transactions of the ASME

journal of heat transfer

Published Quarterly by
The American Society of
Mechanical Engineers
Volume 101 • Number 2
May 1979

EDITORIAL STAFF
Editor, **J. J. JAKLITSCH, JR.**
Production Editor,
STELLA ROBINSON
Editorial Prod. Asst.,
BETH DARCHI

HEAT TRANSFER DIVISION
Chairman, **F. W. SCHMIDT**
Secretary, **C. J. CREMERS**
Senior Technical Editor, **E. M. SPARROW**
Technical Editor, **W. AUNG**
Technical Editor, **B. T. CHAO**
Technical Editor, **D. K. EDWARDS**
Technical Editor, **R. EICHHORN**
Technical Editor, **J. S. LEE**
Technical Editor, **V. E. SCHROCK**
Technical Editor, **R. SIEGEL**

POLICY BOARD, COMMUNICATIONS
Chairman and Vice-President
I. BERMAN

Members-at-Large
J. W. LOCKE
J. E. ORTLOFF
M. J. RABINS
W. J. WARREN

Policy Board Representatives
Basic Engineering, **F. LANDIS**
General Engineering, **D. D. ACKER**
Industry, **M. M. LIVINGSTON**
Power, **R. E. REDER**
Research, **G. P. COOPER**
Codes and Stds., **P. M. BRISTER**
Computer Technology Com.,
A. A. SEIREG
Nom. Com. Rep.,
S. P. ROGACKI

Business Staff
345 E. 47th St.
New York, N. Y. 10017
(212) 644-7789
Mng. Dir., Publ., **C. O. SANDERSON**

OFFICERS OF THE ASME
President, **O. L. LEWIS**
Exec. Dir. & Sec'y, **ROGERS B. FINCH**
Treasurer, **ROBERT A. BENNETT**

EDITED and PUBLISHED quarterly at the offices of The American Society of Mechanical Engineers, United Engineering Center, 345 E. 47th St., New York, N. Y. 10017. ASME TWX No. 710-581-5267. Second-class postage paid at New York, N. Y., and at additional *mailing offices.*

CHANGES OF ADDRESS must be received at Society headquarters seven weeks before they are to be effective. Please send old label and new address.

PRICES: To members, $25.00, annually; to nonmembers, $50.00. Single copies, $15.00 each. Add $1.50 for postage to countries outside the United States and Canada.

STATEMENT *from* By-Laws. *The Society shall not be responsible for statements or opinions advanced in papers or . . . printed in its publications* (B 13, Par. 4).

COPYRIGHT © 1978 by the American Society of Mechanical Engineers. Reprints from this publication may be made on conditions that full credit be given the TRANSACTIONS OF THE ASME, SERIES C—JOURNAL OF HEAT TRANSFER, *and the author and date of publication stated.*

INDEXED by the Engineering Index, Inc.

(continued on page 248)

Downloaded 04 Feb 2011 to 194.85.80.107. Redistribution subject to ASME license or copyright; see http://www.asme.org/terms/Terms_Use.cfm

TECHNICAL NOTES

ERRATA

ANNOUNCEMENTS

M. M. Pimenta
Department of Mechanical Engineering
Universidade de Sao Paulo, Brasil

R. J. Moffat
Department of Mechanical Engineering,
Stanford University,
Stanford, Calif. 94305
Mem. ASME

W. M. Kays
Dean, School of Engineering,
Stanford University,
Stanford, Calif. 94305
Fellow ASME

The Structure of a Boundary Layer on a Rough Wall with Blowing and Heat Transfer

A regular, deterministic, rough surface was tested at four velocities from 11 to 40 m/s, with and without blowing, to evaluate the Stanton number and friction factor characteristics. Hot-wire data were taken to document the turbulence components, the Reynolds stresses, and the turbulent heat flux. Data are presented concerning the streamwise development of the mean and fluctuating components, and the effect of blowing. Correlation coefficients and mixing lengths were deduced from the hot-wire data and are also presented. While the mean velocity data showed only two allowable states for the boundary layer (laminar and "fully rough"), the turbulence structure indicated a third: "transitionally rough". Distributions of $\overline{u'v'}/u_\tau^2$ *and* $\overline{v't'}/u_\tau t_\tau$ *are similar, except for high blowing* ($F = 0.004$)*. The turbulent Prandtl number lies between 0.85 and 1.0 for the entire layer, and a mixing length constant of* $\kappa = 0.41$ *describes the data with good accuracy for all velocities and all values of blowing tested.*

Introduction

There are many situations of engineering importance in which there is heat transfer to or from a permeable, rough wall: ablating rocket nozzles and blast tubes, porous liners for gas turbine combustion chambers, transpiration-cooled turbine blades, nose-tips on re-entry vehicles, and—in the study of flame spread—the behavior of a pyrolyzing wall ahead of an advancing flame front. The heat transfer in each case is determined by the distributions of velocity and temperature and the transport mechanisms within the boundary layer. These are, in turn, affected by both the roughness of the surface and by the injection of fluid through the wall.

Predictions of heat transfer rate can be made at any of several levels, which might be categorized as correlations, integral methods, or differential methods. The categorization depends upon the forms of the input and output information required and produced by the method. Current emphasis is on development of differential predictors, which require phenomenological rate equations describing the transport processes within the boundary layer and produce, as their output, the distributions of velocity and temperature and, sometimes, the distribution of turbulence quantities also. These ancillary outputs are frequently used, during the development of predictor programs, as diagnostics to determine whether or not the program is proceeding satisfactorily. One generally desires to have diagnostics available to at least one level higher than the phenomenon being predicted.

Objective

The experiments reported here are aimed at documenting the details of hydrodynamic and heat transfer behavior in a turbulent boundary layer on a rough wall with blowing. The data are intended to be used to provide inputs to and to test the validity of prediction methods using either "mixing length" or "turbulence kinetic energy" types of closures.

Apparatus and Procedure

Fig. 1 shows the apparatus used in these experiments. Built by Healzer [1], it is a closed-loop, variable-speed tunnel using air at approximately atmospheric conditions both for the main flow and the injected fluid. The test section is 0.5 m wide, 0.1 m high and 2.44 m long. The upper wall can be adjusted to maintan uniform static pressure in the tunnel. The lower surface is the test plate.

Since the measurement of turbulence quantities usually required eight to ten hours, control of the mainstream air temperature was critical. Special precautions were taken to provide a cooling system of large thermal capacity, to reduce temperature drift to less than 0.15°C during an experiment.

The main air circuit contains a heat exchanger, a filter, a screen box (four layers of 40 mesh screen, 3 cm apart), and a smooth approach nozzle with a contraction ratio of 19.8 to 1. A small auxiliary blower maintains the static pressure in the test section equal to the ambient pressure, to prevent leaks.

The test surface consists of 24 plates, each 0.1 m in the flow direc-

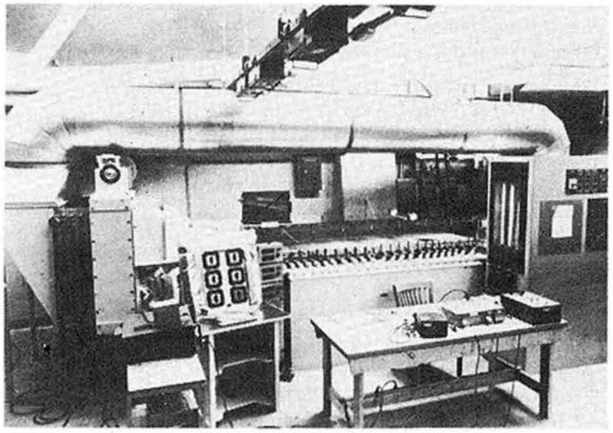

Fig. 1 The roughness apparatus

Contributed by the Heat Transfer Division and presented at the AIAA-ASME Thermophysics and Heat Transfer Conference, Palo Alto, California, May 24–26, 1978.

Revised manuscript received at ASME Headquarters August 28, 1978. Paper No. 78-HT-3.

tion and 0.46 m wide, supported on a rigid aluminum structure. Each plate is 12.7 mm thick and consists of 11 layers of copper balls, each 1.27 mm in diameter, brazed together into a rigid, uniformly permeable wall [1, 2]. Fig. 2 shows a close-up of the surface. The surface is regular and deterministic, which may affect the structure of the turbulence. The crests of the spheres forming the test surface are coplanar and aligned with the smooth surface of the approach nozzle.

Each of the 24 segments is equipped with an electrical heater and is thermally isolated from its neighbors so its heat transfer rate can be calculated by energy balance means. Temperature-controlled transpiration air is metered individually to each plate.

Mean velocities, turbulence quantities, and temperature fluctuations were measured with hot wire anemometers, using both a horizontal wire (U, T, $\overline{u'^2}$, $\overline{t'^2}$, and $\overline{u't'}$) and a rotatable 45 deg slant wire ($\overline{u'v'}$, $\overline{u'w'}$, $\overline{v'w'}$, $\overline{v'^2}$, $\overline{w'^2}$, $\overline{v't'}$). The probes and techniques used are consistent with the recommendations of [3–8]. Calibration of the wires was done in a variable velocity, variable temperature free-jet facility. For a fixed wire resistance, R_w, the results were expressed as

$$\frac{E^2}{R_w - R(T)} = F(U) \tag{1}$$

following Sandborn [9] and Orlando [7]. Results showed no errors as large as 1 percent when using a four-term polynomial for $f(U)$ over the range of temperatures from 60 to 90°F. Fluctuation measurements can be made in non-isothermal flows, but the signal must be regarded as having two components

$$e' = \frac{\partial e}{\partial u} u' + \frac{\partial e}{\partial t} t' \tag{2}$$

as shown by Sandborn [9], Corrsin [10], and Fulachier and Dumas [11]. It was assumed that the dynamic response to fluctuations was the same as the steady state response to mean values; i.e.,

$$\frac{\partial e}{\partial u} = \left.\frac{\partial E}{\partial U}\right|_T \text{ and } \frac{\partial e}{\partial t} = \left.\frac{\partial E}{\partial T}\right|_U \tag{3}$$

The same probe was used for velocity and for temperature measurements, by switching between two separate anemometers: one of constant temperature and one of constant current. This reduced positional ambiguity. Values of t' were corrected for conduction effect following Maye [4]. Values of $\overline{v'^2}$, $\overline{w'^2}$ and $\overline{u'v'}$ were measured with the technique of Fujita and Kovasny [12] also used by Andersen [6] and Orlando [7]. Values of $\overline{v'w'}$ and $\overline{u'w'}$ were found to be less than 1 percent of $\overline{u'v'}$ in every location and, in subsequent data processing, were set to zero for simplicity. The $\overline{v't'}$ correlation was measured using the technique of Arya and Plate [13], also described by Corrsin [10] and Orlando [7]. Values of $\overline{u'v'}$ needed in that interpretation were borrowed from isothermal data for the same flow conditions.

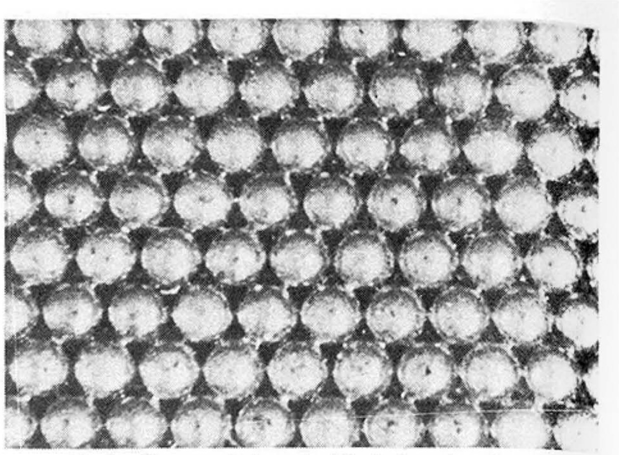

Fig. 2 Close-up photograph of the test rough surface

The test section velocity was shown to be uniform within ±.16 percent with a turbulence intensity of less than 0.4 percent (based upon $\sqrt{\overline{u'^2}}/U_\infty$). Spanwise variation of the momentum thickness was less than ±3 percent across the central one-third of the span, measured at the exit of the test section.

Stanton numbers measured in the present work agreed with previous results by Healzer [1] within ±.0001 units, and his procedures were used throughout. Friction factor values measured here are about 10 percent below Healzers, and were based upon the measured turbulence stresses near the wall, extrapolated to the wall by:

$$\frac{cf}{2} = \frac{-\overline{u'v'}(y)}{U_\infty{}^2} - \frac{U_{(y)}V_0}{U_\infty{}^2} \tag{4}$$

This follows the precedent of Andersen [6]. Healzer based his values on momentum thickness variations, and the present results are felt to be more precise.

Mean velocity profile data were compared with expectations for a dense array of spherical caps of k_s = 0.78 mm (k_s = .62 d), as recommended by Schlichting [14]. The value of Δu^+, the shift in the log

Nomenclature

A = constant used in calibrating hot-wire probes (equation (5))
c = specific heat at constant pressure
$C_f/2$ = friction factor, $g_c\tau_0 = \frac{C_f}{2}\rho_\infty U_\infty{}^2$
$e^{*\prime}$ = fluctuating component of voltage out of the constant current anemometer
e' = fluctuating component of voltage out of the constant temperature anemometer
E = voltage output of hot-wire anemometer
F = blowing fraction, $F = \rho_0 v_0/\rho_\infty U_\infty$
F = constant used in calibrating hot-wire probes (equation (5))
g_c = gravitational constant
G = mass velocity, $G = (\rho U)_\infty$
G = Clauser shape factor (equation (9))
h = heat transfer coefficient
H = Karman shape factor
k_s = equivalent sand-grain roughness size
q^2 = turbulence kinetic energy, $\overline{q^2} = \overline{u'^2} + \overline{v'^2} + \overline{w'^2}$
r = radius of the balls forming the surface
R_w = resistance of the wire, as driven by the anemometer
$R(T)$ = resistance of the wire, at air temperature
St = Stanton number, St = h/Gc
T = mean temperature
T_τ = shear temperature, $T_\tau = (T_0 - T_\infty)\,\mathrm{St}\sqrt{C_f/2}$
t' = fluctuation in temperature
U = mean velocity in the x direction
V = mean velocity in the y direction
u' = fluctuation in streamwise velocity
v' = fluctuation in normal velocity
w' = fluctuation in spanwise velocity
u^+ = dimensionless velocity, $u^+ = u/u_\tau$
u_τ = shear velocity, $u_\tau = \sqrt{g_c\tau_0/\rho} = U_\infty(\sqrt{C_f/2})$
v_0 = velocity of injected fluid, perpendicular to the wall
x = streamwise distance, from the beginning of the rough plate
y = distance perpendicular to the wall
β = pressure gradient parameter (equation (9))
δ = boundary layer thickness
δ_1 = displacement thickness,

$$\delta_1 = \int_0^\infty \left(1 - \frac{U}{U_\infty}\right) dy$$

δ_2 = momentum thickness,

$$\delta_2 = \int_0^\infty \frac{\rho U}{\rho_\infty U_\infty} \times \left(1 - \frac{U}{U_\infty}\right) dy$$

Δ_2 = enthalpy thickness,

$$\Delta_2 = \int_0^\infty \frac{\rho U}{\rho_\infty U_\infty} \times \left(\frac{T - T_\infty}{T_0 - T_\infty}\right) dy$$

θ = rotational position of slant wire, deg
κ = mixing-length constant
ρ = density
τ_0 = wall shear stress
π = pi
$\overline{(\quad)}$ = Time-averaged value of ( )
$(\quad)_0$ = value of ( ) evaluated at the wall
$(\quad)_y$ = value of ( ) evaluated at the elevation y
$(\quad)_\infty$ = value of ( ) evaluated in the free stream
0(3) = terms neglected are of order 3 in the perturbation

region, agreed very well with the predicted form

$$u^+ = \frac{1}{.41}\ln\left(\frac{y}{k_s}\right) + 8.5 \qquad (5)$$

as shown in Fig. 3. The value of y is measured from the crests of the balls (coplanar). The same value was deduced for the equivalent sandgrain roughness, for all locations and all velocities, to within the accuracy with which k_s can be determined based upon friction factor measurements.

The Experimental Data

The data presented here cover several levels of information: Stanton number and friction factor, mean velocity and temperature, turbulence quantities, and turbulence correlation parameters. Streamwise development is recorded by showing two axial locations, velocity dependence by use of three different free stream velocities, and the effects of blowing by two additional sets.

Stanton Number and Friction Factor. Stanton number data are reported for each of the 24 segments of the test section. Friction factor measurements were made, using the slanted hot wire, at six locations spaced 0.3 m apart.

Figs. 4 and 5 show the Stanton number and friction factor in "fully rough" coordinates, St versus Δ_2/r and $C_f/2$ versus δ_2/r. Stanton number data for all three velocities are well represented by a single, compact group, for no blowing. Blowing reduces Stanton number, changing the slope and level of the data trend, as previously shown by Healzer [1]. Friction factor data are less coherent, with the data for 15.85 m/s lying slightly below the data for the higher velocities. Blowing reduces the friction factor, but seems not to alter the slope of the data trend, only the level.

The largest value of Δ_2/r which occurred naturally at 27 m/s was 10. The data for Δ_2/r larger than 10 were obtained by blowing through the first 1.2 m of test plate to thicken it, and allowing the thickened layer to relax into a normal state as it proceeded downstream. This technique was introduced by Healzer, also for the purpose of artificually thickening the layer. The data show that an unblown span of 0.3 m suffices to return the data to the accepted rough-wall correlation.

Mean Velocity. Fig. 6 shows the mean velocity, U/U_∞, versus y/δ_2, the distance above the crests of the balls made dimensionless by the momentum thickness of the boundary layer. Data are shown for four velocities (11, 16, 27, and 40 m/s nominal) and represent seven different axial stations from $x = 0.36$ m to 2.18 m. Three situations exist.

- *A laminar boundary layer.* For 11 m/s, a natural transition occurred between 1.0 and 1.3 m. Upstream of transition the mean velocity profile could be shifted to fall exactly on the classical Blasius profile for a laminar boundary layer by the addition of 0.13 mm to the y value. Monin and Yaglom [15] discussed a systematic way of locating the "virtual wall location" which sharply discriminates for small shifts. Their method, applied to the present turbulent data, requires a y-shift of 0.15 mm for the fully rough situation, regardless of velocity. There is uncertainty in the shift, of the order of ±.01 mm; hence, the hueristic observation of a need for a y-shift of 0.13 mm in the laminar regime is in good agreement with the requirement for 0.15 mm in the fully rough, turbulent state.
- *A fully rough turbulent boundary layer.* For 11 m/s downstream of $x = 1.3$ m and for all higher velocities for all measuring stations, the same profile of mean velocity applies in "outer coordinates", i.e., y/δ_2. The boundary layer seems to have only two states, as far as mean velocity is concerned: classically laminar and fully rough. This is probably related to the uniformity of the roughness elements on the present surface. One might expect distributed particle sizes and shapes to result in a more versatile boundary layer.
- *A fully rough turbulent boundary layer with blowing.* One set of data is shown for $F = 0.004$ at 27 m/s. This is a typical result. For the same velocity, $F = 0.002$ displaces about half as much downward as did $F = 0.004$. The shape of the profile is the same; the wall join point has simply been depressed.

The present data for no blowing are in excellent agreement with

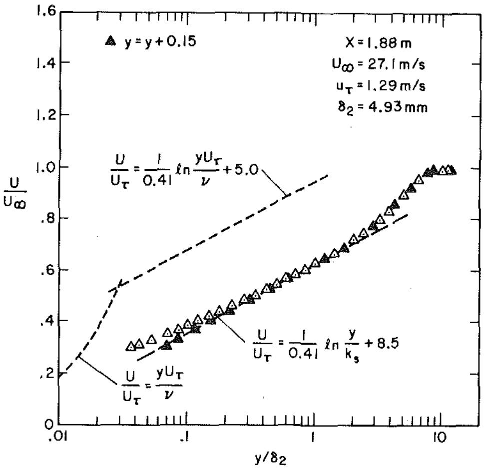

Fig. 3 Fully rough velocity profile—shifted and non-shifted y-coordinates. No blowing

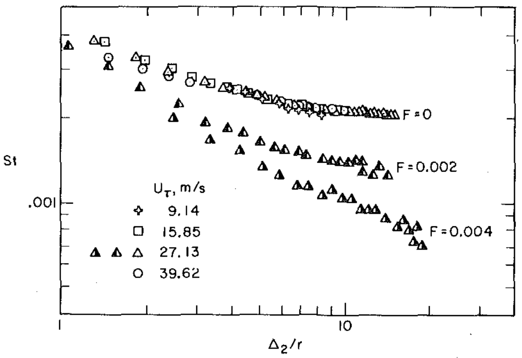

Fig. 4 Stanton number versus boundary layer enthalpy thickness, Δ_2/r

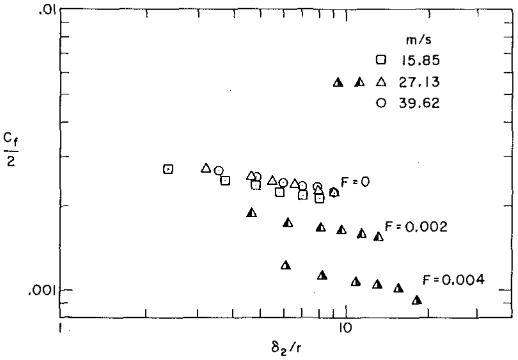

Fig. 5 Friction factor versus boundary layer momentum thickness: δ_2/r

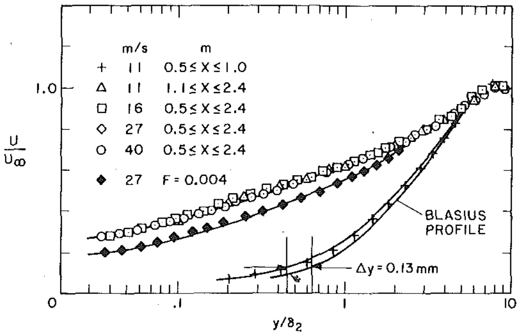

Fig. 6 $\bar{U}/U_\infty$ versus y/δ_2 for velocities between 11 and 40 m/s, including the laminar approach profiles

the wake function of Coles [16], as have been the results of othere (i.e., Hama [17], Moore [18], and Perry, et al. [19]), with

$$\frac{U_\infty - U}{u_\tau} = \frac{1}{.41} \ln \frac{y}{\delta} + \frac{\pi}{.41} \left\{ 2 - W\left(\frac{y}{\delta}\right) \right\} \tag{6}$$

using the Coles values of $W(y/\delta)$. The unblown data also follow Clauser's equilibrium-defect profiles. For the present case, since the flow is not accelerating, $\beta = 0$ and the Clauser shape factor, G, should be about 6.7.

$$G = \frac{\sqrt{C_f/2}}{\delta_1} \int_0^\infty \left(\frac{U_\infty - u}{u_\tau} \right)^2 dy \tag{7}$$

The Clauser shape factor, G, and the Karman shape factor, $H = \delta_1/\delta_2$, are related through

$$H = \frac{1}{1 - G\sqrt{C_f/2}} \tag{8}$$

All of the velocity profiles from the present study satisfy this relationship within the uncertainty of $C_f/2$.

Values of H ranged from 1.53 to 1.45 over the length of the test plate, for all unblown profiles measured except those in the purely laminar condition shown in Fig. 6.

Healzer [1] reported signs of a laminar sublayer inboard of $y/\delta_2 = 0.024$ at a velocity of 9.75 m/s. The profile location was $x = 1.5$ m, which was only 0.2 m downstream of the transition. No trace is visible at 15.85 m/s at $y/\delta_2 = .035$, the closest point reached in the present study, for any x.

Mean Temperature. Fig. 7 shows the mean temperature plotted against the mean velocity. In these coordinates, the same linear relationship exists for all velocities and for all values of blowing. Extrapolation of the line to the location of $U/U_\infty = 0$ (the virtual wall location) shows a value of $T_w - T/T_w - T_\infty$ of about 0.10 for all conditions. This indicates existence of a region near the wall (inside the location where $U/U_\infty \approx .15$) where heat transfer is limited compared to momentum transfer, requiring a sharper temperature gradient. It is believed that this "temperature jump" represents a region where all heat transfer must be by conduction, while the pressure-velocity correlation can transfer momentum. The fact that the correlation between T and U is straight suggests that the turbulent Prandtl number is sensibly constant. This is an observation which is borne out in Fig. 14.

One reason for sequentially measuring T and U with the same wire in the same location was to decrease the uncertainty in the value of $\partial T/\partial U$ which is needed for evaluation of the turbulent Prandtl number.

Turbulence Measurements. Klebanoff's values for the distribution of turbulence components in a boundary layer on a smooth wall [20] are used to provide reference lines in the present work. They are shown as dashed lines in Figs. 8 and 9. The free stream turbulence in the present tunnel was about 0.4 percent, compared to 0.03 percent for Klebanoff's work. This effect is not large compared to the points of interest to be noted in the present data.

Fig. 8 shows the u', v', and w' components of turbulence normalized against the friction velocity, u_τ. Two axial measuring stations were used, $x = 0.97$ m and $x = 1.88$ m, to show the streamwise development. Free stream velocity was 15.85 m/s. With respect to Klebanoff's lines, the present data show high values in the middle and outer regions, and higher overall levels. The "upturn" in $\sqrt{u'^2}/u_\tau$, which is characteristic of the smooth wall, is noted in the rough wall data as well, for this velocity.

Fig. 9 shows the same type of data for 39.62 m/s. The u' data for each velocity shows a pronounced drop near the wall, in the location where the smooth wall data and the rough wall data for 15.85 m/s show the sharp rise. In all other respects, the data for 39.62 m/s are similar to those of 15.85 m/s. Outboard of $y/\delta = 0.1$, the data are nearly congruent for all three velocities tested. The "downturn" was also present at 27.13 m/s.

The salient characteristics are:

- The values of $\sqrt{u'^2}/u_\tau$ drop sharply near the wall (inside $y/\delta = 0.1$) for data taken at 27.13 and 39.62 m/s. This may be a distinguishing characteristic of fully rough flows.
- The values of $\sqrt{u'^2}/u_\tau$ rise sharply near the wall (inside of $y/\delta = 0.1$) for data taken at 15.85 m/s. This may be a characteristic of a transitionally rough boundary layer, since it resembles the smooth plate behavior reported by Klebanoff.
- The levels of turbulence are higher, everywhere in the layer, for a rough wall flow than for a smooth wall flow, even when normalized on the shear velocity.

These data seem to contradict Hinze's remarks [21] on the data of Corrsin, et al. [22], which showed u_τ to be a normalizing parameter that would make the smooth and rough data outboard of $y/\delta = 0.2$ look the same.

Fig. 10 shows the effect on the turbulence components of blowing through the surfaces with $F = 0.004$. The free stream velocity of 27.63

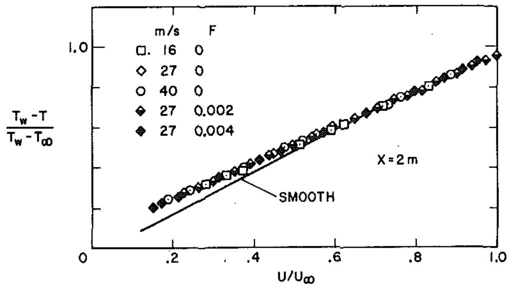

Fig. 7 Mean temperature versus mean velocity

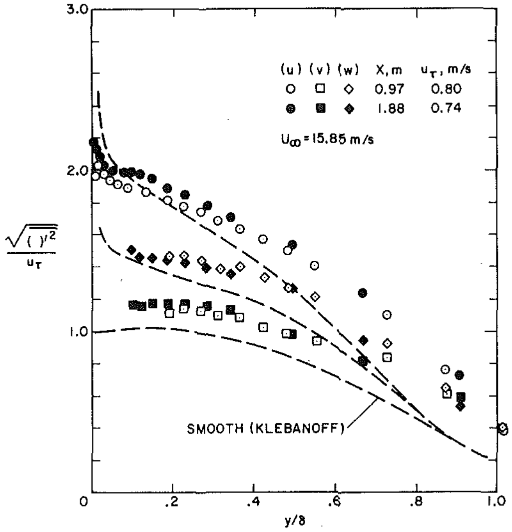

Fig. 8 Turbulence components. Streamwise development at 15.85 m/s. Transitionally rough

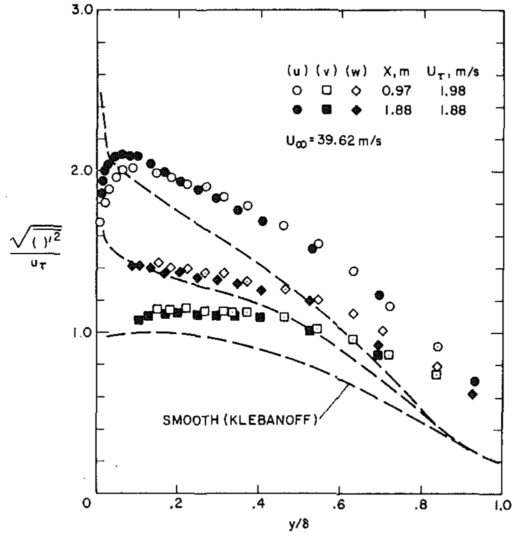

Fig. 9 Turbulence components. Streamwise development at 39.62 m/s. Fully rough

m/s seems to produce typical fully rough behavior of the turbulence components. The data are normalized by U_∞ not by u_τ, which would emphasize the differences. All three components display a drop near the wall, but the shapes of their profiles are different. With blowing, the u' profile peaks at about $y/\delta = 0.1$, while v' and w' peak between $y/\delta = 0.25$ and $y/\delta = 0.3$.

Fig. 11 shows values of $\sqrt{t'^2}/T_\tau$, without blowing, for three velocities and two x-locations to display the streamwise development and the onset of the fully rough state. Reference data from Orlando [7] and Fulachier and Dumas [11] are shown to establish the expectation values for smooth wall behavior. The data of Orlando were recalculated to take out a numerical error in the conduction loss term, as described by Pimenta [23]. Fulachier's data did not reach into the high "bulge" inside $y/\delta = 0.1$. This is the counterpart of the rise in u' near the smooth wall. At 15.8 m/s on the rough wall, the bulge is still visible, though greatly reduced, while at 27.13 m/s only a trace remains.

Fig. 12 shows the effect on temperature fluctuation of blowing through the rough wall. The data are normalized on the overall temperature difference rather than on T_τ. Use of T_τ would expand the differences shown.

Fig. 13 shows the dimensionless values of turbulent shear stress, $-\overline{u'v'}/u_\tau{}^2$, and turbulent heat flux, $\overline{v't'}/u_\tau T_\tau$, versus y/δ. Data are shown for three different velocities, two different x-locations, and three values of blowing. Both the shear stress and heat flux had attained invariant profiles within the first 1 m of run for all three velocities tested. There is little to be seen as far as streamwise development is concerned. The data for $\overline{v't'}/u_\tau T_\tau$ might be judged to lie 3–4 percent below $-\overline{u'v'}/u_\tau{}^2$ in the inner region (inboard of $y/\delta = 0.3$) and 3–4 percent above in the outer region (outboard of $y/\delta = 0.7$), but considering the uncertainty in measurement, not much reliance should be placed in such small differences. Blowing seems to separate the profiles of shear stress and heat flux. At $F = 0.002$ the heat flux data lie slightly above the shear stress data, outboard of $y/\delta = 0.5$. At $F = 0.004$ the two profiles are widely different, with the heat flux 25–30 percent above the shear stress everywhere.

Fig. 14 shows correlations calculated from the turbulence measurements, with and without blowing.

- *Turbulent Prandtl number.* The same distribution applies for all velocities tested, and both without blowing and with blowing, up to $F = 0.004$. The turbulent Prandtl number is between 0.95 and 1.0 near the wall, and drops linearly to 0.8 on the outer edge. No values of Pr_t greater than 1.0 were measured. The data points nearest the wall were at $y/\delta = 0.05$.

Turbulent Prandtl number was calculated from directly measured values by the following form:

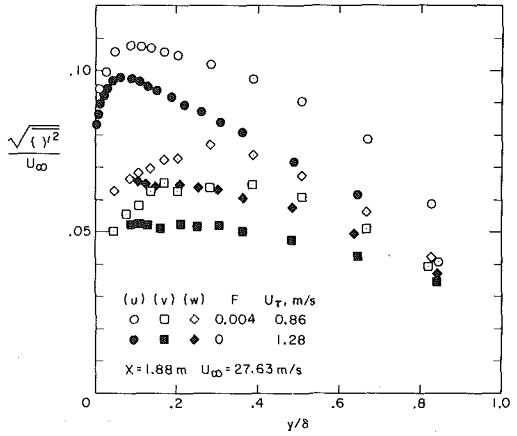

Fig. 10 Turbulence components. Effect of blowing, fully rough

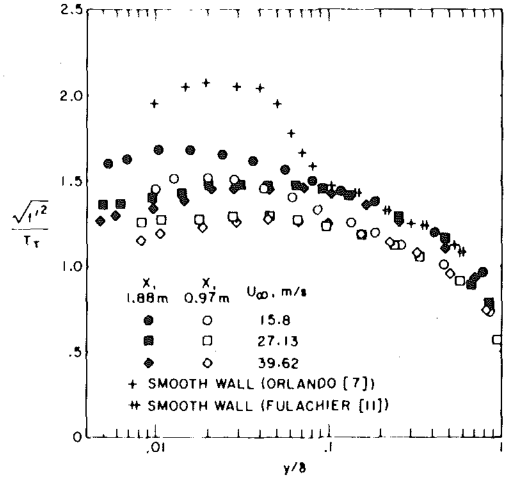

Fig. 11 Temperature fluctuations. Streamwise development at different velocities. $F = 0.000$

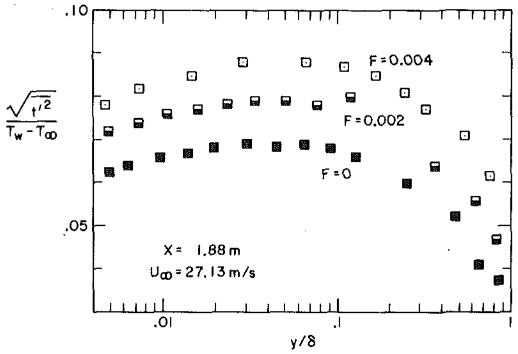

Fig. 12 Temperature fluctuations. Effect of blowing

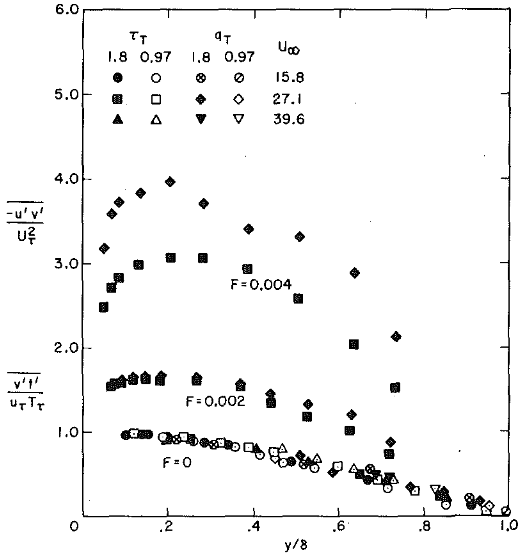

Fig. 13 Reynolds stress and turbulent heat transfer. Streamwise development and effects of blowing

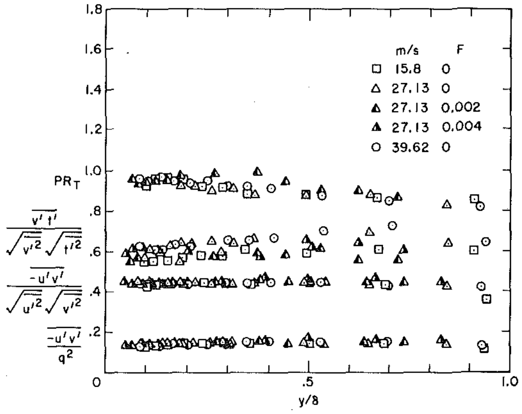

Fig. 14 Turbulent Prandtl number, velocity correlation coefficient, normalized shear stress, and temperature velocity correlation

$$\mathrm{Pr}_t = \frac{-\overline{u'v'}}{\overline{v't'}} \frac{\partial T}{\partial U} \quad (9)$$

Since T and U were measured sequentially, by the same probe at the same location, there is much less uncertainty in the value of $\partial T/\partial U$ than by previous techniques used to get this derivative. Overall, the uncertainty in Pr_t is felt to be ±18 percent, at worst.

- $\overline{u'v'}/\sqrt{\overline{u'^2}}\sqrt{\overline{v'^2}}$, the correlation coefficient between longitudinal and normal velocities. The same distribution applies for all velocities both without and with blowing up to $F = 0.004$. A value of 0.45 accurately represents all of the present data from the rough wall, just as it represents the smooth wall data.
- $-\overline{u'v'}/q^2$, the Reynolds stress normalized on turbulence kinetic energy. A value of 0.14 is maintained over most of the layer. This is the same value used in smooth wall work, and yet it describes the present data for all velocities tested, both with and without blowing.
- $\overline{v't'}/\sqrt{\overline{v'^2}}\sqrt{\overline{t'^2}}$, the correlation coefficient between normal velocity and temperature. The value is between 0.55 and 0.60 at the wall, rising to between 0.60 and 0.70 near the outer edge.
- Note: The correlation coefficient $-\overline{u't'}/\sqrt{\overline{u'^2}}\sqrt{\overline{t'^2}}$ was measured and found to lie between 0.6 and 0.8 for all cases. There was no *tendency for the correlation to be higher near the wall, as reported* by Johnson [24].

The Prandtl mixing length was deduced from mean velocity and shear stress data. From the nearest data point to the wall (0.18 mm) out to $(y + \Delta y)/\delta = 0.15$, the mixing length agreed with $l = 0.41\ (y + \Delta y)$ within experimental error for all velocities, with and without blowing. The value of Δy was 0.15 mm, following the technique of Monin and Yaglom, and was the same for all velocities and all values of blowing ($F = 0$, 0.002, and 0.004).

Discussion and Conclusions

The term fully rough may have to be applied piecemeal to the various descriptors of a turbulent boundary layer. In the present results: the Stanton number data and the mean velocity profile for 16 m/s and even for 11 m/s are typical of fully rough behavior, yet the distribution for $\sqrt{\overline{u'^2}}/u_\tau$ for 16 m/s is distinctly different from the fully rough distribution.

As far as mean velocity profiles are concerned, the results show only two allowable states (fully rough and laminar) for the boundary layer on the surface used here. The uniformity of size and arrangement of the balls making up the surface may have essentially eliminated the transitionally rough domain.

The profiles of mean temperature and mean velocity show that there is a layer very near the wall which could be modeled as a temperature step, responsible for about 10 percent of the temperature drop across the boundary layer, regardless of velocity or blowing fraction.

The fully rough state for the turbulence kinetic energy was found to have a sharp drop in $\sqrt{\overline{u'^2}}/u_\tau$ in the very near-wall region, where smooth-wall data show a sharp rise. In addition to the drop near the wall, the turbulence tended to remain high farther out into the layer, even when made dimensionless on u_τ. The shapes of the distributions for fully rough and smooth are distinctly different, even considering the outer region alone.

Evidence of a transitionally rough state for the turbulence kinetic energy was found in the form of a sharp rise in $\sqrt{\overline{u'^2}}/u_\tau$ inside of $y/\delta = 0.1$ for a relatively low tunnel velocity (15.8 m/s). For all runs shown, the correlation coefficient $-\overline{u'v'}/\sqrt{\overline{u'^2}}\sqrt{\overline{v'^2}}$ has a value of 0.45 in a fully rough boundary layer, even with blowing, and a normalized stress $-\overline{u'v'}/q^2$ of 0.14. These are the same values used in smooth-wall work.

The Prandtl mixing length displays a broad inner region of constant $\kappa = 0.41$, just as does a smooth layer, even with blowing.

Acknowledgments

The authors wish to thank the Office of Naval Research for the support of this work through contract N-00014-67-A-0112-0072. We are grateful to Mr. James Patton for his continued interest, and to Dr. William Thielbahr, of China Lake Naval Weapons Center, for initiating this study.

The first author also wishes to express his gratitude to the agencies which supported his stay at Stanford: Fundacao de Ampara a Pesquisa do Estado de Sao Paulo (FAPESP), Meneracao Matheus Leme Ltda., Escola Politecnica da Universidade de Sao Paulo.

Access to the Data

Tabular data in support of each figure in the present paper, plus detailed supporting arguments regarding calibration and technique, are contained in Report HMT-21, by the present authors. Copies are available through the Thermosciences Division, Department of Mechanical Engineering, Stanford University, Stanford, Calif. 94305.

Dr. Pimenta's thesis is available through University Microfilms, Ann Arbor, Michigan.

References

1 Healzer, J. M., R. J. Moffat, and W. M. Kays, "The Turbulent Boundary Layer on a Rough, Porous Plate: Experimental Heat Transfer wih Uniform Blowing," Report HMT-18, Thermosciences Division, Dept. of Mech. Engrg., Stanford University, 1974.

2 Pimenta, M., and R. J. Moffat, "Stability of Flow through Porous Plates: Coalescent Jets Effects," *AIAA Journal*, Vol. 12, No. 10, Tech. Note, 1974, pp. *1438–1440.*

3 Rasmussen, C. G., and M. Dahm, "Effect of Wire Mounting System on Hot-Wire Probe Characteristics," DISA Information No. 7, pp. 19–24, Jan. 1970.

4 Maye, F. P., "Error Due to Thermal Conduction between the Sensing Wire and Its Supports when Measuring Temperature with a Hot-Wire Anemometer Used as a Resistance Thermometer," DISA Information No. 8, Feb. 1970, pp. 22–26.

5 Thinh, N. V., "On Some Measurements Made by Means of a Hot-Wire in a Turbulent Flow near a Wall," DISA Information No. 7, Jan. 1970, pp. 13–18.

6 Andersen, P. S., W. M. Kays, and R. J. Moffat, "The Turbulent Boundary Layer on a Porous Plate: An Experimental Study of the Fluid Mechanics for Adverse Free-Stream Pressure Gradients," Report HMT-15, Thermosciences Div., Dept. of Mech. Engrg., Stanford University, 1972.

7 Orlando, A. F., R. J. Moffat, and W. M. Kays, "Turbulent Transport of Heat and Momentum in a Boundary Layer Subject to Deceleration, Suction, and Variable Wall Temperature," Report HMT-17, Thermosciences Div., Dept. of Mech. Engrg. Stanford University, 1974.

8 Jorgensen, F. E., "Directional Sensitivity of Wire and Hot-film Probes," DISA Information No. 11, 1971.

9 Sandborn, V. A., *Resistance Temperature Transducers,* Fort Collins, Colo., Metrology Press, 1972.

10 Corrsin, S., "Extended Applications of the Hot-Wire Anemometer," NACA Tech. Note No. 1864, April 1949.

11 Fulachier, L., and R. Dumas, "Repartitions Spectrales des Fluctuations Thermoques dans une Couche Limite Turbulent," AGARD Conference Proceedings No. 93 on Turbulent Shear Flows, Paper 4, 1972.

12 Fujita, H., and L. S. G. Kovasznay, "Measurements of Reynolds Stress by a Single Rotated Hot-Wire Anemometer," *The Review of Scientific Instruments,* Vol. 39, No. 9, Sept. 1968.

13 Arya, S. P. S., and E. J. Plate, "Hot-Wire Measurements in Non-isothermal Flow," *Instruments & Control Systems,* March 1969, p. 87.

14 Schlichting, H., *Boundary Layer Theory,* 6th ed., McGraw-Hill, New York, 1968.

15 Monin, A. S., and A. M. Yaglom, *Statistical Fluid Mechanics,* Vol. 1, The MIT Press, 1971.

16 Coles, D., "The Law of the Wake in the Turbulent Boundary Layer," *Jour. Fluid Mech.,* Vol. 1, p. 191, 1956.

17 Hama, F. R., "Boundary Layer Characteristics for Smooth and Rough Surfaces," *Trans. Soc. NAME,* Vol. 62, 1954, pp. 333–354.

18 Moore, W. L., "An Experimental Investigation of Boundary Layer Development Along a Rough Surface," Ph.D. Dissertation, State Univ. of Iowa, Aug. 1951.

19 Perry, A. W., and P. H. Joubert, "Rough Wall Boundary Layers in Adverse Pressure Gradients," *Jour. Fluid Mechanics,* Vol. 37, 1963, pp. 193–211.

20 Klebanoff, P. S., "Characteristics of Turbulence in a Boundary Layer with Zero Pressure Gradient," NACA Report 1247, 1955.

21 Hinze, J. O., *Turbulence—An Introduction to the Mechanism and Theory,* McGraw-Hill, 1959.

22 Corrsin, S., and A. L. Kistler, "The Free Stream Boundaries of Turbulent Flows," NACA Tech. Note 3133, Jan. 1954.

23 Pimenta, M. M., R. J. Moffat, and W. M. Kays, "The Turbulent Boundary Layer: An Experimental Study of the Transport Momentum and Heat with the Effect of Roughness," Report HMT-21, Thermosciences Div., Dept. of Mech. Engrg., Stanford University, 1975.

24 Johnson, D. S., "Velocity and Temperature Fluctuation Measurements in a Turbulent Boundary Layer Downstream of a Stepwise Discontinuity in Wall Temperature," *Jour. of Appl. Mech., ASME, p. 325, 1959.*

E. M. Sparrow
Fellow ASME

J. W. Ramsey
E. A. Mass
Department of Mechanical Engineering,
University of Minnesota,
Minneapolis, Minn. 55455

Effect of Finite Width on Heat Transfer and Fluid Flow about an Inclined Rectangular Plate

Wind tunnel experiments were performed to study the heat transfer and fluid flow characteristics for finite-width rectangular plates inclined at various angles of attack to an oncoming airflow. Plates having ratios of spanwise width to streamwise length of 0.4 and 2.5 were employed, and the angle of attack was varied from 90 deg (normal incidence) to 25 deg. The Reynolds number range extended from about 20,000 to 90,000. The naphthalene sublimation technique was used in the transfer coefficient determinations, and the fluid flow patterns adjacent to the plate were made visible by the oil/lampblack technique. The flow field was found to be highly complex and three dimensional, with stronger three-dimensional effects in evidence for the narrow plate. A stagnation zone, centered in the plate cross section at normal incidence, moved forward and ultimately disappeared as the plate was inclined at smaller angles of attack. The dimensionless heat (mass) transfer coefficient, expressed in terms of the Colburn j-factor, varied as the square root of the Reynolds number for all angles of attack, both for the narrow and the wider plates. For the wider plate, the transfer coefficients are completely independent of the angle of attack in the range investigated, while for the narrow plate there is an overall variation of twenty percent. An algebraically simple correlation of all the results, accurate to ±10 percent, is given to facilitate their use in applications such as the wind-related heat loss from flat plate solar collectors.

Introduction

There is an extensive literature dealing with boundary layer flow and heat transfer for a flat plate oriented at an angle of attack to an oncoming stream. This literature includes, for example, the well-known wedge-flow solutions and their many variants. Almost without exception, these studies have been analytical in nature and were concerned with plates that are of infinite extent in the spanwise direction, so that the flow is two-dimensional. On the other hand, the few available heat transfer experiments [1, 2] for inclined flat plates were performed with surfaces of finite span, although in [1] baffles were affixed to the lateral edges with the view of avoiding three-dimensional effects. The experiments of [2] were carried out with square plates and were, therefore, involved with three-dimensional flows. Heat transfer coefficients measured in those experiments were found to be insensitive to the angle of attack over a wide range of angles.

The present experiments were undertaken to investigate in greater depth the effect of finite span on the heat transfer and fluid flow characteristics for a flat plate inclined at an angle of attack to an air stream. To this end, rectangular plates having two different ratios of span to streamwise length were employed. One of these, to be designated as the narrow plate, had a span/length ratio of 0.4, whereas the second had a span/length ratio of 2.5 and will be called the moderately wide plate (or, for brevity, the wider plate).

These plates and their angular orientations are illustrated in Fig. 1. The pair of diagrams in the upper part of the figure show the wider plate. At the left, the plate is orientated normal to the oncoming flow which streams from right to left along the XO axis. By a rotation about the OY axis, as portrayed at the right, the plate is inclined relative to the flow direction. The inclination is specified via the angle of attack α, where α = 90 deg corresponds to normal incidence. The narrow plate is shown in the lower pair of diagrams, respectively in the normal

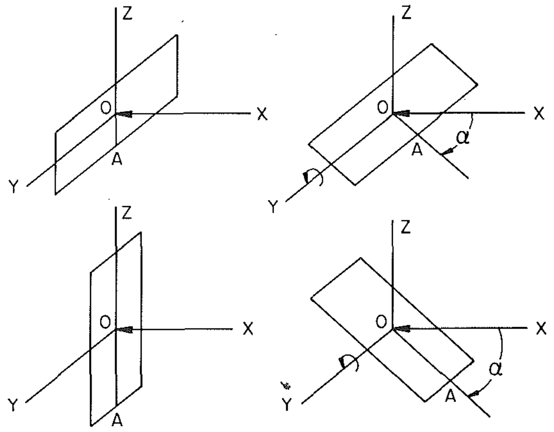

Fig. 1 Schematic views of the wider and narrow plates, upper and lower diagrams, respectively. The airflow is in the direction of XO

Contributed by the Heat Transfer Division for publication in the JOURNAL OF HEAT TRANSFER. Manuscript received by the Heat Transfer Division August 17, 1978.

and inclined orientations. Again, the inclination is specified via the angle of attack α.

If the oncoming stream is uniform and extends over a cross section that is much larger than that of the plate, then at normal incidence (α = 90 deg) both plates have identical flow and heat transfer characteristics. As the plates are respectively inclined and α decreases, the difference in their spans begins to assert itself. Thus, for example, the flow field for the narrow plate should be more three dimensional than that for the wider plate, and this should give rise to differences in the heat transfer characteristics.

The research encompasses both heat transfer experiments and flow visualization. The former were actually performed with mass transfer rather than with heat transfer, and the mass transfer coefficients were converted to heat transfer coefficients via the well-established analogy between the two processes. Specifically, the mass transfer experiments involved the sublimation of naphthalene. The advantages of the naphthalene technique, relative to direct heat transfer experiments, lie in the absence of extraneous losses via structure and supports, easier attainment of boundary condition uniformity, and generally higher accuracy. The heat transfer boundary condition analogous to that of the mass transfer experiments is uniform wall temperature.

To determine the patterns of fluid flow adjacent to the plate surface, the oil/lampblack flow visualization technique was employed. The flow-pattern traces tattooed on the surface by the shear stresses exerted by the air stream were photographed and are presented here. These photographs show both streak lines which are indicative of the flow direction and homogeneous black regions which correspond to stagnation zones. Especially noteworthy among the photographic results is the progression of positions and shapes of the stagnation zone as the orientation of the plate is varied from normal to various inclinations.

The experiments were performed for angles of attack between 90 and 25 deg for both the narrow and wider plates. At each angle of attack, the Reynolds number was varied between 20,000 and 90,000.

The presentation of the heat (mass) transfer results will be concerned with the sensitivity of the transfer coefficients both to the angle of attack and to the ratio of the span to the streamwise length. The correlation of the results for different span/length ratios involves the selection of an appropriate characteristic dimension, and two candidate characteristic dimensions will be examined. In connection with this correlation effort, comparisons will be made between the present rectangular-plate results and those for square plates [2].

Before proceeding with the description of the experiments and the results, brief mention will be made of one of the motivating applications, namely, the wind-related heat losses from the cover plate of a solar collector. In [2], it was shown that the heat transfer coefficients that have been conventionally employed for the calculation of these heat losses are both inappropriate to the application and numerically in error. The coefficients that were measured and correlated in [2] possess the requisite accuracy but are based on square plate experiments. Since present day collectors tend to be rectangular rather than square, it is relevant to generalize the correlation of [2] to rectangular plates and to test the effectiveness of the generalization—as will be done later.

The Experiments

Apparatus and Experimental Procedure. The experiments were performed in a low-turbulence, subsonic wind tunnel (turbulence level ~0.2 percent) having a test section with a 61 × 30.5 cm (2 × 1 ft) rectangular cross section. Operation of the tunnel was in the open-circuit mode with naphthalene-free air drawn into the test section from the laboratory room and naphthalene-laden air discharged outside the building. The velocity range available in the test section ranged from about 4.5 to 24 m/s (15 to 80 ft/s).

The naphthalene plates employed in the experiments were made by a casting process utilizing a two-part mold fabricated from stainless steel. Molten naphthalene was poured into a mold cavity bounded by a highly polished flat plate and a hollowed-out plate. The unmolding process was performed in such a way that the naphthalene surface that had been formed adjacent to the polished plate was exposed while the remainder of the casting remained housed in the hollowed-out plate. Thus, after unmolding, the hollowed-out plate served as a cassette for the naphthalene test plate. The cassette was subsequently mounted in the test section of the wind tunnel and oriented so that the exposed naphthalene surface faced the airflow.

To ensure that the oncoming flow would not be diverted by edge bluntness, all four edges of the cassette were beveled. The bevel angle (i.e., the included angle between the naphthalene face and each beveled edge) was 20 deg. The back side of the cassette was equipped with a fixture which mated with a sting that was suspended from the ceiling of the wind tunnel. The fixture enabled the adjustment of the inclination of the plate relative to the flow direction, thereby facilitating the setting of the angle of attack α (Fig. 1).

When viewed head-on, the naphthalene test surface may be seen to be framed by a thin border which is part of the cassette. The naphthalene plate and its framing border constituted a 5.08 × 12.7 cm (2 × 5 in.) rectangle, which corresponds to an aspect ratio of 1:2.5. The width of the border was about 0.19 cm (0.075 in.).

The cassette and mold employed here bear a filial relationship to those used in [2]. Consequently, the photographs shown in Figs. 2–4 of [2] provide potential assistance in visualizing the present test apparatus.

The temperature of the naphthalene test plate was sensed by a pair of copper-constantan thermocouples positioned just beneath the exposed surface. These thermocouples, which entered the cassette via its rear surface, were cast in place. The thermocouples had been carefully calibrated and, during a data run, their outputs agreed to within a few hundredths of a degree. A similar thermocouple, positioned just downstream and above the plate, measured the air stream temperature. The thermocouple emfs were measured at two-minute intervals during a data run and recorded by a digital millivoltmeter. The velocity in the test section of the wind tunnel was measured by a retractable L-shaped impact tube in conjunction with a wall static tap.

The rate of naphthalene sublimation from the test surface was determined by weighings of the test element (i.e., the naphthalene plate and its cassette). The weighings were accomplished with a Mettler analytical balance having a capacity of 200 g and a smallest scale reading of 0.1 mg.

For each data run, a new naphthalene plate was cast using fresh (i.e., previously unused) reagent grade naphthalene. Subsequent to casting, a sequence of steps similar to those described in [2] was followed to ensure that the naphthalene plate attained a uniform, steady temperature during the data run. This concern about temperature is engendered by the fact that the vapor pressure of naphthalene, the driving force for mass transfer, is quite sensitive to temperature (about 10 percent change per 1°C). Care was also taken as in [2] to minimize and correct for any uncertainties in mass transfer during the setup and disassembly of the experiment.

A typical data run for determining mass transfer coefficients encompassed the aforementioned steps plus several others. These included the weighing of the test element immediately before the run,

Nomenclature

A = surface area of plate

C = circumference of plate

j = j-factor, equations (2) and (3)

K = mass transfer coefficient, $\dot{m}/(\rho_{nw} - \rho_{n\infty})$

L^* = characteristic dimension

$\dot{m}$ = surface-average mass transfer rate

Pr = Prandtl number

Re_D = Reynolds number based on $L^* = \sqrt{(4/\pi)A}$

Re_L = Reynolds number based on $L^* = 4A/C$

Sc = Schmidt number

U_∞ = free stream velocity

α = angle of attack, Fig. 1

ν = kinematic viscosity

ρ_{nw} = naphthalene vapor concentration at plate surface

$\rho_{n\infty}$ = naphthalene vapor concentration in free stream its installation in the wind tunnel and exposure to the air stream for a preselected period of time, removal of the element at the end of the run followed by immediate weighing. Typical wind tunnel exposure times ranged from 25 to 50 min, depending on the Reynolds number, with naphthalene mass transfers in the range of 140 mg.

Flow Visualization. The patterns of fluid flow adjacent to the surface of the test plate were made visible by employing the oil/lampblack technique. According to this technique, the test surface is coated with a thin film of a lampblack and oil mixture and then exposed to the airflow. Under the action of the shear stresses exerted by the air on the surface, the mixture is caused to flow along the surface in the flow direction. The result is a pattern of streaks which reveal the path of the air as it passes over the surface. In a stagnation region, the oil and lampblack mixture remains as it was initially applied, so that a black region without streaks is indicative of stagnation conditions.

The consistency of the mixture must be such that it flows readily under the action of the surface shear stresses, yet it must not be so fluid that it is all blown off the surface. For the present experiments, it was found that a twelve to one mixture (weight proportion of oil to lampblack) gave satisfactory results; the oil was a red manometer fluid. To enable a succession of consecutive runs to be made without having to renew the surface, the exposed face of the plate was covered with a sheet of white plastic-coated contact paper.

With the proper mixture consistency, the flow pattern traces, once established, remained stable. This enabled the plate to be removed from the wind tunnel and photographed head-on, with side lighting by flood lights employed to attain greater sharpness. The photographs were taken with Tri-X film.

Data Reduction. The determination of the average mass transfer coefficients from the measured data follows a pattern similar to that of [2], so that only an overview need be given here. The mass measurements before and after a data run, used in conjunction with the timed duration of the run and the surface area of the naphthalene plate, yield the surface-averaged mass transfer rate $\dot{m}$. By ratioing $\dot{m}$ with the difference in the naphthalene vapor concentrations at the surface and in the free stream, the mass transfer coefficient K is obtained

$$K = \frac{\dot{m}}{\rho_{nw} - \rho_{n\infty}} \tag{1}$$

In the present experiments, there was no naphthalene vapor in the free stream so that $\rho_{n\infty}$ is zero. The wall concentration ρ_{nw} is obtained by first evaluating the naphthalene vapor pressure from the Sogin equation [3] and then using the perfect gas law (molecular weight of naphthalene = 128.17).

For the dimensionless form of the mass transfer coefficient, the Colburn j-factor was selected because it facilitates the application of the analogy between heat and mass transfer. The j-factor for mass transfer is

$$j = (K/U_\infty)\mathrm{Sc}^{2/3} \tag{2}$$

where U_∞ is the free stream velocity and Sc is the Schmidt number (~2.57 for the present experiments). For heat transfer, the j-factor is

$$j = \mathrm{St}\mathrm{Pr}^{2/3}, \ \mathrm{St} = h/\rho c_p U_\infty \tag{3}$$

According to the analogy, the j-factors for heat and mass transfer are equal.

The j-factor results will be parameterized by the Reynolds number

$$\mathrm{Re} = U_\infty L^*/\nu$$

where L^* is a characteristic dimension that will be specified in the course of the presentation of results.

Results and Discussion

In the presentation of the results, attention will first be given to visualization photographs and their interpretation, after which the heat (mass) transfer results will be presented and discussed. This ordering was chosen because the insights gained from a knowledge of the fluid flow patterns are helpful in understanding the trends in the heat transfer results.

Fluid Flow Patterns. Photographs of the traces of the fluid flow adjacent to the plate surface are presented in Figs. 2 and 3 for the wider and the narrow plates, respectively. These traces were made visible by the oil/lampblack technique, the application of which was described earlier in the paper. All of the flow visualization runs were made for a common value of the Reynolds number equal to about 50,000 (the characteristic length L^* appearing in Re will be discussed later). Fig. 2 contains a succession of four photographs arranged one above the other. These photographs are ordered, from bottom to top,

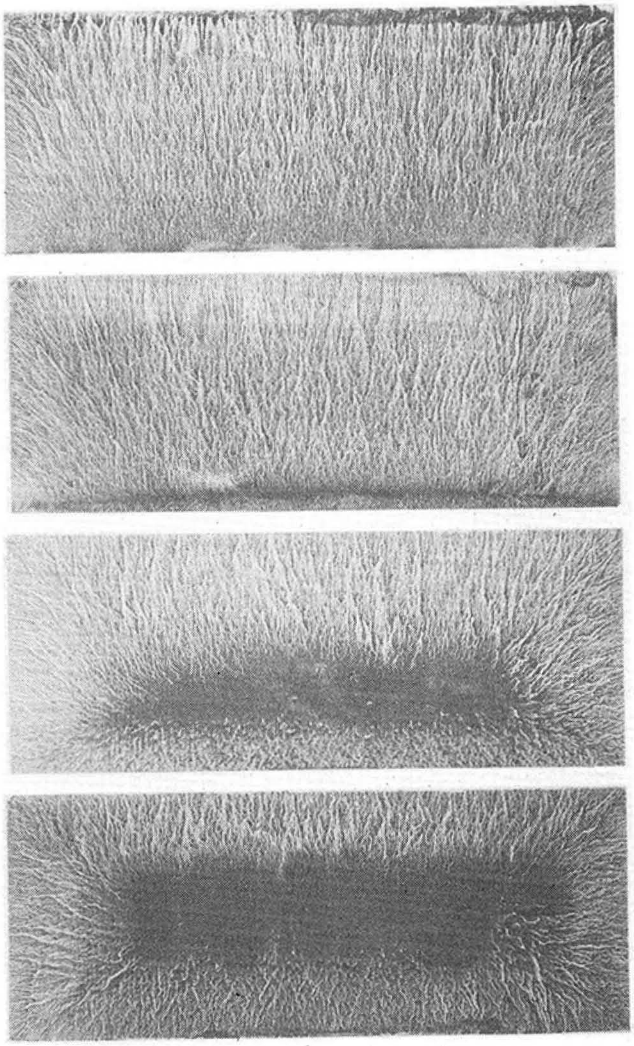

Fig. 2 Fluid flow patterns for the wider plate. From bottom to top, α = 90, 65, 45, and 25 deg; $\mathrm{Re}_L \sim 50{,}000$

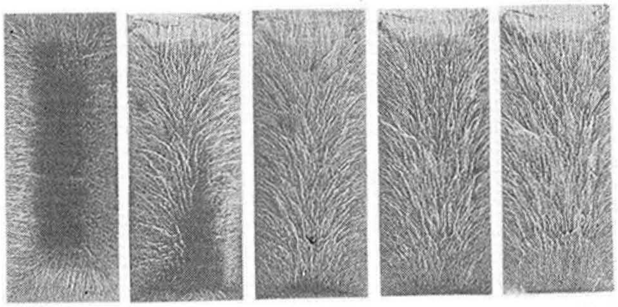

Fig. 3 Fluid flow patterns for the narrow plate. From left to right, α = 90, 65, 45, 35, and 25 deg; $\mathrm{Re}_L \sim 50{,}000$

according to decreasing values of the angle of attack: 90 (normal impingement), 65, 45, and 25 deg. For angles of attack less than 90 deg, the results correspond to orientations in which the lower edge of the plate is thrust forward into the direction of the wind as illustrated in Fig. 1, upper right.

The flow patterns for the narrow plate are displayed via the five photographs that are arranged side by side in Fig. 3. The photo at the left is for normal impingement ($\alpha = 90$ deg) and, proceeding from left to right, the successive photographs correspond to α values of 65, 45, 35, and 25 deg. In common with Fig. 2, the $\alpha < 90$ deg results displayed in Fig. 3 correspond to plates inclined so that the lower edge is thrust forward into the direction of the oncoming airstream.

Attention will first be directed to Fig. 2. For the case in which the plate is situated normal to the flow (lower photo), there is a rectangular stagnation zone (i.e., the black region) centered in the plate cross section. Surrounding the stagnation zone are streak lines indicating that the fluid adjacent to the plate surface is flowing outward toward the respective edges. The three-dimensional effects engendered by the finite span are clearly evidenced by the lateral flows directed toward side edges.

As the plate is inclined and the angle of attack is decreased from 90 to 65 deg, the stagnation zone migrates toward the forward part of the plate (Fig. 2, second photograph). Forward of the stagnation zone, the fluid adjacent to the plate flows upstream toward the leading edge, even though the freestream flow moves downstream. There continue to be significant three-dimensional effects as the flow fans out from the right- and left-hand ends of the stagnation zone toward the lateral edges.

With a further decrease of the angle of attack to 45 deg, the stagnation zone shrinks to a thin line situated just downstream of the leading edge. Careful inspection of the third photograph in Fig. 2 indicates that there is a narrow region between the stagnation zone and the leading edge where the flow moves upstream. It also appears that the three-dimensional effects (i.e., lateral flows) are confined to a somewhat narrower region adjacent to the side edges than at the larger angles of attack. As the angle of attack is decreased still further to 25 deg, the stagnation zone appears to have become coincident with the leading edge. Furthermore, the extent of the three-dimensional effects, as measured by the width of the regions of lateral flow, has definitely diminished.

Thus, there are a number of significant changes in the flow field that occur as the orientation of the wider plate is varied from normal incidence through a sequence of inclinations. Among these, the most prominent are the forward movement and ultimate disappearance of the stagnation zone, the evolution of the longitudinal flow from one having zones of upstream motion and downstream motion to one having only downstream motion, and the diminution of the extent of the three-dimensional effects.

Consideration may now be given to the flow patterns for the narrow plate, Fig. 3. The normal impingement case is represented by a photograph (at the extreme left) which is identical to that in Fig. 2 (lower photo), but turned through an angle of 90 deg. Therefore, the characteristics already identified for the latter are also applicable to the former. The second photo in Fig. 3 shows the flow pattern for a plate at a 65 deg angle of attack. The stagnation zone is now situated in the forward part of the plate and is triangular in form (albeit somewhat skewed). Between the stagnation zone and the leading edge, a narrow region of upstream flow persists. Perhaps even more noteworthy is the dominance of the lateral flow. Indeed, except for a narrow corridor along the longitudinal axis and a small region near the trailing edge, there is little evidence of longitudinal flow (i.e., flow in the direction of the free stream).

The decrease of the angle of attack to 45 deg (third photo) causes further forward migration and diminution of the stagnation zone, with its triangular form being maintained. Although the lateral flow continues to be dominant, the longitudinal component is somewhat more in evidence. These trends are further accentuated as the angle of attack is successively decreased to 35 and 25 deg (fourth and fifth photos). The stagnation zone appears to coincide with the leading edge and the longitudinal component of the flow is more in evidence. Furthermore, there is a tendency for the lateral flows to retreat toward the side edges, leaving a central corridor for the longitudinal flow.

By comparing the characteristics of the flow patterns for the narrow plate with those for the wider plate, it appears that the qualitative trends are common to both. However, it is important to note that at any angle of attack, the three-dimensional effects are much more in evidence for the narrow plate. Thus, for example, at the 25 deg angle of attack, the lateral flow continues to be a dominant feature for the narrow plate but is confined to narrow edge-adjacent regions for the wider plate.

The flow-pattern characteristics discussed in the foregoing are corroborated by those identified in [4] for a square plate inclined at various angles of attack to an oncoming airstream. Qualitatively speaking, the square-plate results are intermediate between those for the narrow plate and the wider plate.

Since much has been said about edge-related flow patterns, it is opportune to illuminate their impact on the heat (mass) transfer coefficients. To this end, results borrowed from [4] are presented in Fig. 4. Although these results are for a square plate, their qualitative behavior should be applicable to the rectangular plates studied here.

Fig. 4 is subdivided into left and right-hand parts. Each part depicts half of a square plate, the other half being omitted by virtue of symmetry. In each part, contour lines are drawn showing the ratio of the local to the average heat (mass) transfer coefficient. The left-hand part is for normal impingement ($\alpha = 90$ deg) while the right-hand part is for an angle of attack of 25 deg, with the lower edge being thrust forward in the direction of the oncoming flow. The results correspond to a Reynolds number of about 80,000 (based on the side of the square as the characteristic dimension).

Turning first to the case of normal impingement, it is seen that the lowest heat transfer coefficients occur in the central region of the plate, that is, in the stagnation zone. The coefficients increase in the radial direction from the center to the edges. This direction of increase coincides with the direction of flow along the plate, thereby implying a decrease in the boundary layer thickness from the center of the plate toward the edges. The thinning of the boundary layer is believed to occur as the radially outflowing streamlines are pressed toward the plate surface by the freestream flow which passes beyond the edges of the plate.

The results for the 25 deg angle of attack (right-hand diagram) indicate the continued prominence of the edge-region heat transfer coefficients that was noted for normal impingement, although the flow patterns for the two cases are quite different. The high coefficients that are in evidence in the forward part of the plate (i.e., near the lower edge) are due to the developing boundary layer. In the neighborhood

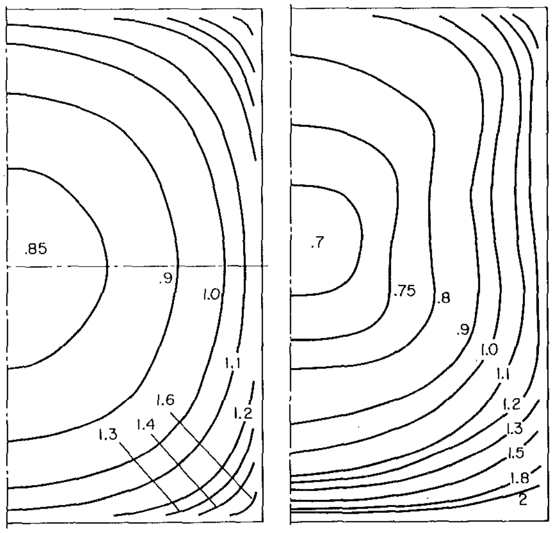

Fig. 4 Contour lines of constant local heat (or mass) transfer coefficient, relative to the plate average, for a square plate (from [4]). Left-hand diagram: $\alpha = 90$ deg; righthand diagram, $\alpha = 25$ deg

of the trailing edge, the boundary layer is thinned as the streamlines are pressed against the surface, as in the normal impingement case. The relatively high coefficients that occur adjacent to the side edges are also due to thinning of the boundary layer. This thinning has been experimentally demonstrated [5, 6] for flow along a flat plate aligned parallel to the free stream and should also occur for inclined plates.

It can be expected that the edge-region heat transfer coefficients for rectangular plates will also be relatively high.

The Characteristic Dimension. The heat (mass) transfer coefficients will be presented in dimensionless form via the j-factor. As can be verified from equations (2) and (3), the j-factor does not contain a characteristic dimension. There is, however, a characteristic dimension in the Reynolds number (equation (4)), and a suitable selection must now be made. In considering the make-up of the characteristic dimension, it is apparent that the surface area A of the plate must somehow be involved. In addition, in view of the just-demonstrated relatively high rates of heat (or mass) transfer adjacent to the edges, the circumference C of the plate should also be considered. The simplest combination of A and C which yields a length dimension is the ratio A/C. For purely cosmetic reasons, a factor of four may be included (so that the characteristic dimensions for a square and a circle are, respectively, the side and the diameter). Thus, we define

$$L = 4A/C, \quad \mathrm{Re}_L = U_\infty(4A/C)/\nu \tag{5}$$

In support of this selection, mention may be made of its successful application in another problem which, although seemingly unrelated, shares some common features with that studied here. In [7], natural convection was studied for upward-facing heated plates including circles, rectangles with aspect ratios ranging from 1:1 to 7:1, and right triangles having various included angles. The heat transfer results for all of these cases were successfully brought together by the use of A/C as the characteristic length. The common bond between the natural convection problem of [7] and the present problem is that both are characterized by relatively high coefficients adjacent to the edges.

Another candidate characteristic length, alternative to that of equation (5), can be defined via a geometric mean. If L_1 and L_2 are the sides of a rectangular plate, then

$$L^* = \sqrt{L_1L_2} = \sqrt{A} \tag{6}$$

where $A = L_1L_2$ is the area of the plate surface. The L^* defined by equation (6) can be interpreted as the side of a square plate whose surface area is equal to that of the rectangular plate. If, for cosmetic purposes, a factor $\sqrt{4/\pi}$ is introduced into equation (6), the resulting L^* can be interpreted as the diameter of a circle whose area equals that of the rectangle, since

$$L^* = \sqrt{(4/\pi)A} \text{ or } \pi L^{*2}/4 = A \tag{7}$$

The presence or absence of the multiplying factor $\sqrt{4/\pi}$ will have no effect on the correlating capabilities of the geometric-mean characteristic length. We have chosen to retain the factor and to designate the L^* of equation (7) as an effective diameter. Correspondingly, the Reynolds number will be evaluated as

$$\mathrm{Re}_D = U_\infty \sqrt{(4/\pi)A}/\nu \tag{8}$$

In the initial presentation of the heat transfer results, where attention is focused on the effect of Reynolds number and inclination angle, either Re_L or Re_D can be employed without affecting the nature of the results. Later, the correlating capabilities of the two characteristic lengths with regard to different plate aspect ratios will be examined.

Heat (Mass) Transfer Results. The heat (mass) transfer results for the narrow and the wider plates are presented in Fig. 5 in the right and left-hand diagrams. The j-factors are plotted as a function of the Reynolds number Re_L, with different data symbols being employed to parameterize the various angles of attack between 25 and 90 deg.

If attention is first turned to the results for the wider plate, it can be observed that the heat transfer coefficients are fully independent of the angle of attack in the range investigated. This finding appears to be all the more remarkable when viewed against the backdrop of the flow visualization photographs of Fig. 2, where significant changes in flow pattern are in evidence. On the other hand, the insensitivity is not completely unexpected, since the square-plate results of [2] showed only a slight sensitivity to angle of attack (~4½ percent decrease over the range from $\alpha = 90$ to 25 deg).

A least-squares straight line has been passed through the data; its equation is

$$j = 0.939\mathrm{Re}_L{}^{-1/2} \tag{9}$$

It is evident from the figure that the line is an excellent representation of the data. It may also be noted that for the square plate, the least squares fit of the data gives $j = 0.927\mathrm{Re}_L{}^{-1/2}$, which differs from equation (9) by about a percent.

Consideration will now be given to the results for the narrow plate (right-hand part of Fig. 5). Since the results for the 90 deg case (circles) are common to both the narrow and the wider plates, it follows that the narrow-plate heat transfer coefficients tend to lie below those for the wider plate. The figure shows that there is an orderly pattern whereby the narrow-plate results lie successively lower as the angle of attack decreases from 90 deg. The decrease in the transfer coefficient is rather slow at first (e.g., the 65 deg results are only slightly different from the 90 deg results) but becomes more rapid as α deviates more and more from 90 deg. The overall spread in the data is about 20 percent, and while this is not large by many standards it is significant compared to the total insensitivity to angle that was displayed by the wider-plate results.

The aforementioned decrease of the transfer coefficient is believed due to the development of a region of low transfer situated near the aft end of the plate. As α decreases toward 0 deg, any fluid which reaches the aft end must first have traversed the fore part of the plate. However, owing to the relative ease with which fluid can escape from the plate, and its friction forces, via the side edges, relatively little fluid reaches the aft end. Furthermore, as α decreases, the streamlines are less and less pressed toward the trailing edge by the free stream flow. Both these factors are believed to contribute to the decrease in the transfer coefficient with decreasing angle of attack.

A least-squares fit of the narrow plate data yields

$$j = 0.870\mathrm{Re}_L{}^{-1/2} \tag{10}$$

with deviations of +8 percent and −12 percent. While this correlation is not as pleasing as that for the wider plate, it is altogether satisfactory for engineering applications.

As a final remark with respect to Fig. 5, it should be noted that the data for each angle of attack and for both plate widths are represented by a relation of the form $j \sim \mathrm{Re}^{-1/2}$. Whereas the $\mathrm{Re}^{-1/2}$ dependence can be established by analysis for flow over a two-dimensional flat plate and at a stagnation region, such a dependence has not heretofore been documented for rectangular plates of finite span and finite length.

The correlation of the results for the various aspect-ratio plates will now be considered, including the narrow and wider rectangular plates

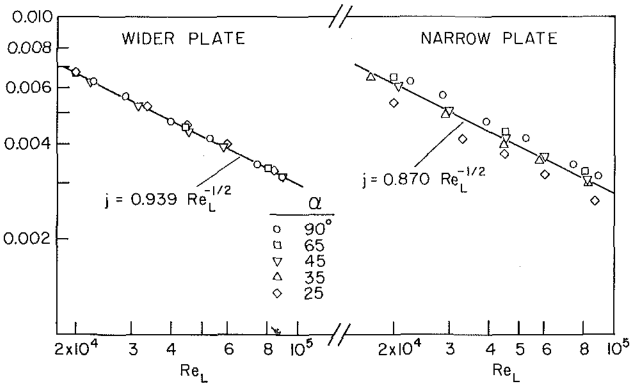

Fig. 5 Heat (mass) transfer coefficients for the wider and the narrow plates

of the present investigation and the square plate of [2]. Since the correlation equations for the latter are already in the literature, they will be used as a basis for comparison with the present results.

Fig. 6 compares the square-plate correlation equations with the results for the wider plate. In [2], the square-plate correlation is expressed as

$$j = 0.947\,\mathrm{Re}_L^{-1/2} \text{ and } j = 0.905\mathrm{Re}_L^{-1/2} \qquad (11)$$

where the first equation is for $\alpha = 90$ and 65 deg, and the second is for $\alpha = 45$ and 25 deg. The comparison is shown in the upper part of the figure—at the left for the 90 and 65 deg angles and at the right for the 45 and 25 deg angles. The former comparison indicates virtually exact agreement, while the latter shows an average deviation of less than four percent. Furthermore, as noted in connection with Fig. 5, the global correlation (equation (9)) of the data for the wider plate differs by only about one percent from its square-plate counterpart. It can thus be concluded that the characteristic dimension defined by equation (5) is highly effective in bringing together the results for the square plate and the wider rectangular plate.

A similar comparison, but made on the basis of the Reynolds number Re_D, is shown in the lower part of Fig. 6. To enable a compact presentation, the quantity $j/2$ is plotted rather than j itself. The square-plate equations, when rephrased in terms of Re_D, are

$$j = 1.006\mathrm{Re}_D^{-1/2} \text{ and } j = 0.961\mathrm{Re}_D^{-1/2} \qquad (12)$$

respectively for $\alpha = 90$ and 65° and for 45 and 25 deg. Clearly, the correlation of the two geometries is not as effective as with the Reynolds number Re_L.

Next, attention will be turned to Fig. 7 and to the narrow-plate results. The structure of the figure is identical to Fig. 6, and the straight lines are the square-plate correlations, equations (11) and (12). Since these lines are common to the two figures, they also provide a convenient reference for comparing the results for the narrow and wider plates.

From Fig. 7, it is seen that the Re_L representation satisfactorily correlates the square- and narrow-plate results for $\alpha = 90$, 65, and 45 deg. For smaller angles, there is an increasing deviation (up to about 15 percent) between the two geometries. The Re_D representation provides a better correlation at the smaller angles (deviations about 10 percent at $\alpha = 25$ deg) but not quite as good at larger angles.

If comparisons are made between Figs. 6 and 7, the narrow and wider-plate results are seen to be in very good agreement for $\alpha = 90$, 65, and 45 deg. Furthermore, these results correlate well with those for the square plate when the Re_L representation is used. For angles less than 45 deg, the data for the three geometries tend to spread, with those for the wider plate lying highest, the square plate next, and the narrow plate lowest. The overall spread at $\alpha = 25$ deg is slightly in excess of 20 percent.

Thus a geometry-independent correlation (based on Re_L) appears to exist for angles between 90 deg and 45 deg, but at smaller angles there are imperfections in the correlation on the order of 20 percent.

As a final matter, it may be noted that possible wind-tunnel blockage effects were not considered in the evaluation of the velocity U_∞ which appears in both j and in Re. At $\alpha = 90$ deg, the cross-sectional blockage due to the plate was about 3½ percent, while at $\alpha = 25$ deg the blockage was about 1½ percent. If a blockage correction were made based on a velocity increase proportional to the blocked area, then the j, Re correlation for $\alpha = 90$ deg would have been shifted by about two percent and that for $\alpha = 25$ deg by about one percent. In view of the smallness of these shifts and the uncertainties of blockage corrections, it was judged that no correction was warranted.

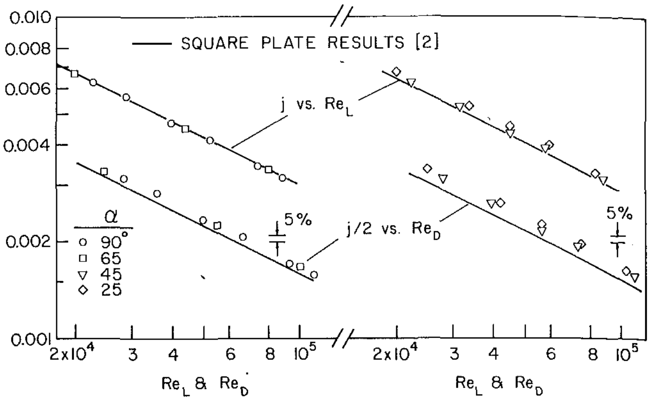

Fig. 6 Comparison between the results for the wider rectangular plate and the square plate of [2]

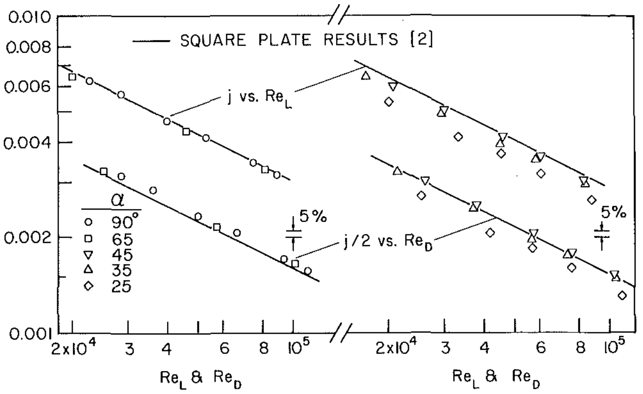

Fig. 7 Comparison between the results for the narrow rectangular plate and the square plate of [2]

Concluding Remarks

With regard to the solar collector application that was discussed at the beginning of the paper, there is need for a predictive equation having a simple form and a minimum number of parameters. In particular, since the wind direction is a timewise variable and is often not known with certainty, an equation involving an angle dependence would not find wide application. Furthermore, an equation which does not include a parametric dependence on aspect ratio would be regarded with favor. Since neither the angle nor the geometry effects have been found to be large, the aforementioned simplicity criteria can be fulfilled.

As a global correlation equation, we propose

$$j = 0.86\mathrm{Re}_L^{-1/2} \qquad (13)$$

with Re_L defined by equation (5). This equation represents the present results and those of [2] for angles of attack between 90 and 25 deg, with maximum errors of ±10 percent. The numerical constant, 0.86, was calculated by averaging the constants C obtained from least-squares fits ($j = C\mathrm{Re}^{-1/2}$) passed through the highest and lowest sets of data.

Acknowledgment

This research was performed under the auspices of NSF Grant ENG77-06762.

References

1 Drake, R. M., Jr., "Investigation of the Variation of Point Unit Heat Transfer Coefficient for Laminar Flow Over an Inclined Flat Plate," ASME *Journal of Applied Mechanics*, Vol. 71, 1949, pp. 1–8.

2 Sparrow, E. M. and Tien, K. K., "Forced Convection Heat Transfer at an Inclined and Yawed Square Plate—Application to Solar Collectors," ASME JOURNAL OF HEAT TRANSFER, Vol. 99, 1977, pp. 507–512.

3 Sogin, H. H., "Sublimation from Disks to Air Streams Flowing Normal to Their Surfaces," Trans. ASME, Vol. 80, 1958, pp. 61–69.

4 Tien, K. K., "Heat/Mass Transfer Characteristics and Fluid Flow Patterns for Airflow About an Inclined and Yawed Flat Plate," Ph.D. Thesis, Department of Mechanical Engineering, University of Minnesota, Minneapolis, Minn., 1978.

5 Elder, J. W., "The Flow Past a Flat Plate of Finite Span," *Journal of Fluid Mechanics*, Vol. 9, 1960, pp. 133–153.

6 Davies, E. B. and Young, A. D., "Streamwise Edge Effects in the Turbulent Boundary Layer on a Flat Plate of Finite Aspect Ratio," Aeronautical Research Council of Great Britain, Reports and Memoranda No. 3367, 1963.

7 Lloyd, J. R. and Moran, W. R., "Natural Convection Adjacent to Horizontal Surface of Various Planforms," ASME JOURNAL OF HEAT TRANSFER, Vol. 96, 1974, pp. 443–447.

R. B. Holmberg,
AB Svenska Fläktfabriken
Åsenvägen 7,
S-551 84 Jönköping
Sweden

Combined Heat and Mass Transfer in Regenerators with Hygroscopic Materials

Simultaneous heat and mass transfer in periodic-flow heat and mass exchangers, or regenerators, with hygroscopic matrix materials has been analyzed. The coupled heat and mass transfer equations are derived for boundary-layer controlled heat and mass transfer and include longitudinal heat conduction in the matrix. A numerical method of the finite-difference type is applied to the steady-state performance. Results for a water vapor-air mixture show the influence of matrix heat and moisture capacities on temperature and humidity efficiencies. Distributions of air temperature, air humidity, matrix temperature and adsorbent moisture content are calculated in drying as well as recovery operations.

Introduction

Periodic-flow heat and mass exchangers, or regenerators, with hygroscopic matrix materials are used in a variety of applications. Periodic-flow exchangers transfer heat and adsorbates cyclically from one fluid stream to a matrix and then from the matrix to the other fluid stream. In chemical engineering, cyclic sorption operations in fixed beds or matrices (with valves in order to alternate the fluid streams) are common and can be considered as sorptive regenerators. Adsorption drying of industrial gases by means of silica gel is an example of this type.

In air conditioning, regenerators with hygroscopic matrix materials are used both for heat and moisture recovery and for dehumidification of moist air. In the recovery case the total heat or enthalpy regenerator has high matrix capacity for heat as well as moisture, while in the dehumidification case, the regenerative dehumidifier has low matrix heat capacity and high matrix moisture capacity. These devices are usually in the form of a rotating matrix with two axial counter-flow streams and are often called rotary exchangers or dryers.

The sizing of regenerative dehumidifiers is usually based upon adiabatic sorption analysis in porous media. The inlet condition of the process stream flowing adiabatically through the porous medium in equilibrium has been suddenly changed and the time response of the adsorbate concentration in the outlet stream has been determined. This approach gives satisfactory predictions for regenerative dehumidifiers only if the entire bed is in equilibrium with the inlet fluid at the end of each period. However, since this condition results in reduced dehumidifying efficiency, it is not often satisfied in practice. Several authors [1–3] have assumed thermal and sorption local equilibrium between fluid and bed in the adiabatic sorption system, in order to obtain uncoupled differential equations describing the coupled heat and mass transfer problem. Other authors [4–8] have without this assumption solved the resulting coupled non-linear differential equations for adiabatic sorption by finite-difference methods. Later, the equilibrium method has been applied to total heat regenerators and regenerative dehumidifiers [9].

The present study of regenerators with hygroscopic matrix materials is concerned with the air-conditioning cases. However, the analysis is applicable to regenerators in other fields. The theoretical analysis is applied to the steady-state behavior, where the cyclic operation is continuously repeated. Each period, hot and cold, of the regenerator is described by equations similar to the equations which describe adiabatic sorption without the equilibrium assumption. The coupled heat and mass transfer equations are derived for boundary-layer controlled heat and mass transfer, and include longitudinal heat conduction in the matrix solid. The set of non-linear differential equations are solved for both periods of the regenerator by a finite-difference method similar to the method, which has been used by the present author [10] in studying the heat and mass transfer in regenerators with non-hygroscopic matrix materials. The solutions of the two periods are coupled together with the boundary conditions of the matrix. In particular, the simultaneous heat and mass transfer is analyzed for different values of the matrix heat and moisture capacities, that is from recovery to drying operations.

Theoretical Analysis

In the total heat regenerator, heat is transferred from the hot air to the matrix, is stored in the matrix material and is subsequently transferred to the cold air. The moisture of the hot air is transferred by adsorption to the matrix as long as the bulk absolute humidity of the hot air is greater than the absolute humidity of the hot air in equilibrium with the adsorbent. Since water will be condensed out of the hot air, the moisture content of the adsorbent will increase. The adsorbed water is then evaporated into the cold air as long as the absolute humidity of the cold air in equilibrium with the adsorbent is greater than the bulk absolute humidity of the cold air. The heat release accompaning the adsorption tends to increase the matrix temperature change caused by the heat transfer.

Contributed by the Heat Transfer Division for publication in the JOURNAL OF HEAT TRANSFER. Manuscript received by the Heat Transfer Division March 6, 1978.

In the regenerative dehumidifier, the heat transfer from hot to cold air is small, due to the low matrix heat capacity. The moisture of the cold air is adsorbed by the matrix as soon as the absolute humidity is greater in the bulk air than in the air in equilibrium with the adsorbent. The moisture content in the adsorbent will thus increase. The released heat will raise the temperatures of the adsorbent and the cold air stream. On the hot air side, the matrix then will be reactivated in the sense that the adsorbed water is evaporated into the hot air stream. The temperatures of the adsorbent and the hot air stream decreases, since the heat of adsorption is expended in evaporating the condensate.

The differential equations describing the simultaneous heat and mass transfer in a regenerator will be considered for a typical element of a rotor matrix (Fig. 1). Although Fig. 1 shows an axial-flow type of rotary exchanger, a typical element can be selected in the same way for a radial-flow type of rotary exchanger or for a periodic-flow exchanger with valves. The equations will be given with the following main idealizations:

1 The thermal resistance of the matrix material is infinite in the tangential direction, finite in the axial direction and small in the radial direction, which is indicated in Fig. 1.

2 The mass diffusion resistance of the matrix material is infinite both in the tangential and the axial direction and small in the radial direction.

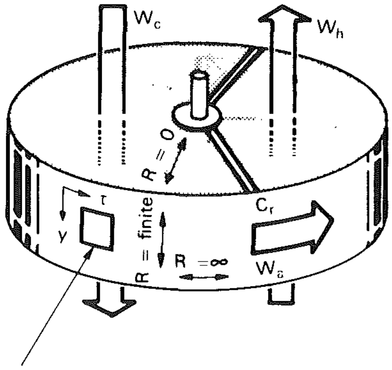

Fig. 1 Illustrative rotor arrangement

3 The fluid heat and mass storage capacities are negligible in comparison with the convective heat and mass transport.

4 The thermal properties of the fluids and of the matrix material are constant.

5 No mixing or bypassing of the fluids occurs.

6 The fluids pass in counter flow directions.

7 Regular periodic conditions are established for all matrix elements, i.e., steady-state operation.

On the basis of these idealizations, a set of differential equations can be expressed for the hot-fluid and cold-fluid sides respectively. The minus signs within brackets are valid for the hot-fluid side and the plus signs for the cold-fluid side.

The mass-transfer rate equation is

$$W\frac{\partial x}{\partial y} = (\mp)\frac{\beta_x A}{L}(x - x_s), \tag{1}$$

the mass-conservation equation

$$W\frac{\partial x}{\partial y} = (\mp)\frac{\alpha_a m_r}{L}\frac{\partial w}{\partial \tau}, \tag{2}$$

the energy-transfer rate equation

$$W\frac{\partial i}{\partial y} = (\mp)\frac{\beta_x A}{L}[\phi c_p(t - t_r) + (x - x_s)(i_{vs} - i_{ws})] \tag{3}$$

and the energy-conservation equation

$$W\frac{\partial i}{\partial y} = (\mp)\left(\frac{m_r}{L}\frac{\partial i_r}{\partial \tau} - kA_k\frac{\partial^2 t_r}{\partial y^2}\right). \tag{4}$$

where $\phi = h/(\beta_x c_p)$ is the psychrometric ratio. In addition to the boundary-layer diffusion the mass transfer coefficient β_x is assumed to take into account also small transverse diffusion effects within the adsorbent similar to Chi and Wasan [7]; likewise, the heat transfer coefficient h can take into account small transverse conduction effects within the rotor material.

The enthalpy of moist air is defined by

$$i = c_{pa}t + i_v x = c_p t + r_0 x$$

and its derivative becomes

Nomenclature

A = heat-transfer area for one period, m^2
A_k = cross-sectional area for longitudinal heat conduction for one period, m^2
A_{kt} = total cross-sectional area for longitudinal heat conduction, $A_{kc} + A_{kh}$, m^2
c = specific heat, J/kg-°C
c_p = specific heat of vapor-gas mixture (at constant pressure), J/kg dry gas-°C
c_r = specific heat of matrix, J/kg-°C
C = heat capacity rate of vapor-gas mixture, Wc_p,W/°C
C_r = heat capacity rate of matrix, $m_r c_r/(\tau_c + \tau_h)$, W/°C
h = heat transfer coefficient, W/m^2-°C
i = enthalpy, J/kg and enthalpy of vapor-gas mixture, J/kg dry gas
i_r = enthalpy of matrix, J/kg
k = thermal conductivity of matrix solid supporter, W/m-°C
K = overall mass transfer coefficient, 1/(A/$(\beta_x A)_c + A/(\beta_x A)_h$), W/m^2-°C
L = flow length of matrix, m
m_r = mass of matrix, kg
N = number of subdivisions
p = pressure, Pa
p_t = total pressure of vapor-gas mixture, Pa
r_{ad} = heat of adsorption, J/kg
r_0 = latent heat of vaporization, J/kg
R = thermal resistance, °C/W
t = temperature of vapor-gas mixture, °C
t_r = temperature of matrix, °C
w = adsorbate concentration, kg adsorbate/kg adsorbent
W = mass flow rate of gas, kg dry gas/s
W_a = mass flow rate of adsorbent, $\alpha_a m_r/(\tau_c + \tau_h)$, kg adsorbent/s
x = absolute humidity of vapor-gas mixture, kg vapor/kg dry gas
y = flow length coordinate measured from hot-fluid inlet, m
α = mass fraction, kg/kg matrix
β_x = mass transfer coefficient, kg vapor/m^2-s-Δx
$\mathcal{H}$ = constant for uneven spacing
τ = time coordinate, s
τ_c, τ_h = time for one cold-fluid and one hot-fluid period, respectively, s
φ = relative humidity of vapor-gas mixture
(i, j) = typical element for hot-fluid period
(f, g) = typical element for cold-fluid period
$\bar{i}_{c2}$ = cold-fluid outlet enthalpy, $(i_{c2} - i_{c1})/(i_{h1} - i_{c1})$
$\bar{t}_{c2}$ = cold-fluid outlet temperature, $(t_{c2} - t_{c1})/(t_{h1} - t_{c1})$
$\bar{x}_{c2}$ = cold-fluid outlet absolute humidity for recovery, $(x_{c2} - x_{c1})/(x_{h1} - x_{c1})$
$\bar{x}^*_{c2}$ = cold-fluid outlet absolute humidity for drying, $(x_{c2} - x_{c1})/(x^*_{h1} - x_{c1})$
W_c/W_h = mass flow rate ratio of fluid streams
C_r/C_n = heat capacity rate ratio of matrix to minimum fluid capacity rate
W_a/W_n = mass flow rate ratio of adsorbent to minimum fluid mass flow rate
$N_{tu,0}$ = overall number of transfer units, KA/W_n
$(\beta_x A)^+$ = diffusion resistance ratio, $(\beta_x A)_c/(\beta_x A)_h$
$A_k{}^+$ = conduction area ratio, A_{kc}/A_{kh}
Λ = total conduction parameter, $kA_{kt}/(LC_n)$
ϕ = psychrometric ratio, $h/(\beta_x c_p)$

Subscripts

1 = inlet
2 = outlet
a = adsorbent in matrix
av = average
b = porous supporter in matrix
c = cold fluid or cold-fluid period (side)
h = hot fluid or hot-fluid period (side)
k = solid supporter in matrix
n = minimum
r = total matrix
s = saturation
v = adsorbate vapor
w = adsorbate

$$\frac{\partial i}{\partial y} = c_p \frac{\partial t}{\partial y} + \mathrm{i_v} \frac{\partial x}{\partial y}, \tag{5}$$

where the specific heat of moist air $c_p = c_{pa} + xc_{pv}$ is assumed to be constant with $x = (x_{h1} + x_{c1})/2$. The results are given for $c_{pa} = 1.005$ kJ/kg-°C for dry air and $c_{pv} = 1.86$ kJ/kg-°C for water vapor.

The rotor matrix can be composed of a solid supporter (k), a porous supporter (b) and an adsorbent (a) with the mass fractions α_k, α_b and α_a respectively ($\alpha_k + \alpha_b + \alpha_a = 1$).

Thus the enthalpy of the rotor matrix is defined by

$$i_r = \alpha_k i_k + \alpha_b i_b + \alpha_a [i_a + w(i_{ws} - \Delta r_w)]$$

and its derivative becomes

$$\frac{\partial i_r}{\partial \tau} = c_r \frac{\partial t_r}{\partial \tau} + \alpha_a (i_{ws} - \Delta r_w) \frac{\partial w}{\partial \tau}, \tag{6}$$

where the specific heat of the rotor matrix $c_r = \alpha_k c_k + \alpha_b c_b + \alpha_a (c_a + wc_w)$ and the differential heat of wetting $\Delta r_w = r_{ad} - (i_{vs} - i_{ws})$ are prescribed to be locally constant in every element with mean water content w of the adsorbent.

Elimination of the enthalpy of moist air from equation (3) with the equations (5) and (1) results in

$$Wc_p \frac{\partial t}{\partial y} = (\mp) \frac{\beta_x A}{L} \phi (t - t_r), \tag{7}$$

where the enthalpy of the condensed water vapor and the enthalpy change of the water vapor during its transport through the air boundary layer are neglected.

Elimination of the enthalpy of moist air and of the rotor matrix from equation (4) with the equations (5), (6) and (2) results in

$$W \left(c_p \frac{\partial t}{\partial y} + r_{ad} \frac{\partial x}{\partial y} \right) = (\mp) \left(\frac{m_r c_r}{L} \frac{\partial t_r}{\partial \tau} - kA_k \frac{\partial^2 t_r}{\partial y^2} \right), \tag{8}$$

where the same neglections as in equation (7) are made. Thus, the system of partial differential equations describing the actual problem consists of the equations (1), (2), (7) and (8).

The absolute humidity of moist air in equilibrium with the local adsorbent is obtained from

$$x_s = 0.62198 \frac{p_{va}}{p_t - p_{va}}$$

and the water vapor pressure in equilibrium with the adsorbent is expressed by

$$p_{va} = \varphi_a p_{vs}$$

where the saturation pressure p_{vs} over liquid water is determined according to Goff formulas [11].

It is assumed that the water content of the adsorbent is a function of the relative humidity of moist air in equilibrium with the adsorbent only and invariable with temperature. Furthermore, sorption hysteresis is neglected and the adsorption isotherm can be expressed by

$$\varphi_a = f(w).$$

Numerical Method

The system of differential equations is solved by a finite-difference method. Fig. 2 illustrates a staggered mesh representing the y-τ plane of the rotary exchanger (Fig. 1). Techniques for uneven spacing are used for the differences in the τ direction in order to be able to handle the steep temperature gradients in cases of low matrix heat capacities.

For the hot-fluid side, the mass-transfer rate equation (1) is represented by an ordinary central difference scheme

$$x_h(i, j) - x_h(i + 1, j) = \frac{(\beta_x A)_h}{W_h} \frac{\Delta y}{L} \Delta x_{h,av}(i, j), \tag{9}$$

where the mean difference between the absolute humidity of the moist air and of the moist air in equilibrium with the adsorbent is assumed as the arithmetic mean value according to

$$\Delta x_{h,av}(i,j) = \frac{1}{2}[x_h(i, j) + x_h(i + 1, j)] - \frac{1}{2}[x_{sh}(i, j) + x_{sh}(i, j + 1)]$$

Similarly, the heat-transfer rate equation (7) is represented by

$$t_h(i, j) - t_h(i + 1, j) = \frac{(\beta_x A)_h}{W_h} \phi \frac{\Delta y}{L} \Delta t_{h,av}(i, j), \tag{10}$$

where the mean temperature difference between the air and the rotor matrix is assumed to be

$$\Delta t_{h,av}(i, j) = \frac{1}{2}[t_h(i, j) + t_h(i + 1, j)] - \frac{1}{2}[t_{rh}(i, j) + t_{rh}(i, j + 1)].$$

The mass-conservation equation (2) is represented by

$$x_h(i, j) - x_h(i + 1, j) = \frac{W_a}{W_h} \frac{\Delta y}{L} \frac{\tau_h}{\Delta \tau_h(j)} [w_h(i, j + 1) - w_h(i, j)] \tag{11}$$

and the energy-conservation equation (8) is represented by the implicit Crank-Nicholson scheme

$$\begin{aligned} t_h(i, j) - t_h(i + 1, j) + \frac{r_{ad}}{c_{ph}} [x_h(i, j) - x_h(i + 1, j)] &= \frac{C_r}{C_h} \frac{\Delta y}{L} \frac{\tau_y}{\Delta \tau_h(j)} [t_{rh}(i, j + 1) - t_{rh}(i, j)] \\ &- \frac{kA_{kh}L}{2LC_h \Delta y} [t_{rh}(i + 1, j) + t_{rh}(i - 1, j) - 2t_{rh}(i, j) \\ &+ t_{rh}(i + 1, j + 1) + t_{rh}(i - 1, j + 1) - 2t_{rh}(i, j + 1)]. \end{aligned} \tag{12}$$

Similarly, the corresponding equations can be expressed for the cold-fluid side.

The boundary conditions are as follows:
For the inlet on the hot-fluid side

$$t_h(1, j) = t_{h1}, \quad j = 1, 2, \ldots N_h$$
$$x_h(1, j) = x_{h1}, \quad j = 1, 2, \ldots N_h$$

For the inlet on the cold-fluid side

$$t_c(1, g) = t_{c1}, \quad g = 1, 2, \ldots N_c$$
$$x_c(1, g) = x_{c1}, \quad g = 1, 2, \ldots \mathrm{N_c}$$

On the cold-rotor seal

$$t_{rh}(i, 1) = t_{rc}(f, N_c + 1), \quad i = 1, 2, \ldots \mathrm{N_r},$$
$$w_h(i, 1) = w_c(f, N_c + 1), \quad f = N_r + 1 - i$$

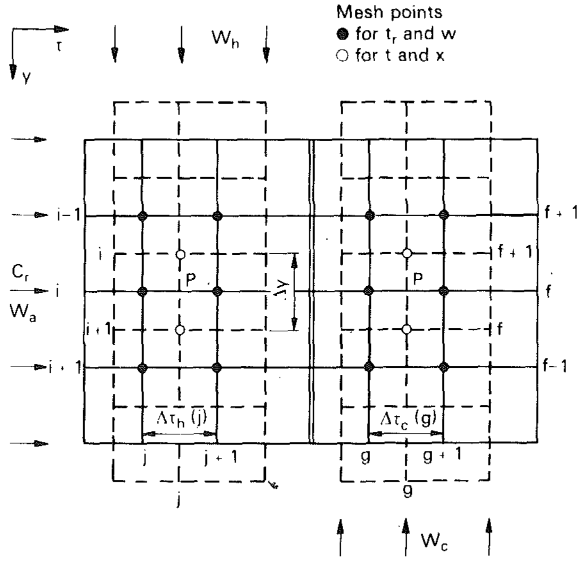

Fig. 2 **A staggered mesh representing the y-τ plane of a rotary exchanger**

which means that the left edge in Fig. 2 is physically the same as the right edge. This will later be referred to as the reversal condition.

On the hot-rotor seal

$$t_{rc}(f, 1) = t_{rh}(i, N_h + 1), \qquad f = 1, 2, \ldots N_r$$

$$w_c(f, 1) = w_h(i, N_h + 1), \qquad i = N_r + 1 - f$$

The longitudinal heat conduction is zero at the ends of the rotor in axial direction, i.e.,

$$t_{rh}(0, j) = t_{rh}(1, j), \qquad j = 1, 2, \ldots N_h$$

$$t_{rh}(N_r + 1, j) = t_{rh}(N_r, j), \qquad j = 1, 2, \ldots N_h$$

$$t_{rc}(0, g) = t_{rc}(1, g), \qquad g = 1, 2, \ldots N_c$$

$$t_{rc}(N_r + 1, g) = t_{rc}(N_r, g), \qquad g = 1, 2, \ldots N_c$$

The difference equations (9–12) for the hot-fluid side and corresponding equations for the cold-fluid side are solved for $t(i + 1, j)$, $x(i + 1, j)$, $t_r(i, j + 1)$ and $w(i, j + 1)$ with the constants expressed in terms of the nondimensional parameters W_c/W_h, C_r/C_n, W_a/W_n, $N_{tu,0}$, Λ, $(\beta_x A)^+$, $A_k{}^+$ and ϕ. In order to obtain convergence an implicit trick has been used for the term $x_s(i, j + 1)$, since this term is highly dependent on the dependent variables $t_r(i, j + 1)$ and $w(i, j + 1)$. The calculation method becomes iterative and the Gauss-Seidel method with successive under-relaxation is used. After each iteration, energy and mass balances are made and, before a solution is accepted for a particular set of parameters, the energy and mass balance errors, together with the reversal condition, must be satisfied to a specified accuracy. The energy balance error is determined from the difference between the hot-fluid and the cold-fluid enthalpy changes compared to the difference between the hot-fluid and the cold-fluid inlet enthalpies. The mass balance error is determined similarly.

The accuracy of the results calculated by this method depends on the error criterion as well as on the number of subdivisions. The error of 0.05 percent for the convergence conditions, which is used for the present calculations, together with the number of subdivisions $N_r = N_h = N_c = 16$, gives the calculated efficiencies, accurate to three significant figures.

The uneven spacings in the τ-direction are determined according to

$$\Delta\tau_h(j) = (\mathcal{H}_h)^j / \sum_{k=1}^{N_h} (\mathcal{H}_h)^k \text{ and } \Delta\tau_c(g) = (\mathcal{H}_c)^g / \sum_{k=1}^{N_c} (\mathcal{H}_c)^k.$$

Results

In studying how the matrix heat and moisture capacities influence the heat and mass transfer, the results are evaluated for the following inlet air conditions:

$$t_{h1} = 40°\text{C}, \varphi_{h1} = 0.30 \text{ for the hot air and}$$

$$t_{c1} = 20°\text{C}, \varphi_{c1} = 0.70 \text{ for the cold air}$$

with the atmospheric pressure $p_t = 101.3$ kPa.

Silica gel is chosen as adsorbent material (mass fraction α_a) and the adsorption isotherm is assumed to be linear within the actual relative humidity range according to

$$\varphi_a = w/0.55.$$

The heat of adsorption is assumed constant within the actual temperature and humidity ranges and is taken to be $r_{ad} = 2600$ kJ/kg. The Lewis relation $\phi = 1$, based on the heat and mass transfer analogy, is assumed to be valid for the air-water-silica gel system. Furthermore, the nondimensional parameters are chosen $W_c/W_h = 1$, $N_{tu,0} = 5$, $\Lambda = 0$, $(\beta_x A)^+ = A_k{}^+ = 1$ in studying the influence of the heat capacity rate ratio C_r/C_n and the mass flow rate ratio W_a/W_n. Since the specific heat of silica gel is nearly equal to the specific heat of air, the relation $(W_a/W_n)/(C_r/C_n) = 1$ is approximately valid for silica gel as matrix material. In order to obtain lower mass flow rate ratios than heat capacity rate ratios with silica gel as adsorbent, the matrix must contain a nonhygroscopic material (mass fraction α_b) besides the silica gel. No solid supporter (k) is included.

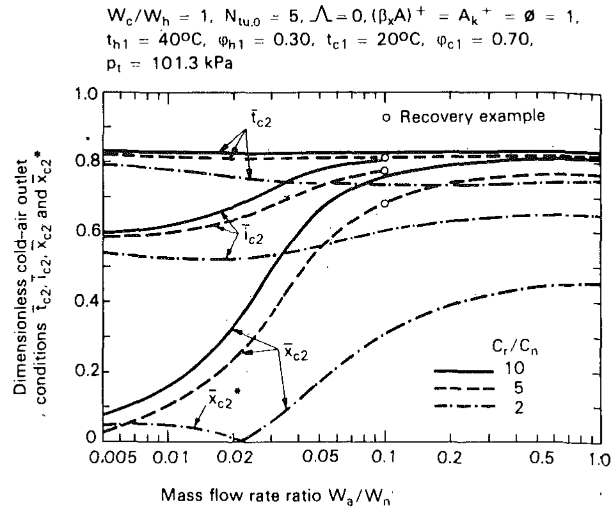

Fig. 3 Outlet conditions of cold air for different matrix heat and moisture capacities giving recovery, with silica gel as adsorbent

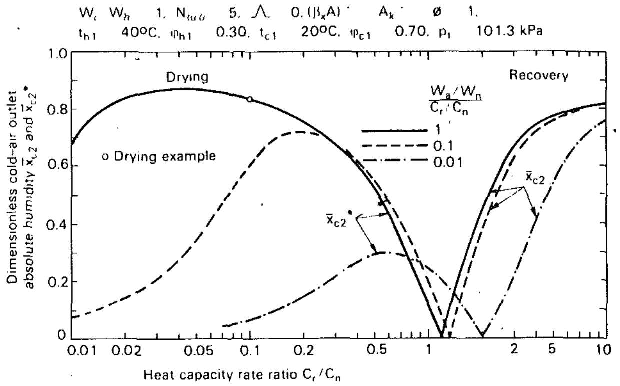

Fig. 4 Outlet absolute humidity of cold air for different matrix heat and moisture capacities giving both recovery and drying, with silica gel as adsorbent

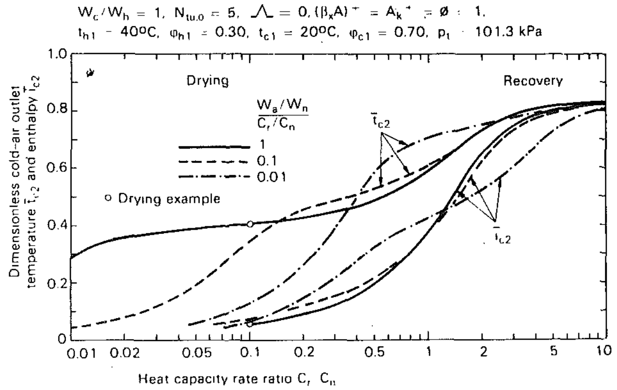

Fig. 5 Outlet temperature and enthalpy of cold air for different matrix heat and moisture capacities giving both recovery and drying, with silica gel as adsorbent

The mean cold-air temperature, absolute humidity and enthalpy at the outlet are given in Fig. 3–5 for different matrix capacities. These parameters are represented in dimensionless form by

$$\bar{z}_{c2} = (z_{c2} - z_{c1})/(z_{h1} - z_{c1}) \text{ and } \bar{z}_{h2} = (z_{h1} - z_{h2})/(z_{h1} - z_{c1}),$$

where z stands for t, x, and i, and the average values for z_{c2} and z_{h2} are calculated from

$$z_2 = \frac{1}{\tau} \sum_{k=1}^{N} z(N_r + 1, k)\Delta\tau(k).$$

For the total heat regenerator, these dimensionless temperatures, absolute humidities and enthalpies are equal to ordinary defined efficiencies on the cold-fluid side.

For the regenerative dehumidifier, the dimensionless enthalpy is equal to the enthalpy efficiency. However, the mean cold-air absolute humidity at the outlet will be defined in a more proper way for drying processes by

$$\bar{x}_{c2}^* = (x_{c2} - x_{c1})/(x_{h1}^* - x_{c1}),$$

where x_{h1}^* represents the lowest attainable absolute humidity on drying, which corresponds to the moist air condition (i_{c1}, φ_{h1}).

This dimensionless absolute humidity $\bar{x}_{c2}^*$ can be considered as a drying efficiency. The ordinary temperature efficiency definition is improper on drying, since the adsorption heat effects the air temperature change, but is not transferred by the rotor matrix as on recovery.

From Fig. 3, it is clear how the heat and moisture recovery in a total heat regenerator varies with the mass flow rate ratio for constant heat capacity rate ratio. The temperature efficiency is almost constant at high matrix heat capacities and decreases somewhat with increasing moisture recovery at lower heat capacities. The humidity efficiency decreases with both heat and moisture capacities and the moisture recovery changes into drying at low heat capacities.

In Fig. 4, the dimensionless mean absolute humidity at the outlet on the cold-fluid side (or the humidity efficiency) is presented as a function of the matrix heat capacity for constant values of the ratio between moisture and heat capacities. This chart will simulate variable times for one cycle, i.e. variable rotational speeds for rotary exchangers. It appears from the figure that moisture recovery will change into drying at heat capacity rate ratios of about 1 to 2, depending on the moisture capacity. At lower heat capacities the drying humidity efficiency will increase up to an optimum value, after which it will decrease again. The optimum value increases in magnitude with increasing moisture capacity. For constant moisture capacity on the other hand, the drying humidity efficiency increases with decreasing heat capacity without any optimum value. Corresponding outlet temperatures and enthalpies (or enthalpy efficiencies) are given in Fig. 5, from which it can be seen that the outlet temperature decreases slowly with decreasing matrix heat capacity, when the drying process starts, since the adsorption heat raises the temperature on the cold-fluid side.

These results in Fig. 3–5 for silica gel can be valid for other adsorbents with linear adsorption isotherms by correcting the mass flow rate ratio W_a/W_n with respect to the adsorption isotherm constant. The calculations have been made with the number of subdivisions $N_r = N_h = N_c = 8$ and uneven spacings with values of $\mathcal{H}_h$ and $\mathcal{H}_c$ between 1 and 2.

One recovering and one drying example have been selected to study the temperature and humidity distributions within the total regenerator and dehumidifier respectively. The recovery example, which is marked in Fig. 3 with $C_r/C_n = 5$, $W_a/W_n = 0.1$ and the remaining data as above, has been calculated with $N_r = N_h = N_c = 16$ and even spacings ($\mathcal{H}_h = \mathcal{H}_c = 1$). The temperature efficiency becomes $\bar{t}_{c2} = \bar{t}_{h2} = 0.813$ $(c_{pc}/c_{ph} = 1)$ and the humidity efficiency $\bar{x}_{c2} = \bar{x}_{h2} = 0.678$. The corresponding temperature efficiency for no mass transfer with $W_a/W_n = 0$ is 0.8289 [10]. Greater values of W_a/W_n and C_r/C_n give humidity efficiencies practically as high as the temperature efficiency.

The drying example, which is marked in Fig. 4, with $C_r/C_n = 0.1$ and $W_a/W_n = 0.1$ and the remaining data as above, has been evaluated with $N_r = N_h = N_c = 16$ and uneven spacings ($\mathcal{H}_h = \mathcal{H}_c = 1.3$). The humidity efficiency for drying becomes $\bar{x}_{c2}^* = 0.834$ and the enthalpy efficiency $\bar{i}_{c2} = \bar{i}_{h2} = 0.051$.

Figs. 6 and 7 show the cold-air temperature and absolute humidity

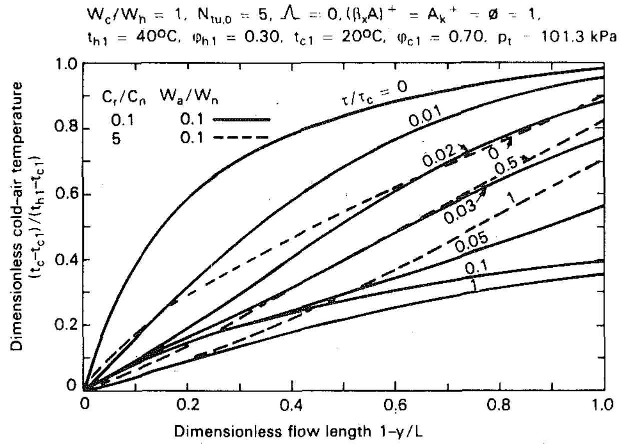

Fig. 6 Temperature distribution of cold air for recovery and drying examples, with silica gel as adsorbent

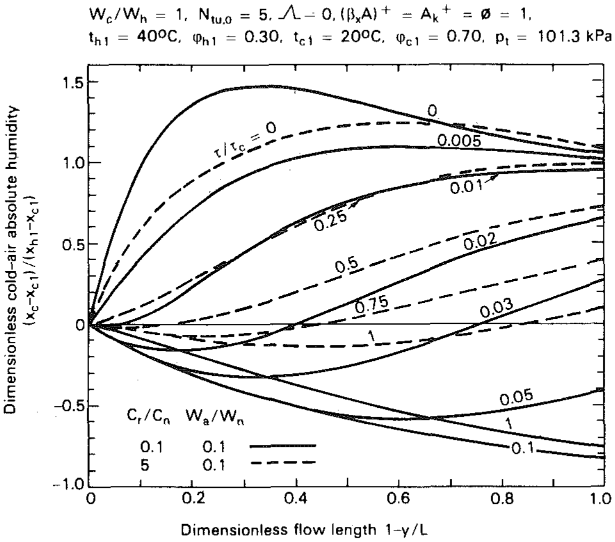

Fig. 7 Absolute humidity distribution of cold air for recovery and drying examples, with silica gel as adsorbent

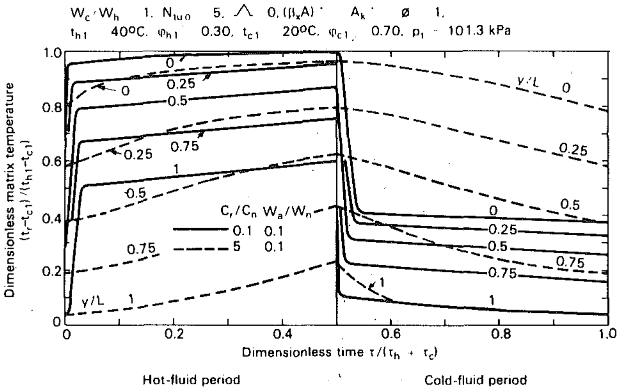

Fig. 8 Matrix temperature distribution for recovery and drying examples, with silica gel as adsorbent

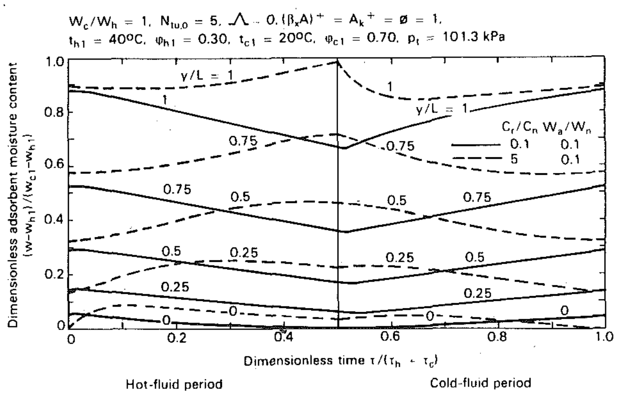

Fig. 9 Adsorbent moisture content distribution for recovery and drying examples, with silica gel as adsorbent

distributions in dimensionless form. Figs. 8 and 9 show the matrix temperature and adsorbent moisture content distributions. In the drying case, the matrix temperature variation from one period to the other is very great due to the low matrix heat capacity. The low heat capacity results also in steep matrix temperature gradients at the beginning of each period. The adsorbent moisture content is fairly small in this example, since the matrix moisture capacity is rather high. Because of these temperature and moisture content variations, the cold air will be moistened at the beginning of the cold-fluid period, but in any case dried during the main part of the period. In the recovery case on the other hand, the matrix temperature variation is fairly small and rather linear throughout the period due to the high matrix heat capacity. This small temperature variation results in moistening of the cold air during the main part of the cold-fluid period.

Conclusions

The presented method for analyzing the heat and mass transfer in regenerators with hygroscopic matrix materials is completely general for the problem of steady-state performance in respect to fluid and matrix capacity rates, heat and mass transfer coefficients, transfer areas, longitudinal heat conduction, adsorption isotherm, and inlet gas conditions.

The method has turned out to be applicable in calculating cyclic sorption operations, such as adsorption drying and heat and mass recovery processes.

Acknowledgment

The author wishes to express his thanks to AB Svenska Fläktfabriken, Jönköping, Sweden, for permission to publish this paper and to Dr. O. Strindehag, the head of the Research and Development Laboratory, for many valuable discussions.

References

1 Henry, P. S. H., "Diffusion in Absorbing Media," *Proc. Roy. Soc.*, Vol. 171, 1939, pp 215–241.

2 Cassie, A. B. D., "Theory of Propagation of Temperature Change-Part II," *Trans. Faraday Soc.*, Vol. 36, 1940, pp. 453–458.

3 Amundson, N. R., Aris, R. and Swanson, R., "On Simple Exchange Waves in Fixed Beds," *Proc. Roy. Soc.*, Vol. 286, 1965, pp. 129–139.

4 Nordon, P., "A Model for Mass Transfer in Beds of Wool Fibres," *Int. J. Heat Mass Transfer*, Vol. 7, 1964, pp. 639–651.

5 Carter, J. W., "A Numerical Method for Prediction of Adiabatic Adsorption in Fixed Beds," *Trans. Instn. Chem. Engrs*, Vol. 44, 1966, pp. T253–T259.

6 Bullock, C. E. and Threlkeld, J. L., "Dehumidification of Moist Air by Adiabatic Adsorption-Part I," *Trans. ASHRAE*, Vol. 72, 1966, pp. 301–313.

7 Chi, C. W. and Wasan, D. T., "Fixed Bed Adsorption Drying," *AIChE Journal*, Vol. 16, 1970, pp. 23–31

8 Chase, C. A., Gidaspow, D. and Peck, R. E., "Adiabatic Adsorption in a Regenerator," *Chem. Engng Prog. Symp.*, Vol. 65, No. 96, 1969, pp. 34–47.

9 Maclaine-Cross, I. L. and Banks, P. J., "Coupled Heat and Mass Transfer in Regenerators-Prediction using an Analogy with Heat Transfer," *Int. J. Heat Mass Transfer*, Vol. 15, 1972, pp. 1225–1242.

10 Holmberg, R. B., "Heat and Mass Transfer in Rotary Heat Exchangers with Nonhygroscopic Rotor Materials," *TRANS. J. Heat Transfer*, Vol. 99, 1977, pp. 196–202.

11 ASHRAE, *Handbook of Fundamentals*, ASHRAE Inc., New York, 1972.

N. Cur
E. M. Sparrow
Fellow ASME

Department of Mechanical Engineering,
University of Minnesota,
Minneapolis, Minn. 55455

Measurements of Developing and Fully Developed Heat Transfer Coefficients along a Periodically Interrupted Surface

The heat transfer and pressure drop characteristics for an array of colinear, equally spaced plates aligned parallel to the flow in a flat rectangular duct have been studied experimentally. The periodic interruptions (i.e., the gaps between the plates) preclude the attainment of hydrodynamic and thermal development of the type that is encountered in conventional duct flows, but a periodic fully developed regime can exist. Measurements of the heat transfer coefficients for the successive plates of the array affirmed the periodically developed regime and demonstrated the developmental pattern leading to its attainment. The thickness of the plates in the array was varied parametrically. In general, the Nusselt number increases with plate thickness. Thickness-related increases in the fully developed Nusselt number of up to 65 percent were encountered. The presence of the interruptions serves to augment the heat transfer coefficients. In the fully turbulent regime, the heat transfer coefficients are on the order of twice those for a conventional duct flow. The pressure drop also increases with the plate thickness.

Introduction

The use of periodic interruptions in plane, flow-aligned heat transfer surfaces is a commonly used technique for increasing the heat transfer coefficients in heat exchange devices. These surfaces may be viewed as a succession of colinear plate segments oriented parallel to the flow, with gaps between the successive plates. Alternatively, they may be regarded as periodically interrupted walls, and the designation, interrupted-wall passages, will be employed here to describe flow passages bounded by such surfaces. Practical examples of periodically interrupted heat transfer surfaces include strip fins and offset fins.

As the flow traverses the length of an interruption, both the velocity and temperature distributions tend to become more uniform because of the absence of the constraints imposed by wall friction and heat transfer. The degree of velocity and temperature homogenization attained by the flow depends on the length of the interruption. When the partially (or fully) homogenized flow encounters the segment of heat transfer surface situated just downstream of the interruption, new velocity and thermal boundary layers develop. Since a developing boundary layer flow is characterized by much higher heat transfer coefficients than a fully developed duct flow, the desired enhancement is achieved. Another factor which contributes to the enhancement is the wake which is shed from the trailing edge of each segment and which washes segments that are situated downstream. The heat transfer augmentation is accompanied by higher pressure drops brought about by the relatively large boundary layer shear and by wake dissipation.

The shapes of the interrupted-wall passages that are employed in actual heat exchangers are quite complex as witnessed, for example, by the Kays-London compilation [1]. As a consequence, information about the heat transfer—pressure drop characteristics of interrupted-wall passages has, in the main, been confined to overall coefficients obtained from tests on either actual or large-scale models of heat exchangers (e.g., [1–5]). While this information is of direct applicability in the design of certain specific types of interrupted-wall heat exchangers, it does not provide insights into the fundamental processes that occur within the individual flow passages.

The fundamental studies of interrupted surfaces which have appeared in the literature have been limited to a pair of colinear plates aligned parallel to the flow direction. Heat transfer results encompassing variations in plate thickness, inter-plate spacing, and Reynolds number are reported in [6] and [7], where heat transfer and mass transfer measurements were made, respectively. Flow visualization, based both on dye injection and the hydrogen bubble technique, was employed in [8] to reveal the nature of the wake in the inter-plate gap. When viewed in the context of duct-flow research, the experiments performed in [6–8] can be regarded as entrance region studies. This is because the velocity fields adjacent to the two plates are quite different.

If, instead of two plates, there were an array of numerous, equally spaced colinear plates aligned parallel to the flow, then, at sufficient

---

Contributed by the Heat Transfer Division for publication in the JOURNAL OF HEAT TRANSFER. Manuscript received by the Heat Transfer Division May 26, 1978.

downstream distances, a special type of fully developed regime would be established. This regime is characterized by identical developing boundary layers on successive plates and, in addition, by identical flow fields in the successive inter-plate spaces. Such a fully developed regime is fundamentally different from the regime of unchanging velocity profiles that characterizes fully developed duct flows. The new type of regime has been referred to in [9] as periodic fully developed and its properties were employed there as the basis for a laminar flow analysis. The periodic fully developed flow admits a periodic thermally developed regime. If the successive plates are at the same uniform temperature, a suitably defined per-plate heat transfer coefficient should become constant at sufficient downstream distances.

The thermal development and ultimate attainment of the periodic fully developed regime has not yet been experimentally investigated for interrupted-wall passages. Such an investigation has been undertaken here for a colinear array of plates that is shown in photographic view in Fig. 1. As seen there, the multi-plate array is situated in a flat rectangular duct (the top wall of the test section has been removed to reveal the plates). To facilitate the research, mass transfer experiments were performed rather than direct heat transfer experiments, and the mass transfer results were converted to heat transfer results via the well-known analogy between the two processes. The naphthalene sublimation technique was used for the mass transfer experiments and, correspondingly, each test plate consisted of a thin naphthalene coating which enveloped a metal substrate. According to the heat/mass transfer analogy, the thermal boundary condition for heat transfer plates that would correspond to the plates of the present mass transfer experiments is uniform wall temperature. Air was the working fluid for the experiments.

Measured mass transfer rates for each plate in the array enabled the evaluation of per-plate transfer coefficients and Sherwood numbers (the Sherwood number is analogous to the Nusselt number). The stream-wise distribution of these results portrays the thermal development and the attainment of the periodically developed regime. The entrance region and fully developed results were obtained for Reynolds numbers ranging from about 1000 to 1400.

A second focus of the research was to investigate the influence of plate thickness on the heat transfer characteristics. The motivation for this phase of the investigation was the realization that the ratios of plate thickness to length encountered in real devices such as compact heat exchangers are not negligibly small. This is because in the general shrinking of dimensions to attain compactness, the plate thickness cannot be reduced below a basic minimum needed for structural integrity. Experiments were carried out for ratios of thickness to plate length t/L of 0.04, 0.08, and 0.12, which encompasses the practical range. Also, in keeping with practice, the inter-plate spacing was made equal to the plate length.

Since the number of wall segments deployed along the length of a flow passage in an interrupted-wall heat exchange device is generally very large, fully developed conditions may prevail in a significant portion of the device. The fully developed heat transfer coefficients are, therefore, of particular interest. Correspondingly, special attention is given here to the variations of the fully developed Sherwood (Nusselt) number with the Reynolds number and with the thickness-length ratio t/L.

In addition to the mass transfer studies, axial pressure distributions were measured to determine the pressure drop associated with the presence of the multi-plate array. These results are made dimensionless with respect to the velocity head and are tabulated as a function of the Reynolds number and the t/L ratio.

The Experiments

The Naphthalene Test Plates. Mass transfer coefficients for each plate of the colinear array were deduced from measurements of of the sublimation rate of naphthalene vapor from the plate surface into the flowing air stream. Each test plate was a composite consisting of a metal core sandwiched between thin layers of naphthalene. The fabrication of the test plates involves both casting and machining operations, the details of which are available in [10]. Only a general description of the fabrication procedures will be presented here.

The basis of each test element was a mild steel plate, rectangular in shape, with dimensions 25.4 × 152.4 mm (1 × 6 in.). A naphthalene coating of dimensions 25.4 × 133.4 mm (1 × 5.25 in.) was applied to each surface of the steel plate. The uncoated portions were situated at the extremities of the plate width and, as will be explained later, were seated in the duct wall to position and support the plate during the experiment. The edges of the steel plate were left uncoated, and the forward and aft edges were squared off in order to present a blunt face to the flow.

Three sets of test plates were prepared, respectively with overall thicknesses of 1.01, 2.03, and 3.04 mm (0.040, 0.080, and 0.12 in.). Since all of the plates were 25.4 mm (1 in.) long in the streamwise direction, the corresponding thickness-length ratios t/L are 0.040, 0.080, and 0.12. For all cases, the thickness of naphthalene coating applied to each face of the metal substrate was maintained at approximately 0.15 mm (0.006 in.). The metal substrates used for the three sets of test plates had thicknesses of 0.71, 1.73, and 2.74 mm (0.028, 0.068, and 0.108 in.), respectively.

In preparation for the coating process, two steps were taken to enhance the adhesion of the naphthalene to the substrate. One of these was a light sandblasting of the surface and the second was the drilling of a closely spaced array of holes all around the perimeter of the area to be coated. These holes permitted a throughflow of molten naphthalene during the casting process, thereby providing a firm anchoring of the coating.

For the casting, an open-topped mold was formed with the steel substrate as the base surface and metal bars as the side walls. Molten naphthalene poured into the mold cavity to a depth of about 2.5 mm (0.1 in.) was allowed to solidify, after which the substrate was turned over and a poured coating was applied to the other surface. Subsequent to casting, each coating was machined to the desired thickness (~0.15 mm) with a vertical milling machine equipped with a fly cutter attachment. The surface quality obtained from the machining operation was excellent, as witnessed both by the glass-like smoothness sensed by touch and by observed reflected highlights. All aspects of the casting and machining procedure were performed under strict conditions of cleanliness in order to avoid contamination of the naphthalene coating.

Experimental Apparatus. The description of the experimental apparatus is facilitated by making reference to Fig. 1. The main

Nomenclature

A = sublimation surface area of a plate
D_e = equivalent diameter, equation (4)
$\mathcal{D}$ = naphthalene-air diffusion coefficient
h = distance between plate surface and duct wall
K_i = mass transfer coefficient for plate i, equation (1)
K_p = pressure loss coefficient, equation (6)
L = plate length
$\dot{M}_i$ = rate of mass transfer at plate i
$\dot{m}_i$ = rate of mass transfer per unit area at plate i
Nu = Nusselt number at a given plate
Pr = Prandtl number
Δp_{array} = net pressure drop for array, illustrated in Fig. 2
Re = Reynolds number, equation (7)
Sc = Schmidt number, $\nu/\mathcal{D}$
Sh = Sherwood number at a given plate, equation (3)
t = plate thickness
V = mean velocity, equation (5)
$\dot{W}$ = rate of flow through duct
w = plate width
x = streamwise coordinate
ν = kinematic viscosity
ρ_{nb} = uniform bulk concentration of naphthalene vapor
ρ_{nw} = concentration of naphthalene vapor at plate surface
$\rho_n{}^*$ = reference concentration of naphthalene vapor
ρ = air density

Subscript

i = pertaining to plate i

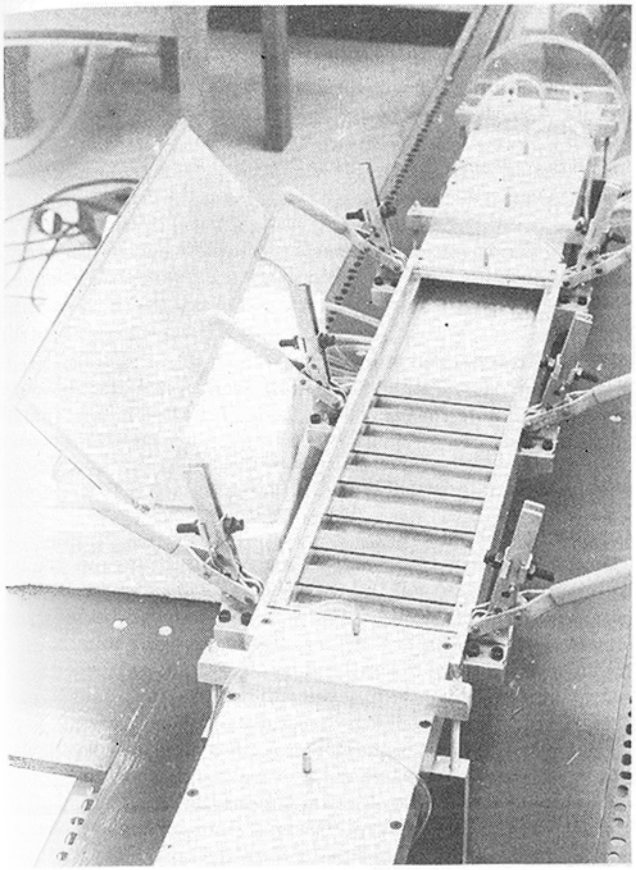

Fig. 1 Photograph of the test section with the upper wall removed

component of the apparatus was a flat rectangular duct whose upstream, middle, and downstream sections respectively served as the hydrodynamic development length, the test section, and the hydrodynamic redevelopment length. As shown in the figure, the duct was designed so that the mid-section of its upper wall could be readily removed to provide easy access to the test section (in the photograph, the removed section of wall is situated just to the left of the open top of the duct). Eight naphthalene-coated plates were employed in each of the final data runs, and these are shown in place in the photograph (most of the first plate is obscured because of the oblique angle of view).

The duct was of 5:1 cross-sectional aspect ratio, dimensions 133.5 × 26.7 mm (5.25 × 1.05 in.), with an axial length of 62 equivalent diameters—37 diameters for the development section, nine for the test section, and the remainder for redevelopment. It was part of an open-loop airflow system which drew air from the laboratory room and which included, along the path of flow, the duct, a rectangular-to-circular transition section, an orifice flow-metering station and control valve, and the blower. The latter was situated in a service corridor outside the laboratory, and the blower-heated, naphthalene-laden air was exhausted at the roof of the building. This arrangement ensured that the air drawn into the duct was free of naphthalene vapor and was at a uniform temperature whose level (~20°C) could be set by the controls of the laboratory room.

In addition to the removable top wall, other features were incorporated into the test section design to enable the experiment to be set up and taken apart rapidly and conveniently. This concern about minimizing the time for assembly and disassembly of the test section stems from the need to avoid extraneous sublimation, i.e., sublimation that is over and above that which occurs during the timed period of forced convection airflow in the duct.

The arrangement employed for holding and positioning the naphthalene test plates was designed with the foregoing considerations in mind. The removable hold-down bars, seen in Fig. 1 in place along the side walls of the test section, were periodically slotted along their lower surfaces to cradle the uncoated extremities of the plates. In addition, locating pins, which protruded upward from the rails supporting the plates, positively positioned both the plates and the hold-down bars. Thus, neither screws nor other threaded fasteners were used in the set-up of the experiment. The closure of the removable wall of the test section was accomplished with quick-acting clamps (see Fig. 1). Because of these features, the test section could be assembled or disassembled in a few minutes.

For the pressure measurements, 23 taps were installed along the axial centerline of the upper wall of the duct. Some of these taps and their associated plastic tubing can be seen in Fig. 1. The axial positions of the taps will be evident from a representative pressure distribution that will be presented later. The pressure signals were passed through a specially designed selector switch whose output was sensed by a Baratron capacitance-type pressure meter with a smallest scale reading of 0.001 mm Hg. One of two calibrated orifices was used for flow metering, respectively for the high and low Reynolds number ranges.

The mass of the naphthalene-coated plates was measured both before and after each data run with a Mettler analytical balance having a capacity of 200 g and a smallest scale reading of 0.1 mg.

Experimental Procedure. Preliminary data runs had indicated that thermally developed conditions were attained with an eight-plate array, and all final runs were made with such arrays. Correspondingly, the naphthalene casting and machining operations were carried out for batches of eight plates. Once the coatings had been applied, the plates were sandwiched between glass and the whole was wrapped with plastic. Then, the wrapped plates were placed in the laboratory to attain thermal equilibrium with the surroundings.

Immediately before the initiation of a data run, the mass of each participating plate was measured with the Mettler balance. The test section was then assembled and air, drawn from the laboratory room by the downstream-positioned blower, was passed through the duct. The duration of a data run was selected to keep the change of the mean thickness of each coating below 0.025 mm (0.001 in.) with the typical change being 0.018 mm (0.0007 in.). Run times ranged from 20 min to two hr, depending on the Reynolds number. Typically, the mass loss per plate was in the 100 to 150 mg range.

To conclude a run, the air flow was terminated, the test section disassembled, and the mass of each plate measured. To avoid potential uncertainties associated with start-up and shut-down transients, the blower was kept running steadily both prior to the initiation and after the conclusion of the run; the activation (or deactivation) of the test section flow was accomplished by deft coupling (or decoupling) of a flexible plastic tube to (from) a metal tube downstream of the duct.

To correct for possible extraneous sublimation during assembly, disassembly, and weighing, each data run was followed by a repetition of all phases of the run but without the period of air flow through the test section. Any mass loss measured during the non air-flow run was subtracted from that for the actual run. Typically, the correction was about two to four percent.

Data Reduction

The data reduction was aimed at evaluating both the mass transfer coefficient (and its dimensionless counterpart, the Sherwood number) at each plate of the array and the pressure loss coefficient for the array. The mass transfer rate $\dot{M}_i$ at plate i was obtained from the measured mass loss and the duration time of the run and, with this, the unit-area transfer rate $\dot{m}_i = \dot{M}_i/A$ was evaluated, where A is the total naphthalene surface area per plate. The per-plate mass transfer coefficient K_i is the ratio of the unit-area transfer rate $\dot{m}_i$ to the concentration difference that drives the mass transfer. If ρ_{nw} and $\rho_n{}^*$ respectively denote the concentrations (i.e., partial densities) of naphthalene vapor at the plate surface and at a reference state, then the driving potential is $(\rho_{nw} - \rho_n{}^*)_i$. The wall concentration ρ_{nw} depends only on temperature and is constant along each plate and has the same value for all plates. It was evaluated from the Sogin vapor pressure—temperature relation [10].

The reference concentration $(\rho_n^*)_i$ can be interpreted variously, especially in view of the complexity of the participating transfer processes. However, from the practical side, it is difficult to see how to evaluate a reference concentration without assuming that the flow is well mixed. The model to be adopted here is that the flow becomes well mixed as it traverses the inter-plate gap and arrives at the leading edge of plate i with a uniform bulk concentration $(\rho_{nb})_i$. A concentration boundary layer develops along the length of plate i, and $(\rho_{nb})_i$ plays the role of the free stream concentration.

We associate $(\rho_{nb})_i$ with $(\rho_n^*)_i$ and write

$$K_i = \frac{\dot{m}_i}{\rho_{nw} - (\rho_{nb})_i} \tag{1}$$

where the concentration $(\rho_{nb})_i$ was evaluated from

$$(\rho_{nb})_i = (\rho_{nb})_0 + \sum_{j=1}^{i-1} \dot{M}_j/Q \tag{2}$$

The quantity Q is the volume flow (a constant throughout the test section) and $(\rho_{nb})_0$ is the naphthalene concentration of the flow approaching the first plate (equal to zero in the present experiments).

The Sherwood number Sh provides a dimensionless representation of the mass transfer coefficient, that is,

$$\mathrm{Sh}_i = K_i D_e/\mathcal{D} \tag{3}$$

The naphthalene-air diffusion coefficient $\mathcal{D}$ was evaluated via the Schmidt number $\mathrm{Sc} = \nu/\mathcal{D}$, where $\mathrm{Sc} = 2.5$ [10] and ν is the kinematic viscosity of pure air.

The equivalent diameter was referred to the flow space above or below a plate. If h represents the distance (i.e., the height) between the plate surface and the duct wall and w is the duct width, then

$$D_e = 4wh/(2w + 2h) \tag{4}$$

For the evaluation of the pressure drop caused by the presence of the multi-plate array, a working graph such as Fig. 2 was prepared for each case (i.e., each plate thickness and Reynolds number). In each of these figures, the static pressure is plotted against the dimensionless axial coordinate x/L, where L is the plate length. The axial stations corresponding to the beginning and the end of the multi-plate array are indicated in the figure. As can be seen from the linear pressure distribution, the flow upstream of the array is hydrodynamically developed. Furthermore, hydrodynamically developed flow is reestablished downstream of the array. The slopes of the upstream and downstream pressure distributions are the same.

In the absence of the array, the upstream and downstream pressure distributions would lie on a continuous straight line. The vertical displacement of the upstream and downstream lines that is in evidence in Fig. 2 is, therefore, due to the presence of the array and is denoted by $\Delta p_{\mathrm{array}}$. Specifically, $\Delta p_{\mathrm{array}}$ is the pressure drop that is over and above that which would otherwise exist in the duct in the absence of the array. For a dimensionless representation of the array pressure drop, the velocity head $\frac{1}{2}\rho V^2$ is employed, where V is the mean velocity in the flow space above or below a plate. If $\dot{W}$ is the rate of mass flow through the duct, then

$$V = (\dot{W}/2)/\rho hw \tag{5}$$

With this, the dimensionless pressure loss coefficient for the array was evaluated as

$$K_p = \Delta p_{\mathrm{array}}/\tfrac{1}{2}\rho V^2 \tag{6}$$

The mass transfer and pressure drop results will be parameterized by the Reynolds number corresponding to the flow space above or below a plate. With the equivalent diameter from equation (4) and the mean velocity from equation (5), the Reynolds number is

$$\mathrm{Re} = VD_e/\nu \tag{7}$$

Results and Discussion

Heat/Mass Transfer. With the aim of generalizing the results, the quantity $\mathrm{Sh}/\mathrm{Sc}^{0.4}$ will be presented rather than Sh itself. Furthermore, in view of the analogy between heat and mass transfer, the numerical values of $\mathrm{Sh}/\mathrm{Sc}^{0.4}$ will be regarded as being equal to $\mathrm{Nu}/\mathrm{Pr}^{0.4}$. The ordinates of the forthcoming figures will be labelled with both quantities, and in the discussion the phrases heat transfer and mass transfer will be used interchangeably.

The motivation for using the aforementioned presentation variables is to extend the range of applicability of the results, which correspond to measurements for $\mathrm{Sc} = 2.5$, to situations characterized by other Prandtl (or Schmidt) numbers. The most common applications situation is heat transfer to (or from) air, which is characterized by $\mathrm{Pr} = 0.7$. In the range between $\mathrm{Pr} = 0.7$ and 2.5, the Prandtl number dependence evidenced by the most recent duct flow correlations [12] and [13] favor the 0.4 power rather than the 1/3 power implicit in the Colburn j-factor.

The plate-by-plate development of the heat transfer coefficient is presented in Fig. 3, where $\mathrm{Nu}/\mathrm{Pr}^{0.4}$ and $\mathrm{Sh}/\mathrm{Sc}^{0.4}$ are plotted as a function of the plate number (1 and 8 denote the most upstream and most downstream plates respectively). The figure contains four sets of data, each of which corresponds to a given Reynolds number in the range from 13,600 (upper part of graph) to 1,100 (lower part of graph).

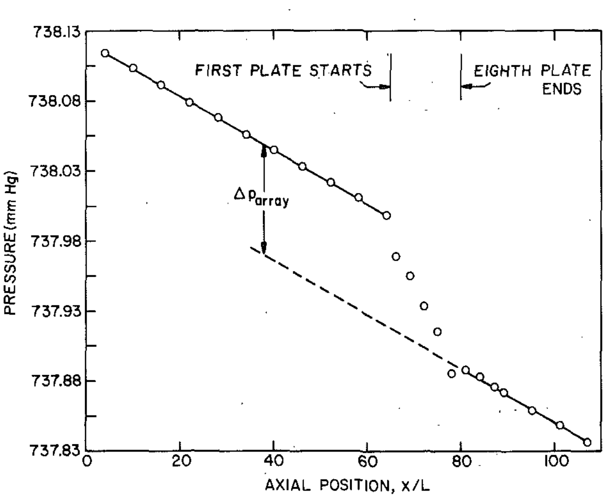

Fig. 2 Representative axial pressure distribution (Re = 8,200, t/L = 0.08)

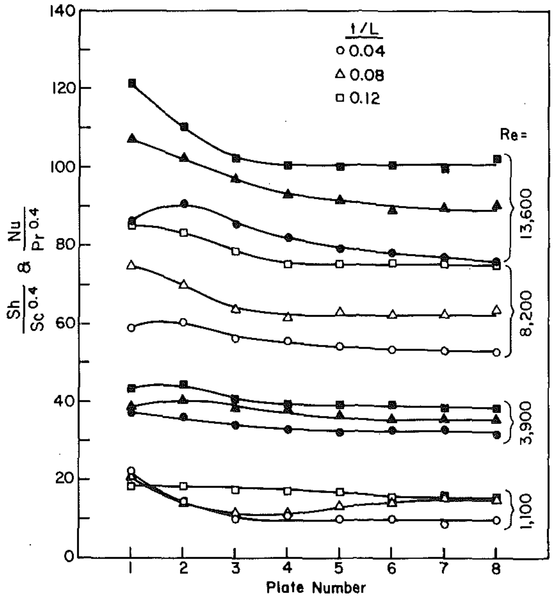

Fig. 3 Variation of the per-plate Nusselt (Sherwood) number along the length of the array

To facilitate their identification, the data points for the successive sets are alternatively blackened or unblackened. Within each set, data are given for three thickness-length ratios t/L equal to 0.04, 0.08, and 0.12.

The figure shows an orderly thermal development whereby, subsequent to the second plate, the heat transfer coefficient decreases monotonically and then attains a constant, fully developed value. Thus, in spite of the complexity of the flow, a regular periodic regime is ultimately established such that each successive plate experiences similar hydrodynamic events and similar thermal events. To the best knowledge of the authors, the results of Fig. 3 constitute the first experimental demonstration of the periodic thermally developed regime for interrupted-wall passages.

The plate-to-plate variations of the Nusselt (Sherwood) number exhibit a degree of regularity (albeit of a complex nature). At the two higher Reynolds numbers, the thermal development becomes less rapid as the plate thickness decreases, and this trend persists in an overall sense for the third Reynolds number. For the lowest Reynolds number, a different pattern is in evidence. It appears that the flow passes from turbulent to transitional to laminar with decreasing plate thickness. The transitional distribution curve for $t/L = 0.08$ was found to be highly reproducible, so that data from a pair of repeated runs could not be distinguished from each other within the scale of the figure. In general, thermal development is attained at or prior to the eighth plate for the cases studied here.[1]

Of some interest is the fact that the second-plate Nusselt numbers are not necessarily lower than those for the first plate. This may happen when the turbulence due to the wake shed by the first plate is especially strong. In [8], studies of the character of the wake between two co-linear plates revealed a turbulent resonance phenomenon which depended in a complex manner on plate thickness, inter-plate spacing, and velocity.

An overall inspection of Fig. 3 shows that both the Reynolds number and the plate thickness affect the magnitude of the Nusselt number. Since the fully developed values are the ones that are most relevant to practice, attention will now be focused on how they depend on Reynolds number and plate thickness.

The influence of plate thickness is presented in Fig. 4, where the fully developed Nusselt number is plotted as a function of the thickness-to-length ratio t/L for parametric values of the Reynolds number. The figure shows that, in general, the Nusselt number increases with increasing plate thickness. The increase is most dramatic at the lowest Reynolds number as a result of the thickness-induced change in flow regime (i.e., the $t/L = 0.04$ plates are in the laminar regime, and the $t/L = 0.08$ and 0.12 plates are in the turbulent regime). With this laminar-turbulent transition, there is an increase of 65 percent in the Nusselt number as t/L varies from 0.04 to 0.12 at the lowest Reynolds number. If, however, the flow had been turbulent for all three plate thicknesses (dashed line), the thickness effect would be only about 12 percent.

At higher Reynolds numbers, the flow is turbulent for all of the plate thicknesses investigated here, so that transition is not a factor. The thickness-related increases in the Nusselt number are about 20 percent for Re = 3900 and about 40 percent for Re = 8200 and 13,600.

From the foregoing remarks, it is evident that the extent of the thickness effect depends on the Reynolds number at lower Re, but becomes independent of the Reynolds number at higher Re where, presumably, the turbulence is fully developed. Furthermore, aside from the triggering of transition, the thickness effects are smaller at lower Reynolds numbers than at higher Reynolds numbers. All of these trends are physically plausible.

Whereas direct comparisons of the just-identified thickness effects with literature information cannot be made because of differences in geometrical and thermal configurations, it is relevant to make all possible comparisons with regard to trend. The only available Nusselt number—plate thickness correlation for any configuration remotely resembling that studied here is that of [4], which is concerned with system-averaged Nusselt numbers for offset-fin plate-fin heat exchangers. The correlation of [4] provides partial verification of the present findings. In the low-Reynolds-number correlation (presumably laminar) of [4], the thickness effect is altogether absent, whereas in the high Reynolds number correlation (presumably turbulent) the thickness appears to a positive exponent. That exponent implies a smaller thickness effect than that found here, which may well be related to the bent and scarfed edges of the plates used in the heat exchangers that served as the basis of [4]'s correlation.

The variation of the fully developed Nusselt number with the Reynolds number is plotted in Fig. 5 on logarithmic coordinates, with the t/L ratio serving to parameterize the data. As expected, the Nusselt number increases markedly with the Reynolds number. Within the small scatter of the data, a straight line representation appears to be adequate except at the smallest thickness. There, the rapid drop-off at the lowest Reynolds number is suggestive of laminar flow. The two uppermost curves are characterized by Reynolds number exponents in the 0.72 to 0.74 range.

The main message to be conveyed by Fig. 5 is the augmentation afforded by the interruptions. To this end, a short line segment (Re

---

[1] Indeed, at Re = 13,600 and $t/L = 0.04$, the development appears to be still in progress at the eighth plate. However, shifts of only one to two percent in the last two data points would alter the distribution curve sufficiently to give it a fully developed character.

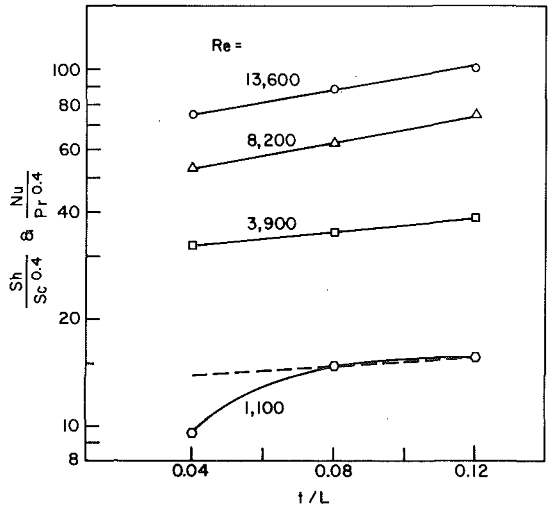

Fig. 4 **Effect of plate thickness on the fully developed Nusselt (Sherwood) number**

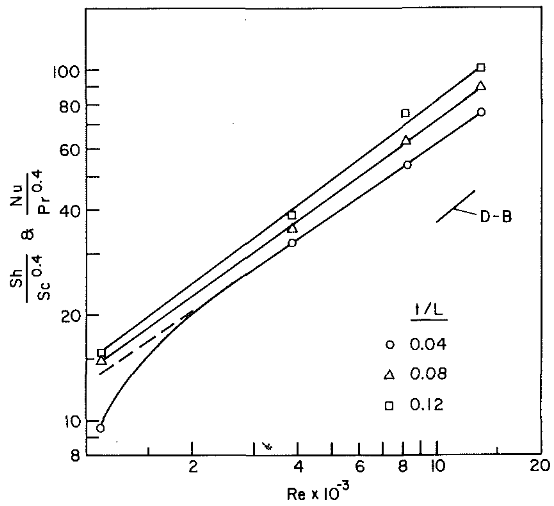

Fig. 5 **Effect of Reynolds number on the fully developed Nusselt (Sherwood) number**

> 10,000) corresponding to the Dittus-Boelter (D-B) equation has been plotted. If the D-B equation is accepted as representing the fully developed turbulent Nusselt number for a continuous-walled duct,[2] then it is seen that the presence of the interruptions gives rise to increases in Nusselt number on the order of a factor of two. This twofold increase in Nusselt number enables a given heat load to be accommodated with only half the surface area of a continuous-walled duct, thereby resulting in substantial materials savings. With regard to turbulent flow at Reynolds numbers less than 10,000, it does not appear that there is a reliable correlation equation for duct-flow Nusselt numbers which can serve as a basis for comparison. Therefore, the augmentation afforded by the interruptions cannot be estimated at this time.

Pressure Drop. The pressure loss Δp_{array} due to the presence of the multi-plate array can be expressed in dimensionless form by the loss coefficient K_p defined by equation (6). It is worth noting here that Δp_{array} is the pressure drop over and above that which would exist in the duct in the absence of the array. The experimentally determined values of K_p are listed in Table 1 for the various Reynolds numbers and thickness-length ratios that were investigated.

The tabulated results show that K_p increases with increasing plate thickness at a given Reynolds number. This is plausible because of the larger thickness-related losses both in the leading edge separation bubble and in the wake. The increase in the K_p values with thickness appears to be greater at higher Reynolds numbers. At any given thickness, the loss coefficient increases as the Reynolds number decreases. This trend is universally encountered whenever there is a significant contribution of wall friction to the pressure drop.

To provide some perspective on the magnitude of the K_p values of Table 1, it is interesting to compare them with the values of $\Delta p/{}^1\!/\!_2\rho V^2$ for fully developed flow in a rectangular duct. The comparison will be made at the highest Reynolds number of the experiments (13,600) so that the duct-flow friction factor can be taken with confidence from the Moody diagram. Furthermore, the L and D_e needed in evaluating the friction factor were respectively taken equal to the total length of the array (eight plates and seven gaps) and to the equivalent diameter of the space above or below a plate.

The $\Delta p/{}^1\!/\!_2\rho V^2$ for the duct flow were found to be 0.448, 0.464, and 0.483. From a comparison with the last column of Table 1, it is seen that the two sets of values are of similar magnitude, with the array value being lower than the duct value at the smallest thickness and vice-versa at the largest thickness. This finding is quite plausible. In the multi-plate array, the presence of the gaps diminishes the contribution of wall friction to the pressure drop, compared with that in the solid-walled duct. However, there are compensating inertial losses due to the presence of the gaps. The inertial losses increase with plate thickness, and this causes the cross-over in the comparison between the $\Delta p/{}^1\!/\!_2\rho V^2$ values for the array and the duct.

Concluding Remarks

The present experiments have demonstrated that thermally developed conditions can be established in a flow where the velocity field experiences geometrically induced periodic variations in the streamwise direction. From measurements of the Nusselt numbers of the successive plates of the multi-plate array, it was found that thermal development is attained at or prior to the eighth plate of the array.

Table 1 Pressure loss coefficient K_p for eight-plate array

	Re			
t/L	1,100	3,900	8,200	13,600
0.04	0.631	0.500	0.365	0.335
0.08	0.861	0.609	0.573	0.472
0.12	1.060	0.814	0.792	0.752

The fully developed Nusselt number increases with plate thickness. At higher Reynolds numbers, the increase was about forty percent over the range from $t/L = 0.04$ to 0.12. Even larger increases were encountered at lower Reynolds numbers owing to the triggering of transition from laminar to turbulent flow.

The presence of the interruptions was shown to bring about a significant increase in the Nusselt number compared with that for a continuous-walled duct. A comparison in the fully turbulent regime (Re > 10,000) showed the augmentation to be about a factor of two.

The dimensionless pressure drop due to the presence of the array also increases with plate thickness. At the smallest thickness, the pressure drop was less than that in a comparable continuous-walled channel, while the opposite relationship was in effect for the largest thickness.

Acknowledgment

This research was performed under the auspices of ONR contract NOOO14-76-C-0246.

References

1 Kays, W. M., and London, A. L., *Compact Heat Exchangers*, Second ed., McGraw-Hill, New York, 1964.

2 Norris, R. H., and Spofford, W. A., "High Performance Fins for Heat Transfer," Trans. ASME Vol. 64, 1942, pp. 489–496.

3 Shah, R. K., and London, A. L., "Offset Rectangular Plate-Fin Surfaces—Heat Transfer and Flow Friction Characteristics," ASME *Journal of Engineering for Power*, Vol. 90, 1968, pp. 218–228.

4 Wieting, A. R., "Empirical Correlation for Heat Transfer and Flow Friction Characteristics of Rectangular Offset-Fin Plate-Fin Heat Exchangers," ASME JOURNAL OF HEAT TRANSFER, Vol. 97, 1975, pp. 488–490.

5 Mochizuki, S., and Yoshinao, Y., "Heat Transfer and Friction Characteristics of Strip Fins," *Heat Transfer, Japanese Research*, Vol. 6, No. 3, 1977, pp. 36–59.

6 Adarkar, D. B., and Kays, W. M., "Heat Transfer in Wakes," Technical Report No. 55, Department of Mechanical Engineering, Stanford University, Stanford, Calif. 1963.

7 Cur, N., and Sparrow, E. M., "Experiments on Heat Transfer and Pressure Drop for a Pair of Colinear, Interrupted Plates Aligned with the Flow," *International Journal of Heat and Mass Transfer*, Vol. 21, 1978, pp. 1069–1080.

8 Loehrke, R. I., Roadman, R. E., and Reed, G. W., "Low Reynolds Number Flow in Plate Wakes," ASME paper 76-WA/HT-30, New York, 1976.

9 Patankar, S. V., Liu, C. H., and Sparrow, E. M., "Fully Developed Flow and Heat Transfer in Ducts Having Streamwise-Periodic Variations of Cross-Sectional Area," ASME JOURNAL OF HEAT TRANSFER, Vol. 99, 1977, pp. 180–186.

10 Cur, N., "Experiments on Heat Transfer and Pressure Drop for an Array of Colinear Interrupted Plates," Ph.D. Thesis, Department of Mechanical Engineering, University of Minnesota, 1978.

11 Sogin, H. H., "Sublimation from Disks to Air Streams Flowing Normal to their Surfaces," Trans. ASME, Vol. 89, 1958, pp. 61–69.

12 Petukhov, B. S., "Heat Transfer and Friction in Turbulent Pipe Flow with Variable Physical Properties," *Advances in Heat Transfer*, Vol. 6, 1972, p. 523.

13 Sleicher, C. A., and Rouse, N. W., "A Convenient Correlation for Heat Transfer to Constant and Variable Property Fluids in Turbulent Pipe Flow," *International Journal of Heat and Mass Transfer*, Vol. 18, 1975, pp. 677–683.

---

[2] Since the equivalent diameter and the Reynolds number employed here are referred to the flow space that is either above or below a plate, the continuous-walled duct used for comparison should bound the same flow space.

S. Bunditkul
Wen-Jei Yang

Department of Mechanical Engineering,
The University of Michigan,
Ann Arbor, Mich. 48109

Laminar Transport Phenomena in parallel Channels with a Short Flow Construction

A finite-difference numerical analysis was conducted in [3] to investigate laminar transport phenomena in constricted parallel ducts with fully developed flow and temperature profiles. The same numerical procedure is employed to determine laminar transfer phenomena in parallel channels with a short flow constriction within which the flow is still developing. Two limiting thermal conditions are treated: uniform surface temperature and uniform surface heat flux. Theoretical results are obtained for the pressure, streamline, velocity and temperature distributions, the loss coefficients, the Fanning friction factor, and the local and average heat transfer coefficients. Two new dimensionless parameters are derived which describe the transfer performance in the ducts with a short flow constriction. Both the hydrodynamic and thermo-hydrodynamic effects at the entrance as well as the exit of the constricted flow geometry are determined. The numerical scheme is capable of treating high velocity flows up to the transition Reynolds number.

Introduction

Exactly one century ago, in 1878, Weisbach [1] published a book on theoretical mechanics in which the analytical and experimental results were presented on resistance to the motion of water flowing through conduits with sudden enlargement and contraction. The head loss in such a system was given as

$$H = \xi \frac{V^{*2}}{2g_0}$$

Here, V^* denotes the outlet velocity; g_0, conversion factor; and ξ, coefficient of resistance which takes a value of 0.480 for a sudden contraction and $(1/\sigma - 1)^2$ for a sudden enlargement. Kays [2] has obtained semi-empirical results on the expansion and contraction coefficients, K_e and K_c, for flows through tubes and ducts with abrupt constrictions, respectively. These coefficients whose magnitude is a measure of pressure drop ΔP^* due to abrupt expansion or contraction can be determined from the Darcy equation

$$\Delta P^* = K\rho \frac{V_b{}^{*2}}{2g_0} \tag{1}$$

where $V_b{}^*$ represents the bulk velocity in the flow passage, and ρ is the fluid density. His results are only valid for the flow passage of large length-to-hydraulic diameter ratio $L^*/D_h{}^*$, since the study was performed on a fully developed flow in either the laminar or turbulent flow range. By numerically integrating the full Navier-Stokes and energy equations for steady flows in a parallel channel, results were obtained in [3], for K_e, K_c, critical constriction length, combined hydrodynamic and thermal entry length and heat transfer performance for both the uniform surface temperature and uniform surface heat flux cases. It is concluded that both pressure drop and heat transfer rate in the conduit have been significantly enhanced due to a sudden expansion or contraction.

A comprehensive survey of the literature pertinent to the friction loss and heat transfer performance in the entrance region, the pressure drop in flows across nozzles, orifices, and other flow constrictions, and the blood pressure change in cardiovascular systems including aortic valves and arterial stenoses is available in [4] together with a review of some numerical techniques suitable for transport analyses and will not be repeated here.

Laminar transport performance in long parallel channel flows is well known. Bunditkul and Yang [3] investigated the performance enhancement in the parallel conduit due to a sudden expansion and contraction in the presence of a long flow constriction, i.e., L^*/D_h is so large that both the velocity and temperature profiles become fully developed in the constriction. The present study's objective is to determine a further enhancement in the transport performance due to the hydrodynamic and thermo-hydrodynamic effects at both the entrance and the exit of the constricted flow geometry when $L^*/D_h{}^*$ is so small that the flow is still developing at the exit.

Theoretical results are obtained by numerically integrating the full Navier-Stokes and energy equations using finite-difference technique. The expressions for the loss coefficients, Fanning friction factor, and average Nusselt number are derived from the numerical results. Two new nondimensional parameters are derived to describe the hydrodynamic and thermo-hydrodynamic effects at the entrance and the exit of the flow constriction.

Contributed by the Heat Transfer Division for publication in The JOURNAL OF HEAT TRANSFER. Manuscript recieved by the Heat Transfer Division August 21, 1978.

Analysis

The physical system to be studied is shown in Fig. 1. It is a viscous, incompressible flow through a parallel channel of width a^* with a short rectangular constriction of width b^* and length L^* situated at a distance $L_1{}^*$ from the channel entrance. The origin of the Cartesian coordinates (x^*, y^*) is fixed at the channel entrance with x^* measuring the distance in the flow direction and y^* the distance from the channel center. The flow is laminar and fully developed as it enters the channel. The fluid temperature at the channel entrance and the wall (excluding the constriction surface) temperature are maintained at $T_a{}^*$. The constriction surface ($L_1{}^* < x^* < L_1{}^* + L^*$) is heated to achieve two limiting thermal conditions, namely constant heat flux and constant surface temperature at $T_w{}^*$. Constant heat rate problems arise in electric heating, radiant heating, nuclear heating, and in counter-flow heat exchangers when the fluid capacity rates are the same. The constant surface temperature case occurs in evaporators, condensers, or any heat exchangers where one fluid has a much higher heat capacity rate than the other. These two cases cover the usual extremes met in heat exchanger design and are thus of great technical importance. It is important to note the difference between [3] and the present study: In [3], the constriction length L^* is so large compared to the hydraulic diameter of the constriction $D_h{}^*$ ($= 2b^*$) that the flow and temperature profiles are fully developed inside the constriction. However, the present study considers the constriction of insufficient length, namely small $L^*/D_h{}^*$, so that the flow is still developing at the exit. The flow is then disrupted again at the abrupt enlargement.

The vorticity, continuity, momentum and heat transfer equations in dimensionless form read

$$u \frac{\partial \omega}{\partial x} + v \frac{\partial \omega}{\partial y} = C \frac{\partial^2 \omega}{\partial x^2} + \frac{\partial^2 \omega}{\partial y^2}$$

$$\frac{\partial u}{\partial x} + \frac{\partial v}{\partial y} = 0 \tag{2}$$

$$u \frac{\partial u}{\partial x} + v \frac{\partial u}{\partial y} = -C \frac{\partial P}{\partial x} + C \frac{\partial^2 u}{\partial x^2} + \frac{\partial^2 u}{\partial y^2} \tag{3a}$$

$$u \frac{\partial v}{\partial x} + v \frac{\partial v}{\partial y} = - \frac{\partial P}{\partial y} + C \frac{\partial^2 v}{\partial x^2} + \frac{\partial^2 v}{\partial y^2} \tag{3b}$$

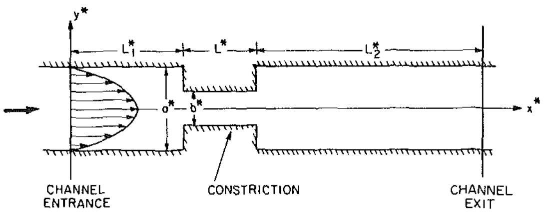

Fig. 1 The conduit model configuration and coordinate system

$$u \frac{\partial T}{\partial x} + v \frac{\partial T}{\partial y} = \frac{1}{\mathrm{Pr}} \left[C \frac{\partial^2 T}{\partial x^2} + \frac{\partial^2 T}{\partial y^2} \right] \tag{4}$$

respectively, where C is defined as $(b^*/L^*)^2$.

The appropriate boundary conditions are specified as follows: the flow at the inlet $x = 0$ is fully developed, that is, $u = 3/2\,\bar{u}[1 - (2y/a)^2]$, $v = 0$, $\psi = 3/2\,\bar{u}[1 - 1/3(2y/a)^2]y$ and $\omega = -12\,\bar{u}\,y/a^2$, where $\bar{u}$ is the mean velocity over the channel cross section. Along the walls including corners, one has zero velocity components, constant stream function and $C\,\partial^2\omega/\partial x^2 + \partial^2\omega/\partial y^2 = 0$. The centerline of the channel geometry $y = 0$ is a streamline for which $\psi = 0$, $\omega = 0$ and, by symmetry, $v = 0$ and $\partial u/\partial y = 0$. The Uchida-Endo scheme [5] is utilized to determine the vorticity, stream function, and temperature at the channel exit. $P = 0$ at $x = 0$ is selected arbitrarily as a reference pressure value.

One primary emphasis in this study is on the practical application of numerical methods to the transport problem of separated viscous flow through parallel ducts of complex axial geometries. Proper treatment of the boundary-region flow is essential to the realistic simulation of the separated flow. Of particular importance is the treatment of the flow in the vicinity of the corners at the two ends of the flow constriction. The latter affects computational instabilities which limit the range of Reynolds numbers. In response to these considerations, the choice of rectangular-mesh systems running parallel to the solid walls was made, with fine grids at the boundary regions near the two ends of the constriction and coarser grids in the remaining bulk of the flow region. The network of finite-difference meshes occupying the flow field consists of four different grid sizes. Accordingly, four difference schemes are formulated for the interior

Nomenclature

a^* = duct width
b^* = constriction width
$B_F = (\mathrm{Re}D_h{}^*/L^*)^{1/3}\sigma 1/4$
$B_H = \mathrm{Gz}^{1/3} \cdot \sigma^{1/4}$ or $B_F \mathrm{Pr}^{1/3}$
C = correction factor or $(b^*/L^*)^2$
C_c = correction factor for contraction coefficient
C_e = correction factor for expansion coefficient
C_f = correction factor for Fanning friction factor
$D_h{}^*$ = hydraulic diameter, $= 2b^*$
f = Fanning friction factor for long constriction [3], $\Delta P^* \Big/ \left(\frac{4L^*}{D_h{}^*} \rho \frac{\bar{u}_c{}^{*2}}{2g_0}\right)$
f^* = Fanning friction factor for short constriction
g_0 = conversion factor
Gz = Graetz number = $\mathrm{RePr}D_h{}^*/L^*$
h_x = local heat transfer coefficient
h = average heat transfer coefficient over heated surface
k_f = fluid thermal conductivity
K_c = contraction coefficient for flow through long constriction
$K_c{}^*$ = contraction coefficient for flow through short constriction
K_e = expansion coefficient for flow through long constriction
$K_e{}^*$ = expansion coefficient for flow through short constriction
L^* = constriction length
$L_1 = L_1{}^*/L^*$
$L_1{}^*$ = distance from channel entrance to constriction entrance
$L_2 = L_2{}^*/L^*$
$L_2{}^*$ = distance from constriction exit to channel exit
Nu_x = local Nusselt number, $h_x D_h{}^*/k_f$
Nu = Nusselt number, $hD^*{}_h/k_f$
$P = P^* g_0 b^{*2}/\nu^2 \rho$
P^* = static pressure
$\Delta P = \Delta P^* g_0\, b^{*2}/\nu^2 \rho$
ΔP^* = pressure drop
Pr = Prandtl number
Re = Reynolds number = $D_h \bar{u}_c{}^*/\nu$
$T = (T^* - T_a{}^*)/(T_w{}^* - T_a{}^*)$ for constant surface temperature case $(T^* - T_a{}^*)/T_a{}^*$ for constant surface heat flux case
T^* = temperature
$T_a{}^*$ = fluid temperature in the inlet region and unheated-wall surface temperature
$T_w{}^*$ = temperature of constriction surface
u = velocity component in x-direction = $u^* b^{*2}/\nu\, L^*$
u^* = velocity component in x-direction
$\bar{u}_c{}^*$ = average velocity in constriction
v = velocity component in y-direction = $v^* b^*/\nu$
v^* = velocity component in y-direction
$x = x^*/L^*$
x^* = distance measured from duct entrance in flow direction
$y = y^*/b^*$
y^* = distance measured from channel center
μ = absolute viscosity
ν = kinematic viscosity
ρ = fluid density
σ = ratio of constriction area to frontal area
ψ = stream function
ω = vorticity = $C \frac{\partial^2 \psi}{\partial x^2} + \frac{\partial^2 \psi}{\partial y^2}$

Subscripts

c = contraction
e = expansion
f = fluid

nodes depending upon their location. The four difference schemes produce four sets of difference equations and boundary conditions covering the entire flow field. Step-by-step iterative procedure is employed for numerical solutions of each interior node, node by node, proceeding downstream from the inlet. The vorticity and temperature for the new nodes are determined by the Gauss-Seidel iterative scheme [6], while the stream function of the node is calculated by means of the successive row iteration method [7]. The velocity components u and v at the node are then evaluated from the definition of the stream function. The iteration procedure is terminated when the desired level of convergence in the stream function and temperature solutions at each node is attained. After the solutions ω, ψ, u and v for all nodes are calculated, the pressure distribution in the flow field is determined using the momentum equations (3). Details of the finite difference expressions and calculation procedure are available in [4].

Results and Discussion

An AMDAHL 470 V/6 digital computer was employed for numerical computations of various flow levels in the laminar range up to the transition Reynolds number (which varies drastically depending upon $L^*/D_h{}^*$ and σ) with various Prandtl numbers. The ratio of free-flow area to frontal area of the constriction σ was varied between two limiting values 0 and 1. The ratio of constriction length to hydraulic diameter (its range appropriate for a short constriction depends on σ and Re) ranged from 0.67 to 240. The channel geometry corresponding to $L^* = L_1{}^* = L_2{}^*/2$ was divided into a grid network of 144 points in the flow direction. In the direction perpendicular to the flow, however, both the number of grid network and the grid size was varied with σ: 35 grid points for $\sigma = 1/4$, 21 grid points for $\sigma = 1/2$, and 21 grid points for $\sigma = 2/3$. The criterion of convergence of ψ and T was set at 0.1 percent. The solution differs from that corresponding to 0.5 percent of convergence criterion by a maximum of 2.5 percent at all grid points in the same network. The computer time for each case was about 100 s.

Numerical results were obtained for the pressure, streamline, velocity and temperature distributions, the loss coefficients, the Fanning friction factor, and the local and average Nusselt number. Both the uniform surface temperature and uniform surface heat flux cases were treated. Results are available in detail in [4]. In the interest of brevity, only a few representative results are presented here.

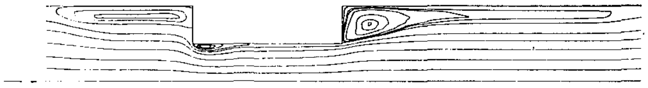

Fig. 2 Streamlines for Re = 500, $L^*/D_h{}^* = 1.0$, $\sigma = 0.5$

Fig. 2 illustrates the streamline distribution in the flow field for $\sigma = 0.5$, $L^*/D_h{}^* = 1.0$ and Re = 500. Three vortices are observed, as expected. They grow as the Reynolds number is increased [4]. In case of a long constriction, the y-component velocity is small in the flow field and pressures at the same cross section of the flow channel are about the same. However, when the constriction is short, pressure distribution which is influenced by the size and strength of the three vortices varies depending upon a combination of the three parameters Re, L^*/D_h and σ. Fig. 3 shows the pressure distribution along the mid-channel corresponding to the case in Fig. 2. The pressure drops ΔP_c and ΔP_e due to an abrupt contraction and expansion determine the loss coefficients $K_c{}^*$ and $K_e{}^*$, respectively, for flows through parallel channels with a short flow constriction using equation (1). The pressure ΔP_f is due to flow friction in the constriction. Here, the average ΔP's across the channel are used in the computations. The hydrodynamic entrance effect is exhibited as a pressure variation immediately downstream from the inlet, $x = 1.0$ to about 1.2, while the hydrodynamic exit effect appears as the pressure change immediately upstream from the exit, $x = 1.6$ to 2.0. As the constriction grows in length, the pressure variations at the entrance and exit reduce in magnitude.

Let us define

$$K_c{}^* = C_c K_c;\ K_e{}^* = C_e K_e;\ f^* = C_f f \tag{5}$$

Here K_c and K_e are the loss coefficients and f denotes the Fanning friction factor for flows through parallel ducts with a long constriction. Both K_c and K_e are determined from Fig. 3 [3], while f corresponds to that for flows through parallel ducts and is equal to 24/Re. The correction factors C_c, C_e and C_f, derived from the numerical computations, are plotted against B_F in Fig. 4, where B_f is defined as (Re $D_h{}^*/L^*)^{1/3}\,\sigma^{1/4}$. They are unity when $B_F \leqslant 2.25$, the criterion for a constriction to be hydrodynamically long. In the present study, parallel ducts with a short constriction must satisfy the condition of $B_F > 2.25$. The correction factors in Fig. 4 can be expressed in the form of

$$C = aB_F + b \tag{6}$$

in which $a = -0.304, 0.792, 0.122$ and $b = 1.684, -0.782, 0.725$ for C_c, C_e and C_f, respectively.

Figs. 5 and 6(a) show the development of temperature profiles in the flow field (Re = 2000, $\sigma = 0.5$ and $L^*/D_h{}^* = 5$, and $T = 0$ at inlet) for the uniform surface temperature and uniform surface heat flux ($\partial T/\partial y = 1.0$) cases, respectively. The Prandtl number was varied to determine the effects of thermal diffusivity on thermal stratification in a laminar flow through the constricted flow geometry. It is observed that all isothermal lines originate from the inlet corner of the con-

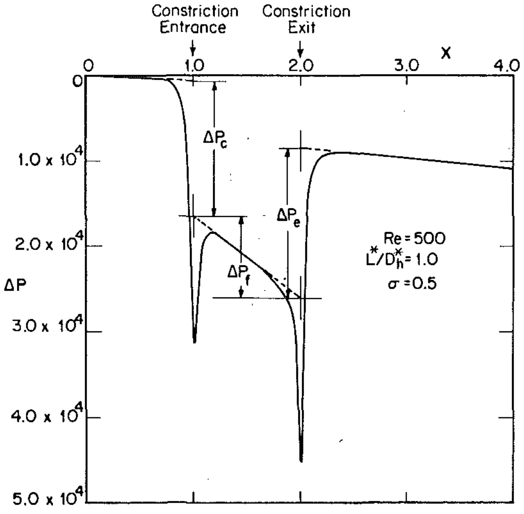

Fig. 3 Pressure drop along mid-channel for Re = 500, $L^*/D_h{}^* = 1.0$ and $\sigma = 0.5$

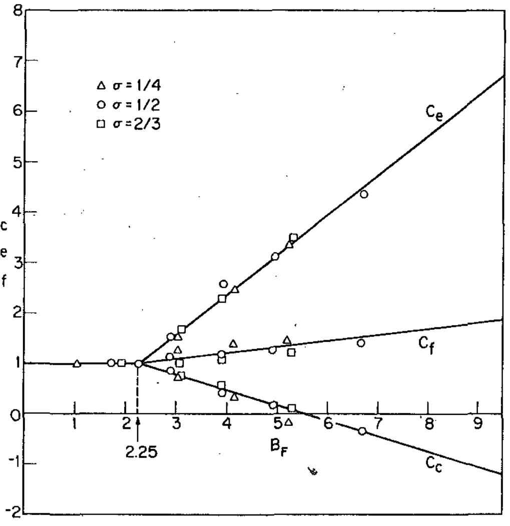

Fig. 4 Correction factors for loss coefficients and Fanning fiction factor for flows through parallel channels with a short flow constriction

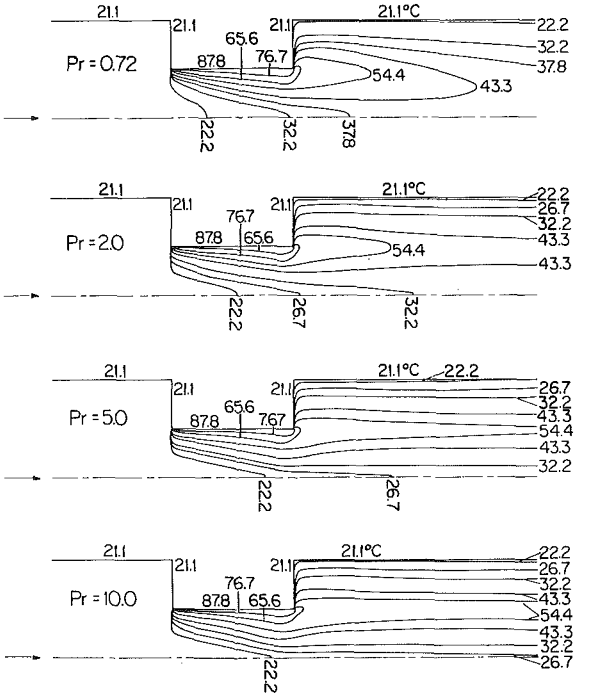

Fig. 5 Temperature distributions for uniform surface temperature case corresponding to σ = 0.5, L^*/D_h^* = 5, Re = 2000, Pr = 0.72, 2.0, 5.0 and 10.0

striction heated at a uniform surface temperature, while the uniform surface heat flux case has some isothermals originating from the heated surface. Under both thermal boundary conditions, isothermal lines stretch downstream as Pr increases or as the L^*/D_h^* ratio decreases. In the limit when L^*/D_h^* takes a large value, all isothermal lines terminate almost perpendicularly at the channel center line as seen in Figs. 4 and 5 of [3]. In the case of uniform surface heat flux, the highest temperature on the heated surface occurs at a distance x^* measured from the exit corner of the constriction:

$$x^*/L^* = 0.94\,\mathrm{Pr}^{1/3}/(\mathrm{Re}^{1/2}\,\sigma L^*/D_h^*) \tag{7}$$

The location x^* is confined within the downstream half of the constriction walls. This suggests a potential hazard in the region due to local heat concentration whose severity depends on Pr, Re, σ and L^*/D_h^*. Fig. 6(*b*) demonstrates the effect of the Reynolds number on temperature distribution for the constant heat rate case. It is observed that the temperature gradients at the heated wall in the constriction entry region grow steeper as the flow rate diminishes, indicating an enhancement in the local Nusselt number with a decrease in the Reynolds number. Particularly noteworthy is the heating of the fluid upstream from the constriction entrance due to thermal diffusion in the fluid. The heating spreads further upstream and outward (in the y direction) as the Reynolds number is reduced.

Fig. 7 demonstrates the effects of σ and L^*/D_h^* on the local heat transfer performance and the thermal entrance length for both the uniform surface temperature and uniform surface heat flux cases at Re = 2000 and Pr = 0.72. A comparison of Figs. 7(*a*) and 7(*b*) reveals that the thermo-hydrodynamic entrance effect is more prominent in a shorter constriction as expected. In a shorter constriction, for example L^*/D_h^* of 5 in Fig. 7(*a*), the thermo-hydrodynamic "exit effect," an augmentation in the local heat transfer performance, is observed under both thermal boundary conditions. This exit effect is not seen in Fig. 7(*b*) for L^*/D_h^* = 25 or Fig. 6 of [3] for large L^*/D_h^*. Both the entrance and exit effects diminish with an increase in the constriction length. When the Reynolds number diminishes, the local Nusselt number increases in the entry region but decreases in the downstream region to the exit such that its average value over the entire constriction Nu would be reduced in compliance with equation (8) or (9) which follows below.

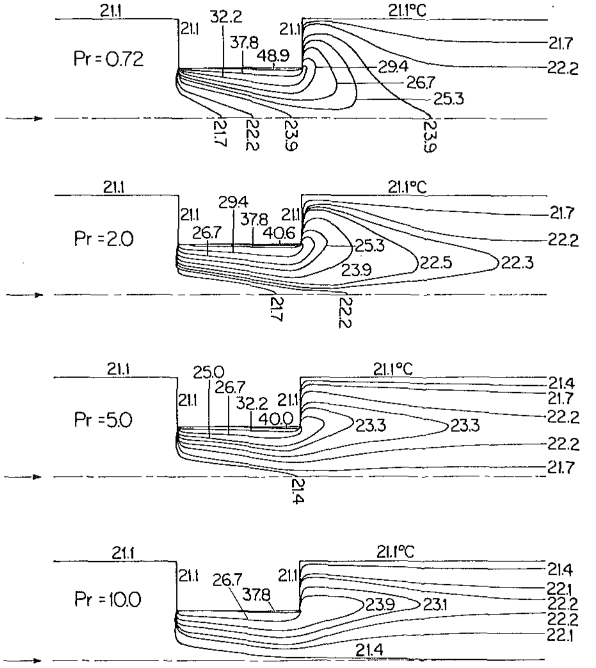

Fig. 6(*a*) Temperature distributions for uniform surface heat flux case corresponding to σ = 0.5, T^*/D_h^* = 5, Re = 2000, Pr = 0.72, 2.0, 5.0 and 10.0

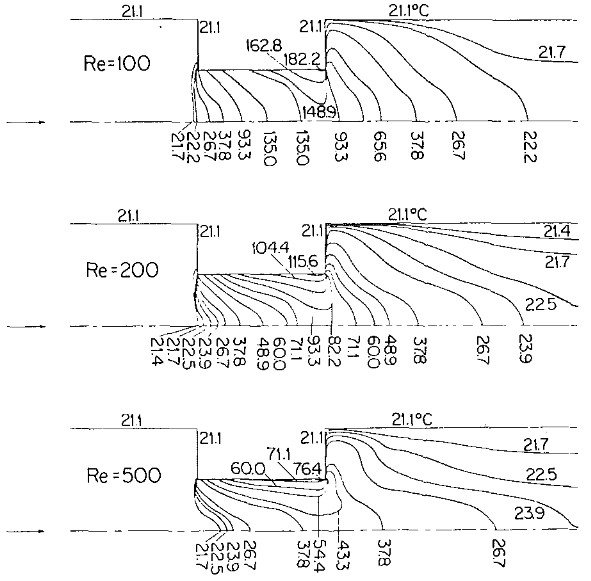

Fig. 6(*b*) Temperature distributions for constant surface heat flux case corresponding to σ = 0.5, T^*/D_h^* = 5, Pr = 0.72, Re = 100, 200 and 500

The following expressions for the mean Nusselt number Nu are derived from the numerical computations:

For the uniform surface temperature case:

$$\mathrm{Nu} = \begin{cases} 9.3 & \text{for } B_H < 3.5 \\ 2.26\,\mathrm{G_z}^{1/3} & \text{for } 4.4 > B_H > 3.5 \\ 3.08\,B_H & \text{for } B_H > 4.4 \end{cases} \tag{8}$$

For the uniform surface heat flux case:

$$\mathrm{Nu} = \begin{cases} 10.7 & \text{for } B_H < 3.5 \\ 2.60\,\mathrm{Gz}^{1/3} & \text{for } 4.4 > B_H > 3.5 \\ 3.85\,B_H & \text{for } B_H > 4.4 \end{cases} \tag{9}$$

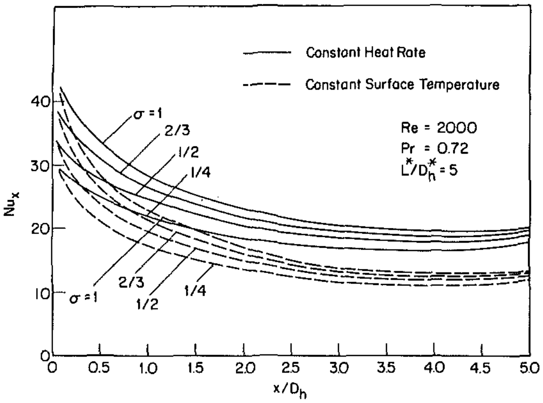

Fig. 7(*a*) Local heat transfer performance in constricted flow systems for $L^*/D_h^* = 5$, Re = 2000, Dr = 0.72

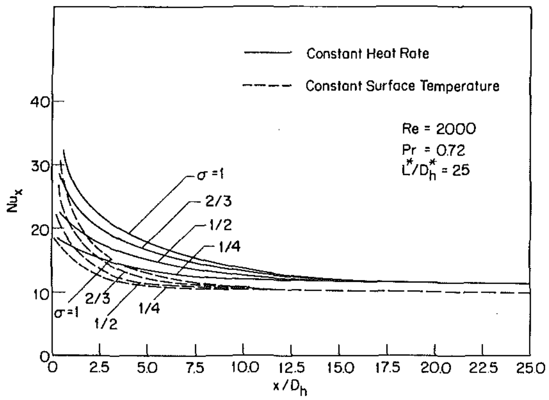

Fig. 7(*b*) Local heat transfer performance in constricted flow systems for $L^*/D_h^* = 25$, Re = 2000 and Pr = 0.72

Here, Gz denotes the Graetz number defined as $\mathrm{RePr}D_h^*/L^*$ and B_H is $\mathrm{Gz}^{1/3}\,\sigma^{1/4}$ or $B_F\mathrm{Pr}^{1/3}$. For a given Peclet number RePr, a large value of Gz signifies a shorter constriction. In the determination of the loss coefficients and the Fanning friction factor, $B_F > 2.25$ is the indication of a hydrodynamically short constriction. For heat transfer performance evaluation, $B_H > 4.4$ is the criterion for a thermo-hydrodynamically short constriction. It is evident in equations (6, 8) and (9) that for short constrictions, both the C-B_F and Nu-B_H relationships are linear. A comparison of equations (8) and (9) discloses that in geometrically similar heat transfer systems, a uniform surface temperature yields smaller convective conductances than a uniform surface heat flux input at the same Reynolds and Prandtl numbers. The limiting Nusselt number for B_H less than 3.5 takes a constant value which is independent of the area ratio: 9.3 and 10.7 for constant surface temperature and constant heat flux, respectively. Both are higher than their counterparts in a long parallel channel flow, 7.54 and 8.235, respectively, as well as those in a circular tube flow, 3.658 and 4.364, respectively.

In order to ascertain the validity of the present finite-difference scheme, both qualitative and quantitative comparisons were made in [4] between the numerical results obtained from this scheme and the empirical and theoretical data available in the literature. Qualitatively, the streamlines in the flow field and the vortices generated at the steps and the constriction entrance, for example in Fig. 2, are confirmed by the visualization studies on channel flows with abrupt expansion or contraction [8, 9], flows along a flat surface with a step [9], and a back step flow [10, 11]. The present numerical scheme was applied to solve the problem of laminar forced convection in the entrance region between parallel flat ducts. Results for the local and average Nusselt number over a wide range of Pr compare very well qualitatively with both theory and test data [12–19], as shown in [4].

Conclusions

Two new dimensionless parameters B_F and B_H are defined to describe transport phenomena in the constricted flow geometry: B_F for flows and pressure drops and B_H for heat transfer performance. B_F corresponds to B_H for Pr of unity. A constriction is hydrodynamically short when B_F exceeds 2.25 and is thermo-hydrodynamically short when B_H is greater than 4.4. Equation (5) defines the loss coefficients and Fanning friction factor for flows through the constricted geometry, in which K_c and K_e are determined from Fig. 3 [3], $f = 24/\mathrm{Re}$, and the correction factors C_c, C_e and C_f are evaluated using equation (6) or Fig. 4. Equation (7) gives the location of the maximum wall temperature in the uniform surface heat flux case. The last expressions of equations (8) and (9) give the average Nusselt numbers in the constricted flow geometry for the uniform surface temperature and uniform surface heat flux cases, respectively. Both the C-B_F and Nu-B_H relationships for the constricted flow system are linear. It is revealed that in geometrically similar flow systems, a uniform surface temperature yields lower heat transfer performance than a uniform surface heat flux input at the same Peclet number. Of interest is the phenomena of both the hydrodynamic and thermo-hydrodynamic effects at the entrance as well as the exit of the constricted flow geometry.

References

1 Weisbach, J., *Theoretical Mechanics, with an Introduction to the Calculus,* D. van Nostrand, New York, 1878.

2 Kays, W. M., "Loss Coefficients for Abrupt Changes in Flow Cross Section with Low Reynolds Number Flow in Single and Multiple Tube System," *Trans. ASME,* Vol. 72, 1950, pp. 1067–1074.

3 Bunditkul, S. and Yang, Wen-Jei, "Laminar Transport Phenomena in Constricted Parallel Ducts," *Letters J. Heat and Mass Transfer,* Vol. 4, 1977, pp. 249–260.

4 Bunditkul, S., "Laminar Transport Phenomena in Parallel Ducts with Abrupt Contraction and Expansion," Ph.D. Thesis of Mechanical Engineering, University of Michigan, 1978.

5 Uchida, S. and Endo, M., "On Some Numerical Solutions of the Flow thriugh a Back-Step Channel," *Memoirs of the Faculty of Engineering,* Nagoya University, Research Report, Vol. 27, No. 1, 1975, pp. 152–161.

6 Fromm, J., "A Method for Computing Nonsteady, Incompressible, Viscous Fluid Flows," Los Alamos Scientific Laboratory, Los Alamos, N.M. Sept. 1963.

7 Bruce, G. H., Peaceman, D. W., Rachford, H. H., Jr., and Rice, J. D., "Calculations of Unsteady-State Gas Flow Through Porous Media," *Petroleum Transactions,* AIME 198, 1953, pp. 79–92.

8 Rouse, H., *Elementary Mechanics of Fluids,* Wiley, New York, 1960, pp. 55–60, p. 259.

9 Van Dyke, M., Vincenti, W. G. and Wehausen, J. V. (eds.), *Annual Review of Fluid Mechanics,* Vol. 5, George Bomta Co., 1973.

10 Eck, B., *Technische Strömungslehre,* Springer Verlag, Berlin, 1966, p. 243.

11 Mueller, T. J. and O'Leary, R. A., "Physical and Numerical Experiments in Laminar Incompressible Separating and Reattaching Flows," AIAA Paper No. 70-763, 1970.

12 Bhatti, M. S. and Savery, C. W., "Heat Transfer in the Entrance Region of a Straight Channel: Laminar Flow with Uniform Wall Heat Flux," ASME JOURNAL HEAT TRANSFER, Vol. 99, 1977, pp. 142–144.

13 Bhatti, M. S. and Savery, C. W., "Heat Transfer in the Entrance Region of a Straight Channel: Laminar Flow with Uniform Wall Temperature," ASME Paper No. 77-WA/HT-4, 1977.

14 Mercer, W. E., Pearce, W. M. and Hitchcock, J. E., "Laminar Forced Convection in the Entrance Region Between Parallel Flat Plates," ASME JOURNAL OF HEAT TRANSFER, Vol. 89, 1967, pp. 251–257.

15 Hwang, C. L. and Fan, L. T., "Finite Difference Analysis of Forced-Convection Heat Transfer in Entrance Region of a Flat Rectangular Duct," *Applied Scientific Research,* Section A, Vol. 13, 1964, pp. 401–422.

16 Naito, E., "Laminar Heat Transfer in the Entrance Region Between Parallel Plates: The Case of Uniform Heat Flux," *Heat Transfer Japanese Research,* Vol. 4, No. 2, 1975, pp. 63–74.

17 Siegel, R. and Sparrow, E. M., "Simultaneous Development of Velocity and Temperature Distributions in a Flat Duct with Uniform Wall Heating," *AIChE Journal,* Vol. 5, No. 1, 1959, pp. 73–75.

18 Sparrow, E. M., "Analysis of Laminar Forced-Convection Heat Transfer in Entrance Region of Flat Rectangular Ducts," NACA Technical Note 3331, 1955.

19 Stephan, K., "Wärmeubergang und Druckabfall bei nicht ausgebildeter Laminarströmung in Rohren und in ebenen Spalten," *Chemi-Ing.-Techn.,* Vol. 31, No. 12, 1959, pp. 773–778.

Y. Kamotani
S. Ostrach
H. Miao
Department of Mechanical and Aerospace Engineering
Case Western Reserve University
Cleveland, OH

Convective Heat Transfer Augmentation in Thermal Entrance Regions by means of Thermal Instability

The effects of thermal instability on a liminar thermally developing entrance flow between two horizontal plates heated from below are studied experimentally. The experiments cover a range of Rayleigh numbers between 2.2 × 10^4 and 2.1 × 10^5, and Reynolds numbers between 50 and 300 using air. Results for the heat transfer rate and entrance length show that they are influenced not only by the Rayleigh number but also by the ratio Re^2/Gr. The heat transfer rate is increased as much as 4.4 times due to thermal instability. The flow visualization experiments show that the critical wavelength is determined by the channel height, not by the thermal boundary layer thickness.

Introduction

The effects of thermal instability on a laminar, hydrodynamically fully developed but thermally developing flow in a channel formed by two horizontal plates heated from below have been studied in recent years by several investigators (Kamotani and Ostrach [1], Hwang and Cheng [2], Hwang and Liu [3]). Kamotani and Ostrach [1] obtained experimentally the critical Rayleigh numbers based on the channel height as a function of downstream distance using air, and found that the thermal entrance region is more stable than the fully-developed region. They also found that the values of $Ra_{,cr}$ are much larger than the theoretical values given by Hwang and Cheng [2]. Later the experimental work by Hwang and Liu confirmed the findings of Kamotani and Ostrach.

Kamotani and Ostrach also investigated the structure of the secondary flow caused by the thermal instability and the associated heat transfer augmentation in the post-critical region. However, because of the aforementioned unexpectedly high critical Rayleigh numbers it was not possible to operate the apparatus much beyond the critical values, and therefore the heat transfer augmentation attained in the experiments was rather small (less than twice the heat transfer rate of a subcritical condition) and the study of the secondary flow structure in the post-critical region was limited. One result by Kamotani and Ostrach showed that the thermal entrance length did not change appreciably in the range of Rayleigh number studied (10^3 to 3.1 × 10^4), which may not be true in a higher Rayleigh number range.

In the present experiments the effects of thermal instability are investigated in the range of Rayleigh number much larger than that of Kamotani and Ostrach [1]. The heat transfer rates and temperature fields are studied in the post-critical region. Flow visualization experiments also are conducted to study the detailed flow structure near the onset point of thermal instability.

Experimental Setup and Procedure

Fig. 1 shows a sketch of the test setup and the coordinate system adopted herein. The setup is similar to the one used by Kamotani and Ostrach [1], but the present one is larger in all dimensions to obtain higher Rayleigh numbers. The test section is 56.4 cm wide and 53.3 cm long. The height of the test section is 3.8 cm. The test section is connected to a 213.4 cm long entrance section in order to obtain a fully developed velocity profile at the entrance of the test section. The bottom plate of the test section is made of a 6.35 mm thick aluminum plate. Seven electrical heating mats are bonded to the back of the plate as shown in Fig. 2. Various size heaters are used in accordance with the heat transfer rate change in the longitudinal direction. Four guard heaters are used to minimize the heat loss to both sides of the plate. The input to each heater is regulated individually by a voltage transformer. The top plate of the test section is made of 6.35 mm thick plexiglas. The temperature of the top plate is controlled by cooling water flowing over it. The top plate temperature is kept at the main stream temperature to eliminate a thermal boundary layer on the top wall surface. The surface temperatures of both top and bottom plates are measured by thermocouples embedded in the plates. To minimize the net heat transfer between the heaters through the aluminum plate the heat input to each heater is carefully adjusted until no consistent trend in the plate temperature distribution is found. The nonuniformity of the plate temperature distribution relative to ΔT is about two percent for the smallest ΔT (about 5°C) tested here and becomes better as ΔT increases.

For each experiment the input of each heater is adjusted until a steady uniform bottom wall temperature is obtained. The total heat

---

Contributed by the Heat Transfer Division for publication in the JOURNAL OF HEAT TRANSFER. Manuscript received by the Heat Transfer Division May 15, 1978.

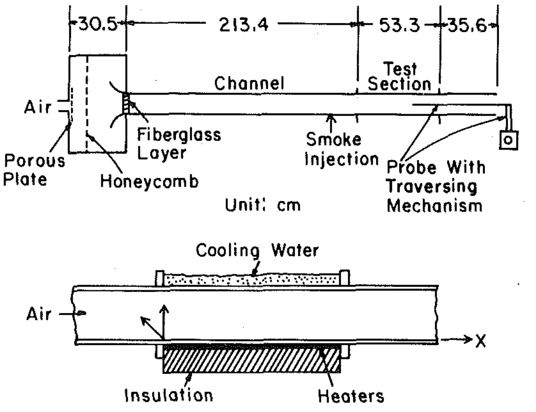

Fig. 1 Experimental apparatus

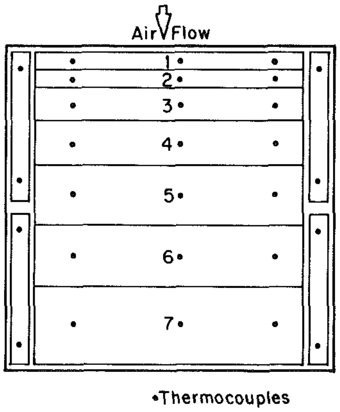

Heater Sizes

No.	W	L
1	2.54	50.8
2	2.54	50.8
3	5.08	50.8
4	7.62	50.8
5	10.16	50.8
6	10.16	50.8
7	12.70	50.8
Guard Heaters	2.54	25.4

Unit: cm

Fig. 2 Heater sizes and thermocouple locations

transfer rate over the region covered by each heater is calculated from the net heat input to the air in the test section. The net heat input of each heater is calculated by subtracting the conduction and radiation loss from the total input to each heater. The details of the calculation are explained in Ostrach and Kamotani [4] and also in Miao, Kamotani and Ostrach [5] from which most of the present data are taken. The heat transfer coefficient of each heater and, its dimensionless form the Nusselt number are defined as:

$$\frac{Q\text{net}}{\text{area}} = h(T_1 - T_0), \text{Nu} = \frac{hD}{k}$$

The experimental error involved in the value of Nusselt number is estimated to be ±12 percent as discussed in Miao, Kamotani and Ostrach [5].

The total flow rate in the test section is measured by a flowmeter. The mean speed at the test section is calculated from the total flow rate. The Reynolds number at the test section is varied between 50 and 300.

Temperature distributions in the test section are measured by a thermocouple probe inserted from the downstream end of the test section.

In the flow visualization experiments a mixture of titanium tetrachloride and carbon tetrachloride is used to generate smoke by slowly blowing humid air through the mixture outside the apparatus. The smoke is clearly visible and neutrally buoyant in air. A small amount of the smoke is injected from small holes in the bottom plate just ahead of the test section as shown in Fig. 1.

Experimental Results and Discussion

At first, as was done by Kamotani and Ostrach [1], the main flow is investigated to check its two-dimensionality and its laminar and fully developed conditions at the test section without heating. It is found that the main stream conditions are very similar to those obtained for the test setup by Kamotani and Ostrach [1], and those conditions are considered to be satisfactory for the present experiments.

Onset of Thermal Instability. The flow structure near the beginning of the thermally unstable region is studied by visual observations. The onset points of thermal instability are determined by detecting the start of small but systematic smoke motions in the thermal boundary layer. The onset points are spaced at certain intervals in the spanwise direction (y-direction). The average axial location of onset of instability is plotted as a function of the Rayleigh number in Fig. 3. The figure also shows the results of similar experiments by Hwang and Liu [3] and those of the work by Kamotani and Ostrach [1] in which the onset points were determined by detecting small spanwise temperature variations. As seen in the figure, the three results agree well. The small discrepancies between the work of [1] and the present data are due to the two different techniques of determining the instability onset. They all show that the experimentally determined critical Rayleigh numbers are much larger than the theoretically predicted values by Hwang and Cheng [2]. As pointed out by Kamotani and Ostrach [1], this discrepancy may be caused by the fact that in the analysis of Hwang and Cheng the channel height, D, was used as the vertical length scale, whereas in the thermal boundary layer the temperature difference exists only over the thermal boundary layer thickness, δ_T. Davis and Choi [6], in their study of thermal instability in a liquid film flow, observed similar discrepancies between the theoretical and experimental $\text{Ra}_{,cr}$. Davis and Choi also computed $\text{Ra}_{,cr}$ using δ_T as the vertical length scale, and found good agreements between the theoretical and experimental values. In the present analysis no theoretical computations of $\text{Ra}_{,cr}$ based on δ_T is available, but a comparison of the experimental data with the theoretical result by Hwang and Cheng indicates that the difference scales roughly with the ratio, $(D/\delta_T)^3$. The fact suggests that δ_T may be the proper vertical length scale of the problem.

If δ_T is indeed the proper vertical length scale in the disturbance equations, the wavelength of the induced secondary flow is expected to increase as δ_T increases in the subsequent downstream flow development. However, Hwang and Liu [3] noted that the wavelength remains constant along the main flow direction after the onset of the secondary flow. To check this the flow structure near the onset points is carefully studied in the present experiment. Smoke injection near the bottom plate surface reveals a rather complex flow structure. Fig. 4 shows a schematic view of the flow structure. At a certain axial location the smoke near the bottom wall starts to bifurcate. Downstream

Nomenclature

D = channel height
Gr = Grashof number, $g\beta\Delta TD^3/\nu^2$
g = gravitational acceleration
k = thermal conductivity
Pe = Peclet number, RePr
Pr = Prandtl number, ν/α
Ra = Rayleigh number, $g\beta\Delta TD^3/\nu\alpha$
$\text{Ra}_{,cr}$ = critical Rayleigh number
Re = Reynolds number, $\overline{U}D/\nu$
T_1 = bottom wall temperature
T_0 = free stream and top wall temperature
$\Delta T = T_1 - T_0$
$\overline{U}$ = mean axial velocity
α = thermal diffusivity
β = thermal expansion coefficient
ν = kinematic viscosity

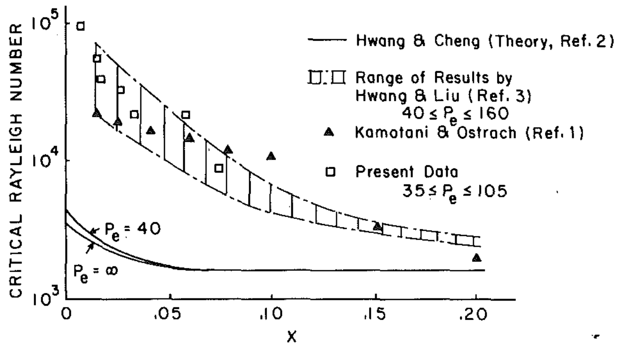

Fig. 3 Critical Rayleigh number versus x

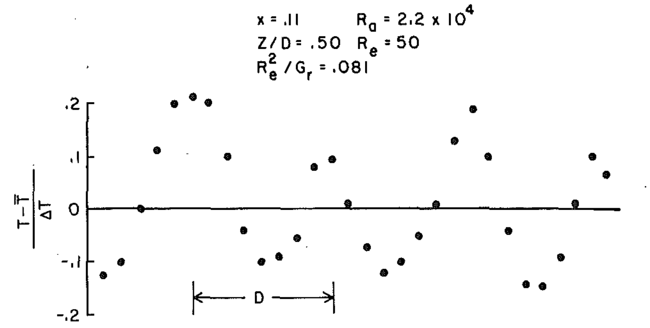

Fig. 5 Spanwise temperature distribution

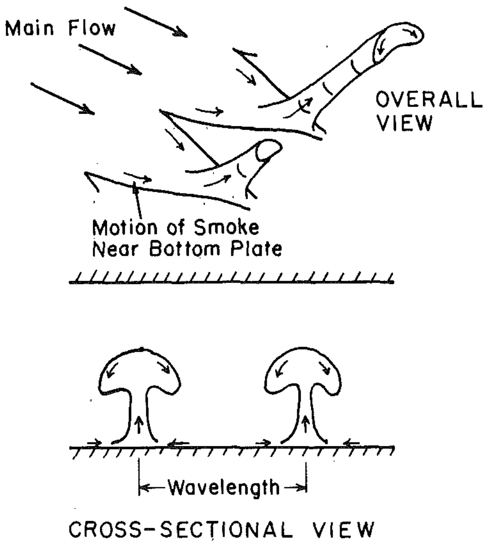

Fig. 4 Flow structure near onset points

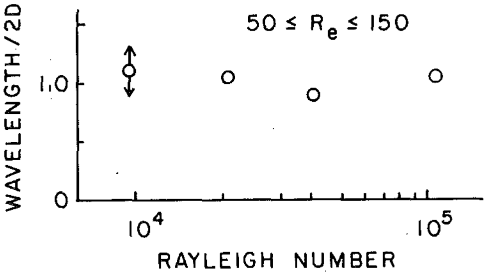

Fig. 6 Critical wavelength

of that position a strong upward motion of the smoke in a nearly columnar shape is observed. As the column rises, it deforms into a mushroom-shape due to the shearing action of the main stream. A similar flow structure is clearly visible also in the pictures taken by Hwang and Liu [3]. The mushroom-shape flow structure eventually reaches the top wall and bifurcates, developing into a longitudinal roll-cell in the downstream region. In the region where the mushroom-shape flow is dominant the spanwise temperature distribution shows alternating appearances of small and large peaks as shown in Fig. 5. The small peaks are considered to be due to the aforementioned bifurcation. The temperature measurements were made without smoke particles, but one can infer from Fig. 5 that the flow is qualitatively like that observed from the smoke study. This would seem to indicate that the aforementioned flow structure is not just caused by the presence of smoke particles. When the ratio $\mathrm{Re}^2/\mathrm{Gr}$ (the ratio of inertia forces [forced convection] to buoyancy, sometimes called modified Froude number) is much smaller than unity ($\mathrm{Re}^2/\mathrm{Gr} < .1$), the smoke columns impinge strongly on the top plate, which causes a noticeable back-flow in the upstream direction along the top wall. The back-flow is eventually pushed back into the main stream, but it disturbs the main stream substantially. When $\mathrm{Re}^2/\mathrm{Gr} > .1$, by the time the smoke columns reach the top wall, they are substantially deflected downstream. The ratio $\mathrm{Re}^2/\mathrm{Gr}$ does not play a role in the linearized stability analysis of the present problem by Hwang and Cheng [2], but the flow structure in the post-critical region is expected to be influenced by the ratio. Fig. 6 shows the spanwise spacing of the onset points measured under various experimental conditions. As seen in the figure the spacing is close to the channel height, D. The spacing remains nearly constant in the subsequent development into longitudinal cells. The observation is in good agreement with the one made by Hwang and Liu [3]. Therefore from the flow visualization tests it can be inferred that the critical wavelength of the thermal instability is determined by D, not by δ_T. According to the stability analysis by Hwang and Cheng [2], the secondary motion associated with the thermal instability is not confined in the thermal boundary layer but engulfs the whole flow passage. In that regard D seems to be more appropriate length scale than δ_T. It is noted, however, that the secondary motion must grow sufficiently after the onset to be detected experimentally. The thinner the thermal boundary layer, it is expected to take more time for the secondary motion to grow because it has to penetrate into the more stable free stream region. That seems to be one reason why the experimentally determined critical Rayleigh numbers are strongly influenced by the thermal boundary layer thickness. Another reason for the discrepancy between the measured and predicted $\mathrm{Ra}_{,cr}$ may be due to the fact that according to the present visual observations the flow does not seem to be unstable to longitudinal cells at the onset point as assumed in the theory. Around the onset point the fluid motion seems to be more three-dimensional. Those rising columns observed in the present experiment resemble the rising center columns of Benard cells. In the present case those columns are deflected and bifurcated, and eventually impinge on the top wall and further bifurcate, developing into longitudinal cells in the downstream region.

Heat Transfer Rate. Fig. 7 shows the variation of measured mean Nusselt number with $x(=X/\mathrm{Pe}D)$ for $2 \times 10^4 < \mathrm{Ra} < 2.2 \times 10^5$ and $\mathrm{Re} = 50$. The mean Nusselt number at x is defined as Nusselt number averaged over the length between $x = 0$ and x, and is a measure of overall heat transfer rate in the region. The solid line in Fig. 7 is the theoretical result given by Hatton and Turton [7] for the heat transfer rate in the thermal entrance region without buoyancy effects. Some of the data from the work by Kamotani and Ostrach [1] are also shown

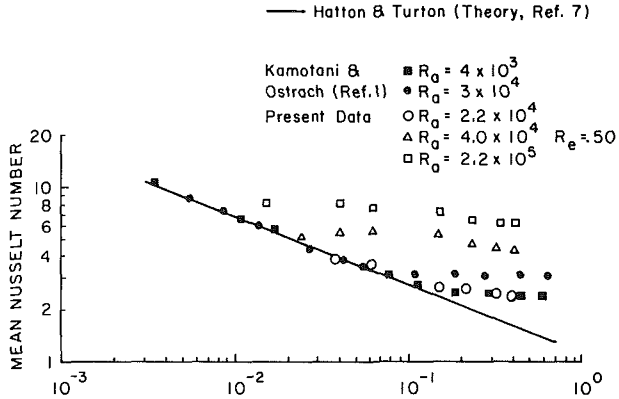

Fig. 7 Mean Nusselt number variation

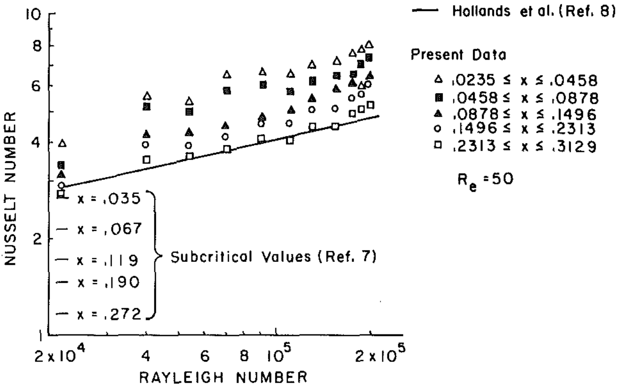

Fig. 8 Heat transfer rate as a function of Rayleigh number

in the figure for comparison. For a given Rayleigh number the variation of the measured mean Nu follows closely the theoretical curve up to a certain x value, which indicates no appreciable effect of thermal instability in that region. Once the secondary flow (caused by the thermal instability) becomes appreciable, the data start to deviate from the theoretical curve indicating an augmentation of the heat transfer rate. The enhanced heat transfer occurs at different axial locations depending on the Rayleigh number. With increasing Rayleigh number the location where the mean Nu deviates from the subcritical value moves upstream, indicating that the thermally unstable region spreads into the upstream region. The same trend was also observed by Kamotani and Ostrach [1] although in that work the effect of thermal instability is much smaller due to smaller Rayleigh numbers. For the maximum Rayleigh number obtained in the present experiment (2.1×10^5) one can observe the effect of thermal instability on heat transfer rate at $x = .01$ and further upstream.

To study the effect of thermal instability locally it is necessary to measure the local heat transfer rate. However, because of the way the heat transfer rate is measured in the present experiment one cannot determine the heat transfer rate at a given point. Instead, the local effect of thermal instability is studied using the average Nusselt number over each heater. The locally averaged Nusselt number Nu $[a \le x \le b]$ is defined as the mean Nusselt number in the interval $a \le x \le b$ where a and b are specified by the size of each heater (nondimensionalized by DPe). Variations of locally averaged Nu with Ra at several locations are presented in Fig. 8. Also shown in the figure for comparison are local Nusselt numbers at $x = \frac{1}{2}(a + b)$ in the subcritical range given by Hatton and Turton [7]. Because the dimensions of the present apparatus is too small to yield a subcritical condition (ΔT becomes too small) no data are taken in the subcritical range. However using a similar setup as the present one Kamotani and Ostrach [1] confirmed the theoretical values of Hatton and Turton. The solid line in Fig. 8 is the empirical curve obtained by Hollands, et al. [8] who measured the heat transfer rate in confined air (no mainstream). According to Ostrach and Kamotani [4] there is no appreciable difference between the heat transfer augmentation due to thermal instability for the confined case and that for the fully developed flow. As seen in Fig. 8, the measured values of Nu approach those for the confined case with increasing x. Due to the experimental error involved in the values of Nu it is difficult to pinpoint in Fig. 8 the location where the flow becomes thermally fully developed. The subject of the thermal entrance length is discussed in the following section. In the region where the flow is not thermally fully developed, one still observes a substantial increase of the heat transfer rate from the subcritical value. At Ra = 2.2×10^4 and Re = 50, according to the present flow visualization experiment the flow becomes unstable at $x \doteq .05$. But Fig. 8 shows that at the corresponding condition there is already a noticeable heat transfer rate increase in the region $.023 \le x \le .046$. In comparison Kamotani and Ostrach [1] observed very little heat transfer augmentation in the region $.035 \le x \le .054$ at Ra = 2.2×10^4 and Re = 170. This may be explained by the difference in the value of Re^2/Gr in the two experiments. Compared to the present experiment the value of Re^2/Gr is about 12 times larger in the previous experiment by Kamotani and Ostrach, and thus one expects a stronger effect of natural convection in the present experiment, once the flow becomes unstable. As explained previously, when Re^2/Gr is much smaller than unity an upward fluid motion becomes very strong at the onset point, which causes a substantial upstream flow disturbance. That seems to be the reason for the increase of heat transfer rate even in the thermally stable region. The aforementioned phenomenon becomes less noticeable as Re^2/Gr increases. Therefore it can be said that in the region of small x, Nu is influenced by Re^2/Gr (in addition to Ra) especially when the ratio is less than one. When the measured locally-averaged Nusselt numbers are compared with the corresponding subcritical values given by Hatton and Turton, it is found that heat transfer augmentation is about 1.6 around $x = .035$, and 4.4 around $x = .272$ in the range of Rayleigh number (and Re^2/Gr) studied herein.

From the above results it seems that Nu in the thermal entrance region is a function of mainly x, Ra, Gr/Re^2 and $Ra_{,cr}$ for air. Some simple attempts were made to correlate the heat transfer data obtained herein and by Kamotani and Ostrach [1], but no satisfactory correlation was found. Considering the number of variables involved and rather complex manners in which Nu changes with x near $Ra_{,cr}$ as shown by Kamotani and Ostrach [1] very extensive work seems to be required to correlate the Nu data. Besides, more experimental data, especially data concerning the effects of Re^2/Gr on Nu are needed. For these reasons the correlation of the heat transfer data is left for future work. It is noted that the correlation equation given by Hollands, et al. [8] for the confined case (also valid for the fully developed region) is not applicable in the region $x < .2$ and $Ra < 2 \times 10^5$ (Fig. 8).

Thermal Entrance Length. To observe the effect of natural convection on the thermal entrance length, temperature distributions in the entrance region are studied. For this study it is found convenient to consider the mean temperature in the spanwise direction at the midheight which is defined as

$$\overline{T}_{1/2}(x) = \frac{1}{L} \int_{y_0}^{y_0+l} T(x, y, z = D/2)dy$$

$\overline{T}_{1/2}$ is close to T_0 at $x = 0$, and becomes equal to the value $\frac{1}{2}(T_0 + T_1)$ in the fully developed region. Fig. 9 shows the distributions of $\overline{T}_{1/2}$ under various experimental conditions. The variation of $\overline{T}_{1/2}$ for the subcritical case (calculated from the data in Kamotani and Ostrach [1]) is also shown in the figure for comparison. When Ra is small (Ra = 9.7×10^3), the variation of $\overline{T}_{1/2}$ follows closely the subcritical variation in most of the entrance region, which agrees with the observation made by Kamotani and Ostrach. At Ra = 1.0×10^5 the thermal entrance length is noticeably shortened. As seen in Fig. 9 at a given Ra value, the variation of $\overline{T}_{1/2}$ and the entrance length depend

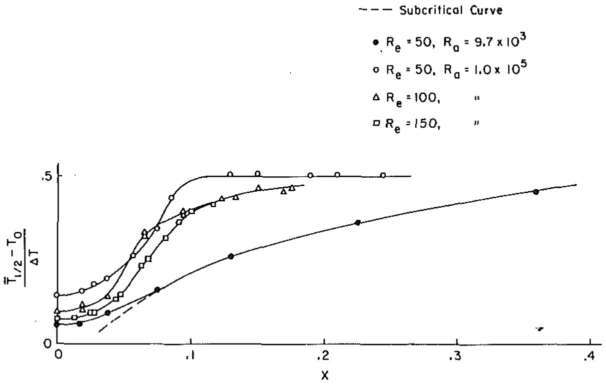

Fig. 9 Axial temperature variation at midheight

very much on Re (or Re^2/Gr). A sharp increase of $\overline{T}_{1/2}$ at a certain axial location is caused by the aforementioned upward fluid motion. At a given Ra if Re is reduced the upward motion carries more heat to the top wall, and thus enhances the mixing of cold and hot air. Consequently the thermal entrance length decreases as Re^2/Gr is reduced. Fig. 9 also shows that the abrupt thickening of the thermal boundary layer in the case of small Re^2/Gr influences the boundary layer upstream substantially.

Conclusions

Experiments were performed to study the effects of thermal instability in the hydrodynamically fully developed but thermally developing region of a channel flow of air on the heat transfer rate and flow field in the Rayleigh number range between 2.2×10^4 and 2.1×10^5. The following conclusions are drawn from the experiments.

1 The heat transfer parameter, Nusselt number, in the thermal entrance region is increased 1.6 to 4.4 times due to the thermal instability. At a given x location Nu depends mainly on Ra, but it is also influenced by the parameter Re^2/Gr near the critical Rayleigh number especially when Re^2/Gr is much less than one.

2 The temperature field and thermal entrance length are also affected by Ra and Re^2/Gr. The entrance length is about $x \div .2$ for Ra = 1.2×10^5 and Re = 50 compared to $x \div .4$ for the subcritical case. The entrance length is reduced as Ra increases, and at a given Ra the length is reduced as Re^2/Gr decreases.

3 The flow visualization experiment shows that when Re^2/Gr is much less than one, there is a strong interaction between the main stream and the flow caused by thermal instability. The wavelength of the secondary flow is nearly constant along the longitudinal direction in the entrance region, and it is determined by the channel height not by the thermal boundary layer thickness.

Acknowledgment

This research was supported by National Foundation grant ENG 76-82247.

References

1 Kamotani, Y., and Ostrach, S., "Effect of Thermal Instability on Thermally Developing Laminar Channel Flow," ASME JOURNAL OF HEAT TRANSFER, Vol. 98, No. 1, Feb. 1976, pp. 62–66.

2 Hwang, G. J., and Cheng, K. C., "Convective Instability in the Thermal Entrance Region of a Horizontal Parallel-Plate Channel Heated From Below," ASME JOURNAL OF HEAT TRANSFER, Vol. 95, No. 1, 1973, pp. 72–77.

3 Hwang, G. J., and Liu, C. L., "An Experimental Study of Convective Instability in the Thermal Entrance Region of a Horizontal Parallel-Plate Channel Heated From Below," *Canadian Journal of Chemical Engineering,* Vol. 54, Dec., 1976, pp. 521–525.

4 Ostrach, S., and Kamotani, Y., "Heat Transfer Augmentation in a Laminar Fully-Developed Channel Flow by Means of Heating From Below," ASME JOURNAL OF HEAT TRANSFER, Vol. 97, No. 2, May 1975, pp. 220–225.

5 Miao, H., Kamotani, Y., and Ostrach, S., "Convective Heat Transfer Augmentation in Thermal Entrance Region by Means of Thermal Instability," Report FTAS/TR-77-133, Dept. of Mechanical and Aerospace Engineering, Case Western Reserve University, Sept., 1977.

6 Davis, E. J., and Choi, C. K., "Cellular Convection with Liquid—Film Flow," *Journal of Fluid Mechanics,* Vol. 81, Part 3, 1977, pp. 565–592.

7 Hatton, A. P., and Turton, J. S., "Heat Transfer in the Thermal Entry Length with Laminar Flow Between Parallel Walls at Unequal Temperatures," *International Journal of Heat and Mass Transfer,* Vol. 5, 1962, pp. 673–679.

8 Hollands, K. G. T., Raithby, G. D., and Konicek, L., "Correlation Equations for Free Convection Heat Transfer in Horizontal Layers of Air and Water," *International Journal of Heat and Mass Transfer,* Vol. 18, 1975, pp. 879–884.

M. Seki
Research Scientist.

H. Kawamura
Research Scientist.

K. Sanokawa
Principal Scientist.
Chief of Heat Transfer Laboratory.

Japan Atomic Energy Institute
Tokai-mura, Ibaraki-ken,
319-11 Japan

Natural Convection of Mercury in a Magnetic Field parallel to the Gravity

Experimental and numerical studies were carried out on the natural convection of mercury in a rectangular container heated from a vertical wall. A magnetic field was applied parallel to the gravity vector and to the heated wall. Experimental results showed that the magnetic field decreased the Nusselt number considerably in the low region of the Grashof number. The effect of the parallel field was found to be less than that for a field normal to the gravity vector, but it is still not negligible. Numerical results on the Nusselt number were found to predict approximately the experimental ones. Calculated velocity profiles displayed noticeable changes due to the application of the magnetic field. A broad stagnation region was formed in the core of the container.

Introduction

Engineering studies on fusion reactors have been made along with the development of plasma confinement techniques. When a liquid metal is used as a coolant for a fusion reactor, its flow and heat transfer are influenced considerably by the magnetic field. The present study was made on natural convection of mercury in an enclosure with a magnetic field applied parallel to the gravity vector.

Many experimental and analytical studies [1-8] have been made on the natural convection of electrically conducting fluids in magnetic fields. To the authors' knowledge, however, the direction of the magnetic field has been perpendicular to the gravity vector in all the studies.

When the direction of the magnetic field is perpendicular to the gravity vector, the flow induced by the buoyant force crosses it. In that case, a term for the electromagnetic retarding force appears in the momentum equation for the vertical velocity component. A term for the buoyancy force also appears in this equation. Therefore, the boundary layer approximation is applicable, so the equation is simplified. Many workers have followed this procedure.

Natural convection with a magnetic field parallel to the gravity vector has not yet been studied. In this case, the magnetic field interacts with the velocity component that is perpendicular to the gravity vector. The momentum equations for the velocities both parallel and perpendicular to the gravity must be solved. The boundary layer approximation is thus not applicable.

In the present work, both experimental and numerical studies were made on the natural convection of mercury in a magnetic field parallel to the gravity vector. In the experiments, mercury was contained in a rectangular vessel and a uniform heat flux was applied through a vertical wall.

Experiment

The experimental apparatus used is shown in Fig. 1. The stainless steel casing is 120 mm high, 175 mm long and 120 mm wide. It contains two chambers. One chamber is filled with mercury to a height of 70-80 mm. The other chamber contains a heater and a copper conductor. The copper conductor is 80 mm in diameter and 44 mm thick with a projecting square finger 45 mm long, the end of which forms a heat transfer surface 20 mm wide and 20 mm high. The casing is so set that the heat transfer surface is parallel to both the gravitational and the magnetic field.

Five thermocouples were inserted into the finger at equal intervals. They were used to measure the heat flux at the surface. The surface temperature was measured with a CA sheathed thermocouple 0.5 mm in OD welded into a groove cut on the surface. Seven sheathed ther-

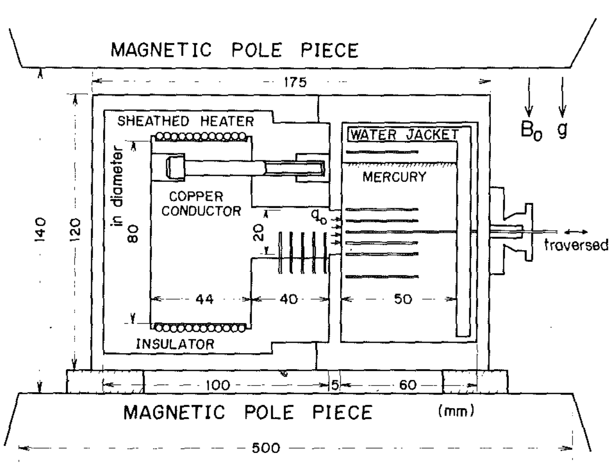

Fig. 1 Experimental apparatus

Contributed by the Heat Transfer Division for publication in the JOURNAL OF HEAT TRANSFER. Manuscript received by the Heat Transfer Division December 30, 1977

mocouples were placed in mercury with each tip 1 mm away from the surface. One of them, just opposed to the center of the heat transfer surface, was driven horizontally by a traversing mechanism, which could provide positioning within 0.01 mm. The temperature distribution in the thermal boundary layer was measured by the traversing thermocouple. The temperature of the mercury near the water jacket was also measured.

Heat was supplied by a sheathed heater wound around the cylindrical base of the copper conductor. The space in the chamber surrounding the heater was filled with thermal insulation and evacuated to minimize heat loss.

The casing was placed between the pole pieces of a large electromagnet, formerly used for MHD experiments. The pole face of the magnet was 250 mm wide and 500 mm long and the separation distance of the pole pieces was 140 mm. Magnetic induction up to 1.5 *T* was available.

The intensity of the magnetic field was increased stepwise with the heat flux held constant. In other runs, the heat flux was varied from 7 to 125 W/cm^2 while the field intensity was kept constant. In each step of a run, measurements were made after steady state was reached.

Experimental Results

Temperature distributions in the boundary layer are shown in Fig. 2(*a*) and those parallel to the heated wall in Fig. 2(*b*). The results of two experimental runs are compared. One is at $B = 0.0$ T and the other is at $B = 0.9$ T with the same heat flux of 30 W/cm^2. The lines show corresponding numerical results, which will be described later. An error in the measuring position was unavoidable due to the relatively large hot junction of the traversed thermocouple. The horizontal bars in Fig. 2(*a*) indicate the range of positional errors.

In the absence of the magnetic field, the temperature at 6 mm away from the heated wall is nearly equal to the cold wall temperature as shown in Fig. 2(*a*). When the magnetic field is applied, the surface temperature rises noticeably; that is, the heat transfer rate is decreased. The temperature near the heated wall is also increased and the thermal boundary layer becomes thicker. The mercury temperature at 1 mm away from the wall is plotted against the vertical position in Fig. 2(*b*). The rise of the temperature becomes remarkable with the application of the magnetic field.

Heat transfer results are shown in Fig. 3 with the Hartmann number as a parameter. The existing empirical correlations for natural convection of liquid metals without a magnetic field indicate that the Nusselt number is proportional to $Gr^{1/4}Pr^{1/2}$ [9, 10]. In this work, to eliminate the effect of the Prandtl number, a modified Nusselt number is defined as $Nu_c^* = Nu_c/(Pr/0.02)^{1/2}$, where $Nu_c = q_0(L/2)/k(T_c - T_\infty)$. This is shown as the ordinate in Fig. 3. The surface temperature was measured at the center of the heated wall; so the characteristic length is chosen as $L/2$ and the suffix *c* is added to the nondimensional quantities in the present paper. Thus, the quantities with the suffix *c* are local values. The broken line in Fig. 3 is the ex-

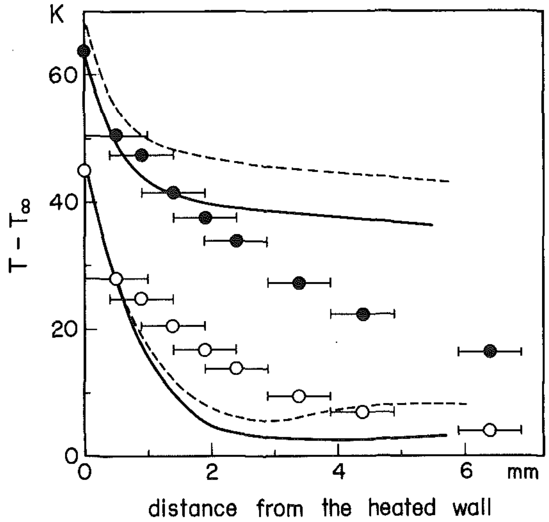

Fig. 2(*a*) Taken at $X = 1.5$

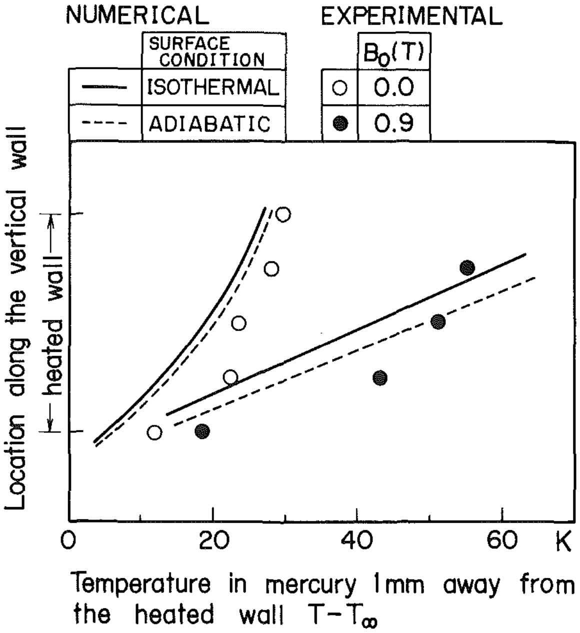

Fig. 2(*b*) Taken at $Y = 0.05$

Fig. 2 Measured temperature distributions in the direction perpendicular and parallel to the heated wall. Lines indicate the corresponding numerical results.

Nomenclature

B_0 = applied magnetic field intensity
$Gr_c = g\beta(L/2)^3(T_c - T_\infty)/\nu^2$, Grashof number
$Gr^* = g\beta L^3(q_0L/k)/\nu^2$
g = gravitational acceleration
$h = \Delta X = \Delta Y$ nondimensional mesh interval
$Ha = \sqrt{\sigma/\eta}\,B_0L$, Hartmann number
$Ha_c = \sqrt{\sigma/\eta}\,B_0(L/2)$
k = thermal conductivity of mercury
L = height of the heating surface
$Ly_c = 2Ha_c^2/\sqrt{Gr_c}$, Lykoudis number
$Nu_c = q_0(L/2)/k(T_c - T_\infty)$, Nusselt number
$Nu_c^* = Nu_c/(Pr/0.02)^{1/2}$
$Nu_0 = Nu_c^*$ for $Ha_c = 0$
p = pressure
$Pr = \nu/\alpha$, Prandtl number (of mercury)
q_0 = heat flux at the heating surface
T = temperature
T_c = temperature of the heating surface at the position of $L/2$
T_∞ = temperature of the cooling wall
u = velocity of x-component
$U = uL/\nu$
U_{max} = maximum of U
v = velocity of y-component
$V = vL/\nu$
x = axis along the direction of the gravity
$X = x/L$
X_1 = the position where heating starts
X_2 = the position where heating ends
X_E = nondimensional depth of mercury. i.e., the position of the free surface
y = axis normal to the heating surface
$Y = y/L$
Y_E = nondimensional distance between hot and cold walls, i.e., the position of the cooling wall
α = thermal diffusivity
β = thermal expansion coefficient
η = dynamic viscosity
$\theta = (T - T_\infty)/(q_0L/k - T_\infty)$, nondimensional temperature
ν = kinematic viscosity
σ = electrical conductivity

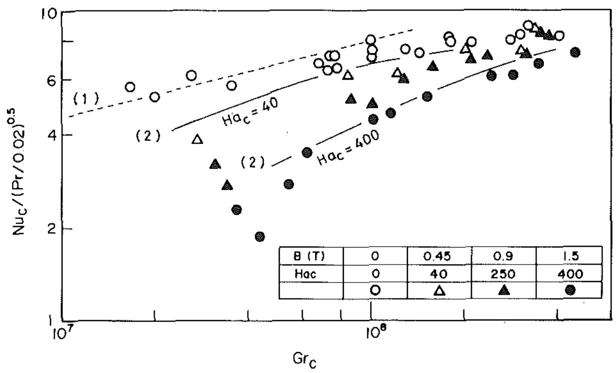

Fig. 3 Experimental results of Nu_c^* versus Gr_c for various magnetic field strength, with the broken line denoting the existing correlation for zero magnetic field (1). Solid lines are obtained from the present empirical correlation in the presence of a magnetic field (2).

(1) $Nu_x = 0.546\, Pr^{1/2}\, Gr_x^{1/4}/(0.800 + Pr)^{1/4}$,

(2) $Nu_c^*/Nu_0 = 1 - 0.13 \times 10^6 (Ha_c/Gr_c) + 7.5 \times 10^9 (Ha_c/Gr_c)^2$

isting correlation without the magnetic field. Our experimental results for $Ha_c = 0$ are proportional to $Gr_c^{1/5}$ rather than $Gr_c^{1/4}$, where $Ha_c = \sqrt{\sigma/\eta} B_0(L/2)$ and $Gr_c = g\beta(L/2)^3(T_c - T_\infty)/\nu^2$. The cause for this difference may be that the presence of the cooling wall is not negligible in the present experiment. Except for this slight difference in the exponent of the Grashof number, the present results for $Ha_c = 0$ agree with those in the literature [9, 10].

When the magnetic field was applied with the wall heat flux constant, the surface temperature increased, the Nusselt number decreased and the Grashof number increased. This effect was especially remarkable in the Grashof number low region (see Fig. 3). At high Grashof numbers, application of the magnetic field reduced the Nusselt number only slightly.

The present data are empirically found to be represented approximately by $Nu_c/Nu_0 = 1 - 0.13 \times 10^6 (Ha_c/Gr_c) + 7.5 \times 10^9 (Ha_c/Gr_c)^2$ for $Ha_c/Gr_c \lesssim 6 \times 10^{-6}$. The Nusselt numbers obtained from the correlation are plotted in Fig. 3 for $B = 0.45$ and $1.5\ T$. For high Hartmann numbers, the effect of the magnetic field on heat transfer changes with the geometrical configuration of the container, especially with the aspect ratio; that is the ratio of the height of the heated section to the distance between the hot and the cold walls. Thus, the correlation is valid only for the present aspect ratio of 0.4.

The ratio Nu_c^*/Nu_0 is plotted against the Lykoudis number, Ly_c, in Fig. 4. This number was introduced by Lykoudis [2] in his similarity analysis on natural convection with the magnetic field normal to the gravity vector. It physically represents the ratio of the pondermotive force to the square root of the product of buoyant and inertial forces.

Unlike the case for a normal magnetic field, there is no theoretical background to show that the effect of a magnetic field parallel to the gravity vector can be correlated by the Lykoudis number. However, to compare it to the effect of the direction of the magnetic field, we choose the Lykoudis number as the abscissa. The dotted-dashed line indicates the analytical results by Sparrow, et al. [1] for a uniform surface temperature with the magnetic field normal to the gravity vector. As expected, the present experimental results appear not to be well correlated with Ly_c. The numerical results for $B = 0.45$ and 1.5 T also do not coincide in a single curve. However, we can roughly compare the difference between the parallel and the normal magnetic fields. The effect of the magnetic field parallel to the gravity vector is less than that of the field perpendicular to it, but it is not negligible.

In Fig. 4, both experimental and numerical plots of Nu_c^*/Nu_0 have a tendency to approach some asymptotic values for high Hartmann numbers. This is because the natural convection is nearly frozen and heat conduction becomes dominant with application of the strong magnetic field.

Numerical Analysis

Governing Equations. The physical situation is illustrated in Fig. 5. At $X = X_E$ is a free surface. The configuration analyzed is similar to the experimental apparatus except that the geometry is two-dimensional and the height X_1 is about one-half of its experimental counterpart. The location of X_1 was found to have a small effect on the heat transfer at the heated wall; thus the height was decreased to reduce the number of mesh points. The flow away from the heated wall may actually be three-dimensional. However, a three-dimensional numerical treatment would require large computer storage and long computation times. So, we used the two-dimensional model.

The following assumptions are made in the analysis:

1 Physical properties are constant except for the density in the buoyancy term.

2 The fluid is Newtonian.

3 Compressibility effects and viscous dissipation are neglected.

4 The flow is laminar and two-dimensional.

5 The induced electric current does not distort appreciably the applied magnetic field.

6 The only nonzero component of the magnetic field is parallel to the gravitational field.

Then, the governing equations are:

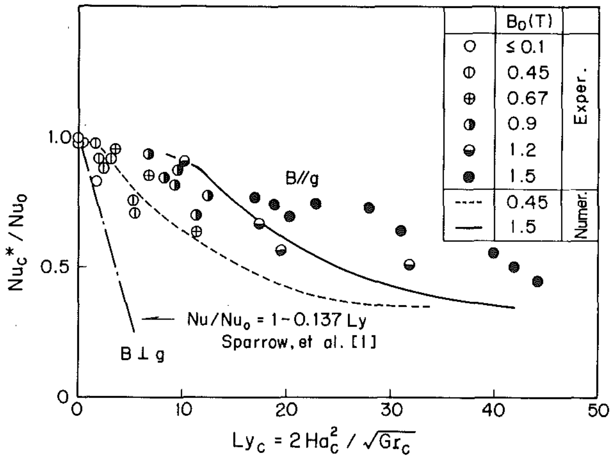

Fig. 4 Plots of Nu_c^*/Nu_0 against Ly_c for various magnetic field strength. The dotted-dashed line indicates the analytical results by Sparrow, et al. [1] for the magnetic field normal to the gravity vector.

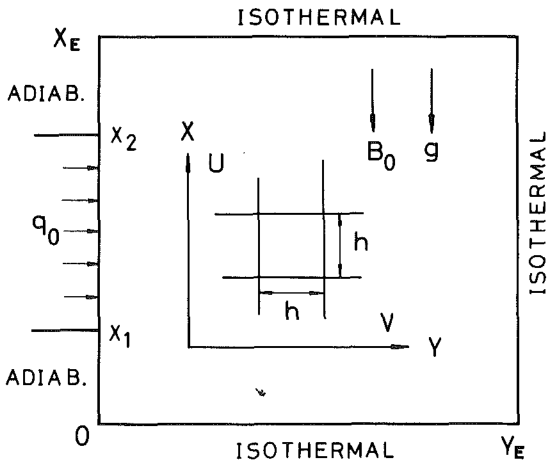

Fig. 5 Physical situation of numerical analysis

Table 1 Preliminary calculations for determination of the mesh size

X_L	Y_L	X_1	X_2	$B = 0$ T Nu$_c$	$B = 0$ T Time (s)	$B = 1.5$ T Nu$_c$	$B = 1.5$ T Time (s)	$B = 1.5$ T Core (kw)
21	26	6	16	4.05	7	2.14	8	32
41	51	11	31	6.01	151	2.70	540	57
61	76	16	46	7.25	580	3.13	1100	73
81	101	21	61	7.27	3150			88
161	201	41	121	7.42*	3600			169

* not yet converged

continuity equation

$$\partial u/\partial x + \partial v/\partial y = 0 \tag{1}$$

momentum equations

$$u\partial u/\partial x + v\partial u/\partial y = -1/\rho\ \partial p/\partial x + \nu\nabla^2 u + g\beta(T - T_\infty) \tag{2}$$

$$u\partial v/\partial x + v\partial v/\partial y = -1/\rho\ \partial p/\partial y + \nu\nabla^2 v - \sigma B_0{}^2 v/\rho \tag{3}$$

energy equation

$$u\partial T/\partial x + v\partial T/\partial y = \alpha\nabla^2 T \tag{4}$$

The momentum equations (2) and (3) are differentiated with respect to y and x respectively, and subtracted to eliminate the pressure terms. The equations are nondimensionalized. The stream function ϕ and the vorticity ζ are introduced.

$$U = \partial\phi/\partial Y,\ V = -\partial\phi/\partial X \tag{5}$$

$$\tilde{\nabla}^2\phi = \left(\frac{\partial^2}{\partial X^2} + \frac{\partial^2}{\partial Y^2}\right)\phi = -\zeta \tag{6}$$

Then, the vorticity and the energy equations become

$$U\partial\zeta/\partial X + V\partial\zeta/\partial Y = \tilde{\nabla}^2\zeta - \mathrm{Gr}^*\partial\theta/\partial Y - \mathrm{Ha}^2\partial V/\partial X \tag{7}$$

$$\mathrm{Pr}(U\partial\theta/\partial X + V\partial\theta/\partial Y) = \tilde{\nabla}^2\theta \tag{8}$$

Boundary Conditions. Uniform heat flux is supplied to the mercury from a part of the vertical wall ($X_1 \le X \le X_2$ at $Y = 0$). The opposite vertical wall and the bottom wall are assumed isothermal. In the experiment, a finite heat transfer rate exists on the free surface, but here two limiting conditions are examined. One assumes an infinite heat transfer coefficient, i.e., an isothermal surface. The other assumes zero heat transfer, i.e., an adiabatic surface. Typical numerical results on temperature distributions are shown in Fig. 2. The condition on the free surface influences considerably the flow and temperature distributions in the core region of the mercury. However, the distributions close to the heating surface change only slightly and the heat transfer coefficient of the heating surface is little influenced. Thus, the isothermal condition was employed because the calculations converge much faster.

The boundary conditions are as follows:

$$\left.\begin{aligned} \theta = 0 \qquad & \text{for } X = 0, X_E \text{ and } Y = Y_E \\ \partial\theta/\partial Y = 0 \qquad & \text{for } Y = 0 \text{ and } 0 \le X < X_1, X_2 < X \le X_E \end{aligned}\right\} \tag{9}$$

$$\left.\begin{aligned} \partial\theta/\partial Y = -1 \qquad & \text{for } Y = 0 \text{ and } X_1 \le X \le X_2 \\ U = V = 0 \qquad & \text{for } X = 0, \text{ and } Y = 0, Y_E \\ U = \partial V/\partial X = 0 \qquad & \text{for } X = X_E \end{aligned}\right\} \tag{10}$$

$$\left.\begin{aligned} \phi = 0 \qquad & \text{for } X = 0, X_E \text{ and } Y = 0, Y_E \\ \partial\phi/\partial X = \partial\phi/\partial Y = 0 \qquad & \text{for } X = 0 \text{ and } Y = 0, Y_E \\ \partial\phi/\partial Y = \partial^2\phi/\partial X^2 = \zeta = 0 \qquad & \text{for } X = X_E \end{aligned}\right\} \tag{11}$$

Numerical Procedure. The set of equations (5–8) was solved by a finite difference method. The desire to use small mesh intervals for higher accuracy had to be compromised by limitations imposed by the available computing equipment (FACOM 230–75). Calculations were made to determine the optimum mesh size. The results are shown in Table 1. The Nusselt number increased with the number of mesh points, but not beyond 61 × 76. So, the 61 × 76 mesh was used in most of the calculations.

Table 2 The effect of the differencing schema on the Nusselt number

q_0 (W/cm^2)	Gr*	Nu$_c$ Central	Nu$_c$ Mixed	Nu$_c$ Upwind
5×10^{-5}	1.48×10^4	0.856	0.845	0.848
5×10^{-2}	1.48×10^7	diverge	2.45	2.35

$B = 0$ T, with 61 × 76 mesh

Upwind difference approximations were used in the spacial derivatives of the convective terms. The upwind difference approximation may lead to significant truncation errors. The most serious error is a false diffusion, which augments the effect of viscosity [11]. When the Grashof number becomes large, however, the upwind difference is required to obtain a stable solution.

Some calculations were made with central differences to examine the convergence of the solutions. These calculations converged for low Grashof numbers up to $\mathrm{Gr}^* = 1.5 \times 10^4$. In this case, $hU_{\max}$ is about equal to unity. The calculations did not converge for larger Grashof numbers, for which $hU_{\max} \gg 1$. The results with the central and the upwind differences are compared in Table 2. Both results agree well.

The convective term in the energy equation (8) is multiplied by the Prandtl number, $\mathrm{Pr} \sim 0.02$ for mercury. A Prandtl number less than unity brings about an effect equivalent to a reduction of the velocities. Thus, the central-difference form of the energy equation is expected to converge for higher Grashof numbers than the vorticity equation. Calculations were made with the central-difference form for the energy equation and with the upwind-difference form for the vorticity equation. These converged for Grashof numbers up to $\mathrm{Gr}^* = 1.5 \times 10^7$. The differencing scheme appears to have only a slight effect on the Nusselt number.

For the high Grashof numbers of practical interest, $U_{\max}$ exceeds 10^3. So, to obtain a stable solution with central differences, more than 10^3 mesh points are required in one direction. This is far beyond the capacity of available computers. Upwind differences were therefore used for the convective terms.

The calculations were made in the following order:

1 The energy equation was solved by SOR.

2 The vorticity equation was solved by block SOR.

3 The stream function was obtained by SOR.

4 New wall vorticities were computed from the stream function as [12, 13]

$$\zeta_{i,1} = \frac{8\phi_{i,2} - \phi_{i,3}}{2(\Delta Y)^2} \tag{12}$$

5 Velocities were calculated from the stream function.

6 If the solutions had not converged, return was made to 1.

The solution was assumed to have converged when the following criteria were satisfied simultaneously for the mth iteration.

$$\|\theta^m\| = \frac{\sum_{i,j}|\theta^m_{i,j} - \theta^{m-1}_{i,j}|}{\sum_{i,j}\theta^m_{i,j}} < 1 \times 10^{-5}$$

$$\|\phi^m\| = \frac{\sum_{i,j} |\phi_{i,j}^m - \phi_{i,j}^{m-1}|}{\sum_{i,j} \phi_{i,j}^m} < 1 \times 10^{-5}$$

$$\epsilon_\zeta = \max\left(\frac{|\zeta_{i,j}^m - \zeta_{i,j}^{m-1}|}{\zeta_{i,j}^m}\right) < 1 \times 10^{-2}$$

Numerical Results

Velocity distributions with and without the magnetic field are shown in Fig. 6. In the absence of the magnetic field, a circulating flow is formed in the container and the velocity V is of the same order of U as seen in Fig. 6. With the application of the magnetic field, the velocity V directly interacts with it and is strongly suppressed. The effect is transmitted to U through the change of the pressure gradient and the mass continuity. Hence, U is also decreased noticeably and a broad stagnation region is formed in the core of the container.

The profile and the magnitude of V may change with the aspect ratio and the condition on the upper surface; a free surface or a solid one. Thus, further studies are needed on these points.

The numerical results for the temperature distributions coincide well with those of the experiments in the absence of the magnetic field (see Fig. 2). When the magnetic field is applied, both results agree only in the vicinity of the wall and the numerical results show higher values away from the wall. At the field strength of 1.5 T, numerical results give higher temperatures than those of the experiments in the whole region.

When the magnetic field is strong, the core region becomes broadly stagnated. The velocity U near the heated wall was suppressed so much that the convective heat transfer rate was decreased. Then, the conducted heat occupies an increasing portion of the total heat flow. Thus, a three-dimensional effect may be inevitable. This is one of the causes of the large difference between numerical and experimental results in the presence of the strong magnetic field.

The values of Nu_c^* obtained numerically are plotted against Gr_c in Fig. 7. The numerical results for $\mathrm{Ha}_c = 0$ agree well with the experimental ones, but those for the high Hartmann number are much lower than those by experiment. One of the causes may be that the mesh interval is not sufficiently small near the heating surface. However, further reduction of the mesh interval requires impractical computing time. So, what is known as "zooming" was tried. In this scheme, calculations are first made with the 61 × 76 mesh, and then the meshes are further divided into two or three meshes. The values at the new mesh points are given by interpolation, and calculations are continued. Repetitions are made only for the several meshes near the boundaries to save computation time, because velocities in the core region are so small that they have little effect on the heat transfer coefficient. However, the temperature is solved for over the whole region, because it is high even in the core region especially for high Hartmann numbers. The Nusselt numbers obtained by the zooming method are shown in Fig. 7 by the dashed line. The improvement is noticeable.

Typical velocity distributions near the heating wall are shown in Fig. 8. The solid line is the result with the 61 × 76 mesh. The velocity U is a maximum at the mesh point adjacent to the heated wall. This is not a desirable effect in the calculation of the velocity profile. And, as the mesh interval is reduced by the zooming, $Y_{\max}$ does not fall on the mesh point adjacent to the wall but on the second mesh point. The peak velocity also beocmes larger. These effects lead to an increase of the convective heat transfer near the surface. Thus, the Nusselt number increases, so it is closer to the experimental one as shown in Fig. 7.

When the Grashof number is low and the Hartmann number is high, the velocity is small and $Y_{\max}$ is very close to the wall. A quite small mesh interval is required near the wall. Further reduction of the mesh interval consumes too much computing time even with the zooming. So, the calculations were made for the limiting case when $Y_{\max}$ coincides with the wall; that is, slip is allowed on the walls. The resulting Nusselt numbers are shown by the dotted line in Fig. 7. They are, of course, generally large compared with the experimental ones because of the overestimate of the convective effect near the wall. As the Grashof number decreases, however, the results with slip become a better approximation.

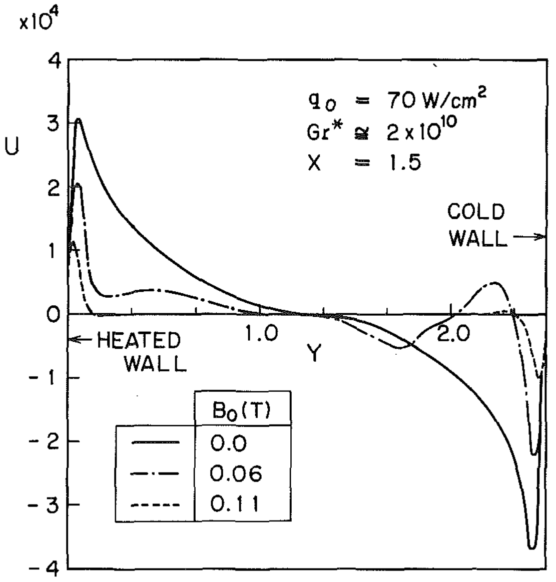

Fig. 6(*a*) Taken at $X = 1.5$

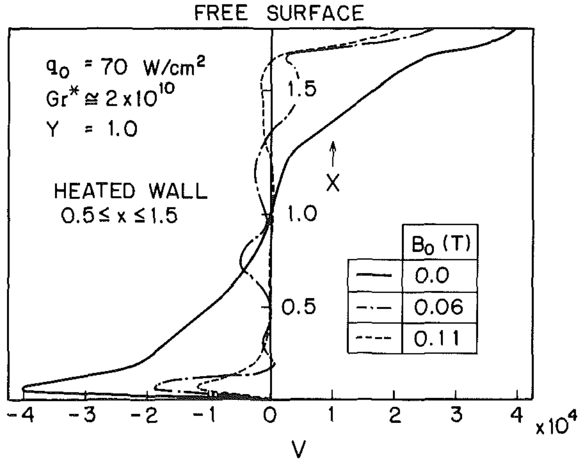

Fig. 6(*b*) Taken at $Y = 1.0$

Fig. 6 Calculated velocity distribution. U and V for $B = 0.0, 0.06, 0.11$ T with the surface heat flux of 70 W/cm^2.

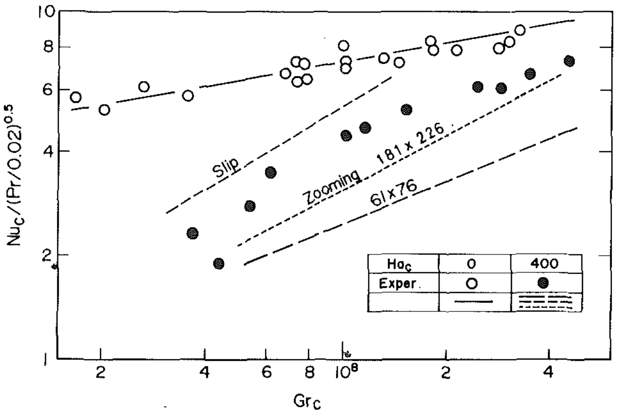

Fig. 7. Comparison of experimental and numerical results on Nu_c^* for $\mathrm{Ha}_c = 0.0$ and 400.

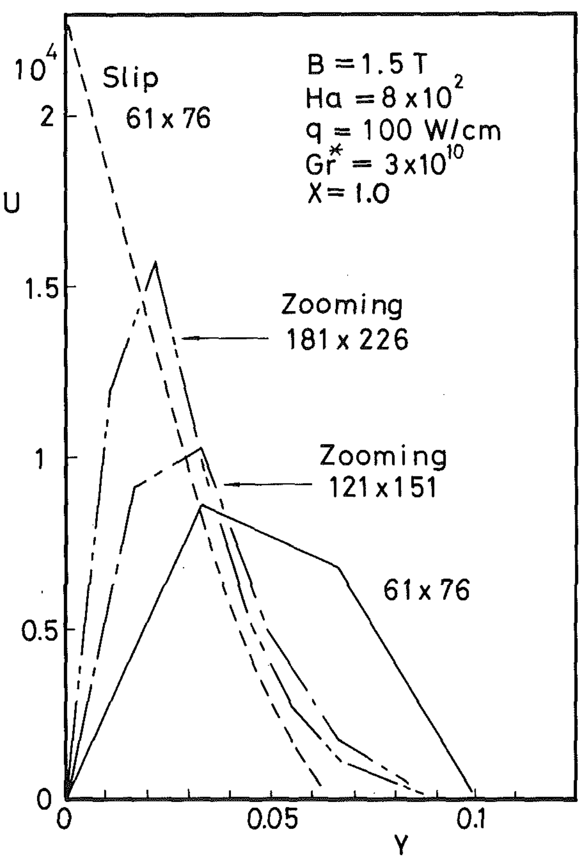

Fig. 8 Calculated velocity distributions near the heated wall with various mesh size.

Conclusions

1 The effect of a magnetic field parallel to the gravity vector is less than that for a field normal to the gravity vector, but it is still not negligible.

2 The experimental results show that the decrease of the Nusselt number is the greatest in the low region of Grashof number.

3 The velocity distribution is influenced noticeably by the application of the parallel magnetic field and a broad stagnant region is formed in the core of the container.

4 The results of numerical calculations with the 61 × 76 mesh coincide well with the experimental ones for zero magnetic field.

5 The numerical values of the heat transfer coefficient are much smaller than the experimental ones for a strong magnetic field, but with the zooming method of computation, they become closer to the experimental ones.

6 The heat transfer rates with the assumption of slip flow are larger than the experimental ones, but they are good approximations for low Grashof and high Hartmann numbers.

References

1 Sparrow, E. M., and Cess, R. D., "The Effect of a Magnetic Field on Free Convection Heat Transfer," *Int. J. Heat Mass Transfer*, Vol. 3, 1961, pp. 267–274.

2 Lykoudis, P. S., "Natural Convection of an Electrically Conducting Fluid in the Presence of a Magnetic Field," *Int. J. Heat Mass Transfer*, Vol. 5, 1962, pp. 23–34.

3 Gupta, A. S., "Steady and Transient Free Convection of an Electrically Conducting Fluid from a Vertical Plate in the Presence of a Magnetic Field," *Appl. Sci. Res. Section A*, Vol. 9, 1960–1961, pp. 319–333.

4 Poots, G., "Laminar Natural Convection Flow in Magneto-Hydrodynamics," *Int. J. Heat Mass Transfer*, Vol. 3, 1961, pp. 1–25.

5 Papaliou, D. D., and Lykoudis, P. S., "Magneto-Fluid-Machanic Laminar Natural Convection—An Experiment," *Int. J. Heat Mass Transfer*, Vol. 11, 1968, pp. 1385–1391.

6 Sapunkov, Ya.G., "Free Convection in a Strong Magnetic Field," *Magnitonaya Gidrodinamika*, Vol. 4, 1974, pp. 24–31.

7 Papailiou, D. D., and Lykoudis, P. S., "Magneto-Fluid-Mechanics Free Convection Turbulent Flow," *Int. J. Heat Mass Transfer*, Vol. 17, 1974, pp. 1181–1189.

8 Romig, M. F., "The Influence of Electric and Magnetic Fields on Heat Transfer to Electrically Conducting Fluids," *Advances in Heat Transfer*, Vol. 1, 1964, pp. 267–354, Academic Press.

9 Kutateladze, S. S., et al., "Liquid Metal Heat Transfer Media," *Consultants Bureau*, Inc., New York, 1959.

10 Sheriff, N., and Davies, N. W., "Review of Liquid Metal Natural Convection Relevant to Fast Reactor Conditions," TRG-2959, 1977.

11 De Vahl Davis, G. and Mallenson, G. D., "An Evaluation of Upwind and Central Difference Approximations by a Study of Recirculating Flow," *Computers and Fluids*, Vol. 4, 1974, pp. 29–43.

12 Barakat, H. Z., and Clark, J. A., "Analytical and Experimental Study of the Transient Laminer Natural Convection Flows in Partially Filled Liquid Containers," *Proc. of the Third Int. Heat Transfer Conf.*, Vol. 2, 1966, pp. 152–162.

13 Wilders, J. O., and Churchill, S. W., "The Finite-Difference Computation of Natural Convection in a Rectangular Enclosure," *AIChE. J.*, Vol. 12, 1966 pp. 161–166.

A. M. C. Chan
Graduate Student.

S. Banerjee
Professor.

Department of Engineering Physics,
McMaster University,
Hamilton, Ontario, L8S 4M1
Canada

A Numerical Study of Three-Dimensional Roll Cells within Rigid Boundaries

Three-dimensional natural convection, roll cells within rigid enclosures have been studied with a previously developed numerical technique based on the marker and cell method. Given identical initial conditions, the velocity and temperatures fields are found to be sensitive to the thermal boundary conditions on the side walls and the aspect ratio of the enclosure. Two-dimensional results are also obtained and compared with the corresponding three-dimensional results. The two-dimensional calculations do not agree well with the three dimensional ones, especially for enclosures having aspect ratios less than unity. This indicates that care must be taken in analyzing natural convection problems of this type with two-dimensional methods.

Introduction

The motivation for our work arose out of a study of natural convection cooling of irradiated nuclear fuel in shipping flasks and storage bays. However, the study of Bernard type cells has been a subject of considerable previous experimental and numerical work. In general, the detailed temperature and velocity profiles are difficult to measure and Nusselt numbers have been used in comparisons between experimental and numerical results.

Because the three dimensional calculations require large computing times, the main numerical investigations have been for two-dimensional flows [1, 2]. The early three-dimensional numerical calculations were by Aziz and Hellums [3] and more recently by Ozoe, et al. [4]. In both cases, the calculations were done for relatively low Rayleigh numbers and used the vorticity-stream function approach.

In the present paper, we present solutions at higher Rayleigh numbers (up to 10^5). The method used is based on the primitive variables and has been described in detail in a previous paper [5]. By this method, we obtain the velocity and temperature fields during the transient from the initial conditions, as well as the steady-state solutions.

The geometry of the system considered is shown in Fig. 1. The effect of adiabatic and isothermal vertical side walls have been studied. Comparisons have also been made between two and three-dimensional calculations.

Conservation Equations, Boundary Conditions and Numerical Technique

The governing equations are the conservation equations for laminar, natural convection flows based on the Boussinesq approximations [6]. The equations shown are for gravitational forces in the y-direction.

$$\frac{\partial u}{\partial x} + \frac{\partial v}{\partial y} + \frac{\partial w}{\partial z} = 0, \tag{1}$$

$$\frac{\partial u}{\partial t} + u\frac{\partial u}{\partial x} + v\frac{\partial u}{\partial y} + w\frac{\partial u}{\partial z} = -\frac{1}{\rho}\frac{\partial P'}{\partial x} + \nu\left[\frac{\partial^2 u}{\partial x^2} + \frac{\partial^2 u}{\partial y^2} + \frac{\partial^2 u}{\partial z^2}\right] \tag{2a}$$

$$\frac{\partial v}{\partial t} + u\frac{\partial v}{\partial x} + v\frac{\partial v}{\partial y} + w\frac{\partial v}{\partial z} = -\frac{1}{\rho}\frac{\partial P'}{\partial y} + \beta g(T - T_0) + \nu\left[\frac{\partial^2 v}{\partial x^2} + \frac{\partial^2 v}{\partial y^2} + \frac{\partial^2 v}{\partial z^2}\right], \tag{2b}$$

$$\frac{\partial w}{\partial t} + u\frac{\partial w}{\partial x} + v\frac{\partial w}{\partial y} + w\frac{\partial w}{\partial z} = -\frac{1}{\rho}\frac{\partial P'}{\partial z} + \nu\left[\frac{\partial^2 w}{\partial x^2} + \frac{\partial^2 w}{\partial y^2} + \frac{\partial^2 w}{\partial z^2}\right], \tag{2c}$$

$$\frac{\partial T}{\partial t} + u\frac{\partial T}{\partial x} + v\frac{\partial T}{\partial y} + w\frac{\partial T}{\partial z} = \frac{k}{\rho C_p}\left[\frac{\partial^2 T}{\partial x^2} + \frac{\partial^2 T}{\partial y^2} + \frac{\partial^2 T}{\partial z^2}\right]. \tag{3}$$

The initial and boundary conditions are described below:

(*1*) *Initial Conditions:*

$$\text{at } t = 0, 0 \leqslant x \leqslant L,\ 0 \leqslant y \leqslant H,\ 0 \leqslant z \leqslant D$$

$$T = T_0, u = v = w = 0.$$

(2) *Boundary Conditions: no slip, rigid walls*

$$\text{at } t \geqslant 0, x = 0, L \text{ or } y = 0, H \text{ or } x = 0, D$$

$$u = v = w = 0.$$

(3) *Thermal Boundary Conditions:*

(a) Isothermal Walls

$$T|_{x=0,L} = T_w;\ T|_{y=0,H} = T_w;\ T|_{z=0,D} = T_w.$$

Contributed by the Heat Transfer Division for publication in the JOURNAL OF HEAT TRANSFER. Manuscript received by the Heat Transfer Division September 15, 1978.

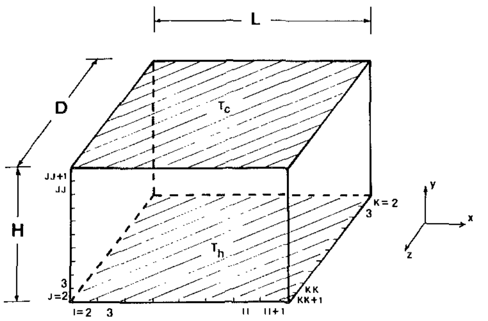

Fig. 1 Diagram of computational geometry

(b) Adiabatic Wall

$$\left.\frac{\partial T}{\partial x}\right|_{x=0,L} = 0; \left.\frac{\partial T}{\partial y}\right|_{y=0,H} = 0; \left.\frac{\partial T}{\partial z}\right|_{z=0,D} = 0.$$

Convective motion is initiated by imposing a constant temperature gradient across the fluid layer with

$$T|_{y=0} = T_h \quad \text{and} \quad T|_{y=H} = T_c$$

at $t \geqslant 0$.

The conservation equations, (1, 2) and (3) are solved by the finite difference method described in detail in our previous paper [5]. The technique uses the primitive form of the conservation equations, using pressure and velocity as dependent variables rather than vorticity and stream function. This results in a simple formulation for the boundary conditions for the three-dimensional problem.

A detailed discussion of the applicability of the technique to two and three-dimensional, laminar, natural convection flows has been presented [5].

The finite difference mesh used for the numerical solution of the conservation equations consisted of cubical computational cells. The velocity components are defined at the cell edges whereas temperature and pressure are defined at the cell centers. We used the fully "donor cell" form in finite differencing the advective terms to retain the "transportive property." However, forms with a certain amount of centered differencing have also been incorporated in the general program. First-order differences are used for the time derivative. A single layer of fictitious cells surrounding the fluid are used to impose the necessary boundary conditions. The finite difference scheme is explicit. The velocity field is computed from the momentum equations using the previous time step values. The new velocity field is then adjusted iteratively to satisfy the mass conservation equation by adjusting the computational cell pressures. When the new adjusted velocity field has been calculated, it is used to compute the new temperature field using the energy equation. The new velocity, pressure and temperature fields are then used as the starting values for the next time step cycle. The temperature gradients at isothermal, constant temperature walls are calculated using second-order differences and the boundary cell temperatures are obtained by quadratic extrapolation. The average Nusselt number is calculated at the heated lower boundary using the computed temperature gradient at $y = 0$. For example,

$$\overline{\mathrm{Nu}} = \frac{hL}{k} = \frac{1}{D(T_h - T_c)} \iint \left(\frac{\partial T}{\partial y}\right)_{y=0} dxdz. \tag{4}$$

Two geometries have been investigated: a cubical enclosure and a rectangular enclosure with a square base. The aspect ratio of the latter is 5/11. For computation purposes, the cubical and rectangular enclosures are divided into $9 \times 9 \times 9 = 729$ (i.e., $II = JJ = KK = 9$) and $11 \times 5 \times 11 = 605$ (i.e., $II = KK = 11, JJ = 5$) computational cells, respectively. The working fluid assumed has $\mathrm{Pr} = 0.72$. Both isothermal and adiabatic vertical side walls are used for the cubical enclosure. Only isothermal vertical side walls boundary conditions have been investigated for the rectangular enclosure. The corresponding two-dimensional solutions have also been obtained for comparison.

The effect of nodalization on the convergence of the solutions was studied. The mesh size near the heated lower boundary was reduced in steps, from $H/7$ to $H/35$. The Nusselt number increases slowly toward its asymptotic value. At $H/35$ it was within one percent of the converged value. The change in Nusselt number between mesh sizes $H/7$ and $H/35$ was less than 15 percent.

The overall flow pattern and temperature distribution remained the same in all cases. However, the velocities and temperatures in the wall region did change, leading to the change in Nusselt numbers.

Noding resolution studies near the side walls were also performed. Results were obtained for the case of $\mathrm{Ra} = 10^4$ using a cubical enclosure and isothermal side wall. Uniform mesh was used. The Nusselt number was found to change only slightly, from 8.04 to 8.13 when the mesh was changed from $9 \times 9 \times 9$ to $16 \times 9 \times 9$. Therefore, we concluded that the Nusselt number was not significantly affected by nodalization near the side walls within the range of node sizes studied.

Numerical stability of the computational scheme has been discussed previously and requires that the Courant number based on the fluid velocity be less than unity [5]. The computer time required on the McMaster University CDC 6400 computer was found to be about 0.006 to 0.01 s per computational cell per time step for these calculations. Steady state is found to be attained much faster for cases with isothermal vertical side walls than adiabatic walls. For the latter cases, steady state is reached for $\tau \sim 0.3$.

Numerical Results

Case I—Cubical Enclosure with Adiabatic Side Walls. Calculations have been made for Rayleigh numbers ranging from 4×10^3 to 10^5. Results for $\mathrm{Ra} = 10^4$ are shown in Fig. 2. It shows the steady-state velocity and temperature fields for the x-y planes at $K = 2, 4, 6, 8$, and 10. Each isotherm shown is ten percent of the overall temperature difference between the heated lower boundary and the cooled upper wall. The three-dimensional effect can be clearly seen from the

Nomenclature

A' = dimensionless speed of flow at x-y plane $= \sqrt{U^2 + V^2}$
A = maximum dimensionless speed of flow at x-y plane
C_p = specific heat of fluid
D = width of enclosure
g = gravitational acceleration
h = heat transfer coefficient
H = height of enclosure
$I, J, K,$ = computational cell (or plane) in x, y, and z directions
II, JJ, KK = total number of cells (or planes) that the enclosure is divided into for computation purpose in x, y, and z directions
k = conductivity of fluid
L = length of enclosure
$\overline{\mathrm{Nu}}$ = average Nusselt number
P' = pressure fluctuation
Pr = Prandtl number
Ra = Rayleigh number $= \dfrac{g\beta(T_h - T_c)H^3}{\nu\alpha}$
t = time
T = temperature
T_0 = reference temperature
u = velocity component in x-direction
U = dimensionless velocity component in x-direction $= uH/\nu$
v = velocity component in y-direction
V = dimensionless velocity component in y-direction $= vH/\nu$
w = velocity component in z-direction
W = dimensionless velocity component in z-direction $= wH/\nu$
β = volumetric coefficient of expansion of fluid
ν = kinematic viscosity of fluid
ρ = density of fluid
τ = dimensionless time $= t\nu/H^2$
θ = dimensionless temperature $= (T - T_c)/(T_h - T_c)$

Subscripts

h = heated surface
c = cold surface
w = wall

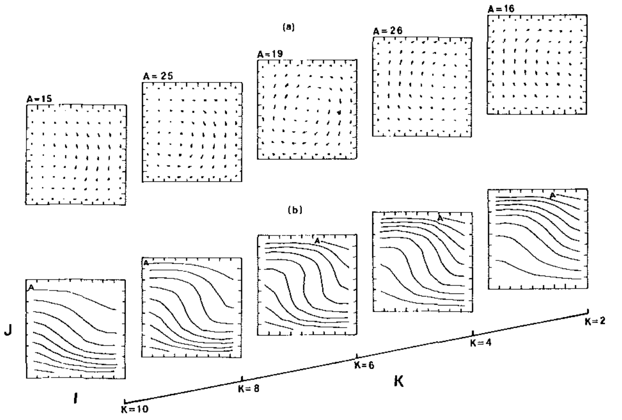

Fig. 2 Three-dimensional steady-state x-y plane solution for a cubical enclosure with adiabatic side walls (Ra = 10^4, Pr = 0.72). (a) velocity plot, (b) isotherms

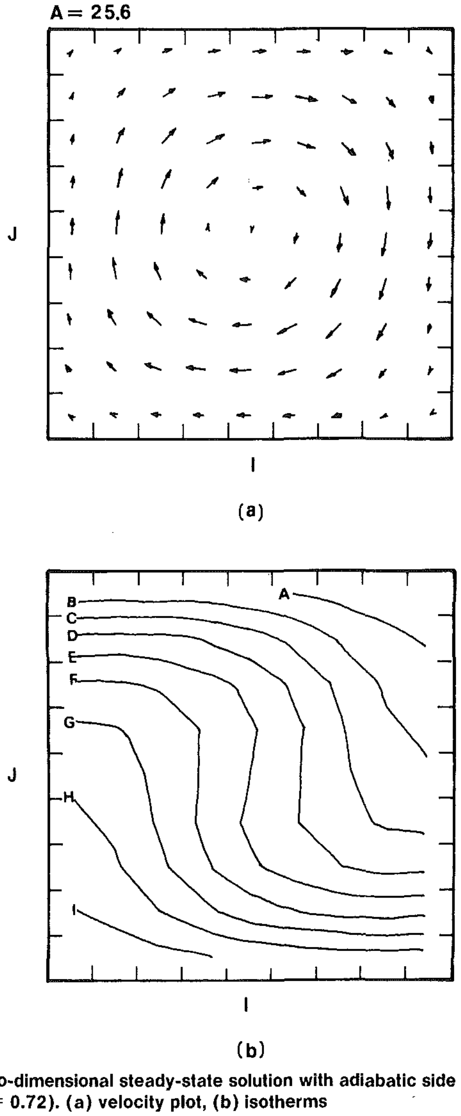

Fig. 3 Two-dimensional steady-state solution with adiabatic side walls (Ra = 10^4, Pr = 0.72). (a) velocity plot, (b) isotherms

figure. Results at the z-y planes for different values of I are identical to the x-y plane results at the corresponding values of K; i.e., the results are symmetric.

At the mid-planes (for I = 6 or K = 6), the effect of the rigid side walls is minimum and the results can be compared directly with the corresponding two-dimensional calculations (Fig. 3). It can be seen that the results agree relatively well. However, the roll cell in the three-dimensional case is not as square. Also, in the three-dimensional case, the velocity and fluid temperatures are lower. The same effect was reported by Aziz and Hellums [3]. It was hypothesized that the addition of rigid side walls reduced the magnitude of the flow.

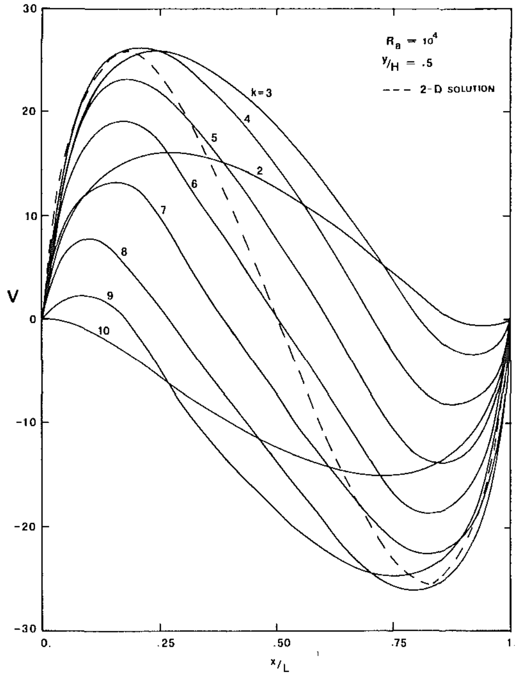

Fig. 4 Vertical velocity profile at mid-height of enclosure with adiabatic side walls

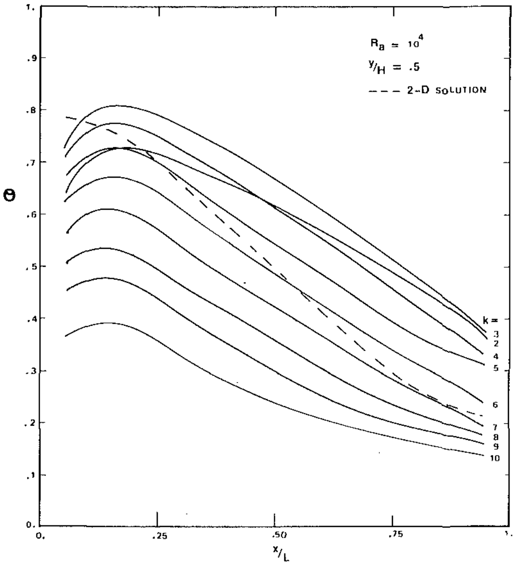

Fig. 5 Temperature profile at mid-height of enclosure with adiabatic side walls

To summarize the results, the vertical velocity and temperature profile at enclosure mid-height are plotted in Figs. 4 and 5 for several x-y planes, i.e., for various values of K. Results for the two-dimensional case are also included for comparison.

The average Nusselt number is computed as a function of Rayleigh number. They are shown in Fig. 6 along with results from other investigators. The agreement is generally good. At higher Rayleigh numbers they agree well with Jakob's experimental results [7], and at lower Rayleigh numbers they are close to Ozoe's calculations [4].

Case II—Cubical Enclosure with Isothermal Side Walls. Results are shown for Ra = 10^4. The side walls were kept at a constant temperature equal to that of the upper boundary. Because the side walls are cooled, the fluid tends to flow downward along them and, hence, forms two vertical roll cells at x-y or z-y planes far from the walls. Fig. 7 shows the x-y plane results at the mid-plane (for K = 6). When compared with the two-dimensional results (Fig. 8), this reveals

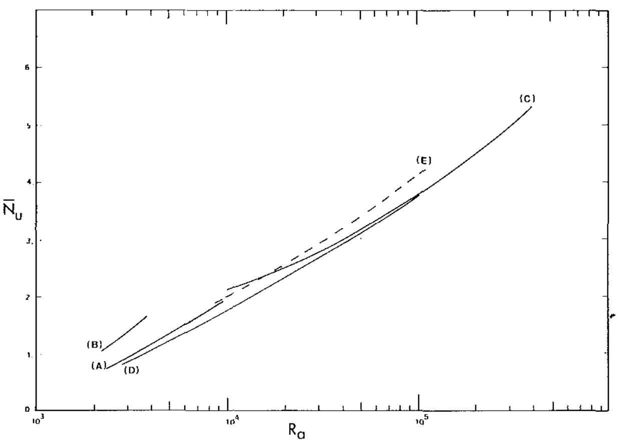

Fig. 6 Average Nusselt number for a cubical enclosure with adiabatic side walls versus Rayleigh number. [A] Ozoe, et al. (three-dimensional, Pr = 1.0), [B] Aziz, et al. (three-dimensional, Pr = 1), [C] Jakob (three-dimensional, Pr = 0.72, expt.), [D] Present authors (three-dimensional, Pr = 0.72), [E] Present authors (two-dimensional, Pr = 0.72)

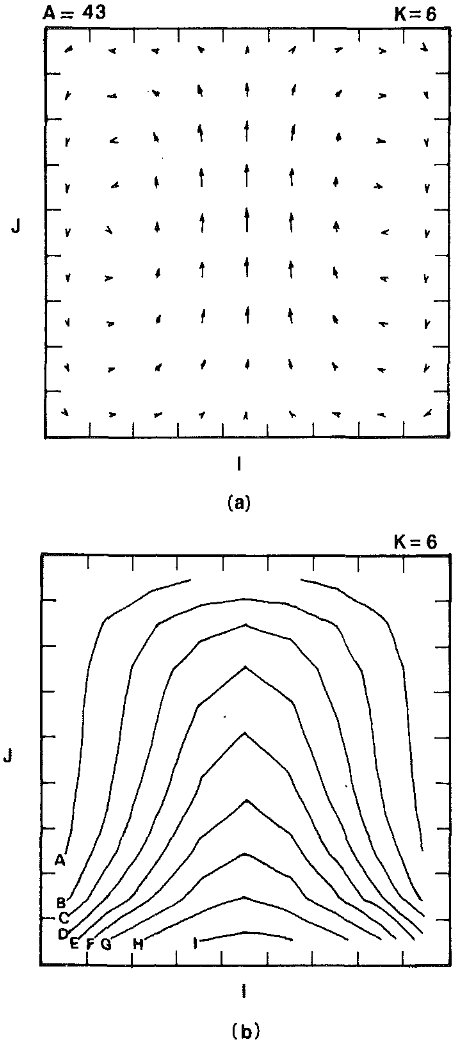

Fig. 7 Three-dimensional steady-state x-y plane solution for a cubical enclosure with isothermal side walls (Ra = 10^4, Pr = 0.72). (a) velocity plot, (b) isotherms.

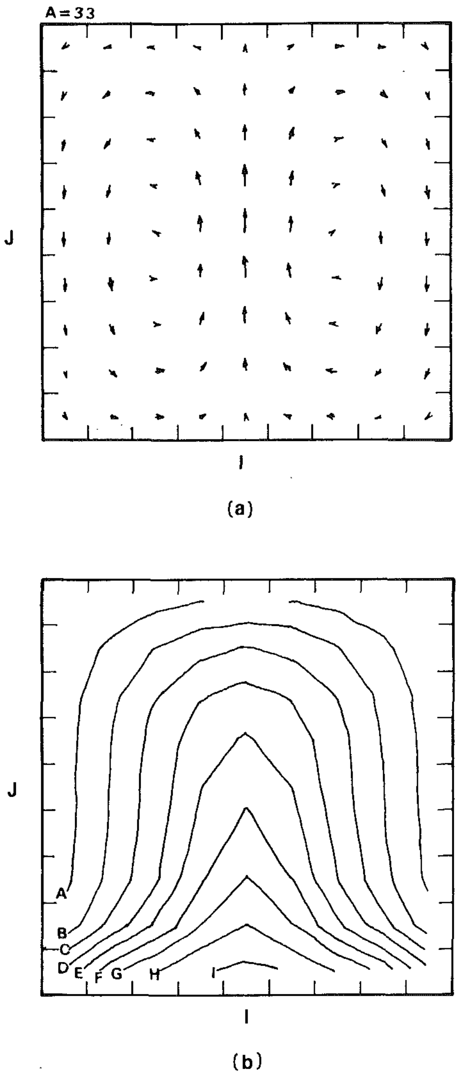

Fig. 8 Two-dimensional steady-state solutions with isothermal side walls (Ra = 10^4, Pr = 0.72). (a) velocity plot, (b) isotherms

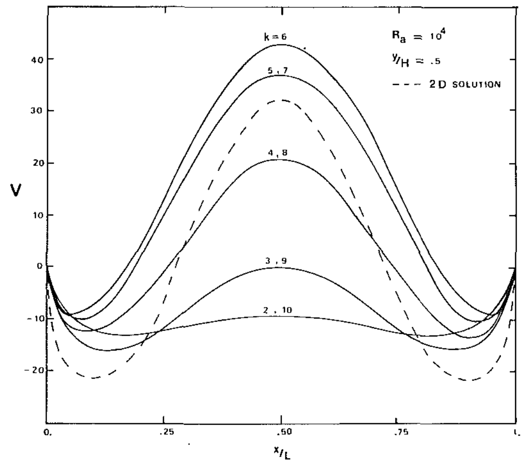

Fig. 9 Vertical velocity profile at mid-height of enclosure with isothermal side walls

the effect of the third dimension. It increases the upward flow stream at the center of the enclosure and decreases the downward flow near the side walls. Figs. 9 and 10 plot the vertical velocity and temperature profile at the enclosure mid-height for several x-y planes along with the two-dimensional solution. It can be seen that the results are symmetrical about the mid-plane ($K = 6$). For the two-dimensional case, the upward flow velocity is lower and the fluid temperature is higher than the three-dimensional case at the mid-plane ($K = 6$). This difference from the "adiabatic side walls" case is not unexpected. The additional rigid walls in the third dimension reduce the magnitude of the motion; however, the additional cold surfaces also enhance fluid circulation. The latter effect appears to dominate and hence results

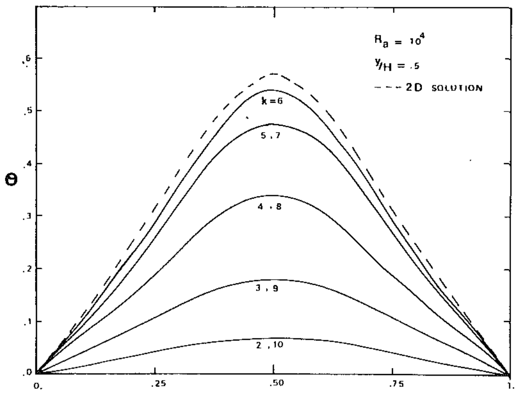

Fig. 10 Temperature profile at mid-height of enclosure with isothermal side walls

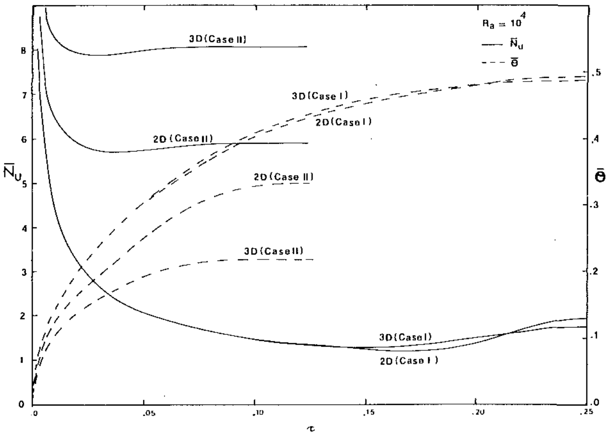

Fig. 11 Transient average Nusselt number and average fluid temperature

in a higher flow velocity at the center.

The transient behaviour of Cases I and II are compared in terms of the average Nusselt number and the average fluid temperature in Fig. 11. For isothermal side walls, the transient is over for τ less than 0.08, whereas for the enclosures with adiabatic side walls, τ greater than 0.25 is required for steady state. Steady-state average Nusselt numbers in the latter situation (Case II) are much higher and show large differences between two- and three-dimensional calculations. For Case I, the steady-state average fluid temperature approaches 0.5 as expected for both two and three-dimensional cases. It should be noted that while the average Nusselt number difference between two-dimensional and three-dimensional calculations is small for Case I, (adiabatic side walls) it is large for Case II (isothermal side wall). We feel that the large variation for the latter situation is more than possible inaccuracies due to nodalization.

Case III—Rectangular Enclosure with Isothermal Side Walls. In order to study the flow patterns for aspect ratios other than unity, a rectangular enclosure with a square base and an aspect ratio of 5/11 was investigated. Isothermal side walls were chosen because steady state could be achieved much faster. Results are shown for Ra = 10^5. The velocity field is shown in Fig. 12 for x-y planes with K = 3, 5, 7, 9 and 11. K = 7 is the mid-plane in the z-direction. The results are almost perfectly symmetric about the center of the enclosure.

Fig. 13 shows the corresponding two-dimensional solutions. The mode of circulation is entirely different. The effect of the three-dimensional calculation is particularly pronounced in this case.

Conclusion

A numerical study on three-dimensional Bernard cells has been made. Given identical initial conditions, the mode of circulation is found to be dependent on the thermal boundary conditions of the side walls and the aspect ratio of the enclosure.

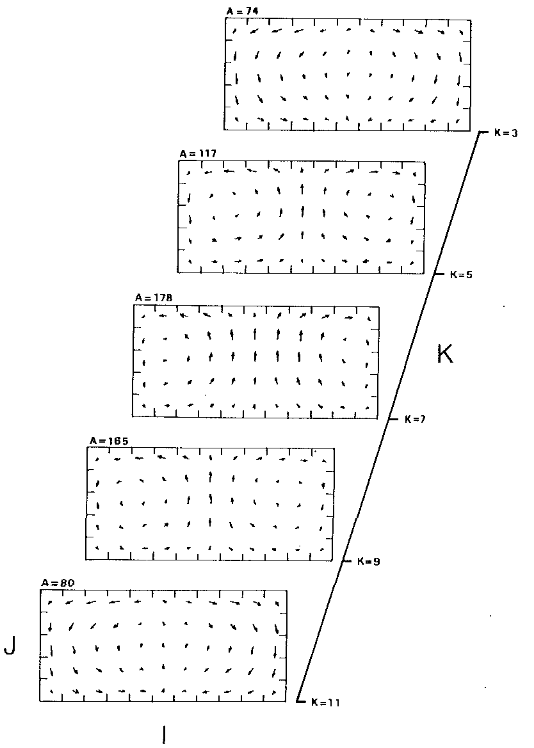

Fig. 12 Three-dimensional steady-state x-y plane solution for a rectangular enclosure with aspect ratio, 5/11 and isothermal side walls (Ra = 10^5, Pr = 0.72)

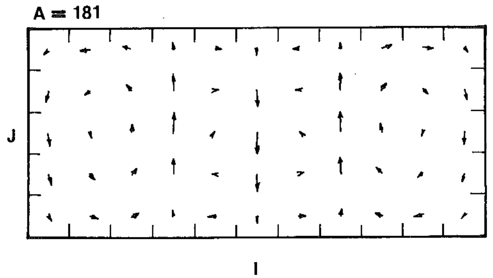

Fig. 13 Two-dimensional steady-state solution for a rectangular enclosure with isothermal side walls (Ra = 10^5, Pr = 0.72)

When the three-dimensional results are compared with the corresponding two-dimensional results, it is evident that the calculations do not agree very well in general. This is especially true for enclosures having an aspect ratio less than unity when different flow patterns are obtained. Therefore, care must be taken when two-dimensional calculations are used to approximate the three-dimensional situation.

References

1 Fromm, J. E., "Numerical Solutions of the Nonlinear Equations for a Heated Fluid Layer," *Phys. of Fluid*, Vol. 8, No. 10, 1965, pp. 1757–1769.

2 Cabelli, A. and DeVahil Davis, G., "A Numerical Study of the Bernard Cell," *J. Fluid Mech.*, Vol. 45, pt. 4, 1971, pp. 805–829.

3 Aziz, K. and Hellums, J. D., "Numerical Solution of the Three-Dimensional Equations of Motion for Laminar Natural Convection," *Phys. of Fluids*, Vol. 10, No. 2, 1976, pp. 314–324.

4 Ozoe, H., Yamamoto, K., Churchill, S. W., and Sayama, H., "Three Dimensional, Numerical Analysis of Laminar Natural Convection in a Confined Fluid Heated from Below," ASME JOURNAL OF HEAT TRANSFER, May 1976, pp. 202–207.

5 Chan, A. M. C. and Banerjee, S., "Three-Dimensional Numerical Analysis of Transient Natural Convection in Rectangular Enclosures," ASME JOURNAL OF HEAT TRANSFER, Feb. 1979, pp. 114–119.

6 Calder, K. L., "In Clarification of the Equations of Shallow-Layer Thermal Convection for a Compressible Fluid Based on the Boussinesq Approximation," *Quarterly J. of the Royal Meteorological Soc.*, Vol. 97, 1968, pp. 88–92.

7 Jakob, M., *Heat Transfer*, Vol. 1, 1949, John Wiley & Sons, New York, p. 535.

S. Ostrach
C. Raghavan

Department of Mechanical and Aerospace Engineering
Case Western Reserve University
Cleveland, OH

Effect of Stabilizing Thermal Gradients on Natural Convection in Rectangular Enclosures[1]

An experimental investigation is described of the effect of stabilizing thermal gradients on natural convection in silicone oils in rectangular enclosures with different aspect ratios. The Prandtl numbers are of the order of 10^5, Grashof numbers range up to 20, and the aspect ratios are 1 and 3. The thermal boundary conditions are established by imposing different temperatures on opposite walls of the enclosure so that there is simultaneous horizontal and vertical heat flow. The effect of stabilizing temperature gradients on flow established by horizontal gradients and the effect of horizontal temperature gradients on a stably stratified fluid are studied for ranges of the parameters. Streamline patterns are observed at steady-state and velocity profiles are calculated from streamline data and extrapolated with approximate theoretical calculations. It is found that the flow generated by a horizontal gradient is retarded by a stabilizing thermal gradient. The reduction is shown as a function of the relevent parameters. For the range of variables investigated complete stabilization of the fluid driven by a horizontal gradient does not seem possible by means of a vertical gradient. The steady state flow patterns obtained do not depend on the manner in which the flow is started, i.e., on the order in which the temperature differences are imposed.

Introduction

The effect of thermal boundary conditions and configuration geometry on the natural convection of confined fluids is of considerable interest in many engineering applications such as crystal growth, solidification of castings, and the circulation of liquids in tanks. Most of the existing work on natural convection in enclosures deals with situations wherein the heat flow is unidirectional, viz., either heating from the side (conventional convection) or heating from below (thermal instability). A summary of research on convectional convection is given in [1] and for a rectangular enclosure which is of primary interest herein, it is indicated therein that the work of Elder [2] is the most comprehensive.

In many practical applications, however, the heat flow can be multidirectional. The earliest work that treats natural convection with simultaneous vertical and horizontal temperature gradients seems to be that of Ostrach [3, 4]. Consideration was given therein to the fully-developed flow in vertical channels whose wall temperatures varied linearly with the axial coordinate. Thus, both a horizontal and a vertical temperature gradient are imposed on the fluid. The presence of the axial temperature gradient has a marked effect on the structure of the natural convection. Furthermore, the nature of this effect differs depending on whether the heat flow is upward (negative gradient) or downward. Since the former case led to unusual features similar to those encountered due to thermal instability in horizontal fluid layers, greater emphasis was given to it. For the latter case of a stabilizing (positive) vertical temperature gradient it was shown that the conventional natural convection is retarded but the importance of this result was not fully appreciated. However, the imposition of a stabilizing gradient seems to offer a valuable design option for minimizing natural convection in applications where it is undesirable. For that purpose it is necessary to have more detailed information on retardation effects for stabilizing temperature gradients of different magnitudes under various conditions, e.g., for different horizontal temperature gradients, aspect ratios, etc. Unfortunately, relatively little work has been done on problems of this type. Birikh, et al. [5] investigated both the hydrodynamic and thermal instability of the problem treated in [3, 4] and Unny and Niessen [6] numerically investigated the effect of a horizontal temperature gradient on the thermal instability in a low aspect ratio rectangular cavity.

Somewhat similar work has been done in relation to oceanographic phenomena. Investigations were made to find the effects of a horizontal temperature gradient on a fluid that is stably stratified due to a salinity gradient [7, 8]. This work attempts to define the mechanism that generates the observed motions.

Since the existing work emphasizes the stability aspects, the type of data needed to determine the suitability of using stabilizing gradients as a design option is not available. The present work represents the first phase of a research program to provide such information and, as such, is intended to give an overall view of the flow fields. Results

---

[1] This research was supported by the U. S. Air Force Office of Scientific Research under grant No. AFOSR 72-2342D

Contributed by the Heat Transfer Division for publication in the JOURNAL OF HEAT TRANSFER. Manuscript received by the Heat Transfer Division January 20, 1978.

from an experimental study of two-dimensional natural convection in rectangular enclosures are presented herein. The effect of imposing stabilizing vertical temperature gradients on flows established by horizontal gradients is considered for a range of Grashof numbers and two aspect ratios. Also, similar to the work of [7] and [8] the convection induced by a small horizontal temperature gradient in a stably (temperature) stratified fluid is investigated.

Experimental Equipment and Procedure

The test enclosure consists of four copper plates machined from 0.95 cm stock to form the four conducting walls. The lateral width is 15.24 cm and was chosen so that end effects are negligible in the test section and so that photographic equipment used in the tracking process could focus accurately on the test section. Six such conducting plates were made, four of width 10.16 cm and two of width 3.38 cm. With these, two configurations are investigated.

1 Apparatus I: $H = L = 10.16$ cms; $W = 15.24$ cms; Aspect ratio $= 1$

2 Apparatus II: $H = 10.16$ cms; $L = 3.38$; $W = 15.24$ cms; Aspect ratio $= 3$

The ends of the enclosure are sealed off with clear plexiglas windows and cork-neoprene gaskets. Between the conducting plates and running along the width of the enclosure are four rubber blocks 0.64 cm square and 15.24 cm long to provide insulation and prevent leakage. The components are all maintained in position by two steel inverted U frames, to which levelling screws are attached, as shown in Fig. 1.

The thermal boundary conditions are established by heating, cooling, or insulating the conducting walls from outside. Some of the plates are provided with strips of heating elements and maintained at a uniform temperature by adjusting the electrical input to the heaters. The cold plates have heat exchanger fluid flow passages milled in them. Distilled water is circulated through them to an accuracy of ±0.006°C by constant temperature circulators. The entire experiment is carried out in a temperature controlled room at a constant temperature of 22.22°C.

The temperature distribution on the walls is measured by 28 B & S gage copper-constantan thermocouples, seven on each plate. Four are fixed near the four corners and three along the center plane. The emf's are measured using a Leeds and Northrup 8686 mV potentiometer, accurate to 5 μV or ±0.11°C in the operating range.

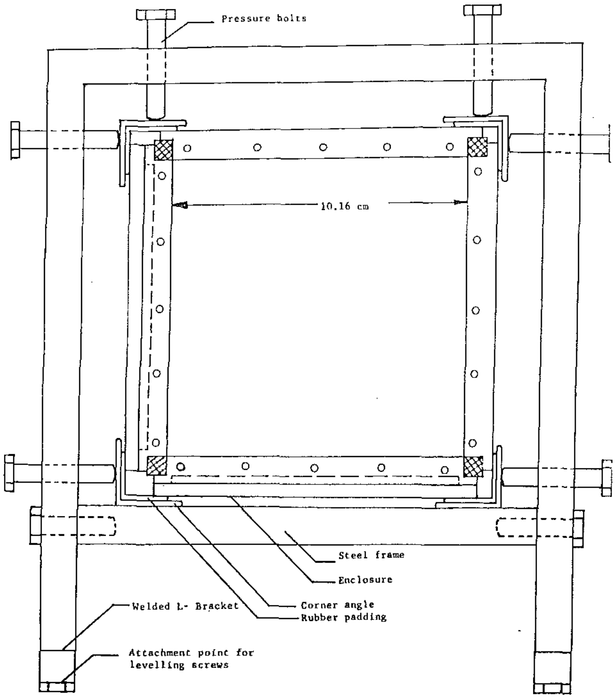

Fig. 1 The test enclosure

The working fluids are silicone oils known commercially as Viscasil 10,000 and SF-96 (2000) [9]. They have a kinematic viscosity of 10,000 and 2000 centistokes, respectively, at 25°C. They are transparent and an optical scheme for tracking the streamlines [10] can be employed. To this end, Pliolite plastic particles [11] from 177 to 205 μ are mixed into the fluid. The particles are tracked by focusing a camera with a 135 mm lens axially through one end of the enclosure to the midplane. The camera film pack is replaced by a ground-glass viewer. Clear plastic inserts are placed in the viewer and the position of the particles in the fluid are marked on the plastic at regular time intervals. At steady state, this gives the streamline patterns of the flow.

More details on the test procedure, optical system alignment and calibration, and experimental error analysis are given in [12], which is a more readily available version of the M.S. degree thesis by the second author. As pointed out therein, due to the high refractive index of the oil the actual section on which the camera focused was 3.05 cm behind the midplane. An axial variation of velocities of about seven percent was found over a region ±1.78 cm from the focus plane. This variation is not due entirely to end effects but also includes experimental errors and, thus, should not affect the overall trends indicated herein. Furthermore, all data presented were obtained in the same plane which would not be possible if significant axial flows were present.

After assembling the apparatus, it is filled with the test fluid and air bubbles are allowed to escape through the air vent. The constant temperature circulators are then switched on and the voltages to the heaters adjusted by trial and error to obtain the desired boundary conditions. The maximum temperature variation on the walls with heaters was 0.22°C and on those with heat exchangers it was less than 0.11°C.

The streamline tracks, in addition to giving the trajectory of a particle in the fluid, also give an approximate value for its velocity. This has been measured for each streamline in a section adjacent to the center of the hot vertical plate. Velocity profiles based on the equation derived in Elder [2] have been fitted to this data. For the test section shown in Fig. 2 we have

$$V_z = C[e^{-mx/L}\,\mathrm{Sin}\,(mx/L) - e^{-m(1-x/L)}\,\mathrm{Sin}\,m(1-x/L)]$$

where C and m are curve fitting constants.

Results and Conclusions

Steady-state results are obtained for the natural convection flow of a fluid in a rectangular enclosure subjected to the boundary conditions as tabulated in Table 1. In all cases, the time elapsed for the flow to become fully established and reach steady state exceeded 24 hr. The main similarity parameter in the experiments are the Grashof numbers ($g\beta\Delta TL^3/\nu^2$) since we have chosen to deal mainly with velocities and an important quantity is the ratio of the vertical stabilizing

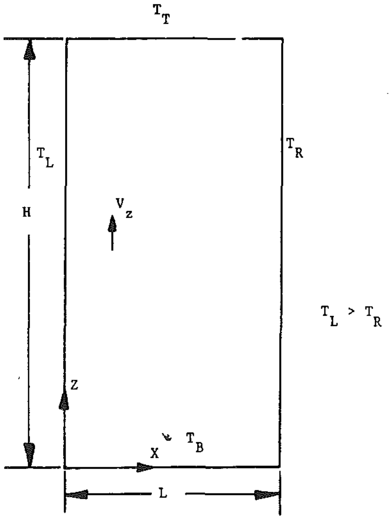

Fig. 2 Coordinate system

Table 1 Experimental parameters

	Expt. No.	T_L °C	T_R °C	T_T °C	T_B °C	ΔT_H °C	ΔT_v °C	Gr_H	Gr_v	P_r	$\mathrm{Gr}_v/\mathrm{Gr}_H$
Set I											
Viscasil 10,000	1	33.3	28.0	30.7	30.7	5.3	0.0	.558	0.0	88,000	0.0
Aspect Ratio 1	2	33.3	28.0	38.1	28	5.3	10.1	.584	1.102	87,000	1.89
Set II	3	33.3	28.0	30.7	30.7	5.3	0.0	.021	0.0	88,000	0.0
Viscasil 10,000	4	33.3	28.0	37.8	28.0	5.3	9.8	.02	1.071	87,000	49.58
Aspect Ratio 3	5	33.1	33.1	37.8	28.3	0.0	9.4	0.0	1.069	86,000	—
	6	29.8	28.3	37.8	28.3	1.4	9.4	.005	1.018	88,000	176.7
Set III	7	*30.6*	*28.0*	*29.3*	*29.3*	*2.6*	*0.0*	*.246*	*0.0*	*18,000*	*0.0*
SF-96 (2000)	8	30.6	28.0	36.1	28.0	2.6	8.1	.25	21.049	18,000	83.23
Aspect Ratio 3	9	31.8	31.8	35.7	28.0	0.0	7.7	0.0	20.98	17,000	—
	10	29.8	28.3	35.7	28.0	1.4	7.7	.14	20.49	18,000	140.3

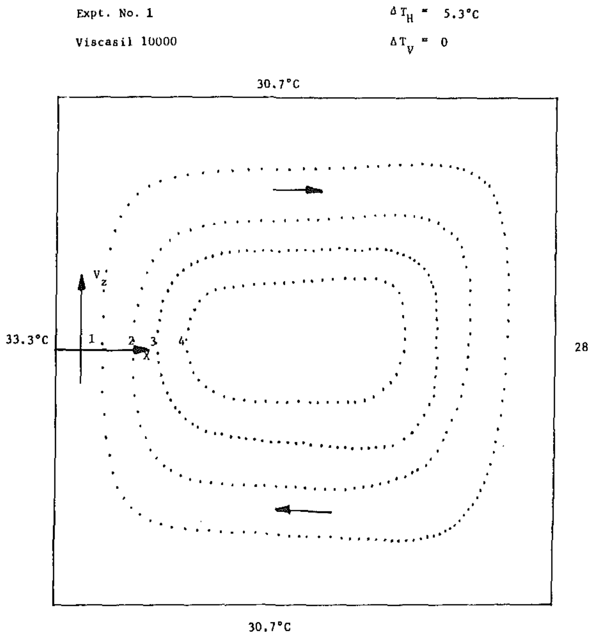

Streamline	Interval (min.)	Total time (mins.)	V_z (cm/min.)	at	X (cm)
1	1	113	0.498		0.917
2	1	92	0.389		1.570
3	1	95	0.224		2.055
4	2	114	0.208		2.647

Fig. 3 Streamline pattern, $\mathrm{Gr}_H = 0.558$, $\mathrm{Gr}_v = 0$, $H/L = 1$

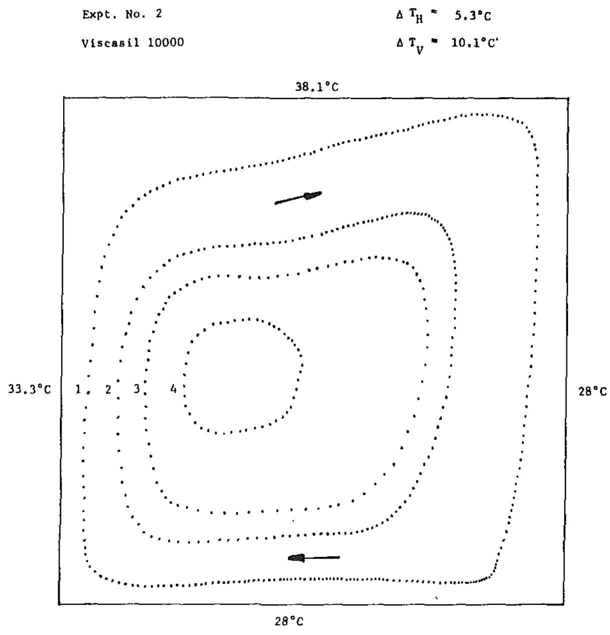

Streamline	Interval (min.)	Total time (mins.)	V_z (cm/min.)	at	X (cm)
1	1,2	271	0.302		0.640
2	1	140	0.348		1.219
3	2	170	0.236		1.758
4	4	188	0.216		2.438

Fig. 4 Streamline pattern, $\mathrm{Gr}_H = 0.584$, $\mathrm{Gr}_v = 1.102$, $H/L = 1$

Grashof number to the horizontal destabilizing Grashof number ($\mathrm{Gr}_v/\mathrm{Gr}_H$). The vertical temperature gradients are all imposed by heating the upper surface and cooling the lower surface and have a stabilizing effect on the flow. The streamline patterns and velocity profiles are found for two different geometries with aspect ratio 1 and 3 for a range of horizontal and vertical Grashof numbers from 0 to 21.

Figs. 3 and 4 are the streamline patterns obtained for aspect ratio 1 and unit order Grashof numbers. The fluid is Viscasil 10,000. In Fig. 3 the fluid is heated on one side and cooled on the other. The top and bottom surfaces are kept insulated from the outside, i.e., no stabilizing gradient is imposed.

As expected, the flow is a clockwise rotation being upward near the hot wall and downward near the cold wall. The streamlines are approximately symmetric about the horizontal axis and follow the geometry of the apparatus close to the boundary, but near the center the shape is more or less elliptic with the major axis horizontal. The velocity is maximum at a small distance from the wall and is very slow in the interior.

Fig. 4 shows a vertical gradient imposed on the fluid. The vertical to horizontal Grashof number ratio is 1.89. There is a pronounced elongation of the streamlines towards the upper right corner across which there is a large temperature change. In this investigation the complexities introduced by large temperature changes at corners have not been eliminated. Comparing the velocities with the previous case, we notice that the flow has been retarded. Along a streamline (No. 1 on Fig. 4, for example) there is a marked reduction in velocity from 0.302 cm/min at the horizontal centerline near the hot plate to 0.05 cm/min at the lower right corner, and the time interval between successive markings has been doubled. The flow in the interior has a maximum velocity on the innermost streamline of 0.216 cm/min.

Fig. 5 shows the velocity profiles at the center line plotted out for these two experiments. We see that a stabilizing gradient with a Grashof number ratio of 1.89 has reduced the maximum velocities by 26.4 percent. For large temperature gradients, there is a large viscosity-temperature change. In experiment 2, Fig. 4, there is a ten percent decrease in viscosity from the lower to the upper plate and this causes an increase in flow velocities.

The next set of experiments, 3 to 6, are conducted in an enclosure with an aspect ratio of 3 and the Grashof numbers range from 0 to 1.1 and the Grashof number ratio from 0 to 176.7. The reference pattern is Fig. 6 in which a horizontal gradient alone is imposed on the fluid with the upper and lower plates insulated. Due to the enclosure geometry, the streamlines are all elliptic with the major axis along the vertical centerline. They are straight in the vertical portion along the side walls but curved in the upper and lower regions while taking the

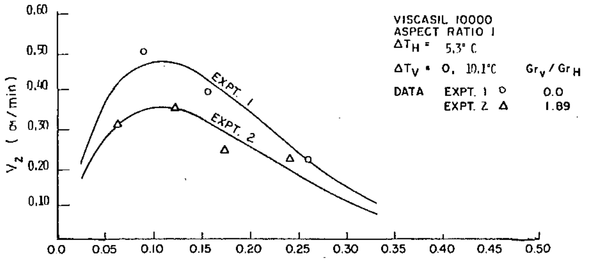

Fig. 5 Velocity profiles for experiments 1 and 2

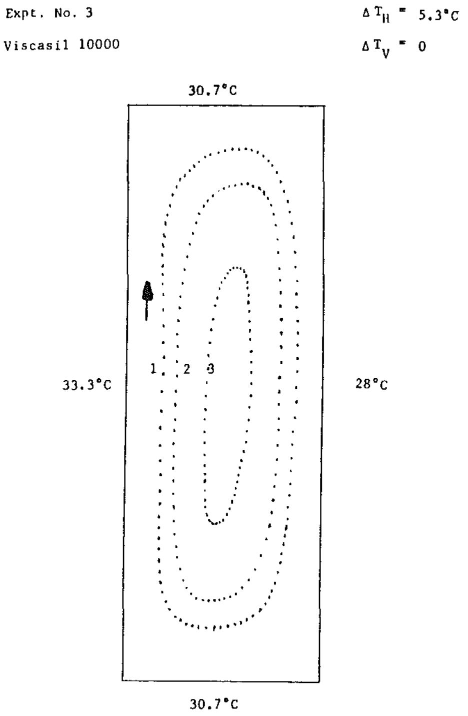

Streamline	Interval (min.)	Total time (mins.)	V_z (cm/min.)	at X (cm)
1	1	104	0.373	0.615
2	1	82	0.297	0.848
3	1	63	0.211	1.382

Fig. 6 Streamline pattern, $Gr_H = 0.021$, $Gr_v = 0$, $H/L = 3$

180 deg turns. The horizontal Grashof number is 0.021 as compared to 0.558 for experiment 1 and the flow velocities are, therefore, lower.

When a stabilizing gradient with a Grashof number ratio of 49.0 is imposed, the temperature differences have increased and the corner effect is more pronounced as in Fig. 7. There is a slowing down of the flow due to the vertical stabilization. Comparing streamlines 2 in Figs. 6 and 7 where they are positioned in approximately the same location, we notice a change in loop velocities from 0.2 cm/min. to 0.163 cm/min., a decrease of 18 percent.

Fig. 8 shows the pattern obtained for a different approach to the problem. In experiment No. 6, a vertical gradient alone is imposed on the fluid which is then allowed to become stably stratified. When no motion is observed, a small horizontal gradient [$Gr_H = 0.0058$) is then imposed. Fig. 8 shows the resulting steady-state flow pattern. The Grashof number ratio is 176.7. The corner effects are very pronounced, and there are two cells in the pattern.

The velocity profiles for this set of data are plotted in Fig. 9. In increasing the Grashof number ratio from 0 to 49.6, there is a 13.3 percent decrease in maximum flow velocities and in increasing the ratio from 49.6 to 176.7, there is a 41.6 percent decrease. The total decrease from 0 to 176.7 is 49.4 percent. Compared to the stabilization

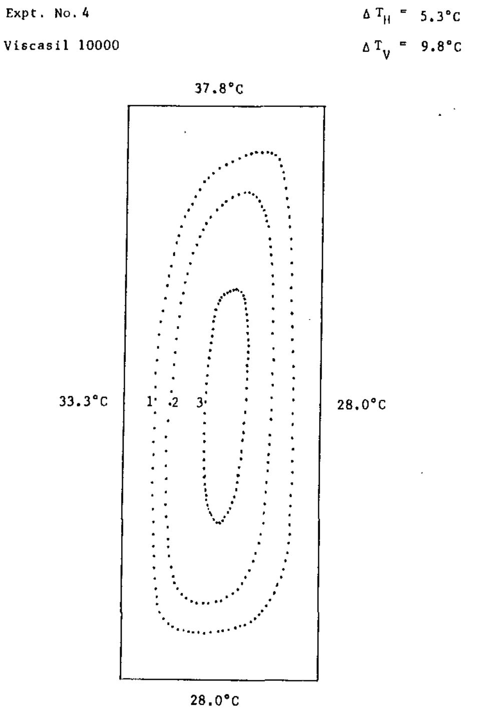

Streamline	Interval (min.)	Total time (mins.)	V_z (cm/min.)	at X (cm)
1	1	117	0.239	0.561
2	1	95	0.254	0.775
3	1	76	0.170	1.425

Fig. 7 Streamline pattern, $Gr_H = 0.022$, $Gr_v = 1.071$, $H/L = 3$

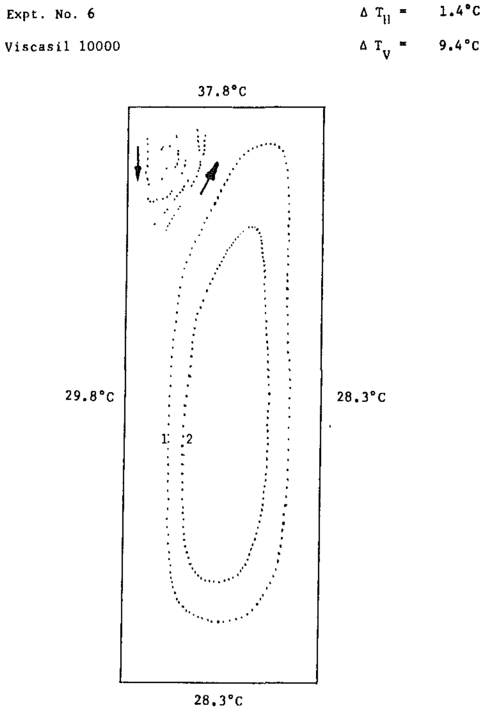

Streamline	Interval (min.)	Total time (mins.)	V_z (cm/min.)	at X (cm)
1	2	280	0.152	0.795
2	2	248	0.173	1.087

Fig. 8 Streamline pattern, $Gr_H = 0.0058$, $Gr_v = 1.018$, $H/L = 3$

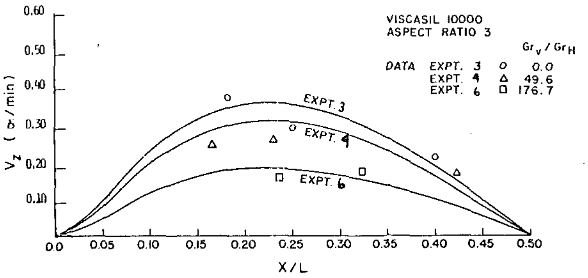

Fig. 9 Velocity profiles for experiments 3, 4, 6

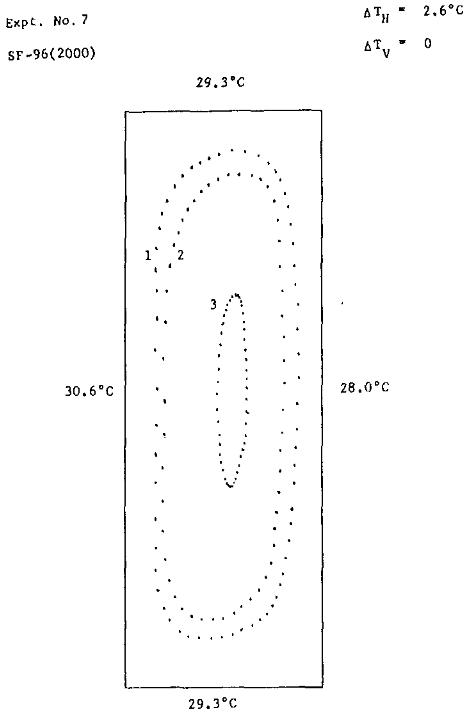

Streamline	Interval (min.)	Total time (mins.)	V_z (cm/min.)	at X (cm)
1	1	61	0.561	0.554
2	1	53	0.615	0.691
3	1	49	0.234	1.641

Fig. 10 Streamline pattern, Gr_H = 0.246, Gr_v = 0, H/L = 3

obtained in the aspect ratio 1 configuration, the stabilizing vertical gradients are not as effective for the higher aspect ratio.

In order to study the stabilizing effect at a higher Grashof number range for the same configuration without drastically increasing experimental run times, a fluid SF-96 (2000) with one-fifth the viscosity of Viscasil 10,000 was chosen. With this, the Grashof numbers have been increased by an order of magnitude. In the reference pattern, Fig. 10, the horizontal Grashof number is 0.25 as compared to 0.02 in experiment 3, Fig. 6, for Viscasil 10,000 and the flow velocities are nearly doubled. The shape of the streamlines in these two patterns are quite similar and symmetric about the horizontal and vertical center lines.

In imposing a vertical stabilizing gradient with a Grashof number ratio of 83, we observe in Fig. 11, a slowing down of the flow and a pronounced elongation towards the upper right corner similar to that observed in experiment 4, Fig. 7.

The last experiment is performed in a way similar to experiment 6, Fig. 8. The fluid is stably stratified with a vertical gradient and then a small horizontal gradient applied. The flow pattern, Fig. 12, has a Grashof number ratio of 140.3. The corner effects are very pronounced and two cells are seen, a large clockwise rotating cell comprising the

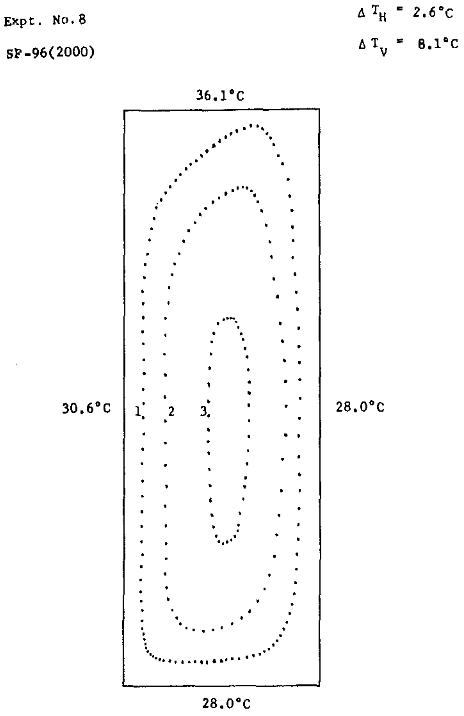

Streamline	Interval (min.)	Total time (mins.)	V_z (cm/min.)	at X (cm)
1	1	118	0.264	0.320
2	1	67	0.384	0.709
3	2	71	0.122	1.504

Fig. 11 Streamline pattern, Gr_H = 0.253, Gr_v = 21.049, H/L = 3

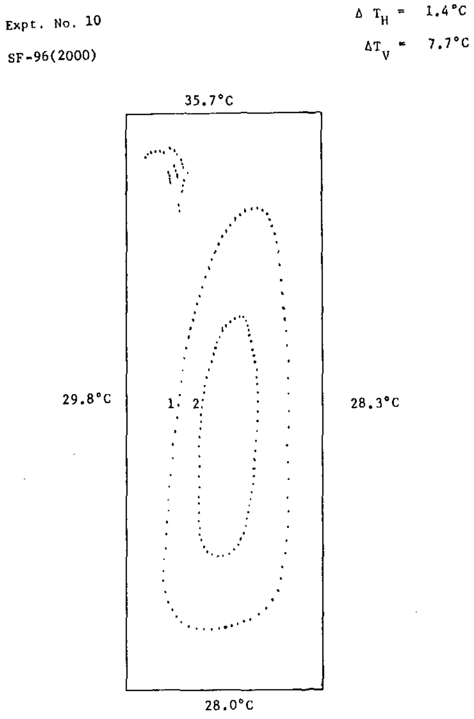

Streamline	Interval (min.)	Total time (mins.)	V_z (cm/min.)	at X (cm)
1	1	88	0.241	0.914
2	1	71	0.170	1.303

Fig. 12 Streamline pattern, Gr_H = 0.143, Gr_v = 28.49, H/L = 3

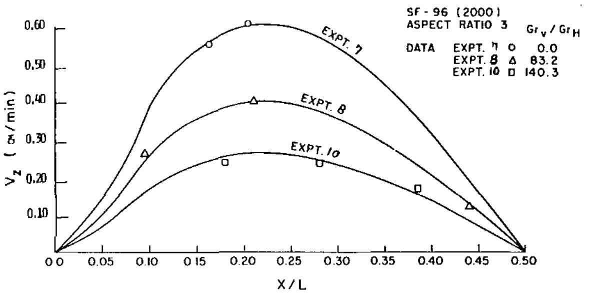

Fig. 13 Velocity profiles for experiments 7,8, 10

main flow and a small counterclockwise rotating cell at the upper left corner, similar to that obtained for a Grashof number ratio of 176.7 in Fig. 12 for the same aspect ratio.

The velocity profiles for this final set are plotted in Fig. 13. The three profiles correspond to Grashof number ratios of 0, 83.2, and 140.3. In increasing the ratio from 0 to 83.2, there is a 34.4 percent decrease in maximum velocities and in increasing it from 83.2 to 140.3 there is a 34.2 percent decrease. The total decrease from 0 to 140.3 is 56.9 percent. The Grashof numbers are in the range 0 to 21. For the same aspect ratio of 3 and Grashof numbers between 0 and 1.1, the decrease was 49.4 percent for a Grashoff number ratio of 176.7. Thus the stabilizing gradient appears to be more effective at a higher Grashof number range. However, for the lower aspect ratio of 1, a decrease in velocities of 26.4 percent was obtained by increasing the Grashof number ratio from 0 to 1.89.

Conclusions

1 A stabilizing vertical gradient imposed on the fluid driven by a horizontal gradient in a rectangular enclosure slows down the flow. The reduction in flow velocities depends on the aspect ratio, the Grashof number range and the ratio of vertical to horizontal Grashof numbers. The stabilizing effect of a vertical gradient is greater for lower aspect ratios and a higher Grashof number range.

2 For a given aspect ratio and horizontal Grashof number, an increase in the Grashof number ratio leads to retardation of the flow.

3 For the range of variables studied, complete stabilization of the fluid driven by a horizontal gradient does not appear possible purely by means of a vertical gradient.

References

1 Ostrach S., "Natural Convection in Enclosures," *Advances in Heat Transfer*, Vol. 8, J. P. Hartnett and T. F. Irvine, Jr., ed., Academic Press, 1972.

2 Elder, J. W., "Laminar Free Convection in a Vertical Slot," *Jour. Fluid Mech.*, Vol. 23, pt. 1, 1965.

3 Ostrach, S., "Combined Natural- and Forced-Convection Laminar Flows and Heat Transfer of Fluids With and Without Heat Sources in Channels with Linearly Varying Wall Temperatures," NACA TN 3141, 1954.

4 Ostrach, S., "On the Flow, Heat Transfer, and Stability of Viscous Fluids Subject to Body Forces and Heated From Below in Vertical Channels," 50 Jahre *Grenzschichtforschung*, H. Görtler, ed., Vieweg, 1955.

5 Birikh, R. V., Gershuni, G. Z., Zhukhovitskii, E. M., and Rudakov, R. H., "Stability of the Steady Convective Motion of a Fluid with a Longitudinal Temperature Gradient," PMM, Vol. 33, No. 6, 1969.

6 Unny, T. E. and Niessen, P., "Thermal Instability in Fluid Layers in the Presence of Horizontal and Vertical Temperature Gradients," *Jour. Appl. Mechanics*, March 1969.

7 Thorpe, S. A., Hutt, P. K., and Soulsby, R., "The Effect of Horizontal Gradients on Thermohaline Convection," *Jour. Fluid Mechanics*, Vol. 38, pt. 2, 1969.

8 Chen, C. F., Briggs, D. G., and Wirtz, R. A., "Stability of Thermal Convection in a Salinity Gradient Due to Lateral Heating," *Int. Jour. Heat Mass Transf.*, Vol. 14, 1971.

9 General Electric Co., *Silicone Fluids*, Tech. Data Book S-9B, Silicone Products Dep. Waterford, NY.

10 Brooks, I. H. and Ostrach, S., "Experimental Investigation of Natural Convection in a Horizontal Cylinder," *Jour. Fluid Mech.*, Vol. 44, pt. 3, 1970.

11 The Goodyear Tire and Rubber Co., Tech. Book Facts, *Pliolite S-5 Bases*, Chemical Division, Akron, OH.

12 Raghavan, C. and Ostrach, S., "Stabilizing Thermal Gradients on Confined Natural Convection Flows," Case Western Reserve University, Dep. of Mech. and Aero. Eng. FTAS/TR-76-118, June 1976

B. Chhuon
J. P. Caltagirone

Laboratoire d'Aérothermique du Centre National
de La Recherche Scientifique,
4 ter, route des Gardes
Meudon, F 92190,
France

Stability of a Horizontal Porous Layer with Timewise Periodic Boundary Conditions

The stability of a horizontal porous layer bounded by two impermeable planes is investigated. A time dependent periodic temperature profile is imposed on the lower boundary while the upper plane is kept at constant temperature. Starting from the preconvective temperature distribution, and using the linear stability theory, a criterion for the onset of convection is defined as a function of the perturbation wavenumber and of the amplitude and frequency of the temperature oscillation. Experimental work with a setup allowing both the amplitude and the frequency of the thermal signal to vary is done. Finally, the equations are also solved numerically and the results are compared to the previous ones. A synthesis of all results is included.

1 Introduction

The stability of a fluid layer with periodic boundary conditions has been widely investigated both experimentally and theoretically. We refer the reader to S. H. Davis [1] where a complete bibliography is given.

For a porous layer under the same boundary conditions, J. P. Caltagirone [2] uses a linear theory and gives the critical Rayleigh number as a function of the amplitude and the frequency of the periodic wave. The Galerkin method is used but its series expansion is limited to only the first term.

This work compares the results obtained when applying the Floquet theory to those given in [2]. An experimental investigation is also performed and shows that convective phenomena can develop within a period. Finally, a numerical model, with the nonlinear terms accounted for, permits us to show the appearance of finite amplitude thermoconvective cells.

2 Problem Formulation

Consider a horizontal porous layer of height H bounded at its upper face by a surface at constant temperature T_1' and, at the lower surface, the temperature varies periodically

$$T_2' = T_3' + (T_4' - T_3') \sin \omega' t'$$

$\omega' = 2\pi f'$, f' is the frequency

The porous matrix, of permeability K and porosity ϵ, is saturated with an interstitial fluid of kinematic viscosity ν, heat capacity per unit volume $(\rho c)_f$ and coefficient of thermal expansion α. The ensemble formed by the solid substrate and the fluid is treated as a unique fictitious fluid of thermal conductivity λ^* and heat capacity per unit volume $(\rho c)^* = \epsilon(\rho c)_f + (1-\epsilon)(\rho c)_s$. This hypothesis has been extensively studied by M. Combarnous and S. Bories [3].

The governing equations are

$$\nabla \cdot \mathbf{V}' = 0 \tag{1}$$

$$(\rho c)^* \frac{\partial T'}{\partial t'} - \lambda^* \nabla^2 T' + (\rho c)_f \mathbf{V}' \cdot \nabla T' = 0 \tag{2}$$

$$\epsilon^{-1} \rho \frac{\partial \mathbf{V}}{\partial t} + \nabla p' - \rho \mathbf{g} + \mu K^{-1} \mathbf{V}' = 0 \tag{3}$$

$\mathbf{V}' = V_1\mathbf{e}_1 + V_2\mathbf{e}_2 + V_3\mathbf{e}_3$ is the fluid's filtration velocity, p is the pressure, T is the temperature and $\mathbf{g} = -g\mathbf{e}_3$ is the acceleration due to gravity.

The fluid's state equation is

$$\rho = \rho_1 [1 - \alpha (T' - T_1')]$$

In order to render the equations dimensionless, the following reference values are used: H, $(\rho c)^* H^2/\lambda^*$, $\lambda^*/H(\rho c)_f$, $\lambda^*\mu/K(\rho c)_f$ and $\Delta T = T_3' - T_1'$ for the length, time, velocity, pressure and temperature scales respectively.

The dimensionless lower surface temperature is thus

$$T_2 = 1 + \beta \sin \omega t \tag{4}$$

with

$$\beta = (T_4' - T_3')/(T_3' - T_1') \text{ and } \omega = \omega' (\rho c)^* H^2/\lambda^*$$

Using the Boussinesq approximation, equations (1–3) become, in dimensionless form,

$$\nabla \cdot \mathbf{V} = 0 \tag{5}$$

$$\frac{\partial T}{\partial t} - \nabla^2 T + \mathbf{V} \cdot \nabla T = 0 \tag{6}$$

$$\epsilon^{-1} F\, \mathrm{Pr}^{*-1} M \frac{\partial \mathbf{V}}{\partial t} + \nabla p - \mathrm{Ra}^* \mathbf{k} T + \mathbf{V} = 0 \tag{7}$$

$\mathbf{k} = -\mathbf{e}_3$.

Contributed by the Heat Transfer Division for publication in the JOURNAL OF HEAT TRANSFER. Manuscript received by the Heat Transfer Division December 27, 1977.

The following dimensionless parameters appear: the Rayleigh number $\mathrm{Ra} = g\alpha(\rho c)_f \Delta T H K/\lambda^* \nu$, the Prandtl number $\mathrm{Pr} = \nu(\rho c)_f/\lambda^*$, and three numbers which characterize the medium: the porosity ϵ, the ratio of heat capacities $(\rho c)_f/(\rho c)^*$ and the fineness of the medium $F = K/H^2$.

The reference states are: a uniform zero velocity field ($\mathbf{V}_0 = 0$) and a temperature distribution satisfying

$$\frac{\partial T_0}{\partial t} = \frac{\partial^2 T_0}{\partial z^2} \tag{8}$$

with

$$T_0 = 0 \qquad \text{for } z = 1$$

$$T_0 = 1 + \beta \sin \omega t \text{ for } z = 0$$

Using separation of variables, we obtain

$$T_0 = (1 - z) + \beta\alpha(z) \sin(\omega t + \phi(z)) \tag{9}$$

$$\alpha(z) = |q|, \phi(z) = \mathrm{Arg}\,|q|;$$

$$q(z) = \sinh[k(1+i)(1-z)]/\sinh[k(1+i)], k = (\omega/2)^{1/2}$$

The critical stability conditions are determined with $T_0(z, t)$ as the starting point.

3 Linear Stability

We introduce temperature and velocity perturbations, $\theta = T - T_0$ and $\mathbf{v} = \mathbf{V} - \mathbf{V}_0$ respectively, into (5–7), neglect the second order terms in the energy equation and consider the component on $\mathbf{e}_3$ of the velocity perturbation.

Since the layer is bounded by two infinite horizontal planes, the perturbations are developed as periodic wave functions on the two horizontal directions [4]

$$\theta(x, y, z, t) = \theta(z, t) \exp[i(s_x x + s_y y)]$$

$$w(x, y, z, t) = w(z, t) \exp[i(s_x x + s_y y)] \tag{10}$$

s_x and s_y are two perturbation wavenumbers.

We obtain

$$\frac{\partial \theta}{\partial t} = (D^2 - s^2)\theta - w \frac{\partial T_0}{\partial z} \tag{11}$$

$$\epsilon^{-1} \mathrm{Pr}^{*-1} MF \frac{\partial}{\partial t}(D^2 - s^2)w = -\mathrm{Ra}^* s^2 \theta - (D^2 - s^2)w \tag{12}$$

$$D = d/dz \quad \text{and} \quad s^2 = {s_x}^2 + {s_y}^2$$

The boundary conditions for isothermal and impermeable planes are:

$$\theta = w = 0 \qquad \text{for } z = 0 \text{ and } z = 1 \tag{13}$$

$F = K/H^2$ is generally less than 10^{-4} so we set it equal to zero (D.D. Joseph, Vol. 2, 1976 [5]).

Equations (11–13) are solved using the Galerkin method [6]; the perturbations θ and w are represented by linearly independent functions satisfying the boundary conditions

$$\theta(z, t) = \sum_{k=1}^{N} a_k(t)\Theta_k(z)$$

$$w(z, t) = \sum_{k=1}^{N} b_k(t) W_k(z) \tag{14}$$

The chosen trial functions are $\Theta_k = W_k = \sin(k\pi z)$.

Replacing θ and w in (11–12) by their expression (14), multiplying the two equations by Θ_l and W_l respectively and integrating over the height of the layer, we obtain

$$\sum_{k=1}^{N} \frac{da_k}{dt} \int_0^1 \Theta_k \Theta_l \, dz = \sum_{k=1}^{N} a_k \int_0^1 (D^2 - s^2)\Theta_k \Theta_l \, dz - \sum_{k=1}^{N} b_k \int_0^1 W_k \Theta_l \frac{\partial T_0}{\partial_z} dz \tag{15}$$

$$0 = -\mathrm{Ra}^* s^2 \sum_{k=1}^{N'} a_k \int_0^1 \Theta_k W_l \, dz - \sum_{k=1}^{N} b_k \int_0^1 (D^2 - s^2) W_k W_l \, dz \tag{16}$$

The system of ordinary differential equations (15–16) is written in matrix form

$$\sum_{k=1}^{N} A_{lk} \frac{da_k}{dt} = \sum_{k=1}^{N} B_{lk} a_k + \sum_{k=1}^{N} C_{lk} b_k \tag{17}$$

$$0 = \mathrm{Ra}^* \sum_{k=1}^{N} D_{lk} a_k + \sum_{k=1}^{N} E_{lk} b_k \tag{18}$$

$A_{lk}, B_{lk}, C_{lk}, D_{lk},$ and E_{lk} are square matrices, C_{lk} is time dependent and of period $\tau = 1/f$.

$$C_{lk} = \int_0^1 [(1 - z) + \beta\alpha \sin(\omega t + \theta)] (DW_k \Theta_l + W_k D\Theta_l) \, dz = \frac{1}{2}\delta_{lk} + \beta [G_{lk} \sin \omega t + H_{lk} \cos \omega t] \tag{19}$$

δ_{lk} is the Kronecker delta.

Equations (17–18) become

$$\frac{da_l}{dt} = \left\{ \frac{\mathrm{Ra}^* s^2 - (l^2\pi^2 + s^2)^2}{(l^2\pi^2 + s^2)} \delta_{lk} + \mathrm{Ra}^* \beta [R_{lk} \sin \omega t + T_{lk} \cos \omega t] \right\} a_k \tag{20}$$

$$R_{lk} = G_{\ell k} {\delta_{lk}}^2 s^2/(l^2\pi^2 + s^2) \quad \text{and} \quad T_{lk} = H_{\ell k} \cdot {\delta_{lk}}^2 s^2/(l^2\pi^2 + s^2)$$

Equation (20) is then written as

$$\frac{da_l}{dt} = F_{lk} a_k, \quad F_{lk}(\tau) = F_{lk}(0) \tag{21}$$

with initial condition $a_l(0)$.

If N different solutions are known, $a_{l1}, a_{l2}, \ldots a_{lN}$; a more general solution is $C_1 a_{l1} + C_2 a_{l2} + \ldots C_N a_{lN}$.

The N column matrices a_{lm} define a fundamental system of solutions ($m = 1, 2, \ldots N$).

Nomenclature

a, b = functions of time
c = specific heat
$\mathbf{e}_1, \mathbf{e}_2, \mathbf{e}_3$ = unit vectors
f = frequency
F = fineness of the medium = K/H^2
g = acceleration due to gravity
H = layer thickness
$\mathbf{k} = -\mathbf{e}_3$
K = permeability
M = ratio of heat capacities $(\rho c)_f/(\rho c)^*$
N = order of approximation
p = pressure
Pr^* = Prandtl number
Ra^* = Rayleigh number
s = wavenumber
t = time
T = temperature
$\mathbf{v}$ = velocity
x, y, z = dimensionless coordinates
α = coefficient of thermal expansion
δ = Kronecker delta
ϵ = porosity
λ^* = thermal conductivity
μ = dynamic viscosity
ν = kinematic viscosity
ρ = density
τ = period
θ = temperature perturbation
ψ = stream function
$\omega = 2\pi f$
primes = real variables

Thus,

$$\frac{da_{lm}}{dt} = F_{lk} a_{km} \tag{22}$$

Taking into account the periodic nature of the coefficients, we have:

$$\frac{da_{lm}(t+\tau)}{dt} = F_{lk}(t+\tau) a_{km}(t+\tau) = F_{lk}(t)\, a_{km}(t+\tau) \tag{23}$$

The stability discussion is based on Floquet's theory. It is possible to find a solution a_{km} of system such that

$$a_{km}(\tau) = a_{kn}(0) Q_{nm}(\tau) \tag{24}$$

$Q(\tau)$ is called a "monodromy matrix."

If the initial condition is

$$a_{km}(0) = \delta_{km}, \tag{25}$$

we obtain

$$a_{km}(\tau) = Q_{km}(\tau) \tag{26}$$

The eigenvalues of Q are called the Floquet multipliers $\lambda_1, \lambda_2 \ldots \lambda_N$ and $\mu_1, \mu_2 \ldots \mu_N$ defined by

$$\lambda_j = \exp(-\mu_j \tau) \tag{27}$$

are the Floquet exponents and they determine the system stability. If the real part of μ_1 is the greatest, the system is stable if

$$re(\mu_1) > 0 \tag{28}$$

The matrix $a_{km}(\tau)$ is determined by solving (22) with initial conditions (25). The Runge-Kutta method is employed. Next, the eigenvalues of $a_{km}(\tau)$ are calculated and let us suppose λ_1, is the greatest. A different approach would be to search for the critical Rayleigh number given $\lambda_1 = 1$ ($\mu_1 = 0$). This is equivalent to

$$\det(Q - I) = 0 \tag{29}$$

In Galerkin's method, the number of terms kept in the series is two. The difference between the values obtained for the critical Rayleigh number ($N = 2$ and $N = 3$) is always less than 2×10^{-4}. If $\beta = 0$, the result for $\mathrm{Ra}_c{}^*$ is $4\pi^2$, evidently.

The results are shown in Figs. 1–3; they show the critical Rayleigh number as a function of the frequency, the amplitude and the wavenumber respectively $\mathrm{Ra}_{ct}{}^*$ varies weakly with f and are of opposite sign as those in [7] for a liquid layer. For $f > 100$, the oscillation has no influence on the stability.

4 Experimental Investigation

The experimental setup is shown in Fig. 4. The test cell is made up of two isothermal blocks. The porous medium consists of glass balls (3 mm dia) and a saturating fluid (water). The test cell dimensions are 190 mm × 60 mm × 20 mm. Thermocouples are placed on the lower and upper faces and, inside the cell ($h_1 = 15$ mm, $h_2 = 30$ mm, $h_3 = 45$ mm).

The surface temperatures are provided by water circulation. The periodic temperature of the lower wall is obtained employing a computer, a data acquisition system and a timing generator. The precision of this modulation is checked by a Fourier analysis giving the rate of harmonics by reference to the fundamental one (<2 percent). The data acquisition system collects and registers the voltage, the current passing through the heating resistor of the heat exchanger and the electromotive forces of the thermocouples.

The temperature evolution within the layer permits us to observe the onset of convection and to define the critical value of $\mathrm{Ra}_{ct}{}^*$. In fact, for $f = 4.23$, the periodic temperature evolution proves the existence of conduction at $\mathrm{Ra}^* = 21.4$ (Fig. 5), symmetry of the increasing and decreasing parts of each period and some value of peaks. At $\mathrm{Ra}^* = 35.6$ (Fig. 6), the influence of convection is noted since the temperature curves are no longer symmetrical, the declining section is more elongated than the rising section.

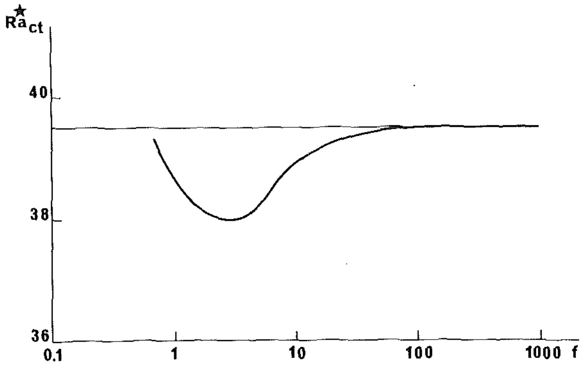

Fig. 1 $\mathrm{Ra}_{ct}{}^*$ as a function of f for $\beta = 1$ and $s = \pi$

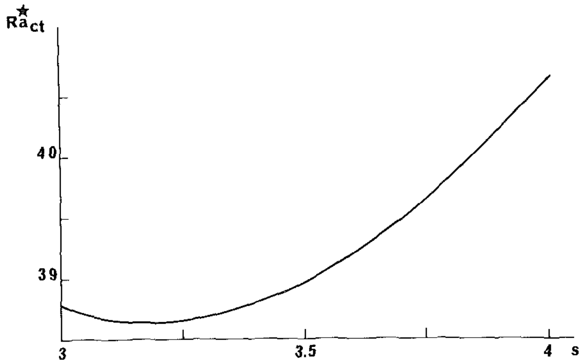

Fig. 2 $\mathrm{Ra}_{ct}{}^*$ as a function of β for $f = 1$ and $s = \pi$

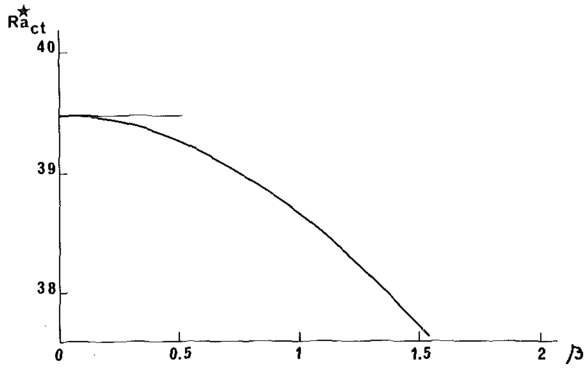

Fig. 3 $\mathrm{Ra}_{ct}{}^*$ as a function of s for $\beta = 1$ and $f = 1$

At higher Ra*, a regime of convection with a strong peak of first oscillation is seen.

Attempting to compare theory with experiment in order to determine the value of $\mathrm{Ra}_{ct}{}^*$ (β) when close to the marginal state definited by the linear theory is very difficult.

Though the experiments can not lead us to define a precise stability criterion, they clearly show that convective phenomena can develop for Rayleigh numbers less than $4\pi^2$, thus leading to a perturbation of the temperature field.

Fig. 7 shows a summary of results for $f = 4.23$.

5 Numerical Model

Considering equations (5–7) with $F = 0$, taking the curl of (7) and introducing the stream function ψ, such that $V_x = \partial\psi/\partial z$ and $V_z = -\partial\psi/\partial x$, we obtain

$$\frac{\partial T}{\partial t} - \nabla^2 T + \mathbf{V} \cdot \nabla T = 0 \tag{30}$$

$$\nabla^2 \psi - \mathrm{Ra}^* \frac{\partial T}{\partial x} = 0 \tag{31}$$

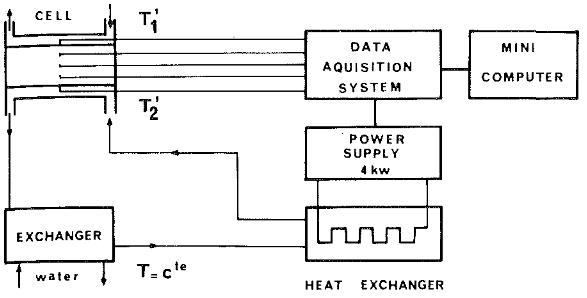

Fig. 4 Experimental setup

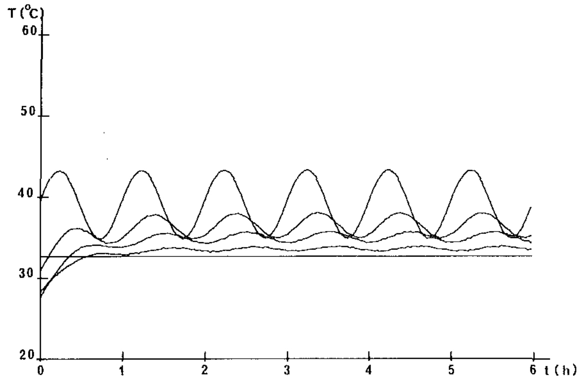

Fig. 5 Temperature modulation as a function of *t* for *f* = 4.23 and Ra* = 21.4

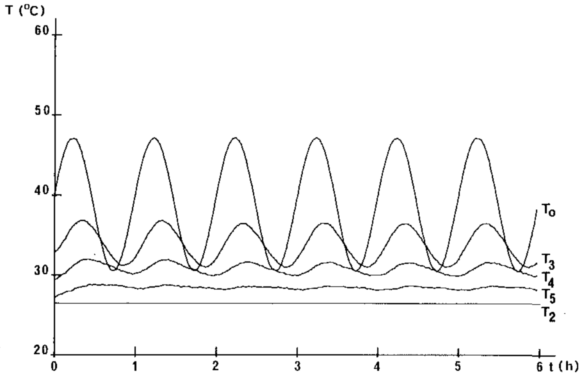

Fig. 6 Temperature modulation as a function of *t* for *f* = 4.23 and Ra* = 35.6

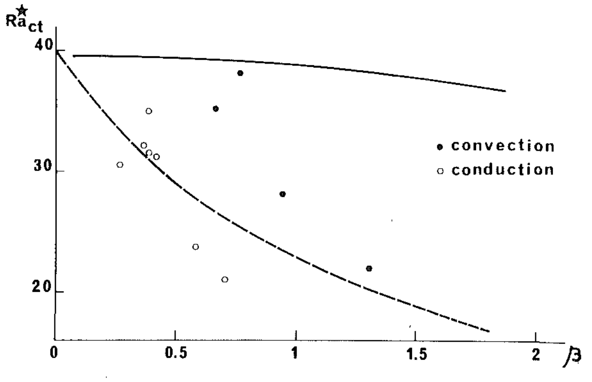

Fig. 7 Critical Rayleigh numbers for *f* = 4.23
● ○ experiment, — — — linear theory [2], — Floquet theory

where $\mathbf{V} = V_x\,\mathbf{e}_1 + V_z\,\mathbf{e}_3$.

The horizontal surfaces are isothermal and impermeable while the lateral surfaces are adiabatic. The aspect ratio is $A = L/H = 1$ (square cell), L is the cell width. The boundary conditions are

$$
\begin{aligned}
&T = 0, \quad \psi = 0 \quad \text{for } z = 1, \forall x \\
&T = 1 + \beta \sin \omega t, \psi = 0 \quad \text{for } z = 0, \forall x \qquad (32)\\
&\frac{\partial T}{\partial x} = 0, \quad \psi = 0 \quad \text{for } x = 0 \text{ and } x = A, \forall z
\end{aligned}
$$

We superimpose on the initial temperature distribution ($T_0 = (1 - z) + \beta\alpha \sin(\omega t + \phi)$) in the cell, an arbitrary perturbation of the form $\alpha_1 \cos(n\pi x) \sin(m\pi z)$. α_1 is an amplification coefficient; m and n are wavenumbers. This introduction has an interesting effect; convective phenomena appear and they can increase or decrease during the period. Equations (30–31) are written in finite difference form and solved with the A.D.I. method. A grid of 25 × 25 is used.

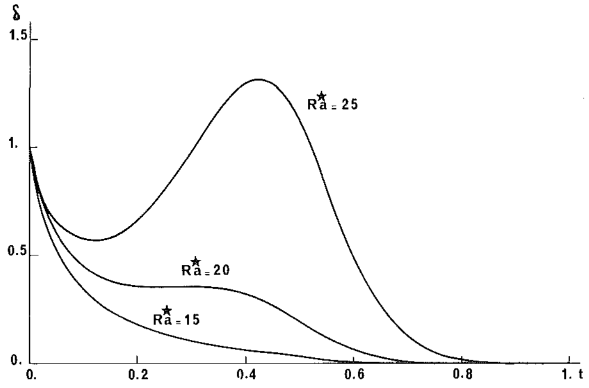

Fig. 8 Numerical model; perturbation variation with *t* for *f* = 1 and β = 1

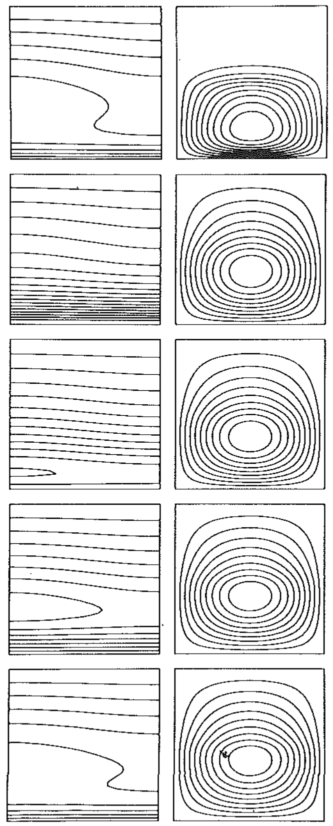

Fig. 9 Streamlines and temperature profile evolution for Ra* = 50, *f* = 10, and for *t* = 0, 0.025, 0.05, 0.075 and 0.1 (numerical model)

The results are plotted and show the time variation of the maximum temperature deviation along horizontal straight line $[\delta = [T(0,z) - T(1,z)]/\alpha_1]$. Fig. 8 shows this for $f = 1$ and $\beta = 1$. When Ra* = 15, the introduced perturbation decreases very rapidly; when Ra* = 20, $\delta(t)$ remains constant temporarily and then decreases and, when Ra* = 25, the initial thermoconvective cell tends to grow since $\delta(t)$ exhibits a positive slope during part of the period. The temperature and stream function fields, for $f = 10$ and Ra* = 50, are shown on Fig. 9.

6 Synthesis

When a periodic boundary condition is imposed on the lower face of a porous layer, one question immediately arises: does the periodic condition lead to a stabilization, compared to stationary condition?

Before answering this, one must clearly define the stability criterion. In [2], the stability criterion is $a(t) < 0$, $a(t)$ being the amplitude of the temperature perturbation. Here, the differential system also has periodic coefficients but another critical Rayleigh number is defined because the Floquet theory is used.

Both theories give the same frequency range for which $\mathrm{Ra}_{ct}{}^*$ varies significantly. However, in the Floquet theory, $\mathrm{Ra}_{ct}{}^*$ varies slightly with f while, in [2], $\mathrm{Ra}_{ct}{}^*$ varies from 40 at $f \to \infty$ to $40/(\beta + 1)$ for $f = 0$.

Both theories predict a destabilization from the stationary case. The Floquet theory breaks down when $f \to 0$ since the critical Rayleigh number must necessarily approach $4\pi^2/(\beta + 1)$. This is confirmed experimentally since, for $f = 4.3$, convective phenomena are observed for Rayleigh numbers between those given by the two theories (Fig. 7).

The numerical model shows that during part of the period of oscillation, the initial perturbation is attenuated considerably and then it increases.

For high frequencies, the results agree very well. All theories predict that the temperature oscillation has no effect on the stability of the layer and that the critical Rayleigh number approaches the constant lower surface value when the frequency tends towards infinity.

Acknowledgment

The authors wish to thank the referees of the *Journal of Heat Transfer* for their important comments and Professor E. M. Sparrow for his valuable suggestions for the preparation of the present paper.

References

1 Davis, S. H., "The Stability of Time-Periodic Flows," *Annual Review of Fluid Mechanics*, Vol. 8, 1976, pp. 57–74.

2 Caltagirone, J. P., "Stabilité d'une Couche Poreuse Horizontale Soumise à des Conditions aux Limites Périodiques," *Int. J. Heat and Mass Transfer*, Vol. 19, 1976, pp. 815–820.

3 Combarnous, M. and Bories, S., "Modélisation de la Convection Naturelle au Sein d'une Couche Poreuse Horizontale à l'Aide d'un Coefficient de Transfert Solide-Fluide," *Int. J. Heat Mass Transfer*, Vol. 17, 1974 pp. 505–515.

4 Chandrasekhar, S., *Hydrodynamic and Hydromagnetic Stability*, Oxford University Press, Clarendon, 1961.

5 Joseph, D. D., *Stability of Fluid Motions*, t. 1–2, Springer, Berlin, 1976.

6 Finlayson, B. A., *Method of Weighted Residuals*, Academic Press, New York, 1972.

7 Rosenblat, S. and Tanaka, G. A., "Modulation of Thermal Convection Instability," *The Phys. of Fluids*, Vol. 14, 1971, pp. 1319–1322.

J. A. Liburdy
Clemson University,
Clemson, SC

E. G. Groff
General Motors Research Laboratory,
Warren, MI

G. M. Faeth
214 Mechanical Engineering Building,
The Pennsylvania State University,
University Park, PA 16802

Structure of a Turbulent Thermal Plume Rising along an Isothermal Wall

The weakly buoyant region of a turbulent thermal plume formed by a line heat source along the base of a vertical isothermal wall was investigated. The turbulence quantities: u', v', w', t', $\overline{u'v'}$, $\overline{u't'}$, *and* $\overline{v't'}$ *were measured, supplementing existing measurements of mean quantities in this flow. The plumes exhibited local similarity in terms of local plume thermal energy flux and height above the source. In the outer portions of the flow, the shear stress agreed with conventional mixing length models and the turbulent Prandtl number approached 0.5. Near the wall, however, turbulent stress and transport quantities do not approach zero when gradients in mean quantities are zero and eddy viscosity models do not properly represent the turbulence characteristics. Predictions of mean quantities were examined using a local similarity hypothesis and various eddy viscosity models. The theoretical results are in fair agreement with the measurements, in spite of the inaccurate representation of turbulence quantities near the wall. The theory indicates that local similarity for mean quantities is only approximately observed, and suggests the presence of systematic Grashof number effects that were not apparent in the measurements due to data scatter.*

Introduction

The structure and heat transfer characteristics of a two-dimensional, turbulent, thermal plume rising along a vertical constant temperature wall is considered. This flow is caused by a line source of heat parallel to the base of the wall and is observed during fires on vertical surfaces, above baseboard heating elements, on large electronic circuit boards, and in other confined natural convection processes. Aside from direct applications, studies of wall plumes are important for increasing understanding of turbulent buoyant flows, since these flows uniquely involve both plume and wall layer phenomena.

Earlier studies have considered turbulent plumes along both adiabatic and isothermal walls [1, 2]. These studies were confined to the weakly buoyant region of the plumes, where property variations (except buoyancy) and radiation can be ignored. Measurements of profiles of mean velocity, streamwise velocity intensity and mean temperature were completed in the adiabatic wall plume [1]. Profiles of mean velocity and temperature, and the wall heat flux distribution, were measured for the isothermal wall plume [2]. Integral models, based on methods used for free line plumes [3, 4], were reasonably successful in correlating the data for both flows. The adiabatic wall plume exhibited similarity to about the same degree as free line plumes [1]. The thermal energy flux is not conserved in the isothermal wall plume due to heat loss to the wall; in this case, *local* similarity was observed, based on the local thermal energy flux in the plume [2]. Both flows exhibited non-similar effects in the wall layer.

The present investigation continues the study of turbulent wall plumes, beginning the development of a more complete theoretical description than that provided by integral models. Model development is greatly enhanced by the availability of information on the turbulent structure. Therefore, new measurements of profiles of u', v', w', t', $u'v'$, $u't'$ and $v't'$ were completed in the isothermal wall plume to supplement existing information on mean quantities. Similar to earlier wall plume studies [1, 2], experimental difficulties were minimized by limiting the measurements to the weakly buoyant region.

Theoretical studies of natural convection boundary layers have progressed from models which assume eddy diffusivity distributions based on forced convection flows [7–9], to methods involving higher-order turbulence closure [10]. The present investigation initiates this process for wall plumes by solving the turbulent boundary layer equations with various eddy diffusivity models.

Experimental Apparatus and Procedure

The details of the experimental apparatus have been described elsewhere [2]. Briefly, the arrangement consists of a smooth vertical wall, 1.22 m wide and 2.44 m high, with side walls to help provide a two-dimensional flow. Cooling water is circulated through coils mounted on the back surface of the wall, maintaining wall temperatures within ±.3 K of the ambient temperature. The heat source is provided by an array of small diffusion flames, burning carbon

---

Contributed by the Heat Transfer Division of THE AMERICAN SOCIETY OF MECHANICAL ENGINEERS and presented at the AIAA/ASME Thermophysics and Heat Transfer Conference, Palo Alto, California, May 25–26, 1978. Manuscript received by the Heat Transfer Division July 21, 1978. Paper No. 78-HT-24.

monoxide, located along the base of the wall and flush with the front surface.

The measurements of mean and turbulent quantities in the flow utilized a fine-wire thermocouple (0.0254 mm dia chromel-alumel wires; 12.7 mm exposed length, parallel to wall) and various arrangements of tungsten hot-wire sensors (0.00508 mm dia wire, 1 mm exposed length). The hot wires were calibrated in a heated air stream, for the complete gas temperature range at all overheat ratios used in the tests. The calibrations were correlated using a temperature dependent Nusselt number-Reynolds number relationship, similar to the formula proposed by Collis and Williams [11].

The hot-wire measurements employed two Thermo Systems, Inc., Model 1050 anemometers, a Model 1015 C correlator, and a Model 1060 true rms meter. All signals were processed with a Hewlett-Packard, Model DY2401B, integrating digital voltmeter, using one-minute intervals of integration, which were timed with a Model 2509 A, digital clock.

The quantities that were measured, and the procedures used for each measurement are summarized in Table 1. Hot-wire measurements at various overheat ratios were used to back-out values of the turbulence quantities. The details of these procedures are described in [12].

In order to establish confidence in the measurements, test conditions were limited to a narrow gas temperature range (13.2 K maximum mean temperature defect), tests were repeated, redundant overheat ratios were used, and many quantities were cross-checked using different methods. Within the range of test conditions reported here, experimental accuracy is within 15 percent except when $y/x < .01$ where the measurements are considered to be less accurate due to wall effects [12]. There was less than a one percent mean temperature variation and less than a ten percent mean velocity variation for distances up to 0.14 m on either side of the centerline of the wall [2, 12].

Experimental Results and Discussion

The present turbulence measurements were obtained at four different test conditions (tests 2–5 summarized in [2]). These test conditions are for plume thermal energy fluxes in the range 116.2–283.8 W/m, and distances from the source of 0.47 and 0.94 m. The present data is plotted in terms of y/x and $y/\delta_{1/2}$, since the latter quantity is useful for comparison with other flows. The $10y/x$ values on the abscissa of each plot only pertain to the isothermal wall plume data; however, the $y/\delta_{1/2}$ values pertain to all the flows. Profiles of mean quantities may be found in [2] and Figs. 10–12 of this paper, the present discussion only considers the new turbulence measurements.

Fig. 1 is an illustration of the fluctuating velocity components, normalized by the maximum streamwise velocity. Turbulent kinetic energy profiles are illustrated in Fig. 2. The results are similar for the different test conditions, the fluctuations are nearly constant across the bulk of the flow, decreasing near the wall.

Table 1 Summary of measurement techniques

Technique	*Quantities Measured*
Single hot wire normal to flow, constant temperature at various overheat ratios	u, u'
Fine-wire thermocouple	ΔT
Single hot wire, constant current	$\Delta T, t'$
Single hot wire normal to flow, constant temperature at three overheat ratios	$u, u', \overline{u't'}, t'$
Crossed hot wires, constant temperature	$u, \Delta T, u', v', w', \overline{u'v'}$
Crossed hot wires, constant current at low overheat ratio	$\overline{v't'}, t'$

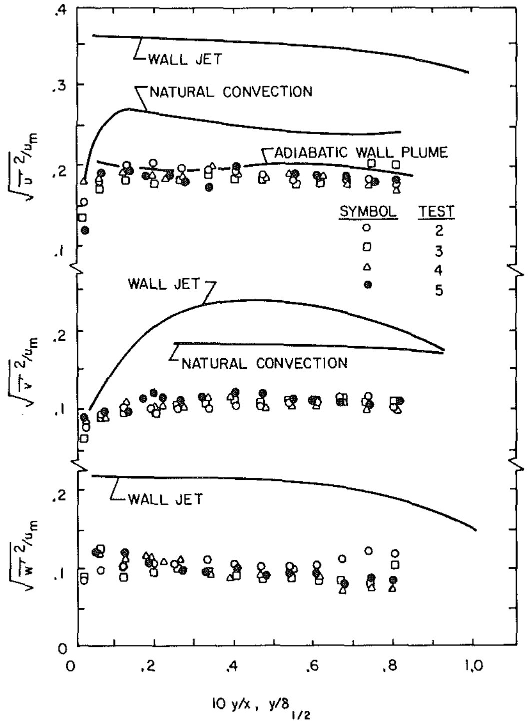

Fig. 1 Profiles of fluctuating velocity components. Symbols represent present isothermal wall plume data. Lines correspond to adiabatic wall plume data [1], natural convection data [5], and wall jet data [6].

The streamwise velocity fluctuations for the adiabatic wall plume [1], are very similar to the present measurements. The natural convection measurements by Smith [5], for $\mathrm{Gr}_x = 4.93 \times 10^{10}$ have a similar shape, but the intensities are roughly 50 percent higher in comparison to u_m. The wall jet intensities of Poreh, et al. [6] are generally higher than the buoyant flows. Towards the edge of the

Nomenclature

A = parameter, equation (24)
C_p = specific heat at constant pressure
f = dimensionless stream function, equation (14)
g = acceleration of gravity
Gr_x = local Grashof number, $g\beta x^3 \Delta T_m/\nu^2$
Gr_x^* = modified local Grashof number, $g\beta x^3 Q_x/\rho C_p \nu^3$
h = heat transfer coefficient = $q_w/\Delta T_m$
k = turbulent kinetic energy
L = momentum mixing length
Nu_x = Nusselt number, hx/λ
Pr, Pr_t = laminar and turbulent Prandtl numbers
q_w = heat flux to wall
Q_x = thermal energy flux in plume
Ra_x^* = modified Rayleigh number, $\mathrm{Gr}_x^* \cdot \mathrm{Pr}$
Re_x = Reynolds number, $u_m x/\nu$
$R_{x'y'}$ = correlation coefficient $\overline{x'y'}/(\overline{x'^2})^{1/2}(\overline{y'^2})^{1/2}$
St = Stanton number, $q_w/\rho C_p u_m \Delta T_m$
t' = temperature fluctuation
T = temperature
u', v', w' = fluctuating velocity components; vertical, normal and parallel to wall
u, v = mean velocity components; vertical and normal to wall
x = distance along wall
y = distance normal to wall
$y^+ = (y/\nu)(\tau_w/\rho)^{1/2}$
α = parameter, equation (17)
β = coefficient of volumetric expansion
$\delta, \delta_{1/2}$ = plume width, $u = 0.1\ u_m$ and $0.5\ u_m$
ϵ = eddy diffusivity
η = dimensionless distance normal to wall, y/x
θ = dimensionless temperature, equation (14)
λ = thermal conductivity
ν = kinematic viscosity
ρ = density
τ = shear stress

Subscripts

m = maximum value
w = at the wall
∞ = ambient condition

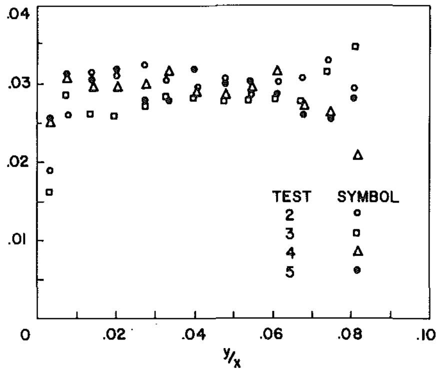

Fig. 2 Profiles of turbulent kinetic energy data for the isothermal wall plume

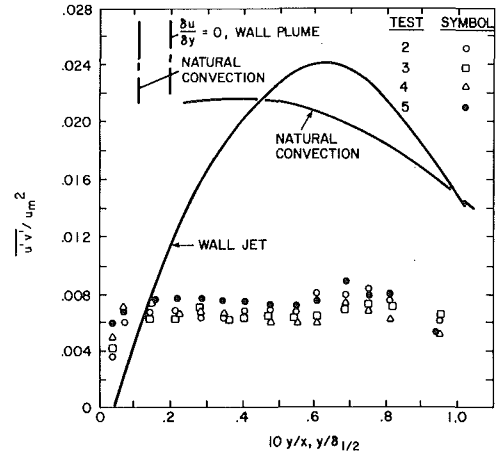

Fig. 3 Profiles of Reynolds stress. Symbols represent present isothermal wall plume data. Lines correspond to natural convection data [5] and wall jet data [6].

boundary layer for the isothermal wall plume, $\overline{u'^2}:\overline{v'^2}:\overline{w'^2} = (1.24:.42:.34)k$. Smith [5] did not determine w', however, if it is assumed that $w' = v'$, the ratios for natural convection in the outer region are $\overline{u'^2}:\overline{v'^2}\ \overline{w'^2} = (.94:.53:.53)k$ which are typical values for nonbuoyant shear layers [13].

Profiles of Reynolds stress appear in Fig. 3, along with measurements for natural convection and the radial wall jet. The present values are nearly constant across much of the flow, with a small peak near the inflection point of the velocity profile. The present Reynolds stresses are lower than the other cases, in keeping with the lower values of k. The Reynolds stress does not change sign at the maximum velocity position, similar to the findings for the wall jet. The natural convection measurements do not extend to the maximum velocity position, but these results also show little tendency to approach zero at this point. The wall jet measurements and the extrapolation of the present measurements, indicate that sign reversal for the Reynolds stress occurs between the maximum velocity position and the wall. This behavior is observed in other flows with asymmetric mean velocity profiles [13]. The buoyant flows have additional buoyant generation of $\overline{u'v'}$ near the wall, which further impedes the Reynolds stress from approaching zero as the sign of the velocity gradient changes. Buoyant generation of $\overline{u'v'}$ is not present for the wall jet which exhibits a more peaked Reynolds stress profile.

The temperature fluctuation intensities are illustrated in Fig. 4, along with natural convection measurements obtained by Smith [5]. The shape of the profile is similar for the two cases, but the natural convection values are generally lower and exhibit a sharper peak near the wall. This behavior is probably due to the fact that the maximum temperature is right at the wall for natural convection which inhibits turbulent transport of peak temperature levels. In contrast, the peak temperature region of the isothermal wall plume is well into the fully-turbulent portion of the flow and fully contributes to fluctuations.

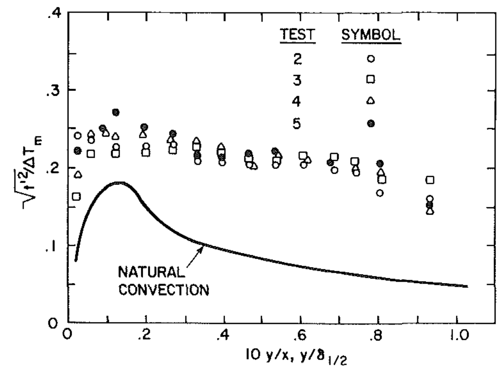

Fig. 4 Profiles of fluctuating temperature intensities. Symbols represent present isothermal wall plume data. Line corresponds to natural convection data [5].

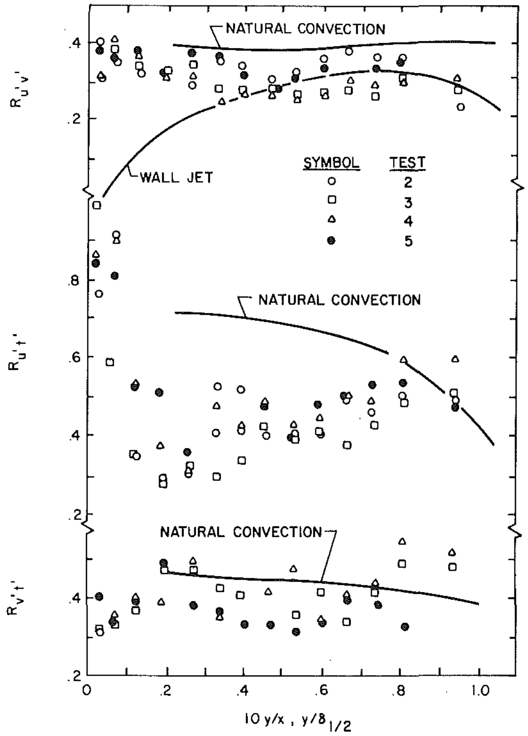

Fig. 5 Profiles of correlation coefficients. Symbols represent present isothermal wall plume data. Lines correspond to natural convection data [5] and wall jet data [6].

Several correlation coefficients for the flow are illustrated in Fig. 5. The velocity correlation coefficient, $R_{u'v'}$, is nearly constant across much of the boundary layer, with values somewhat below those for natural convection. In the outer regions of the flow, the present values approach those measured for the wall jet.

The streamwise velocity correlation, $R_{u't'}$ is high near the wall in the isothermal wall plume. For the bulk of the flow the present values are lower then the natural convection measurements, falling in the range .4–.6.

The values of $R_{v't'}$ for the wall plume and natural convection are nearly the same. Similar to the Reynolds stress and $R_{u'v'}$, which do not change sign at the maximum velocity position, $R_{v't'}$ does not change sign at the maximum temperature position due to the asymmetrical temperature profile.

Fig. 6 is a plot of the ratio of momentum and heat transport by turbulence. This ratio is an effective Prandtl number defined as

$$\mathrm{Pr}_t = \overline{u'v'}\,\frac{\partial T}{\partial y}\Bigg/\left(\overline{v't'}\,\frac{\partial u}{\partial y}\right) \tag{1}$$

The values are roughly constant, except near the wall, falling in the

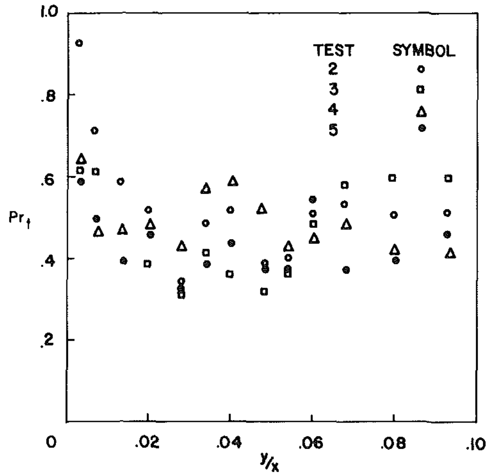

Fig. 6 Profiles of turbulent Prandtl number data for the isothermal wall plume

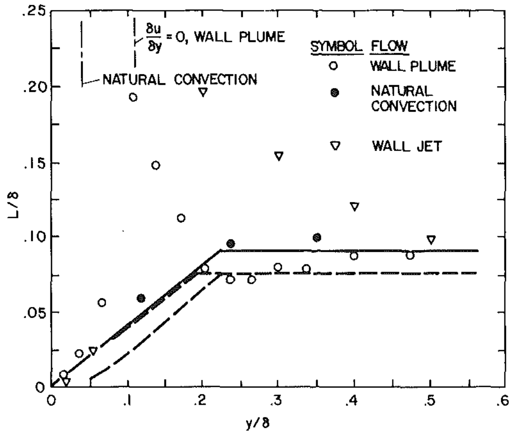

Fig. 7 Profiles of mixing lengths. Symbols represent present isothermal wall plume data, natural convection data [5], and wall jet data [6]. Solid line corresponds to correlation of Escudier [14]. Dashed lines correspond to correlation of Cebeci and Khattab [9], Re_x = 12900 and 28700 (nearest wall).

range 0.4–.6, which is a typical value for two-dimensional flows [13]. Pr_t increases near the wall, however, the values are questionable in this region since both $\overline{u'v'}$ and $\overline{v't'}$ do not change sign at the respective maxima of mean velocity and temperature.

Fig. 7 illustrates mixing lengths calculated for the three flows, using the following stress-mean gradient relationship [13]

$$\overline{u'v'} = L^2 \left|\frac{\partial u}{\partial y}\right| \frac{\partial u}{\partial y} \tag{2}$$

which yields a turbulent diffusity

$$\epsilon = L^2 \left|\frac{\partial u}{\partial y}\right| \tag{3}$$

The natural convection data is for $Gr_x = 4.93 \times 10^{10}$ [5], the present data represent the average value of the four tests. While mixing lengths are plotted for the full width of the flow, between the wall and the maximum velocity position the square of the mixing length calculated from equation (3) is negative and a mixing length is not properly defined. Another difficulty is that the mixing length is infinitely large at the maximum velocity position for the wall plume and wall jet, and large values are encountered near this position.

The mixing length correlations proposed by Escudier [14], and Cebeci and Khattab [9] are compared with the measurements in Fig. 7, (two curves are presented for the Cebeci and Khattab relation, representing the Reynolds number limits [2], of the present tests). The wall plume data generally fall between the two models beyond the maximum velocity position, with higher mixing length values observed for natural convection and the wall jet. Quantitative comparison, however, is difficult due to the problem of accurately determining δ for the three flows.

The mixing length based on the turbulent kinetic energy

$$\epsilon = k^{1/2} L \tag{4}$$

was also evaluated [12]. The trends are similar to Fig. 7, however, the values are 20–30 percent lower. Thermal mixing lengths have similar characteristics, except the values are larger in the outer region, as dictated by Pr_t.

Theoretical Model

There are many known instances where the use of a turbulent viscosity model provides satisfactory predictions of mean quantities (velocity and temperature profiles, wall friction, heat transfer rates, etc.) even though the model does not provide an accurate description of the turbulent stress distribution [13]. Turbulent natural convection on a vertical flat plate provides a recent example of this behavior. Existing data, e.g., Fig. 3, suggest that the Reynolds stress is not zero at the point where the mean velocity gradient is zero, contrary to the behavior prescribed by a turbulent viscosity [5]. Computations with a multi-stress turbulence model support this behavior [5]. Yet reasonably good predictions of this flow were recently obtained with turbulent viscosity models [7–10]. Since the eddy viscosity parameters measured for the isothermal wall plume were qualitatively similar to those found for natural convection on a vertical flat plate, it was of interest to examine whether wall plumes could also be approximated by an eddy viscosity model. Another objective of the calculations was to determine the degree to which theory supports local similarity for these flows.

Both the adiabatic and isothermal wall plumes were considered in the analysis. The maximum temperature defect for the adiabatic wall plume data was 24.2 K, while the present data had a maximum temperature defect of 13.2 K. Since property variations are relatively small for this range of temperatures, the Boussinesq approximation was employed in the analysis. This and other assumptions of the theory are similar to earlier eddy viscosity models of natural convection boundary layers [7–9]. Since profiles of mean quantities in the wall plumes exhibited local similarity, the local similarity method of Noto and Matsumoto [7] has been followed. The similarity variables were selected to conform with earlier wall plume measurements [1, 2].

The basic equations are as follows:

$$\frac{\partial u}{\partial x} + \frac{\partial v}{\partial y} = 0 \tag{5}$$

$$u\frac{\partial u}{\partial x} + v\frac{\partial u}{\partial y} = g\beta(T - T_\infty) + \frac{\partial}{\partial y}\left[(\nu + \epsilon)\frac{\partial u}{\partial y}\right] \tag{6}$$

$$u\frac{\partial T}{\partial x} + v\frac{\partial T}{\partial y} = \frac{\partial}{\partial y}\left[\left(\frac{\nu}{\Pr} + \frac{\epsilon}{\Pr_t}\right)\frac{\partial T}{\partial y}\right] \tag{7}$$

We also define the thermal energy flux in the plume as

$$Q_x = \int_0^\infty \rho u C_p (T - T_\infty) dy \tag{8}$$

Common boundary conditions for both wall plumes are

$$y = 0, \quad u = v = 0; \quad y = \infty, \quad u = 0, \quad T = T_\infty \tag{9}$$

The remaining boundary condition at the wall differs for each plume type as follows

$$y = 0, \quad \frac{\partial T}{\partial y} = 0 \text{ (adiabatic)}, \quad T = T_\infty \text{ (isothermal)} \tag{10}$$

The conservation equations and equation (10) imply that Q_x is a constant for the adiabatic wall plume. For the isothermal wall plume, we define the wall heat flux and heat transfer coefficient as follows

$$q_w = \lambda \left.\frac{\partial T}{\partial y}\right)_{y=0} = h(T_m - T_\infty) \tag{11}$$

which implies that

$$\frac{dQ_x}{dx} = -q_w \tag{12}$$

Now introduce the stream function

$$u = \frac{\partial\psi}{\partial y}, \quad v = -\frac{\partial\psi}{\partial x} \tag{13}$$

and the following dimensionless variables

$$\eta = y/x$$

$$f(x, \eta) = \mathrm{Gr}_x{}^{*-1/3}\psi/\nu \tag{14}$$

$$\theta(x, \eta) = Gr_x{}^{*-2/3}\mathrm{g}\beta \mathrm{x}^3(\mathrm{T} - \mathrm{T}_\infty)/\nu^2$$

which transform equations (5–7) to the following:

$$\mathrm{Gr}_x{}^{*-1/3}\left(1 + \frac{\epsilon}{\nu}\right)f''' + (1 + \alpha)ff'' + \mathrm{Gr}_x{}^{*-1/3}\mathrm{f}''\frac{\partial}{\partial\eta}\left(\frac{\epsilon}{\nu}\right) - \alpha(f')^2 + \theta = x\left(f'\frac{\partial f'}{\partial x} - f''\frac{\partial f}{\partial x}\right) \tag{15}$$

$$\mathrm{Gr}_x{}^{*-1/3}\left(\frac{1}{\mathrm{Pr}} + \frac{\epsilon}{\nu\mathrm{Pr}_t}\right)\theta'' + \left[\mathrm{Gr}_x{}^{*-1/3}\frac{\partial}{\partial\eta}\left(\frac{\epsilon}{\nu\mathrm{Pr}_t}\right) + (1 + \alpha)f\right]\theta' + (1 - 2\alpha)f'\theta = x\left(f'\frac{\partial\theta}{\partial x} - \theta'\frac{\partial f}{\partial x}\right) \tag{16}$$

where derivatives with respect to η are denoted by primes and

$$\alpha = \frac{1}{3}\frac{d \ln Q_x}{d \ln x} \tag{17}$$

The boundary conditions become

$$\begin{aligned} \eta = 0, &\quad f = f' = \theta' \text{ (adiabatic)} = \theta\text{(isothermal)} = 0 \\ \eta = \infty, &\quad f' = \theta = 0 \end{aligned} \tag{18}$$

Equation (8) provides the following integral condition to be satisfied for both flows

$$\int_0^\infty f'\theta d\eta = 1 \tag{19}$$

while equations (11) and (12) yield

$$\frac{xq_w}{Q_x}\mathrm{Pr}^{2/3}\mathrm{Ra}_x{}^{*1/3} = -3\alpha\mathrm{Pr}\,\mathrm{Gr}_x{}^{*1/3} = \theta'(\mathrm{x}, 0) \tag{20}$$

Employing the local similarity method, variations of f and θ in the x-direction are neglected, and the RHS of equations (15) and (16) is set equal to zero. The equations may then be integrated for parametric values of $\mathrm{Gr}_x{}^*$, including any x dependency introduced by the eddy diffusivity distributions. The parameter α is identically zero for the adiabatic wall plume; for the isothermal wall plume, α is an eigenvalue of the solution determined from equation (20). The resulting fifth-order system is apparently overspecified since six boundary conditions are given by equations (18) and (19). However, similar to solutions for two-dimensional laminar free plumes and wall plumes [15, 16], equation (16) trivially satisfies the condition $\theta(x, \infty) = 0$ and this condition is extraneous, providing a well posed problem with the remaining five boundary conditions.

Three eddy diffusivity formulas were examined in the calculations. The first formula was used by Noto and Matsumoto [7] during their calculations for turbulent natural convection

$$\epsilon/\nu = 0.4\,y^+[1 - \exp(-0.0017\,y^{+2})] \tag{21}$$

The second formula employs the mixing length distribution proposed by Escudier [14]

$$\begin{aligned} \epsilon &= (0.41\,y)^2\left|\frac{\partial u}{\partial y}\right|, \quad y/\delta \leqslant .22 \\ &= (0.09\delta)^2\left|\frac{\partial u}{\partial y}\right|, \quad y/\delta > .22 \end{aligned} \tag{22}$$

The third formula is the relationship employed by Cebeci and Khattab [9]. In this case, the eddy diffusivity is taken as the smaller of the following expressions, at each point in the boundary layer.

$$\begin{aligned} \epsilon &= [0.4y(1 - \exp(-y/A))]^2\left|\frac{\partial u}{\partial y}\right| \\ &= (0.075\delta)^2\left|\frac{\partial u}{\partial y}\right| \end{aligned} \tag{23}$$

where

$$A = 26\nu(\rho/\tau_w)^{1/2} \tag{24}$$

These three methods span a range of possibilities for mixing length models. The first only employs a near-wall correction, the second a free-stream correction, while the third contains corrections in both areas.

Constant turbulent Prandtl numbers of 0.5 and 1.0 were used in the calculations. The first value is suggested by the results of Fig. 6, except for the region very near the wall. The second value was used by Noto and Matsumoto [7] and also approximates the more complex prescription employed by Cebeci and Khattab [9].

Theoretical Results and Discussion

Figs. 8–11 are illustrations of the comparison between predicted and measured mean velocities and temperatures for both the adiabatic and isothermal wall plumes. The bars on the data symbols represent the bounds of the data for several tests over the indicated $\mathrm{Gr}_x{}^*$ range. The Cebeci and Khattab (C-K) model, with $\mathrm{Pr}_t = .5$ gave generally the best results and this version is directly compared with the data, using two parametric values of $\mathrm{Gr}_x{}^*$ which bound the test conditions. The Escudier (E), Noto and Matsumoto (N-M) and C-K ($\mathrm{Pr}_t = 1$) models are illustrated in the inset figure for $\mathrm{Gr}_x{}^* = 10^{10}$.

All the models indicate that local similarity is only approximately observed for the mean profiles. In general, maximum quantities tend to increase, the positions of the maxima move toward the wall, and the boundary layer thickness decreases as $\mathrm{Gr}_x{}^*$ increases. An exception to this behavior is the temperature profile for the adiabatic wall plume, where the maximum is always at the wall and remains relatively constant. The changes are not large, however, and these tends are not clearly discernable in the data, due to scatter.

While the C-K model with $\mathrm{Pr}_t = .5$ is reasonably successful, the use of $\mathrm{Pr}_t = 1$ in this model overestimates the maximum temperature, particularly for the adiabatic wall plume (Fig. 9). The N-M and E models with $\mathrm{Pr}_t = .5$, underestimate the maximum temperature values and overestimate the boundary layer thickness. This is particularly true for the N-M model, which prescribes overly large values of the eddy diffusivity near the edge of the boundary layer. The profile predictions of the E and N-M models are improved for $\mathrm{Pr}_t = 1$, however, this results in poorer wall heat flux predictions for the isothermal wall plume, as we shall see next.

Fig. 12 is an illustration of the comparison between measured and predicted wall heat flux for the isothermal wall plume. The C-K and N-M models with $\mathrm{Pr}_t = .5$ provide the best predictions, the results for the other cases are less satisfactory.

The results shown in Figs. 8–12 illustrate that even though mixing length models do not accurately represent all the turbulence characteristics of the flow, prescriptions for the mixing length distribution and the turbulent Prandtl number can be found which yield reasonably good predictions of mean quantities and overall heat transfer characteristics, e.g., the C-K model with $\mathrm{Pr}_t = .5$ in the present case. This is not a new finding, Launder and Spalding [13] present a number of other examples.

The fact that $\mathrm{Pr}_t = .5$, which was found from the turbulence measurements, yields the best predictions of mean quantities for the wall plumes is probably related to the thickness of these flows. In terms of y/x, which is a reasonably satisfactory local similarity coordinate for all the flows, the adiabatic and isothermal wall plumes are two to three times thicker than the natural convection boundary layer. The turbulent Prandtl number generally decreases with distance from the wall, e.g., Fig. 6 and [5, 9, 10] and [13], and is found to be 0.5 for two-dimensional free flows, jets, mixing layers, etc. [13]. Therefore, since

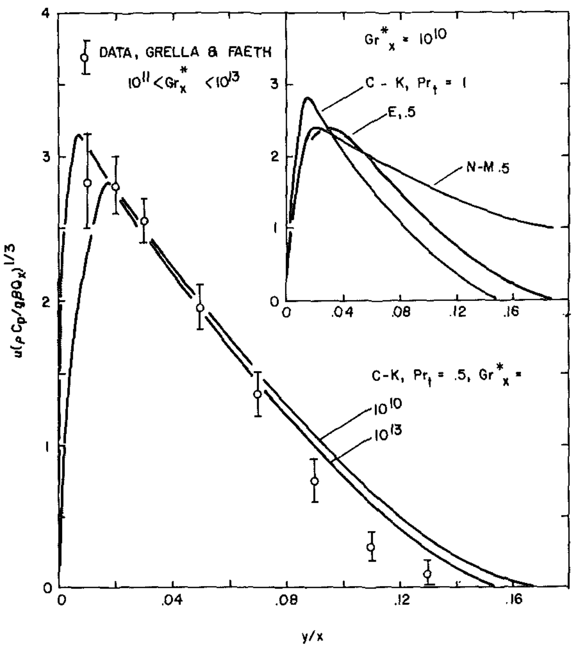

Fig. 8 Predicted and measured mean velocity profiles for the adiabatic wall plume

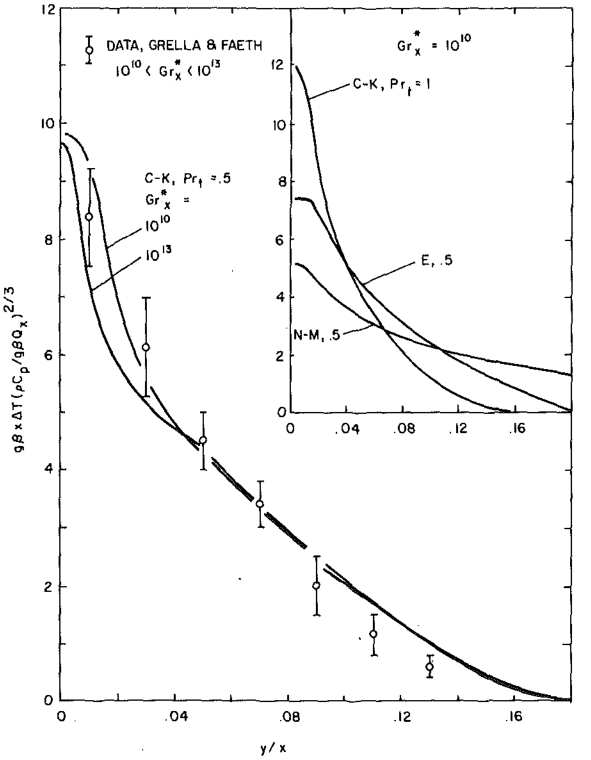

Fig. 9 Predicted and measured mean temperature profiles for the adiabatic wall plume

the wall plumes extend farther from the wall, it is not unexpected that they can be modeled better with a lower Pr_t.

Concluding Remarks

Turbulence quantities in the isothermal wall plume exhibited local similarity to about the same degree as the mean quantities [2]. While specific quantities such as u'/u_m, $\overline{u'v'}/u_m{}^2$, etc., were not the same for the isothermal wall plume and the natural convection boundary layer, mixing lengths calculated for both flows approach values typical of nonbuoyant boundary layers in the region away from the wall. In this same region, however, $\overline{u'^2}$:$\overline{v'^2}$:$\overline{w'^2}$ had ratios of 1.24:.42:.34, rather than the values .94:.53:.53 found for nonbuoyant shear layers [13],

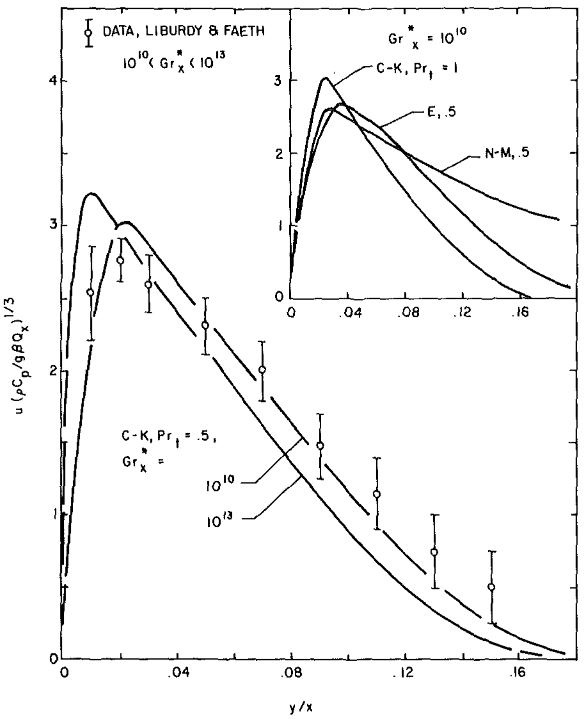

Fig. 10 Predicted and measured mean velocity profiles for the isothermal wall plume

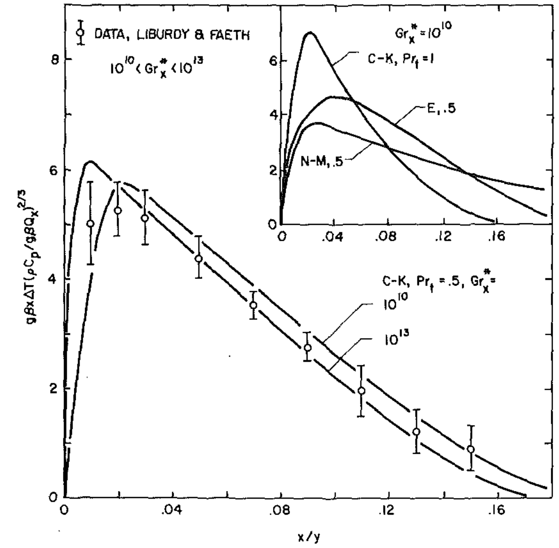

Fig. 11 Predicted and measured mean temperature profiles for isothermal wall plume

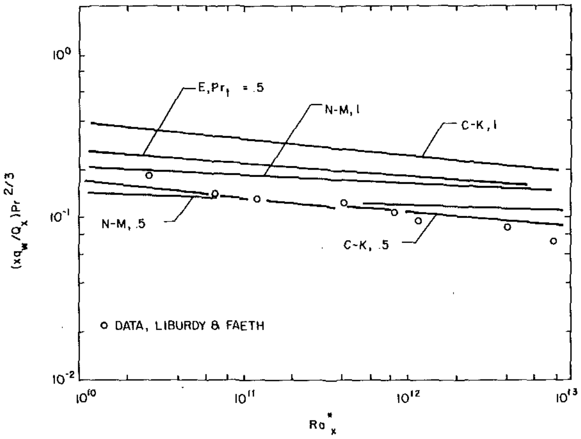

Fig. 12 Predicted and measured wall heat flux correlation for the isothermal wall plume

suggesting a buoyant contribution which increases streamwise velocity fluctuations. The turbulent Prandtl number was approximately 0.5 toward the edge of the boundary layer similar to other two-dimensional flows far from surfaces [13].

Turbulent stresses and transport quantities did not approach zero at the positions where the mean quantities reached maximum values, representing an obvious defect for eddy viscosity models of the turbulence characteristics of this flow. This behavior is not unusual for flows with asymmetrical profiles of mean quantities [13].

The use of a local similarity approximation and an eddy viscosity model for the solution of the boundary layer equations was reasonably successful for the wall plumes. The mixing length constants recommended by Cebeci and Khattab [9] yielded the best overall predictions of mean quantities for both wall plumes and the wall heat flux for the isothermal wall plume. The only modification of the prescription of [9] required during the present calculations was the use of $\mathrm{Pr}_t = 0.5$, a value which also agrees with the present turbulence measurements.

The theories suggest that local similarity does not completely represent wall plumes and that a parametric variation of mean profiles with $\mathrm{Gr}_x{}^*$ should also be observed. Unfortunately, existing data are not sufficiently accurate to confirm this prediction. Since the calculations indicate that local similarity is not exact, higher-order local nonsimilarity solutions similar to those described by Sparrow, et al. [17], are also needed to evaluate the accuracy of the local similarity approximation. Work along these lines is being undertaken in this laboratory.

Eddy viscosity models do not properly represent the turbulent transport characteristics near the wall for the wall plumes, and examination of this flow with higher order models, similar to the study of Smith [5] for natural convection, would be desirable. The turbulence data reported here should be of value in undertaking theories of this type.

Acknowledgment

This research was supported by the United States Department of Commerce, National Bureau of Standards, Grant No. 5-9020, under the technical management of Dr. John Rockett of the Center for Fire Research.

References

1 Grella, J. J. and Faeth, G. M., "Measurements in a Two-Dimensional Thermal Plume along a Vertical Adiabatic Wall," *Journal of Fluid Mechanics*, Vol. 71, 1975, pp. 701–710.

2 Liburdy, J. A. and Faeth, G. M., "Heat Transfer and Mean Structure of a Turbulent Thermal Plume Along Vertical Isothermal Wall," ASME JOURNAL OF HEAT TRANSFER, Vol. 11, May 1978, pp. 177–183.

3 Rouse, H., Yih, C. S., and Humphreys, H. W., "Gravitational Convection from a Boundary Source," *Tellus*, Vol. 4, 1952, pp. 201–210.

4 Lee, S. L. and Emmons, H. W., "A Study of Natural Convection above a Line Fire," *Journal of Fluid Mechanics*, Vol. 11, 1961, pp. 353–368.

5 Smith, R. R., "Characteristics of Turbulence in Free Convection Flow Past a Vertical Plate," Ph.D. Thesis, Queen Mary College, University of London, 1972.

6 Poreh, H., Tsuei, Y. C., and Cermak, J. E., "Investigation of a Turbulent Radial Wall Jet," ASME *Journal of Applied Mechanics*, Vol. 89, 1967, pp. 457–463.

7 Noto, K. and Matsumoto, R., "Turbulent Heat Transfer by Natural Convection Along an Isothermal Vertical Flat Surface," ASME JOURNAL OF HEAT TRANSFER, Vol. 97, 1975, pp. 621–624.

8 Mason, H. B. and Seban, R. A., "Numerical Predictions for Turbulent Free Convection from Vertical Surfaces," *International Journal of Heat and Mass Transfer*, Vol. 17, 1974, pp. 1329–1336.

9 Cebeci, T. and Khattab, A., "Prediction of Turbulent Free Convection from Vertical Surfaces," ASME JOURNAL OF HEAT TRANSFER, Vol. 97, 1975, pp. 469–471.

10 Plumb, O. A. and Kennedy, L. A., "Application of a K-E Turbulence Model to Natural Convection from a Vertical Isothermal Surface," ASME JOURNAL OF HEAT TRANSFER, Vol. 99, 1977, pp. 79–85.

11 Collis, D. G. and Williams, M. J., "Two-dimensional Convection from Heated Wires at Low Reynolds Numbers," *Journal of Fluid Mechanics*, Vol. 6, 1959, pp. 357–384.

12 Liburdy, J. A., "Investigations of Thermal Plumes along Vertical Walls," Ph.D. Thesis, The Pennsylvanis State University, University Park, PA, 1976.

13 Launder, B. E. and Spalding, D. B., *Mathematical Models of Turbulence*, Academic Press, London, 1972, pp. 23–45, p. 49.

14 Escudier, M. P., "The Distribution of Mixing-Length in Turbulent Flow Near Walls," Heat Transfer Section Report TWF/1, Imperial College, London, 1966.

15 Fujii, T., Morioka, I., and Uehara, H., "Buoyant Plume above a Horizontal Line Heat Source," *International Journal of Heat Mass Transfer*, Vol. 16, 1973, pp. 755–768

16 Liburdy, J. A. and Faeth, G. M., "Theory of a Steady Laminar Thermal Plume Along a Vertical Adiabatic Wall," *Letters in Heat and Mass Transfer*, Vol. 2, 1975, pp. 407–418.

17 Sparrow, E. M., Quack, H., and Boerner, C. J., "Local Nonsimilarity Boundary-Layer Solutions," *AIAA Journal*, Vol. 8, 1970, pp. 1936–1942.

R. D. Flack, Jr.
Assistant Professor.
Department of Mechanical and Aerospace Engineering,
University of Virginia,
Charlottesville, Va.
Assoc. Mem. ASME

C. L. Witt
Engineer.
Hayes, Seay, Mattern and Mattern,
Roanoke, Va.
Assoc. Mem. ASME

Velocity Measurements in Two Natural Convection Air Flows Using a Laser Velocimeter

Velocities in two laminar free convection air flow fields were measured using a laser velocimeter. Velocities were first measured in the boundary layer around a heated vertical flat plate and results compare within two percent of theoretical and previous experimental (streak photography) data. Second, velocities were measured throughout a two-dimensional triangular enclosure, which consisted of two isothermal side walls (one heated and one cooled), an insulated bottom, and glass end plates. Enclosure data are compared to simple inclined isothermal plate data and are also presented so that the flow patterns can be observed.

Introduction

Free convection has been of interest in heat transfer applications for decades. Theoretical techniques used to solve natural convection problems yield both heat transfer rates and velocity information [1, 2]. Experimentally, more data are oriented toward heat transfer rates or convection coefficients. Mach-Zehnder interferometers [3] or Wollaston prism interferometers [4] are usually used in two-dimensional and axisymmetric free convection problems. Some velocity field data are available for several specific cases and such data are usually obtained from streak photography [5, 6]. However, with all of these experimental techniques, the flow must exhibit a simple geometric dependence, usually two-dimensionality, or in some cases axisymmetry. In three-dimensional free convection flow fields the above experimental techniques are not acceptable for checking forthcoming three-dimensional theoretical solutions. One technique for measuring velocities in free convection gas flows which has been exploited only minimally is a laser velocimeter (LV). For this paper, a laser velocimeter was used to measure the velocities of free convection in air around a vertical isothermal flat plate. Data are compared to previously determined velocities. Also, the LV was used to measure the velocity field in an air filled triangular enclosure for which the heat transfer characteristics were simultaneously examined [7]. This geometry is representative of attic enclosures and some electronic consoles. For this case velocity data are presented and compared to previously presented results for inclined isothermal plates.

The purpose of this paper is thus two-fold: first, to determine acceptable light scattering particles for and to demonstrate the capability of laser velocimeter in small scale free convection gas flow fields, and second, and most importantly, to provide some quantitative velocity data for a specific natural convection problem which has only recently been studied with heat transfer measurements.

Laser Velocimeters

Over the past fifteen years, laser velocimeters have been used in various applications for measuring fluid velocities. The advantage of using an LV is that the "probe volume" does not disturb the flow as a mechanical probe does. Applications range from very low speed liquid flow such as blood [8] to high speed gas flows [9]. LV's have also been used for both laminar and turbulent flows. The principle of the laser velocimeter stems from the fact that small particles in a flow scatter light. Several arrangements are possible for an LV system as discussed by Durst, et al. [10] and others. For the arrangement of the LV used here two laser beams cross at the "probe volume" (see Fig. 1). This crossing produces a set of parallel fringes due to the coherence of the beams. As particles cross the fringes they scatter light in a periodic fashion. The scattered light is collected by a lens and focused on a photodiode which converts the light signal to an electrical signal. This signal will have a "Doppler" frequency, f_D, which can be converted to particle velocity (V_p) by:

$$V_p = \lambda f_D / 2 \sin(\theta/2) \tag{1}$$

where λ is the wavelength of light used.

Previous to this time LV's have only been used sparingly in free convection gas flows. Abshire, et al. [11], Lawrence, et al. [12] and

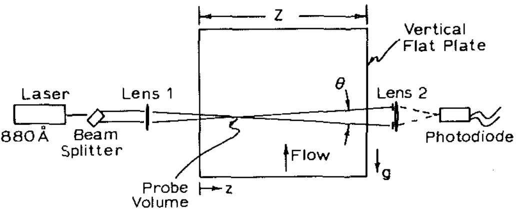

Fig. 1 Laser velocimeter system and flat plate assembly

Contributed by the Heat Transfer Division for publication in the JOURNAL OF HEAT TRANSFER. Manuscript received by the Heat Transfer Division June 12, 1978.

others have used LV's to measure convective velocities in the atmosphere. Also, Amenitskii, et al. [13] used an LV in free convective liquid flows (glycerin and water), in which the impurities in the liquids were used as particles. Adrian [14] used an LV to measure forced convection velocities in water. Overall, however, very little work of this nature has been done with small scale apparatuses.

Errors in LV data can be present due to high acceleration rates, large turbulence intensities, particle dynamics, and the finite size of the probe volume as discussed by Durst, et al. [10] and others. For the laminar velocities, size of the particles, and acceleration rates used here, such inaccuracies were not encountered.

Experimental Apparatus

Vertical Flat Plate. First, an aluminum flat plate assembly 152 mm wide (Z) and 152 mm high (L) was constructed. A water bath was attached behind the assembly with an electrical heater coil and stirrer. The plate was also instrumented with imbedded copper constantan thermocouples.

The laser velocimeter was used in a dual beam forward scatter mode as shown in Fig. 1. The laser is a 0.5 watt Argon ion laser and the beam crossing angle, θ, was equal to 5.14 deg, which resulted in an elliptical probe volume approximately 200 μm in diameter and 2900 μm long. The laser was run at approximately 0.1 watts. Since a photodiode was used (as opposed to a photomultiplier tube) and since relatively small particles were used, running the laser below this level reduced the signal to noise ratio. Due to the small active size of the photodiode and the depth of field of the lens the effective length of the probe volume was 800 μm. The two laser beams were in a plane parallel to the flat plate. Thus, the vertical velocity component was measured. Velocity components in other directions could be measured by rotating the beam splitter.

Smoke (which filled the room) was used as the scattering particles. The smoke was generated with oil soaked paper which was smoldering in a closed container. Most of the particles were very small and did not contribute Doppler signals. The particles that did contribute Doppler signals were estimated to be approximately 1 μm (as discussed in the following section). Many small particles were in the probe volume simultaneously. This resulted in a d-c voltage (output by the photodiode) being detected even when no Doppler signal particles were in the probe volume. When larger particles were in the probe volume the Doppler signals were clearly evident.

Scattered light was focused onto a United Detector Model PIN 020B silicon photodiode. The output of the photodiode was amplified by a factor of 100 and each "burst" signal was displayed on a storage oscilloscope, which had been calibrated using a frequency generator and counter. The Doppler frequency was determined for each particle by counting ten cycles of each burst signal on the oscilloscope.

Only laminar flow was examined and very little "scatter" was found in the reduced data at a given point in the flow. Collecting a large number of samples was not necessary and recording data from an oscilloscope was possible. 30 to 50 samples at each position were recorded and the Doppler frequencies of all particles were determined. The average of all particle velocities (u) at a point in the flow was used in the correlation of the data. The data rate was typically 0.2 sample/s. Only rarely did multiple particles appear in the probe volume.

Due to the finite size of the probe volume some gradient broadening was expected due to the high velocity gradient near the wall. Due to this effect, a minimum ratio of standard deviation/average velocity of 0.05 was expected. Near the wall a value of 0.08 was measured while in the free stream values from 0.02 to 0.04 were measured.

The positioning of the probe volume in the flow field was attained by moving the vertical plate with micrometer heads relative to the stationary optics. Thus, the plate was moved in the y direction for the traversal of the boundary layer with the LV probe volume. Positioning was performed with accuracies of 0.05 mm in the y direction and 0.1 mm in the x direction.

Due to temperature and related index of refraction gradients the position of the probe volume will be shifted. However, for the cases considered here shifts of 0.5 μm and less were present. Also, since the plate was moved the flow field was periodically disturbed. Periods of ten min or more were allowed for the flow field to settle between movements.

The probe volume was located midway between the ends of the plate. The flow field could have been easily traversed in the third direction, z, to determine any three-dimensional dependence of the velocity components. In this respect the laser velocimeter has a great advantage over other experimental techniques in that any three-dimensionality of the flow can be quantified experimentally. In the Appendix a velocity profile at the corner of the plate is presented to demonstrate the three-dimensional traversing capability of the LV.

Triangular Enclosure. The air filled triangular enclosure consisted of two constant temperature tanks and one horizontal adiabatic bottom, as shown in Fig. 2(a). Concurrently with these tests, a Wollaston prism schlieren interferometer was used to measure the heat transfer rates in the same enclosure [7].

Two polished aluminum plates (1.27 cm thick) formed the two inclined sides of the triangular enclosure. Six copper-constantan thermocouples inbedded in the aluminum walls and were within 0.16 cm of the faces similar to other enclosures [4]. The temperatures of the surfaces were uniform within 1°C. The bottom surface of the enclosure was fabricated from a 2.54 cm thick Bakelite plate and was heavily insulated with urethane foam underneath. The two end plates were sealed onto the ends with silicon sealant/adhesive.

The idealized enclosure is presented in Fig. 2(b). One should note that the x direction is defined differently for the hot and cold walls due to the anticipated development of the flow.

The same LV as described above was used to measure the velocities within the enclosure. Two components of velocity were measured: those in the x_C and x_H directions. The flow field was traversed in five approximately equally spaced horizontal planes at distances, h, from the insulated floor. As before, the test section was moved relative to

Nomenclature

f_D = Doppler Frequency of scattered light
g = acceleration due to gravity
Gr = Grashof number, see equation (3)
$\widehat{\mathrm{Gr}} = g\beta_m \cos\gamma(T_H - T_C)L^3/\nu_m{}^2$
h = distance from bottom of triangular enclosure
H = height of triangular enclosure
$\overline{H} = h/H$
L = length of isothermal surface
T = temperature
u = average velocity
$\hat{u}$ = nondimensionalized velocity, see equation (3)
U = nondimensionalized similarity velocity, see equation (3)
V_p = velocity of a single particle
W = width of triangular enclosure
x = direction tangent to an isothermal surface
$X = x/L$
y = direction normal to an isothermal surface
$Y = \mathrm{Gr}^{1/4}y/L$
z = longitudinal direction in the test section
Z = length of the test section
β = volumetric coefficient of expansion = $1/T$
γ = angle between an isothermal surface and the gravity vector
$\eta = Y/(4X)^{1/4}$
θ = angle between laser beams
θ_1, θ_2 = angles in triangular enclosure, see Fig. 2
λ = wavelength of laser light
ν = kinematic viscosity

Subscripts

H,C = pertaining to hot and cold surfaces in triangular enclosure
m = pertaining to mean value of temperature, $T_m = (T_H + T_C)/2$
r = reference condition at which fluid properties are evaluated
w = pertaining to a wall condition
∞ = pertaining to free stream value

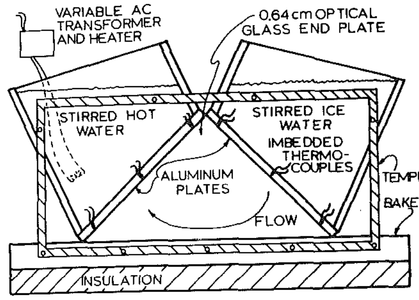

(a) Enclosure Schematic

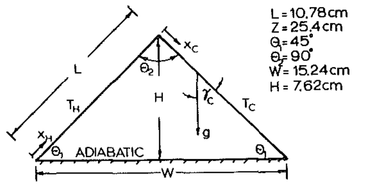

(b) Idealized Enclosure

Fig. 2 End view of triangular enclosure

the LV probe volume with micrometer heads. Both components of velocity were independently measured across the entire test section.

For the enclosure the angle between the laser beams, θ, was decreased to 0.91 deg so that the probe volume could be positioned very close to the surfaces. This was necessary for the measurement of the velocity component normal to the surfaces, particularly in the corner regions. For the enclosure geometry the diameter of the probe volume was approximately 300 μm. The probe volume length was 30,000 μm and again the effective length was approximately 800 μm.

Small chalk dust particles were used for the seeding material in the enclosure. Initially, smoke was attempted for this case, but regulating the size distribution of the smoke was not possible, as the smoke generated very small particles and few large Doppler signal particles as discussed earlier. Injecting smoke into the enclosure produced a small signal to noise ratio and only seldom were burst signals seen. Also, using aluminum powder as seeding material was attempted. The particle sizes were measured with a microscope to be approximately 1 to 3 μm. This powder was injected into the chamber but reseeding was often necessary as the particles tended to drop out of the flow.

The most effective particles were found to be chalk dust. Chalk powder was placed in a hypodermic syringe with air and shaken to suspend the particles. The air/powder was injected into the channel. This resulted in a concentration of approximately 20 particles/cm^3 in the channel. The mean particle size was measured as 1 μm with a microscope. Data rates of 0.5 samples/s were obtained. With these particles, run times in excess of one hour were achieved, as the particle dropout rates were very low. The ratio of standard deviation/average velocity was typically 0.03 for the enclosure.

The smoke was more convenient for use around the flat plate, since seeding the entire room with chalk dust would not have been possible. By examining the voltage amplitudes for the chalk dust and large smoke particles the size of the Doppler signal smoke particles was estimated to be approximately 1 μm since the two types of signals were approximately of the same magnitude.

Experimental Data

Vertical Flat Plate. Measurements were taken for several values of x, and approximately ten values of y were used for each x. The reference temperature rule initiated by Sparrow and Gregg [15] was used in correlating the data. This rule is that a reference temperature, T_r, is used to calculate all fluid properties where

$$T_r = T_w - 0.38(T_w - T_\infty) \tag{2}$$

and that T_∞ be used to evaluate the coefficient of volumetric expansion, β.

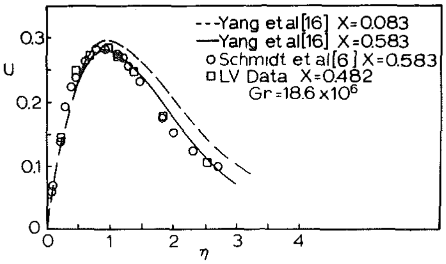

Fig. 3 LV data for vertical flat plate

Velocity and position data have been nondimensionalized as follows so that velocity profiles for vertical and inclined plates approximately collapse to one curve [5, 16]:

$$\left.\begin{aligned} U &= (\mathrm{Gr}/4X)^{1/2}\hat{u} \\ \mathrm{Gr} &= g\beta\cos\gamma(T_w - T_\infty)L^3/\nu_r{}^2 \\ X &= x/L \\ \hat{u} &= u\nu_r/g\beta(T_w - T_\infty)L^2 \end{aligned}\right\} \tag{3}$$

$$\left.\begin{aligned} \eta &= Y(4X)^{1/4} \\ Y &= (\mathrm{Gr})^{1/4}y/L \end{aligned}\right\} \tag{4}$$

Typical data are presented in Fig. 3. These data were collected midway between the ends of the plate at $T_w = 86°\mathrm{C}$, $T_\infty = 25°\mathrm{C}$, and $X = 0.482$. The data are compared to the analysis of Yang and Jerger [16] and the data of Schmidt and Beckmann [6]. Two values of X from [16] are presented primarily to indicate how much results change with X.

Present results are in excellent agreement with the data of [6]. Differences are generally less than two percent. Although the data were not taken at exactly the same value of X, Yang and Jerger's analysis indicates very little difference should exist between $X = 0.482$ and 0.583. The present values of U should be slightly higher than those for $X = 0.583$. As can be seen in Fig. 3, this is true. The recorded peak value of U of the present data are 0.285 ($X = 0.482$) as compared to 0.280 ($X = 0.583$).

One problem which arose with making velocity measurements in the open free convective field was with room currents. Since an LV is making point measurements, such currents are more pronounced than for interferometers, which average over a test section.

Triangular Enclosure. Measurements were taken midway between the end plates for five values of h in the chamber and at 20 to 30 horizontal positions for each component. To correlate the velocity data tangent to the nearest surface, nondimensionalization in equations (2–4) was used once again.

To present heat transfer data for rectangular enclosures in a form comparable to vertical plate data, Eckert and Carlson [3] utilized the temperature at the center plane to represent the temperature at "infinity" (T_∞). For a triangular enclosure, however, defining such a temperature becomes very difficult near the corners. Therefore, for this work, the free stream temperature (T_∞) was replaced by the mean temperature (T_m), such that comparison to simple inclined plate data was possible.

Nondimensionalized velocity profiles for the tangential velocity components midway up the isothermal walls are presented in Fig. 4. The conditions for which this data were collected are $T_H = 64°\mathrm{C}$ and $T_C = 0°\mathrm{C}$ and the overall Grashof number based on the total temperature difference ($\hat{\mathrm{G}}\mathrm{r}$) is 6.5×10^6 for this case. In Fig. 4, velocity profiles near the two isothermal surfaces are presented and compared to that of the LV results for the isothermal vertical flat plate.

Also in Fig. 4, two theoretical velocity profiles are presented. These two theoretical profiles were calculated using the method of Kierkus [5] for heated inclined plates. The dotted line corresponds to the velocity data near the hot wall of the triangular enclosure. The solid line represents an inclined heated surface facing upwards, which is approximately the same condition as an inclined cooled plate facing downward. Thus, the solid line corresponds to the cold wall of the

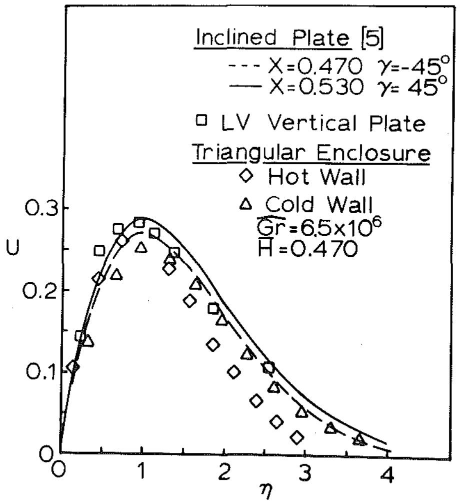

Fig. 4 LV data for $\overline{H}$ = 0.470 for triangular enclosure as compared to simple inclined plate correlations

enclosure. Different values of X were used in the application of the analysis of Kierkus, since X was measured differently for each surface (see Fig. 2(*b*)), while $\overline{H}$ was the same near both walls. Kierkus demonstrated the accuracy of the theoretical solution for several values of X and γ, but did not present experimental data near $X = 0.5$ and $\gamma = \pm 45$ deg, which could be used for direct comparison here. Since his method was accurate for other values, however, it will be used for comparison here.

In Fig. 4, one can see the three experimental velocity profiles are in approximate agreement. Both of the experimental velocity profiles for the enclosure are somewhat thinner than the Kierkus theoretical analysis for simple inclined surfaces. This is due to the fact that in the enclosure larger buoyancy forces are present due to the two walls rather than a single wall, particularly near the apex. The data nonetheless do correspond approximately to the theory of Kierkus with the cold wall agreeing slightly better than the hot wall data. Also, for the data presented in Fig. 4, the flow was almost exactly one-dimensional near the surfaces. No velocities normal to either surface were measured for $\overline{H} = 0.470$.

In Figs. 5 (*a*) and (*b*) nondimensionalized tangential velocity profiles are presented for both walls for five values of $\overline{H}$. In general, velocity profiles near both walls show a strong dependence on the parameter $\overline{H}$. The experimental data and theoretical method of Kierkus [5] are on the other hand rather insensitive to the value of X. For example, one can use Fig. 3 to appreciate the relative changes of the profile shape for vertical or inclined plates with changing X.

The five profiles near the hot wall are presented in Fig. 5(*a*). The curve with the lowest velocity peak is for $\overline{H} = X = 0.783$ while the largest peak occurs for $\overline{H} = 0.310$. For values of η between 1 and 3 the plots for $\overline{H} = 0.157, 0.310, 0.470$ and 0.627 approximately collapse to one curve. Qualitatively, the behavior for the hot enclosure wall is somewhat the same as for the simple inclined plate. For example, the largest peaks occur for small values of X for both cases. Differences do occur, however, particularly near the corners. The width of the boundary layer for $\overline{H} = 0.783$ is larger than for small values of $\overline{H}$. Also, the largest peak does not occur at $\overline{H} = 0.157$. Neither of these observations agree with inclined flat plate behavior.

In Fig. 5(*b*), the profiles near the cold wall are presented. Due to the definition of x the values of $\overline{H} = 0.783, 0.627, 0.470, 0.310$ and 0.157 correspond to $X = 0.217, 0.373, 0.530, 0.690$ and 0.843, respectively. Overall, these profiles agree much better qualitatively with the inclined flat plate behavior. The largest peak occurs for the smallest value of X and vice versa. Also, in general, the width of the boundary layer decreases with increasing X. Only for $X = 0.843$ does the trend deviate from simple inclined plate behavior. For this value of X the width of the boundary layer is larger than for $X = 0.690$. Again, however, the differences in boundary layer shapes for different values of X only are in qualitative agreement with simple inclined plate behavior. In general, the magnitudes of the differences are much larger due to the corner effects on the flow.

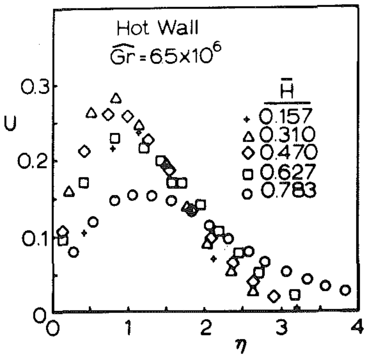

(a) Hot Wall

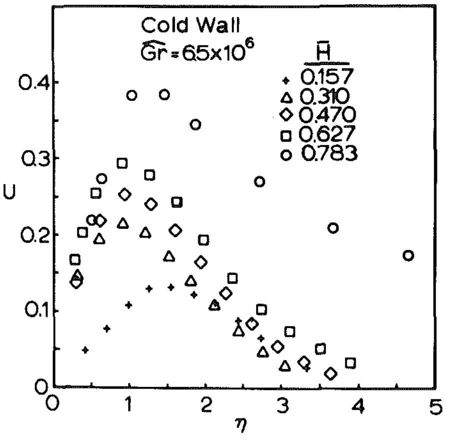

(b) Cold Wall

Fig. 5 LV data near walls of enclosure for five values of $\overline{H}$

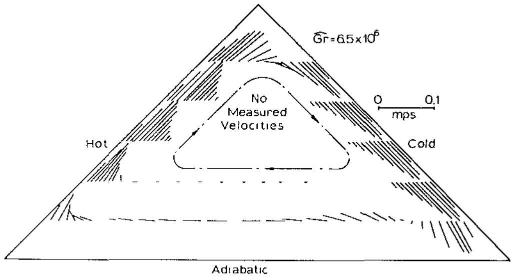

Fig. 6 Flow patterns in enclosure

Finally, by using the two velocity components at selected points in the chamber, a flow map was constructed and is presented in Fig. 6. This figure clearly shows boundary layer type flow with no flow in the central region of the chamber. In [7] this geometry was found to have an approximately constant temperature region in the central portion, which is also indicative of the "boundary layer regime". Thus, the two sets of experimental data are in agreement.

Particle Dynamics. Two different free convective flow fields were investigated here. For the first case (external flow), velocities were measured with the LV with smoke and were within two percent of previously measured (streak photography) velocities and within two percent of theoretical results. For this case it is rather obvious that particle dynamics were not influential.

For the second case (internal flow), atomized chalk dust particles were injected into the test cell. Nondimensionalized velocity profiles were presented near both the hot and cold surfaces of the enclosure and compared to an inclined plate correlation. Near the central horizontal plane of the enclosure corner effects should be minimal and the flow should be essentially one-dimensional, and tangent to the walls. As can be seen by Fig. 6, the flow is tangent to the walls and no velocity components normal to the walls were measured. This indicates that the vertical gravity vector was not influencing the measurements. Also, near the central horizontal plane, the nondimensional velocity profiles did approximately collapse onto one curve as might be expected and compared well to the simple inclined plate correlation. The small differences between the enclosure data and inclined plate correlation near $\overline{H} = 0.5$ can be attributed to the fact that the boundary layer development will be different for simple inclined walls and the enclosure walls because of the flow near the corners.

Also, for the large Grashof numbers used in the enclosure the flow was expected to be in the "boundary layer regime" as was found for rectangular enclosures [3]. By examining Fig. 6 one can see that no velocities were detected in this region (only a low level d-c voltage was output from the photodiode in this region). By Stoksian flow theory the settling velocities of these particles is estimated to be 2×10^{-4} mps. Had particle lag been present a significant number of signals in the vertical direction would have been measured here due to the particles falling out of the flow near the apex. This observation agrees with the fact that very little reseeding was necessary after each test began.

Thus, since in the central region of the test section the flow was tangent to the walls and the velocity profiles approximately collapsed onto one nondimensionalized curve, since no vertical velocities were measured in the center of the flow field, and since the settling velocity is considerably less than the measured velocities the effects of particle dynamics in the enclosure have been concluded to be negligible.

Conclusions

Overall, accurate LV results were obtained for free convection over a vertical isothermal flat plate where flows had previously been examined with streak photography and in a triangular enclosure where results were not available. Specific conclusions include: (1) The LV measurements for flow around the flat plate were within two percent of previous measurements and theoretical results. (2) Smoke was the most convenient seeding material for external flows. (3) Injected atomized chalk dust was the most efficient seeding material for internal flows. (4) For the particular enclosure geometry and conditions examined the flow was in the "boundary layer regime", which agrees with the observation in the heat transfer measurements. (5) The nondimensionalized velocity profiles near the walls of the enclosure were strong functions of X, as compared to the velocity profiles on inclined isothermal plates, which are weak functions of X.

Acknowledgments

The authors gratefully acknowledge the support of the Department of Mechanical and Aerospace Engineering, University of Virginia, for the experimental apparatus and optical system.

References

1 Ostrach, S., Natural Convection in Enclosures," *Advances in Heat Transfer*, Vol. 8, Academic Press, New York, 1972, pp. 161–227.

2 Raithby, G. D. and Hollands, K. G. T., "A General Method for Obtaining Approximate Solutions to Laminar and Turbulent Free Convection Problems," *Advances in Heat Transfer*, Vol. 11, Academic Press, New York, 1975, pp. 265–315.

3 Eckert, E. R. G., and Carlson, W. O., "Natural Convection in an Air Layer Enclosed Between Two Vertical Plates with Different Temperatures," *Int. J. Heat Mass Transfer*, Vol. 2, Nos. 1/2, March 1961, pp. 106–120.

4 Sernas, V., Fletcher, L. S., and Aung, W., "Heat Transfer Measurements with a Wollaston Prism Schlieren Interferometer," ASME Paper, 72-HT-9, presented at the AIChe-ASME Heat Transfer Conference, Denver, Col., Aug., 1972.

5 Kierkus, W. T., "An Analysis of Laminar Free Convection Flow and Heat Transfer About an Inclined Isothermal Plate," *Int. J. Heat Mass Transfer*, Vol. 11, No. 2, Feb. 1968, pp. 241–253.

6 Schmidt, E. and Beckmann, W., "Das Temperatur-und Geschwindigkeitsfeld vor einer Warme abgebenden senkrechten Platte bei naturlicher Knovektion," Tech. Mech. u. Thermodynamic, Bd. 1, Nr. 10, Oct. 1930, pp. 341–349; cont. Bd. 1, Nr. 11, Nov. 1930, pp. 391–406.

7 Flack, R. D., Konopnicki, T. T., and Rooke, J. H., "The Measurement of Natural Convective Heat Transfer in Triangular Enclosures," ASME Paper 78-WA/HT-9, presented at the ASME Winter Annual Meeting, San Francisco, Cal., Dec. 1978.

8 Vlachos, N. S. and Whitelaw, J. H., "The Measurement of Blood Velocity with Laser Anemometry," In: *Proceedings of the Second International Workshop on Laser Velocimetry*, Purdue University, March 27–29, 1974, pp. 521–544.

9 Flack, R. D., and Thompson, H. D., "Comparison of Pressure and LDV Velocity Measurements with Predictions in Transonic Flow," *AIAA Journal*, Vol. 13, No. 1, Jan. 1975, pp. 53–59.

10 Durst, F., Melling, A., and Whitelaw, J. M., *Principles and Practice of Laser—Doppler Anemometry*, Academic Press, New York, 1976.

11 Abshire, N. L., Schweisow, R. L., and Derr, V. E., "Doppler Lidar Observations of Hydrometers," *J. Appl. Meteorology*, Vol. 13, Dec. 1974, pp. 951–953.

12 Lawrence, T. R., Wilson, D. J., Craven, C. E., Jones, I. P., Huffaker, R. M., and Thompson, J. A. L., "A Laser Velocimeter for Remote Wind Sensing," *Rev. Sci. Instr.*, Vol. 43, 1972, pp. 512–518.

13 Amenitskii, A. N., Rinkevichyus, B. S., and Solovev, G. M., "Measurements Using the Doppler Effect of Small Velocities in Flows Occurring in the Free Convection of Fluids," *Soviet Physics-Doklady*, Vol. 17, No. 11, May 1973, pp. 1078–1079.

14 Adrian, R. J., "Turbulent Convection in Water Over Ice", *J. Fluid Mech.*, Vol. 69, Pt. 4, 1975, pp. 753–781.

15 Sparrow, E. M., and Gregg, J. L., "The Variable Fluid Property Problem in Free Convection," *Trans. ASME*, Vol. 80, 1958, pp. 879–886.

16 Yang, K. T., and Jerger, D. W., "First Order Perturbations of Laminar Free Convection Boundary Layers on a Vertical Plate," ASME, JOURNAL OF HEAT TRANSFER, Vol. 86, 1964, pp. 107–115.

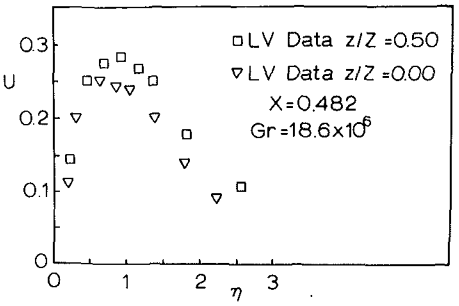

Fig. 7 LV data near corner of vertical flat plate

APPENDIX

Data for the vertical flat plate are presented in Fig. 3 for velocities near the midplane of the plate. To demonstrate that an LV is capable of traversing the z direction, in this Appendix typical data are presented for measurements at the corner of the plate ($z/Z = 0.00$). Other parameters are the same as for Fig. 3. These corner data are presented in Fig. 7 and compared to data at the center ($z/Z = 0.50$). Velocities are lower in the major part of the boundary layer for $z/Z = 0.00$ as opposed to those for $z/Z = 0.50$. This should be expected since near the corner the "driving force" per unit fluid volume will be less than a centrally located point. Resulting fluid velocities will, thus, be less. For small values of η, differences between these two sets of data are small.

C. Quon
Atlantic Oceanographic Laboratory,
Bedford Institute of Oceanography,
Dartmouth, Nova Scotia, B2Y 4A2
Canada

A Study of Penetrative Convection in Rotating Fluid[1]

The effects of rotation on penetrative convection in an annulus of fluid are studied numerically by finite difference method. The axisymmetric flows for 14 sets of parameters are presented. It is found that rotation compresses the cell heights and increases the horizontal cell number in the r-z plane. The curvature of the container strongly affects the cell structure only at low rotation rate. The upper dynamical boundary conditions have virtually no effect on the flow fields if the upper temperature is sufficiently high.

Introduction

Penetrative convection in an unstable fluid layer underneath a stable layer in a stationary frame of reference has been studied by Veronis [11], Townsend [10], Musman [6], Faller and Kaylor [4], Moore and Weiss [5], and others. Since this problem has astro-geophysical applications it would be interesting to study the effect of rotation on penetrative convection. For simplicity, only axisymmetric flows will be considered.

Let us consider the following model problem. An annulus of fresh water has its upper and lower boundaries maintained at two different temperatures T_1 and T_0 (Fig. 1): $T_1 > 3.98°C$ and $T_0 = 0°C$. Due to thermal diffusion, the fluid will in time develop into a two-layer system with $T = 3.98°C$ as the dividing line. The upper layer with $3.98°C \leq T < T_1$ is a gravitationally stable layer and the lower layer with $0 \leq T \leq 3.98°C$ is a gravitationally unstable layer, because fresh water has maximum density at 3.98°C.

In this system, instability sets in at two stages. The first stage is infinitesimal in which the meridional motion due to an imposed random disturbance organizes into cells. The cells grow very gradually in strength and lead to finite amplitude instability. After the onset of this second instability, the kinetic energy of the whole system rapidly increases. The structure of isotherms in the lower layer alters with the convective motion. This second stage of instability will either strengthen the existing convection cells or induce finite amplitude oscillation. Rotation has only a slight effect on the onset of the initial stage of instability; but its effect on the structure of the finite amplitude cells is considerable. It was suggested that the azimuthal current induced by Coriolis effect can give rise to centrifugal instability and possibly baroclinic instability. The development of centrifugal instability in the system has been discussed by Quon [9].

In this paper we shall give a report on the effects of rotation, temperature differentials between the upper and lower boundaries, and curvature of the container on the axisymmetric motion in an annulus of square cross section. Although the problem considered here cannot be directly applied to any natural system, nor can the results be compared with any existing theories on Benard convection, which are mostly formulated for infinite domains, the present problem is of general interest because of its exploratory nature. It is believed that this is the first attempt to describe penetrative convection in a rotating fluid. As Daniels [2] and Daniels and Stewartson [3] have shown recently, Benard type of convection in a rotating fluid in a finite domain does pose some extra constraint because of the vertical boundaries, and hence requires fresh interpretation.

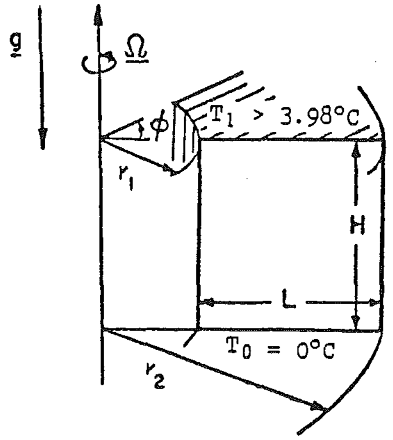

Fig. 1 The physical system

Mathematical Formulation

The nondimensional equations of axisymmetric flow for an incompressible fluid in the rotating frame of reference can be written as follows (Chandrasekhar [1], p. 83):

$$\partial\zeta/\partial t = \mathrm{J}(\zeta/r, \psi) + (1 + 2v/r)\partial v/\partial z - \beta\partial\theta^2/\partial r + \epsilon L\zeta \tag{1}$$

$$\partial(r^2 v)/\partial t = \mathrm{J}(rv, \psi) + r\partial\psi/\partial z + \epsilon r^2 L v \tag{2}$$

$$\partial(r\theta)/\partial t = \mathrm{J}(\theta, \psi) + (\epsilon/\sigma)r\left(L + \frac{1}{r^2}\right)\theta \tag{3}$$

---

[1] A Bedford Institute contribution.

Contributed by the Heat Transfer Division for publication in the JOURNAL OF HEAT TRANSFER. Manuscript received by the Heat Transfer Division December 4, 1978.

$$\frac{1}{r}\left(\partial^2/\partial r^2 - \frac{1}{r}\,\partial/\partial r + \partial^2/\partial z^2\right)\psi = -\zeta \tag{4}$$

where $L = (\nabla^2 - 1/r^2)$, ∇^2 being the Laplacian operator, and $J(f, h) = (\partial f/\partial r \cdot \partial h/\partial z - \partial f/\partial z \cdot \partial h/\partial r)$, the Jacobian. Boussinesq approximation has been applied with the following equation of state

$$\rho = \rho_0[1 - \alpha(T - 3.98\ \mathrm{C})^2]$$

$$\alpha = 8.0 \times 10^{-6}/(°\mathrm{C})^2 \tag{5}$$

In (1) to (4), ζ and ψ are the vorticity and the Stokes' stream function in the meridional (r-z) plane, respectively. υ is the azimuthal velocity. The total velocity vector is then

$$\boldsymbol{q} = \left(-\frac{1}{r}\,\psi_z, \upsilon, \frac{1}{r}\,\psi_r\right) \tag{6}$$

A characteristic time $\tau = (2\Omega)^{-1}$, length L and velocity $U = (2\Omega L)$ have been used. Hence the characteristic stream function is $2\Omega L^3$. The normalized temperature θ is defined as

$$\theta = (T - 3.98)/3.98.$$

Three useful nondimensional parameters are defined as follows:

$\epsilon = \nu/2\Omega L^2$	Ekman number
$\beta = \dfrac{\alpha g(3.98)^2}{4\Omega^2 L}$	Thermal Rossby number
$\sigma = \nu/\kappa$	Prandtl number

The boundary conditions for (1) to (4) are:

$\upsilon = \psi = \partial\psi/\partial\eta = 0$	on all walls
$\theta = \lambda > 0$	on upper boundary
$= -1$	on lower boundary
$\partial\theta/\partial r = 0$	on the cylindrical walls,

where $\partial/\partial\eta$ denotes normal gradients on the walls. In this paper $\partial\psi/\partial\eta = 0$ on the side walls has been relaxed and replaced by $\zeta = 0$. This relaxation is intended to reduce viscous drag produced by the vertical walls. It does not make the side walls completely slippery, however, because $\upsilon = 0$ instead of $\partial\upsilon/\partial\eta = 0$ is maintained.

Method of Solution and the Initial Condition

Since we are mainly interested in nonlinear convection, we shall investigate the problem numerically by finite difference method. The essence has been given in Quon [8]. The finite difference formulation is stable enough to suppress the disturbance due to truncation and roundoff errors. Hence the integration starts from zero initial condition, the $\partial\theta^2/\partial r$ term in (1) would remain zero at all times because the ensuing temperature development is by conduction in the z-direction only. Consequently no motion can be generated. In all computations initially a random θ field with maximum amplitude of 0.1 percent of $(1 + \lambda)$ had to be imposed.

The parameters for all computations are given in Table 1.

Table 1 Details of Computation

Case	ϵ	β	λ	Ω (rad/s)
$Q10$	5.39×10^{-1}	9.76×10^{3}	6.0	1.03×10^{-3}
$Q11$	3.54×10^{-1}	4.20×10^{3}	6.0	1.57×10^{-3}
$Q12$	1.77×10^{-1}	1.05×10^{3}	6.0	3.14×10^{-3}
$Q13$	8.84×10^{-2}	2.62×10^{2}	6.0	6.28×10^{-3}
$Q14$	4.42×10^{-3}	6.56×10^{-1}	6.0	1.26×10^{-1}
$Q15$	3.30×10^{-3}	3.65×10^{-1}	6.0	1.68×10^{-1}
$Q16$	2.46×10^{-3}	2.02×10^{-1}	6.0	2.26×10^{-1}
$Q17$	2.21×10^{-3}	1.64×10^{-1}	6.0	2.51×10^{-1}
$Q18$	2.21×10^{-3}	1.64×10^{-1}	2.5	2.51×10^{-1}
$Q19$	2.21×10^{-3}	1.64×10^{-1}	0.3	2.51×10^{-1}
$Q20$	2.46×10^{-3}	2.02×10^{-1}	4.0	2.26×10^{-1}
$Q21$	2.31×10^{-3}	1.80×10^{-1}	2.1	2.40×10^{-1}
$Q22$	2.39×10^{-3}	1.92×10^{-1}	1.5	2.32×10^{-1}
$Q23$	2.76×10^{-3}	2.56×10^{-1}	2.1	2.01×10^{-1}

$L = 3$ cm, $\kappa = 1.4 \times 10^{-3}$, $\nu = 1.0 \times 10^{-2}$, $\alpha = 8.0 \times 10^{-6}$ for all cases.

$\epsilon = \dfrac{\nu}{2\Omega L^2}$, $\beta = \dfrac{\alpha g(3.98)^2}{4\Omega^2 L}$.

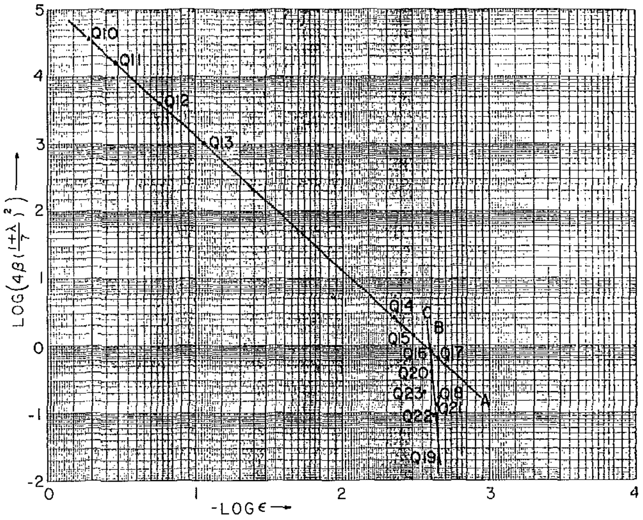

Fig. 2 Summary of the computations

Results and Discussion

Fig. 2 summarizes the various cases of computation in $\epsilon - \beta$ parameter space. Line A contains all cases which are different from one another only in the rate of rotation. The rotation rate increases from $\Omega = 1.03 \times 10^{-3}$ rad s^{-1} for $Q10$ to $\Omega = 2.51 \times 10^{-1}$ rad s^{-1} for $Q17$ at a constant $\lambda = 6$. Line B contains three cases of different values of λ at a constant $\Omega = 2.51 \times 10^{-1}$ rad s^{-1}: $Q17$ ($\lambda = 6$), $Q18$ ($\lambda = 2.5$), and $Q19$ ($\lambda = 0.3$). Line C divides the cases of three-cell formation to the left from the four-cell formation to the rigt. Line C is roughly represented by

$$\left\{\beta\left(\frac{1+\lambda}{7}\right)^2\right\}^\mu = 390\,\epsilon,$$

where $\mu = 0.0444$.

In this section we shall examine the various effects on the structure of the convection cells.

1 **Effects of Rotation.** The most obvious effect of rotation on the convective motion is the existence of an azimuthal velocity. Without rotation, axisymmetric convection rolls may have two-dimensional motion only. Coriolis effect has generated an additional azimuthal velocity. Circular motion in axisymmetric rolls has become helical although the motion is still axisymmetric. The magnitude of the azimuthal velocity υ can be estimated by

$$-\psi_z = \epsilon\left(\frac{\partial^2\upsilon}{\partial x^2} + \frac{\partial^2\upsilon}{\partial z^2}\right)$$

Nomenclature

J = Jacobian operator
$L = \nabla^2 - 1/r^2$, a differential operator
$\boldsymbol{q}$ = velocity vector
r = radial coordinate
t = time
υ = azimuthal velocity
z = vertical coordinate
α = coefficient of cubic expansion
β = thermal Rossby number
ϵ = Ekman number
ζ = vorticity
$\partial/\partial\eta$ = normal gradient at the boundaries
θ = normalized temperature
κ = thermometric conductivity of fluid
λ = normalized temperature at the upper boundary
ν = kinematic viscosity
ρ = density of fluid
σ = Prandtl number
$\tau = (2\Omega)^{-1}$, characteristic time
ψ = Stokes stream function
Ω = rotation rate

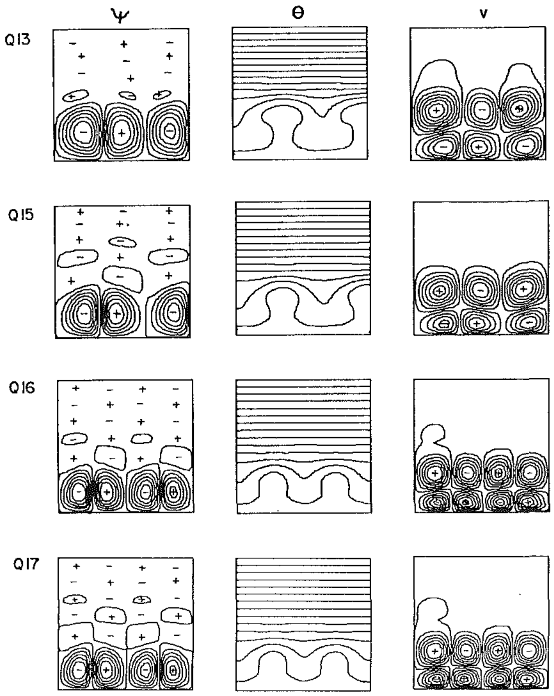

Fig. 3 Steady-state contours of various fields for selected cases along line A in Fig. 2. The varying parameter is the rotation rate Ω. Isotherm spacings are $(\lambda + 1)/13$ with $\theta = \lambda$ at upper and $\theta = -1$ at lower boundary. Clockwise meridional motions are represented by + ψ cells. + Contours in v indicate flows into the page.

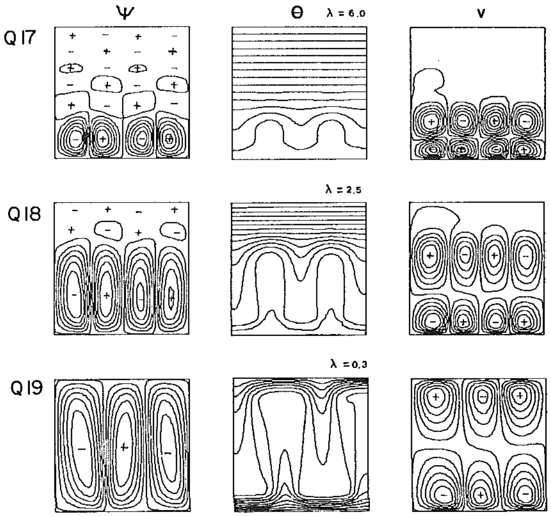

Fig. 4 Steady-state contours for the three cases along line B in Fig. 2. Note how the unstable layer increases when λ decreases. See caption of Fig. 3 for explanation.

with $\psi = \psi_0 \sin \pi z/d \sin k\pi x$ where $x = (r - r_1)$, d the cell height of ψ, and k the horizontal number of cells shown in Fig. 3.

The second noticeable effect of rotation is on the permissible number of horizontal cells as shown in Fig. 3. As one descends from left to right along Line A in Fig. 2, the number of cells increases from 3 in $Q15$ to 4 in $Q16$. The classical theory of Benard convection in a rotating fluid predicts that asymptotically the cell scales vary with $\Omega^{-1/3}$ [1]. The transition from three cells to four cells is not clear cut in the computation. However, the increase in cell number with increasing rotation is in keeping with the classical theory.

The third effect of rotation is in the reduction of cell heights by rotation as shown in Fig. 3. This effect is not surprising. If the horizontal scale decreases, the vertical scale also decreases with increasing rotation according to the classical theory.

2 **Effect of Temperature on Upper Boundary.** Fig. 4 depicts the various fields for the three cases on Line B in Fig. 2. They illustrate the effect by varying the upper temperature while the rotation rate is held constant. The cell heights increase with decreasing upper temperature. For $\lambda = 0.3$, or the upper temperature = 5.2°C, the whole cavity becomes unstable. The cell number decreases from 4 for $Q18$ to 3 for $Q19$. In the classical theory of Benard convection, there is a definite cell height to cell width ratio. In the present system, this ratio depends strongly on the upper temperature as shown in $Q17$,$Q18$ in Fig. 3. One must not, however, compare infinitesimal instability theory valid for an infinite domain to finite amplitude instability in a finite container.

3 **Effects of the Upper Dynamical Boundary Condition and Curvature.** When the temperature on the upper boundary is sufficiently large [say, $\lambda \sim 0(1)$], the dynamical boundary condition on the upper boundary produces no appreciable effect either on the onset of instability or on the final cell structure. Fig. 5 shows the results of two computations: the upper diagrams are for a free upper surface ($v_z = 0$, $\zeta = 0$) and the lower diagrams are for a rigid upper boundary with non-slip conditions, while all other parameters are held constant with $\lambda = 2.5$ or $T_1 = 9.95$°C. The stable layer occupies about one-third of the cavity. There is virtually no difference between the two cases. The reason for this insensibility to the upper boundary conditions is that the real boundary of the vigorous cellular motion lies within the fluid at the bottom of the stable layer. The motion near the upper boundary is virtually zero, provided that the stable layer is sufficiently thick so that the motion will be damped out as it propagates from the bottom to the top of the cavity.

The curvature has a strong effect on the flows at low rotation rate. Fig. 6 compares two computations for $Q16$: the upper diagrams for $r_2/r_1 = 5/4$, and the lower diagram for $r_1 \rightarrow \infty$. The effect of curvature is almost imperceptible. Fig. 7 shows, on the other hand, a great deal of change due to elimination of curvature for $Q10$: three cells have been reduced to two cells as the curvature effect is removed. The two cells are symmetric about the centre line. The difference in the rotation rate between $Q16$ and $Q10$ is about two orders of magnitude (see Table 1).

4 **Comparison with Previous Works.** It is not appropriate to compare the details of the present work with the previous works mentioned above, because they do not include the constraint of rotation; nevertheless, there are similar features. Townsend's measurement for the mean temperature in the unstable layer is ~3.2°, corresponding to a normalized temperature ~−0.20. In our computations, the mean temperatures range from −0.20 to −0.30. There is a tendency for the mean normalized temperature to decrease from zero (corresponding to 3.98°C) with (*a*) increasing rotation when the upper temperature is held constant, and with (*b*) increasing upper temperature when the rotation is kept constant. Both (*a*) and (*b*) would result in the compression of cell heights as pointed out above, and reduce meridional motion (cells are less vigorous). This may permit diffusion to play a relatively strong role and bring the mean temperature closer to that at the lower boundary.

The temperature inversions observed by Townsend are also present in the present system. These inversions correspond to the mushroom-shaped isotherms as shown in the contour diagrams. It is obvious that inversion is more pronounced for cases with weak rotation or small λ. Mushroom-shaped isotherms are associated with strong advection.

Musman's computations show a number of closed isotherms which are dynamically impossible in a steady state unless there is a heat source or heat sink in the body of fluid. Similar residual effect also appeared in Poot's [7] computation of convection in a slot. Musman used the mean field approximation. He considered one wave number ratio at a time. Poot used a truncated series expansion for the solution. In both cases the closed isotherms perhaps can be eliminated by including more terms in the expansion.

Consideration of Damping in the Stable Layer

It suffices to note from Fig. 8 that damping of the motion in the stable layer is extremely strong. Townsend considered the damping of a spectrum of internal waves in an inviscid fluid generated at the bottom of the stable layer due to penetration of the convective cells.

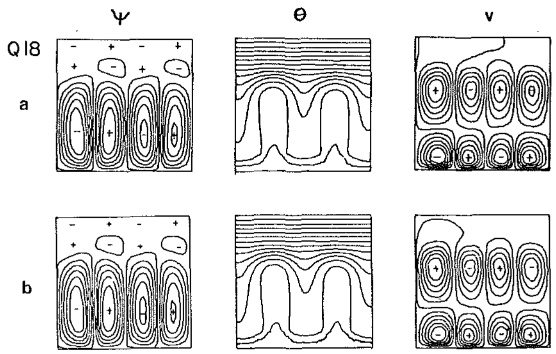

Fig. 5 Upper boundary conditions have no appreciable effect for *Q*18. (a) upper boundary free, (b) upper boundary rigid, while all other parameters held constant

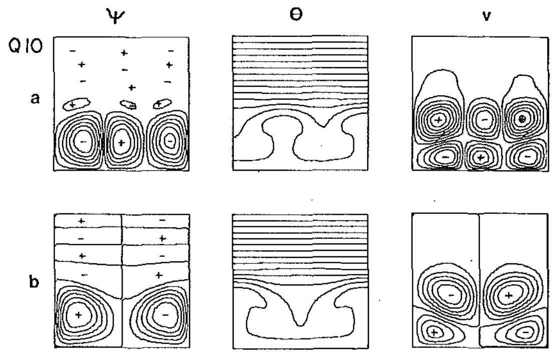

Fig. 7 Elimination of curvature has not only symmetricized the fields of *Q*10 but also changes the cell number from 3 to 2. (a) $(r_2 - r_1)/r_1 = 1/4$; (b) $(r_2 - r_1)/r_1 \to 0$.

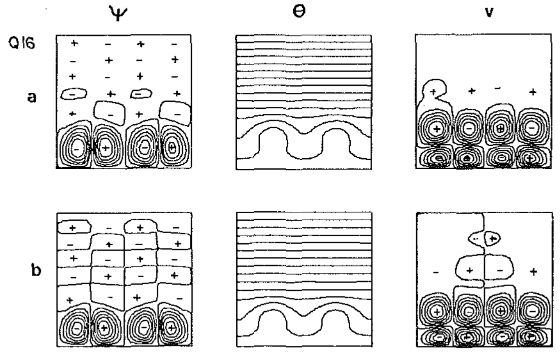

Fig. 6 Elimination of curvature has little effect on *Q*16, except to symmetricize the fields (a) $(r_2 - r_1)/r_1 = 1/4$; (b) $(r_2 - r_1)/r_1 \to 0$. Note this case has relatively high rotation rate.

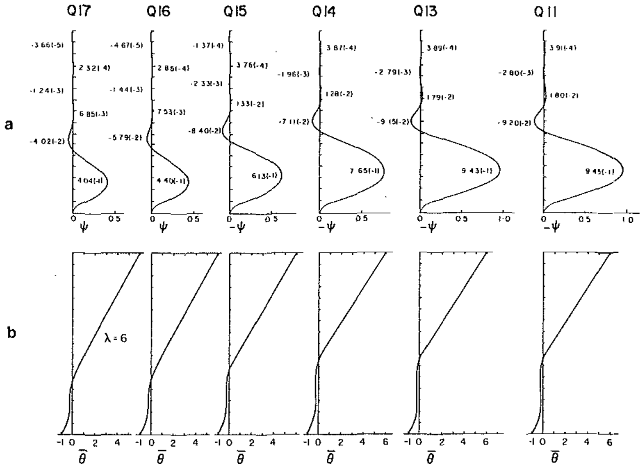

Fig. 8 (a) The *z*-dependence of the right-most ψ cells of cases along line A in Fig. 2. All stream functions have been normalized. Multiply the values of ψ by 0.225 $cm^3 s^{-1}$ to obtain absolute values of the Stokes' stream function. (b) The horizontally averaged temperature

He obtained airy wave solutions which are not sufficiently damped at low frequency. For the present problem, one should take viscosity, diffusivity and rotation into consideration. The problem can then be solved as an eigenvalue problem. However, the complication does not warrant the effort here.

Conclusion

Two-dimensional computations have shown that both the rotation and the imposed upper temperature tend to compress the scale of the convective cells, and that the upper dynamical boundary conditions do not affect the flow to any appreciable extent when the imposed upper temperature is sufficiently high. However, suppressing the dependence on the third dimension in the computation may have oversimplified the motion. It would be interesting to perform a laboratory experiment to see whether or not two-dimensional motion can exist, and if they do, to see whether or not the cell numbers can vacillate under appropriate conditions as discussed by Quon [9].

References

1 Chandrasekhar, S., *Hydrodynamic and Hydromagnetic Stability*, Oxford University Press, 1961.

2 Daniels, P. G., *Geophysical Fluid Dynamics*, Vol. 7, 1976, p. 297.

3 Daniels, P. G., and Stewartson, K., *Mathematical Proceedings of the Cambridge Philosophical Society*, Vol. 81, 1977, p. 325.

4 Faller, A. J., and Kaylor, R., *Journal of Geophysical Research*, Vol. 75, 1970, p. 521.

5 Moore, D. R., and Weiss, N. O., *Journal of Fluid Mechanics*, Vol. 61, 1973, p. 553.

6 Musman, S., *Journal of Fluid Mechanics*, Vol. 31, 1968, p. 343.

7 Poots, G., *Quarterly Journal of Applied Mathematics*, Vol. 11, 1958, p. 157.

8 Quon, C., *Journal of Computational Physics*, Vol. 22, 1976, p. 459.

9 Quon, C., "Finite Amplitude Instability and Penetrative Convection in a Rotating Fluid," ASME Paper 78-HT-39, 1978.

10 Townsend, A. A., *Quarterly Journal of the Royal Meteorological Society*, Vol. 90, 1964, p. 248.

11 Veronis, G., *Astrophysical Journal*, Vol. 137, 1963, p. 641.

Y. Katto
M. Shimizu

Department of Mechanical Engineering,
University of Tokyo,
Hongo, Bunkyo-Ku,
Tokyo, Japan

Upper Limit of CHF in the Saturated Forced Convection Boiling on a Heated Disk with a Small Impinging Jet

Critical heat flux (CHF) in the forced convection boiling on an open heated disk being supplied with saturated liquids through a small high-speed jet impinging at the center of disk is studied experimentally employing Refrigerant 12 at comparatively high pressures from 6.0 to 27.9 bars as well as water and Refrigerant 113 at atmospheric pressure. Generalized correlations of CHF are obtained for two characteristic regimes: V-regime where CHF is variable and I-regime where CHF is invariable for the change of jet velocity. Then, the boundaries of each regime are discussed clarifying the aspects for the lower limit of jet velocity capable of generating I-regime as well as the upper limit of CHF.

Introduction

Boiling on an open heated surface being supplied with a liquid by means of a small round or a thin plane high-speed jet may be regarded as one of the simplest systems associated with the forced convection boiling. Studies of critical heat flux (CHF) in such simple systems are important not only for industrial applications but also for obtaining basic information which may be useful in clarifying the mechanism of CHF in forced convection boiling.

Recently, Monde and Katto [1], employing water and Refrigerant 113 at atmospheric pressure, performed an experimental study for CHF in forced convection boiling on open heated disks (both upward- and downward-facing) supplied with liquid through a round jet of very small d/D impinging perpendicularly at the center of the heated disk, and the following correlation was obtained:

$$q_c = q_{co}\left\{1 + 2.7\left(\frac{\rho_\ell}{\rho_v}\right)^{0.5}\left(\frac{\Delta H_i}{H_{fg}}\right)^2\right\} \tag{1}$$

where q_{co}, critical heat flux for $\Delta H_i = 0$, was given by

$$\frac{q_{co}}{\rho_v H_{fg} u} = 0.0745\left(\frac{\rho_\ell}{\rho_v}\right)^{0.725}\left(\frac{\sigma}{\rho_\ell u^2 D}\right)^{1/3} \tag{2}$$

where u is the velocity of liquid jet measured at the exit of the nozzle. Then, CHF in another type of boiling system, where a thin plane jet supplied saturated liquid to just upstream of an edge of rectangular heated surface (downward-facing only), was investigated by Katto and Ishii [2], and their data obtained for water, R-113 and trichloroethane at atmospheric pressure were correlated by

$$\frac{q_{co}}{\rho_v H_{fg} u} = 0.0164\left(\frac{\rho_\ell}{\rho_v}\right)^{0.867}\left(\frac{\sigma}{\rho_\ell u^2 \ell}\right)^{1/3} \tag{3}$$

where ℓ is the length of heated surface in direction of flow. In Chapter 5 of [2], a comparison was made between equations (2) and (3) by replacing D in equation (2) by 2ℓ, because ℓ can be regarded as the maximum flow length measured from the location of incidence of liquid jet; and it indicates that $q_{co}/\rho_v H_{fg} u$ of equation (2) is not so different quantitatively from that of equation (3) within the experimental range. Then, it may be presumed that the difference in the exponent of ρ_ℓ/ρ_v between equations (2) and (3) is attributable to the different type of flow on the heated surface: that is, the radial flow in the former and the parallel flow in the latter.

It is interesting that the experimental data of CHF in the forced convection boiling systems mentioned above can be correlated by equations of simple form such as equations (2) and (3); and in justification of the form of these equations, a discussion based on dimensional analysis has been given in Sections 5.2 and 5.3 of [1]. Also, with respect to the common appearance of $(\sigma/\rho_\ell u^2 D)^{1/3}$ in equations (2) and (3), an explanation based on both hydrodynamic instability theory and vectorial dimensional analysis has been given in Chapter 2 of [14]. However, there is still a problem that equations (2) and (3) imply that q_{co} can increase boundlessly as the velocity of the liquid jet u is raised. Previous studies of boiling suggest that their dependence is unlikely to persist for all u, and therefore it is necessary to determine the upper limit for CHF in the forced convection boiling on open heated surface with a liquid jet, and also to examine the applicability of equations (2) and (3) at different pressures from atmospheric pressure.

In the present paper, CHF in the forced convection boiling of saturated R-12 at the comparatively high pressures of 6.0 to 27.9 bars is studied on a downward-facing heated disk surface of diameter $D = 0.01$ m with a small round impinging jet of diameter $d = 0.002$ m. The jet velocity u cannot exceed 20 m/s in the experiment due to the limit of experimental apparatus employed, but the surface tension of R-12 is smaller than those of water and R-113, and besides, it decreases as the pressure rises, so that the experimental range of $\sigma/\rho_\ell u^2 D$ is extended to much smaller value of $\sigma/\rho_\ell u^2 D$ with the same effect as that of increasing u. Furthermore, experiments of CHF of saturated water and R-113 at the atmospheric pressure are also made to test the reliability of the experimental apparatus in the present

---

Contributed by the Heat Transfer Division for publication in the JOURNAL OF HEAT TRANSFER. Manuscript received by the Heat Transfer Division May 30, 1978.

study as well as to extend the experimental range of ρ_ℓ/ρ_v.

Experimental Apparatus and Measuring Method of CHF

The experimental apparatus is shown schematically in Fig. 1. At the top of a pressure vessel (1) (the details of which are shown in Fig. 2) a copper block (2) is set up with eleven plate-type heaters in the upper conical part, to which electric power is supplied from an a-c transformer (3). The flat, end surface of the lower cylindrical part of the copper block provides a downward-facing heated circular surface of diameter D = 0.01 m. The circumferential surface of this cylindrical part is insulated with a ceramic sleeve, and the clearance between the cylindrical part and the insulator is filled with a plastic packing to prevent the contact between Refrigerant vapor and the very high temperature, inner region of the copper block, then avoiding thermal decomposition of the Refrigerant. The test liquid, which is pressurized by a peripheral pump (8) and then adjusted with the nozzle-heater (5) up to the saturation temperature corresponding to the internal pressure of the vessel, flows out of a nozzle (10) of inner diameter d = 0.002 m, impinging at the center of the heated disk. The velocity of the liquid jet at nozzle exit u can be determined by measuring the pressure difference between the inlet and the outlet of nozzle by means of a differential pressure transducer (14). The lower half of the inside of the pressure vessel is filled with the test liquid (about 0.4 to 0.5 m deep), which is heated by a vessel-heater (4), while the vapor above the liquid is condensed by a pair of cooling coils (7). The prescribed saturation pressure inside the vessel is maintained by controlling the vessel-heater as well as the cooling coils.

The heat flux across the heated disk as well as the temperature of heated surface is determined by means of three Chromel-Alumel thermocouples set up at regular intervals along the axis of the cylindrical part of copper block. The actual thermal conductivity of the copper block employed, indispensable to an accurate estimate of the heat flux, has been carefully determined in the preliminary experiment in the same way as that of [1, 2].

Critical heat flux is determined by the following means. Increasing the input to heaters in the copper block stepwisely with each increment less than five percent of the preceding heat flux, it finally arrives at the state in which the heated surface temperature cannot have a steady state rising very rapidly, when CHF is determined with an error within five percent. The flow state at the onset of CHF cannot be observed in the present study due to the employment of the pressure vessel, but it has been revealed in the preceding study [1] that once CHF takes place, the dryout occurs at the outer edge of the heated disk to extend toward the central impinging zone.

Experimental Data and Correlation of CHF

Experimental Result of CHF. Fig. 3 represents the experimental variation of CHF for R-12 with the jet velocity u, obtained at pressures p = 6.00, 11.6, 17.7, 23.5 and 27.9 bars respectively. It can be seen in Fig. 3 that at the lowest pressure, q_{co} increases with u over nearly the entire experimental range of u. As pressure rises, however, the region in which q_{co} is independent of u extends gradually from the high velocity region toward the low velocity region. In other words, two characteristic regimes can be distinguished for CHF in Fig. 3: one regime of variable q_{co} and the other regime of invariant q_{co}. In this paper, the former regime will be called V-regime, and the latter will be called I-regime for simplicity.

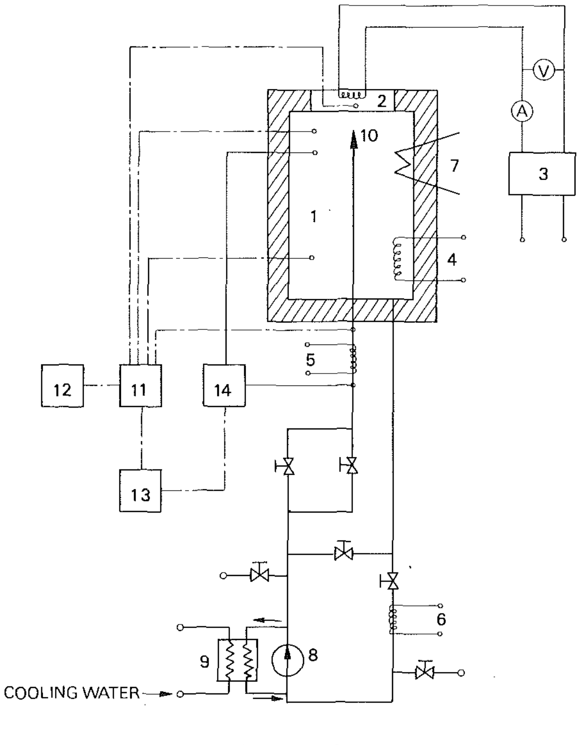

Fig. 1 System of experimental apparatus

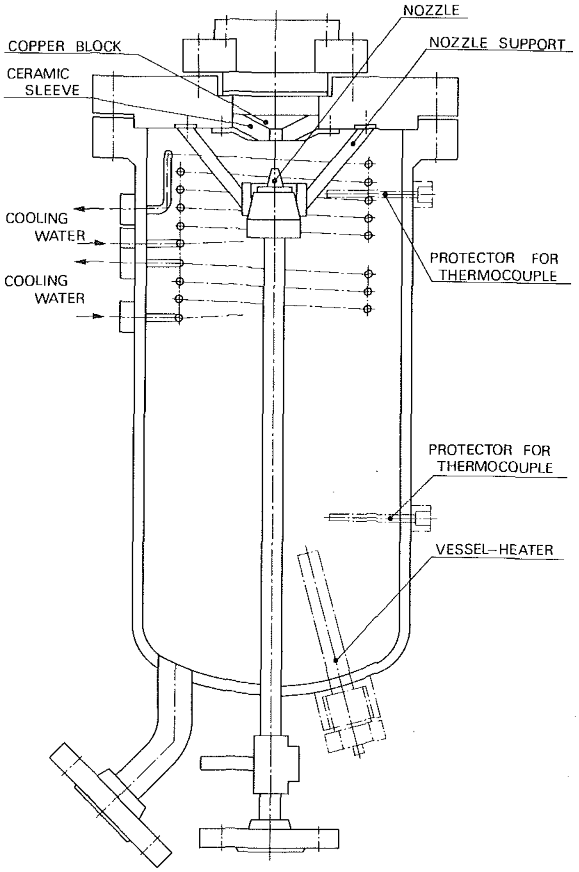

Fig. 2 Pressure vessel

Nomenclature

d = inner diameter of nozzle
D = diameter of heated disk
H_{fg} = latent heat of evaporation
ΔH_i = inlet subcooling enthalpy of liquid
p = absolute pressure
q_c = critical heat flux
$q_{co} = q_c$ for $\Delta H_i = 0$
$q_{co,\max}$ = upper limit of q_{co}
u = velocity of liquid jet at nozzle exit
$u_{\min}$ = lower limit of u capable of generating $q_{co,\max}$
ρ_ℓ = density of liquid
ρ_v = density of vapor
σ = surface tension

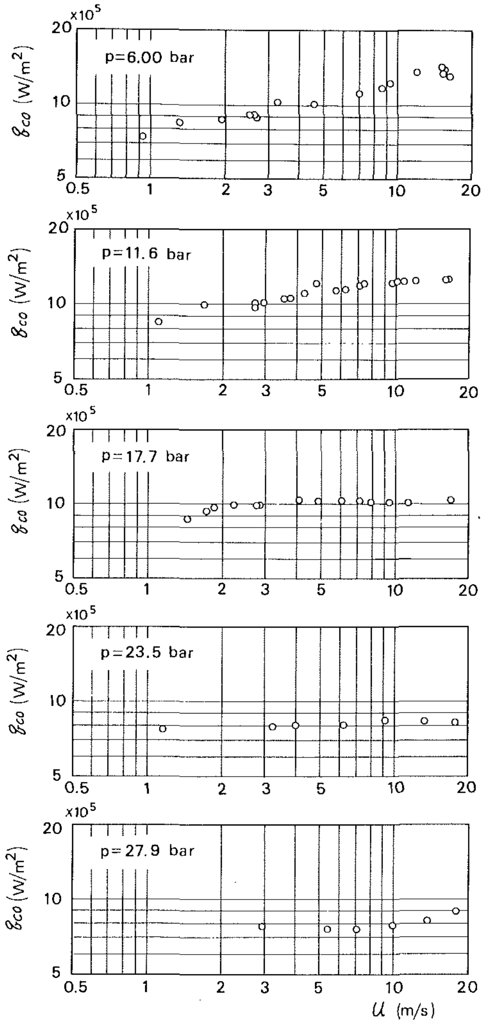

Fig. 3 Relation between CHF and jet velocity obtained for R-12

Analysis of CHF Data in *V*-regime. The relation between $(q_{co}/\rho_v H_{fg} u)/(\sigma/\rho_\ell u^2 D)^{1/3}$ and (ρ_ℓ/ρ_v) suggested by equation (2) for the experimental data classified to be in the V-regime is examined in the right side of Fig. 4. It may be noted in Fig. 4 that the V-regime data scatter to some extent, but the data of R-12 at pressures from 6.0 to 17.7 bars together with the data of water and R-113 at atmospheric pressure can be correlated by the higher solid line, yielding the following correlation equation:

$$\frac{q_{co}}{\rho_v H_{fg} u} = 0.188 \left(\frac{\rho_\ell}{\rho_v}\right)^{0.614} \left(\frac{\sigma}{\rho_\ell u^2 D}\right)^{1/3} \tag{4}$$

Among the V-regime data in Fig. 4, the R-12 data at $p = 17.7$ bars show a somewhat greater deviation from equation (4) than other data, but it should be noted that these data are situated within a limited range near the border with I-regime as seen in Fig. 3.

Equation (2) obtained in the experiment of [1] for water and R-113 at atmospheric pressure is also illustrated by the broken line in Fig. 4, and it is noted that the prediction of equation (2) agrees approximately with the present data for water, but falls a little lower than the present data for R-113. Recently, Monde, Kusuda and Uehara [3] carried out experiments for CHF of water and R-113 at atmospheric pressure for the boiling system with plural impinging jets on a heated disk of diameter $D = 0.0252$ m, giving a correlation equation of their experimental data, and if this correlation equation is reduced to the case of a single jet, it yields

$$\frac{q_{co}}{\rho_v H_{fg} u} = 0.170 \left(\frac{\rho_\ell}{\rho_v}\right)^{0.608} \left(\frac{\sigma}{\rho_\ell u^2 D}\right)^{1/3} \tag{5}$$

Equation (5) is illustrated by the chain line in Fig. 4, showing better agreement with the present result.

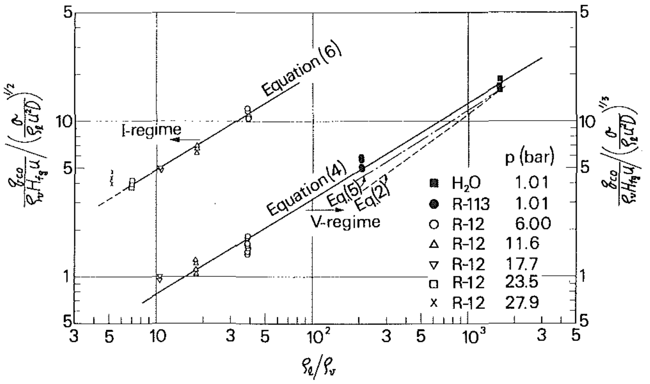

Fig. 4 Nondimensional correlations of CHF in *V* and *I*-regime

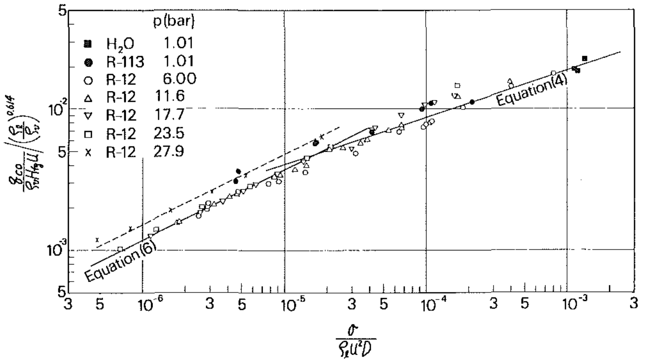

Fig. 5 Comparison of correlation equations (4) and (6) with experimental data

Analysis of CHF Data in *I*-regime. Regarding the experimental data for q_{co} classified to be in I-regime where q_{co} is regarded as independent of u, it may not be useless to test the correlation of data employing $(q_{co}/\rho_v H_{fg} u)/(\sigma/\rho_\ell u^2 D)^{1/2}$ and (ρ_ℓ/ρ_v), because $(q_{co}/\rho_v H_{fg} u)/(\sigma/\rho_\ell u^2 D)^{1/2}$ appears to be a dimensionless group which is substantially independent of u; and fortunately it gives acceptable results such as shown in the left side of Fig. 4. It is noted in Fig. 4 that all the I-regime data for R-12 except those at the highest pressure $p = 27.9$ bars can be correlated by the upper solid line, to give the following equation:

$$\frac{q_{co}}{\rho_v H_{fg} u} = 1.18 \left(\frac{\rho_\ell}{\rho_v}\right)^{0.614} \left(\frac{\sigma}{\rho_\ell u^2 D}\right)^{1/2} \tag{6}$$

The problem of discrepancy of data at $p = 27.9$ bars will be discussed later relating to characteristic regimes.

Consolidation of Equations (4) and (6). It is of interest to note that generalized correlation equations (4) and (6) derived for V and I-regime respectively take a common value for the exponent of ρ_ℓ/ρ_v, and owing to such circumstances, Fig. 5 can be presented, showing another type of comparison between all the experimental data obtained in the present study and the correlation equations (4) and (6). The aspect of transition between V and I-regime can be seen in Fig. 5. As for the data for R-113, however, somewhat dubious features are observed; the reason for this is unknown, leaving a problem to be solved in the future. At the present stage, therefore, it should be understood that the accuracy of the proposed equations (4) and (6) has a tolerance such as indicated by the experimental data in Fig. 5 at least. On the other hand, the singular data for R-12 at $p = 27.9$ bars are discriminated, in Fig. 5, from other data by the broken line, which is parallel to the line of equation (6) yielding the following relation:

$$\frac{q_{co}}{\rho_v H_{fg} u} \propto \left(\frac{\sigma}{\rho_\ell u^2 D}\right)^{1/2} \tag{7}$$

so that q_{co} is independent of u for these singular data too.

Boundaries of Characteristic Regimes

Boundary between *D*-regime and *V*-regime. As has been observed in the experiment by [4] and discussed briefly in the appendix of [2], there is a simple kind of CHF which takes place only due to the deficiency of liquid supply as compared with the heat load. If it can be assumed for simplicity that all the liquid supplied is vaporized because the fraction of liquid splashing away from the heated surface is so small, and that the jet velocity is high enough to neglect the effects of surface tension and gravity, the critical heat flux q_{co} in this case is related to the liquid supply via the heat balance as follows:

$$\frac{q_{co}}{\rho_v H_{fg} u} = \frac{\rho_\ell}{\rho_v}\left(\frac{d}{D}\right)^2 \tag{8}$$

where d is the diameter of nozzle supplying liquid. The regime responsible to this type of CHF will be called D-regime in this paper, because it is concerned with CHF due to the dryout of heated surface. In many cases, D-regime is situated in the range of low jet velocities.

The boundary between D and V-regime, where q_{co} is presumably continuous, may be determined by eliminating q_{co} from equations (4) and (8) as,

$$\frac{\sigma}{\rho_\ell u^2 D} = 150\left(\frac{\rho_\ell}{\rho_v}\right)^{1.16}\left(\frac{d}{D}\right)^6 \tag{9}$$

In the experiments of the present study, $d/D = 1/5$, and the minimum density ratio is $\rho_\ell/\rho_v = 5.20$ for R-12 at $p = 27.9$ bars, so that equation (9) gives the following possible minimum value of $\sigma/\rho_\ell u^2 D$ for D-regime:

$$\frac{\sigma}{\rho_\ell u^2 D} = 6.50 \times 10^{-2}$$

Since this value is much higher than those value of $\sigma/\rho_\ell u^2 D$ experienced in the present study as shown in abscissa of Fig. 5, it is concluded that the present study has no relation to D-regime.

Boundary between V-regime and I-regime. As in the preceding section, the boundary between V and I-regime is determined by eliminating q_{co} from equations (4) and (6) to give

$$\frac{\sigma}{\rho_\ell u^2 D} = 1.64 \times 10^{-5} \tag{10}$$

Of course, equation (10) corresponds exactly to the value of $\sigma/\rho_\ell u^2 D$ at which two solid lines intersect in Fig. 5.

Possibility of the Fourth Regime. As mentioned before, the R-12 data at $p = 27.9$ bars deviate from the prediction of equation (6), and this fact suggests the possibility of a fourth regime existing at very high pressures. Such a characteristic regime at high pressures is known to exist in forced convection boiling in round tubes and will be discussed in the next chapter. At present, it is recommended that a restriction be placed on the pressure range where equation (6) is applicable as follows:

$$\rho_\ell/\rho_v > 6.0 \tag{11}$$

In case of water, for instance, inequality (11) of the density ratio corresponds to the pressure range: $p < 152$ bars, or $p/p_c < 0.69$ where p_c is the critical pressure.

Upper Limit of CHF

Equation (6) has been so far expressed in the form including the jet velocity u, but u has in fact no effects on q_{co} in I-regime. Therefore, it is preferable that the q_{co}, namely the upper limit of q_{co} be denoted by $q_{co,\max}$, and equation (6) be rewritten as:

$$\frac{q_{co,\max}}{\rho_v H_{fg}\sqrt{\sigma/(\rho_\ell D)}} = 1.18\left(\frac{\rho_\ell}{\rho_v}\right)^{0.614} \tag{12}$$

Also, the lower limit of the jet velocity u capable of generating $q_{co,\max}$ is denoted by $u_{\min}$, when equation (10) gives the following indication for $u_{\min}$:

$$\frac{\sigma}{\rho_\ell u_{\min}^2 D} = 1.64 \times 10^{-5} \tag{13}$$

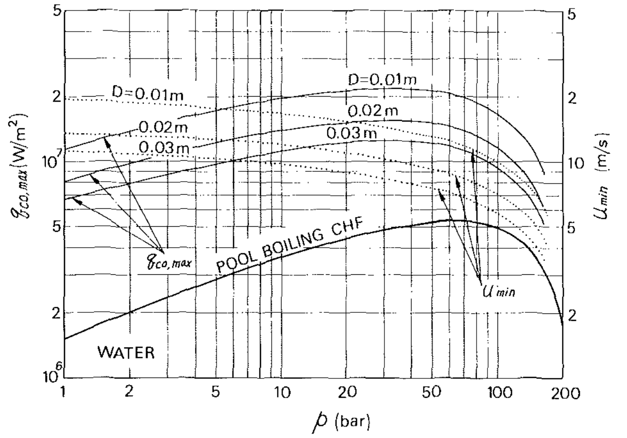

Fig. 6 Upper limit of q_{co} and corresponding lower limit of u for water boiling on heated disks

Pressure variation of $q_{co,\max}$ and $u_{\min}$, which is predicted by equation (12) and (13), is shown in Fig. 6 for the case of water boiling on heated disks of diameter $D = 0.01, 0.02$ and 0.03 m. Fig. 6 also shows critical heat flux q_{co} in saturated pool boiling at the standard gravitational acceleration, which is predicted by Zuber correlation modified by Rohsenow [5]:

$$\frac{q_{co}}{\rho_v H_{fg}} = 0.18\left[\frac{\sigma g(\rho_\ell - \rho_v)}{\rho_v^2}\right]^{1/4}\left[\frac{1}{1 + (\rho_v/\rho_\ell)}\right]^{1/2} \tag{14}$$

where g is the gravitational acceleration. It may be of interest to note in Fig. 6 that the prediction of equation (12) for $q_{co,\max}$ versus p and that of equation (14) for q_{co} versus p are somewhat similar in character.

Discussion. With respect to the result mentioned above, it may be useful to note the following remarks: Examining CHF in forced convection boiling in vertical uniformly heated round tubes for instance, it is found that there are many data showing CHF saturation trend accompanying the increase of mass velocity, particularly in case of $\Delta H_i = 0$ (cf. Fig. 2(a) of Thompson, et al. [6], Figs. 17–20 of Stevens, et al. [7], Fig. 6–11 of Becker, et al. [8], and Collier [9], Hewitt [10], and Lee [11]). For such a state of CHF, and presumably for CHF in I-regime in the present study too, it may be presumed that, owing to high mass velocity of liquid, the vapor generated on the heated surface is captured by the liquid flow, and CHF takes place due to near wall bulk crowding and vapor blanketing.

In addition, it is well known that when the system pressure is highly elevated in the forced convection boiling in round tubes, characteristics of CHF change to quite different ones from those at low pressures (cf. Becker, et al. [12], Campolunghi, et al. [13], and Katto [14]).

Of course, simple comparison should not be made on CHF between the forced convection boiling on heated disks with only one dimension of radial length and the much more complicated convection boiling in heated round tubes with two dimensions of axial length and inner diameter. However, it may be of use as well as of interest to notice that there are many common characters between the two boiling systems in elemental aspects of CHF.

Conclusions

1 CHF in the forced convection boiling on an open heated disk surface supplied with saturated liquids at various pressures through a small impinging jet has been studied, yielding equations (4) and (6) for the generalized correlation of CHF in V-regime and I-regime, and equations (9), (10) and (11) to predict the boundaries of D, V and I-regime. At present, equations (4) and (6) should to be used with attention to a tolerance of accuracy as indicated by the experimental results, including equations (2) and (5) in Figs. 4 and 5.

2 For the prediction of upper limit of CHF as well as the lower limit of the jet velocity capable of generating the upper limit of CHF, equations (12) and (13) are presented.

3 The possibility is suggested that a fourth regime other than the D, V and I-regimes may exist at elevated pressures.

Acknowledgment

The financial support specially provided by the Ministry of Education, Science and Culture to this study is gratefully acknowledged. The authors also express their appreciation to Messrs. M. Neki and S. Yano for their valuable assistance with the experiments.

References

1 Monde, M. and Katto, Y., "Burnout in a High Heat-Flux Boiling System with an Impinging Jet," *International Journal of Heat and Mass Transfer*, Vol. 21, 1978, pp. 295–305.

2 Katto, Y. and Ishii, K., "Burnout in a High Heat Flux Boiling System with a Forced Supply of Liquid through a Plane Jet," Sixth International Heat Transfer Conference, Toronto, Vol. 1, 1978, pp. 435–440.

3 Monde, M., Kusuda, H. and Uehara, H., "Burnout in a High Heat-Flux Boiling System with Impinging Jets," *Proceedings of the Fifteenth Japan National Symposium of Heat Transfer*, 1978, pp. 157–159.

4 Katto, Y. and Kunihiro, M., "Study of the Mechanism of Burn-Out in Boiling System of High Burn-Out Heat Flux," *Bulletin JSME*, Vol. 16, 1973, pp. 1357–1366.

5 Rohsenow, W. M. and Hartnett, J. P. (editors), *Handbook of Heat Transfer*, Section 13, McGraw-Hill, 1973, p. 32.

6 Thompson, B. and Macbeth, R. V., "Boiling Water Heat Transfer Burnout in Uniformly Heated Round Tubes: A Compilation of World Data with Accurate Correlations," United Kingdom Atomic Energy Authority, AEEW-R 356, 1964.

7 Stevens, G. F., Elliott, D. F. and Wood, R. W., "An Experimental Investigation into Forced Convection Burn-Out in Freon, with Reference to Burn-Out in Water, Uniformly Heated Round Tubes with Vertical Up-Flow," United Kingdom Atomic Energy Authority, AEEW-R 321, 1964.

8 Becker, K. M. Bager, J. and Djursing, D., "Burnout Correlation in Simple Geometries: Most Recent Assessments," Seminar on Two-Phase Flow Thermohydraulics, Rome, 1972, pp. 51–91.

9 Collier, J. G., *Convective Boiling and Condensation*, McGraw-Hill, 1972, p. 251.

10 Hewitt, G. F., *Mechanism and Prediction of Burnout, in Two-Phase Flows and Heat Transfer*, II, Hemisphere Pub. Corp., 1976, p. 722.

11 Lee, D. H., *Prediction of Burnout, in Two-Phase Flow and Heat Transfer*, Oxford Univ. Press, 1977, p. 297.

12 Becker, K. M., Djursing, D., Lindberg, K., Eklind, O. and Österdahl, C., "Burnout Conditions for Round Tubes at Elevated Pressures," *Progress in Heat and Mass Transfer*, Vol. 6, Pergamon Press, 1972, pp. 55–73.

13 Campolunghi, F., Cumo, M., Ferrari, G., Leo, R and Vaccaro, G., "Burn-Out Power in Once-Through Tubular System Generators," *Proceedings of Fifth International Heat Transfer Conference*, Vol. IV, 1974, pp. 280–284.

14 Katto, Y., "A Generalized Correlation of Critical Heat Flux for the Forced Convection Boiling in Vertical Uniformly Heated Round Tubes," *International Journal of Heat and Mass Transfer*, to be published in the near future.

D. M. France
R. D. Carlson
T. Chiang
R. Priemer

Argonne National Laboratory,
Components Technology Division,
Argonne, Il. 60439

Characteristics of Transition Boiling in Sodium-Heated Steam Generator Tubes

Thermal fluctuations were measured in the tube wall in the transition boiling zone of a full-scale LMFBR sodium-heated steam generator tube. The tube had an inside diameter = 10 mm, wall thickness = 2.90 mm, heated length = 13.1 m, and material = $2^1/_4$ Cr-1 Mo steel. Water flowed vertically upwards inside the straight tube, and sodium flowed counter-currently in a surrounding annulus. Results of thermal, spectral, and thermal stress analyses are presented for a test within the normal operating range of LMFBR steam generators. Results of other tests are presented that show the effects and sensitivity of sodium temperature and water pressure on the severity of the thermal fluctuations.

Introduction

The critical heat flux (CHF) phenomenon in flow boiling has been the subject of major engineering study for many years and has included a variety of applications. The majority of the more recent investigations has been directed towards the prediction of the occurrence of CHF in water-cooled nuclear reactor cores where CHF is avoided under normal operating conditions. There is also no transition boiling zone under normal operating conditions, and, as a result, it was unnecessary to study many aspects of transition boiling in detail. Thus, little information is available in the engineering literature on this subject. In contrast to water reactor cases, many sodium heated steam generators designed worldwide for use in liquid metal fast breeder reactor (LMFBR) electric power plants operate with CHF and transition boiling in the water tubes under all or partial load ranges. For this LMFBR application, thermal-hydraulic details of the transition boiling zone represent important design inputs. The major thermal-hydraulic design problem associated with the transition boiling zone is related to the characteristics of thermal fluctuations induced in the water tube walls. Since transition boiling and the associated thermal fluctuations may occur under all or most operating conditions, the potential for high cycle fatigue due to thermal stress is an important consideration in determining the lifetime of the water tubes. The purpose of this investigation was to experimentally determine the characteristics of transition boiling and the associated thermal fluctuations required for sodium-heated steam generator design.

Direct application of experimentally measured thermal fluctuations to sodium-heated steam generators requires a temperature controlled, rather than a heat flux controlled, experimental system. Electrical heating of an experimental water tube, for example, may lead to significantly different thermal fluctuations in the transition boiling zone as compared to fluctuations occurring when heating is accomplished via a hot fluid, like sodium. (The subject is discussed in some detail in [1], and very limited experimental results are available in [2–5].) It is anticipated on a qualitative basis that the thermal fluctuations will be less severe in a temperature controlled situation than in the heat flux controlled case [1]. However, the amplitude of the fluctuations may be large enough to limit the life of sodium-heated steam generator tubes. Frequency and other characteristics of transition boiling also contribute to this lifetime condition.

The experimental program established at Argonne National Laboratory (ANL) to obtain transition boiling information for direct application to LMFBR steam generators employed a sodium-heated, vertically mounted, straight, steam/water tube typical of full-scale LMFBR steam generator tubes. Tests were performed in the ANL Steam Generator Test Facility (SGTF). The facility is described, and the results of observations related to transition boiling zone characteristics are presented and discussed. Further experimental results are presented in detail from a test with parameters within the normal operating range of LMFBR steam generators. The effects of steam pressure and sodium temperature (heat flux) on the severity of thermal fluctuations in the tube wall were studied independently. The results of these studies are also presented.

Experimental Facility

The Steam Generator Test Facility (SGTF), described briefly in [6], employs sodium to boil water in the test section. The SGTF will accommodate test sections having vertical lengths in excess of 15 m. The closed sodium and water circuits are shown in Fig. 1. The electric power supply and electro-magnetic pump have maximum capacities of 1 MW and 0.0044 m^3/s at 650°C, respectively. The water circuit shown in Fig. 1 operates in the recirculation mode with saturated water/steam flowing vertically upwards from the test section to a separation tank (steam drum). Steam from the top of the drum is condensed in the condenser while the liquid from the bottom of the drum is subcooled in another heat exchanger (cooler). The water temperature at the test section inlet is controlled by heat rejection from the cooler and condenser. This dual heat exchanger (condenser and cooler) heat rejection system precluded the necessity for a high pressure water preheater. The condensate and water from the cooler

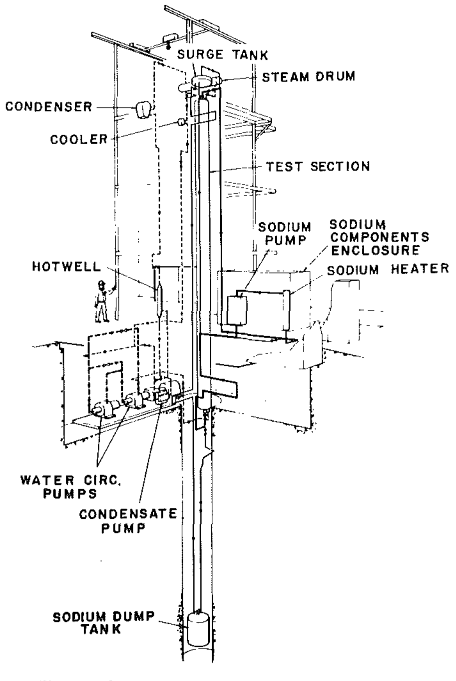

Fig. 1 Steam generator test facility (SGTF)

Contributed by the Heat Transfer Division for publication in the JOURNAL OF HEAT TRANSFER. Manuscript received by the Heat Transfer Division June 30, 1978.

are recombined before entering the canned rotor, high pressure, centrifugal pump circuit from which the flow enters the test section through a throttling valve. The water circuit has maximum pressure and flow of 16.5 MPa and 0.0082 m^3/s, respectively.

A somewhat unique aspect of the SGTF is the condenser/cooler arrangement with both components at full system pressure. In order to maintain fine system control with fast feedback, a high temperature synthetic oil is used as the heat rejection fluid in the condenser and cooler; the oil in turn rejects heat to a water cooling tower. The oil system, not shown in Fig. 1, utilizes pneumatically controlled valves to change load quickly by changing oil flow rather than temperature.

System instrumentation includes numerous thermocouples, pressure transducers, flowmeters, and automatic-feedback proportional gain controllers. The water flowmeters are of the turbine type while electro-magnetic flowmeters are used in the sodium circuit. All instruments used for data purposes have calibrations traceable to the National Bureau of Standards, and all of these instruments were systematically checked for continued accuracy at regularly scheduled intervals throughout the test series.

The chemical quality of the water in the SGTF was maintained at a level in the range typical of LMFBR steam generators. Calibrated meters were employed in a continuously operating mode during testing, and readings out of preset ranges automatically energized alarms. A volatile water treatment was utilized in the SGTF high pressure water circuit, and makeup water was demineralized and deoxygenated prior to introduction into the circuit. The following parameter ranges were maintained in the high pressure water circuit:

Dissolved oxygen	10 ppb maximum
pH	9 to 10
Hydrazine residual	10 to 50 ppb
Cation conductivity at 25°C	3 micro-mho/cm maximum

Test Section

The test section, shown in Fig. 2, consisted of a $2\frac{1}{4}$ Cr-1 Mo steel tube with an inside diameter of 10 mm and a wall thickness of 2.90 mm, in which water flowed vertically upward. Sodium flowed countercurrent in the annulus between the water tube and the 304 stainless steel sodium tube (31.5 mm ID). The tubes were held in concentricity by support spacers designed for minimum heat transfer between tubes and minimum flow perturbation. The heat transfer length between the centerlines of the sodium nozzles was 13.1 m.

102 shell thermocouples were spot welded axially along the outside of the sodium tube (shell) with a minimum spacing of 0.076 m. An additional eleven stainless steel sheathed thermocouples were embedded into the water tube wall. These internal thermocouples (tube thermocouples) were fed through the sodium annulus, held in place by provisions in the support spacers, and brazed into the tube wall from the sodium side with the junction approximately midway through the wall. The internal thermocouples were located at nominal increments of 1.52 m along the tube, and each junction was located independently at radii r_m with respect to the tube centerline. Isothermal tests provided calibration for internal and shell thermocouples as well as test section heat loss measurement.

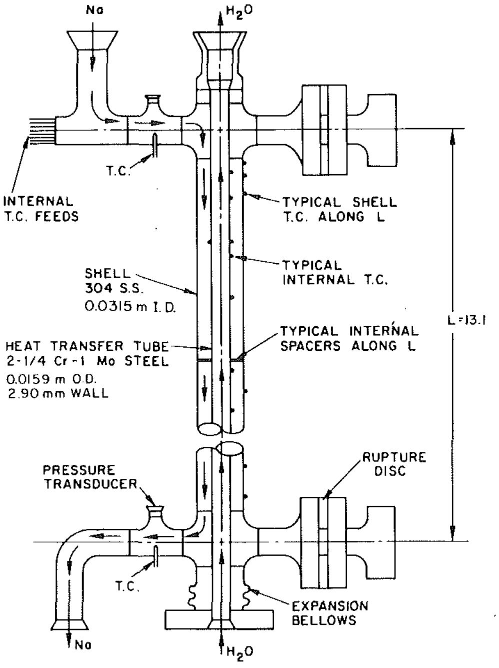

Fig. 2 SGTF test section

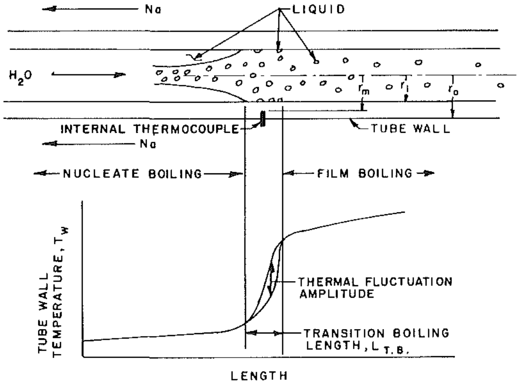

Fig. 3 Transition boiling in two-phase annular flow

Experimental Procedure and Transition Boiling Characterization

Five parameters completely specify a test in the SGTF. Tests were run by fixing four of the five parameters, namely sodium mass flowrate, water inlet temperature, water flowrate, and water pressure, and then adjusting the fifth parameter, sodium inlet temperature, until CHF was detected at a predetermined internal thermocouple located in the tube wall.

The pertinent two-phase flow regime for the tests was annular flow. The hydrodynamic structure is shown in Fig. 3. Upstream (with respect to the water flow) of transition boiling, a liquid film exists on the tube wall with entrained liquid droplets in the vapor core. The

Nomenclature

$A_k, B_k, C_k, D_k = k = 0, 1, 2 \ldots$ Fourier series coefficients, for use in equation (1), °C
f = frequency, Hz ($\omega = 2\pi f$)
f_0 = fundamental frequency, Hz
$L_{T.B.}$ = length of transition boiling zone, m
r = radial coordinate measured from centerline of water tube, m
S = stress, MPa
$S\ EQ\ ALT$ = equivalent alternating stress, MPa
T = temperature, °C
t = time, s
X_{CHF} = CHF quality
Y_1 = amplitude of inherent thermal fluctuations within transition boiling, °C
$Y_{1,max}$ = maximum amplitude of inherent thermal fluctuations within transition boiling, °C
Y_2 = amplitude of system induced thermal fluctuations due to transition boiling zone movement, °C
ΔZ = axial movement of transition boiling zone, m
ω = frequency, rad/s ($\omega = 2\pi f$)

Subscripts

a = alternating stress
B = sodium bulk
H_2O = water
i = tube inside radius
m = measurement point at internal thermocouple junction
mean = mean stress
Na = sodium
o = tube outside radius
w = water tube wall

excellent heat transfer and high heat fluxes in this region have given rise to the name nucleate boiling, by analogy to pool boiling terminology. Dryout of the liquid film yields a drastic reduction in heat flux, followed by a region of mist flow with relatively poor heat transfer and low heat flux, this region being termed film boiling, also by analogy to pool boiling. The maximum heat flux is the CHF by definition, and the transition boiling zone between nucleate and film boiling is shown in Fig. 3. Thermal fluctuations occurring in the tube wall as a consequence of the local unstable condition of the flow were detected in the SGTF test section by an internal thermocouple positioned as shown in Fig. 3. The amplitude of the fluctuations is also shown schematically in Fig. 3. Experimental data were recorded while the transition boiling zone was positioned over the internal thermocouple.

Details of the tube wall temperature within the transition boiling zone are depicted schematically in Fig. 4. These results are based on experimental observations. First, it should be noted that the amplitude of the thermal fluctuations in the tube wall varies along the length of the zone. Shown in Fig. 4(*a*) is this amplitude, Y_1, which is maximum near the center of the zone. A qualitative representation of amplitude versus length, based on experimental observations, is shown in Fig. 4(*b*). This figure agrees well with similar results reported in [3]. Results similar to Fig. 4(*b*) were experimentally obtained, and typical measurements of fluctuation amplitude are shown in Fig. 5. The amplitudes, measured by an internal thermocouple located 12.2 m downstream of the water inlet to the test section with the junction at r_m = 6.73 mm, are shown in Fig. 5 over the length of the transition boiling zone. The amplitudes are plotted against the mean temperatures of the fluctuations, and the results are consistent with Fig. 4(*b*). The test conditions corresponding to Fig. 5 were water pressure = 11.5 MPa, water mass flux = 2450 kg/m^2.s, sodium mass flowrate = 0.566 kg/s, CHF quality = 0.26, and heat flux = 1.00 MW/m^2. These conditions are within the range of normal operation of LMFBR steam generators. The maximum amplitude occurring in the transition boiling zone was usually found to be significantly less than the maximum potential amplitude, Y_2, representing the difference between the tube wall temperatures under nucleate and film boiling conditions, as shown in Fig. 4(*a*). However, for a given potential amplitude, Y_2, the value of $Y_{1,\max}$ was found to vary considerably as a function of test parameters. Various observations are shown schematically in Fig. 4(*a*).

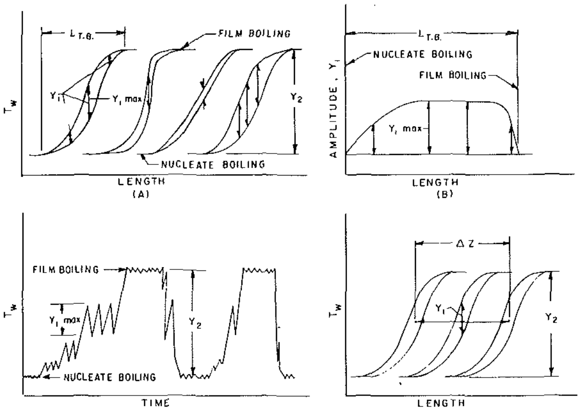

Fig. 4 Variations in transition boiling

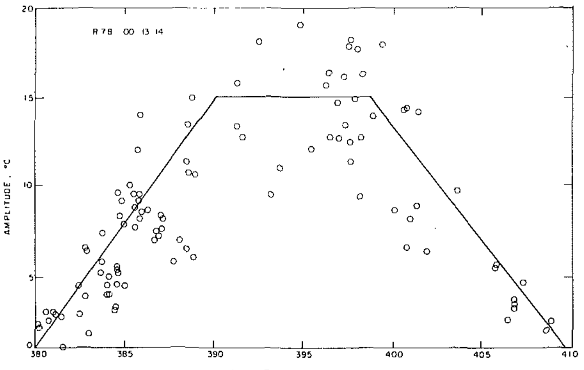

Fig. 5 Fluctuation amplitudes measured in transition boiling

The temperature at a given axial (and radial) point in the tube wall varies as a function of time. The plot shown in Fig. 4(*c*) is typical of the range of responses of an internal thermocouple during a single test. The maximum amplitude of the thermal fluctuations, $Y_{1,\max}$, is shown occurring when the point is well centered in the transition boiling zone. This maximum amplitude is generally observed over a portion of the length of the transition boiling zone, as shown in Figs. 4(*b*) and 5. When the transition boiling zone moves downstream (with respect to water flow) of the thermocouple, minimal amplitude is measured in the nucleate boiling zone. Similarly, minimal amplitude is recorded when the thermocouple is within the film boiling zone when transition boiling is upstream of the thermocouple. Axial movement of the transition boiling zone is a direct result of small changes in the system parameters of water pressure, fluid flowrates, or fluid inlet temperatures to the test section. These system parameters are controlled in the SGTF by electronic feedback controllers which have periods nominally of the order of 1 min. This movement of the transition boiling zone results in thermal fluctuations of amplitude Y_2 with a period of the order of 1 min. The amplitude, Y_2, is shown in Figs. 4(*a*), 4(*c*), and 4(*d*), and the length of movement of the zone is labeled ΔZ in Fig. 4(*d*). Thermal stress in the tube wall is produced by the relatively high frequency fluctuations with amplitude Y_1 that are inherent in transition boiling, plus the lower frequency fluctuations with larger amplitude Y_2, which are system induced. The frequency of the system induced fluctuations and the length of the transition boiling zone movement, ΔZ, are peculiar to each individual experimental system or power plant. These parameters were varied in the SGTF by altering the electronic controllers. The amplitude of the system fluctuation, Y_2, may be calculated from steady state heat transfer analysis, but little quantitative data are available concerning the inherent fluctuations in the transition boiling zone. In this investigation, the frequency and maximum amplitude, $Y_{1,\max}$, were determined for parameters in the range of normal LMFBR steam generator operation.

Accurate recording of the test section sensor outputs required a sampling time significantly faster than the period of the system oscillations. It was found that only the tube thermocouples were sensitive to the higher frequency, inherent oscillations of transition boiling, but the shell thermocouples did respond to the system induced fluctuations as observed in [7]. Thus, a computerized data acquisition system was employed to measure all 150 SGTF sensors used for data purposes. All sensors were read in a time period of 30 ms representing one data scan. Scans were taken at 0.5 s intervals, and some scans were stored on a disc file for future data reduction. Multiple scans were stored for each test, and simultaneous recordings were made, of the voltage from the internal thermocouple located in the transition boiling zone, on an analog FM tape recorder with a frequency response in the kHz range. The response of the internal thermocouple in its place in the tube wall was calculated to be satisfactory up to a frequency of approximately 8 Hz.

Thermal Fluctuation Results and Discussion

Nominal Test. A test was conducted in the SGTF with conditions within the normal operating range of LMFBR sodium heated steam generators. The system conditions for this test, R662, are given in Table 1. The transition boiling zone was adjacent to a tube thermocouple located 12.2 m downstream of the water inlet to the test section (close to the water exit). Water exiting the test section was saturated and had a quality of 0.26. The SGTF system controllers were refined to enable the transition boiling zone to be maintained over the thermocouple for a period of time long enough for the data to have statistical significance. This task was accomplished while maintaining a minimum controller period of 30 s, well above the period of the inherent fluctuations. Segments of temperature versus time recordings were obtained that were similar in form to the section marked $Y_{1,\max}$ in Fig. 4(*c*). A segment of the measurements for Test R662 is shown in Fig. 6.

Table 1 Test R662 parameters

Water	
Mass flux	= 2480 kg/m²·s
Pressure	= 12.9 MPa
Test section inlet temperature	= 293°C
Saturation temperature	= 330°C
Test section exit quality	= 0.26
Sodium	
Mass flowrate	= 0.59 kg/s
Test section inlet temperature	= 438°C
Test section outlet temperature	= 303°C
CHF	
Water side heat flux	= 0.81 MW/m²
Quality	= 0.19
Sodium bulk temperature	= 420°C
Sodium heat transfer coefficient	= 28.9 kW/m²·K

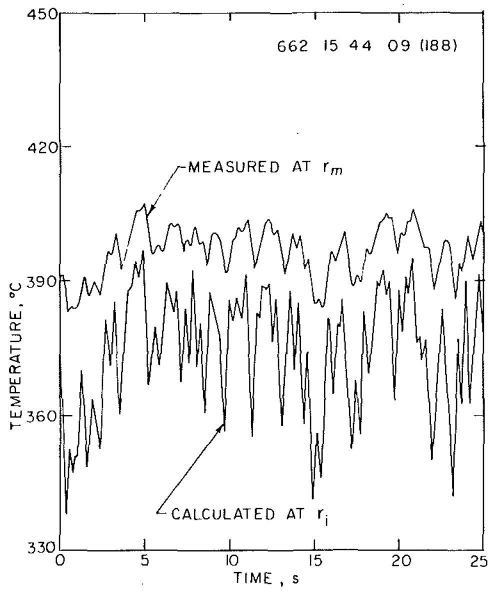

Fig. 6 Test R662 thermal fluctuations

The junction of the thermocouple that produced the signal of Fig. 6 was accurately located within the tube wall at a radial location, $r_m = 6.73$ mm. This measurement formed the basis for a calculation of the temperature distribution in the entire tube wall. The measured temperature formed one boundary condition at $r = r_m$, and the sodium bulk temperature and heat transfer coefficient determined from analysis of the shell thermocouples formed the second boundary condition at $r = r_o$. (The method of [8] was employed in the sodium heat transfer coefficient calculation, and it was found that its magnitude, as given in Table 1 for Test R662, did not vary more than a few percent in the tests presented.) Solution of the one-dimensional, transient, heat conduction equation in the region $r_m \leq r \leq r_o$ was straightforward. Extension of the solution to $r = r_i$ involved solution of a problem of the inverse heat transfer type. Results are shown in Fig. 6 for the calculated temperature at $r = r_1$. This result was verified by using the calculated temperature at $r = r_i$ as one boundary condition, and the sodium bulk temperature and heat transfer coefficient as the other, in a standard, transient, finite difference, heat conduction computer code. The temperature calculated from the code at $r = r_m$ was in excellent agreement with the measured temperature at $r = r_m$.

Fourier series representations were made of the two temperatures of Fig. 6. The temperature at the tube inside diameter, $r = r_i$, may be reproduced from the following relation:

$$T(t, r_i) = A_o + \sum_{k=1}^{64} [A_k \cos (2\pi k f_o t) + B_k \sin (2\pi k f_o t)] \qquad (1)$$

where the coefficients A_k and B_k are given in Table 2. The measured thermocouple temperature, $T(t, r_m)$, may be obtained by substituting coefficients C_k and D_k from Table 2 for A_k and B_k, respectively, in equation (1).

The power spectral density of the measured thermal fluctuations for Test R662 is shown in Fig. 7. The large amplitudes below approximately 0.3 Hz are system induced components, while the major components of the inherent transition boiling fluctuations are seen to be bracketed by 0.3 Hz and 1.0 Hz. This frequency band was found to occur in all SGTF tests. The same time segment was analyzed over frequency ranges of 0–10 Hz and 0–20 Hz with no change in results. In addition, it was found that 25.6 s time segments were sufficient for statistical significance, and analyses of longer time segments produced

Table 2 Test R662 Fourier series coefficients for tube temperatures. Fundamental frequency = 0.03906 D = 02 Hz

	THERMOCOUPLE		INNER WALL .			THERMOCOUPLE		INNER WALL	
K	CK	DK	AK	BK	K	CK	DK	AK	BK
0	3.9661D+02	0.0	3.7575D+02	0.0					
1	-1.6698D+00	1.0103D+00	-3.1620D+00	2.1609D+00	33	1.1305D-01	-2.9176D-01	-8.9118D-01	-7.1792D-01
2	-2.7341D+00	-2.5734D+00	-5.9095D+00	-4.4428D+00	34	6.8260D-02	2.8760D-02	1.7532D-01	-2.1423D-01
3	-2.5339D+00	-1.3107D-01	-4.9918D+00	5.6894D-01	35	1.4289D-01	3.8503D-01	1.5617D+00	-1.3952D-01
4	2.1429D+00	-1.1851D+00	3.6593D+00	-3.2381D+00	36	1.6805D-01	-1.3176D-02	1.0970D-01	-6.4801D-01
5	1.1520D+00	-1.3475D+00	1.5046D+00	-3.2398D+00	37	-3.8078D-01	-1.2976D-01	-8.4328D-01	1.3615D+00
6	1.5363D+00	-1.2231D+00	2.1725D+00	-3.3627D+00	38	-3.4757D-01	-4.3999D-02	-4.6495D-01	1.3455D+00
7	1.0204D-01	-9.1900D-01	-5.0128D-01	-1.8436D+00	39	2.5728D-02	1.4174D-01	5.9732D-01	4.9714D-03
8	-1.6449D-01	1.4031D-01	-1.9256D-01	4.1061D-01	40	-2.4091D-01	-2.8344D-01	-1.3536D+00	8.0238D-01
9	7.9911D-01	-1.4726D+00	8.0170D-02	-3.5723D+00	41	2.6422D-02	-1.3757D-01	-5.6958D-01	-2.0215D-01
10	-3.9627D-01	-9.6990D-01	-1.7959D+00	-1.3963D+00	42	2.6790D-01	-3.9252D-01	-1.5544D+00	-1.3980D+00
11	8.8232D-01	1.1163D+00	2.9746D+00	1.0323D+00	43	3.8529D-01	2.7517D-01	1.4260D+00	-1.5730D+00
12	1.3169D+00	-8.7033D-01	1.3036D+00	-3.3171D+00	44	3.3825D-01	-3.5168D-01	-1.4462D+00	-1.6973D+00
13	-1.4171D+00	-1.3643D+00	-4.5076D+00	-5.0294D-01	45	-7.4749D-03	1.6071D-01	7.4290D-01	9.6338D-02
14	6.9549D-01	-1.1940D+00	-5.4877D-01	-3.2092D+00	46	2.7415D-01	-4.1307D-01	-1.8690D+00	-1.4268D+00
15	-4.9266D-01	-2.7996D-01	-1.3325D+00	2.9804D-01	47	1.4965D-01	-3.5093D-01	-1.6568D+00	-8.0657D-01
16	8.1878D-01	5.8730D-01	2.4545D+00	-3.7911D-01	48	-1.4916D-01	3.7974D-02	1.6160D-01	7.3944D-01
17	-4.7430D-01	1.1723D+00	1.3249D+00	2.9020D+00	49	3.2382D-01	-3.5846D-01	-1.7639D+00	-1.6539D+00
18	3.1866D-01	-3.0342D-01	-4.4045D-02	-1.1354D+00	50	1.0097D-01	6.4690D-03	3.4609D-02	-5.1422D-01
19	1.4696D-01	3.5063D-01	9.6316D-01	2.8806D-01	51	-1.4765D-01	-1.7414D-01	-8.9336D-01	7.7586D-01
20	-1.6552D-01	6.7691D-02	-1.2724D-01	4.6725D-01	52	-1.2064D-01	-4.8601D-02	-2.3912D-01	6.4263D-01
21	5.8634D-01	-5.2627D-01	-2.3902D-01	-2.1720D+00	53	1.7291D-01	1.1328D-01	5.6848D-01	-9.5138D-01
22	6.7063D-01	-6.2260D-01	-4.0775D-01	-2.5670D+00	54	-1.2220D-01	-2.5075D-02	-9.9304D-02	6.7276D-01
23	-5.8990D-01	-5.7673D-01	-2.3332D+00	5.6102D-01	55	-4.4246D-02	-2.0191D-02	-9.4450D-02	2.5243D-01
24	-6.8229D-02	-3.7582D-01	-1.0679D+00	-3.9240D-01	56	1.8293D-01	-6.5497D-02	-4.5420D-01	-9.9572D-01
25	-2.3479D-01	-2.0205D-01	-8.8532D-01	3.2974D-01	57	5.7965D-02	2.2235D-01	1.2341D+00	-4.5472D-01
26	-1.0052D+00	8.2344D-02	-1.2112D+00	2.9068D+00	58	2.9965D-01	-6.3151D-02	-5.5923D-01	-1.6907D+00
27	1.0395D-01	-5.7073D-02	-1.9635D-02	-3.7847D-01	59	2.3846D-01	-1.1807D-02	-2.4520D-01	-1.3888D+00
28	-4.9015D-01	-1.1701D-01	-1.0094D+00	1.3028D+00	60	2.5035D-01	-1.7343D-02	-3.1065D-01	-1.4731D+00
29	2.3880D-01	-2.1755D-01	-3.5914D-01	-1.0195D+00	61	-4.5016D-02	-1.5043D-01	-8.6432D-01	4.0974D-01
30	1.0732D-01	3.0571D-01	1.1081D+00	4.2839D-02	62	1.1777D-01	-7.0138D-03	-1.6243D-01	-7.1134D-01
31	-2.7164D-02	-4.1499D-01	-1.3958D+00	-4.1295D-01	63	1.3240D-01	1.5275D-01	7.9670D-01	-9.8785D-01
32	-3.6244D-01	6.4079D-02	-2.0389D-01	1.3011D+00	64	1.2490D-01	-1.0872D-01	-8.3112D-01	-6.5006D-01

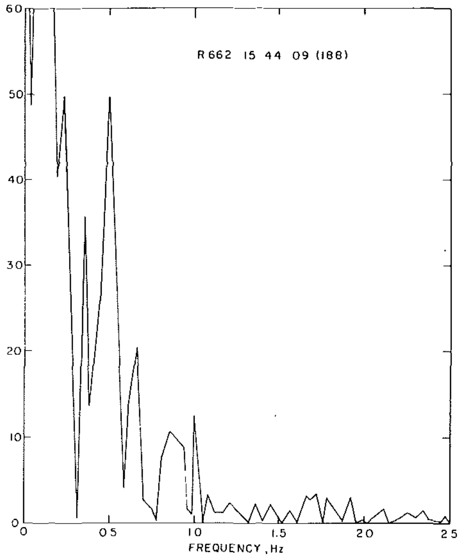

Fig. 7 Power spectral density of measured thermal fluctuations

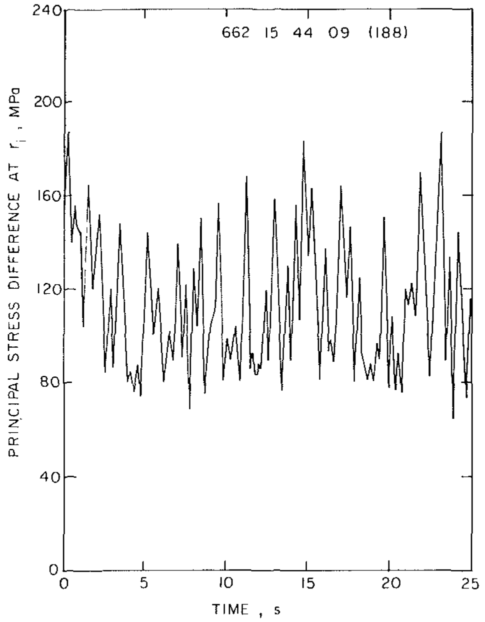

Fig. 8 Test R662 thermal stress

similar results. Multiple 25.6 s time segments from the test were analyzed as a control on reproducibility and to insure that the largest amplitudes, $Y_{1,\max}$, had been included.

Determination of the relative severity of the thermal results presented in Figs 6 and 7 is best accomplished by calculating the thermal stress in the tube wall. Using the temperature distribution in the entire tube wall, $r_o \geq r \geq r_i$, as a function of time, thermal stress was calculated by the method of [9]. The difference in the principal stresses is plotted as a function of time in Fig. 8. The maximum and minimum stresses from Fig. 8 were combined to yield alternating and mean stresses, and the equivalent alternating stress at zero mean stress was calculated by the Goodman diagram method which reduces to

$$S\,EQ\,ALT = S_a/[1 - S_{\text{mean}}/344.7] \quad (2)$$

Other methods for calculating thermal stress and equivalent alternating stress have been proposed [10–12], but the present method is adequate for establishing the *relative* severity of the test results and for providing a basis for intercomparing test results. The equivalent alternating stress for Test R662 was calculated to be 100 MPa which is quite large and makes it marginal for meeting the ASME Code requirement for 30 years tube lifetime.

Pressure and Temperature Tests. Four tests were performed in the SGTF to determine the influence and sensitivity of water pressure and sodium temperature on the severity of the thermal fluctuations measured in Test R662. The sodium temperature is an important parameter since the driving potential for thermal fluctuations in the transition boiling zone may be considered as the temperature difference between the water and sodium, $T_B - T_{H_2O}$. (Equivalently, the critical heat flux could replace this temperature difference parameter.) Tests R190 and R297 were performed in a manner similar to Test R662. In all three tests, CHF occurred 12.2 m downstream of the water inlet to the test section, and the water pressure, water flowrate, and CHF quality were essentially the same in Tests R190 and R297 as measured in Test R662. Test R190 was performed with the bulk sodium temperature at CHF 22°C higher than Test R662, thus increasing the thermal potential, $T_B - T_{H_2O}$, from 90 to 112°C. The resulting equivalent alternating stress increased from 100 MPa in Test R662 to 136 MPa in Test R190, as given in Table 3. Decreasing T_B in Test R297 to 411°C reduced the stress to 90 MPa.

Tests R318 and R319 were performed with CHF quality, water flowrate, and sodium bulk temperature at CHF essentially the same as in Test R662. The water pressure was changed in each case. Reducing the water pressure to 11.3 MPa in Test R318 resulted in an increase in the thermal potential, $T_B - T_{H_2O}$, to 108°C, and the equivalent alternating stress increased to 130 MPa. Comparing this result with Test R190 indicates that the reduction of pressure produced a higher stress than can be attributed to the change in thermal potential alone. Increasing the water pressure in Test R319 decreased the thermal potential to 80°C, and the stress decreased to 70 MPa. Comparing this result with Test R297 again indicates a pressure effect; stress is inversely proportional to water pressure. Thus, the effects of both sodium bulk temperature and water pressure on the severity of thermal fluctuations in the transition boiling zone have been demonstrated. A more quantitative evaluation of this severity may be derived from thermal cycle limits for fatigue damage to the tube. Based upon the frequencies of the thermal fluctuations measured in transition boiling, equivalent alternating stress levels above 100 MPa are marginal for meeting the ASME Code requirement for 30 years tube lifetime. This result is independent of the additional stress imposed by the system induced fluctuations.

Conclusions

1 Two types of thermal fluctuations contribute to the thermal stress in sodium-heated steam generator tubes in the transition boiling zone. The first type is attributed to system induced fluctuations which possess the maximum potential amplitude, Y_2, and generally occur at relatively low frequencies. The inherent transition boiling fluctuations constitute the second type and occur at higher frequencies with amplitude Y_1.

2 The maximum amplitude, $Y_{1,\max}$, occurs in the central part of the transition boiling zone.

3 The ratio of amplitudes, $Y_{1,\max}/Y_2$ varies as a function of test parameters.

4 The frequencies of the inherent fluctuations are bounded by 0.3 and 1.0 Hz. This frequency band is independent of test parameters.

5 The amplitude of the high frequency thermal fluctuations increases as sodium temperature (heat flux) increases.

Table 3 Comparison of parametric results

Test No.	Water Pressure MPa	Water Flowrate kg/m²·s	T_B °C	$T_B - T_{H_2O}$ °C	X_{CHF}	S EQ ALT MPa
R662	12.9	2480	420	90	.19	100
R190	12.9	2540	442	112	.18	136
R297	13.0	2480	411	81	.23	90
R318	11.3	2500	427	108	.20	130
R319	15.4	2450	424	80	.20	70

6 The amplitude of the high frequency thermal fluctuations decreases as water pressure increases.

7 Thermal stresses in the tube walls of sodium-heated steam generators in the transition boiling zone may be significantly large in the normal operating range of the unit and may limit tube lifetime as a consequence of thermal fatigue.

Acknowledgment

This work was performed under the auspices of the United States Department of Energy.

References

1 Bailey, N. A. and J. G. Collier, "The Estimation of Tube Wall Temperatures in the Evaporator Region of Subcritical Once-Through Sodium Heated Steam Generators," AEEW-M-1000, Aug. 1970.

2 deMunk, P. J., "Wall Temperature Fluctuations-Realization of the Criteria for Steam Generators," Paper No. G3, *Summary Report of International Atomic Energy Agency Study Group Meeting on Steam Generators for LMFBRs*, Bensberg, IWGFR/1, 1975, pp. 250–253.

3 Nekrasov, A. V., S. A. Logvinov, and I. N. Testov, "Heat-Transfer Crisis in a Steam-Generating Tube on Heating with a Liquid-Metal Heat Carrier," *Soviet Atomic Energy*, Vol. 36, 1976, pp. 595–598.

4 Kebadze, B. V., V. S. Sroelov, B. V. Kul'pin, and A. I. Gavrilin, "Statistical Characteristics of the Temperature Fluctuations in a Direct-Flow Sodium Water Steam Generator," *Soviet Atomic Energy*, Vol. 39, No. 4, 1976, pp. 870–873.

5 Wolf, S. and D. H. Holmes, "Critical Heat Flux in a Sodium-Heated Steam Generator Tube," *Reprints of AIChE Papers*, 17th National Heat Transfer Conference, Am. Inst. Chm. Engr., New York, Aug. 1977, pp. 275–282.

6 Stevens, H. C. and D. M. France, "Development of a Thermal/Hydraulic Test Facility for Full-Scale LMFBR Steam Generator Tubes," *Trans. Am. Nucl. Soc.*, Vol. 22, 1975, pp 538–540.

7 France, D. M., "DNB in Liquid Metal Heated Forced Convection Boiling," *Int. J. Heat Mass Transfer*, Vol. 16, 1973, pp. 2343–2354.

8 France, D. M., T. Chiang, R. D. Carlson, and W. J. Minkowycz, "Measurement and Correlation of Critical Heat Flux in a Sodium Heated Steam Generator Tube," ANL Technical Report, ANL-CT-78-15, Jan. 1978.

9 Chiang, T., D. M. France, and T. R. Bump, "Calculations of Tube Degradation Induced by Dryout Instability in Sodium-Heated Steam Generators," *Nuclear Engineering and Design*, Vol. 41, No. 2, 1977, pp. 181–191.

10 Chu, C. L., S. Wolf, and A. W. Dalcher, "Oscillatory Dryout Related Thermal Stresses in Clean Steam Generator Tubes," ASME Paper No. 76-JPGC-NE-2, Sept. 1976.

11 Gabler, M. J., "The Nature and Effect of DNB in the Evaporator Steam Tubes," AI Document TI-036-610-023, Apr. 1975.

12 Chu, C. L., J. M. Roberts, and A. W. Dalcher, "DNB Oscillatory Temperature and Thermal Stress Responses for Evaporator Tubes Based on Rivulet Model," ASME Paper No. 77-WA/NE-5, 1977.

John H. Lienhard
Professor.
Fellow ASME

Md. Mojibul Hasan
Research Assistant.

Boiling and Phase Change Laboratory,
Mechanical Engineering Department,
University of Kentucky
Lexington, KY 40506

On Predicting Boiling Burnout with the Mechanical Energy Stability Criterion[1]

The mechanical energy stability criterion has been used in the past to predict burnout in flow boiling and is extended here to describe pool boiling burnout. Its use replaces the need for a knowledge of the Helmholtz wavelengths, which is needed in the conventional hydrodynamic theory, with a need to know the surface area of departing bubbles. The hitherto unpublished data of Sun are used to predict the latter. The geometries investigated include the infinite horizontal flat plate, the cylinder, and the sphere.

Introduction

The energy criterion for stability can be written in the form (see, e.g., [1]): *A system is in a state of stable equilibrium if for all possible variations:*

$$\Delta E|_s > 0, \tag{1}$$

where E denotes the system energy and the subscript, s, indicates that the change, ΔE, occurs at constant entropy.

Lienhard and Eichhorn [2] adapted this criterion in 1976 to predict the boiling burnout heat flux, $q_{\max}$, in a liquid crossflow over a cylindrical heater. More recently they used it again [3] to predict the burnout data of Katto and others [4, 5] for liquid jets directed onto plane heaters. In their adaptation, they first noted that, in such configurations, burnout occurs when the vapor escape "wake" becomes unstable. The word wake in this case refers to the vapor escape path beyond the heater but still close to it. In the wake, the system is virtually isothermal at the local saturation temperature. Therefore the important energy interactions are mechanical and isentropic. In such wake systems the energy criterion for stability can be written in the form:

The vapor-escape wake system in a boiling process remains stable as long as the net mechanical energy transfer to the system is negative.

When this criterion is violated, a generally very effective vapor removal system will collapse and be replaced with a far less efficient one. This usually will be some form of film boiling. At this point, the temperature will rise dramatically to accomodate the same heat flux, and we call the process "burnout" whether or not the heater actually melts.

It is important to note that there is no contradiction between this burnout mechanism and the hydrodynamic theory as articulated by Kutateladze [6], Zuber [7], and Lienhard, Dhir, and others [8, 9, 10]. The formulation of either burnout mechanism begins with the general relation

$$q_{\max} = \rho_g h_{fg} u_g (A_j/A_h), \tag{2}$$

where ρ_g and h_{fg} are the vapor density and latent heat, and A_j and A_h are the cross-sectional area of the vapor jets and the heater area that they subtend. The vapor velocity, u_g, is the value which is just sufficient to cause the system to collapse. In the hydrodynamic formulations, it is calculated as the value which causes a known or assumed vapor escape configuration to become Helmholtz unstable.

The mechanical energy stability criterion should predict the same value of u_g, because Helmholtz instability is still responsible for the jet breakdown. However, in using it we replace the assumptions required to make a Helmholtz stability analysis with another set of assumptions that may or may not be easier to formulate. To illustrate how this works, consider the flow boiling vapor escape path dealt with in [2]. This situation, depicted in Fig. 1, is a thin vapor sheet moving away from the cylinder and breaking off periodically in sausage-shaped bubbles. The Helmholtz wavelength in the vapor sheet was unknown in this case, and no one has succeeded in predicting it directly. However, the energy criterion made it possible to circumvent the need for that wavelength.

We equate the rate at which kinetic energy of the vapor is added to the sheet, to the rate at which the sheet gives up its rather high capillary energy per unit volume when it breaks into bubbles. This specifies the correct value of u_g and permits us to predict the peak heat flux using equation (2).

The purpose of this paper is to further demonstrate the usefulness of the mechanical energy stability criterion by using it to replace the hydrodynamic descriptions of pool boiling. This exercise will have the added benefit of making useful commentary on certain of the assumptions that are involved with that body of theory.

The Prediction of Pool Boiling Burnout

The Infinite Horizontal Flat Plate. The infinite, upward-facing, horizontal, flat plate is useful geometry to begin with because it is reasonably simple, and because the hydrodynamic theory and experimental data specify a reliable final result [9]. The peak heat flux, $q_{\max}$, in this case is 14 percent higher than Zuber originally predicted:

$$q_{\max F} = 1.14\left[\frac{\pi}{24}\,\rho_g{}^{1/2} h_{fg} \sqrt[4]{g\sigma(\rho_f - \rho_g)}\right]. \tag{3}$$

To predict $q_{\max F}$ using the mechanical energy stability criterion, we consider the idealized vapor escape configuration shown in Fig. 2 and then equate the rate at which vapor kinetic energy leaves the surface to the rate at which surface energy is carried off by the bubbles. We first calculate:

$$\frac{\text{no. of bubbles}}{\text{column-s}} = \frac{\pi(b\lambda_d)^2 u_g \rho_g}{(4/3)\pi(a\lambda_d)^3\rho_g} = \frac{3b^2 u_g}{4a^3\lambda_d} \tag{4}$$

where λ_d is the dominant Taylor-unstable wavelength on which the jets are spaced, and a and b are defined as shown in Fig. 2 by:

$$\left.\begin{array}{l} R_b\text{, the radius of departing bubbles} \equiv a\lambda_d \\ R_j\text{, the radius of the vapor jet} \equiv b\lambda_d \end{array}\right\} \tag{5}$$

The remaining symbols are conventional ones, included in the Nomenclature.

The energy-rate balance is then:

$$\underbrace{[\pi(b\lambda_d)^2 u_g\rho_g]\frac{u_g{}^2}{2}}_{\substack{\text{rate of kinetic energy}\\ \text{per column}}} = \underbrace{\left[\frac{3b^2u_g}{4a^3\lambda_d}\right]}_{\substack{\text{rate of}\\ \text{bubbles}\\ \text{per column}}} \times \underbrace{[4\pi(a\lambda_d)^2\sigma]}_{\substack{\text{capillary energy}\\ \text{of a bubble}}}. \tag{6}$$

This gives:

$$u_g = \sqrt{6\sigma/a\lambda_d\rho_g}\,. \tag{7}$$

---

[1] This work was funded under N.S.F. Grant ENG 77-25029.

Contributed by the Heat Transfer Division for publication in the JOURNAL OF HEAT TRANSFER. Manuscript received by the Heat Transfer Division August 11, 1978.

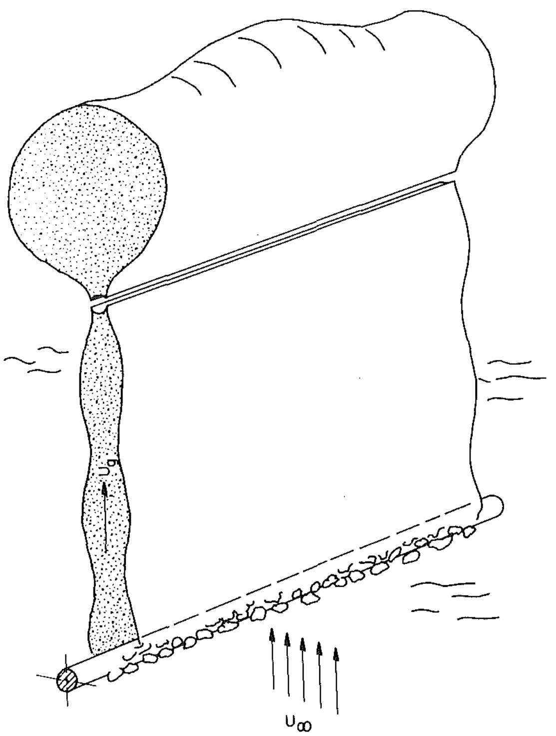

Fig. 1 Vapor removal by the action of two-dimensional jets before burnout occurs in flow boiling

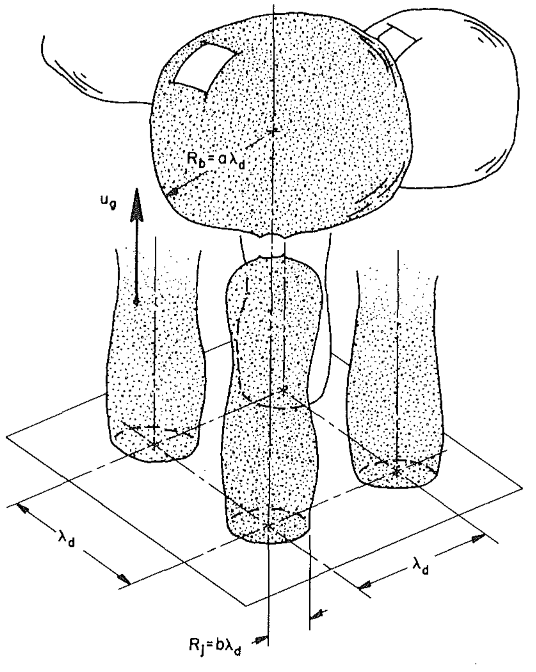

Fig. 2 Idealization of vapor removal from an infinite flat plate during pool boiling

Using the well-known dominant Taylor wavelength (see, e.g., [7] or [8]):

$$\lambda_d = 2\pi\sqrt{3}\sqrt{\sigma/(\rho_f - \rho_g)g}\,, \tag{8}$$

in equation (6) and substituting the result in equation (2), we obtain the $q_{\max}$ prediction:

$$q_{\max} = \left[2.3327\,\frac{b^2}{\sqrt{a}}\right]\,[\rho_g{}^{1/2}h_{fg}\sqrt[4]{\sigma g(\rho_g - \rho_g)}]. \tag{9}$$

We now need to specify the values of a and b. Zuber guessed that $b \equiv R_j/\lambda_d = 0.25$ and that has received considerable approximate experimental support over the years. In 1962–63, Moissis and Berenson [11] quoted previous work which suggested the slightly lower value of $b = 0.216$.

The hydrodynamic theory does not include any information as to the value of $a \equiv R_b/\lambda_d$. Furthermore, the boiling literature says a great deal about bubble sizes in the region of isolated bubbles (as they depart from heater surfaces), but it includes very little on bubbles breaking away from the vapor jets. We therefore turn to unpublished photographs that Sun [12] made in connection with [13].

Fig. 3 is a typical photograph from Sun's data books. It shows vapor jets leaving a cylindrical heater and breaking into bubbles. Such measurements could not very well be made during boiling from a horizontal plate, but we expect that bubbles will break away from any cylindrical jet in the same way, regardless of the heater configuration below it.

Measurements of R_b from 78 of Sun's photographs for isopropanol, methanol, and acetone are shown in Fig. 4. These data are all for relatively large cylinders ($R' \gtrsim 0.2\lambda_d$). It turns out that bubble departure pictures for smaller wires are unclear, owing to an increasing number of small bubbles mixed in with the obvious larger ones. In such situations, the average values of R_b would have to include all bubbles passing a given plane. Such information cannot be obtained from still photographs, so we cannot complete the present development for small heaters.

The bubble radii are reported in terms of $R_b' \equiv R_b\sqrt{g(\rho_f - \rho_g)/\sigma}$, which in turn is equal to $2\pi\sqrt{3}a$. The fact that R_b' does not vary significantly with R' means that R_b is determined by gravity and surface tension without reference to the jet diameter. From Fig. 4, we get:

$$R_b' = 9.57 \pm 1.49 \tag{10}$$

or

$$a = 0.879 \pm 0.120 \tag{11}$$

Combining equation (11) and either Zuber's value of $b = 0.25$ or Berenson's value of $b = 0.216$ in equation (9), we obtain

$$q_{\max} = \begin{bmatrix} 0.155 \text{ for Zuber's } b \\ 0.116 \text{ for Berenson's } b \end{bmatrix} \rho_g{}^{1/2}h_{fg}\sqrt[4]{\sigma g(\rho_f - \rho_g)}\,. \tag{12}$$

The value of the lead constant which is consistent with the data is 0.149. This would give $b = 0.245$.

The mechanical energy stability criterion thus yields results that agree with the hydrodynamic theory well within the available data, and it shows that we can retain Zuber's assumed value of the jet radius. It does so by replacing an assumption as to the nature of the Helmholtz unstable wavelength with an empirical observation of the bubble departure diameter.

Nomenclature

$a = R_b/\lambda_d$

A_j = area of jet

A_h = area of heater subtended by one jet

$b = R_j/\lambda_d$

g = acceleration of gravity

h_{fg} = latent heat of vaporization

$q_{\max}$, $q_{\max F}$, $q_{\max Z}$ = peak pool boiling heat flux; subscript F denotes infinite flat plate value; subscript Z denotes Zubers prediction of $q_{\max}$ (bracketed term in equation (3))

R_j = radius of jet of vapor leaving surface

R_b = radius of the departing bubble at burnout

$R' = R\sqrt{g(\rho_f - \rho_g)/\sigma}$, a dimensionless radius

$R_b' = R_b\sqrt{g(\rho_f - \rho_g)/\sigma}$, a dimensionless vapor departure radius

u_g = the velocity of vapor in a jet at burnout

δ = vapor blanket thickness

$\Delta E|_s$ = isentropic variation of the energy of a system

λ_d, λ_H = most susceptible Taylor wavelength in a horizontal liquid-vapor interface, and the Helmholtz unstable wavelength in a vapor jet, respectively.

ρ_f, ρ_g = saturated liquid and vapor densities, respectively

σ = surface tension of a liquid in contact with its vapor

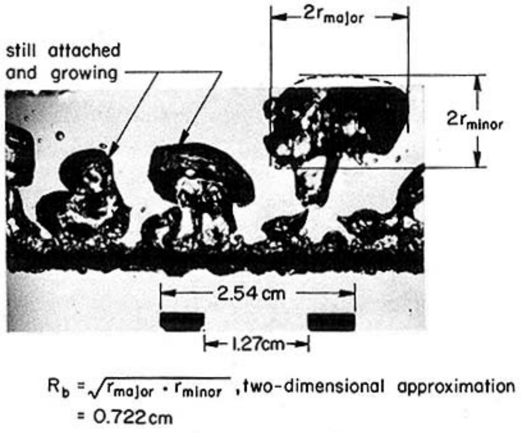

Fig. 3 The measurement of a bubble from one of Sun's unpublished photographs. Isopropanol boiling on a 2.06 mm dia wire near q_{max}

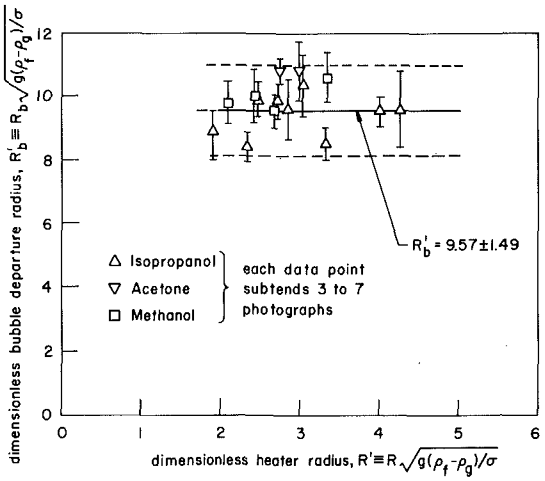

Fig. 4 Dimensionless radius, $R_b' \equiv R_b\sqrt{g(\rho_f - \rho_g)/\sigma}$, of bubbles breaking away from a vapor jet

The Large Horizontal Cylinder. In this case, we replace equation (4) with

$$\frac{\text{no. of bubbles}}{\text{column-s}} = \frac{\pi(R+\delta)^2 u_g \rho_g}{\frac{4}{3}\pi R_b^{\,3}\rho_g} = \frac{3(R+\delta)^2 u_g}{4R_b^{\,3}} \tag{13}$$

and the mechanical energy balance becomes

$$[\pi(R+\delta)^2 u_g \rho_g]\frac{u_g^{\,2}}{2} = [(4\pi R_b^{\,2})\sigma]\ [\text{no. of bubbles/column-s}] \tag{14}$$

Combining equations (13) and (14), we find

$$u_g = \sqrt{\frac{6\sigma}{\rho_g R_b}} \tag{15}$$

It was observed by Lienhard and Dhir [8, 10] that for large cylinders $A_j/A_h = 0.155$. Using this result in equation (2) along with equation (5), we obtain for the large cylinder heater

$$q_{\max_{cyl}} = 0.380\rho_g^{\,1/2} h_{fg}\sqrt{\sigma/R_b} \tag{16}$$

Finally, we divide this result by $q_{\max_Z}$ to nondimensionalize it in the usual way. The result is

$$\left.\frac{q_{\max}}{q_{\max_Z}}\right|_{\text{large cyl}} = \frac{2.90}{\sqrt{R'_b}} = 0.937 \pm 0.062 \tag{17}$$

Equation (17) is compared with Sun's [13] prediction,

$$\frac{q_{\max}}{q_{\max_Z}} = 0.89 + 2.27\exp(-3.44\sqrt{R'}), \tag{18}$$

where $R' = R\sqrt{g(\rho_f - \rho_g)/\sigma}$, in Fig. 6.

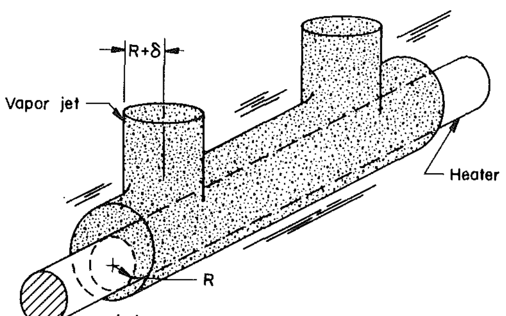

(a) Vapor removal configuration

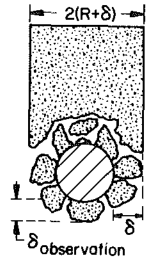

(b) Cross-sectional view of a vapor jet.

Fig. 5 Model for peak pool boiling heat flux on horizontal cylinder

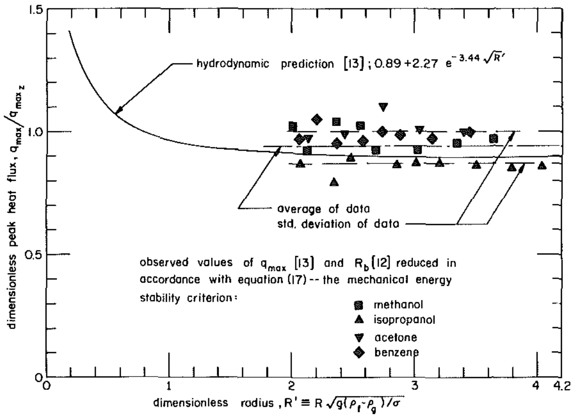

Fig. 6 Comparison of the mechanical energy stability theory prediction of burnout on cylinders with the hydrodynamic theory

Fig. 6 reveals that, when we predict burnout on large cylinders using the mechanical energy stability criterion and measured values of R_b, we get the same result as we do with the hydrodynamic theory and an assumed value of the Helmholtz unstable wavelength. The two results overlap within about ½ of a standard deviation of the data points.

The Large Sphere. For large spheres, the ration A_j/A_h is predicted by Ded and Lienhard [8, 14] and verified experimentally. The result is

$$A_j/A_h = 0.143 \tag{19}$$

Using this result in equation (2), along with equation (14), we obtain for large, spherical heaters

$$\left.\frac{q_{\max}}{q_{\max_Z}}\right|_{\text{large sphere}} = \frac{2.68}{\sqrt{R_b'}} \tag{20}$$

We assume that R_b' for large spheres or for any other large heater should be the same as it is for a large cylinder, since the situation in the upper interface is similar. This assumption replaces one of the assumptions of hydrodynamic theory, that the Helmholtz unstable wavelength, $\lambda_H = \lambda_d$ for any large finite heater. We have seen that R_b' is 9.57 ± 1.49 above large cylinders, so equation (20) becomes

$$\left.\frac{q_{\max}}{q_{\max_Z}}\right|_{\text{large sphere}} = 0.866 \pm 0.053 \tag{21}$$

The hydrodynamic theory [8, 13] gives the comparable value of

$$\left.\frac{q_{\max}}{q_{\max Z}}\right|_{\text{large sphere}} = 0.84 \tag{22}$$

Conclusions

1 The mechanical energy stability criterion can be used to develop the conventional peak pool boiling heat flux equations. The result includes a constant which depends upon the average departing bubble radius.

2 The departing bubble radius can be established empirically on the basis of hitherto unpublished photographs of vapor bubbles leaving large horizontal cylinders near burnout. The result, $R_b' = 9.57 \pm 1.49$, should be generally valid for a bubble leaving a cylindrical jet.

3 Based on these data, $q_{\max}$ is predicted for infinite flat plates, large spheres, and large cylinders. The predictions of $q_{\max}$ or R_j all fall within five percent of the established results. This is better than experimental accuracy and probably reflects the uncertainty in our measurements of R_b.

4 Zuber's conjecture that $R_j = \lambda_d/4$; and Sun, Lienhard, and Dhir's conjecture that $\lambda_H = \lambda_d$ above large bodies; are both supported.

5 The success of the mechanical energy stability criterion in the present rationalization of pool boiling burnout, and in the prior cases of flow boiling burnout, strongly suggest that it is a tool that should be further exploited in such fluid stability problems.

References

1 Kennan, J. H. *Thermodynamics,* John Wiley and Sons, New York, 1941, et. seq., Chapter 23.

2 Lienhard, J. H. and Eichhorn, R. "Peak Boiling Heat Flux on Cylinders and in a Cross Flow," *Int. Jour. Heat Mass Transfer,* Vol. 19, 1976, pp. 1135–1142.

3 Lienhard, J. H. and Eichhorn, R. "On Predicting Boiling Burnout for Heaters Cooled by Liquid Jets," *Int. Jour. Heat Mass Transfer,* (in press).

4 Monde, M. and Katto, Y. "Burnout in High Heat-Flux Boiling System with an Impinging Jet," *Int. Jour. Heat Mass Transfer,* Vol. 21, 1978, pp. 295–305.

5 Katto, Y. and Monde, M. "Study of Mechanism of Burnout in High Heat-Flux Boiling System with an Impinging Jet," *Proc. 5th Int. Heat Transfer Conf., Tokyo,* Vol. IV, B6.2, Japan, 1974.

6 Kutateladze, S. S. "On the Transition to Film Boiling Under Natural Convection," *Kotloturbostroenie,* No. 3, 1948, p. 10.

7 Zuber, N. "Hydrodynamic Aspects of Boiling Heat Transfer," AEC Report No. AECU-4439, Physics and Mathematics, 1959.

8 Lienhard, J. H. and Dhir, V. K. "Extended Hydrodynamic Theory of the Peak and Minimum Pool Boiling Heat Fluxes," NASA CR-2270, July, 1973.

9 Lienhard, J. H., Dhir, V. K. and Riherd, D. M. "Peak Pool Boiling Heat-Flux Measurements on Finite Horizontal Flat Plates," ASME JOURNAL OF HEAT TRANSFER, Vol. 95, No. 4, 1973, pp. 477–482.

10 Lienhard, J. H. and Dhir, V. K. "Hydrodynamic Prediction of Peak Pool-boiling Heat Fluxes from Finite Bodies," ASME JOURNAL OF HEAT TRANSFER, Vol. 95, No. 2, 1973, pp. 152–158.

11 Moissis, R. and Berenson, P. J. "On the Hydrodynamic Transisions in Nucleate Boiling," ASME JOURNAL OF HEAT TRANSFER, Vol. 85, No. 3, 1963, pp. 221–229.

12 Unpublished photographs from the data books of K. H. Sun, Boiling and Phase Change Laboratory Files, Mech. Engr. Dept., Univ. of Kentucky.

13 Sun, K. H. and Lienhard, J. H. "The Peak Boiling Heat Flux in Horizontal Cylinders," *Int. Journ. Heat. Mass Transfer,* Vol. 13, 1970, pp. 1425–1439.

14 Ded, J. S. and Lienhard, J. H. "The Peak Boiling Heat Flux from a Sphere," *AICHE Journal,* Vol. 18, No. 2, 1972, pp. 337–342.

R. E. Henry
H. K. Fauske

Argonne National Laboratory
Argonne, Ill. 60439

Nucleation Processes in Large Scale Vapor Explosions

A spontaneous nucleation model is proposed for the mechanisms which lead to explosive boiling in the free contacting mode. The model considers that spontaneous nucleation cannot occur until the thermal boundary layer is sufficiently thick to support a critical size vapor cavity, and that significant bubble growth requires an established pressure gradient in the cold liquid. This results in a prediction that, for an interface temperature above the spontaneous nucleation limit, large cold liquid droplets will remain in film boiling due to coalescence of vapor nuclei, whereas smaller droplets will be captured by the hot liquid surface and rapidly vaporize, which agrees with the experimental observations. The model also predicts that explosions are eliminated by an elevated system pressure or a supercritical contact interface temperature, and this is also in agreement with experimental data.

1 Introduction

A vapor explosion is the rapid generation of vapor at a rate which exceeds the ability of the surrounding environment to acoustically respond. Extensive experimental investigations have resulted in the formulation of a list of necessary but not sufficient conditions for these explosions. These are (1) two liquids, one hot and one cold, must be present; (2) the liquids must come into intimate contact; and (3) the hot liquid temperature must be greater than some minimum value. These investigations have led to the formulation of several parametric models [1, 2, 3] which basically assume that fine fragmentation and intimate mixing of the hot and cold liquids has already occurred. Other mechanistic approaches have been formulated based on vapor bubble collapse [4, 5, 6] and shock wave induced fragmentation [7] for achieving the intimate mixing. One unique difference between the observed explosive interactions and these models is the definite temperature threshold observed experimentally, below which no violent explosive interactions occur, whereas the above models do not predict such behavior. A proposed explanation for this threshold [8] is that spontaneous nucleation of the cold liquid, upon contact with the hot liquid, is a necessary condition for the occurrence of a large-scale vapor explosion. (A large-scale vapor explosion is one in which the energy is transferred on a time scale comparable to, or less than, the acoustic relief time of the liquid-liquid system. This can be contrasted with small scale, or superheat explosions in which the energy is stored within the cold liquid on a time scale that is long compared to the acoustic relief, i.e., classical liquid superheat measurements [9–12].) Assuming the applicability of the parabolic heat conduction equation, semi-infinite liquid masses on the time scale of interest, and constant thermal properties in both liquids, the time independent contact interface temperature is given by [13]

$$T_i = \frac{T_H + \sqrt{k_C \rho_C C_C / k_H \rho_H C_H}\, T_C}{1 + \sqrt{k_C \rho_C C_C / k_H \rho_H C_H}} \qquad (1)$$

Detailed calculations [14, 15] with the hyperbolic heat conduction equation have demonstrated that the parabolic equation is valid for time scales longer than 10^{-12} s, which is much less than the time intervals of interest in this study.

2 Spontaneous Nucleation

Spontaneous nucleation is a mechanism by which critical size vapor embryos or cavities are formed as a result of density fluctuations independent of any pre-existing liquid-vapor or liquid-gas interfaces. As discussed in [16], this nucleation may either be heterogeneous (vapor embryo is formed as a lense at the poorly wetted liquid-liquid interface) or homogeneous for well-wetted liquid pairs (site is formed completely within the cold liquid), but for simplicity, well-wetted systems will be considered in this paper. The homogeneous nucleation frequency is given by the classic equation for nucleation [9]

$$J = A(T) e^{-(W/k_1 T)} \qquad (2)$$

The pre-exponential factor $A(T)$, which is approximately 10^{33} if the volumetric site density is given in sites/cm^3 s [17], includes the detailed effects of molecular vaporization and condensation, but this term can be in error by several orders of magnitude and have little effect on the temperatures calculated for spontaneous nucleation. Equation (2) exhibits a strong temperature dependence as illustrated in Table 1 for homogeneous nucleation of Freon-22; i.e., the frequency of nucleation increases many orders of magnitude within a narrow temperature band. From the results given in Table 1, it is apparent that order of magnitude errors in the preexponential term, $A(T)$, do not significantly change the temperature level at which homogeneous nucleation becomes important. Small-scale, definitive experiments have verified the temperature threshold predicted by equation (2) for a wide variety of liquids at several different pressure levels [9–12]. In such systems, the cold liquid is basically in thermal equilibrium with its surroundings, and can thus, be best classified as isothermal. For large-scale vapor explosive systems in which the two liquids are at greatly different temperatures, intimate contact causes the cold liquid surface temperature to rise rapidly [14, 15]. *For these transient conditions, nucleation cannot proceed until a sufficiently thick thermal boundary layer has been developed to support vapor em-*

Contributed by the Heat Transfer Division for publication in the JOURNAL OF HEAT TRANSFER. Manuscript received by the Heat Transfer Division January 26, 1978.

Table 1 Homogeneous nucleation for Freon-22 at 1 atm

Temperature °C	Vapor Pressure MPa	Surface Tension N/m × 10^3	Critical Cavity Radius Å	Nucleation Rate sites/ ($\mathrm{cm^3 \cdot s}$)	Waiting Time per $\mathrm{cm^3}$
50	1.94	4.71	49	3.9×10^{-18}	8×10^9 yrs
52	2.03	4.46	44	2.0×10^{-6}	5.8 days
54	2.12	4.22	40	2.4×10^3	400 μs
56	2.23	3.97	36	7.2×10^{10}	10^{-11} s
58	2.32	3.73	32	1.6×10^{16}	6×10^{-17} s
60	2.43	3.49	29	3.7×10^{20}	3×10^{-21} s
65	2.70	2.91	22	2.1×10^{27}	5×20^{-28} s
70	3.00	2.35	16	4.3×10^{30}	2×20^{-31} s
80	3.66	1.30	7.3	5.6×10^{32}	2×20^{-33} s
90	4.44	0.39	1.8	1.0×10^{33}	10^{-33} s

bryos of the critical size. This is equivalent to the criterion proposed by Hsu [18] for preferred site nucleation in standard nucleate boiling.

3 Thermal Boundary Layer Model

The model proposed here is specifically concerned with the free contacting mode in which one liquid is merely poured into the other liquid, and this contact mode will be investigated by considering the behavior of an arbitrary mass of cold liquid as it contacts a hot liquid surface. As will be discussed later, modest impact velocities (~1–2 m/s) may be important, but for these phenomenological arguments, such impact velocities will be neglected initially.

The instantaneous increase in the interface temperature resulting from contact is accompanied by a pressurization due to the local expansion of the liquid. This single-phase pressurization is sustained by the growth of the thermal boundary layer, which grows as the square root of time, and it is relieved by an acoustic wave, which travels at a uniform speed. As the acoustic wave moves away from the interface, the pressure resulting from single-phase heating will decay, and for Freon-22, after approximately 10^{-7} s, the pressure will approach the ambient value. During this interval, the spontaneous nucleation can be suppressed since the local pressure can be quite high, but the thermal boundary layer will grow as dictated by the error function solution, and as illustrated in Fig. 1 for Freon-22 with a contact interface temperature of 60°C. The limit of mechanical stability, or critical size, for a vapor embryo is also shown in Fig. 1 for $P_\ell = 0.1$ MPa and P_v the corresponding saturation value. After the decay of the single-phase pressurization, if the thermal layer has not become sufficiently thick to support a critical size vapor bubble, embryos will collapse before they reach the critical size, and the thermal layer will continue to develop.

As shown in Fig. 1, once the thermal boundary layer is sufficiently developed, the frequency of formation for critical size cavities is given by the product of the frequency per unit volume, which is a function of the local temperature, and the volume of fluid, V, having a temperature equal to or greater than that value. The cold liquid has a nucleation waiting time given by $t_w = [1/(J \cdot V)]$.

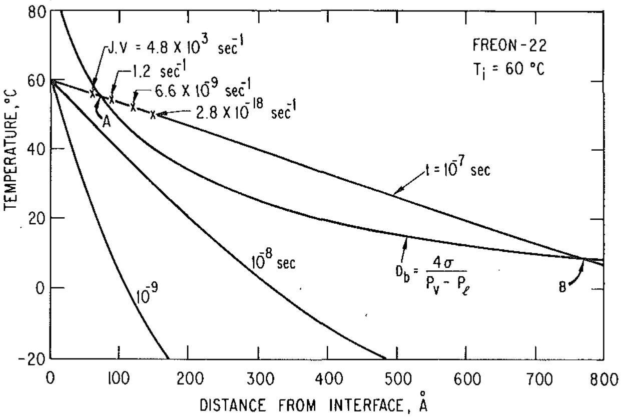

Fig. 1. Thermal boundary layer development and mechanical stability criterion

When the first critical embryo is formed, the bubble will attempt to grow from this radius to its next stable radius indicated by the intersection of the mechanical stability line and the thermal boundary layer (point B on Fig. 1). This growth, which is initiated from high superheats, low liquid pressures, and small dimensions, is a very complex process involving rapid acoustic growth into comparatively cold regions of the thermal boundary layer, condensation on the portion of the vapor space which penetrates the thermal boundary layer and continued heat addition at the interface. As an approximation to this complex behavior, it is assumed that the growth is inertially dominated and that the pressure profile required for such growth is developed in one acoustic transmission time from the contact interface, through the cold liquid droplet to the free surface on the opposite side, and back to the interface. It is assumed that inertial growth can proceed after this time interval ($t_a = 2\ell/c$), where ℓ is the distance from the interface to the free surface on the opposite side of the liquid mass. During this acoustic relief time, the thermal boundary layer continues to develop.

The time to nucleation and growth is then the sum of these relief times and the waiting time for a critical size cavity to appear.

$$t_n = 10^{-7} + \frac{1}{J \cdot V} + \frac{2\ell}{c} \tag{3}$$

After the time delay given in equation (3), the vapor embryo is assumed to grow. The growth time from inception size to the limit of mechanical stability, point B in Fig. 1, can be calculated from the inertial growth equation, and this represents the minimum lifetime of the bubble under these conditions.

$$t_g = \frac{\Delta r}{\sqrt{2/3\,\dfrac{\Delta P}{\rho_\ell}}} \tag{4}$$

ΔP is the average driving pressure between the minimum and maximum stable limits for the vapor bubble. With this time interval, the number of bubbles that can coexist during the minimum lifetime of

Nomenclature

C = specific heat
c = speed of sound
D = droplet diameter
D_b = critical size cavity = $4\sigma/(P_v - P_\ell)$
D_B = maximum stable diameter
h_{fg} = latent heat of vaporization
J = volumetric nucleation rate
Ja = Jakob number $\rho_\ell C_\ell (T_\ell - T_{\mathrm{sat}})/(\rho_v h_{fg})$
k = thermal conductivity
k_1 = Boltzmann's constant
ℓ = characteristic length

N = number of nucleation sites
P = pressure
r = radius
T = temperature
t = time
V = volume
W = work to form a critical size cavity = $16\pi\sigma^3/(3(P_v - P_\ell)^2)$
α = thermal diffusivity
ρ = density
σ = surface tension

Subscripts

a = acoustic
C = cold
c = capture
g = growth
H = hot
i = interface
ℓ = liquid
0 = initial
sat = saturation
t = transition from inertial to thermal
v = vapor

one bubble can be estimated and this is equal to the product of $J \cdot V \cdot t_g$.

The number density of bubbles calculated by this product is applicable as long as the bubbles do not become so numerous as to pressurize the liquid phase by their very presence. When the interface temperature upon contact considerably exceeds the minimum spontaneous nucleation value, the nucleation rate is so large that the formation of additional nuclei will pressurize the liquid which decreases the nucleation rate and slows down the bubble growth. A maximum site density can be estimated from the compressibility of the liquid phase, which is related to the sonic velocity by $c^2 = (\Delta P/\Delta\rho)$. Compression of the liquid volume, which is assumed to exist over a depth of one critical size bubble diameter, is equal to the increase in the vapor volume which can be specified by

$$V_v = \frac{N\pi D^3}{6} \sim \frac{ND^3}{2} \tag{5}$$

Therefore the increase in density of the liquid phase, per unit surface area of contact, can be related to the number and size of the incipient critical embryos by

$$\Delta\rho_\ell = \frac{\rho_\ell}{D} \cdot \frac{ND^3}{2} = \frac{\rho_\ell N D^2}{2} \tag{6}$$

Consequently the pressure increase within the liquid can also be related to these two parameters and sonic velocity of the liquid phase itself.

$$\Delta P = 1/2\, N \rho_\ell D^2 c^2 \tag{7}$$

It is assumed that an overpressure of bars is sufficient to suppress further nucleation sites within the remainder of the liquid Freon-22. (The analysis is rather insensitive to this assumption, i.e., a value of 2 bars or 15 bars could have been chosen without dramatically altering the results.) A characteristic diameter of 50 Å is assumed for the vapor bubbles and with these two parameters the number of nucleation sites per sq cm of contact area which suppresses further sites is 10^9. If the number of sites that can be formed within the growth time of one bubble is considerably less than this value, no significant pressurization will occur within the liquid. From a practical standpoint, when the interface temperature upon contact is significantly greater than the minimum spontaneous nucleation temperature, the nucleation site density is determined by this compressible limitation.

4 Drop Stability

In this study the characteristic length is assumed to be the droplet diameter and with the equations outlined above (see Appendix) one can assess the stability of a cold drop impacting upon a hot surface. Upon contact, the interface temperature is established and the thermal boundary layer develops during the relief times and waiting interval discussed above. As illustrated in Fig. 1, this establishes not only the inception criteria for the vapor bubble but also the maximum stable diameter to which it could grow. If this number of coexisting vapor cavities results in physical interference at the maximum stable bubble diameter (point B in Fig. 1), it is assumed that the interface between the two liquids will be vapor blanketed and the energy transfer is terminated. This interference site density can be evaluated from the maximum stable diameter at point B by $N = (1/D_B^2)$, where N cannot be greater than 10^9 sites per sq cm. If physical interference does not occur, the high pressure vapor will rapidly grow into a condensing zone and the droplet will be captured on the surface. These two different results are illustrated in Fig. 2. A prediction for this capture behavior is shown in Fig. 3 for Freon-22. This illustrates the result that, for a given temperature, droplets larger than a critical size will remain in film boiling despite initial, intimate, liquid/liquid contact, whereas those smaller than this value will wet and be captured by the surface.

This stability limit characterizes the size of cold liquid droplets which are capable of initiating explosive vapor formation. It is clear from the sizes shown in Fig. 3 that one drop captured on the surface does not result in sufficient vapor to represent either the explosion itself or even the initiator. However, as the cold liquid is broken down and fragmented in the film boiling mode, significant fractions of the liquid mass can attain sizes characterized by the stability criterion given in Fig. 3, which only represents order of magnitude arguments and analyses, and these fractions of the liquid mass can then initiate an explosive event. Consequently, the stability prediction shown in Fig. 3 represents only the initiating condition for a large-scale vapor explosion in the free contacting mode.

It is noteworthy that a similar stability prediction can be obtained if impact velocities of 1 or 2 m/s are assumed. The impact pressure resulting from a 1 m/s impact of Freon-22 is approximately 1.0 MPa. This pressure would last for one acoustic relief time and would inhibit nucleation. After the acoustic relief, bubbles could occur according to the extent of the thermal boundary layer as discussed above. Consequently, such assumptions also lead to the conclusion that capture and rapid vaporization are dependent upon the diameter of the cold liquid droplets. The experiments, which are discussed later, typically had such impact velocities, but experiments in which the cold liquid was initially floating on the surface in film boiling, i.e., no impact velocity, also demonstrated capture at essentially the same droplet diameter. Therefore, such impact velocities do not appear to be a requirement for capture, but it is notable that such assumptions would yield a similar prediction.

5 High Interface Temperatures

As illustrated in Table 1 for the homogeneous nucleation of Freon-22, when the contact temperature approaches the thermodynamic critical point (96°C), the nucleation rates become unrealistic. At these conditions, the calculated critical size cavities are smaller than one molecule. Consequently, it is unreasonable to assume that

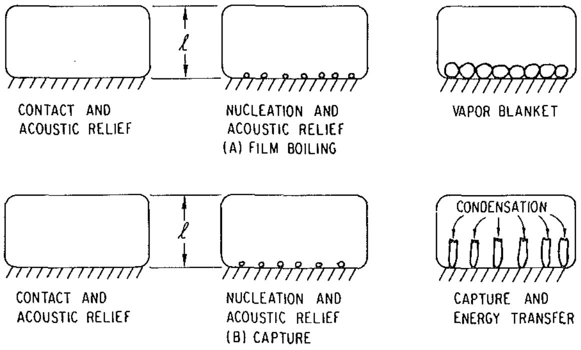

Fig. 2. Droplet film boiling and capture behavior

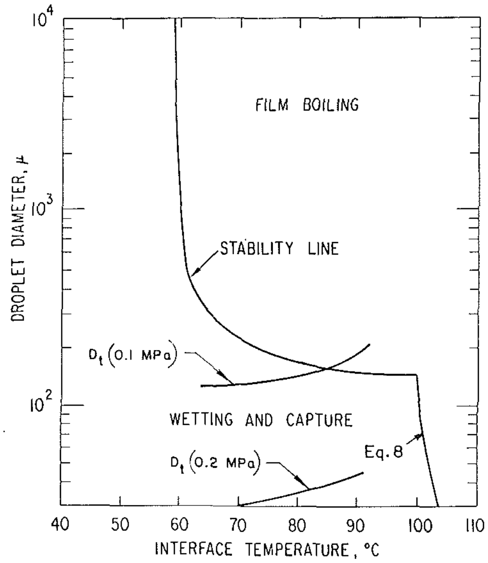

Fig. 3. Predicted droplet capture and bubble transition diameters as a function of interface temperature

continuum theory still applies in this thermodynamic range. It is uncertain what the nucleation behavior would be at these temperatures, but as a first approximation, it is assumed that a minimum of 40 molecules are required to produce a vapor cavity. (This number is arbitrary, but it makes little difference if it is varied by a factor of three or four.) Therefore, at very high interface temperatures, nucleation is assumed not to begin until the thermal layer is sufficiently developed to support a vapor cavity containing 40 molecules.[1] If the interface temperature is sufficiently high so that the thermal boundary layer can support such a nucleus at the critical pressure within the acoustic relief intervals, mutual pressurization is no longer applicable. Under such conditions, film boiling is inevitable. These interface temperatures can be estimated from

$$\frac{T_i - T_{\text{crit}}}{T_i - T_0} = \frac{D_b'}{\sqrt{8\alpha_C t_a}} \tag{8}$$

where D_b' is the vapor cavity diameter containing 40 molecules at the critical pressure.

6 Experimental Verification

Small Drop Experiments. An experiment was conducted to determine the viability of the predicted drop stability criterion. In this experiment, Fig. 4, small Freon-12 drops of varying diameters were impinged upon a mineral oil surface and high speed movies (5,000 pps) were taken of the resulting interactions. Since these experiments were conducted in air, Freon-12 was used because it is less hygroscopic than Freon-22. The drops were generated from a mechanically oscillated hypodermic needle and fell through a heated collimator tube onto the target area on the mineral oil surface. The collimator tube temperature was sufficiently hot so that the drops were in film boiling during their transit through the tube which also insured that the drops were saturated at atmospheric pressure when they impinged upon the mineral oil surface. A small wire ring was utilized to raise the oil surface, which formed a concave region of the target area that kept the drops centrally located within the focal plane of the camera.

For interface temperatures less than the homogeneous nucleation value, all sized drops wet the surface and proceeded to vaporize in thin film vaporization or by entrapment and incoherent nucleation after significantly long heating times (small-scale explosive interactions). For interface temperatures considerably greater than the homogeneous nucleation value large sized drops penetrated the surface and developed their own protective vapor envelopes, which was clearly evident when they returned to the surface as drops floating in their own protective vapor pockets. When these large drops either fragmented or vaporized to a small enough size, they would become captured on the surface and vaporize completely within 1 to 2 ms. Complete vaporization is evidenced by the fact that the volume of the bubble cloud left on the surface after this violent boiling essentially corresponds to complete vaporization of the initial droplet. Based on the projected area of the droplet such vaporization corresponds to a heat flux of approximately 8000 w/cm^2 as compared to a critical heat flux for Freon-12 at one atmosphere of 23 w/cm^2 [19]. Consequently, such heat fluxes are far beyond those previously observed in standard nucleate boiling. While this vaporization rate is still comparatively long for explosive interactions, it should be noted that this type of experiment inherently produces drops at the limit of stability, and these have the largest diameters and the longest time constants for energy transfer of all capturable sizes at that temperature.

Three different behaviors were observed when the drops contacted the oil surface. Some drops penetrated the surface and returned to the surface surrounded by a vapor film while others wetted upon contact and vaporized immediately. Other droplets, with diameters close to the stability prediction, would bounce on the oil surface and then finally wet. A summation of all these small drop experimental results and the analytical predictions are shown in Fig. 5 and the experimental results are in excellent agreement with the stability predictions arising from spontaneous nucleation and thermal boundary layer considerations.

The capture size is strongly influenced by the interface temperature which principally reflects the dominant role of the spontaneous nu-

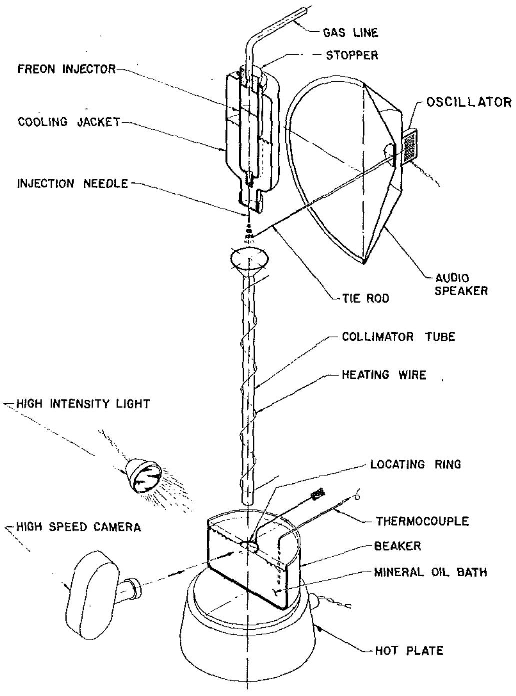

Fig. 4. Drop interaction apparatus

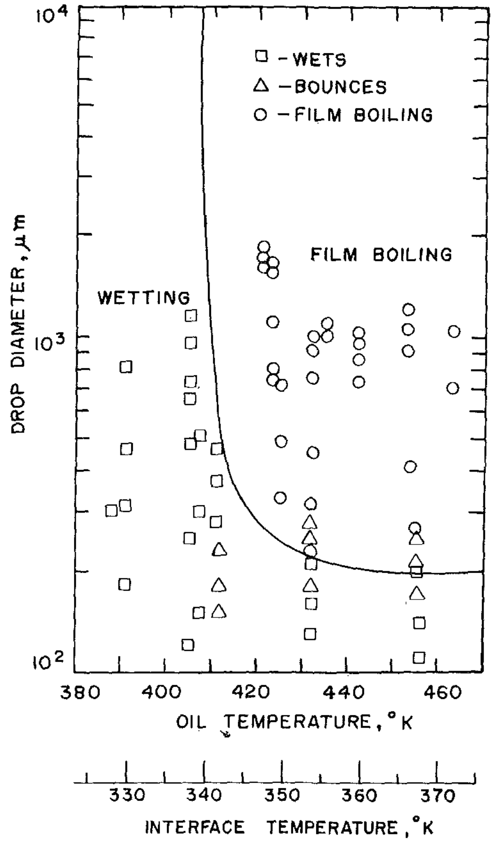

Fig. 5. Comparison of predicted and observed Freon-12 droplet behavior

---

[1] This is one area of spontaneous nucleation that has been of little interest in isothermal experiments because, as shown in Table 1, any experiments with slow heating rates in the order of 10^6 °C/s or less would be unable to achieve these high temperatures. In fact, from the practical standpoint, they can only be achieved by instantaneous contact.

cleation process. For interface temperatures less than the spontaneous nucleation limit, all drop sizes are captured which means that no significant prefragmentation of the cold liquid occurs and the interfacial area per unit mass is minimal at the initiation of direct liquid-liquid energy transfer. This results in a system that does not produce an explosive configuration for large-scale events. (These data are presented later.) However, when the interface temperature is greater than the spontaneous nucleation value (homogeneous nucleation for Freon-12 and mineral oil), significant prefragmentation of the cold liquid occurs before capture, and as will be discussed later, this also provides a propagation mechanism in large-scale events.

The predicted variation of capture diameter as a function of interface temperature is in agreement with the additional experimental observation that systems with interface temperatures barely into the explosive range have experienced interactions upon contact, while at higher temperatures, a sustained period of film boiling is observed [6, 20].

Large-Scale Experiments. Many large-scale experiments are reported in the literature with a wide variety of liquids and contact modes [6, 20–35]. In this paper, we are specifically concerned with large-scale explosions in the free contacting mode with no significant potential for chemical interaction between the two liquids, and for simplicity as well as a demonstration of the relevant physical principles, a well-wetted system is considered.

Henry, et al. [28, 29] have reported large-scale vapor explosion experiments with Freon-22 and mineral oil in which both liquid temperatures were systematically varied in order to study the relevance of the interface temperature criterion. These results are shown in Fig. 6 in terms of explosive and nonexplosive events as compared to the interface temperature prediction for a temperature of 60°C.[2] As shown, the interface temperature is a valid characterization of the explosive region. It should be noted that when highly subcooled liquid is used, only the initial temperatures of the liquids are known. When delay times of 1 s or longer are encountered before an explosive interaction is initiated, the temperature of the Freon could have increased considerably. This accounts for the scatter in the immediate vicinity of the prediction.

Other large-scale experiments with saturated Freon-22 and mineral oil have illustrated the dependence between the maximum explosive pressure (with rise times to this pressure less than 1 ms) and the degree to which the interface temperature exceeds homogeneous nucleation. These experimental results are illustrated in Fig. 7 for contacting modes of Freon poured into oil and oil poured into Freon. When the interface temperature is 60°C, weak explosive interactions are initiated, but they become progressively stronger as the interface temperature is increased. This is in agreement with the thermal boundary layer model since a higher interface temperature yields a more extensive prefragmentation and consequently a more energetic explosion. Anderson and Armstrong [6] have also shown that stronger explosions can be correlated with a longer delay time, and a more extensive prefragmentation of the system would also mean a longer delay time. Therefore, these experimental observations are all consistent with the thermal boundary layer model.

The existing data for very high temperature oil systems is limited and this particular aspect of both the proposed model and the experimental observations should be examined in detail. The proposed model predicts that aluminum-water and nitrogen-water systems are not explosive in a free contacting mode since the contact temperatures are far above the critical temperature. As observed by Long [21] and Hess and Brondyke [24], the aluminum-water system requires the presence of a wetted solid wall for explosions to occur. Hence, the system is no longer in a free contacting mode when explosions begin, but while the fluids were in a free configuration, no explosions were observed. Aluminum-water shock tube results [25, 33] have also produced explosive events, but again this is not the mode of contact considered herein. Water-liquid nitrogen systems have been observed to be nonexplosive in a free contacting mode but can explode in a shock tube test [34], and the same behavior has been observed with liquid ethane and water [27]. For the experiments described above, which were performed in air, the mineral oil temperature was sufficiently high to allow oxidation (~200°C). Such oxidation changes the thermophysical properties of the oil and renders inaccurate an interface temperature calculation based on pure liquid properties. These high temperature tests have been recently repeated [31] in an argon environment to eliminate oxidation, and the results, which are illustrated in Fig. 8, demonstrate the elimination of explosive interactions when the interface temperature exceeds the thermodynamic critical point (96°C) as predicted by the model.

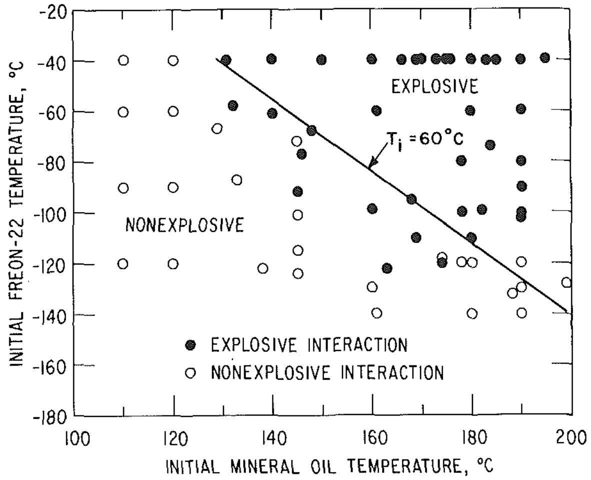

Fig. 6. **Large-scale explosive interactions compared to the contact interface temperature criterion**

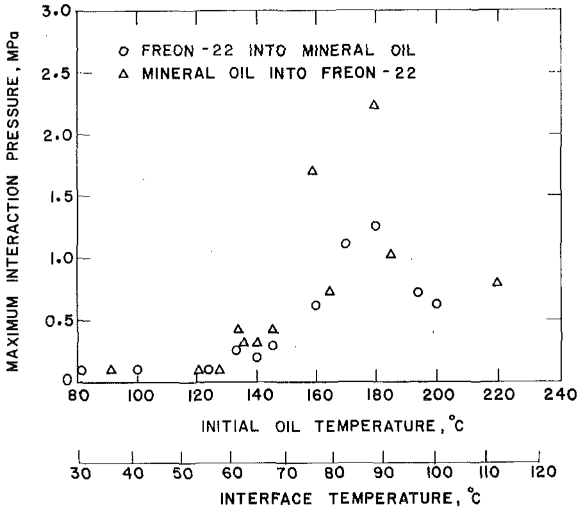

Fig. 7. **Large-scale explosive interactions for various contact interface temperatures**

This oxidation behavior may be an important consideration in liquid metal-water explosions. Since oxides generally have thermal conductivities that are one to two orders of magnitude less than the pure metal, any significant oxidation of the system, either during the heatup period or upon contact, will change the interface temperature and perhaps the explosive nature of the system. This was observed by Zyszkowski [35] for molten copper dropped into water. When the copper was heated in air, violent explosions occurred. However, when the copper was heated in an argon atmosphere, no explosive interactions were observed. This change in the interaction behavior may be due to a lower interface temperature because of the oxide properties or it may be due to the gas solubility arguments presented by Epstein [36]. In either case, the presence of oxygen changes the basic behavior of the system as has been experimentally observed by Dahlgren, et al. [37] for oxide mixtures.

---

[2] At this temperature the nucleation rate becomes significant on the time scale of interest in the thermal boundary layer.

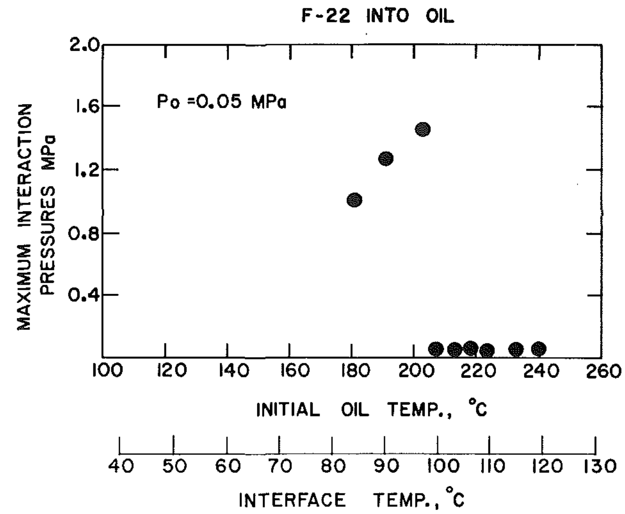

Fig. 8. Freon-22 and mineral oil explosive behavior at contact interface temperatures near the thermodynamic critical value

7 Elevated Ambient Pressures

To have a vapor explosion, vapor must be formed from the liquid phase and grow at a pressure higher than the ambient. The details of bubble growth characteristics found in [38], show that there are many effects which must be considered in the integrated growth behavior. However, *from a first order point of view, there are two basic regimes* of interest. These are the inertially and thermally dominated growth regimes. In inertially dominated systems, the pressure inside the vapor space is higher than that of the surrounding liquid and the temperature within the bubble is essentially equal to that of the surrounding liquid. The growth under these circumstances is limited by the rate at which the surrounding liquid can be pushed out of the way and the bubble radius versus time can be calculated from Rayleigh's equation

$$r = \sqrt{\frac{2}{3}\frac{P_v - P_\ell}{\rho_\ell}}\,t. \tag{9}$$

In a thermally dominated system, the pressure inside the vapor space is essentially the same as the surrounding liquid and the temperature within the bubble is considerably different than the temperature far removed from the vapor-liquid interface. Under these conditions, the growth is determined by the rate at which thermal energy can be conducted from the liquid to the interface, and the bubble radius verse time is approximated by [19]

$$r = 2\,\mathrm{Ja}\,\sqrt{\alpha_\ell t}\,. \tag{10}$$

Since the controlling behavior is the one with the slowest growth, the initial growth is inertially limited and the latter portions are thermally dominated. The approximate radius where inertial to thermal growth transition occurs is obtained from equations (9) and (10) and is given by

$$r_t = \frac{4\,\mathrm{Ja}^2\alpha_\ell}{\sqrt{\frac{2}{3}\frac{P_v - P_\ell}{\rho_\ell}}} \tag{11}$$

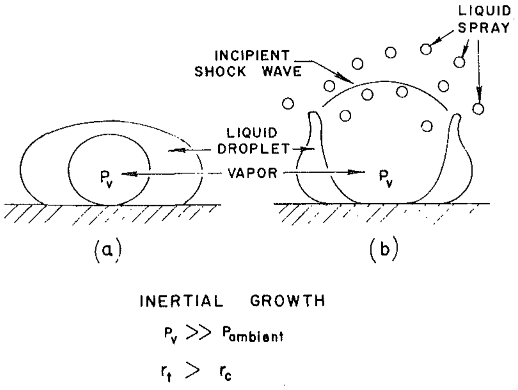

INERTIAL GROWTH

$P_v >> P_{ambient}$

$r_t > r_c$

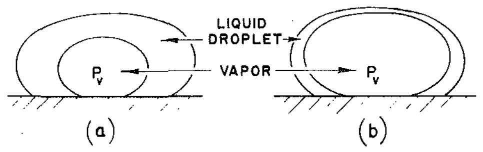

THERMAL GROWTH

$P_v = P_{ambient}$

$r_t < r_c$

Fig. 9. Boiling fragmentation mechanism

Therefore, if a vapor explosion is to occur, it must take place under the conditions where the inertially dominated growth can exist to a significant radius. The proposed model predicts the droplet size of cold liquid which can be captured by the hot liquid and thus initiate an explosion. When the interface temperature upon contact is above the homogeneous nucleation temperature but below the critical temperature, the capture diameter for Freon-22 is an order of magnitude 100 μ as shown in Fig. 3 and this is almost invariant with pressure. The transition diameter for a system pressure of 0.1 MPa is shown in Fig. 3 as is the corresponding diameter for a system pressure of 0.2 MPa. The transition dimension is essentially the same as the capture diameter for system pressure of 0.1 MPa, but for a pressure of 0.2 MPa it is an order of magnitude less than the capture size. Consequently, at atmospheric pressure the inertially dominated growth is capable of growing through the entire drop dimension with a vapor pressure higher than the surrounding liquid pressure. As illustrated in Fig. 9, as a high pressure vapor source inside of a liquid droplet approaches the opposite surface, the droplet will burst open producing a fine liquid spray and releasing the stored high pressure vapor which is an incipient shockwave to start the interaction. However, the most important aspect is the highly fragmented liquid spray which would be produced as the droplet is ruptured. It is this very fine liquid spray, which is much smaller than the parent droplet and therefore certainly less than the capturable size, which can provide the highly fragmented cold liquid material necessary for sustained propagation. Since the dimensions of this liquid spray may be order of magnitude 1 to 10 μ, nucleations within these small liquid droplets, as they contact additional hot liquid surface, are capable of experiencing inertially dominated growth through their entire dimensions at liquid pressures considerably greater than 0.1 MPa. This process of nucleation, inertial growth, and liquid fragmentation from within is the proposed mechanism by which the explosion escalates and propagates throughout the mixture. The time required for this inertial growth, can be estimated from

$$t_t = \frac{6\,\mathrm{Ja}^2\,\alpha_\ell\,\rho_\ell}{P_v - P_\ell} \tag{12}$$

and is five μs for Freon-22 at an interface temperature of 60°C and a system pressure of 0.1 MPa. Consequently, this mechanism can occur on a time scale which is two orders of magnitude shorter than the overall pressure rise, and thus, this internal fragmentation mechanism can be extremely effective in providing propagation for the explosive event.

The above behavior can be contrasted to a system in which the growth becomes thermally limited well inside the liquid droplet dimension; i.e., there is no high pressure source to rupture the surrounding liquid and no release of high pressure vapor as an incipient shockwave. Without the fragmentation and propagation mechanism, any initiating event is essentially incapable of escalating and propagating throughout the remainder of the system. This also emphasizes the importance of prefragmentation; i.e., if large drops are captured, the propagation mechanism can be eliminated. Therefore, the droplet capture, bubble growth arguments predict that there should be a significant difference between the behavior observed at a system pressure of 0.1 MPa and 0.22 MPa when Freon-22 is the cold liquid.

Large-scale experiments have been reported with Freon-22 and mineral oil [31] for different ambient pressures and the results are shown in Fig. 10. For a system pressure of 0.1 MPa, explosions were observed when the contact interface temperature was greater than the homogeneous nucleation value but less than the thermodynamic critical temperature. However, when the system pressure was increased to 0.22 MPa and 0.8 MPa, no explosive interactions were observed. This is in excellent agreement with the prediction of the thermal boundary layer model.

Similar calculations for water show that explosive interactions should be terminated at approximately 0.9 MPa. Recent water experiments [39] at various pressure levels have demonstrated explosive events for system pressures less than or equal to 0.5 MPa, but no explosions were observed at a pressure of 0.75 MPa.

9 Conclusions

A model, based on spontaneous nucleation, has been proposed to describe the inception and propagation mechanisms for vapor explosions in the free contacting mode. The proposed model predicts that the capture and resultant rapid vaporization is dependent upon the contact interface temperature and upon the droplet size.

This mechanism proposes that spontaneous nucleation and the resultant vapor growth is the mechanism for describing: (1) film boiling in a liquid/liquid system after intimate contact, (2) the limit of stability at a given temperature, (3) the spontaneous trigger for an explosive interaction, and (4) the propagation of the initiating event in these systems. The model formulated in these considerations provides a good representation of the explosive character for well-wetted liquid-liquid systems including the onset of explosive events and the sensitivity of such events to the ambient pressure.

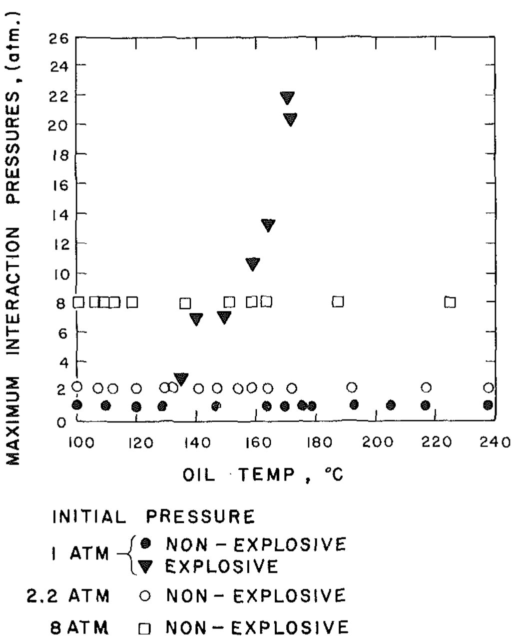

Fig. 10. Explosive behavior as a function of system pressure

References

1 Cho, D. H., Ivins, R. O., and Wright, R. W., "Pressure Generation by Molten Fuel-Coolant Interactions During LMFBR Accident Conditions," *Proc. of the Conference on New Developments in Reactor Mathematics*, Idaho Falls, ID, CONF-710302, Vol. 1, March 1971, p. 25.

2 Simon, R., "Computer Model Study of the Smelt-Water Physical Explosions," AIChE Preprint 15, presented at the 14th Natl. Heat Transfer Conference, Atlanta, GA, Aug. 5–8, 1973.

3 Caldarola, L., and Kousouvelis, G., "A Theoretical Model with Variable Masses for Molten Fuel-Sodium Thermal Interactions," *Proc. Fast Reactor Safety Meeting*, Beverly Hills, CA., CONF-740401-P2, April 1974, pp. 969–991.

4 Buchanan, D. J., *Journal of Physics D: Applied Physics*, Vol. 7, 1974, pp. 1441–1457.

5 Caldarola, L., and Kastenberg, W. E., "On the Mechanism of Fragmentation During Molten Fuel-Coolant Thermal Interactions," *Proc. Fast Reactor Safety Meeting*, Beverly Hills, CA., CONF-740401-P2, April 1974, pp. 937–954.

6 Anderson, R. P., and Armstrong, D. R., "R-22 Vapor Explosions," paper presented at ASME Winter Annual Meeting, Nuclear Reactor Safety and Heat Transfer Section, Atlanta, GA., Nov. 1977, pp. 31–45.

7 Board, S. J., Hall, R. W., and Hall, R. S., *Nature*, Vol. 254, March 1975, p. 319–321.

8 Fauske, H. K., *Trans. ANS*, Vol. 15, 1972, p. 813.

9 Skripov, V. P., *Metastable Liquids*, Halstead Press, Jerusalem, 1974.

10 Blander, M., et al., "Chemical Engineering Division Physical Inorganic Chemistry Semiannual Report," July–December, 1971, ANL-7878, 1972.

11 Wakeshima, H., and Takata, K., *Journal of the Physical Society of Japan*, Vol. 13, 1958, p. 1398.

12 Moore, G. R., *AIChE Journal*, Vol. 5, No. 4, 1959, pp. 458–466.

13 Carslaw, H. S., and Jaeger, J. C., *Conduction of Heat in Solids*, 2nd Ed., Clarendon Press, Oxford, 1959.

14 Baumeister, K. J., and Hamill, T. D., ASME JOURNAL OF HEAT TRANSFER, Vol. 91, 1969, pp. 543–548.

15 Kazimi, M. S., *Trans. ANS*, Vol. 21, 1975, p. 321.

16 Fauske, H. K., "Some Aspects of Liquid-Liquid Heat Transfer and Explosive Boiling," *Proc. Fast Reactor Safety Meeting*, Beverly Hills, CA., CONF-740401-P2, April 1974, pp. 992–1005.

17 Apfel, R. E., "Vapor Cavity Formation in Liquids," Technical Memorandum No. 62, Acoustic Research Laboratory, Harvard University, Cambridge, MA, Feb. 1970.

18 Hsu, Y. Y., ASME JOURNAL OF HEAT TRANSFER, Vol. 84, Aug. 1962, pp. 207–213.

19 Tong, L. S., *Boiling Heat Transfer and Two-Phase Flow*, John Wiley and Sons, New York, London, Sydney, 1965.

20 Board, S. J., Hall, R. W., and Brown, G. E., "The Role of Spontaneous Nucleation in Thermal Explosions: Freon/Water Experiments," CEGB Report RD/B/N3007, 1974.

21 Long, G., *Metal Progress*, May 1957, p. 107.

22 Henry, R. E., et al., "Large Scale Vapor Explosions," *Proc. Fast Reactor Safety Meeting*, Beverly Hills, CA., CONF-740401-P2, April 1974, pp. 922–934.

23 Johnson, T. R., Baker, L., Jr., and Pavlik, J. R., "Large-Scale Molten Fuel-Sodium Interaction Experiments," *Proc. Fast Reactor Safety Meeting*, Beverly Hills, CA., CONF-740401-P2, April 1974, pp. 883–896.

24 Hess, P. D., and Brondyke, K. J., *Metal Progress*, Vol. 93, April 1969.

25 Wright, R. W., et al., "Kinetic Studies of Heterogeneous Water Reactors—Annular Summary Report, 1965," USAEC Report No. STL-372-30, Dec. 1965.

26 Zivi, S. M., et al., "An In-Pile Study of Thermal Interactions Between High-Energy Molten UO$_2$ Fuel and Liquid Sodium," *Nuclear Science and Engineering*, Vol. 56, 1975, pp. 229–240.

27 Porteous, W. M., and Reid, R. C., *Chemical Engineering Progress*, Vol. 72, No. 5, 1976, pp. 83–89.

28 Henry, R. E., Fauske, H. K., and McUmber, L. M., "Vapor Explosions of Subcooled Freon," *Proc. Third Specialists Meeting on Sodium-Fuel Interactions in Fast Reactors*, Tokyo, Japan, Vol. 1, March 1976, pp. 231–246.

29 Henry, R. E., and McUmber, L. M., "Vapor-Explosion Experiments with Subcooled Freon," ANL-77-43, June 1977.

30 Henry, R. E., Fauske, H. K., and McUmber, L. M., "Vapor Explosion Experiments with Simultant Fluids," *Proc. ANS Topical Meeting on Fast Reactor Safety and Related Physics*, Chicago, IL., CONF-761001, Vol. 4, Oct. 1976, pp. 1862–1869.

31 Henry, R. E., and McUmber, L. M., "Vapor Explosion Potentials Under LWR Hypothetical Accident Conditions," *Proc. Light Water Reactor Safety Meeting*, Sun Valley, ID, CONF-770708, Vol. 3, Aug 1977, pp. 414–425.

32 Henry, R. E., and Fauske, H. K., "Nucleation Characteristics in Physical Explosions," *Proc. Third Specialists Meeting on Sodium-Fuel Interactions in Fast Reactors*, Tokyo, Japan, PNC N251 76-12, Vol. 2, March 1976, pp. 595–620.

33 Guest, J. N., Turner, R. G., and Rees, N. J. M., "Al/Water Shocktube Experiments at A.W.R.E. Foulness Since January 1972," FPR-1-74, Jan. 1974.

34 Anderson, R. P., and Armstrong, D. R., "Experimental Study of Vapor Explosions," *Proc. Third International Conference on Liquefied Natural Gas*, Washington, DC, 1972.

35 Zyszkowski, W., *International Journal of Heat and Mass Transfer*, Vol. 19, 1976, pp. 849–868.

36 Epstein, M., *Nuclear Science and Engineering*, Vol. 55, 1974, pp. 462–467.

37 Dahlgren, D. A., et al., "Molten LWR Core Material Interactions with Water and Concrete," *Proc. Light Water Reactor Safety Meeting*, Sun Valley, ID, CONF-770708, Vol. 3, Aug. 1977, pp. 426–440.

38 Theofaneous, T., et al., *Chemical Engineering Science*, Vol. 24, 1969, pp. 885–897.

39 Nelson, L. S., and Buxton, L. D., *Trans. ANS*, Vol. 28, 1978, p. 448.

APPENDIX

The proposed model generally involves a graphical solution. However, when the site density is limited by the maximum value of 10^9 sites/cm^3 s, the solution can be achieved straightforwardly. The interference diameter for this site density is

$$D_B = \frac{1}{\sqrt{N}} = 3.2 \times 10^{-5} \text{ cm} \tag{A1}$$

A critical size bubble (Freon-22) at this dimension would have an internal pressure of

$$P_v = \frac{4\sigma}{D_B} + P_\ell = 0.29 \text{ MPa} \tag{A2}$$

where $\sigma \approx 0.015$ N/m. The saturation temperature at this pressure is $T_B = -15.6$°C and using a linear approximation for the error function,

$$\frac{T_i - T_B}{T_i - T_{\text{sat}}} = \frac{D_B}{2\sqrt{\alpha t}}, \tag{A3}$$

one can calculate the time required to develop, a sufficiently thick thermal boundary to establish film boiling. For example, with an interface temperature of 80°C and saturated Freon-22 at 0.1 MPa, the time required is 6.1×10^{-7} s, which corresponds to an acoustic transmission time of 5.1×10^{-7} s. With a liquid sonic velocity of 763 m/s, the diameter of a drop at the stability limit would be 195 μm.

E. N. Ganić
Department of Energy Engineering,
University of Illinois at Chicago Circle,
Chicago, IL 60680

W. M. Rohsenow
Department of Mechanical Engineering,
Massachusetts Institute of Technology,
Cambridge, MA 02139

On the Mechanism of Liquid Drop Deposition in Two-Phase Dispersed Flow

The deposition motion of liquid drops (the migration of drops toward the wall) in dispersed flow heat transfer is analyzed. Equations of drop motion penetrating the laminar sublayer are derived taking into account inertia forces arising from change in the velocity of drop, drag forces, buoyancy forces, gravity forces, lift forces (forces due to rotation of the drop inside laminar sublayer caused by high vapor velocity gradient) and reaction forces due to asymmetrical drop evaporation inside laminar sublayer. A new expression for the reaction force is derived. The application of the developed drop deposition model is illustrated by calculating several quantities of practical interest for analysis of heat and mass transfer in dispersed systems. Also, the model has been applied to explain the behavior of the dispersed flow boiling heat transfer data.

Introduction

The behavior of liquid drops suspended in a fluid stream, drop or dispersed flow, is of interest in a wide range of areas of technical importance. A knowledge of the trajectories of drops is important in the design of a number of industrial applications such as evaporators, nuclear reactors, spray coolers, and combustion devices involving sprays of liquid fuels. The theoretical approach in analyzing drop motion is generally similar to that of analyzing bubble motion. Equations of the motion of bubbles (bubbly flow) are analogous to drop motion. In spite of that, there are qualitative differences between the behavior of drops and bubbles. Those differences are most noticeable when the density difference between the components is high, as in gas-liquid systems at low pressure. In bubbly flow most of the inertia is in the continuous phase and as a result the drag forces on bubbles are large compared with their momentum. Bubbles therefore follow the motion of the surrounding fluid very closely in forced convection flow. Drops, however, take far longer to adjust to the motions of the surrounding gas. Also, in the dispersed flow heat transfer some additional specific forces are associated with the drop motion.

The most important phenomenon in the dispersed flow is the deposition motion of drops. By deposition motion, we mean the migration of drops toward the wall. Up to now, a theoretical analysis of drop deposition from the gas stream on the hot wall has not been reported. Also, no experimental data exist for the trajectories of drop inside the thermal boundary layer of the gas stream.

In recent years there have been several investigations related to the problem of particle migration in a shear field. When a particle enters a shear flow it moves across fluid streamlines as a consequence of fluid dynamic forces. This kind of a particle motion can also be a consequence of the temperature gradient in the fluid stream, as we will show in this study. The forces on a particle in the fluid stream analyzed in most of the studies [1] are inertia, drag, gravity, buoyancy and lift forces. Deposition of water drops in adiabatic turbulent downward air flow has been studied by Kondic [2]. The theoretical analysis of the rigid particle motion within the laminar sublayer has been made by Rouhiainen and Stachiewicz [3]. The characteristics of the motion of a drop in a two-phase boundary layer on a flat plate have been reported by Deich and Ignat'evskaya [4]. Denson, et al. [5] analyzed the motion of a single rigid sphere entrained in a glycerine-water solution flowing downward through a cylindrical tube. The comparison of the theoretical and experimental values for the deposition velocities of liquid drops and solid particles in dispersed flow systems has been summarixed by Liu and Ilori [6]. The experimental data obtained by Farmer [7] are included in their analysis. A stochastic model for deposition of particles and drops from turbulent gas streams was developed by Hutchinson, et al. [8]. The model was critically examined by McCoy [9]. In a paper by Gauvin, et al. [10] the work on spray dryers has been summarized and extended. A theory of a vaporizing drop motion in the laminar entry region of a straight channel with isothermal walls was presented by Bhatti [11].

In spite of a large number of published studies, the problem of drop deposition in dispersed flow with heat addition (dispersed flow heat transfer) has remained largely unexplored. This study is devoted to this problem.

Analysis

Dispersed flow heat transfer is a high void fraction flow. Because of this, the drop concentration is low, the interference of neighboring drops may be neglected, and the single drop may be treated as if it were alone in the medium. Also, since we are focusing our analysis on the drop motion through the boundary layer (laminar sublayer), we are assuming that the drop diameter is small compared to the thickness of this layer [12]. This is the kind of continum criterion to be satisfied. This basically means that the forces on the drop are de-

---

Contributed by the Heat Transfer Division for publication in the JOURNAL OF HEAT TRANSFER. Manuscript received by the Heat Transfer Division August 23, 1978.

pendent on the local vapor velocity and temperature of the stream.

In order to obtain some useful and reliable results the additional following simplifying assumptions for the motion inside the laminar sublayer are made:

1 The drop has a spherical shape.

2 Flow in the two-component, two-phase stream is laminar, two-dimensional, steady and incompressible.

3 The change of the drop diameter due to evaporation during deposition motion is not significant.

The list of forces during accelerated motion of the drop includes:

1) *Inertia Force,* 2) *Drag Force.* Since the drop Reynolds number for our conditions is close to one, the drag of the medium due to viscosity μ_g is given by the Stokes law [12].

The motion of the drop inside the boundary layer is unsteady, but it is customary to assume that the Stokes law may be used [13]. On the other hand, the drag problem becomes more complicated because of the evaporation of the drop and the possibility for circulation of liquid inside the drop. Evaporation can reduce the drag coefficient due to mass flux from the surface, for which Bailey, et al. [14] suggests the following correlation:

$$C_{D_0} = C_D/(1 + B) \tag{1}$$

The transfer coefficient B is generally small compared to unity for an evorating drop.

The correction to the drag coefficient due to the circulation of the liquid inside the moving drop is negligible for the conditions under consideration as shown in [12].

Also the Stokes drag for the sphere is derived for the case of uniform flow passing a sphere but Kohlman and Mollo-Christensen [15] experimentally demonstrated that shear flow does not affect the drag for the low Reynolds number.

3) *Gravity and Buoyancy Forces,* 4) *Lift Force.* Rotation of the drop occurs in the presence of the velocity gradient in the boundary layer. This is a well known phenomenon that the velocity gradient can cause a solid particle to rotate. At low Reynolds numbers rotation causes fluid entrainment, increasing the velocity on one side of the body and lowering the velocity on the other side. This tends to move the particle toward the region of higher velocity. Most of the experimental data related to the radial migration of solid particles and liquid drops in shear flow have been interpreted on the basis of the Rubinow-Keller lift force on a spinning translating sphere in an unbounded fluid at rest (or in uniform flow) at infinity. The force is given by [16]

$$\vec{F}_L = \frac{\pi a^3}{8}\rho_g\vec{\omega} \times (\vec{V} - \vec{V}_a)[1 + 0(\mathrm{Re}_a)] \tag{2}$$

For the steady motion inside the boundary layer the angular velocity of the sphere ω is equal to the angular velocity of the flow ω_g where

$$\omega_g \simeq -\frac{1}{2}\frac{dU}{dy} \tag{3}$$

This is experimentally verified by Kohlman and Mollo-Christensen [15] in the constant shear flow. Rather remarkably, the Rubinow-Keller lift force is independent of viscosity for small values of Re_a.

5) *Reaction Force.* As we mentioned before, this force is due to asymmetrical drop evaporation inside the boundary layer. There is a high temperature gradient in the fluid stream close to the heated wall and since the fluid temperature is larger than the drop temperature (saturation temperature assumed), the evaporation of the drop occurs. The difference in these two temperatures is larger for the drop side facing the wall than for the other side of the drop because of the temperature gradient in the fluid stream. This causes the vapor velocity generated on the drop side facing the wall (bottom side) to be higher than the vapor velocity generated on the other side. This produces a reaction force which tends to prevent a deposition of the drop on the wall.

The derivation of the reaction force is based on the following assumptions:

1 The temperature profile inside the boundary layer is a linear one:

$$T = T_s + (T_w - T_s)\left(1 - \frac{y}{\delta}\right) \tag{4}$$

2 The Nusselt number related to the drop heat transfer is given by the relation [17]

$$\mathrm{Nu}_a = 2.0 + 0.6\,\mathrm{Re}_a{}^{0.5}\,\mathrm{Pr}^{0.33} \tag{5}$$

and the circumferential variation of this number is negligible at low Reynolds number [18]. Since the drop Reynolds number for our condition is close to one, then

$$\mathrm{Nu}_a \simeq 2.6 \text{ as } \mathrm{Pr} \simeq 1. \tag{6}$$

Nomenclature

a = drop diameter, μm
a_c = drop deposition diameter, μm
A = surface, m^2
$B = C_p(T - T_s)/H_{lg}$ = transfer coefficient
C_D = drag coefficient
C_{D_0} = drag coefficient, equation (1)
C_p = specific heat, J/kg K
D = tube diameter, m
f = cumulative factor, equation (23)
$f_g = 0.0791/\mathrm{Re}^{0.25}$ = friction factor
F = force, N
F_{cy} = reaction force, equations (13) and (14), N
F_{ry} = reaction force, equation (16), N
g = gravitational acceleration, m/s^2
h = heat transfer coefficient, W/m^2 K
$H_{\ell g}$ = latent heat of evaporation, J/kg
$\mathrm{Nu}_a = ha/k_g$ = Nusselt number
p = pressure, N/m^2
$P(a)$ = drop size distribution fraction
$\mathrm{Pr} = C_p\mu_g/k_g$ = Prandtl number
$\mathrm{Re} = \rho_g U_0 D/\mu_g$ = flow Reynolds number
$\mathrm{Re}_a = \rho_g(V - V_a)a/\mu_g$ = drop Reynolds number
$S = U_0/u_0$ = slip ratio
t = time, ms, s, or hr
T = Temperature, K
u_0 = initial drop velocity in the x-direction, equation (19), m/hr
U = local vapor velocity, m/hr
$U_{\max}$ = maximum vapor velocity in the tube, m/hr
U_0 = mean or free stream vapor velocity, m/hr
$U^* = U_0[f_g/2]^{1/2}$ = friction velocity, m/hr
v_0 = drop deposition velocity, equations (20) and (21), m/hr
$\Delta u_0 = (U_0 - u_0)$ = slip velocity, m/hr
V = local vapor velocity (note: $V = U$), m/hr
V_a = local drop velocity, m/hr
x = axial distance, m
$\frac{dx}{dt}$ = drop velocity in the x-direction, m/hr
y = radial distance, m
$\bar{y}$ = mean film thickness, equation (15), m
$\frac{dy}{dt}$ = drop velocity in the y-direction, m/hr
δ = laminar sublayer thickness, μm
ϵ = thermal emissivity
κ = constant, equation (21)
μ = viscosity, N s/m^2
ν = vapor velocity, equations (11–13) and (15) m/hr
ν_y = vapor velocity in the y-direction, equation (13), m/hr
ρ = density, kg/m^3
σ = Stefan-Boltzman constant, W/m^2 K^4
ω = angular velocity, rad/s

Subscripts

a = drop
g = gas or vapor
ℓ = liquid
L = lift
s = saturation
w = wall
1 = upper half of the drop
2 = lower half of the drop
$c.s.$ = control surface

Equation (5) is good for small heat transfer rate. In the case of high evaporation rate (drop is very close to the hot wall), the correction to the Nusselt number is needed, similar to that suggested by Bailey [14].

3 The boundary layer thickness around the spherical drop moving in shear flow is approximately given by the potential flow theory. This thickness is then of the correct order of magnitude of drop diameter when the drop Reynolds number is close to one [15, 19].

As we mentioned before, the drop diameter is much smaller than the thickness of the laminar sublayer. This leads us to the conclusion that the drop residence time (deposition time or time measured from the moment a drop entered the boundary layer until it touches the wall) is much larger than the time for a heat diffusion through the drop boundary layer. As long as this conclusion is valid, the drop motion inside the boundary layer is influenced by the temperature distribution in it.

The evaporation of the drops occurs due to convective heat transfer from the fluid stream (vapor) to the drop and radiative heat transfer from the hot wall to the drop. The vapor participation in radient energy exchange is assumed to be small. We will first analyse the evaporation due to convective heat transfer.

Let the drop be at distance y from the wall (Fig. 1). The corresponding vapor temperature at that distance is $T_i(y)$. As we assumed the linear temperature distribution, the average vapor temperature for the upper and lower portions of the drop are then respectively

$$T_{i+1}(y) = T_i(y) + \frac{dT_i}{dy}\Delta y \qquad (7)$$

$$T_{i-1}(y) = T_i(y) - \frac{dT_i}{dy}\Delta y \qquad (8)$$

where $\Delta y = a/k$ and $k = 4$. The value of k was obtained by calculating the average fluid (gas) temperature for the upper or lower surface portion of the sphere. Introducing equation (4) into (7) and (8) gives

$$T_{i+1}(y) = T_i(y) - \frac{(T_w - T_s)}{\delta}\frac{a}{4} \qquad (9)$$

$$T_{i-1}(y) = T_i(y) + \frac{(T_w - T_s)}{\delta}\frac{a}{4} \qquad (10)$$

The average vapor velocities leaving the upper and lower portion of the drop are then [12], respectively,

$$\nu_1 = \frac{h}{H_{\ell g}\rho_g}\left[(T_w - T_s)\left(1 - \frac{y}{\delta}\right) - \frac{(T_w - T_s)}{\delta}\frac{a}{4}\right] \qquad (11)$$

$$\nu_2 = \frac{h}{H_{\ell g}\rho_g}\left[(T_w - T_s)\left(1 - \frac{y}{\delta}\right) + \frac{(T_w - T_s)}{\delta}\frac{a}{4}\right] \qquad (12)$$

where h is the heat transfer coefficient given by equation (6). Since $\nu_2 > \nu_1$ the upward force on the sperical drop is produced. We choose the volume of the spherical drop as a control volume. The upward force (reaction force) is then approximately given as the net rate of efflux of momentum through the control surface in the y direction

$$F_{cy} = \iint_{c.s.} \nu_y(\rho_g \vec{\nu}\, d\vec{A}) \qquad (13)$$

Introducing equations (11) and (12) into (13) gives

$$F_{cy} = \frac{\pi a^2 h^2}{4 H_{\ell g}{}^2 \rho_g}(T_w - T_s)^2 \frac{a}{\delta}\left(1 - \frac{y}{\delta}\right) \qquad (14)$$

It is seen from equation (14) that the reaction force, F_{cy}, is a function of the drop distance y from the wall for the given wall temperature and drop diameter.

If the distance of the drop from the wall is less than the drop boundary layer thickness, the expression (14) is not valid any more. In that case, the thermal conduction through the vapor film existing between the wall and the bottom of the drop is the most important mechanism of heat transfer. If we assume that conduction is in the y direction only, then the velocity of the vapor leaving the lower portion of the drop due to evaporation is

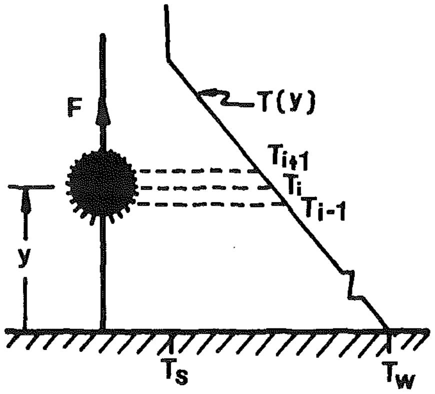

Fig. 1 Direction of the recation force acting on the evaporating drop in the thermal boundary layer

$$\nu_2 = \frac{k_g}{\bar{y}}\frac{(T_w - T_s)}{H_{\ell g}\rho_g} \qquad (15)$$

where $\bar{y}$ is the current mean film thickness between the wall and lower portion of the drop through which heat is conducted [20].

In this case the pressure increase in the vapor layer does influence the saturation temperature T_s and the latent heat of evaporation $H_{\ell g}$. Also, the effect of the wall roughness is important. Further details of this analysis include application of equation (13) and iterative evaluation of the saturation temperature [12]. They are omitted here because the most critical effects of the resistance forces on the drop occur near the edge of the laminar sublayer, or sufficiently far away from the wall. More clearly, whenever a drop approaches the distance that is equal to or less than the drop boundary layer thickness, deposition of the drop will occur. This will be shown below.

The evaporation of the drop due to radiative heat transfer becomes more important as the wall temperature increases. Assuming that the wall and the lower half of the drop are separated by a nonabsorbing, nonemitting medium, an approximate expression for the reaction force on the spherical drop due to radiation heat transfer reads,

$$F_{ry} = \frac{\pi a^2 \sigma^2}{4H_{\ell g}{}^2 \rho_g}(T_w{}^4 - T_s{}^4)^2 \left\{\frac{1}{([(1/\epsilon_\ell) - 1] + 1/0.682)^2} - \frac{1}{([(1/\epsilon_\ell) - 1] + 1/0.318)^2}\right\} \qquad (16)$$

A derivation of this equation is given in details in [12]. The total reaction force on the drop due to nonuniform evaporation is then the sum of the forces given by equations (14) and (16).

It is not likely that the shape of the spherical drop will be changed due to evaporation. As we mentioned before, a drop rotates inside the boundary layer due to velocity gradient. Therefore the whole surface of the drop is equally exposed to the hot wall during deposition.

For the case of the drop motion inside the tube the component of the reaction force due to radiation heat transfer, F_{ry}, is zero since the average configuration factors for radiation between the lower and upper halves of the drop and the wall have the same numerical values.

Other forces known to influence the drop motion in addition to the forces we analyzed so far are listed in [12]. Since they are important only for the motion of the submicron drop size their analysis is omitted here.

Differential Equations of Liquid Drop Motion (Trajectory of the Drop), Analyses and Discussion

Denoting the coordinates of the center of a spherical drop by x and y we write the equations of motion of a drop moving in the laminar sublayer when the main flow in the channel is directed vertically upward:

$$\rho_\ell \frac{\pi}{6} a^3 \frac{d^2x}{dt^2} = \frac{\pi}{16} a^3 \rho_g \frac{dU}{dy}\left(\frac{dy}{dt}\right)$$

$$- 6\pi \mu_g \frac{a}{2}\left(\frac{dx}{dt} - U\right) - (\rho_\ell - \rho_g)\, g \frac{\pi}{6} a^3 \quad (17a)$$

$$\rho_\ell \frac{\pi}{6} a^3 \frac{d^2y}{dt^2} = - \frac{\pi}{16} a^3 \rho_g \frac{dU}{dy}\left(\frac{dx}{dt} - U\right)$$

$$- 6\pi \mu_g \frac{a}{2}\left(\frac{dy}{dt}\right) + \frac{\pi a^2 h^2}{4H_{\ell g}{}^2 \rho_g}(T_w - T_s)^2 \frac{a}{\delta}\left(1 - \frac{y}{\delta}\right) \quad (17b)$$

Equation (17*a*) is obtained from the equilibrium of forces acting on the drop in the direction of flow (x-direction), x being taken as positive upward. Force acting upwards in the x-direction are taken as positive. Equation (17*b*) is obtained from the equilibrium of forces acting on the drop in the y-direction, y being taken as zero at the wall, increasing positively toward the center line of the channel (tube). The first terms on the right side of equations (17*a*) and (17*b*) represent the lift forces. The second terms on the right side of equations (17*a*) and (17*b*) represent the drag forces. The third term on the right side of equation (17*a*) represents the gravity and buoyancy force. The third term of the right side of equation (17*b*) represents the reaction force. The terms on the left side of equations (17*a*) and (17*b*) represents the inertial forces.

In order to solve the equations (17*a*) and (17*b*) the linear velocity profile of the gas stream across the laminar sublayer was assumed:

$$U = U_0 \left(\frac{y}{\delta}\right) \quad (18)$$

The laminar sublayer thickness was calculated assuming [21] that $y = \delta$ when $U = \frac{1}{3} U_{\max}$. The following initial conditions were used:

$$t = 0, \quad x = 0, \quad \frac{dx}{dt} = u_0 \quad (19)$$

$$t = 0, \quad y = \delta, \quad \frac{dy}{dt} = - v_0 \quad (20)$$

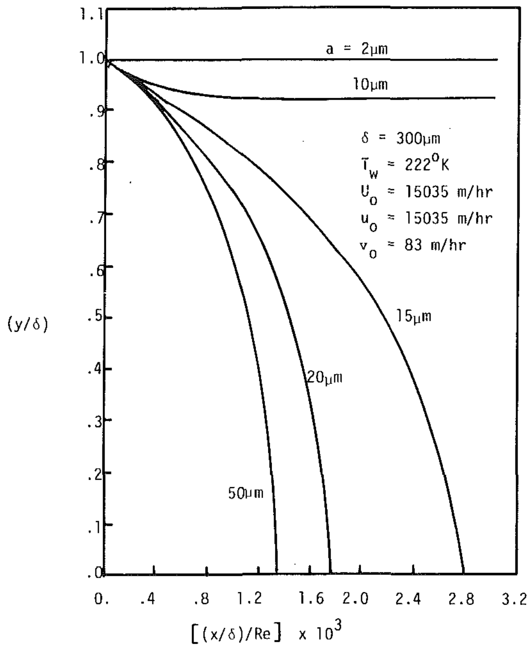

Fig. 2 The effect of the drop diameter on the drop trajectory

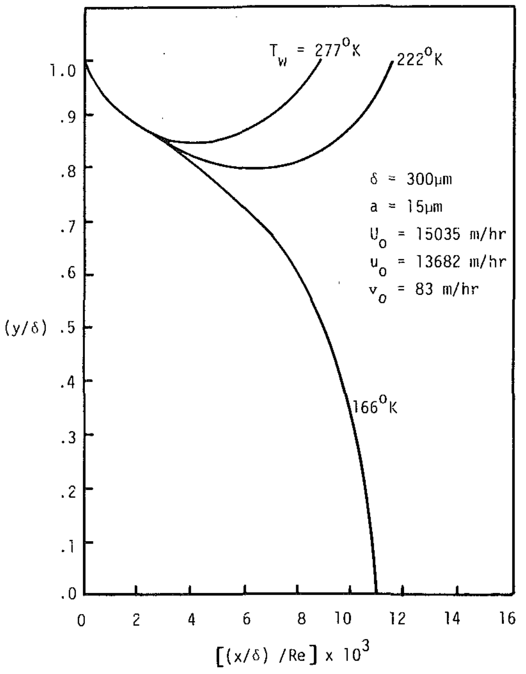

Fig. 3 The effect of the wall temperature on the drop trajectory

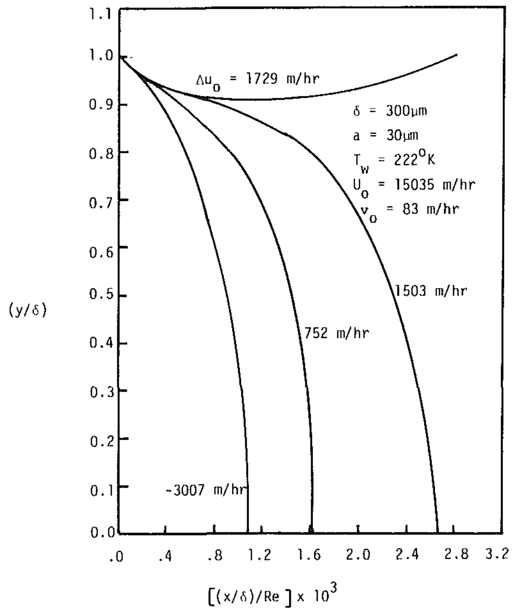

Fig. 4 The effect of the slip velocity on the drop trajectory

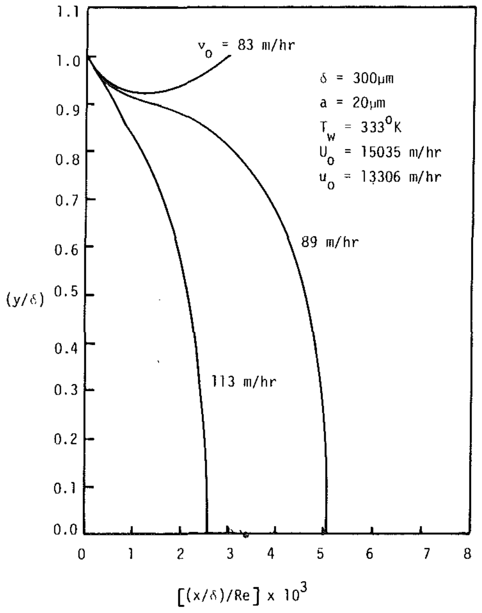

Fig. 5 The effect of the drop deposition velocity on the drop trajectory

The initial velocity in the radial direction v_0 is usually called the deposition velocity of the drop and it is imparted to the drop by free stream turbulence. Equations (17*a*) and (17*b*) are solved analytically in [12].

The main results of calculating the trajectories of the drop in the region of the laminar sublayer are presented in Figs. 2–5 where the effects of the drop diameter, wall temperature and the initial drop velocities in the x and y directions, on the drop trajectories, are demonstrated. Nitrogen data ($p = 140 \times 10^3$ N/m^2) were used in the calculation.

In order to summarize the studies on the drop motion inside the sublayer the history of the drop (the position and forces on the drop in the radial direction) that penetrated the sublayer to certain depth and was forced back to the main stream is presented in Fig. 6.

The same analysis for the drop that has been deposited on the wall is presented in Fig. 7.

From Fig. 6 one can see that the direction of the lift force has been changed at $y/\delta = 0.91$ as $(U - dx/dt)$ becomes negative, but the lift force has been overcome by the reaction and Stokes forces and the drop returned to the main stream. So if $(U - dx/dt)$ is negative, the lift force on the drop is directed toward the wall (equation (17*b*)), but this condition is not sufficient for the deposition of the drop. From Fig. 7 one can see that the drop penetrates sufficiently far into the sublayer where, at $y/\delta = 0.89$ the lift force overcomes the reaction and Stokes forces, and the drop begins to accelerate toward the wall.

When the drop is approaching a wall the drop Reynolds number is becoming larger than 1.0 due to drop acceleration. The same is true for the drop leaving the sublayer. In this case the Stokes expression for the drag of the drop is not applicable, but since the lift force dominates in these regions, the correction to the drag coefficient does not play a significant part on the drop trajectory. More details about drop trajectories on Figs. 6 and 7, including also the analysis of the forces on the drop in x-direction and the values of the drop Reynolds number, are given in [12].

The analysis of drop trajectories in Figs. 2–5 and 7, lead to the conclusion that the drops are being deposited on the wall with a definite impact. This is in qualitative agreement with the results of Cousin and Hewitt [22].

The significant conclusion concerning the drop trajectories in Figs. 2–7 is that since the most critical effects of the lift, reaction, and drag forces on the drop deposition take place sufficiently far away from the wall, the effect of the wall may be neglected, as assumed in equations (17*a*) and (17*b*). Also, the effect of the evaporation on the drag coefficient and drop Nusselt number is negligible as the values of the transfer coefficient B for $y > y_{cr}$ are small (y_{cr} is the critical distance, i.e., the distance where the critical effects of the forces occur). For example, the values of B for the trajectories in Fig. 4($\Delta u_0 = 1729$ m/hr), 5($v_0 = 83$ m/hr) and 6 at $y = y_{cr}$ are 0.035, 0.073, and 0.079, respectively.

Since the vapor superheat increases when a drop is approaching a wall, then B, which is a function of the local vapor superheat, increases and effects of the evaporation on the drag coefficient and drop Nusselt number may be significant. On the other hand, the lift force dominates when the drop is approaching a wall, as we mentioned before, and any correction for the drag coefficient and drop Nusselt number does not play a significant part on the drop trajectory.

Equations (17*a*) and (17*b*) were solved assuming that decrease of the drop diameter due to evaporation during deposition motion inside the sublayer was negligible. This assumption holds very well as shown in [12].

Little error is introduced in the analysis by assuming that the angular velocity of the drop is the same as that of the fluid stream. It is also shown in [12].

The Rubinow-Keller lift force was not derived for a shear flow but on the other hand, the experimental and theoretical studies of the drop trajectories by Dension, et al. [5], Goldsmith [23], Repetti [24], and Kondic [2] indicated that it yields a force of the correct order of magnitude for such a flow.

Model Application

In order to determine the drops deposition rate on the wall (i.e., the number of drops deposited per unit area of the wall and unit time) a drop size spectrum $P(a)$ was introduced into the analysis. Predictions of drops trajectories for $a_0 \leq a \leq a_m$ (where a_0 and a_m are minimum and maximum drop diameter, respectively, in dispersed flow under consideration) was done by increasing initial drop diameter a_0 step by step and solving equations (17*a*) and (17*b*) for each value of a. The initial boundary condition given by equation (20) was expressed as a function of the friction velocity,

$$v_0 = \kappa\, U_0 \sqrt{f_g/2} \tag{21}$$

Relation (21) was obtained from the summarized study of deposition of solid particles and liquid drop in two phase mixture by Liu and Ilori [6]. In our analysis we used $\kappa = 0.15$ as suggested by Iloeje, et al. [25].

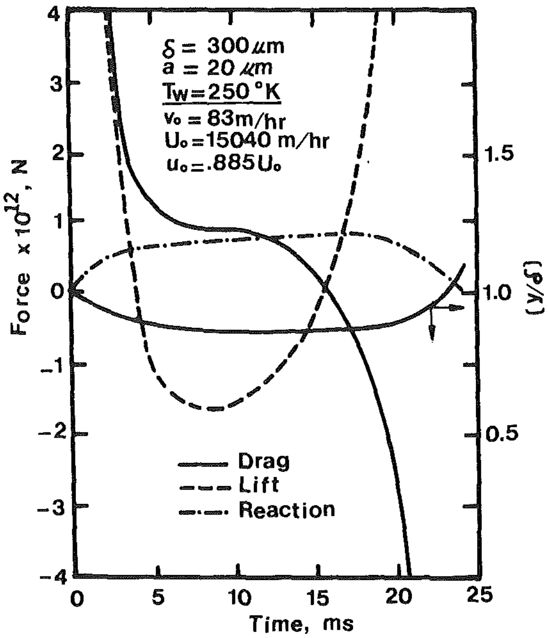

Fig. 6 History of the drop motion in the *y*-direction

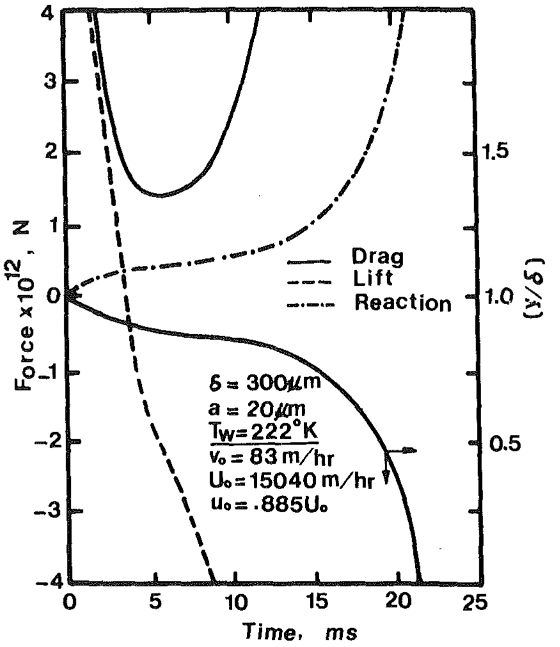

Fig. 7 History of the drop motion in the *y*-direction

Cumo, et al. [26] performed visual observations of the dispersed flow employing high speed cinematography. Analyzing more than 10,000 drops, they found that the drop velocity in the direction of flow is independent of drop diameter and almost equal for all drops. They also found that the drop transversal velocity profile in the flow channel is very close to the vapor velocity profile with local slip ratio close to one (see, for instance, Fig. 9 in their article). Since their observation was basically outside of the laminar sublayer one can assume that the drop velocities in the flow direction at the edge of the sublayer is

$$u_0 = \frac{U_0}{S} \tag{22}$$

where S is the slip ratio at the edge of the laminar sublayer. The methods of the evaluation of the slip ratio S are summarized in [12].

For a given mass flux G and vapor quality x the initial boundary conditions, equations (21) and (22), were evaluated. Equations (17a) and (17b) were then solved and trajectories obtained for each value of $a_0 < a < a_c$, for one particular value of the wall temperature. The value of a_c is the minimum size of drop deposited on the wall (drops with diameter $a_c < a < a_m$ were deposited on the wall and drops with diameter $a < a_c$ where returned to the main stream). The value of a_c increases with the wall temperature (Fig. 3).

For the known value of the deposition diameter a_c, and assumed drop size distribution low $P(a)$, the mass cumulative factor $f(a_c)$ is given as

$$f(a_c) = \frac{\int_{a_c}^{a_m} a^3 P(a)\, da}{\int_0^{a_m} a^3 P(a)\, da} \tag{23}$$

The summarized results of calculation of $f(a_c)$ for $G = 171$ Kg/sm^2 and $x = 0.31$ are presented in Fig. 8. When the wall temperature increase $f(a_c)$ decreases since a_c increases. The curve on Fig. 8 was obtained for the step increase in drop diameter of $\Delta a = 1$ μm, for one particular value of the wall temperature. The step increase in wall temperature was $\Delta T_w = 10$K and the drop size distribution was given by equation (8) of [27].

Knowing the cumulative mass of liquid drops deposited on the wall, the heat transfer to the liquid drops was determined by applying the semi-empirical correlation for the evaporation of the liquid drop on the hot wall. Details of this calculation and discription of the experiment are presented in [27]. Three sets of the dispersed flow heat transfer data are shown in Fig. 9. The solid line, Fig. 9, is related to the calculated total heat flux applying deposition model developed in this study. The dotted line is related to the calculated heat flux assuming no drops deposition occurs, i.e., only heat transfer to the vapor component of the flow is considered. It can be seen in Fig. 9 that as the wall temperature increases the heat flux decreases in the transition boiling region, because the number of the drops deposited per unit time (drop deposition flux [27]) decreases. This is in qualitative agreement with the results in Fig. 8. In the high temperature region (film boiling region), the drop deposition is becoming negligible and the heat transfer coefficient between the wall and flow is given by the single-phase relationship.

Summary and Conclusion

Deposition of liquid drop in dispersed flow with heat addition is analyzed. The expression for the reaction force on the drop due to nonuniform drop evaporation inside the laminar sublayer is developed. This force as well as other forces acting on the drop, lift, drag, gravity, buoyancy, and inertia, are analyzed and trajectories of the drops are calculated. A drop trajectory inside the laminar sublayer is prescribed by magnitude of the forces mentioned above.

The effects of the drop diameter, deposition velocity, slip velocity, and wall temperature on the drop trajectory are examined.

The application of the developed drop deposition model for the prediction of the dispersed flow heat transfer data is illustrated.

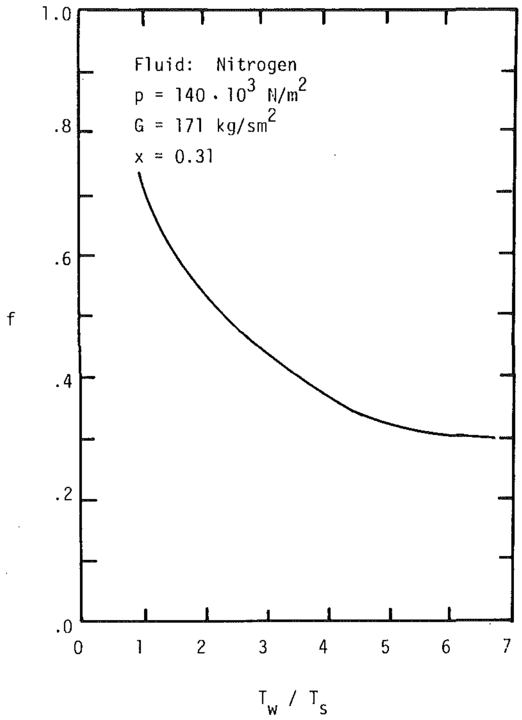

Fig. 8 The effect of the wall temperature on the cumulative deposition factor

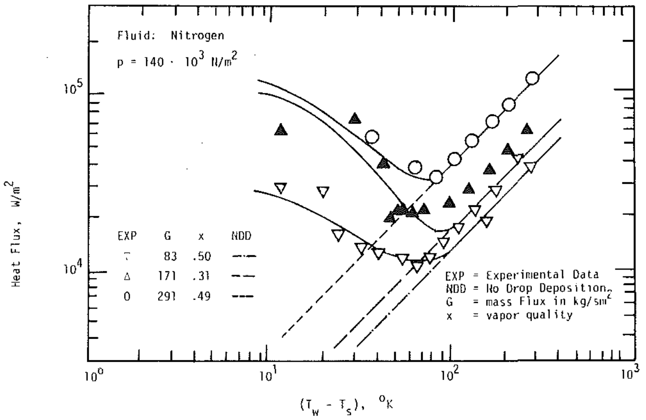

Fig. 9 Heat flux versus wall superheat

Acknowledgment

This work was supported by the National Science Foundation. Mr. R. Moose from UICC assisted in preparation of Figs. 2–5.

References

1 Brenner, H., "Hydrodynamic Resistance of Particles at Small Reynolds Numbers," *Advances in Chemical Engineering,* 1966, pp. 287–439.

2 Kondic, N. N., "Lateral Motion of Individual Particles in Channel Flow-Effect of Diffusion and Interaction Forces," ASME JOURNAL OF HEAT TRANSFER, Sept. 1970, pp. 419–428.

3 Rouhiainen, P. O. and Stachiewicz, J. W., "On the Deposition of Small Particles From Turbulent Streams," ASME JOURNAL OF HEAT TRANSFER, Sept. 1970, pp. 169–177.

4 Deich, M. E. and Ignat'evskaya, L. E., "Characteristics of the Motion of a Drop in a Two-Phase Boundary Layer on a Flat Plate", *Tepl. Vys. Tem.,* Vol. 9, No. 2, 1971, pp. 335–340.

5 Denson, C. D., Christiansen, E. B. and Salt, D. L., "Particles Migration in Shear Fields," *A.I.Ch.E. Journal,* Vol. 12, No. 3, 1966, pp. 589–595,

6 Liu, Y. H. and Ilori, T. W., "On the Theory of Aerosol Deposition in Turbulent Pipe Flow," University of Minnesota, Particle Technology Lab. Publication, No. 210, 1973.

7 Farmer, R., Griffith, P. and Rohsenow, W. M,, "Liquid Droplet Deposition in Two-Phase Flow," ASME Paper No. 70-HT-1, 1970.

8 Hutchinson, P., Hewitt, G. F., and Dukler, A. E., "Deposition of Liquid or Solid Dispersions From Turbulent Gas Streams: A Stockastic Model,"

Chemical Engineering Science, Vol. 26, 1971, pp. 419–439.

9 McCoy, D. D., "Particle Deposition in Turbulent Flow," M.S. Thesis, University of Illinois at Urbana, 1975.

10 Gauvin, W. H., Katta, S. and Knelman, F. H., "Drop Trajectory Predictions and their Importance in the Design of Spray Drayers," *Int. J. Multiphase Flow,* Vol. 1, 1975, pp. 793–816.

11 Bhatti, M. A., "Dynamics of a Vaporizing Droplet in Laminar Entry Region of a Straight Channel," ASME JOURNAL OF HEAT TRANSFER, Vol. 99, 1977, pp. 574–578.

12 Ganić, E. N., "Post Critical Heat Flux Heat Transfer," Sc. D. Thesis, M.I.T., 1976.

13 Hidy, G. M. and Brock, J. R., *The Dynamics of Aerocolloidal Systems,* Pergamon Press, 1970.

14 Bailey, G. H., Stater, I. W. and Eisenklam, P., "Dynamic Equations and Solutions for Particles Undergoing Mass Transfer," *Brit. Chem. Eng.,* Vol. 15, 1970, pp. 912–916.

15 Kohlman, D. L. and Mollo-Christensen, E., "Measurement of Drag of Cylinders and Spheres in a Couette-Flow Channel," *The Physics of Fluids,* Vol. 8, No. 6, 1965, pp. 1013–1017.

16 Rubinow, S. I. and Keller, J. B., "The Transverse Force on a Spinning Sphere Moving in a Viscous Fluid," *J. Fluid Mech.,* Vol. 11, 1961, pp. 447–459.

17 Bird, R. B., Stewart, W. E. and Lighfoot, E. N., *Transport Phenomena,* J. Wiley and Sons, New York, 1960.

18 Kreith, F., *Principles of Heat Transfer,* Chap. 9, Intext Educational Publishers, New York, 1973.

19 Prandth, L. and Tietjens, O. G., *Appkied Hydro- and Aeromechanics,* Dover, New York, 1934.

20 Gottfried, B. S., Lee, C. J. and Bell, K. J., "Leidenfrost Phenomenon: Film Boiling of Liquid Droplets on a Flat Plate," *Int. J. Heat Mass Transfer,* Vol. 9, 1966, pp. 1167–1187.

21 Krillov, P. L., and Smogalev, I. P., "Analysis of Heat Transfer Crisis in Terms of a Drop Deposition Model," *Tepl. Vys. Temp.* Vol. 11, No. 4, 1973, pp. 794–804.

22 Cousins, L. B. and Hewitt, G. F., "Liquid Phase Mass Transfer in Annular Two-Phase Flow: Droplet Deposition and Liquid Entrainment," AERE-R-5657, 1968.

23 Goldsmith, H. L. and Mason, S. G., *Colloid Science,* Vol. 17, 1962, p. 458.

24 Repetti, R. V. and Leonard, E. F., "Serge–Silberberg Annulus Formation: A Possible Explanation," *Nature,* Vol. 203, 1964, pp. 1346–1348.

25 Iloeje, O. C., Plummer, D. N., Rohsenow, W. M. and Griffith, P., "A Study of Wall Rewet and Heat Transfer in Dispersed Vertical Flow," M.I.T. Report No. 72718-92, 1971.

26 Cumo, M., Ferrari, G. and Farello, G. E., "A Photographic Study of Two-Phase, Highly Dispersed Flows," CNEN-PT/ING(72)19, 1972, pp. 241–268.

27 Ganić, E. N, and Rohsenow, W. M., "Dispersed Flow Heat Transfer," *Int. J. Heat Mass Transfer,* Vol. 20, pp. 855–866, 1977.; also, MIT Report No. 82672-97, 1976.

S. Banerjee
P. Yuen
M. A. Vandenbroek

Department of Engineering Physics,
McMaster University,
Hamilton, Ontario L8S 4M1
Canada

Calibration of a Fast Neutron Scattering Technique for Measurement of Void Fraction in Rod Bundles

A technique based on scattering and transmission of fast neutron beams has been developed for measuring void fraction in two-phase flow through rod bundles. Experiments indicate that the scattered neutron flux varies linearly with void fraction and is largely independent of phase distribution. Measurements of the transmitted neutron flux have been used to determine phase distribution (or flow regime). The technique gives good sensitivity and count rates and appears suitable for void fraction and phase distribution measurements in transient flow boiling.

1 Introduction

Two-phase flow through systems with complex internal geometries occur in many industrial situations. Examples are flow boiling in nuclear reactor cores and in steam generators, gas-liquid mass transfer in packed beds and fluidized bed reactors. To understand the transfer mechanisms and predict transfer rates in these systems, it is often desirable to know the volume fraction of each phase at a cross-section and the phase distribution (or flow regime). These quantities may be measured by a variety of techniques, many of which are discussed in a recent review [1]. Techniques based on transmission and scattering of various types of radiation are particularly attractive because there is usually no need to make system penetrations or disturb the flow. In particular, multi-beam gamma ray techniques have been developed by Banerjee, et al. [2] and Heidrick, et al. [3], among others, for measurements of both void fraction and phase distribution. However, gamma ray attenuation techniques only give good sensitivity in systems containing small amounts of high atomic number solid materials. This is because gamma rays are affected much more by the solid materials than the fluid in these situations. For example, gamma ray techniques are not really suitable for measuring void fraction in two-phase flow through rod bundles, because much of the beam attenuation and scattering is due to the bundle elements. Fast neutrons, however, are less affected by many solid materials than by a hydrogeneous liquid phase (like water or oil). Thus measurements of void fraction and phase distribution in systems like rod bundles or packed beds may, in principle, be made with good sensitivity using fast neutron scattering and transmission.

Void fraction measurement using neutron beams have been studied previously. Moss and Kelly [4], Harms, et al. [5], Younis [6], and Hancox, et al. [7] have used thermal neutron transmission. The basic technique is very similar to that based on gamma or x-ray transmission and relies on the exponential attenuation of intensity to give a measure of the average mixture density in the beam path. The thermal neutron technique is limited to relatively thin test sections in systems containing light water, since the neutrons are strongly absorbed. It is not really suitable for bundle geometries.

Semel and Helf [8] and Jackson, et al. [9] have considered thermalization of fast neutrons by hydrogeneous material as a basis for methods of determining hydrogen content in various materials. Because neutron thermalization theory involves complex interactions, the mathematical treatment for this approach is much more difficult than for thermal neutron transmission. Thus, the usual approach has been to develop standard calibration curves by passing fast neutron beams through samples of known hydrogenous material content. Interpretation of fast neutron transmission data in terms of void fraction is however difficult, and strongly dependent on phase distribution.

A further possibility is to use fast neutron scattering for void fraction measurement. This method has already been used to measure void fractions for two-phase flow in pipes. Preliminary work was reported by Rousseau [10] and Banerjee [11]. These investigations indicated that the technique was promising. However no systematic direct calibration was done. In order to increase confidence in the technique, we first undertook an extensive calibration program for void fraction in pipes [12]. These experiments indicated that for purposes of calibration, the gas phase could be adequately simulated by a relatively neutron transparent material like aluminum. Initial calibration experiments in rod bundles therefore used aluminum to simulate the gas phase. (The volume fraction of aluminum in the test section will sometimes be called void fraction in later sections). These initial tests were then followed by a series of experiments in which void fraction in air-water downflow through rod bundles was measured both by the neutron scattering technique, and directly, by trapping the flow between two quick closing valves and measuring the contents.

The calibration experiments using both aluminum to simulate the gas phase, and the flowing air-water mixture, are discussed in this paper.

Contributed by the Heat Transfer Division and presented at the Winter Annual Meeting, December 10–15, 1978, San Francisco, California. Manuscript received by the Heat Transfer Division August 24, 1978.

2 Experimental Aspects

Description of the Technique. The experimental technique has been discussed in our previous paper on void fraction measurements in pipes [12] and will not be detailed here. Details of hardware and experimental equipment are extensively discussed in the thesis by Yuen [13].

In brief, a collimated fast/epithermal neutron beam was produced at a beamport in the 5 MW(*t*) McMaster Nuclear Reactor. The cross section of the beam was rectangular. For the investigations described here, the horizontal sides of the rectangle were 100 mm wide and the vertical sides were 10 mm high. (We have also experimented with 100 mm long americium/beryllium line sources of neutrons and these appear to give acceptable beams). The neutron beam is made incident on the test section containing the two-phase mixture, and the scattered and transmitted flux are counted. If the incident beam is of uniform intensity at a test section cross-section, then the scattered thermal flux would, to a first approximation, depend on the mass of hydrogeneous material at the cross-section and not on its distribution. This is because several collisions (primarily with hydrogen) are required to downscatter the neutrons into the thermal region. Therefore, the thermal neutrons do not convey information regarding the position of the hydrogeneous material.

On the other hand, the transmitted flux may be counted with collimated detectors and this gives a measure of the amount of hydrogen in the detector's collimation zone. (Gamma beams would give similar results, but the attenuation is much more sensitive to the amount of high atomic number material in the detector collimation zone, than to the amount of hydrogeneous material). Thus by counting the transmitted neutron flux at several locations, the distribution of hydrogeneous material can be reconstructed enough that the main two-phase flow regimes can be determined as discussed later.

Experimental Setup. A plan view of the experimental setup is shown in Fig. 1. The neutron beam is passed through cadmium sheets to remove thermal neutrons before being made incident on the test section. The axis of the neutron beam is perpendicular to the test section axis. The scattered flux is counted by a detector with its axis perpendicular to both the beam and test section axes. The scattered flux is collimated so that the test section lies in the field of view of the detector.

The transmitted neutrons are counted by detectors placed with their axes parallel to the beam axis. The field of view of each detector is collimated so that only a portion of the transmitted beam is counted. The transmitted flux profile may be measured by moving the detector across the beam or by placing several detectors in the beam. For the experiments described here the transmitted beam profile was determined by moving a detector with a collimated field of view in the horizontal plane.

The first series of experiments was done with aluminum being used to simulate the gas phase. This appeared to be a reasonable first step based on our experience with void fraction measurements in pipes [12]. However, to verify that this calibration technique was indeed adequate for rod bundles, a series of experiments was done in the portable air-water loop shown in Fig. 2. The rod bundle test section was placed between two quick closing gate valves. To minimize inlet and outlet effects, rod bundle sections were placed on either side of the test section as shown in the figure. The void fraction in the test section was measured directly by trapping the air-water mixture between the quick closing valves and measuring the amount of trapped water. Each measurement was repeated several times to obtain an ensemble average. Considerable care was needed to make the 100 mm gate valves since they could be closed in about 45 ms, and with a maximum mismatch of about 20 ms. The details are not discussed here but may be obtained from the senior author.

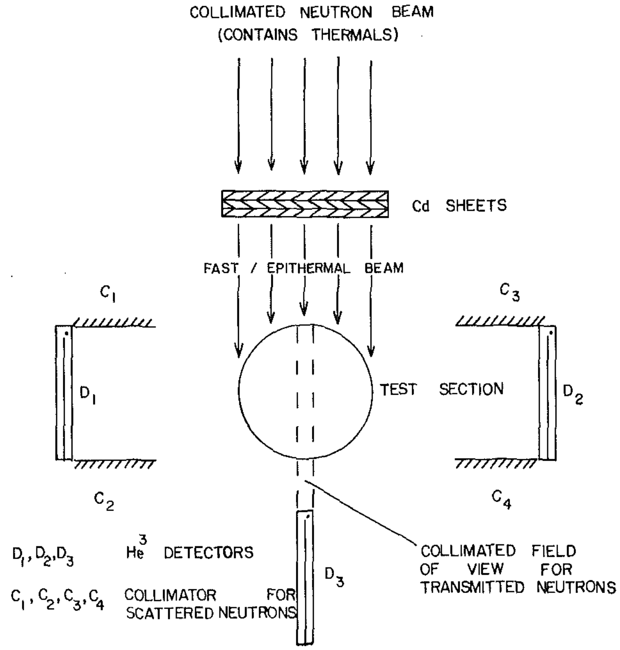

Fig. 1 Plan view of experimental setup showing position of detectors, test section and neutron beam

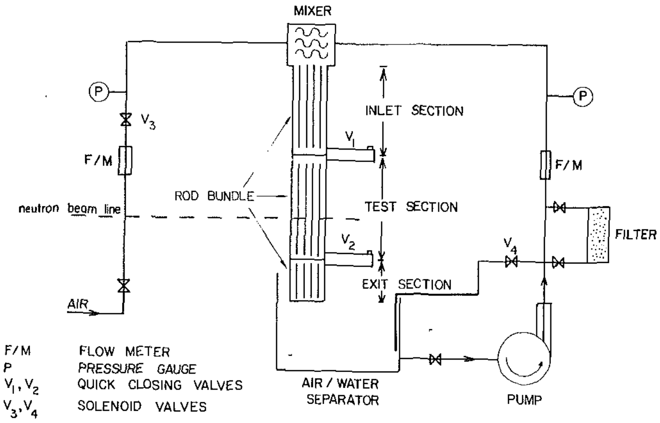

Fig. 2 Diagram of air-water loop

3 Results and Discussion

Aluminum-Water Measurements. To determine how the scattered and transmitted flux were related to void fraction and phase distribution a series of experiments was first done with aluminum water mixtures.

The rod bundles used were of the geometry shown in Fig. 3. (This bundle geometry is of direct relevance to Canadian heavy water reactors, but the conclusions are of significance for other geometries.) The rods were empty zirconium tubes and meant to simulate direct resistance heated bundles. Such bundles are used in many critical heat flux and nuclear reactor safety related experiments.

Experiments were done by filling the bundle subchannels with water and then displacing the water with aluminum rods. The aluminum rods simulated the gaseous phase and were distributed in several different overall patterns such that the water was mainly in (1) the central region of the bundle (core pattern) (2) the periphery of the bundle (annular pattern) or (3) on one side (stratified pattern). The overall patterns were approximately as shown in Fig. 4. These are simulated overall void distributions that might develop in two phase flow through the bundle.

For the experiments at the higher void fractions (>0.6), the subchannels were completely filled with aluminum inserts and holes were drilled in these inserts to accommodate water. The overall distribution

Nomenclature

$N(\alpha)$ = scattered neutron count rate at void fraction α

α = actual or directly measured void fraction

α_E = void fraction from the scattered neutron measurements

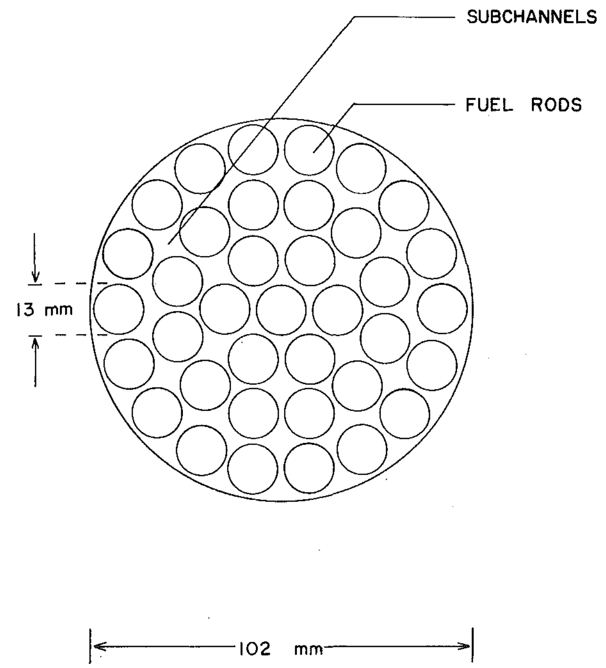

Fig. 3 Cross-sectional view of rod bundle used

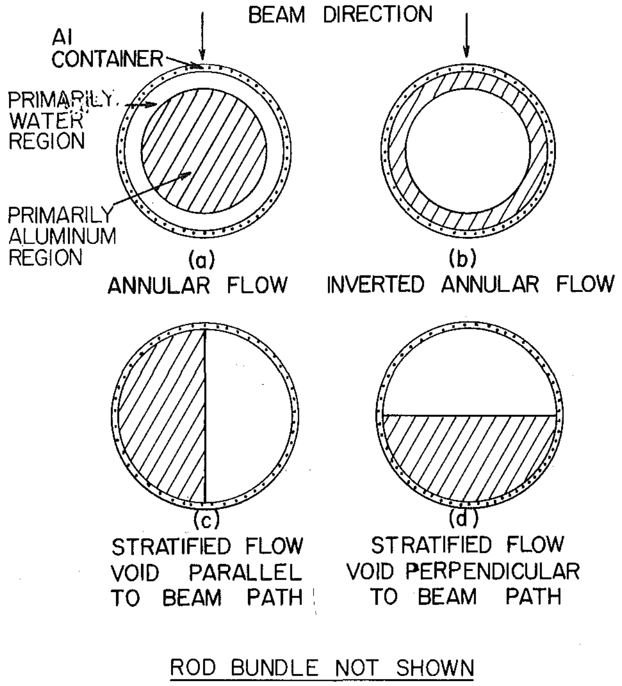

Fig. 4 Cross-sectional view of aluminum shapes for $\alpha = 0.5$

of the water was again varied to give core, annular and stratified patterns.

The volume fraction of aluminum (i.e., the void fraction) was known and compared with the void fraction calculated from the scattered neutron count rate using

$$\alpha_E = \frac{N(0) - N(\alpha)}{N(0) - N(1)} \qquad (1)$$

The results obtained are shown in Fig. 5. The void fractions based on the scattered neutron flux were calculated using equation (1). There is one set of results at void fractions between 0.6 and 0.7 consistently higher than the actual values. This is the lowest void fraction at which the aluminum inserts were made to fill the subchannels completely, with holes drilled to accommodate the water. It was found after the experiment that the holes had not been drilled deep enough and that the actual void fraction (volume fraction of aluminum) in the beam path was somewhat higher than the "actual" values shown in Fig. 5. Except for this set of results there is good agreement between the actual void fractions and those calculated from the scattered neutron flux for all the void distributions tested.

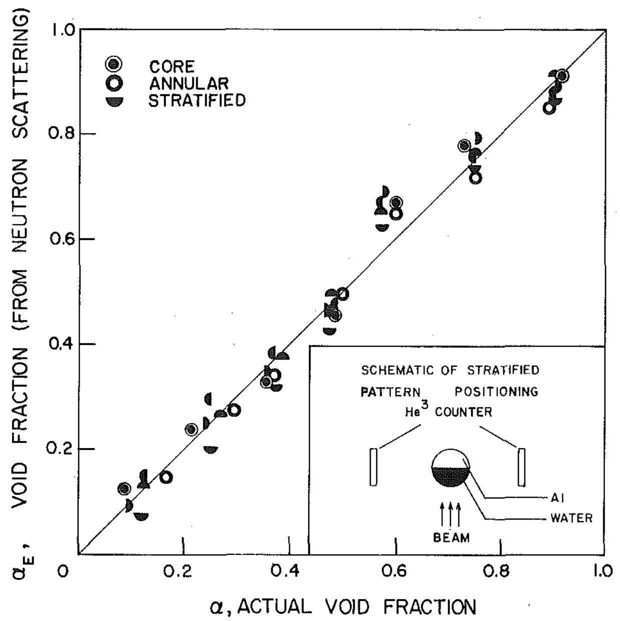

Fig. 5 Comparison of void fractions in rod bundle determined by neutron scattering method with actual values. (Count rates were averaged for two detectors on either side of test section)

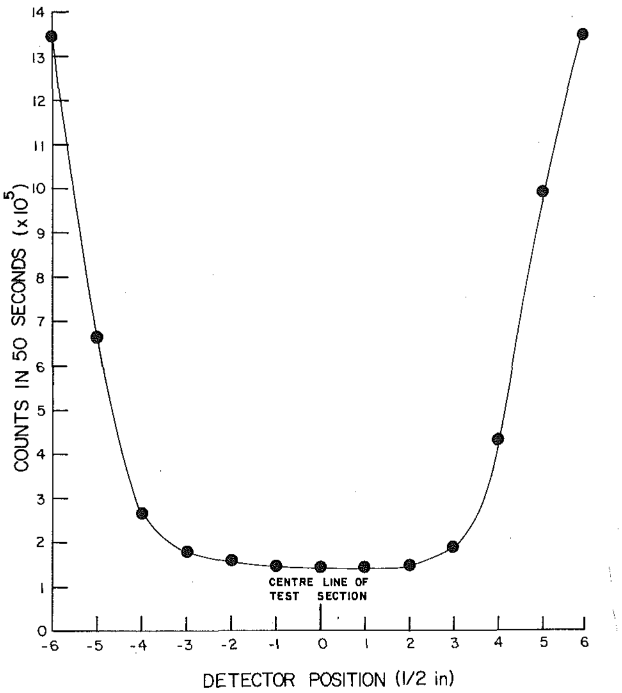

Fig. 6 Transmitted flux profile with rod bundle subchannels filled with water. Counts are shown over 50 seconds because beam was reduced by a factor of 50 from maximum value to allow use of existing electronics system for detectors.

The transmitted flux was also measured with collimated 25.4 mm diam He^3 counters. With the bundle subchannels full of water (α = 0) the transmitted flux had the profile shown in Fig. 6. As expected the count rate is reduced most in the beam containing the greatest path length through the water. Figs. 7 and 8 show the transmitted flux profile for different void fractions and void distributions.

The actual count rate of the transmitted beam is shown rather than

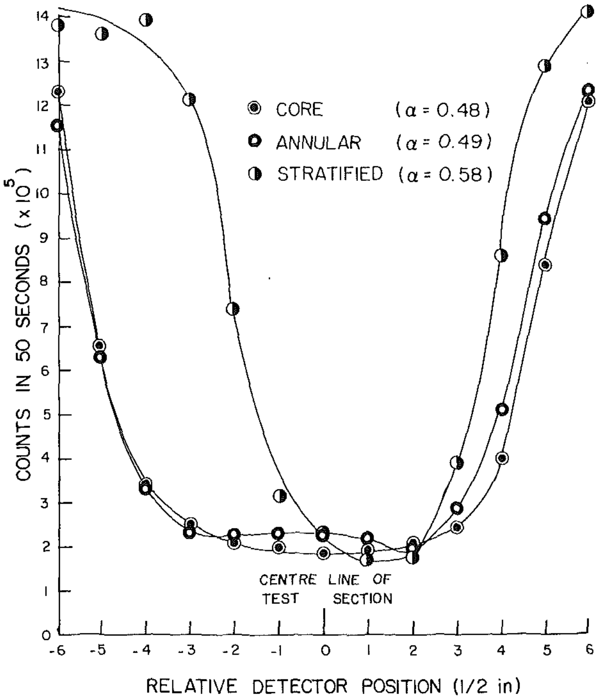

Fig. 7 Transmitted beam profiles for various void distributions in rod bundles, $\alpha \sim 0.5$

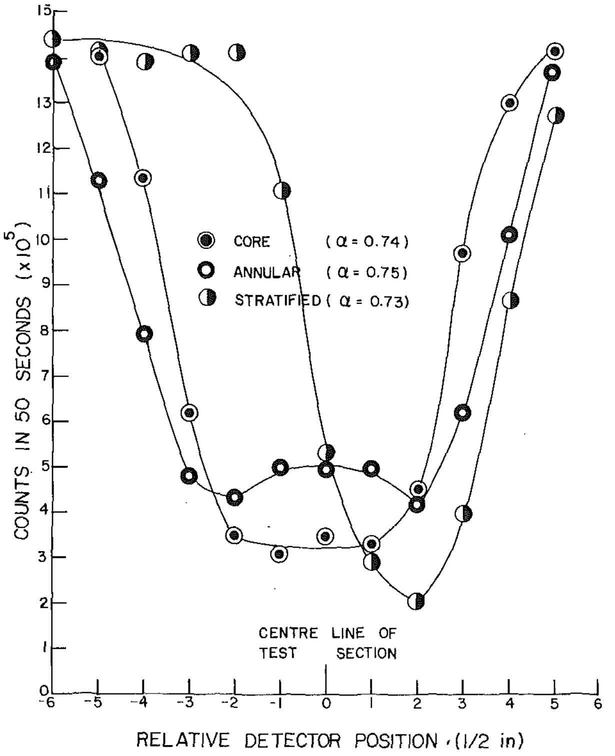

Fig. 8 Transmitted beam profile for various void distributions in rod bundles, $\alpha \sim 0.75$

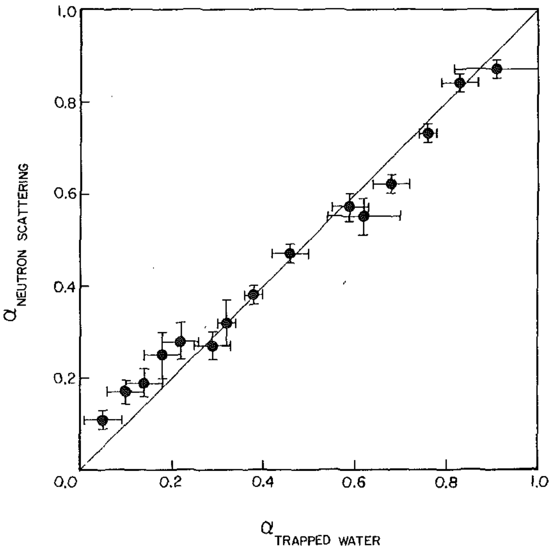

Fig. 9 Comparison of void fractions determined by neutron scattering method and values measured by trapping air-water downflow through rod bundles between two quick closing gate valves

void fraction in these figures because no simple relationship exists between the transmitted flux and the void fraction. This is because neutron thermalization, absorption and scattering in a rod bundle geometry is difficult to calculate. Rather we wish to use the transmitted flux, at this stage, as a qualitative indicator of flow regime rather than as a measure of void fraction. From this viewpoint, it is evident that the count rate is reduced most in the regions where the path length through the hydrogeneous material is the greatest. For example, the count rate is a minimum at the center for the inverted annular flow pattern, where it is a minimum close to the two edges for the annular flow pattern in Fig. 8. The same type of transmitted flux profile has been observed in applying the technique to phase distribution measurements in pipes [12]. The patterns are somewhat less sharply defined in rod bundles than in pipes because some subchannels in the bundle experiments always contain a mixture of water and aluminum, i.e., the void distribution is not obtained by filling some subchannels only with water and some only with aluminum. However, there appears to be sufficient difference between the transmitted flux profiles to allow determination of the various overall patterns for the higher void fractions shown in Fig. 8. For lower void fractions (Fig. 7), stratified flow can be clearly distinguished from the other flow pattern. However, annular flow cannot be clearly discriminated from core flow at these low void fractions.

Air-Water Experiments. Following the aluminum-water experiments, the neutron scattering method was calibrated using an actual two-phase flow system. The void fraction calculated from the scattered neutron flux using equation (1) was compared with void fractions measured by trapping water between two quick closing valves in the air-water loop described previously. The results are shown in Fig. 9. The void fraction measured by trapping water is an average of several measurements.

The main sources of error in the experiments have been analysed and are discussed in Yuen's thesis [13]. The error-bars on the results shown in Fig. 9 show the 95 percent confidence limits calculated on the basis of this analysis for both the trapped water and the neutron scattering method.

It is evident from the figure that the void fractions calculated from the scattered neutron flux, and measured by trapping the two-phase flow, are in good agreement. This appears to be true over the whole range of void fraction and for all the flow regimes obtained in vertical flow, within the precision of the measurement techniques.

4 Conclusions

From the results obtained it appears that fast neutron scattering may be used to determine void fraction for two-phase flow in complex geometries like rod bundles. The scattered neutron flux varies linearly with void fraction and is essentially independent of void distribution. Some of our recent unpublished work in packed beds made of alumina beads suggests the same conclusion. The transmitted neutron flux profile may also be used to indicate the overall void distribution pattern.

Work is continuing on developing a portable instrument for making these measurements using americium/beryllium line sources to produce the fast neutron beams. Void fractions are also being measured in packed beds to determine whether the technique can be used.

With portable neutron sources, drift becomes more of a problem and methods of compensating for this are being investigated. The most promising technique at present, appears to be the use of a reference beam from the source to correct for drift. More details regarding the work with portable sources will be provided in subsequent publications.

Acknowledgment

This work was supported by the Chalk River Nuclear Laboratories of Atomic Energy of Canada Limited.

References

1 Atomic Energy Research Establishment, Harwell, England, "Experimental Methods in Two-Phase Flow Studies—Final Report," Electric Power Research Institute Report EPRINP-118, March 1976.

2 Banerjee, S., Heidrick, T. R., Saltvold, J. R., and Flemons, R. S., "Measurement of Void Fraction and Mass Velocity in Transient Two-Phase Flow," presented at OECD/NEA Specialists Meeting on Transient Two-Phase Flow, Toronto, Aug. 1976.

3 Heidrick, T. R., Saltvold, J. R. and Banerjee, S., "Application of a 3-Beam γ Densitometer to Two-Phase Flow Regime and Density Measurements," *AIChE Symposium Series,* Vol. 73, No. 164, 1976, pp. 234–255.

4 Moss, R. A., and Kelly, A. J., "Neutron Radiographic Study of Limiting Planar Heat Pipe Performance," *Int. J. Heat and Mass Transfer,* 13, 1970, pp. 491–502.

5 Harms, A. A., Lo, S., and Hancox, W. T., "Measurement of Time-Average Voids by Neutron Diagnosis," *J. Appl. Physics,* 42, 1971, pp. 4080–4082.

6 Younis, M. H., "Void Disturbances in Two-Phase Flow Systems," Ph.D. Thesis, McMaster University, 1978.

7 Hancox, W. T., Forrest, C. F., and Harms, A. A., "Void Determination in Two-Phase Systems Employing Neutron Transmission," *Proceedings of AIChE-ASME Heat Transfer Conference,* Denver, Colorado, ASME Paper No. 72-HT-2, 1972.

8 Semel, S., and Helf, S., "Measurement of Low Concentrations of Moisture by Fast Neutron Moderation," *Int. J. App. Rad. and Isotopes,* 20, 1969, pp 229–239.

9 Jackson, C. N., Alleman, R. T., and Spear, W. G., "Neutron Densitometer for Measuring Void Fraction in Steam-Water Flow," *Trans. Am. Nucl. Soc.,* 11, 1968, pp. 366–367.

10 Rousseau, J. C., Czerny, J., and Reigel, B., "Void Fraction Measurements During Blowdown by Neutron Absorption and Scattering Methods," presented at OECD/NEA Specialists Meeting on Transient Two-Phase Flow, Toronto, Aug. 1976.

11 Banerjee, S., "Radiation Methods for Two-Phase Flow Measurements," Invited lecture at USNRC Two Phase Instrumentation Review Meeting, Washington, Jan. 1977.

12 Banerjee, S., Chan, A. M. C., Ramanathan, N., and Yuen, P. S. L., "Fast Neutron Scattering and Attenuation Technique for Measurement of Void Fractions and Phase Distributions in Transient Flow Boiling," *Proc. Sixth Int. Heat Transfer Conf.,* Vol. 1, 1978, pp. 351–355.

13 Yuen, P. S. L., "Fast Neutron Scattering and Attenuation Technique for Measurement of Void Fractions and Phase Distributions in Transient Flow Boiling," M.Eng. Thesis, McMaster University, 1978.

R. L. Collins
Associate Professor,
Department of Mechanical Engineering,
University of Louisville,
Louisville, KY

R. B. Lovelace
Design Engineer,
Perry Ocean Engineering,
Riviera Beach, Fla.

Experimental Study of Two-Phase Propane Expanded through the Ranque-Hilsch Tube

When air or other gases flow through the Ranque-Hilsch vortex tube, the well known temperature separation effect can be produced. This effect has been utilized for many purposes and is especially useful in providing cooling in applications not requiring the higher efficiencies of more sophisticated refrigeration systems. When the inlet fluid to the tube becomes a mixture of saturated liquid and vapor, one intuitively expects the temperature separation to diminish. Experimental data were obtained using propane to quantitatively determine the deterioration of temperature separation when the condition of the inlet fluid becomes a saturated mixture. Observations indicate that temperature separation diminishes rapidly for inlet qualities of less than 80 percent due largely to the decrease in "hot side" temperature. For qualities above 80 percent, significant temperature separation can be maintained.

Introduction

The Ranque-Hilsch vortex tube is a simple device which can separate a single inlet fluid stream into two fluid streams of high and low temperatures. Although the device itself is simple, having no moving parts, the fluid mechanics and heat transfer effects are quite complicated. Experimental and theoretical studies have been made to analyze this phenomenon. Examples of the literature available are Fulton's [1, 2] and Scheper's [3] observations on the theory and application of the Ranque-Hilsch vortex tube; Lay's [4, 5] contributions to the complex flow problem and the excellent works on general vortex flows [6–10]. A more recent general discussion and collection of experimental data is found in Soni's thesis [11] and his note [12].

This paper is primarily concerned with the gross or overall flow effects obtained when the inlet fluid to the vortex tube becomes a two-phase, liquid-vapor mixture. A standard counter-flow vortex tube configuration is used with the tube mounted vertically, cold outlet down. It is intuitively obvious that the vortex tube's performance should diminish when condensation occurs and the cooler liquid collects on the outer, hot walls. It is expected that the higher temperature outer vortex will be cooled appreciably by the interacting liquid and thereby reduce the hot side discharge fluid temperature. Experiments with propane are performed to quantitatively observe the performance of the vortex tube under these conditions. The results indicate that temperature separation does diminish as the inlet quality is reduced but that significant separation is possible when the quality is not too low.

Apparatus

The test apparatus was designed so that a standard propane tank could be used to supply the vortex tube. In order to vary the inlet conditions to the tube a pressure regulator and heat exchanger were placed between the propane supply tank and the vortex tube inlet. A schematic diagram of the test system is shown in Fig. 1.

Propane flows from the supply through the pressure regulator and heat exchanger No. 1 into the vortex tube inlet. Hence the pressure and temperature or quality of the vortex tube inlet fluid can be controlled with this equipment. The line is insulated from the supply tank to the vortex tube so that the water flowing through the heat exchanger is adiabatic to the surroundings. All test runs were performed with the pressure, p_1 regulated to 100 psig (.689 MN/m^2) while cooling water was run through the heat exchanger at varying rates to produce the desired propane inlet temperature T_1 or quality, x_1.

The vortex tube is illustrated on Fig. 2. As shown in Fig. 1, it is mounted vertically with the hot tube mounted upward. Cold side and hot side temperatures (T_2, T_3) are measured at the tube discharges. The flow continues through the No.'s 2 and 3 heat exchangers and flow meters. These discharge heat exchangers are provided to superheat the discharge fluid so that standard gas rotameters can be used to measure flow rates. Steam is passed through these heat exchangers to provide sufficient heat transfer for superheating the discharged propane. The discharge pressures are measured between the heat exchangers and the flowmeters. After the propane passes through the flowmeters it is collected and burned. Tests were performed on the vortex tube both with and without insulation at normal room temperature, ambient conditions.

All temperatures were measured using copper-constantan thermocouples terminated at a Leeds and Northrup, Speedo-Max, 12 channel recorder. The thermocouples measuring T_0, T_1, T_2, and T_3 were inserted through small, sealed support tubes which allowed the

---

Contributed by the Heat Transfer Division for publication in the JOURNAL OF HEAT TRANSFER. Manuscript received by The Heat Transfer Division June 15, 1978.

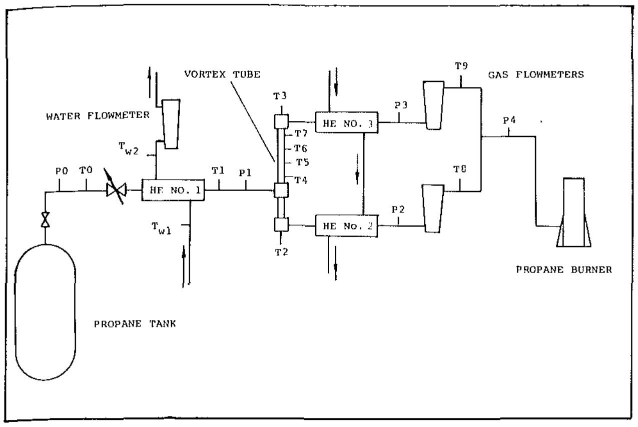

Fig. 1 Schematic diagram of vortex tube test system

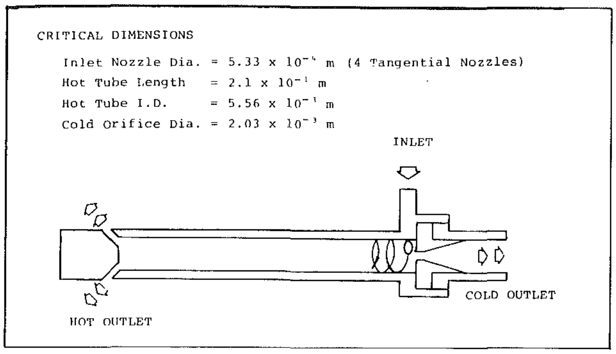

Fig. 2 Schematic diagram of vortex tube

junction to be properly positioned in the flow field. The junction and insulated wires were epoxied to the support tube so that the junction extended about 1/8 in. beyond the end of the support tube and into the flow field. Four thermocouples (T_4, T_5, T_6, T_7) were bonded to the outside of the hot tube to indicate possible temperature gradients along this tube. Pressures were measured with Bourdon Tube gages and well type H_2O manometers as needed. Since the estimated maximum pressure drop in the pipe downstream from the hot and cold tube discharges is only about 80 N/m^2, the exact location of the pressure taps for p_2 and p_3 is not important for these gross performance tests.

The measurement instruments used were standard, commercial type and therefore the expected errors are as normally found in such instruments. For these tests the maximum likely errors are approximately: T_0, T_1, T_2, T_3 = ±1.2 C; P_0, P_1 = ±.015 MN/m^2; P$_2$ = ±.003 MN/m^2; P$_3$ = ±.008 MN/m^2; $\dot{m}$ = ±8 E-5 kg/s; $\dot{m}_w$ = ±1.7 E-4 kg/s

Test Procedure

The data were taken so that the tube inlet fluid was initially in the superheated vapor region and then, holding the inlet pressure p_1 constant, the inlet temperature T_1 was reduced (using cool water in heat exchanger No. 1) until the saturated vapor state was reached. Further removal of heat in the exchanger causes small liquid droplets to form so that the inlet state becomes a two-phase mixture with quality dependent upon the amount of heat removed in the exchanger.

Data taken at a fixed vortex tube inlet condition are called a test. For each test there are several sub-tests on runs obtained by varying the flow through the hot side discharge at the flowmeter. The discharge cone on the vortex tube hot side was left in its full open position and the flow rate was adjusted with the hot side flowmeter needle valve. The hot side flowmeter would initially be closed, with the cold side full open. Propane valves would then be opened to begin the test. The recorder would print out the response of each thermocouple as different temperature effects were noted along the tube and the system. The thermocouples were monitored and when steady flow conditions persisted for a significant time, the pressures and flowrates were recorded. The next run would begin by readjustment of the hot side valve. Throughout a test only the hot side flowrate was changed to vary the propane flowrate ratio. Occasionally, the inlet pressure regulator needed slight adjustment. It was noted that the total flowrate of propane did not vary significantly throughout a test and hence the inlet quality (or temperature) could be maintained essentially constant without changing the water flowrate of the inlet heat exchanger. On some occasions surging was noted while taking flow readings. An average value was recorded and the surging effects noted in the log.

Data Analysis and Results

A sample of the test results are shown in Tables 1 and 2. For brevity, only selected results from [13] and follow up testing are presented in this paper. The temperatures shown were obtained directly from the temperature recorder. The pressures listed are absolute MN/m^2 (=10^6 N/m^2). The flowrates of propane in the hot and cold side tubes were measured using rotameters calibrated for standard air and corrected to the propane flow conditions as discussed in [14]. The total propane flow $\dot{m}$ is given in Tables 1 and 2 along with the "cold fraction" μ which is the ratio of cold side flow to total flow.

The inlet quality x_1 was determined by writing the First Law of Thermodynamics or an "energy balance" for the inlet heat exchanger. Since the inlet piping is insulated it is assumed that no significant heat transfer takes place with the surroundings. Therefore, the total enthalpy entering heat exchanger No. 1 is the total enthalpy of propane leaving the supply tank (h_0) determined at p_0, T_0. An energy balance for the heat exchanger gives:

$$h_1 = h_0 - C_p(T_{w2} - T_{w1})\dot{m}_w/\dot{m} \quad (1)$$

The enthalpy of saturated liquid and vapor at the inlet to the vortex tube are h_{f1} and h_{g1} which are functions of p_1. The quality x_1 is written in terms of these quantities as:

$$x_1 = (h_1 - h_{f1})/(h_{g1} - h_{f1}) \quad (2)$$

Therefore the measured values T_{W_1}, T_{w_2}, $\dot{m}_w$, p_0, p_1 and $\dot{m}$ are sufficient to determine the quality x_1. The values for enthalpy of propane were obtained from the data provided in [15]. The specific heat of water used is C_p = 4186 J/kgK. Note that, although quality is not strictly defined for nonsaturated mixtures a value may be computed even in the superheated vapor region where $h_1 > h_{g1}$ so that $x_1 > 1$. This concept is used in presenting data as a function of quality.

In Tables 1 and 2 a single column is used to present either temperature T_1 or quality x_1. When the inlet is superheated T_1 is presented and when it is a saturated mixtured x_1 is given.

The test results indicate that total flowrate remained constant within about ±8 percent or less. The flowrate measurements exhibit a peculiar effect in tests 8, 12, and 13 in that the total flowrate diminishes slightly when the hot side flow valve is first opened. Although contrary to intuitive reasoning, this effect was measured in several cases and is another example of the complicated flow phenomena of the counter flow vortex tube.

The basic objective of these tests was to observe the vortex tube

Nomenclature

C$_p$ = specific heat of water
h = specific enthalpy
$\dot{m}$ = mass flowrate
p = pressure
q = specific heat transferred
T = temperature
x = quality
μ = cold fraction

Subscripts

0, 1, 2, . . . 7 = locations of Fig. 1
c = cold side vortex tube
h = hot side vortex tube
f = flüssig or liquid (saturated)
g = gas or vapor (saturated)

Table 1 Measured and reduced test data. Vortex tube not insulated P_1 = .791 MN/m^2

Test-Run	T_1/x_1 c/−	P_2 MN/m^2	T_2 C	P_3 MN/m^2	T_3 C	$\dot{m}x10^2$ kg/s	μ −
8-1	38.9	.103	25.0	.229	25.0	.136	1.000
2	41.7	.102	22.8	.165	56.1	.121	.856
3	41.7	"	19.4	.143	52.8	.125	.717
4	38.3	"	14.4	.133	43.3	.126	.577
5	37.8	"	13.3	.127	37.8	.129	.436
9-1	20.6	.103	6.7	.225	32.2	.126	1.000
3	18.9	.103	−1.1	.169	38.9	.128	.865
4	18.9	.102	−2.2	.157	36.1	.133	.792
6	18.3	.102	−6.1	.136	23.9	.138	.606
8	18.3	.102	−6.7	.125	15.6	.150	.453
10-1	.766	.103	−21.7	.227	27.8	.154	1.000
5	.801	"	−27.8	.183	10.0	.157	.833
6	.798	"	−28.9	.173	6.7	.155	.772
9	.808	"	−32.2	.132	−8.9	.163	.421
12-1	.721	.103	−43.9	.215	−15.0	.183	1.000
3	.702	"	−30.0	.205	−24.4	.171	.898
4	.709	"	−30.6	.191	−26.1	.175	.848
5	.705	"	−31.7	.181	−27.2	.172	.793
6	.696	"	−33.3	.163	−30.0	.169	.677
8	.645	"	−38.9	.136	−28.3	.175	.456
13-1	.602	.103	−41.1	.201	−23.9	.184	1.000
3	.570	"	−31.7	.201	−24.4	.172	.899
4	.584	"	−32.2	.183	−27.2	.179	.801
5	.579	"	−33.3	.165	−29.4	.175	.688
7	.597	"	−38.3	.136	−34.4	.183	.476
20-1	.915	.103	−8.3	.206	33.3	.149	1.000
4	.886	.103	−12.2	.187	29.4	.143	.879
5	.888	.102	−13.3	.180	26.7	.144	.817
6	.888	"	−15.0	.172	22.8	.144	.755
9	.894	"	−17.8	.152	11.1	.152	.517

Table 2 Measured and reduced test data. Vortex tube insulated P_1 = .791 MN/m^2

Test-Run	T_1/x_1 °C/−	P_2 MN/m^2	T_2 °C	P_3 MN/m^2	T_3 °C	$\dot{m}x10^2$ kg/s	μ −
22-1	25.0	.102	8.9	.203	43.3	.135	1.000
2	25.6	"	6.1	.187	50.0	.132	.931
3	"	"	4.4	.177	48.3	.132	.871
4	"	"	1.7	.158	41.1	.135	.740
5	"	"	0.0	.148	32.8	.138	.612
6	"	"	−1.1	.141	26.1	.134	.640
23-1	.846	.103	−11.1	.220	37.8	.153	1.000
2	.855	"	−13.3	.205	32.8	.151	.939
3	.844	"	−14.4	.197	27.8	.152	.887
4	.842	"	−16.7	.177	20.0	.151	.765
5	.861	.102	−17.8	.158	14.4	.152	.648
6	.879	"	−17.8	.150	7.8	.158	.538
7	.883	"	−17.8	.140	3.3	.161	.421
24-1	.803	.103	−23.3	.225	7.2	.170	1.000
2	.821	"	−23.3	.213	3.3	.166	.945
3	.843	"	−24.4	.205	2.2	.165	.896
4	.813	"	−25.6	.187	1.1	.160	.780
5	.815	"	−26.7	.167	−1.7	.162	.668
6	.821	"	−27.8	.155	−4.4	.166	.560
7	.840	"	−27.8	.148	−8.3	.162	.420
25-1	.918	.103	−24.4	.246	0	.171	1.000
2	.868	"	−25.6	.219	−6.7	.171	.946
3	.865	"	−25.6	.208	−5.6	.167	.896
4	.815	"	−27.2	.190	−6.7	.165	.785
5	.814	"	−28.9	.169	−7.2	.166	.674
6	.812	"	−31.1	.157	−12.2	.167	.560
7	.819	.102	−32.2	.148	−14.4	.170	.444
8	.823	.102	−32.2	.139	−18.3	.174	.329
26-1	.803	.103	−23.3	.250	−4.4	.171	1.000
2	.698	"	−23.9	.219	−4.4	.172	.947
3	.694	"	−24.4	.210	−5.6	.169	.898
4	.692	"	−26.7	.191	−6.1	.167	.788
5	.690	"	−28.3	.170	−7.8	.167	.677
6	.693	"	−30.0	.157	−11.1	.171	.568

discharge temperature variation with changes in the cold fraction μ and with inlet conditions varied from superheated to a saturated mixture of liquid and vapor. Some of the temperature data are plotted in Figs. 3–7.

Fig. 3 shows the hot and cold side discharge temperatures obtained during the flow-rate adjustments performed in test No. 9. The inlet condition for these runs is superheated vapor and, as expected, the resulting temperature curves are very similar to those for air and other

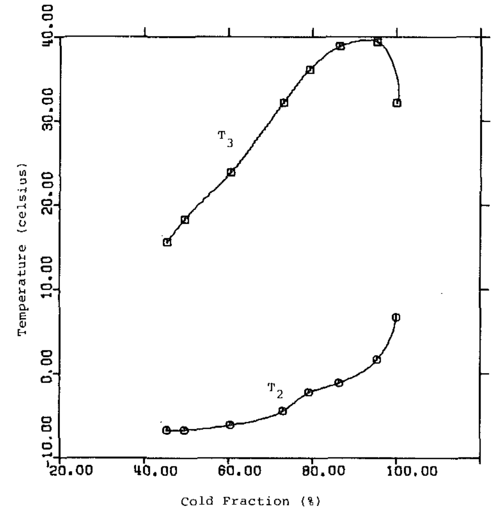

Fig. 3 Discharge temperature variation with cold fraction (percent) for test No. 9 where $p_1 = .791$ MN/m^2, $T_1 = 18.9°$C, $x_1 = 1.01$ at $\mu = .8$

gases. There is a large temperature separation ($T_3 - T_2$) over the entire range of the cold fraction (μ) with the maximum separation occurring at a cold fraction of around 85–95 percent.

When the inlet propane is cooled to a liquid-vapor mixture state, some temperature separation at the hot and cold discharges still remains. In Fig. 4, the inlet propane is at 80 percent quality but at the same pressure as that of Fig. 3. A hot-cold temperature separation of about 40 °C is still maintained but both the cold and hot side temperatures are lower than those of Fig. 3.

Continued reduction of the inlet quality rapidly diminishes the discharge temperature separation as noted from the data plotted in Fig. 5. The inlet quality for Fig. 5 is about 71 percent and the temperature separation has diminished to only a few degrees. The "hot" and cold side discharge temperatures are well below the inlet temperature of about 17°C.

The relatively large cold side temperature decrease, at cold fractions (μ) near 100 percent in Fig. 5, are not indicated in the data at higher qualities. At these cold fractions there is very little net flow from the hot side discharge and the main flow is through the cold side. The authors are not certain why this large temperature drop occurs but it is likely that, under these conditions, many of the liquid droplets formed at the inlet are rapidly vaporized at the vortex tube nozzle

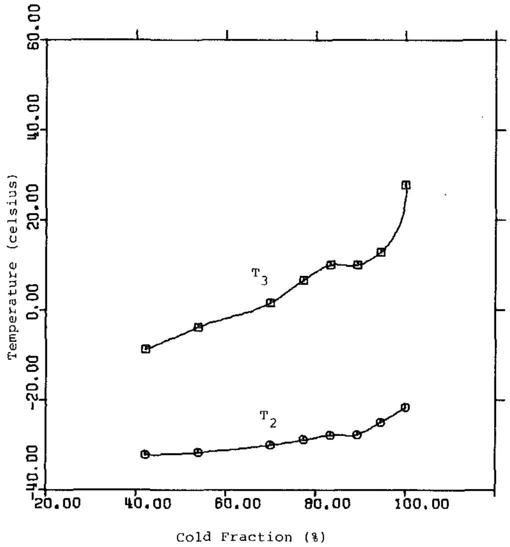

Fig. 4 Discharge temperature variation with cold fraction (percent) for test No. 10 where $p_1 = .791$ MN/m^2, $T_1 = 17.2°$C, $x_1 = .799$ at $\mu = .8$

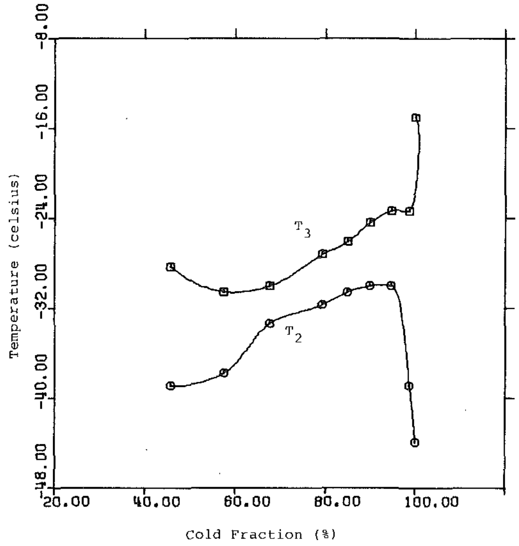

Fig. 5 Discharge temperature variation with cold fraction (percent) for test No. 12 where $p_1 = .791$ MN/m^2, $T_1 = 18°$C, $x_1 = .706$ at $\mu = .8$

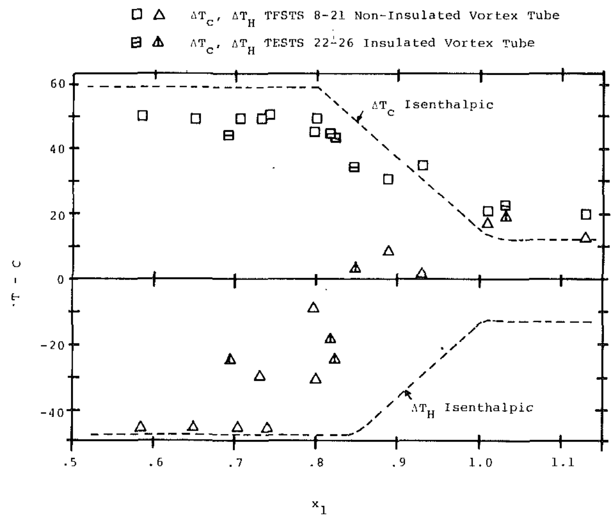

Fig. 6 Temperature differences versus inlet quality x_1 for $p_1 = .791$ MN/m^2 and interpolated to $\mu = .8$ for each test. $\Delta T_H = T_3 - T_1$, $\Delta T_c = T_1 - T_2$.

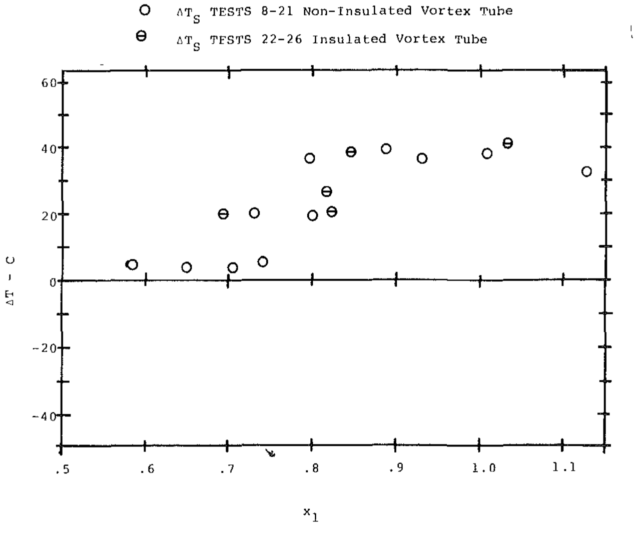

Fig. 7 Temperature separation versus inlet quality x_1 for $p_1 = .791$ MN/m and interpolated to $\mu = .8$ for each test. $\Delta T_S = T_3 - T_2$.

discharge, thereby reducing the heating effect normally occurring in the hot side flow. This situation would result in lower temperatures through the cold discharge. The one high temperature (−15°C) at $\mu = 1$ represents data taken at the hot side discharge tube with zero net flow and the heat transfer mechanism causing this temperature anomaly is likely due to extensive wall friction effects on the hot side vortex flow downstream from the inlet nozzle.

The effect of varying inlet quality on the discharge temperatures is summarized in Figs. 6 and 7, where the pertinent temperature differences are plotted against inlet quality. Each of these temperature differences are obtained from the data of a test run series by interpolating to the cold fraction flow ratio of $\mu = 0.8$.

In Fig. 6 hot side temperature difference $\Delta T_H = T_3 - T_1$ is at about 15 °C for superheated ($x_1 > 1$) inlet flows. As the inlet quality is reduced the hot side temperature difference is reduced and the hot side discharge temperature is equal to the inlet temperature at an inlet quality of about 90 percent. For lower inlet qualities the hot side temperature difference becomes negative and appears to approach a definite lower limit, which is about −50°C for this particular test system.

The cold side temperature difference $\Delta T_C = T_1 - T_2$ is also shown on Fig. 6. At superheated inlet conditions the difference is about 20°C and as the inlet quality is reduced the cold side temperature difference increases to an upper limit of about 50°C.

The temperature difference between the hot and cold side of the vortex tube is called the temperature separation and is sometimes the item of primary importance in applications. The temperature separation is $\Delta T_S = T_3 - T_2 = \Delta T_H + \Delta T_C$ and can be easily found from the data of Fig. 6. The temperature separation is plotted in Fig. 7. It can be observed that the temperature separation for superheated inlets is around 35–40°C and then drops off to zero for inlet qualities below about 70 percent. Note that the temperature separation of about 5°C at the lower inlet qualities on Fig. 7 are due mainly to the back pressure difference on the hot and cold side discharges rather than vortex flow effects in general.

Observation of the data of Figs. 6 and 7 leads to the conclusion that significant temperature separation can be maintained in the vortex tube when the inlet becomes a saturated mixture of liquid and vapor as long as the inlet quality is not too low. For this test system the lower inlet quality limit is about 80 percent.

Application of the first law of thermodynamics can aid in understanding the vortex tube flow phenomena. In its simplest form the law can be written for this system as:

$$q = [\mu h_2 + (1 - \mu)h_3] - h_1 \tag{3}$$

where q is the heat transfer through the walls of the tube per unit mass of propane flowing. Quite often in vortex tube flows the heat transfer term q is negligible or the tube is insulated; therefore, the discharge enthalpies must be related to the inlet enthalpy as:

$$\mu h_2 + (1 - \mu)h_3 = h_1 \tag{4}$$

Because of the highly complicated flow pattern, a fundamental process law has not yet been established relating the separate discharge properties h_2 and h_3 to h_1 so that only the general relationship (4) can be asserted at the present. The effectiveness of the Ranque-Hilsch process may be observed by comparing this process to one of pure throttling, or the isenthalpic process. That is, if each side (hot and cold) of the tube were considered to be simple throttling processes to the lower discharge pressure p^*; then $p_2 = p_3 = p^*$ and $h_2 = h_3 = h^* = h_1$ so that $T_2 = T_3 = T^*$ also. A separation of h_2 from h_3 and of T_2 from T_3 indicates a Ranque-Hilsch process is occurring.

The pressure-enthalpy diagram for propane [15] is useful when considering the thermodynamic process which takes place from inlet to discharge. Such a diagram is illustrated schematically as Fig. 8. The slope of the saturated vapor line is positive from low pressures to the inlet pressure (0.791 MN/m^2) used in these tests. If the vortex tube flow process were similar to adiabatic throttling, the process line would be one of constant enthalpy to the appropriate discharge pressure. When the inlet state is superheated at p_1 = .791 MN/m^2 the isenthalpic temperature drop remains essentially the same for all inlet temperatures (not too highly superheated) and the discharge state becomes even more superheated relative to the saturation temperature at the discharge pressure. This effect is noted by considering processes I and II in Fig. 8. When the inlet state is reduced to the saturation temperature (17.9°C at p_1) and is moved into the saturated mixture region, as indicated by process III in Fig. 8, the discharge for an isenthalpic expansion will remain in the superheat region until the inlet reaches a quality of about 80 percent. Further reduction of inlet quality (at constant p_1) causes no additional isenthalpic temperature changes since isotherms in this region are horizontal lines.

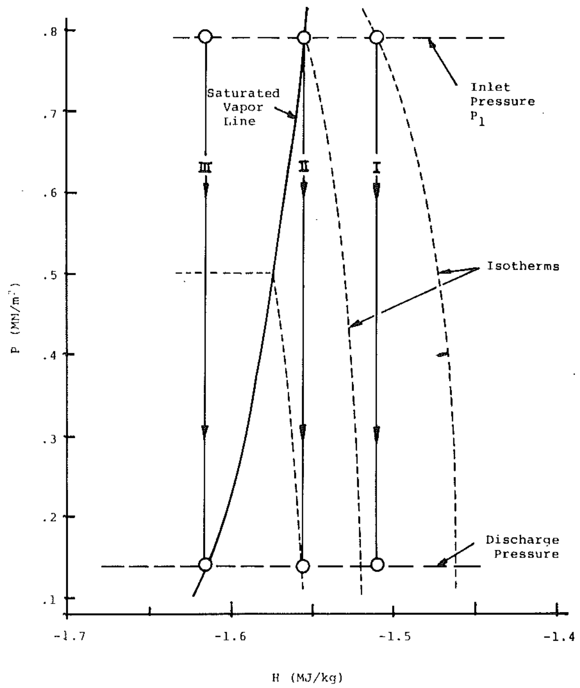

Fig. 8 Schematic plot of pressure-enthalpy diagram for propane (see data of [15]). Also shown are three isenthalpic process lines labelled I, II, III

Again considering the isenthalpic processes indicated in Fig. 8, the temperature differences for various inlet qualities can be determined. For instance, assuming the hot and cold side discharges are at the same pressure then $T_3 = T_2$ so that $\Delta T_H = -\Delta T_C$ and $\Delta T_S = 0$. It is qualitatively easy to see how ΔT_C changes with inlet quality x_1. For superheated ($x_1 > 1$) inlets ΔT_C has a value (like 12°C) and as the inlet condition is changed to saturated vapor ($x_1 = 1$), ΔT_C remains about the same. As the inlet quality is further reduced ($x_1 < 1$), ΔT_C increases since the inlet temperature T_1 now remains constant while T_2 continues to get smaller. Then, when the discharge condition reaches the saturated vapor line, no further increase in ΔT_C can occur since T_2 now remains constant. In the actual process the hot and cold side pressures are different due to the flow control valve on the hot discharge side. Hence, even if the actual process were isenthalpic there would be a difference in discharge temperatures T_2 and T_3 due to this pressure difference p_2 and p_3. Taking this pressure difference into account but assuming isenthalpic flow the temperature differences ΔT_H and ΔT_C were computed. The resulting temperature differences ΔT_H and ΔT_C for an assumed isenthalpic expansion are plotted on Fig. 6 for comparison with the experimental vortex tube data.

From Figs. 6 and 7 it may be observed, by comparing the isenthalpic results with the experimental data, that the vortex tube temperature separation phenomena is exhibited in the superheated region and into the mixture region for higher inlet qualities and the process is definitely not isenthalpic. However, as lower inlet qualities are encountered the hot and cold side expansions become more closely associated with pure throttling or the constant enthalpy process.

Heat exchanger data at the hot and cold discharges was not obtained so that h_2 and h_3 cannot be determined by a method similar to that used to determine h_1. However, as long as the discharges remain superheated the enthalpies can be determined from measure-

Table 3 Enthalpy and quality data

Units of h are MJ/kg

Test-Run	μ –	h_2 Cold	h_1 In	h_3 Hot	x_2 Cold	x_1 In	x_3 Hot
8-2	.856	−1.519	−1.511	−1.466	1.25	1.13	1.35
9-4	.792	−1.565	−1.552	−1.502	1.14	1.01	1.26
10-6	.772	−1.648	−1.626	−1.552	.94	.80	1.14
12-5	.792	−1.671	−1.658	−1.607	.89	.71	1.00
13-4	.801	−1.723	−1.700	−1.607	.77	.58	1.00
20-5	.817	−1.611	−1.594	−1.519	1.03	.89	1.21
22-3	.870	−1.552	−1.543	−1.480	1.17	1.04	1.31
23-4	.765	−1.635	−1.610	−1.530	.97	.84	1.19
24-4	.780	−1.636	−1.620	−1.562	.97	.81	1.11
25-4	.785	−1.633	−1.620	−1.574	.98	.81	1.08
26-4	.788	−1.687	−1.663	−1.573	.85	.69	1.08

Note: $p_1 = .791, p_2 \doteq .103, p_3 \doteq .157 - .191$ MN/m^2

ment of the pressures and temperatures. When the cold side discharge becomes saturated and begins to condense, equation (4) can be used to determine h_2 (x_2) as long as the hot side remains (sufficiently) superheated. When both the hot and cold side discharges are saturated mixtures, there can be no determination of the enthalpies from this data.

Of course the use of equation (4) to establish the enthalpy h_2 depends on the validity of neglecting the heat transfer term q in equation (3). A heat transfer analysis was performed on the system assuming conditions which would produce the greatest possible heat transfer. The heat transfer term q was found to be negligible for these energy levels. Radial heat flow considerations show that a maximum q of .005 MJ/kg could possibly be expected to flow into the propane at the lowest temperature conditions where the inlet is at about $x_1 = 60$ percent and the propane flow rate is about $.18 \times 10^{-2}$ kg/s. A second, fin-like longitudinal analysis indicates a maximum possible heat flow of .01 MJ/kg. Even if these heat flow rates were realized the error in using equation (4) would be small. It is realistic to expect heat flows of an order of magnitude less than these "conservative" computations, hence equation (4) should predict h_2 with reasonable accuracy. The test data of Figs. 6 and 7 indicate no significant differences between the insulated and non-insulated vortex tubes and tend to verify this conclusion.

Since the thermocouples produce an error in indicated temperature reading it is not possible to determine, by pressure and temperature readings alone, when the fluid becomes a two-phase, liquid-vapor mixture. Therefore equation (4) was used to determine the enthalpy of the cold discharge h_2 whenever h_3 could be determined from the (superheated) pressure and temperature conditions: $h_2 = [h_1 - (1 - \mu)h_3]/\mu$. The discharge enthalpies and qualities were computed for several test runs and are tabulated for the readers convenience in Table 3. From these values the deviation of the process from one of pure throttling is easily noted.

The use of a mass basis or quality (x_1) can be misleading in determining the type of two-phase flow which exists. In these tests the flow at the inlet in the saturated mixture region should be of the "mist" or "fog" type since the volume basis or void fraction (α_1) is quite high. For the inlet pressure of .791 MN/m^2 the void fractions are: $\alpha_1 = .97$, .99, 1.0 corresponding to qualities of: $x_1 = .5, .8, 1.0$. The relation between the two being: $\alpha_1 = v_{g1}x_1/v_1$ where $v_1 = v_{f1} + (1 - x)v_{fg1}$. Therefore, the liquid droplets which may form are expected to be of very small diameter and to essentially pass into the tube with the vapor.

The major conclusions which can be observed from these data follow:

1 For a vortex tube using propane with a .791 MN/m^2 inlet pressure, the hot and cold side discharge tube temperature separation remains significant when the inlet quality is above about 80 percent.

2 When the inlet quality drops below 80 percent the temperature separation diminishes to an insignificant level with both hot and cold tube producing similar effects.

3 Although the discharge temperature separation diminishes for inlet qualities below 80 percent, the discharge enthalpies still exhibit considerable difference between hot and cold sides indicating that the Ranque-Hilsch process is still in effect.

References

1 Fulton, C. D., "Ranque's Tube," *ASRE Refrigeration Engineering*, 1950, pp. 473–479.

2 Fulton, C. D., "Comments on the Vortex Tube," *ASRE Refrigeration Engineering*, 1951, p. 984.

3 Scheper, George W., "The Vortex Tube-Internal Flow Data and a Heat Transfer Theory," ASRE Refrigeration Engineering, 1951, pp. 985–989.

4 Lay, J. E., "An Experimental and Analytical Study of Vortex Flow Temperature Separation by Superposition of Spiral and Axial Flows—Part 1.," ASME JOURNAL OF HEAT TRANSFER, Aug. 1959, pp. 202–212.

5 Lay, J. E., "An Experimental and Analytical Study of Vortex Flow Temperature Separation by Superposition of Spiral and Axial Flows—Part 2.," ASME JOURNAL OF HEAT TRANSFER, Aug. 1959, pp. 213–222.

6 Deissler, R. G., and Perlmutter, M., "Analysis of the Flow and Energy Separation in a Turbulent Vortes," *International Journal of Heat and Mass Transfer*, Vol. 1, 1960, Pergammon Press, pp. 173–191.

7 Holman, J. P., and Moore, G. D., "An Experimental Study of Vortex Chamber Flow," ASME *Journal of Basic Engineering*, Dec. 1961, pp. 632–636.

8 Smith, J. L., "An Experimental Study of the Vortex in the Cyclone Separator," ASME *Journal of Basic Engineering*, Dec. 1962, pp. 602–608.

9 Smith, J. L., "An Analysis of the Vortex Flow in the Cyclone Separator," ASME *Journal of Basic Engineering*, Dec. 1962, pp. 609–617.

10 Love, William J., "Prediction of Pressure Drop in Straight Vortex Tubes," *AIAA Journal*, Vol. 12, No. 7, July 1974, pp. 959–965.

11 Soni, Y., "A Parametric Study of the Ranque-Hilsch Tube," University of Idaho, Chemical Engineering, Ph.D. Thesis, 1973, University Microfilms International, Ann Arbor, Michigan, 74-17, 647.

12 Soni, Y., "Optimal Design of the Ranque-Hilsch Vortex Tube," T. N., ASME JOURNAL OF HEAT TRANSFER, May 1975, pp. 316–317.

13 Lovelace, R. B., "Effect of Condensing Flows in the Ranque-Hilsch Vortex Tube," M. Eng. Thesis, Mech. Engrg. Dept., University of Louisville, Louisville, Ky, 1978.

14 Cross, D. E., "Rotameter Calibration Nomograph for GASES," *Instrumentation Technology*, April 1969, pp. 53–55.

15 Canjar, L. N., and Manning, F. S., "Thermodynamic Properties and Reduced Correlations for Gases," Gulf Publishing Company, Houston, 1967, pp. 33–43.

T. Kumada
Assoc. Professor.

R. Ishiguro
Professor.

T. Sato
Graduate Student.

Department of Nuclear Engineering,
Faculty of Engineering, Hokkaido University,
North 13, West 8, Kita-ku,
Sapporo 060, Japan

T. Abe
Research engineer,
Central Research Institute of Electric Power
Industry

Natural Evaporation of Sodium with Mist Formation

Part I—Measurement of Evaporation Rates and Comparison of Values against Theoretical Predictions

Measurements were made of the rate of natural evaporation into a stagnant argon or helium atmosphere from a rectangular-shaped surface of liquid sodium placed on the bottom floor of an evaporation test box. The tests were carried out at various levels of sodium temperature and inert gas pressure under conditions where mist formation could be expected. The values obtained as the Sherwood number were compared with those predicted by various theoretical models. The overall results revealed that the enhancement of evaporation brought about by mist formation significantly increased as the sodium temperature did. It was concluded that the previous theoretical models were not adequate for obtaining correct values for the evaporation rate.

1 Introduction

Many unexamined phenomena have appeared in recent developments of sodium-cooled fast breeder reactor technology. One of them is sodium evaporation into the argon gas phase under conditions of mist formation. In practice, such evaporation may take place from either the free surface of a sodium pool in a reactor vessel or the sodium wetted surface of a spent fuel assembly removed from the pool. The process of evaporation is, in general, complicated by the interdependent relations which hold among and between fields of flow, temperature and vapor concentration. In the present case, however, the physical conditions were not as complicated due to the low partial pressure of the sodium vapor, which prevails under normal conditions of fuel handling. The low vapor pressure caused the velocity of evolving vapor from the sodium surface to become negligible; consequently, the flow and temperature could be treated as independent of the sodium concentration in the gas phase.

On the other hand, the importance of the sodium mist generation in the argon atmosphere must be considered. Sodium mist is generated when liquid sodium of a certain temperature is brought into contact with argon gas at a distinctly lower temperature. This mist gives rise to a steepening of the gradient of the sodium vapor concentration in the vicinity of the surface of evaporation, which, in turn, enhances the evaporation rate.

While a few experimental studies are available on sodium evaporation [1–3], these reports deal mainly with its practical aspects and lack adequate bases for theoretical evaluation. In Hayashi's, et al. [4] studies of naphthalene fogging in the stream of the natural convection from a vertical plate, the temperature difference between the plate and its surroundings was so small (20–40°C) that the enhancement of the evaporation rate was not large and same order comparable to the conventional evaporation rate of water or alcohol in a cold atmosphere. Some of the authors [5] have measured the rate of evaporation from a narrow rectangular sodium surface at the bottom of a duct at temperatures from 320 to 500°C into a forced argon flow at various temperature levels. Their results revealed that the Sherwood number for evaporation varied significantly according to the temperature differences occurring between the sodium and argon atmosphere.

The same authors [6] measured the rate of natural evaporation from a narrow rectangular sodium surface on an isothermal horizontal plate, and the heat transfer from the same geometry as the evaporation apparatus. The enhancement of both the forced and the natural evaporations was of the same order in spite of the difference in geometrical and physical conditions.

The present paper presents the measurements of the natural evaporation of sodium from a similar apparatus into calm argon and helium atmospheres. The theoretical Sherwood numbers were numerically calculated with both the conventional method of mass transfer and the models proposed by Hills, et al. [7] and Turkdogan [8]. In order to evaluate the theoretical models, the resulting Sherwood numbers were compared with those obtained experimentally.

2 Experimental

2.1 Apparatus and Procedure. Figure 1 shows the arrangement of the present equipment for the sodium evaporation experiments. The equipment consists of an evaporation test section, a sodium tank, and an argon gas supply and vacuum system. Details of the evaporation test section are shown in Fig. 2. The section consists of a box and

---

Contributed by the Heat Transfer Division for publication in the JOURNAL OF HEAT TRANSFER. Manuscript received by the Heat Transfer Division March 29, 1978.

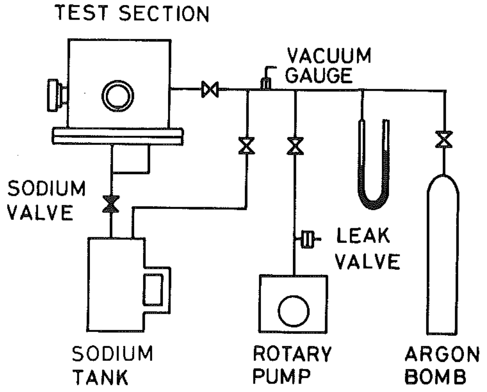

Fig. 1 Schematic diagram of sodium evaporation system

a bottom plate. The box is 260 mm in width, length and height with three windows on the side walls which are used to observe the levels and surface conditions of the sodium. The bottom plate is equipped with a funnel-shaped pot 20 mm in width, 100 mm in length, and 98 mm in height. A gap of 2.5 mm is made between the pot and the bottom plate as shown in Fig. 2. This permits the decrease of heat conduction from the pot to the bottom plate. The outer surface temperature of the box was measured at various points with glass-sheathed thermocouples. The sodium surface temperature was measured with two stainless-steel, sheathed thermocouples of 1 mm OD which are immersed into the sodium to a depth of 10 mm.

The test section was first evacuated to about 0.05 torr. and charged with argon to the atmospheric pressure or higher. All of the equipment exposed to sodium were electrically heated to a prescribed temperature at which they were maintained by means of voltage regulators, with the exception of the sodium pot. During the evaporation of the sodium, the temperature of the sodium pot was controlled by a proportional, integral and differential regulator which was within ±0.5°C of the prescribed temperature. The liquid sodium was then pushed up to the pot by applying pressure to the sodium tank. A temperature equilibrium was established over the sodium pot within 10 min after sodium charging. The sodium level was carefully adjusted flush with the floor of the box. Most of the evaporated sodium became mist and was deposited on the top and bottom surfaces of the test section.

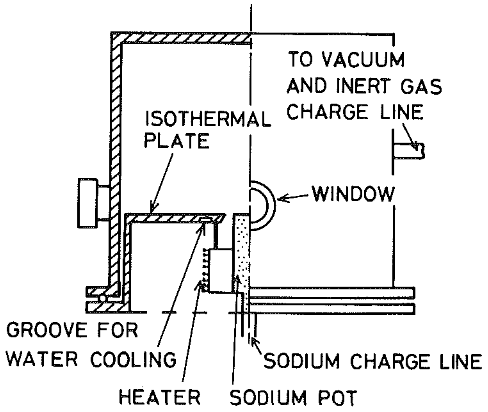

Fig. 2 Details of evaporation test section

The deposited sodium mist was collected by wiping the surfaces several times with clear, wet gauzes after the apparatus was cooled. The residual sodium on the surfaces was within 1.0 percent of the total deposited sodium. The deposition of mist on the evaporation surface was not observed during testing. The collected sodium was dissolved in 1 liter of distilled water for measurement.

2.2 Sherwood Number and Physical Properties.

1 Sherwood number: The evaporation rate is expressed by

$$m = h_D \rho_M (w_{\mathrm{Na},w} - w_{\mathrm{Na},\infty}). \tag{1}$$

Using the ideal gas law, the partial density of gas is given by

$$\rho_M = M_M P_M / RT. \tag{2}$$

Neglecting the term $w_{\mathrm{Na},\infty}$ since $w_{\mathrm{Na},\infty} \ll w_{\mathrm{Na},w}$, the mass transfer coefficient h_D can be expressed by

$$h_D = m/\rho_M w_{\mathrm{Na},w} = m(RT/P_{\mathrm{Na},eq,w} M_{\mathrm{Na}}). \tag{3}$$

The Sherwood number is readily expressed as

$$\mathrm{Sh}_e = h_D \ell / D = m(R\ell/P_{\mathrm{Na},eq,w} M_{\mathrm{Na}})(T/D)_r \tag{4}$$

where $(T/D)_r$ is the value determined from a reference temperature.

2 Diffusion coefficient: To evaluate the diffusion coefficients, Moulaert's theoretical expression [9] for the Na-Ar mixture, and

Nomenclature

a = thermal diffusivity
B, C = constant in equation (11)
d = half-width of sodium or heated surface
c_p = specific heat
D = diffusion coefficient
e = gap between a heated surface and an isothermal plate
g = gravitational acceleration
H = heat of condensation or evaporation
h_D = mass transfer coefficient
J = volumetric steady-state nucleation rate (number of droplets per unit volume and time)
ℓ = width of sodium surface
M = molecular weight
m = evaporation rate
P = total pressure
P_v = vapor pressure
R = universal gas constant
s_{crit} = supersaturation ratio
T = absolute temperature
ΔT = temperature difference between sodium and inert atmosphere
u, v = velocities in the x and y directions, respectively
w = mass fraction of sodium vapor
x, y = coordinates of horizontal and vertical directions
α_m = mass accommodation coefficient
β = coefficient of thermal expansion
ν = kinetic viscosity
ρ = density
σ = surface tension force
Ω = vorticity $(= -\nabla^2\psi)$

Dimensionless Quantity

Gr = Grashof number $(= \ell^3 g\beta\Delta T/\nu^2)$
Le = Lewis number $(= a/D)$
Pr = Prandtl number $(= \nu/a)$
Ra = Rayleigh number (= Pr·Gr)
Sc = Schmidt number $(= \nu/D)$
Sh = Sherwood number $(h_D\ell/D)$
X, Y = dimensionless coordinate in equation (17)
θ = dimensionless temperature $\left(= \dfrac{T - T_\infty}{T_w - T_\infty}\right)$
ω = ratio of mass fraction $\left(= \dfrac{w_{Na} - w_{Na,\infty}}{w_{Na,w} - w_{Na,\infty}}\right)$
ψ = dimensionless stream function in equation (18)

Subscript

a = actual vapor pressure
ACSM = analytical expression by Rosner
Ar = argon
crit = critical supersaturation
e = experiment
eq = equilibrium vapor pressure
HI = by equation (10)
L = liquid
M = gas mixture
Na = sodium
n = position of nucleation
NM = numerical calculation without mist formation
NCSM = numerical calculation with mist formation
r = reference temperature
v = vapor
w = evaporation or heated surface
∞ = atmosphere or isothermal plate

Aref'yev's semiempirical expression [10] for the Na-He mixture were used. These expressions are as follows;

$$\text{for the Na-Ar mixture, } D = 5.16 \times 10^{-5} T^{3/2}/P \tag{5}$$

$$\text{for the Na-He mixture, } D = 2.5 \times \left(\frac{T}{723}\right)^{1.65} \tag{6}$$

Recently some authors [11] have measured the diffusion coefficient of sodium in argon or helium gas on the basis of the Stefan method and have verified that the values calculated by these expressions agreed with experimental diffusion coefficients ±10 percent.

3 Sodium vapor pressure: The equilibrium vapor pressure of sodium was evaluated using the equation of Ditchburn, et al. [12]:

$$\ell\text{og}\, P_{\mathrm{Na},eq} = -5567/T - 0.5\ell\text{og}T + 9.235. \tag{7}$$

4 Critical supersaturation s_{crit}: Epstein, et al. [13] derived the following relation between s_{crit} and T,

$$2[\ell\text{n}s_{\mathrm{crit}}]^3 + \left\{\ln\left[\alpha_m \left(\frac{P_{v,eq}}{T}\right)^2 \left(\frac{\sigma M_v}{\rho_L}\right)^{1/2}\right] + 59.82 - \ell\text{n}\, J_{\mathrm{crit}}\right\}[\ell\text{n}\, s_{\mathrm{crit}}]^2 - 17.49\left(\frac{\sigma}{T}\right)^3\left(\frac{M_v}{\rho_L}\right) = 0. \tag{8}$$

The s_{crit} is calculated by substituting an assumed value of J_{crit} into equation (8). The authors allowed the nucleation rate J_{crit} (nuclei $\mathrm{cm}^{-3}\mathrm{s}^{-1}$) to be as high as 10^5, then the value of s_{crit} by the following simple expression was approximated,

$$s_{\mathrm{crit}} = \exp(2957.1/T - 2.2142). \tag{9}$$

If we allow the other value of J_{crit} to be as high as 10^{10} or as low as 1, we arrive at a Sherwood number of ∓ 10 percent, which is different from that obtained by assuming $J_{\mathrm{crit}} = 10^5$, because J_{crit} has relatively little effect on the corresponding value of s_{crit}.

5 Physical properties of mixtures: The equilibrium vapor pressure of sodium at 500°C is approximately 0.005 atm; therefore, the transport properties for the present case may be identified with those of argon or helium gas.

6 Reference temperature for evaluation of the physical properties: The temperature to which parameters should be referred is not well defined in the case where mist formation significantly enhances evaporation. The Sherwood number was, therefore, evaluated on the basis of a film temperature, as done in conventional heat and mass transfer calculations, since the main purpose of this paper was to show the enhancement in evaporation brought about by mist formation.

2.3 Error Evaluation in Determination of Experimental Sherwood numbers. To evaluate errors in experimental Sherwood numbers, the following discussion was made regarding the several errors sources inherent in the present data arrangement.

1 *Temperature of sodium surface.* For measurement purposes, two sheathed-thermocouples of 1 mm OD were used. These were calibrated within ±0.5°C error at the melting point of zinc (purity: 99.9995 in weight percent, melting point 419.46°C). The maximum error of the sodium surface temperature can be expected at least to be within ±1.0°C, which corresponds to 2 ~ 3 percent error of the sodium vapor pressure. Uncertainty coming from the nonuniformity of the sodium surface temperature ±0.5 percent was also included in this error.

2 *Residual sodium on the box surfaces.* The deposited sodium mist collected by wiping the surfaces several times with clear, wet gauzes after the apparatus was cooled. The residual sodium on the surfaces was within 1.0 percent of the total deposited sodium.

3 *Sodium vapor pressure.* The equilibrium vapor pressure of sodium by Ditchburn, et al. [12] may include the uncertainty of about 4 percent in the low temperature range of the present experiments.

4 *Diffusion Coefficient.* Recently some authors [8] have measured the diffusion coefficient of sodium in argon or helium gas on the basis of the Stefan method and have verified that the values calculated by Moulaert's theoretical expression for the Na-Ar mixture and Aref'yev's semi-empirical expression for the Na-He mixture agreed with the experimental diffusion coefficients within ±10 percent.

As the experimental diffusion coefficient was evaluated on the basis of the sodium vapor pressure, it needs not to add the uncertainty of the sodium vapor pressure for account of the total error in determination of the experimental Sherwood numbers. Hence, the maximum possible uncertainty in determination of the experimental Sherwood numbers amounts to ±14 percent in the low temperature range of the present experiments.

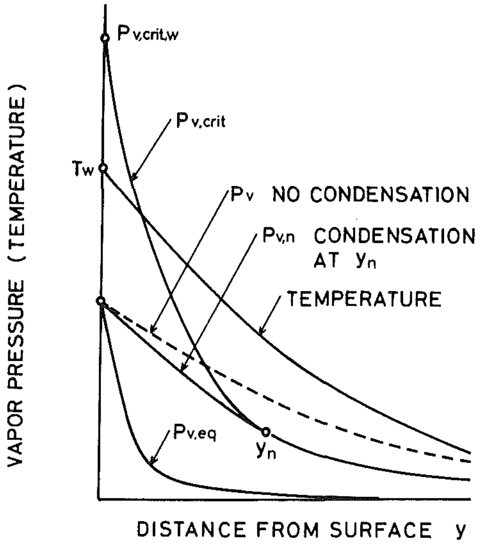

Fig. 3 **Vapor profiles versus distance from evaporation surface**

3 Theoretical

3.1 An Outline of Previous Evaporation Theories. For simplicity, it is assumed that a steady state boundary layer is established and an evaporation surface is maintained at an equilibrium vapor pressure. The vapor pressure is low in comparison with the total pressure of the system. The Stefan flow at the evaporating surface is considered to be negligible, and the heat released upon condensation does not significantly affect the steady state temperature distribution near the heated surface. Under these circumstances, the evaporation theory models can be understood with reference to Fig. 3, which displayed the actual and hypothetical vapor pressure profiles in the vicinity of the evaporating surface.

Two extreme cases can be shown. In the first case, condensation did not occur within the thermal boundary layer. The profile of the vapor pressure was shown by P_v in Fig. 3. This led to conventional mass transfer, and, hence, the minimum rate of evaporation. For natural convection from the present geometrical system, the so-called boundary layer approximations could not be applied; therefore, a numerical analysis can be attempted for an enclosure similar to the geometry of the evaporation test section.

The second extreme was that in which condensation maintained the local vapor pressure at a thermodynamic equilibrium $P_{v,eq}(T)$, corresponding to each temperature T in the boundary layer. For this simpler case Hills and Szekely [7] have proposed an evaporation theory which takes into account the temperature disturbance due to the heat released upon condensation. For a case of low equilibrium vapor pressure in this equation we have:

$$\frac{\mathrm{Sh}_{HI}}{\mathrm{Nu}} = \frac{C}{T_w}\left(1 - \frac{T_\infty}{T_w}\right), \tag{10}$$

where Sh_{HI} is the Sherwood number for the case of mist occurrence, and Nu is the Nusselt number for a similar geometry system of evaporation, which corresponds to the first extreme if the Lewis number is equal to unity. In the following vapor fraction-temperature relationship, C is constant:

$$w = e^{B - C/T}. \tag{11}$$

Recently Turkdogan [8] proposed a quantitative treatment of the intermediate case, which is the so-called critical supersaturation model (CSM). In the model they assumed that the actual vapor pressure profile $P_v(y)$ is tangent to the pressure $P_{v,\mathrm{crit}}(y)$ of critical supersaturation at the point of intersection y_n. The assumption is expressed in the equations:

$$P_v(y_n) = P_{v,\mathrm{crit}}(y_n)$$
$$\left(\frac{\partial P_v}{\partial y}\right)_{y=y_n} = \left(\frac{\partial P_{v,\mathrm{crit}}}{\partial y}\right)_{y=y_n}. \qquad (12)$$

In other words, these conditions mean that, physically, the vapor pressure is steadily maintained at a critical supersaturation where the plane of homogeneous nucleation occurs. Later the CSM was analytically formulated and generalized by Rosner [13] with further generalizations made by Epstein et al. [14]. Rosner proposed a simple expression for the enhancement ratio (Sh/Nu) in terms of a universal function implicitly containing condensation kinetics. However, it appears to be doubtful that a direct application of the expression to the present geometrical system can be made, because the following Rosner assumptions were not strictly satisfied in the present system:

1 The distance y_n to the point of nucleation is small compared with the local radius of the curvature of the surface.
2 The actual temperature profile up to the point of nucleation is linear with the slope $(\partial T/\partial y)_{y=0}$.

3.2 Numerical Method. *1 Sherwood number with no mist formation.* Some of the present authors [15] have proposed a method of numerical calculation for natural convection from a narrow hot strip on a large isothermal horizontal plate, and have shown that the calculated results are in good agreement with their experimental Nusselt number. In this system the governing differential equations are expressed by

$$\frac{\partial u}{\partial x} + \frac{\partial v}{\partial y} = 0, \qquad (13)$$

$$u\frac{\partial u}{\partial x} + v\frac{\partial u}{\partial y} = -\frac{1}{\rho_\infty}\frac{\partial p}{\partial x} + \nu\nabla^2 u, \qquad (14)$$

$$u\frac{\partial v}{\partial x} + v\frac{\partial v}{\partial y} = -\frac{1}{\rho_\infty}\frac{\partial p}{\partial y} + \nu\nabla^2 v + g\frac{T - T_\infty}{T_\infty}. \qquad (15)$$

In the present case, the boundary conditions were the same as the system [6] proposed previously, except for the gap between the heated surface and the isothermal plate, as shown in Fig. 4. The boundary conditions were expressed as,

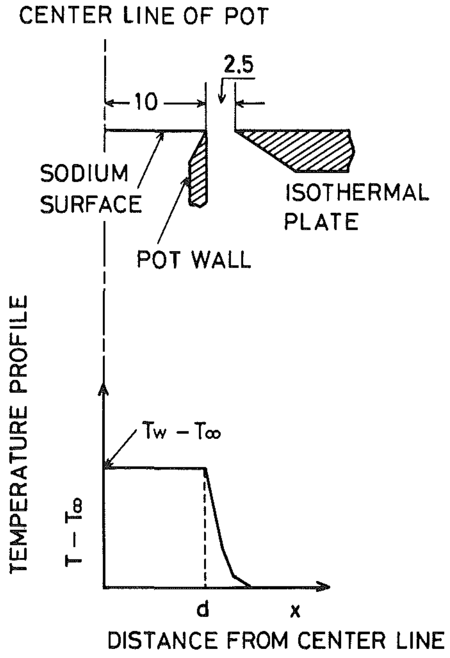

Fig. 4 Details and temperature profile around the gap

$$\left.\begin{aligned}
&0 \leqq x < \infty,\ y \to \infty{:}\ T = T_\infty,\ u = v = 0\\
&0 \leqq x < d,\ y = 0{:}\ T = T_w,\ u = v = 0\\
&d \leqq x < d + e,\ y = 0{:}\ T = T_w + (T_\infty - T_w)\frac{x - d}{e},\\
&\frac{\partial u}{\partial y} = v = 0\\
&d + e \leqq x < \infty,\ y = 0{:}\ T = T_\infty,\ u = v = 0\\
&x \to \infty,\ 0 \leqq y < \infty{:}\ T = T_\infty,\ u = v = 0\\
&x = 0,\ 0 \leqq y < \infty{:}\ \frac{\partial T}{\partial x} = 0,\ u = \frac{\partial v}{\partial x} = 0
\end{aligned}\right\} \qquad (16)$$

The dimensionless variables were introduced by taking d as the reference length,

$$X = \frac{x}{d},\ Y = \frac{y}{d},\ \theta = \frac{T - T_\infty}{T_w - T_\infty}. \qquad (17)$$

The dimensionless stream function ψ was defined by

$$u = \frac{\alpha}{d}\frac{\partial \psi}{\partial X},\ v = -\frac{\alpha}{d}\frac{\partial \psi}{\partial Y}. \qquad (18)$$

Then, combining equations (14) and (15), the vorticity equation is expressed by

$$\nabla^4\psi = \frac{1}{\mathrm{Pr}}\left\{\frac{\partial}{\partial X}(\nabla^2\psi)\frac{\partial\psi}{\partial Y} - \frac{\partial}{\partial Y}(\nabla^2\psi)\frac{\partial\psi}{\partial X}\right\} + \mathrm{Ra}_d\frac{\partial\theta}{\partial X}, \qquad (19)$$

and the transformed energy equation was

$$\nabla^2\theta = \frac{\partial\theta}{\partial X}\frac{\partial\psi}{\partial Y} - \frac{\partial\theta}{\partial Y}\frac{\partial\psi}{\partial X}. \qquad (20)$$

The boundary conditions are also transformed to

$$\left.\begin{aligned}
&0 \leqq X < \infty,\ Y \to \infty{:}\ \theta = 0,\ \psi = \frac{\partial\psi}{\partial Y} = 0\\
&0 \leqq X < 1,\ Y = 0{:}\ \theta = 1,\ \psi = \frac{\partial\psi}{\partial Y} = 0\\
&1 \leqq X < 1 + \frac{e}{d},\ Y = 0{:}\ \theta = 1 - \frac{x - d}{e},\\
&\frac{\partial^2\psi}{\partial X\partial Y} = \frac{\partial\psi}{\partial Y} = 0\\
&1 + \frac{e}{d} \leqq X < \infty,\ Y = 0{:}\ \theta = 0,\ \psi = \frac{\partial\psi}{\partial Y} = 0\\
&X \to \infty,\ 0 \leqq Y < \infty{:}\ \theta = 0,\ \psi = \frac{\partial\psi}{\partial X} = 0\\
&X = 0,\ 0 \leqq Y < \infty{:}\ \frac{\partial\theta}{\partial X} = 0,\ \psi = \frac{\partial^2\psi}{\partial X^2} = 0
\end{aligned}\right\} \qquad (21)$$

The simultaneous differential equations (19) and (20) which were subject to the boundary conditions (21) could be solved numerically by the successive over-relaxation method. Calculations were carried out for two Rayleigh numbers of 40,000 and 900 which corresponded to the argon and helium atmospheres, respectively.

The resulting velocity and temperature distributions were used to analyze numerically the differential equation of mass transfer,

$$u\frac{\partial w}{\partial x} + v\frac{\partial w}{\partial y} = D\nabla^2 w. \qquad (22)$$

The following dimensionless variable was introduced

$$\omega = \frac{w_{\mathrm{Na}} - w_{\mathrm{Na},\infty}}{w_{\mathrm{Na},w} - W_{\mathrm{Na}\,\infty}}, \qquad (23)$$

and then equation (22) was transformed to

$$\nabla^2\omega = \mathrm{Le}\left\{\frac{\partial\omega}{\partial X}\frac{\partial\psi}{\partial Y} - \frac{\partial\omega}{\partial Y}\frac{\partial\psi}{\partial X}\right\}. \qquad (24)$$

The boundary conditions in the dimensionless form were expressed in the following form in place of θ to ω,

$$\left.\begin{array}{l} 0 \leqq X < \infty,\ Y \rightarrow \infty:\ \omega = 0 \\ 0 \leqq X < 1,\ Y = 0:\ \omega = 1 \\ 1 \leqq X < 1 + \dfrac{e}{d},\ Y = 0:\ \omega = 1 - \dfrac{x-d}{e} \\ 1 + \dfrac{e}{d} \leqq X < \infty,\ Y = 0:\ \omega = 0 \\ X \rightarrow \infty,\ 0 \leqq Y < \infty;\ \omega = 0 \\ X = 0,\ 0 \leqq Y < \infty:\ \dfrac{\partial \omega}{\partial X} = 0 \end{array}\right\} \quad (25)$$

Equation (24) subject to equation (25) was also analyzed numerically with precalculated velocity and temperature fields.

2 *Sherwood number by CSM.* The prescribed tangency condition could not be applied directly to the present numerical method. Instead of the tangency condition, the following condition, in which the dimensionless concentration ω never exceeds the critical supersaturation s_{crit}, is imposed in addition to the boundary condition (25),

$$\omega \leqq s_{\text{crit}}. \quad (26)$$

The main difference between the present calculation and that by Rosner et al. was our taking into account the gas flow.

3 *Sherwood number by Hills, et al.* In a similar manner to the CSM, the Sherwood number by Hills et al. was readily obtained by assuming $\omega \leqq 1 (= P_v/P_{v,eq})$ in addition to the boundary condition (25).

4 *Calculation.* The variations in the Rayleigh number evaluated on film temperature were from 38,000 to 42,000 for argon, and 800 to 1,000 for helium, respectively, against the temperature change of the surface of sodium from 300°C to 500°C at the surrounding temperature of 30°C. The variations of the Lewis number were from 1.50 to 1.84 for argon, and 3.05 to 3.12 for helium, respectively, against the same range of sodium temperature. Thus, the numerical calculations by CSM were performed on the assumption of constant Rayleigh and lewis numbers of 40,000 and 1.67 for argon, and 900 and 3.1 for helium, respectively.

4 Comparison and Discussion

4.1 Argon Atmosphere. The Sherwood numbers were presented in Fig. 5 against sodium temperature T_{Na}.

The figure revealed, notably, that:

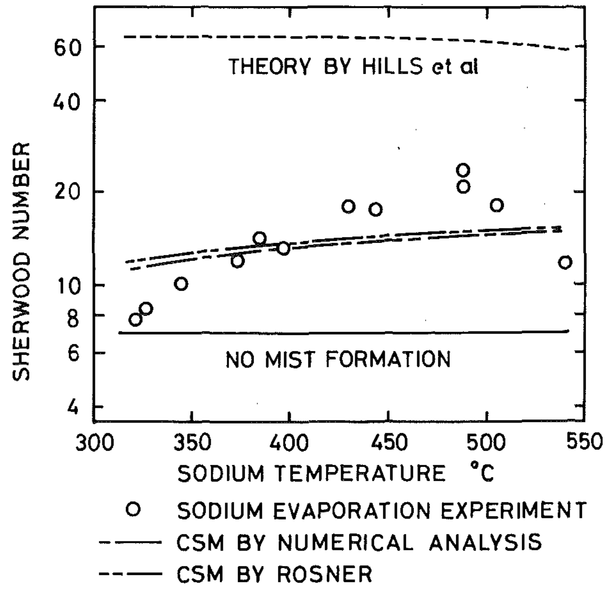

Fig. 5 Effect on Sherwood number brought about by variation of sodium temperature (argon atmosphere)

1 Sh_e increased from one to three times as large as those predicted numerically by assuming no mist formation with increasing T_{Na}, while Sh_{NM} remained nearly constant.

2 The Sh_{HI} curve was significantly higher than that of Sh_e.

3 Sh_{ACSM} slightly increased with the increasing of T_{Na} in a similar manner to Sh_e, but it was considerably smaller in higher T_{Na}, and larger in lower T_{Na}, in comparison with Sh_e.

4 Agreement between the analytical Sh_{ACSM} and numerical Sh_{NCSM} was satisfactory within the range of the present experiment range.

5 The absolute values of Sh_e and Sh_{NCSM} did not indicate an essential difference, whereas their increasing rates with T_{Na} showed a marked difference.

With the decreasing of T_{Na}, Sh_e decreased to Sh_{NM} and the enhancement of evaporation was so small enough to be negligible, despite the presence of sparse mist in the vicinity of the sodium surface. This fact is well experienced in the evaporation of commonly used liquids such as water or alcohol, and in this case, the generation of mist depended mainly on foreign nuclei. The evaporation of sodium was more enhanced with the increasing of T_{Na}, which was accompanied by a denser mist generation. Thus, as T_{Na} increases, the enhancement may decrease, because the latent heat release decreases the gradient of temperature in the vicinity of an evaporating surface, as shown theoretically in [13].

Equation (10) was derived under the assumption that any supersaturated vapor cannot exist in a gas phase. The assumption means, physically, that a great number of particles exist in sufficient quantity to suppress the vapor pressure equilibrium condition. This assumption was not satisifed in the present experiment; thus, it is valid only for indicating the upper limit of evaporation when there is mist formation.

Both curves made by the CSM were slightly elevated due to the fact that the nucleation zone was close to the evaporating surface with increasing T_{Na}, which made it possible to enhance evaporation at higher rates.

The difference between Sh_{ACSM} and Sh_{NCSM} was so small that the simplification of heat being transferred through a boundary layer by conduction was valid in most cases of this type of system. Fig. 6 also represented the Sherwood numbers against the pressure of argon phase P_{Ar}. Sh_e decreased to Sh_{NM} with the decreasing of P_{Ar}, while Sh_{NCSM} did not decrease at such a high rate as Sh_e did. This may be

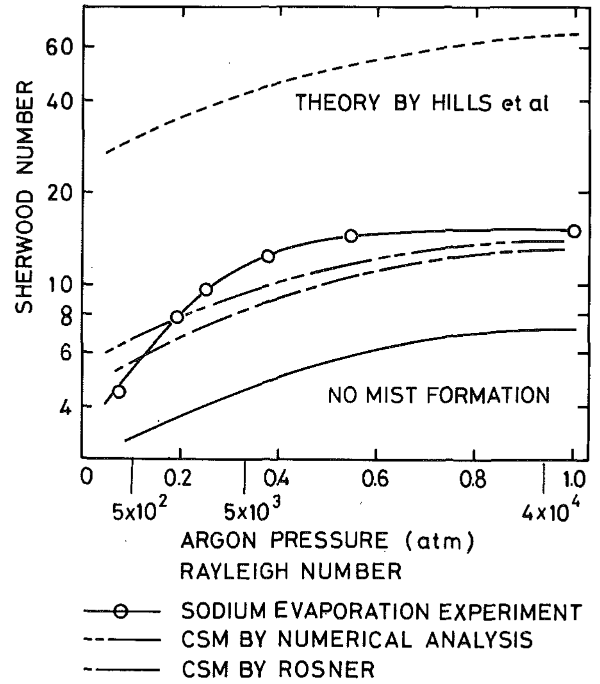

Fig. 6 Effect on Sherwood number brought about by variation of argon pressure

dependent on the significant decrease of the Rayleigh number in a reduced pressure of inert gas, which resulted in a diminishing of the temperature gradient. The difference between Sh_{NCSM} and Sh_{ACSM} increased with the decreasing of argon pressure, but this difference was not so large that it was impossible to apply the analytical expression in order to obtain the estimated Sherwood number in place of a stricter numerical method. However, a detailed discussion of this point is difficult because the mechanism of mist formation still remains largely unknown.

4.2 **Helium Atmosphere.** Fig. 7 showed the variation of Sherwood numbers against T_{Na} at a helium atmosphere the surrounding temperature being fixed at room temperature. In this figure the Sherwood number curves followed roughly a similar pattern, as shown in Fig. 6. There were significant differences in the Rayleigh and Lewis numbers in experiments of the argon and helium atmospheres. However, the enhancement of evaporation was not so different as in the case of argon atmosphere and the results agreed well with those predicted by the CSM at higher temperatures.

4.3 **Evaporation of Molten Iron-Nickel Alloy.** Turkdogan and Mills [16] measured the evaporation rate of inductively heated, molten drops of iron-nickel alloy (nominal diameter = 0.64 cm) magnetically levitated in 80°C quiescent helium at atmospheric pressure. The enhancement ratio decreased from five times to one time as large as those predicted by assuming that there is no mist generation with increasing droplet temperatures from 1900 ~ 2300 K.

On the contrary, sodium evaporation increased from one to three times as large as the theoretical prediction without mist generation in increasing sodium temperatures. The authors reasoned that this difference did not depend on the different geometrical feature of the experimental apparatus, but depended rather on the higher vapor pressure in the evaporation of the molten iron-nickel drops and the error of the predicted Sherwood number caused by the significant difference in temperature and flow fields between the theoretical and the practical models.

5 Conclusions

An experiment was performed to obtain the evaporation rate (or Sherwood number) from a rectangular-shaped free surface of sodium into argon or helium atmospheres with varying sodium temperatures and gas pressures. A numerical analysis was also conducted to verify the increase expected in the evaporation rate by mist formation from supersaturated vapor. The following are the salient results obtained from comparisons among and between the experimental and the theoretical results.

1 The evaporation rates were one to three times as large as those predicted numerically under the assumption of no mist formation in the range of sodium temperatures of 280 ~ 530°C.

2 Regarding magnitude, the values of Sh_e and Sh_{NCSM} did not indicate any essential difference in spite of the fact that the CSM included some unfeasible assumptions.

3 On the other hand, the increasing Sh_e and Sh_{NCSM} rates with sodium temperatures showed a distinct difference, namely, that the former increased constantly with the increasing sodium temperatures, and that latter rate did not indicate such a high rate of increase. The evaporation rate from the Ni-Fe droplets slightly decreased with the increasing droplet temperatures in a range of 1900 ~ 2300 K. The authors reasoned that this difference did not depend on different geometrical features of the experimental apparatus but that it depended rather on the higher vapor pressure and the temperature difference in the evaporation of Ni-Fe droplets.

4 The enhancement of evaporation by equation (10) was too large to be realistic. This may have been due to the assumption that condensation maintains the local vapor pressure at a thermodynamic equilibrium value.

5 The Sh_e/Sh_{NM} value for argon atmosphere decreased to unity with the reducing argon pressure.

6 The Sherwood and Lewis numbers for argon and helium atmospheres were significantly different, whereas the enhancements of evaporation were in good agreement over the range of experimental sodium temperatures.

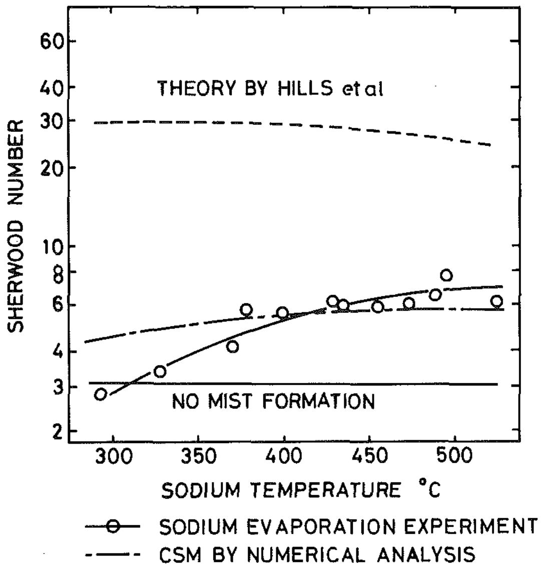

Fig. 7 Effect on Sherwood number brought about by variation of sodium temperature (helium atmosphere)

In our present discussion, it may be important to seek the order of enhancement or the means for predicting evaporation rates under various geometrical and physical conditions. The Sh_e/Sh_{NM} values used in the present evaporation test and the values of forced convection given by some of the present authors did not indicate any essential difference in spite of the difference in the geometrical and convective condition.

The main purpose of the present paper was to provide experimental data under the condition that mist formation occurred and, thus, made possible the evaluation of currently proposed physical models.

The critical supersaturation model (CSM) predicted the values in good agreement with the experiment, except for the lower temperature range of experiment, while the model proposed by Hills, et al. predicted the values to be much larger than the experimental ones. The present experiment, however, did not yield any information on the condensation structure. To confirm the validity of the assumptions in the CSM, more study is required on the physical conditions and behavior of mist formation.

Acknowledgment

We wish to express our appreciation to Mr. Takayuki Shimizu, a graduate student at Hokkaido University for his valuable contributions and help in the present work.

References

1 Horst, K. M., "Southwest Experimental Fast Oxide Reactor Development Program," 2nd Quarterly Report, July–Sept., 1964, GEAP-4742, Oct. 1964.

2 Sutherland, J. D., Markley, R. A., and Mckinney, J. E., "Sodium Vapor Deposition in Inert Enclosures," ASME JOURNAL OF ENG. FOR POWER 92, 1970, pp. 2–107.

3 Dievoet, J. V., Michel A., and Lanckman, R., "Sodium Evaporation in an Argon Flow," ANL-7520, Part 1, 1969, p. 418.

4 Hayashi, Y., Aoki A., and Hori, K., "Transport-Reaction Mechanism of Mist Formation Based on the Critical Supersaturation Model," Trans. ASME 98, 1976, pp 1–114.

5 Kumada, T., Kasahara, F., and Ishiguro, R., "Sodium Evaporation into a Forced Argon flow," (I), *J. Nucl. Sci. Technol.*, Vol. 13 1976, p. 2–74.

6 Ishiguro, R., Kumada T., and Abe, T., "Natural Convection and Evaporation from a Free Surface of Liquid Sodium," *Proc. Int. Heat Transfer Conf.*, 5th, Tokyo, CT 1974, pp 4–15.

7 Hills A. W. D., and Szekely, J., "Notes on Vaporization into very Much Colder Surroundings," *Chem. Engng. Sci.* 17, 79, 1964.

8 Turkdogan, E. T., "The Theory of Enhancement of Diffusion Limited Vaporization Rates by Convection-Condensation Process-Part I, Theoretical," *Trans. Am. Inst. Chem, Engrs.*, Vol. 230, 1964, p. 740.

9 Moulaert, G., "Etude de Proprietes du Melange Argon Sodium," These de fin detudes, Institut de Libre de Bruxelles, 1970.

10 Aref'yev, K. M., Borishansky, V. M., Vorontsova, L. A., Zablotskata, T. V., Ivaschenko, N. I., Paleyev I. I., and Khomchenko, B. M., "Diffusion Coef-

ficients of Alkali Metal Vapors in inert Gases," *Heat Transfer-Soviet Research* 6, 1974, pp. 6–66.

11 Kumada, T., Ishiguro R., and Kimachi, Y., "Diffusion Coefficients of Sodium Vapors in Argon and Helium, Nuclear Science and Engineering," to be published.

12 Ditchburn R. W., and Gilmour, J. C., "Vapor pressure of monatomic vapors," *Revs. of Mod. Phys.* 13, 1941, pp. 310–327.

13 Rosner, D. E., "Enhancement of Diffusion-Limited Vaporization Rates by Condensation within the Thermal Boundary Layer 1. The Critical Supersaturation Approximation," *Int. J. Heat Mass Transfer* 10, 9–1267, 1967.

14 Epstein M., and Rosner, D. E., "Enhancement of Diffusion-Limited Vaporization Rates by Condensation within the Thermal Boundary Layer 2. Comparison of Homogeneous Nucleation Theory with the Critical Supersaturation Model," *Int. J. Heat Mass Transfer* 13, 11–1393, 1970.

15 Abe T., and Ishiguro, R., "Natural Convection over a Heated and Upward-Facing Horizontal Plate-First Report, Numerical analysis," *Trans. JSME* 41, 352–3577 in Japanese 1975.

16 Turkdogan, E. T., and Mills, K. C., "The Theory of Enhancement of Diffusion Limited Vaporization Rates by Convection-condensation Process-Part II, Experimental," *Trans. Am. Inst. Chem, Engrs.* 230, 750, 1964.

N. W. Wilson
Associate Professor.
Mem. ASME

B. D. Vyas
Postdoctorate Fellow.

Faculty of Engineering and Applied Science,
Memorial University of Newfoundland,
St. John's, Newfoundland
Canada

Velocity Profiles near a Vertical Ice Surface Melting into Fresh Water

An experimental determination is made of the velocity profiles which result from the free convective melting of a vertical ice sheet into fresh water at temperatures in the range from 2.0°C to 7.0°C. The results suggest that upward flows exist for water temperatures below 4.7°C. Entirely downward flowing boundary layers are suggested for temperatures above 7.0°C. For intermediate temperatures, an oscillatory dual flow regime is indicated.

Introduction

The phenomena related to the free convective melting of a vertical ice surface into a fesh water medium have been investigated to some extent in the past. Such investigations as are reported in the literature establish that the density extremum in pure water at about 4°C has a complex effect on the fluid flow and heat transfer processes. Consideration of the density dependency on temperature suggests that for ambient water temperatures below a certain critical value, which would be equal to or below 4°C, the fluid would flow upwards in a boundary layer region near the ice surface. Similarily, for a sufficiently high ambient water temperature, predominantly downwards flowing boundary layers should occur in the near wall region. These two flow patterns are substantiated in the review of the literature reported in the introductory comments of Bendell and Gebhart [1].

The analytical works of Merk [2] and Vanier and Tien [3], which are based on boundary layer analyses for isothermal surfaces provide successful solutions for various ambient temperature regimes corresponding to the above mentioned boundary layer flows. However, for some temperature ranges, the analysis of Vanier and Tien does not provide stable analytical solutions. The description of the analysis of Gebhart and Mollendorf [4] which is given in [1] substantiates this with no solutions being reported for ambient fluid temperatures in the range $4.0 < T_\infty < 6.8$°C. It can be postulated that such analytical difficulties occur when the density extremum occurs within a thermal boundary layer in a position such that upwards flow occurs on one side of this position with downwards flow occuring on the other side. Such "dual flows" would preclude adequate analysis by boundary layer methods.

For melting spheres Dumore, et al. [5] and Vanier and Tien [6] have found convective inversions at 4.8°C and 5.3°C, by experimental means. These results compare favorably with the prediction from Merk's analysis of 5.31°C for a convective inversion temperature. Tkachev [7] has found a minimum Nusselt number at $T_\infty = 5.5$°C for a melting vertical cylinder. Ede [8,9] studied the heat transfer from a heated vertical isothermal wall to cold water, and although his results are not directly applicable to a melting ice wall, they exhibit a similar minimum Nusselt number characteristic. Schecter and Isbin [10] have reported on experimental observations of the dual nature of the flow for the transfer of heat from a vertical isothermal plate to cold water. Velocity and temperature distributions are also reported.

Bendell and Gebhart have conducted experiments on the melting of a vertical ice sheet and obtained a minimum Nusselt number at a water temperature of 5.6°C. In addition, by observing the differential in temperature between positions near the top and bottom of the ice sheet, they deduced whether the net flow is upwards or downwards. When $T_\infty = 5.6$°C downflow was observed and when $T_\infty = 5.5$°C upflow was indicated. Watts [11] reports on dunking a colored ice cube in water at about 10°C and observing a vigorously downward flow of the colored melt.

Watts' work represents, to the knowledge of the authors, the only direct experimental observation which is reported in the literature of the fluid flow characteristics near a vertical ice wall melting into a surrounding water medium. Therefore, the present work was undertaken to provide visualizations and direct measurements of the velocity profiles in the temperature range from 2° to 7°C.

Apparatus

The experiments were conducted by melting 25 cm high by 15 cm wide by 3.7 cm thick ice slabs located at one end of a 60 cm by 30 cm by 38 cm glass tank as shown in Fig. 1. The ice slabs were formed in a mold around a lucite fitting which could be clamped to the end wall of the tank to hold the ice in a vertical position to within ±1 deg with the bottom of the ice slab 7 cm above the bottom of the tank. The tank was filled to a depth of 32 cm with a 0.01 percent solution (by weight) of Thymol Blue pH indicator dissolved in distilled water. This permitted the adaptation of the method of Baker [12] for the measurement of the free convective velocity profiles.

Thus, the velocity measurements were effected by first preparing the pH indicator–distilled water mixture by titration to the end point (pH $\simeq$ 8.0) against Na OH until the solution just turned a deep blue

---

Contributed by the Heat Transfer Division for publication in the JOURNAL OF HEAT TRANSFER. Manuscript received by the Heat Transfer Division March 8, 1978.

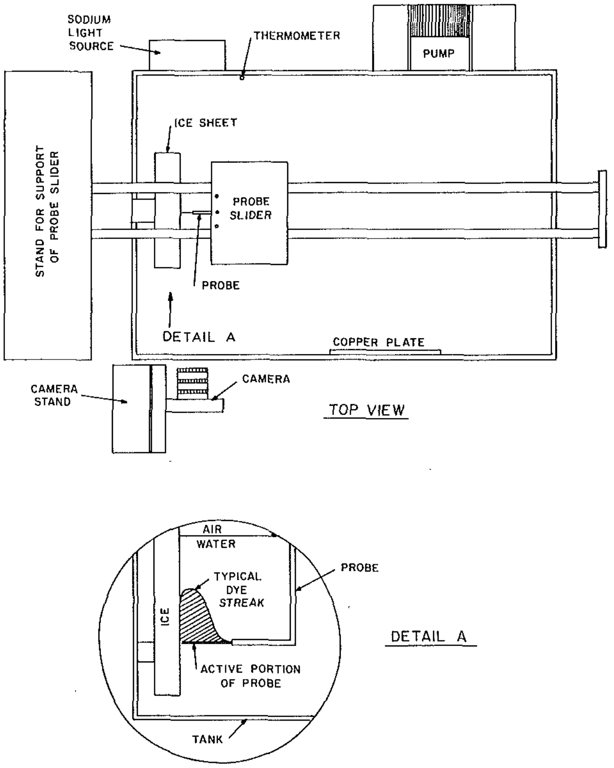

Fig. 1 Apparatus

color. Then by the drop addition of H Cl the solution was brought back to the acidic side of the end point where it possessed a characteristic orange color. According to Raoult's law the presence of the Na OH would depress the fusion temperature of the water by 2×10^{-6} °C. The small amount of chlorine ion produced negligible salinity. Thus, the presence of the electrolytes in the solution produced negligible effect on the fusion temperature and buoyancy.

Two electrodes were situated in the tank. The first electrode consisted of a 0.51 mm dia by 22 mm long platinum wire connected through a stainless steel tube probe holder to the positive side of a d-c power supply. The stainless steel holder was insulated from the tank water by means of shrink tubing and the platinum wire was positioned normal to the ice slab along its center line and 5 cm above the bottom edge of the ice. The second electrode was situated along one side of the tank. Therefore, when the electrodes were energized, a cylinder of dark blue colored fluid was formed around the platinum wire portion of the positive electrode as in Baker's paper. This blue fluid differs from the surrounding fluid only by a small difference in its pH value. It possesses the local fluid density and temperature and will follow along with any motion in the surrounding fluid.

As Fig. 1 also shows, light from a sodium vapor lamp passed through a ground glass diffuser, through the tank walls and water and into a 35 mm camera located outside of the tank. Alignment of the ice slab with the camera axis was ensured within 1 deg. Because of the relatively low transmissibility of the thymol indicator solution (orange on the acidic side) ASA 400 film was utilized at a shutter speed of $\frac{1}{4}$ s at f1.8 to record the color traces throughout the experiments.

In order that elapsed time could be recorded from the energization of the electrodes until a photograph was taken of the ensuing color traces, an electronic timer was employed. The timer was connected to start when the d-c power was first supplied to the electrodes and to stop when the flash contacts of the camera were closed as the shutter was released.

Finally, the whole of the apparatus was housed in a thermostatically controlled cold room to prevent the generation of ambient thermal convection currents within the tank fluid.

Procedure

For a typical run, the cold room temperature was first set at the desired value and the tank fluid was permitted to come to thermal equilibrium with the aid of a mechanical stirrer. When the tank temperature was stabilized to within ±.05°C of the desired value as measured on an immersed mercury in glass thermometer, the stirring was stopped. A lucite piece with a scribed known grid was located at the probe position and photographed to provide a calibration frame on the film. The calibration piece was then withdrawn and the tank permitted to stabilize for a further 30 min to permit any eddies to die out.

The ice slab, initially at 0°C, was equilibrated in air at 20°C for 5 min and then slowly immersed and clamped at the end of the tank and the positive electrode was positioned so that it was just nearly touching the ice sheet. This could be observed through the camera viewfinder by viewing the probe end and its image reflected by the ice surface. To minimize vibrations the cold room compressor was then shut off. After a further waiting period of 5 min the velocity profiles could be recorded.

This was done by energizing the electrodes which started the generation of blue colored fluid at the same instant as the timer was started. During this period the development of the fluid displacement traces was continuously monitored through the reflex camera viewfinder. Close attention was paid to note the formation of any gas bubbles at the electrode since the applied emf of 2 volts exceeded the decomposition voltage of 1.69 volts for the NaOH solution. Consideration of the electrochemical kinetics of the initial stages of the electrolosis of weak aqueous solutions [13] suggests that gas bubble formation at an electrode requires a certain minimum time from the initial energization of the electrodes. In preliminary experiments, it was determined that for this apparatus the minimum time for the generation of a single observable gas bubble was 14 s at an emf of 2 volts and the average time was 17 s. Therefore, the fluid displacement traces were generated until either they filled a significant portion of the field of view or about 15 s had elapsed, and the camera shutter was released which stopped the interval timer.

After a further wait of 4 min to permit the flow to clear the blue dye traces from the field of view, another photograph could be taken to permit comparisons for reproducibility. Typically, a maximum of four or five photographs could be taken before noticeable degeneration occurred on the ice surface.

The film was then processed by standard techniques and mounted on in a Nikon Model 6 C optical comparator at 10x magnification. The negative image of the lucite piece was aligned with the cross hairs of the comparator and x and y direction photographic scale factors were determined using the comparator micrometer heads. These agreed to three significant figures vindicating the alignment. A negative of a particular fluid displacement image in which gas bubble generation had not been observed was then aligned in the comparator. Successive readings were taken on the micrometer heads and averaged to determine the centerline of the probe and the position of the ice surfaces as indicated by the mid point between the probe end and the reflected image. Having thus determined an origin to within ±0.02 mm actual size, the x–y co-ordinates of points on the edge of the dye image could be found typically for 21 points with approximately equal spacing in the y direction. Using the photographic scale factors, the actual size of the dye traces could then be determined. The x coordinate values so obtained divided by the energization time yields the approximation to the u component of velocity provided that the streamlines have a

Nomenclature

T_∞ = temperature of water far from ice surface, °C
x = distance along ice surface, mm
y = distances normal to ice surface, mm
ρ = fluid density, gm/cm^3
u = velocity of water, upwards is positive, mm/s
v = velocity normal to ice surface, mm/s

large radius of curvature and the period of any flow oscilliation is large compared to the energization time.

Results and Discussion

Because of the density extremum at about 4°C, an upwards flowing boundary layer is expected near an ice surface melting into pure water at a temperature, T_∞, below about 4°C under free convective conditions. In the experiments, such flows were noted for water temperatures of 2.0, 3.2, 4.4, and 4.7°C as shown in the data of Figs. 2 and 3. In these cases, fluid was entrained at the lower edge of the ice sheet and was "pumped" upwards by the buoyancy forces. At the measurement station 5 cm above the lower edge, the flow was essentially parallel to the ice sheet and possessed boundary layer characteristics. As the flow neared the free surface it turned away from the wall and its velocity diminished. It then moved across the tank eventually to flow downward again to be entrained. This was observed in preliminary experiments where dye streaks were watched carefully until they diffused beyond recognition. For the data shown above, the maximum changes in mixed tank temperatures were calculated using Bendell and Gebhart's [1] results to be 0.033°C and the maximum change in ice slab thickness is estimated as 0.75 mm. For the greater total elapsed times and higher water temperatures of Figs. 4–8, the maximum estimated tank temperature change was .09°C with an ice slab thickness change of 2.1 mm.

Having established a characteristically upflowing boundary layer at the measurement station for $T_\infty < 4.7°C$, it is possible to compare, in Fig. 2, the data to the predictions obtained from free convective boundary layer theories. In the first instance, the effects of melting were assumed to be negligible and the simple analysis outlined by Bayley, Owen and Turner [14] was applied for $T_\infty = 2°C$ at $x = 5$ cm with $T_w = 0°C$. This predicts a maximum velocity higher than that of the data, and a significantly thinner boundary layer. Vanier and Tien's [3] analysis predicts an even larger maximum velocity and a greater boundary layer thickness than is exhibited by the data. For each of these profiles, fluid densities were obtained from the work of Kell [15]. Disagreement between the analyses and the data may be attributed to the high degree of sensitivity of the analyses to the fluid density. Vanier and Tien's work suggests that the effects of melting are slight, and it is not possible to confirm or contradict this with the present data. By comparing the one set of data in Fig. 2 to the other, it can be estimated that the errors in velocity measurement are of the order of ±0.05 mm/s or ±6.3 percent of the maximum. The apparent broadening of the disagreement between the two sets of data for $y >$ 8 mm could be attributed either to such errors or to slight oscillations or recirculations in a difficult measurement environment.

As the water temperatures increase up to about 4°C the net buoyancy forces increase resulting in increased maximum velocities. This effect can be observed in the data by comparing Fig. 3(*a*) to Fig. 3(*b*). At 4.4°C the flow is still upward, although the maximum velocity is lower and the boundary layer is slightly thinner than at 3.2°C. This can be attributed to the downward buoyancy force occurring in that portion of the profile with temperatures between 4.0 and 4.4°C. In Fig. 3(*c*) a similar but stronger tendency is noted as the result of the increased downwards buoyancy existing in the outer portion of the boundary layer, and the two sets of data shown exhibit distinctly different maximum velocities. On the basis of other profiles taken in the same set but not shown here, it is clear that the flow was oscillating at this temperature. In addition, qualitative observations during the period of energization of the electrode indicated that small downward oscillations in the flow occurred in the outer portion of the boundary layer from time to time. The magnitude of these downward velocities was well below .05 mm/s and could not adequately be measured with the present instrumentation. That is, if the electrodes were energized for sufficient time for the colored fluid to be displaced enough to be measured, either the local flow direction would change, indicating a period of oscillation of the order of between ten and thirty seconds, or gas bubble generation would begin at the anode and disturb the flow. Nevertheless, $T_\infty = 4.7°C$ appears to be the lower limit for the onset of an oscillatory dual flow regime.

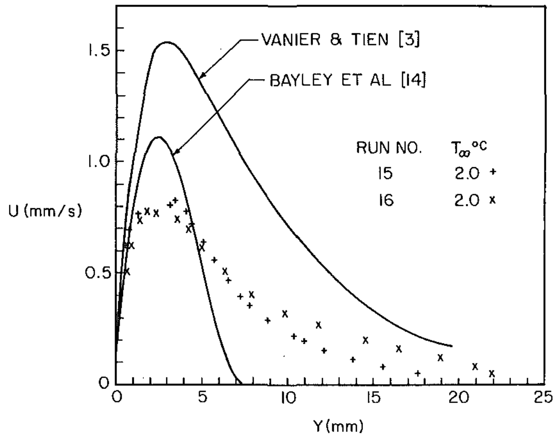

Fig. 2 Velocity profiles for $T_\infty = 2.0°$ C

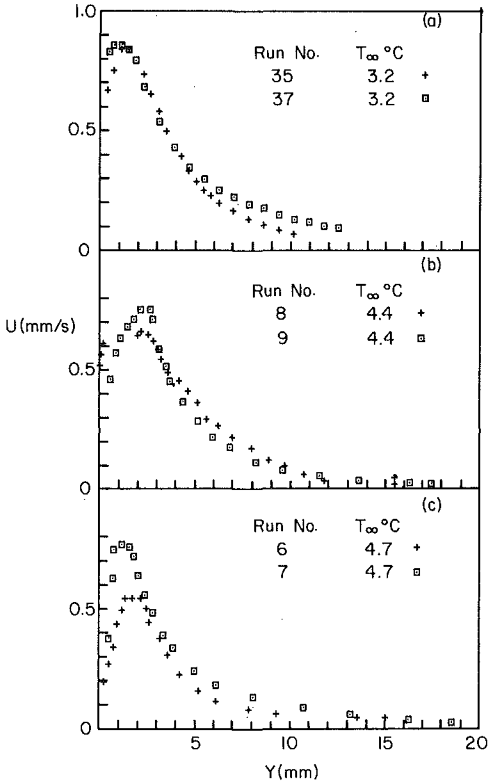

Fig. 3 (*a*) Velocity profiles for $T_\infty = 3.2°C$; (*b*) velocity profiles for $T_\infty = 4.4°C$; (*c*) velocity profiles for $T_\infty = 4.7°C$

When the water temperature was increased to 5.0°C, the oscillatory dual flow characteristic was clearly established and measurable as can be seen in Fig. 4. In comparison with Fig. 3(*c*) the upward flowing portion is substantially thinner with a decrease in the maximum upward velocity when downflow exists. In addition, when the downward flow velocities are large, the boundary layer region thickens substantially to values somewhat larger than the active anode length.

The continuation of this same trend can be seen for 5.4°, 5.6°, and 5.9°C in Figs. 5, 6, and 7, respectively. In each of these cases, oscillatory dual flow existed continuously; i.e., upward flows were not observed at any time beyond the near wall upward flow regions. At 5.3°C the position of the maximum downward velocity oscillated between about 7.3 mm and 11.5 mm from the wall. For 5.6°C these observed locations vary between 6 mm and 18 mm, but at 5.9°C the oscillation in the position is only from 5.2 mm to 8.0 mm. In addition the profiles at 5.9°C possess much greater self similarity than those at the two lower temperatures. Thus, the flow phenomena for 5.3° and 5.6°C seem to be substantially more complex than that at 5.9°C.

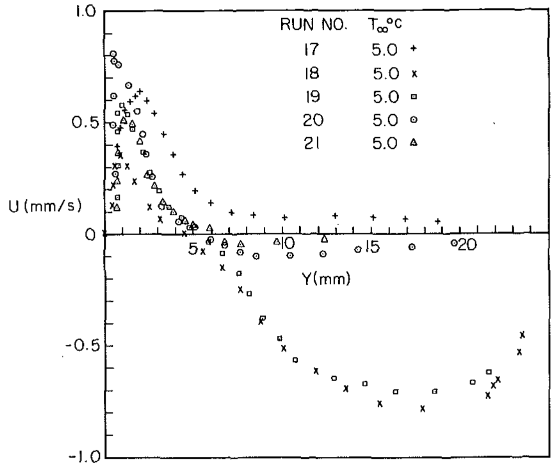

Fig. 4 Velocity profiles for $T_\infty = 5.0°C$

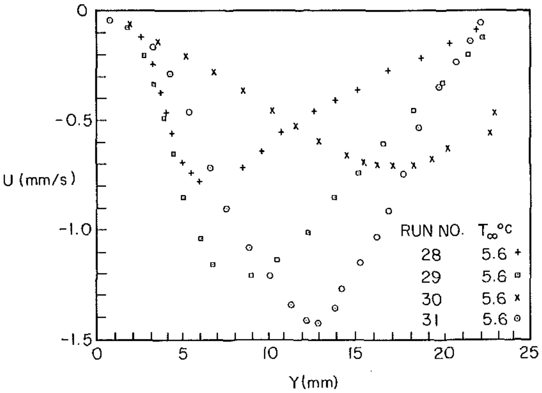

Fig. 6 Velocity profiles for $T_\infty = 5.6°C$

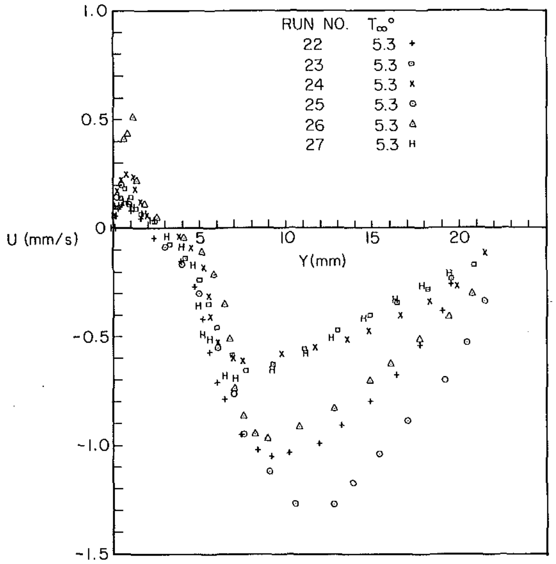

Fig. 5 Velocity profiles for $T_\infty = 5.3°C$

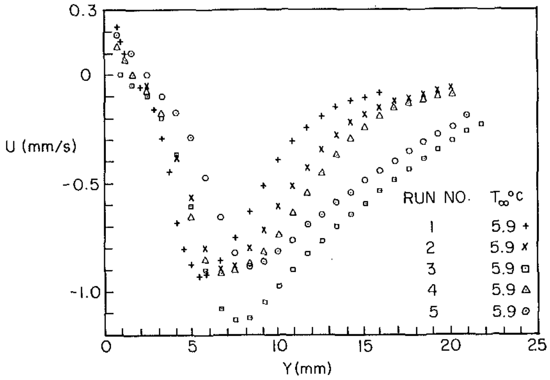

Fig. 7 Velocity profiles for $T_\infty = 5.9°C$

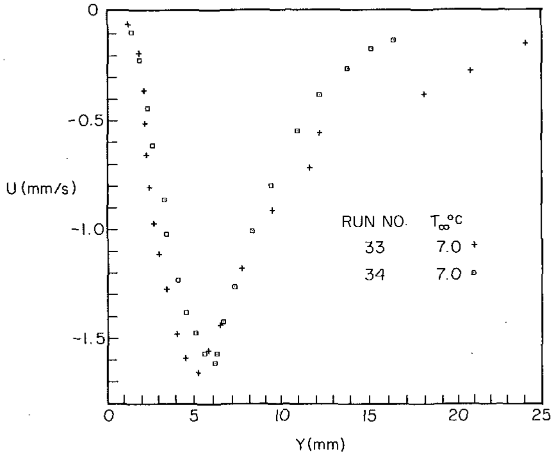

Fig. 8 Velocity profiles for $T_\infty = 7.0°C$

Both Figs. 5 and 7 clearly indicate small regions of the order of 1 to 2 mm in thickness near the wall where upwards flow existed at measurable velocities. At 5.6°C much smaller velocities were observed qualitatively within the same region but with maximum upwards velocities less than .1 mm/s. This apparent anomaly can perhaps be attributed to the strong oscillations in the downward region resulting in near wall transverse velocity oscillations tending to sweep the colored water away from the wall.

For the data in Figs. 4–7, only a very approximate estimate can be made of the period of oscillation. No oscillatory effects were noticed through the camera viewfinder during any single electrode energization, but the flow patterns obtained in successive photographs differed appreciably. Thus the period is between 15 s and 4 min. Mechanisms can be speculated for the oscillatory nature of the dual flow. Transient large recirculations could produce such oscillations; however, at T_∞ = 4.7°C the effect occurred only slightly and at T_∞ = 5.0°C the flow was clearly oscillatory. It is questionable that large scale recirculation could account for such an abrupt change in the flow regime. On the other hand, as the temperature was changed from 4.7°C to 5.0°C the position of the density extremum moved toward the wall and the proportion of the boundary layer where $\partial\rho/\partial y$ is negative increased substantially. It is noted that oscillations become appreciable exactly within the dual flow regime which corresponds to the region where the boundary layer analyses by Vanier and Tien [3], and Gebhart and Mollendorf [4] were unable to obtain solutions. Current unpublished work by one of the present authors uses a two-dimensional finite difference analysis, based on [16], capable of accounting for steady-state recirculation. For free stream temperatures above or below the dual flow regime, stable solutions are obtained in close agreement with [3] and [4]. In the dual flow regime, no solutions have converged, but at T_∞ = 4.8°C one solution has continuously oscillated. This suggests that in the dual flow regime a condition exists between the region where $\partial\rho/\partial y$ is positive and the region where $\partial\rho/\partial y$ is negative such that a steady-state force balance cannot exist for constant local fluid velocity, and the flow oscillates.

In Fig. 8, the results presented for a water temperature of 7°C are characteristic of a relatively stable downward flow regime. In this case, the portion of the boundary layer with upward buoyancy forces is approximately 0.5 to 1 mm in thickness. The downward buoyancy forces in the outer portion are much stronger and the whole flow is downward. Because the viscous forces, which tend to draw the fluid downward, approximately balance the upward buoyant forces near the ice the velocity gradient, du/dy, is approximately zero at the ice surface. At greater temperatures the velocity gradient at the wall would become negative.

Conclusions

1 Visualizations have been made of the free convective flows resulting near a vertical ice sheet melting into fresh water with temperatures in the range from 2.0 to 7.0°C. These visualizations have been interpreted as velocity profile data.

2 For water temperatures in the range from 0 to 4.0°C a relatively stable upward flowing free convective boundary layer exists. The outer portion of the boundary layer may exhibit slight oscillations.

3 The density extremum affects the velocity profiles by decreasing the maximum velocity for temperatures in the range from 4.0 to 4.7°C.

4 At 4.7°C an oscillatory dual flow situation begins to occur. As the temperature is increased this phenomenon is increasingly prevalent, with increasing downward velocities, reaching a maximum at 5.6°C.

5 From 5.6 to 7.0°C the oscillatory nature of the downward flow diminishes.

Acknowledgments

The authors wish to acknowledge support by the National Research Council of Canada under grant number A-9204. The use of the cold room and other facilities of Memorial University, St. John's, Newfoundland made the work possible.

References

1 Bendell, M. S., and Gebhart, B., "Heat Transfer and Ice Melting in Ambient Water Near its Density Extremum," *Int. J. Heat Mass Transfer,* Vol. 19, 1976, pp. 1081–1087.

2 Merk, H. J., "The Influence of Melting and Anomolous Expansion on the Thermal Convection in Laminar Boundary Layers," *Appl. Scient. Res.*, Vol. 4, 1953, pp. 435–452.

3 Vanier, C. R., and Tien, C., "Effect of Maximum Density and Melting on Natural Convection Heat Transfer from a Vertical Plate," *Chem. Eng. Prog. Sym. Ser.*, Vol. 64, pp. 240–254.

4 Gebhart, B., and Mollendorf, J., "Buoyancy Induced Flow in a Liquid under Conditions in which a Density Extremum May Occur," submitted to *J. Fluid Mech.*

5. Dumore, J. M., Merk, H. J., and Prins, J. A., "Heat Transfer from Water to Ice by Thermal Convection," *Nature,* London, Vol. 172, 1953, pp. 460–461.

6 Vanier, C. R., and Tien, C., "Free Convection Melting of Ice Spheres," *AIChE Journal*, Vol. 16, 1970, pp. 76–82.

7 Tkachev, A. G., "Heat Exchange in Melting and Freezing of Ice," Problems of Heat Transfer During a Change of State: A Collection of Articles," AEC-tr-3405, (translated from a publication of the State Power Press, Moscow), 1953, pp. 169–178.

8 Ede, A. J., "Heat Transfer by Natural Convection in a Refrigerated Liquid," *Proc. 8th Int. Cong. Refrig.,* London, 1951, pp. 260.

9 Ede, A. J., "The Influences of Anomolous Expansion on Natural Convection in Water," *Appl. Scient. Res.,* Vol. 5, 1955, pp. 458–460.

10 Schecter, R. S., and Isbin, H. S., "Natural Convection Heat Transfer in Regions of Maximum Fluid Density," *A.I.Ch.E. Journal,* Vol. 4, 1958, pp. 81–89.

11 Watts, R. G., discussion on "Heat, Mass and Momentum Transfer During the Melting of Glacial Ice in Seawater," by O. M. Griffin, Trans. ASME JOURNAL OF HEAT TRANSFER, Vol. 96, 1974, pp. 119–120.

12 Baker, D. J., "A Technique for the Precise Measurement of Small Fluid Velocities," *J. Fluid Mech.,* Vol. 26, No. 3, 1966, pp. 573–575.

13 Glasstone, S., *The Elements of Physical Chemistry,* Van Nostrand, New York, 1958, pp. 475–479.

14 Bayley, F. J., Owen, J. M., and Turner, A. B., *Heat Transfer,* Thomas Nelson and Sons Ltd., 1972, pp. 211–212.

15 Kell, G. S., "Thermodynamic and Transport Properties of Fluid Water," *Water: A Comprehensive Treatise,* ed. F. Franks, Plenum Press, New York, 1972.

16 Gosman, A. D., Pun, W. M., Runchal, A. K., Spalding, D. B. and Wolfshtein, M., *Heat and Mass Transfer in Recirculating Flows,* Academic Press, London and New York, 1969.

K. Taghavi-Tafreshi
Research Assistant.

V. K. Dhir
Associate Professor. Mem. ASME

I. Catton
Professor. Mem. ASME

Chemical, Nuclear and Thermal Engineering
Department,
School of Engineering and Applied Science,
University of California, Los Angeles
Los Angeles, CA 90024

Thermal and Hydrodynamic Phenomena Associated with Melting of a Horizontal Substrate Placed beneath a Heavier Immiscible Liquid[1]

The melting of a horizontal slab of frozen olive oil placed beneath a pool of warm water has been studied experimentally. The interfacial heat flux data are taken in quasi-static mode by noting the time rate of change of enthalpy of the pool of water. Because of little agitation of the pool due to low melt volume flux ($\rho_{water}/\rho_{olive\ oil} \simeq 1.09$; $\Delta T \simeq 5\text{–}45$ K)*, the pool was found to stratify with time. Hence, heat transfer coefficient data have been based on the interfacial temperature rather than on the mean pool temperature. Visual observations show that melt removal is governed by Taylor instability and that melt releasing nodes lie about a Taylor wavelength apart. Predictions of the growth of the interface based on equilibrium between surface tension and buoyant forces have been made and found to compare well with the data obtained from the movies. The heat transfer coefficient data obtained at higher pool temperatures are found to correlate well with the predictions based on the proposed model.*

Introduction

These days a concerted effort is being made to understand various physical phenomena which play a role in the safety evaluation of nuclear reactors under hypothetical core disruptive accident conditions. At different stages of a hypothetical core disruptive accident scenario, the molten fuel or fuel steel mixture may come in contact with a horizontal structural material (steel), sacrificial material in a core catcher or may fall on a concrete foundation of the containment. These materials are generally lighter than the fuel and an understanding of the thermal and hydrodynamic aspects related to their melting is essential to determine the physical state of the fuel and its penetration rate into the substrate. This in turn, will provide quantitative assessment of many of the potential safety related questions.

Recently Dhir, et al. [1] suggested that a phase change process in which the melt density is less than the pool density, would be governed by Taylor instability [2, 3]. In that work, heat transfer from pools of warm water or warm benzene to a horizontal slab of dry ice was studied in both steady and quasi-static modes. It was observed that the sublimation process was very similar to film boiling on a horizontal plate and the bubbles were released from a nearly square grid spaced about a Taylor wavelength apart. In [1], a film boiling model similar to that of Berenson [4, 5] was developed by assuming that only one bubble per λ_d^2 area of the slab was released instead of two as assumed by Berenson. This resulted in a reduction of about 15 percent in the numerical constant (changing it from 0.42 to 0.36) of Berenson's expression for the heat transfer coefficient:

$$h = 0.36 \left[\frac{k_g{}^3 h_{sg} g\,(\rho_f - \rho_g)\,\rho_g}{\mu_g \Delta T\,\sqrt{\sigma/g(\rho_f - \rho_g)}}\right]^{1/4} \tag{1}$$

Experimental data [1] were found to compare well with equation (1), as long as a stable gas film separated the overlying liquid from the dry ice surface and the gas film was laminar. However, when the temperature difference across the film was such that a stable film could no longer be maintained, a partial freezing of the overlying liquid started to occur at the interface. The heat flux quickly dropped to zero as the temperature of the pool approached its freezing temperature. At high pool temperatures at which the gas film was thought to become ripply or turbulent, the heat transfer coefficient was found to increase as square root of Reynolds number. Most of the observations of [1] have subsequently been corroborated by Alsmeyer and Reimann [6]. Alsmeyer and Reimann also qualitatively observed melting of frozen benzene and frozen o-xylene under water at about 298 K. They noted that melting process was indeed governed by

---

[1] This work was supported by Reactor Safety Research Division of U.S. Nuclear Regulatory Commission under Agreement No. AT(04-3)-34 P.A. 223, Mod. 5.

Contributed by the Heat Transfer Division and presented at the Winter Annual Meeting of the AMERICAN SOCIETY OF MECHANICAL ENGINEERS, December 10–15, 1978, San Francisco, California. Paper No. 78-WA/HT-44.

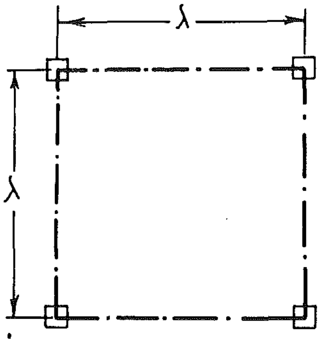

Fig. 1(*a*) Droplet releasing nodes at the melting surface

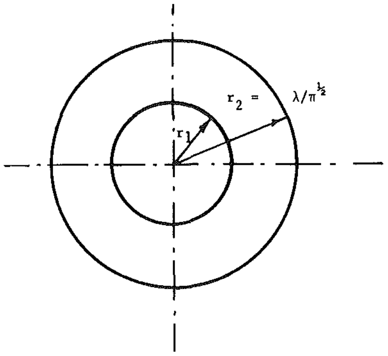

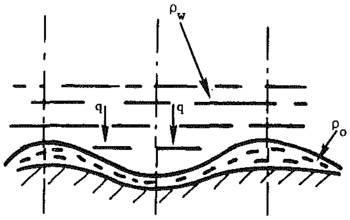

Fig. 1(*b*) Melting process

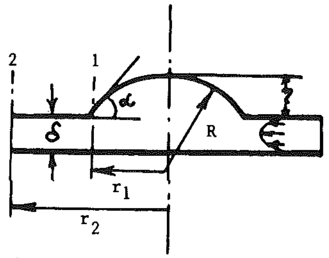

Fig. 1(*c*) Hydrodynamic and heat transfer model

Fig. 1 Physical model of the melting process

Taylor instability even for small density difference between the melt and the overlying liquid.

The aim of the present work is to study quantitatively the hydrodynamic and thermal processes associated with melting of a lighter material placed beneath a heavier immiscible liquid. In many respects the melting process will be similar to film boiling on a flat plate studied by Berensen [4] or to pseudo film boiling studied in [1]. A liquid film will be formed on the surface of the melting solid from which melt droplets governed by Taylor instability will be released cyclically. Because there is less melting beneath a droplet release node than in the region between two adjacent release nodes, the melt surface will become uneven and a standing wave pattern will be established on the surface. Subsequently, the droplets will be released only from nodes of the wave which coincide with ridges on the surface and no droplet will be released from antinodes of the wave which coincide with valleys on the surface. Droplets are not released from the valleys because the interface there becomes relatively stable due to the negative curvature. Figs. 1(*a*) and 1(*b*) show the physical process. To make the experimental investigation, water-olive oil combination is chosen ($\rho_w/\rho_o \simeq 1.09$). Olive oil is chosen as the lighter material because it provides a density ratio of interest in some of the applications, it is easy to work with and is readily available. Study of crust formation was not the subject of this work and olive oil provided a freezing temperature ($\simeq$271.5 K) which was close to the freezing temperature of water. While obtaining these advantages in using olive oil, one had to sacrifice a little in terms of well-defined and well-listed thermophysical properties of olive oil.

Analysis

The melting process will be significantly slower than pseudo film boiling [1] because of the higher density of the melt phase (relative to a gas film) and much smaller density difference between the overlying pool and the melt. This can easily be seen from the expression for linear interface growth rate between two immiscible, inviscid liquids of infinite depth. The local interface position as a function of time can be written as

$$\eta = \eta_0 e^{\omega_{\max} t}, \tag{2}$$

where ω_d is the growth frequency of the "fastest" growing Taylor wave and is given as [3]:

$$\omega_d \sim \left[\frac{\{g(\rho_f - \rho_g)\}^3}{\sigma(\rho_f + \rho_g)^2}\right]^{1/4} \tag{3}$$

The notation here conforms with that of earlier work describing a gas

Nomenclature

C = constant
c_p = specific heat of the liquid
g = gravitational acceleration
h = heat transfer coefficient
h_{sf} = latent heat of fusion
h'_{sf} = latent heat of fusion corrected for sensible heat, $h_{sf}(1 + c_{po}\Delta T/2h_{sf})$
k = thermal conductivity
q = heat flux
R = droplet radius
r = radius
Re = Reynolds number, $q\lambda/\mu_g h_{sf}$
T = temperature
t = time
$\bar{u}$ = mean film velocity in the radial direction
v = velocity in the vertical direction
Δp = pressure difference
ΔT = temperature difference between interface and melting or subliming surface
α = thermal diffusivity of the frozen olive oil
δ = film thickness
η = interface height
λ = wavelength
λ_c = critical wavelength, i.e., wavelength which has zero growth rate (neutrally stable)
λ_d = most dangerous, i.e., wavelength which has the fastest growth
μ = viscosity
ρ = density
σ = surface tension between two immiscible fluids

Superscript

* = quantities nondimensionalized with $\sqrt{\sigma/g(\rho_w - \rho_0)}$

Subscripts

f = liquid
g = gas
i = interface
m = mean
o = liquid olive oil
s = melt surface
w = water

film, g, underlying a liquid, f. The buoyancy tends to move the disturbed interface upward, while surface tension tends to hold it back. As the density of the lighter fluid approaches the heavier liquid, the magnitude of the growth rate would become very small. In this case it may be appropriate to say that, "the interface between two fluids moves so slowly that at each quasi-static position of the interface the surface tension force is in equilibrium with the bouyancy force."

Assuming that the growing interface (droplet) is part of a sphere as shown in Fig. 1(c) the base radius (half chord length) of the droplet can be written in terms of the maximum droplet height and droplet radius as

$$r_1^2 = R^2 - (R - \eta)^2. \tag{4}$$

The volume of this droplet is obtained as

$$V = \pi R \eta^2 \left(1 - \frac{\eta}{3R}\right). \tag{5}$$

Equating the buoyant and surface tension forces acting upon an oil droplet in water yields:

$$\pi R \eta^2 \left(1 - \frac{\eta}{3R}\right)(\rho_w - \rho_o) g = 2\pi R \sigma \sin^2 \alpha$$

$$= 2\pi \eta \sigma \left(2 - \frac{\eta}{R}\right)$$

or

$$R = \frac{2\left(2 - \dfrac{\eta}{R}\right)}{\eta\left(1 - \dfrac{\eta}{3R}\right)} \frac{\sigma}{(\rho_w - \rho_o) g}$$

Using $\sqrt{\sigma/g(\rho_w - \rho_o)}$ as a characteristic length, a dimensionless droplet radius can be written in terms of a dimensionless interface height as

$$R^* = \frac{(\eta^{*2}+12) + \sqrt{(\eta^{*2} + 12)^2 - 72\eta^{*2}}}{6\eta^*} \tag{6}$$

The dimensionless droplet radius from equation (6) is plotted in Fig. 2. In this figure, the dimensionless droplet base radius and dimensionless droplet volumes obtained from equations (4) and (5), respectively, are also plotted with R^* defined by equation (6). It is observed that droplet radius decreases rapidly with droplet height while the droplet base radius decreases slightly. The droplet radius and base radius are equal at $\eta^* = \sqrt{3}$, , when the droplet becomes a hemisphere. The droplet volume increases with η^* and becomes maximum when $\eta^* \simeq 1.5$. A further increase in droplet height would demand a decrease in droplet volume if equilibrium between buoyant and surface tension forces is to hold. A decrease in droplet volume is not possible in the present process because an increase in droplet height is associated with influx of melt into the droplet. Thus, with additional mass flux, the droplet would acquire another shape, which, probably would give it a larger height and a smaller base than dictated by the equilibrium condition. This in turn would cause the buoyant force to significantly exceed the surface tension force and the droplet would break away from the interface. Generally in a cyclical process the droplet will always have some initial volume at the start of the growth period. Thus, through one cycle a droplet will start with some value of $\eta^* > 0$ and teminate with $\eta^* > 1.5$.

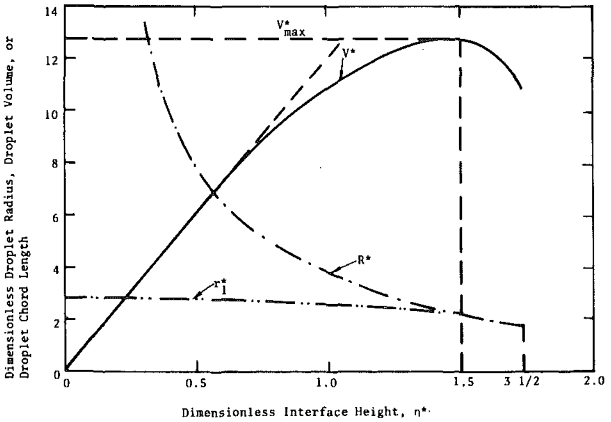

Fig. 2 Dependence of droplet volume, droplet radius, and droplet chord length on the interface height

Next, to develop a model for the heat transfer, we assume that one droplet is released per λ^2 area per cycle (Fig. 1(b)) and that this area can be replaced by an equivalent circle of radius r_2 (Fig. 1(c)) such that

$$r_2 = \lambda/\sqrt{\pi}. \tag{7}$$

Also, the center of the base of the droplet coincides with the center of the equivalent circle. We further assume that, the film is thin and inertialess, melt flow in the film is laminar, melt flows radially into the droplet and does not affect the droplet spacing, and the effect of evolution of the melt at the surface of the solid in reducing shear stress and heat transfer is small. Detailed discussion of these assumptions is given in [1].

For a constant temperature difference across the film, the radial pressure gradient with rigid wall condition at the melting surface and at the outer edge of the film (Fig. 1(c)) can be written as

$$\frac{dp}{dr} = \frac{12\mu_o k_o \Delta T}{\delta^4 \rho_o h'_{sf}} \frac{(r_2^2 - r^2)}{2r} \tag{8}$$

Assuming that the film thickness remains constant in the radial direction, the integration of equation (8) between points 2 ($=r_2$) and 1 ($=r_1$) yields

$$(\Delta p)_{2-1} = \frac{12\mu_o k_o \Delta T}{\delta^4 \rho_o h'_{sf}} \left(\frac{r_2^2}{2} \ln \frac{r_2}{r_1} + \frac{r_1^2}{4} - \frac{r_2^2}{4}\right) \tag{9}$$

The hydrostatic pressure difference between points 2 and 1 can be written while accounting for the contribution of surface tension as

$$(\Delta p)_{2-1} = (\rho_w - \rho_o) g \eta - \frac{2\sigma}{R}. \tag{10}$$

Equation (10) assumes that the pressure inside the droplet is uniform. Also, while writing equation (10), it is assumed that this equation grossly represents the pressure difference available to move the fluid in the film and in the same manner equation (8) is not expected to consistently hold good at any arbitrary location between points 1 and 2.

Elimination of $(\Delta p)_{2-1}$ between equations (9) and (10) yields

$$\delta = C_1 \left[\frac{\mu_o k_o \Delta T \sqrt{\sigma/g(\rho_w - \rho_o)}}{h'_{sf} \rho_o (\rho_w - \rho_o) g}\right]^{1/4} \tag{11}$$

where

$$C_1 = \left[\frac{3\left(2r^{*2}_2 \ln \dfrac{r^*_2}{r^*_1} + r^{*2}_1 - r^{*2}_2\right)}{(\eta^* - 2/R^*)}\right]^{1/4} \tag{12}$$

Once r^*_2 is fixed, constant C_1 can be evaluated in terms of η^* while using equation (6) for R^* and equation (4) for r_1^*. Equation (11) for δ has been arrived at by assuming that heat is transferred only through the unit cell area not covered by the droplet and no heat is transferred through the droplet. Thus, to obtain the film thickness which would give an average heat transfer over the unit cell area, equation (11) should be multiplied by the ratio of the area of the cell to the area not covered by the droplet. Or

$$\delta = C_1 \left(\frac{r^{*2}_2}{r^{*2}_2 - r^{*2}_1}\right) \left[\frac{\mu_o k_o \Delta T \sqrt{\sigma/g(\rho_w - \rho_o)}}{h'_{sf} \rho_o (\rho_w - \rho_o) g}\right]^{1/4} \tag{13}$$

The average heat transfer coefficient over the melting surface can, finally be written as[2]

---

[2] The melt properties are evaluated at the average film temperature and the slab has been assumed to have little or no subcooling.

$$h = \frac{k_o}{\delta} = C\left[\frac{{k_o}^3 h'_{sf}\rho_o(\rho_w - \rho_o)g}{\mu_o \Delta T\sqrt{\sigma/g(\rho_w - \rho_o)}}\right]^{1/4} \tag{14}$$

where

$$C = \left(\frac{1 - {r^*_1}^2/{r^*_2}^2}{C_1}\right). \tag{15}$$

The constants C_1 and C are plotted in Fig. 3 as a function of η^* for $\lambda = \lambda_d$, $0.8\lambda_d$, and λ_c. The wavelength $0.8\lambda_d$ has been chosen because it represents approximate average between critical and "most dangerous" wavelengths. Fig. 3 shows that film thickness for each wavelength depends weakly on η^* and can be considered nearly constant for η^* between $\simeq 0.4$ and 1.5. This observation is of significant importance as it suggests in addition to the earlier assumption of constant film thickness between adjacent droplets that the film thickness also remains constant throughout most of the droplet growth period. The predicted film is thinnest for the critical wavelength and is thickest for the most dangerous wavelength. For all wavelengths, the constant C for average heat transfer coefficient increases with η^* because a unit cell fractional area occupied by the droplet decreases with η^*. The constant C based on critical wavelength is more sensitive to the area change than if it were based on longer wavelengths (wavelengths closer to most dangerous wavelength). Physically, the rapid change in heat transfer during the interface growth period demanded by the critical wavelength may not be possible. Therefore, wavelengths greater than critical which give nearly uniform heat transfer rate during the growth period should be preferred. Perturbations most susceptible to growth are ones which give a wavelength close to the fastest growing Taylor wavelength. But, as we see from Fig. 3, wavelengths shorter than the most dangerous wavelength yield more efficient heat transfer process. To compromise the conflicting constraints imposed by heat transfer and wave growth rate, the process would try to adjust itself so that wavelengths somewhat shorter than the most dangerous wavelength will be preferred. This predicted behavior is similar to experimental observations made during film boiling of CO_2 near the critical pressure [7]. In film boiling of liquid CO_2 wavelengths between critical and most dangerous wavelengths are found to be dominant.

The wavelengths used in plotting the constants C_1 and C are obtained for viscous immiscible liquids of finite depth. The effect of liquid viscosity is generally to lengthen the wavelength and to reduce the growth rate [8, 9]. Using the general method outlined in [3] and [8] for liquids of infinite depth, most dangerous wavelength for olive oil-water combination was calculated. The most dangerous wavelength calculated by viscous analysis for liquids of infinite depth was about 17 percent longer and the corresponding growth rate was about 11 percent smaller than would be predicted by inviscid analysis [10]. The finite layer tends to shorten the most dangerous wavelength by about 14 percent [11] and to reduce the growth rate by about 29 percent. The net effect of liquid viscosity and finite liquid layer depth is to yield a most dangerous wavelength that is about the same as would be obtained with analysis based on infinite inviscid liquid assumptions. However, the effect of finite liquid layer and the liquid viscosity on growth rate is cumulative, i.e., to reduce the growth rate by about 40 percent. Now if we assume that during one cycle the interface grows from $\eta^* = 0.3$ (droplet starts with some initial volume) to $\eta^* = 1.5$ and that the dominant wavelength is $0.8\lambda_d$ then the value of the constant C averaged over η^* is obtained from Fig. 3 as 0.21. In reality C should be evaluated by averaging it over time. This can only be done when dependence of η^* on time is available from the experimental data. Very weak dependence of C on η^*, however, suggests that in the present situation the two averaging procedures should give about the same value of C.

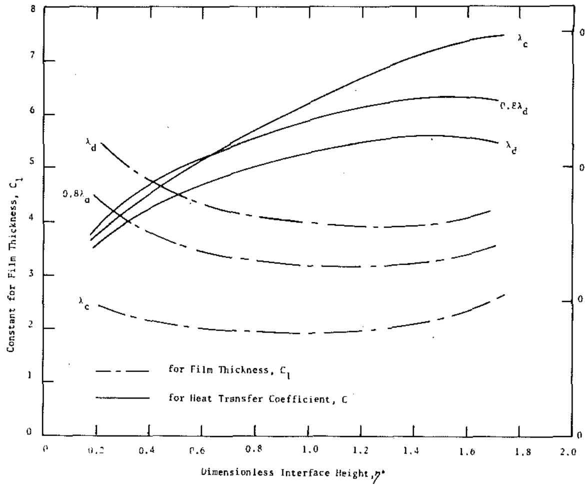

Fig. 3 Dependence of coefficients of film thickness, C_1, and heat transfer coefficient, C, on interface height and wavelength

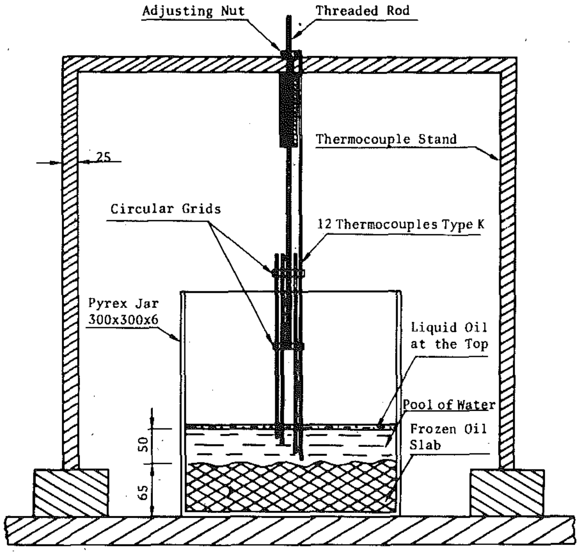

Fig. 4 Test apparatus

Experimental Apparatus and Procedure

The data for heat transfer from a pool of warm water to an underlying slab of frozen olive oil were taken in a quasi-static state. A 6.5 cm thick layer of olive oil was formed in a 30 cm dia, 30 cm high and 0.62 cm thick pyrex jar. Olive oil was frozen by placing the jar for several hours in a refrigerator. The inside temperature of the refrigerator during this period was generally found to remain constant at about 266 K. A 5 cm deep pool of warm water was formed over the slab. Preliminary experiments showed that the pool tended to stratify with time because of little agitation due to escaping of olive oil droplets. Therefore, a thermopile of ten chromel-alumel thermocouples located at different heights in the pool was formed. The thermocouples were held in two circular disks made out of aluminum. The disks were mounted on a threaded spindle and could be moved in the vertical direction with a nut.

Provision was made so that height of the thermocouples could be adjusted at the disks and independent observations of each of the thermocouples in the thermopile could be made. Two additional thermocouples were used to measure the temperature of the interface and the olive oil floating on the pool surface. The thermopile assembly was mounted on a stand made out of 2.5 cm thick square aluminum rod. Fig. 4 shows the test apparatus. The thermocouple output was recorded on two independently operable Houston X-Y recorders equipped with time bases. A selector switch was used to monitor the thermocouple output to the recorders.

Prior to each experiment, the pyrex jar containing frozen olive oil was placed on a styrofoam sheet and visual observations were made to assure that the slab was not cracked and the free surface of the slab was as nearly horizontal as possible. Thereafter, the position of the thermopile was adjusted so that the lowest thermocouple touched the slab surface. About 4 kg of distilled water was then heated to about the desired temperature. The precise weight of water was then noted and it was quickly poured into the pyrex jar. The X-Y recorder was started and temperature of the pool was recorded as a function of time. Usually experiment lasted a total of about ten minutes while data for the first three to four minutes were ignored because during this time strong transient effects due to heat absorbed by the cold pyrex jar were present. Also during this time, enough olive oil would melt to form a thin layer of olive oil over the pool free surface. The presence of olive oil over the free surface significantly cut down the heat losses due to evaporation of water. Due to melting, the frozen olive oil surface tended to recede with time from the fixed location of thermocouples in the thermopile. Thus, after an interval of about two minutes, the thermopile was moved downward by rotating the nut so that the lowest thermocouple was at about the oil-water interface. Simultaneously the temperatures of the oil-water interface and of the olive oil layer floating on the top were recorded on a second X-Y recorder. The temperature of the oil-water interface was noted by visually locating the tip of the thermocouple at the outer edge of the melt layer.

A typical temperature-time plot of the thermopile output is shown in Fig. 5 by the line AB. At point B output of the thermopile suddenly drops to C when the thermopile position is changed so that lowest thermocouple again nearly touches the interface. Actual pool temperature trace given by the thermopile would have been line AC, had one been moving the thermopile at the same rate at the receding melt surface. The average rate of decrease of water temperature with time was obtained by dividing the slope of line AC by ten (the number of thermocouples in the thermopile). Thus, to calculate the total enthalpy loss of the pool per unit area, the average rate of decrease of water temperature with time was multiplied by specific heat and mass of water in the pool and was divided by the surface area of the slab. The error in obtaining the raw heat flux is expected to be less than ±6 percent [10]. To obtain the net energy utilized in melting of the slab, heat losses are to be subtracted from the observed raw heat flux. The following mechanisms contributed to the heat losses not accounted for in the theoretical model.

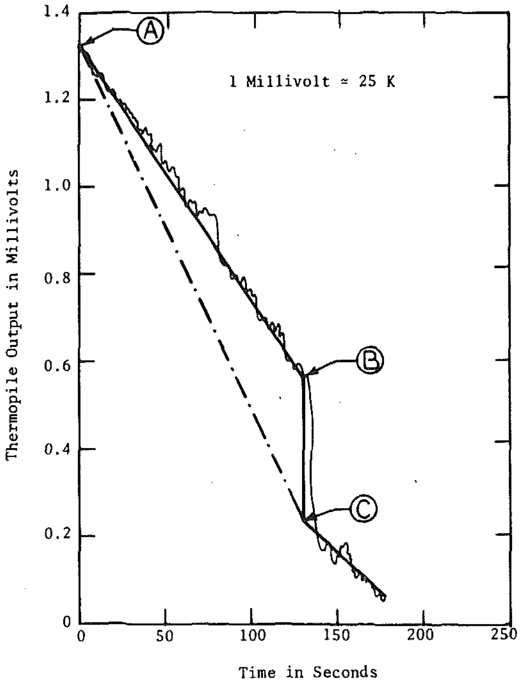

Fig. 5 Typical temperature output of the thermopile

1 Heat loss to the pyrex jar and to the surroundings: This heat loss was calculated by performing experiments for the rate at which enthalpy of the pool decreased when the slab of frozen olive oil was replaced by a 6.5 cm thick slab of bakelite (an insulating material).

2 Heat loss by conduction to the subcooled slab: The slab temperature was generally 5 K lower than the melting temperature of olive oil. The heat lost by conduction to the slab was calculated by using transient heat conduction equation in a semi-infinite slab.

3 Heat loss, as sensible heat to olive oil: Additional sensible heat (apart from that to the film) was supplied to olive oil droplet during its growth into the pool and escape through the pool as part of the olive oil layer overlying the pool free surface. This heat flux was calculated by knowing the mass flux of the melt and the temperature difference between the overlying layer of olive oil and mean temperature of the film.

Details of the heat loss calculations are given in [12]. Maximum uncertainty in calculating the net heat flux is expected to be less than ±8 percent. Error in measuring the interface temperature should be less than ±10 percent. This gives a maximum possible error of ±13 percent in the heat transfer coefficient.

To ascertain the melting temperature of olive oil, a pyrex jar containing frozen olive oil was left in the open for several hours and the temperature of the solid surface beneath the melt layer was measured precisely. This temperature was found to be 271.5 K; which is about the value reported in the literature. Values of viscosity of olive oil at different temperatures could not be found from a single source in the literature. Thus viscosity data from various sources (e.g., [13, 14]) were collected and were found to be correlated well with a correlation based on viscosity at two different temperatures reported in [14] only. Only one data point for interfacial tension between water and olive oil at 293 K was available from [13]. The interfacial tension between olive oil and water has been reported in [15] to be very weakly dependent on temperature in the temperature range 295–313 K. In the present work, the temperatures of interest generally lie in this range. Thus a constant value of interfacial tension at 293 K was used in making the predictions. The heat transfer coefficient depends only on $\sigma^{-1/8}$, thus a few percent error in surface tension would contribute to insignificant error in calculation of heat transfer coefficient from equation (14). Maximum uncertainty was encountered in obtaining the value of the latent heat of fusion of olive oil. Experiments performed with olive oil samples chilled to different temperatures and for different times showed that the latent heat of fusion significantly depended on these parameters. Thus the latent heat of fusion of olive oil was determined in the laboratory by using samples frozen in the same manner as the olive oil slabs used in the experiments. Typical values of viscosity, interfacial tension, latent heat of fusion and other thermophysical properties of olive oil are given in Table 1. Complete details of evaluation of these properties can be found in [10].

Results and Discussion

Heat transfer at water-olive oil interface led to preferential cooling of the water pool at the bottom. This was a thermally stable situation and the movement of the oil droplets through the pool was unable to agitate the pool enough to destabilize the stable liquid layer. The pool thus tended to stratify while pool temperature varied both with vertical position and with time. However, after about 4–5 min, the pool temperature in the vertical direction reached a quasi-static value.

Table 1 Used values for the properties of olive oil (all properties are evaluated at 288 K unless otherwise stated.)

Viscosity μ, centipoise	Surface tension between oil and water σ, dynes/cm	Latent heat of fusion h_{sf}, joule/gm	Thermal conductivity k, w/cm K	Specific heat c_p, joule/gm K	Density ρ, gm/cm^3	Nondimensionalizing parameter $\sqrt{\sigma/g(\rho_w - \rho_o)}$, cm
99	20 (293 K)	60	0.00169	2.00	0.916	0.493

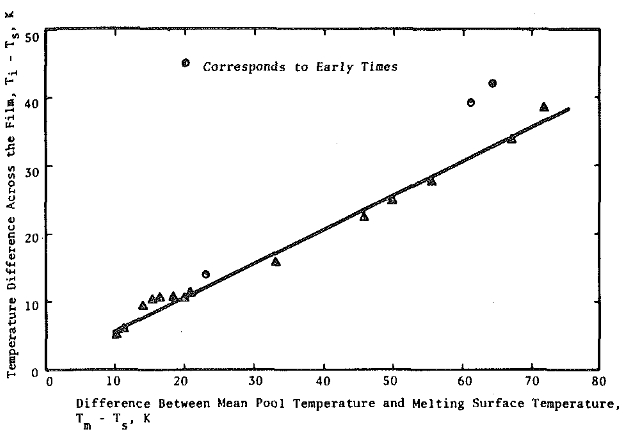

Fig. 6 Relation between mean pool temperature and interface temperature

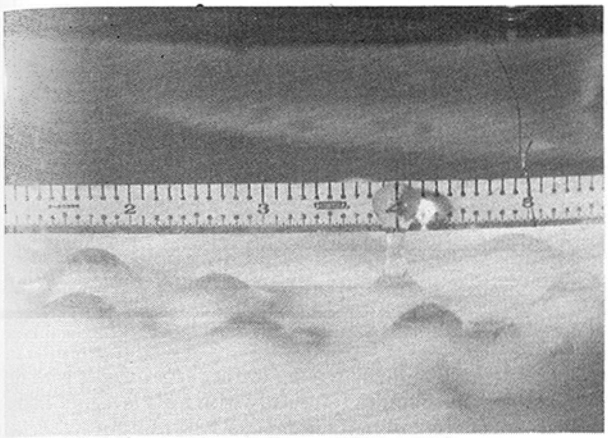

Fig. 7(*a*) Side view

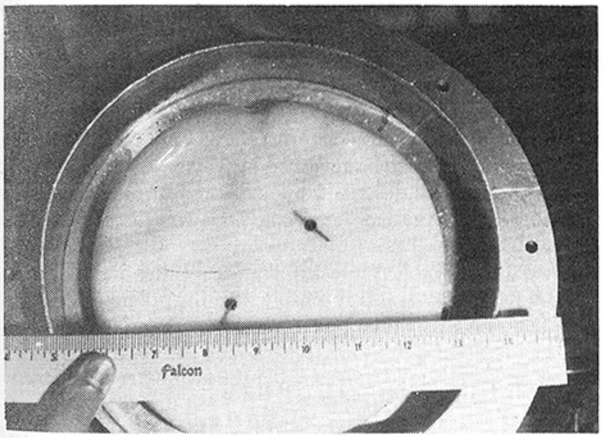

Fig. 7(*b*) Top view

Fig. 7 Photograph of melting of olive oil $\lambda \simeq 5.4$ cm (scale in picture is in inches)

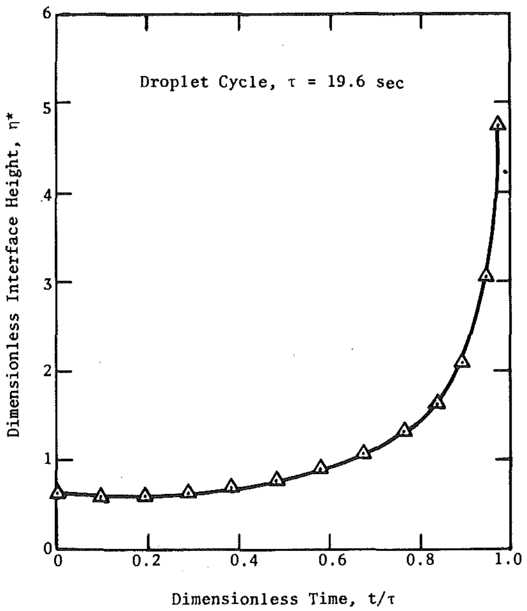

Fig. 8 Interface height as a function of time during one cycle

Thereafter, the ratio of maximum or mean pool temperatures to the interface temperature remained nearly constant with time. The quasi-static oil-water interface temperature at the melting surface is plotted in Fig. 6 as a function of the mean pool temperature. Few data points marked in circles and not correlated by the straight line drawn through most of the data, correspond to times shortly after forming the pool of warm water over the frozen olive oil surface. For these times (<5 min) transient effects were present.

Photographs in Fig. 7 show the side and top views of the melt removal process when a pool of water at a mean temperature of about 325 K was formed over the slab. The ridges and valleys show a definite wave pattern. The distance measured between two consecutive nodes lying over the middle portion of the slab (Fig. 7(*a*)) measures about 5.4 cm ($\simeq \lambda_d$). The droplet spacing as well as droplet arrangement are distorted near the edges. The first row of droplets seen in Fig. 7(*a*) lies adjacent to the slab edge and in this row the droplet spacing is less than that in the interior. A square grid pattern and a three-dimensional wave is clearly visible in this photograph. The spacing between nodes of the droplets was measured to lie between 4.0 to 5.5 cm, whereas two-dimensional most dangerous Taylor wavelength based on viscous and finite layer analysis is predicted to be 5.5 cm. The height difference between peaks and valleys tended to increase as the melting progressed and was observed to reach a limiting value of about $\lambda/6$.

Interface height as a function of time during one droplet cycle is shown in Fig. 8. During the first quarter period, the interface is seen to maintain its near equilibrium position. Visual observations showed that during this period, interface tended to smooth out any distortions caused to the interface during the previous droplet pinching-off period. At $\eta^* = 1.5$, the droplet height starts to increase very rapidly with time. This is indicative of the breaking away of the droplet from the interface. This value of η^* at which the droplet starts to break away is exactly the same as has been predicted from the theoretical analysis. The droplet height, η^*, at half the time period for one cycle is observed to be about 0.85. Various other droplet parameters such as droplet radius, R^*, droplet base radius, r_1^*, radius of equivalent circle, r_2^*, and droplet height observed at half period are compared in Table 2 with the predictions based on $\lambda = 0.8\lambda_d$ and λ_d. It is observed that predictions are in fair agreement with the data.

The growth rate of the olive oil-water interface predicted by Taylor stability theory for viscous immiscible liquids of finite depth is plotted in Fig. 9 as a function of wavelength of the disturbance. In this figure the range of observed wavelength and the growth rates during early periods when linear stability theory is applicable are also plotted. It is noted that the interface growth rate in the experiments is about 30 times slower than would be predicted for the most dangerous or the fastest growing Taylor wavelength. This confirms the assumption made earlier, while doing the analysis, that equilibrium between surface tension and buoyant forces exists and the interface has little or no inertia. Furthermore, the observed wavelengths lie between the critical and the most dangerous wavelengths. As seen from Fig. 9, for wavelengths near the critical, a slight change in wavelength results in a large increase in growth rate. Therefore, taking into consideration the experimental constraints such as edge effects, it is possible to have much smaller growth rate than demanded by the observed wavelengths.

Table 2 Comparison of droplet data with the predictions

	Dimensionless droplet radius R^*	Dimensionless droplet chord length r_1^*	Dimensionless cell radius $r_2^* = \lambda^*/\sqrt{\pi}$	Mean interface height η^*	Constant for heat transfer coefficient C
Data (1)	3.6	2.3	5.7	0.85	0.20
(2)	4.1	2.2	5.9	0.80	0.20
Predictions based on					
$\lambda = 0.8\,\lambda_d$	4.3	2.6	5.0	0.9	0.21
$\lambda = \lambda_d$	4.3	2.6	6.3	0.9	0.20

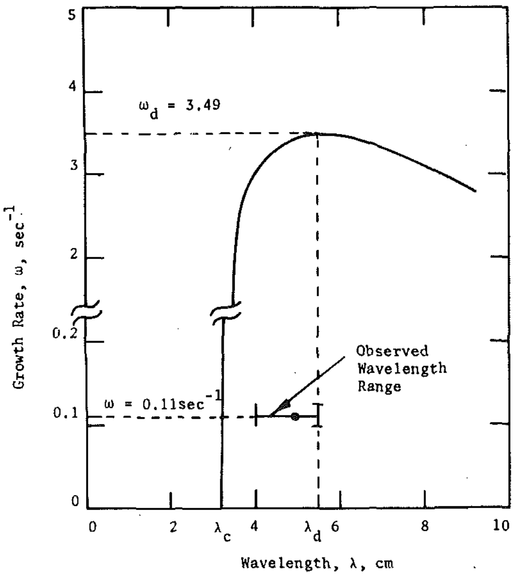

Fig. 9 Comparison of observed and predicted wavelength and growth rate

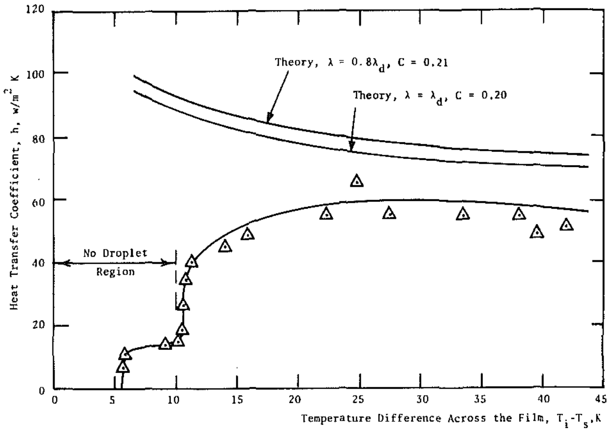

Fig. 10 Dependence of heat transfer coefficient on temperature difference across the film

Fig. 10 shows the data for heat transfer coefficient as a function of temperature difference across the film. In this figure equation (14) with constant C (=0.21) predicted a priori is also plotted. For $\Delta T >$ 20 K, the heat transfer coefficient is seen to depend on $\Delta T^{1/4}$ as has been predicted from the analysis. The prediction, however, is about 20 percent higher than the data for $\Delta T \geq 20$ K. It should be noted that the prediction is based on a prejudged value of λ and average value of η^*. However, if the prediction was based on observed value of λ and η^* as given in Table 2, the data would be about ten percent below the theory. As ΔT decreases below 20 K, the heat transfer coefficient decreases slowly till ΔT is slightly higher than 10 K. For ΔT less than 20 K, cyclic release of droplets breaks down and droplets are released randomly. For these temperature differences the film model developed earlier does not hold well. At $\Delta T \doteq 10$ K, the heat transfer coefficient decreases very rapidly and thereafter, remains nearly constant until $\Delta T \simeq 5.5$ K (T_i = 277 K). Visual observations showed that at $\Delta T \simeq 10$ K, the droplets ceased to appear at the slab surface. In the temperature range of (5.5 K $\leq T \leq$ 10 K) constant heat transfer coefficient, the heat transfer between pool and the slab takes place by direct conduction. The small temperature differences are insufficient to cause enough melting to maintain a continuous flow of melt to the droplets. At interface temperature of 277 K (ΔT = 5.5 K), the heat transfer coefficient suddenly drops to near zero. At this temperature water is heaviest and offers a stable situation such that water adjacent to the interface stays at 277 K until the temperature of the whole of the pool drops to 277 K. The experiments were, however, terminated much earlier.

It should be pointed out that the cut off temperature (ΔT = 20 K) at which the heat transfer coefficient no longer depends on $\Delta T^{-1/4}$ may be peculiar to the present set of fluid combinations. The present work only demonstrates that departure of heat transfer coefficient from $\Delta T^{-1/4}$ dependence is related to certain minimum melt volume flux. Its generalization would require further experiments with different melt and pool liquids (especially with melt layers of higher thermal conductivity). Also, if the data for heat transfer coefficient based on mean pool temperature were plotted [10], the predictions based on the mean pool temperature would be about two times higher. Erroneous heat transfer coefficients may be obtained if stratification of the pool is not considered and the heat transfer coefficients are not based on the melt-water interface temperature.

Conclusions

1 Melting of a less dense material placed underneath a heavier liquid has been shown to be governed by Taylor instability theory, and to be completely described by a theoretical model based on equilibrium between surface tension and buoyant forces acting on a perturbed interface.

2 Data for the droplet radius, droplet base radius and the droplet height are found to compare favorably with the predictions.

3 The observed dominant wavelengths are found to lie between critical and most dangerous wavelengths and the observed interface growth rates are about 30 times smaller than would be predicted for the fastest growing Taylor wave.

4 The pool has been found to stratify with time because the flow induced by the movement of the droplets through the pool is insufficient to agitate the pool.

5 Heat transfer coefficient data obtained for interface and melting surface temperature differences greater than 20 K are found to be about 20 percent lower than predictions. The obtained heat transfer coefficients may be much lower than the prediction if the heat transfer coefficients were based on the difference between mean pool temperature and the melting temperature of the slab.

References

1 Dhir, V. K., Castle, J. N., and Catton, I., ASME JOURNAL OF HEAT TRANSFER, 1977, pp. 411–418.
2 Taylor, G. I., *Proceedings Royal Society London*, A-201, 1950, p. 192.
3 Bellman, R., Pennington, R. H., *Quarterly Applied Mathematics*, Vol. 12, 1954, p. 151.
4 Berenson, P. J., ASME JOURNAL OF HEAT TRANSFER, 1961, pp. 351–362.

5 Berenson, P. J., *International Journal of Heat and Mass Transfer,* Vol. 5, No. 10, 1962, pp. 985–999.

6 Alsmeyer, H. and Reimann, M., "On the Heat and Mass Transport Processes of a Horizontal Melting or Decomposing Layer Under a Molten Pool," paper presented at the Nuclear Reactor Safety Heat Transfer Symposium, ASME Winter Annual meeting, 1977.

7 Abadzic, E. and Goldstein, R. J., *International Journal of Heat and Mass Transfer,* Vol. 13, No. 11, 1970, pp. 1163–1175.

8 Dhir, V. K., and Lienhard, J. H., *International Journal of Heat and Mass Transfer,* Vol. 16, No. 11, 1973, pp. 2097–2109.

9 Plesset, M. S., and Whipple, C. G., *Physics of Fluids,* Vol. 17, No. 1, 1974.

10 Taghavi-Tafreshi, K., "Study of Thermal and Hydrodynamic Processes Associated with Melting of Horizontal Substrate," M.S. Thesis, University of California, Los Angeles, CA, Sept. 1978.

11 Hsieh, D. Y., ASME *Journal of Basic Engineering* 1972, pp. 156–162.

12 Taghavi-Tafreshi, K., Dhir, V. K., and Catton, I., "Thermal and Hydrodynamic Phenomena Associated with Melting of A Horizontal Substrate Placed Beneath a Pool of Heavier Immiscible Liquid," Paper No. 78-WA/HT-44, presented at the 1978 ASME Winter Annual Meeting, San Francisco, CA, 1978.

13 Batchelor, G. K., *An Introduction to Fluid Dynamics,* Cambridge University Press, 1967.

14 Eckey, E. W., *Vegetable Fats and Oils,* Reinhold Publishing Corp., 1954.

15 Hartridge, H., and Peters, R. A., "Surface Tension Between Olive Oil-Water," Proceedings Physiology, Oct. 16, 1920, *Journal of Physiology,* 54 xli.

B. Rubinsky
Research Assistant.
Cryogenic Engineering Laboratory,
Massachusetts Institute of Technology,
Cambridge, MA 02139

E. G. Cravalho
Matsushita Professor of Mechanical
Engineering in Medicine.
Department of Mechanical Engineering,
Massachusetts Institute of Technology
Cambridge, MA 02139

The Determination of the Thermal History in a One-Dimensional Freezing System by a Perturbation Method

A perturbation method is employed to determine the thermal history of a biological organ frozen with a constant cooling rate at its outer surface. Solutions were obtained for the time history of the propagating phase front and the distribution of cooling rates within the organ. By means of a one-dimensional analysis, a new dimensionless group has been found to correlate the range of cooling rates in a frozen organ of complex shape. The analytical model has been confirmed by experimental measurements on a one-dimensional freezing system. The results of this treatment are useful in the design and analysis of experiments dealing with freezing in one dimension, particularly in the preservation of organs by freezing.

Introduction

One of the technical difficulties encountered by surgeons in organ transplantation is the shortage of available organs and the need for close donor-recipient interaction in terms of time and compatibility of the organ. One possible solution to this problem is an organ bank similar to the existing blood banks.

Biological cellular preparations have been preserved successfully at low temperatures for prolonged periods of time. This method of preservation is already used extensively for red blood cells and spermatozoa [1].

Experimental evidence indicates that, when storing a cellular preparation at low temperatures, the survival of the cells depends upon the cooling rate, and subsequently, the heating rate in the temperature range close to the temperature of the change of phase [2]. The plots depicting the dependence of survival on cooling rate have a shape that is approximately Gaussian with a maximum survival peak at a certain optimal cooling rate and with the survival decreasing at both higher and lower cooling rates. Each cell type has its own particular survival curve and the range of cooling rates for the various types of human cells covers several orders of magnitude. A generally accepted theory, due initially to Mazur [2] suggests a dual mechanism responsible for the damage occurring in the frozen cell. At suboptimal cooling rates the damage is a consequence of the increased concentration of electrolytes in the cellular solution as water leaves the solution in the form of ice, while at above optimal cooling rates damage correlates with the formation of intracellular ice.

Organs and cellular preparations have a certain similarity, and therefore it is most tempting to postulate that the viability of a frozen organ will depend upon the cooling rate. Finding such a relation is complicated by the fact that organs are composed of large numbers of different types of cells, their volumes tend to be much larger than those of cellular preparations, and their shapes are irregular; therefore, it is much more difficult to determine the optimum range of cooling rates when freezing an organ.

The purpose of this paper is to deal with the complexity introduced by the volume and shape factors of the organ. A dimensionless analytical study based on perturbation methods and experimental measurements will be performed for the temperature profile and cooling rates in the frozen organ when a constant cooling rate is imposed on the outer surface of the organ. A criterion for the range of cooling rates in the frozen organ will be sought in terms of a dimensionless number. Although the analysis performed for the one-dimensional case is in cartesian coordinates, it can be extended to cylindrical and spherical coordinates.

Analysis

Heat transfer problems dealing with phase change are referred to as Stefan-type problems. The boundary conditions in those problems are nonlinear and cannot be solved by conventional analytical methods of solution; thus, a variety of analytical and numerical methods have been devised to overcome this difficulty. Most of these methods are described in [3].

Perturbation methods for a situation involving a change of phase employ Stefan number, Ste, as a perturbation parameter. In the solution presented here, the moving phase boundary is immobilized by a transform proposed by Landau [4], and subsequently used in a perturbation method [5], which makes the nonlinearity appear explicitly in the heat transfer equation. Further, the relation between the position of the freezing front and the heat flux through it derived

---

Contributed by the Heat Transfer Division for publication in the JOURNAL OF HEAT TRANSFER. Manuscript received by The Heat Transfer Division August 3, 1978.

from a heat balance on the front, is introduced into the heat transfer equation. Then, a long-time solution can be found by a regular perturbation for the temperature distribution. A peculiarity of this approach is that the square of the position of the freezing front rather than the position itself is presented as a regular perturbation series.

The geometry of the biological tissue is presented schematically in Fig. 1. It is assumed that the entire tissue is initially at the phase transition temperature, while the temperature on the outer boundary at $x = 0$ changes with a constant cooling rate, until some minimum temperature established by the apparatus and tissue properties is reached. Since biological tissue has a water content of 60–90 percent, it will be assumed, in this simple analysis, that the tissue has the thermal properties of water and is initially homogeneous.

The mathematical formulation for the problem stated above is:

$$\frac{\partial T}{\partial t} = \alpha \frac{\partial^2 T}{\partial x^2} \tag{1}$$

$$0 \leq x \leq s(t); \quad t > 0$$

with the initial conditions,

$$T(x, 0) = T_{ph}; \quad 0 \leq x \tag{2}$$

The boundary conditions are,

$$T(s(t), t) = T_{ph} \tag{3}$$

$$T_o(0, t) = T_{ph} - Ht \tag{4}$$

and the heat balance on the freezing front,

$$k \frac{\partial T}{\partial x}(s(t), t) = \rho L \frac{ds(t)}{dt} \tag{5}$$

and,

$$s(0) = 0 \tag{6}$$

The temperature of the outer surface changes at a constant rate, H, and the minimum temperature, $T_{\min}$, that can be achieved on the outer surface, for each value of H, is a function of the freezing system used and the tissue properties. The position of the phase boundary when $T_o = T_{\min}$ is defined as $s = a$.

The normalized dimensionless variables employed in this analysis are,

$$u = \frac{T_{ph} - T}{T_{ph} - T_{\min}}; \quad \zeta = \frac{x}{|s(t)|} \tag{7}$$

$$S = \frac{s}{a}; \quad \tau = \frac{H.t}{T_{ph} - T_{\min}}$$

The dimensionless parameters used in this analysis are

$$\mathrm{Ste} = \frac{c_p(T_{ph} - T_{\min})}{L}; \quad B = \frac{Ha^2}{(T_{ph} - T_{\min})\alpha} \tag{8}$$

where Ste is the Stefan number and B, a dimensionless number similar to the Fourier number. The square of the position of the freezing front will be called

$$[S(\tau)]^2 = A \tag{9}$$

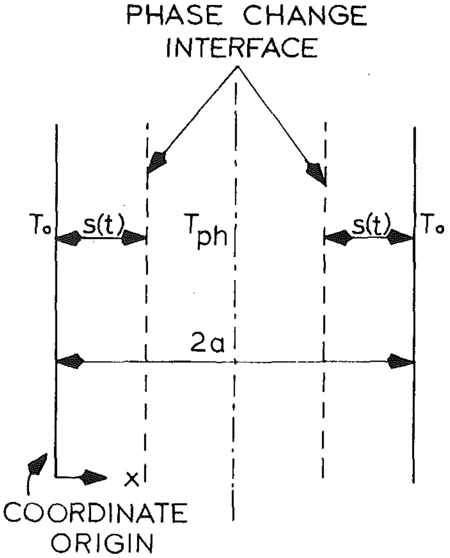

Fig. 1 Schematic drawing of model

When equations (6–8) are introduced into equations (1–5), the results are

$$\frac{\partial^2 u}{\partial \zeta^2} = B\left[A \frac{\partial u}{\partial \tau} - \frac{\zeta}{2} \frac{\partial u}{\partial \zeta} \frac{dA}{d\tau}\right] \tag{10}$$

$$0 \leq \zeta \leq 1; \quad 0 < \tau \leq 1$$

$$u(\zeta, 0) = 0 \tag{11}$$

and

$$u(1, \tau) = 0 \tag{12}$$

$$u(0, \tau) = \tau \tag{13}$$

$$\frac{\partial u}{\partial \zeta}(1, \tau) = -\frac{B}{2\,\mathrm{Ste}} \frac{dA}{d\tau} \tag{14}$$

and,

$$A(0) = 0 \tag{15}$$

From equations (14) and (15) it can be found that

$$A = -\frac{2\,\mathrm{Ste}}{B} \int_0^{\tau} \frac{\partial u}{\partial \zeta}(1, \tau)\, d\tau \tag{16}$$

and when (16) is introduced into (10), it yields

$$\frac{\partial^2 u}{\partial \zeta^2} = -\,\mathrm{Ste}\left[2 \frac{\partial u}{\partial \tau} \int_o^{\tau} \frac{\partial u}{\partial \zeta}(1, \tau) d\tau - \zeta \frac{\partial u}{\partial \zeta} \frac{\partial u}{\partial \zeta}(1, \tau)\right] \tag{17}$$

$$0 \leq \zeta \leq 1; \quad 0 < \tau \leq 1$$

The values for the Stefan number in biological tissue (water) for the temperature range in which experiments are conducted are smaller than 1 and decrease for higher minimal temperatures $T_{\min}$. Thus the Ste number can be regarded as a perturbation parameter.

Nomenclature

a = tissue half width
A = square of the dimensionless location of the freezing front
B = dimensionless number defined in equation (8)
B^* = dimensionless number defined in equation (32)
Bi = Biot number, $\frac{h.a}{k}$
c = specific heat
h = heat transfer coefficient
H = cooling rate
k = thermal conductivity
$\ell_{\min}$ = half of the smallest dimension of an organ
L = latent heat
s = temporary position of freezing front
S = dimensionless position of freezing front
Ste = Stefan number defined in equation (8)
u = dimensionless temperature
t = time
T = temperature
T_o = temperature of outer surface
T_{ph} = change of phase temperature
T_f = fluid temperature
$T_{\min}$ = minimum temperature for a certain freezing protocol
x = length
α = thermal diffusivity
ρ = density
τ = dimensionless time
ζ = dimensionless length

Equation (17) suggests the following form for the long-time perturbation solution for the temperature profile:

$$u = u_0 + \mathrm{Ste}\, u_1 + \mathrm{Ste}^2\, u_2 + \cdots 0(\mathrm{Ste}^3) \tag{18}$$

Introducing equation (18) into equation (17) and equating powers of the Stefan number, we obtain

$$\mathrm{Ste}^0, \frac{\partial^2 u_0}{\partial \zeta^2} = 0 \tag{19}$$

$$\mathrm{Ste}^1, \frac{\partial^2 u_1}{\partial \zeta^2} = -2\frac{\partial u_0}{\partial \tau}\int_0^{\tau}\frac{\partial u_0}{\partial \zeta}(1, \tau)d\tau + \zeta\frac{\partial u_0}{\partial \tau}\frac{\partial u_0}{\partial \zeta}(1, \tau) \tag{20}$$

$$\begin{aligned}\mathrm{Ste}^2, \frac{\partial^2 u_2}{\partial \zeta^2} = {} & -2\frac{\partial u_0}{\partial \tau}\int_0^{\tau}\frac{\partial u_1}{\partial \zeta}(1, \tau)\mathrm{d}\tau \\ & + 2\frac{\partial u_1}{\partial \tau}\int_0^{\tau}\frac{\partial u_0}{\partial \zeta}(1, \tau)d\tau - \zeta\frac{\partial u_0}{\partial \zeta}\frac{\partial u_1}{\partial \zeta}(1, \tau) \\ & - \zeta\frac{\partial u_1}{\partial \zeta}\frac{\partial u_0}{\partial \zeta}(1, \tau)\end{aligned} \tag{21}$$

Substituting equation (18) into equations (12) and (13), we obtain for the boundary conditions

$$u_0(0, \tau) = \tau \tag{22}$$

$$u_i(0, \tau) = 0, i = 1, 2 \cdots \tag{23}$$

$$u_i(1\ \tau) = 0, i = 0, 1, 2 \cdots \tag{24}$$

In this problem the initial condition is immaterial as seen in equation (6) and therefore the long-time solution found here is the solution of the problem in the whole domain of time.

The solution of equations (19–24) is

$$\begin{aligned}u = {} & \tau(1-\zeta) - \frac{\mathrm{Ste}\,\tau\,\zeta(1-\zeta)}{2} \\ & + \frac{(\mathrm{Ste}\,\tau)^2\zeta(1-\zeta)(2\zeta+5)}{18} + \cdots 0(\mathrm{Ste}^3) \\ & 0 \le \zeta \le 1; \quad 0 < \tau \le 1\end{aligned} \tag{25}$$

This solution has apparently secular terms in τ and ζ, but it should be remembered that τ and ζ are normalized with respect to their maximum values and therefore in the discussed time-space domain, the perturbation solution will not break down. From equations (9, 16) and (25) the dimensionless position of the freezing front was obtained

$$S(\tau) = \left[\frac{\mathrm{Ste}\,\tau}{B}\left(1 - \frac{\mathrm{Ste}\,\tau}{3} + \frac{7(\mathrm{Ste}\,\tau)^2}{36} + \cdots 0(\mathrm{Ste})^3\right]^{1/2} \tag{26}$$

From the definitions of $S(\tau)$ and τ in equations (7) and (8) as normalized variables, it follows that when their maximum values are introduced in equation (26) (i.e. $S(1) = 1$), we obtain

$$1 = \left[\frac{\mathrm{Ste}}{B}\left(1 - \frac{\mathrm{Ste}}{3} + \frac{7\,\mathrm{Ste}^2}{36} + \cdots 0(\mathrm{Ste}^3)\right)\right]^{1/2} \tag{27}$$

From equations (7, 8) and (27) the value of a becomes

$$a = (T_{ph} - T_{\min})\left(\frac{\alpha\, c_p}{\mathrm{HL}}\right)^{1/2}\left[1 - \frac{\mathrm{Ste}}{3} + \frac{7\,\mathrm{Ste}^2}{36}\right]^{1/2} \tag{28}$$

The cooling rate on the freezing front at its maximum penetration can be found from equations (7) and (25) viz.

$$\frac{\partial T}{\partial t}(s(t), t) = -H\frac{\left(1 - \frac{\mathrm{Ste}}{2} + \frac{7\,\mathrm{Ste}^2}{18}\right)^2}{\left(1 - \frac{\mathrm{Ste}}{3} + \frac{7\,\mathrm{Ste}^2}{36}\right)} \tag{29}$$

From consideration of the continuity of the solution it can be concluded that when freezing a tissue with a constant cooling rate on its outer surface, the extent of the frozen area a when $T_0 = T_{\min}$ will be given by equation (28) and the range of cooling rates to be found in this area will vary between H and the value given by equation (29).

An order of magnitude analysis of equation (27) shows that

$$\frac{\mathrm{Ste}}{B} = 0(1) \tag{30}$$

Equation (30) can supply a criterion for evaluating the range of cooling rates in a complex organ frozen by a cooling protocol similar to that discussed in this paper. If

$$B^* \le \mathrm{Ste} \tag{31}$$

where B^* is defined as

$$B^* = \frac{H\, l_{\min}}{(T_{ph} - T_{\min})\alpha} \tag{32}$$

and $l_{\min}$ is half of the smallest dimension of the organ, then the cooling rates in the frozen tissue will vary between

$$\begin{aligned}& H \ge \frac{\partial T}{\partial t}(x, t) \ge H\frac{\left(1 - \frac{\mathrm{Ste}}{2} + \frac{7\,\mathrm{Ste}^2}{18}\right)^2}{\left(1 - \frac{\mathrm{Ste}}{3} + \frac{7\,\mathrm{Ste}^2}{36}\right)} \\ & \text{for } 0 \le x \le a; \quad 0 \le t \le \frac{T_{ph} - T_{\min}}{\mathrm{H}}\end{aligned} \tag{33}$$

At this point it is useful to consider the experimental procedure used in order to achieve a constant cooling rate on the outer surface of the tissue. This cooling rate is usually achieved by controlling either the temperature or the flow rate of a cooling fluid (e.g., liquid nitrogen). The heat balance on the outer boundary requires that

$$-k\frac{\partial T(0, t)}{\partial x} = h(t)(T_f - T) \tag{34}$$

or

$$-k\frac{\partial T(0, t)}{\partial x} = h(T_f(t) - T)$$

at the instant the minimum temperature, T_{min} is reached on the outer surface, equations (25) and (34) show that the Biot number, Bi, becomes

$$\mathrm{Bi} = \left(1 + \frac{\mathrm{Ste}}{2} - \frac{5\,\mathrm{Ste}^2}{18}\right)\left(\frac{T_{ph} - T_{\min}}{T_{\min} - T_f}\right) \tag{35}$$

where the Biot number is defined

$$\mathrm{Bi} = \frac{h.a}{k} \tag{36}$$

By equating equations (35) and (36) the value of the required heat transfer coefficient, h, is determined for a specific freezing protocol. A comparison between the required heat transfer coefficient and the one available in a certain experimental apparatus could supply information concerning the possibility of actually freezing the organ according to the desired protocol (i.e., reaching the required minimal temperature $T_{\min}$ and freezing the required amount of tissue, a, in the specified time period).

Discussion

A numerical analysis of the solution has been performed for a biological tissue whose physical and thermal properties were assumed to be those of water.

In Fig. 2 temperature distribution in a frozen tissue is shown at different times after the freezing started. These results were obtained from equations (25) and (27) for a constant cooling rate of 10°C/min. Different order solutions were found to give similar temperature distributions for the case in which the temperature on the outer surface has reached −100°C.

The range of cooling rates in a frozen organ for different Stefan numbers as defined by equation (8) were obtained from equation (29) and presented in Fig. 3. The range of cooling rates has been found up to a Ste number of 0.6 since it has been observed that the accuracy of the second order solution decreases considerably for higher Ste numbers.

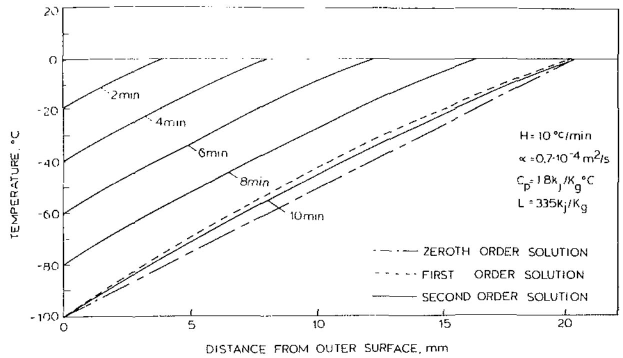

Fig. 2 Temperature distribution in the frozen medium

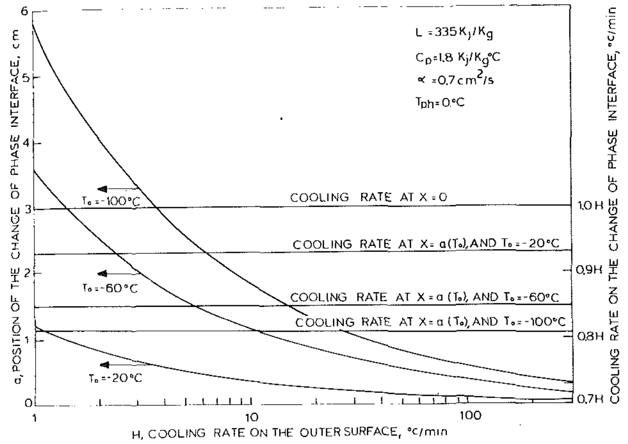

Fig. 4 Position of the freezing front as a function of the outer surface cooling rate for different outer surface temperatures; cooling rates on the freezing front for different outer surface temperatures

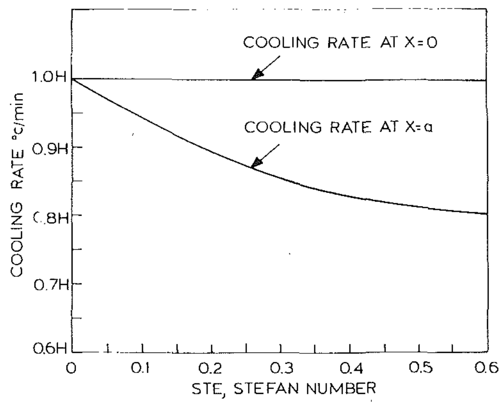

Fig. 3 The range of cooling rates in frozen tissue for different Stefan numbers

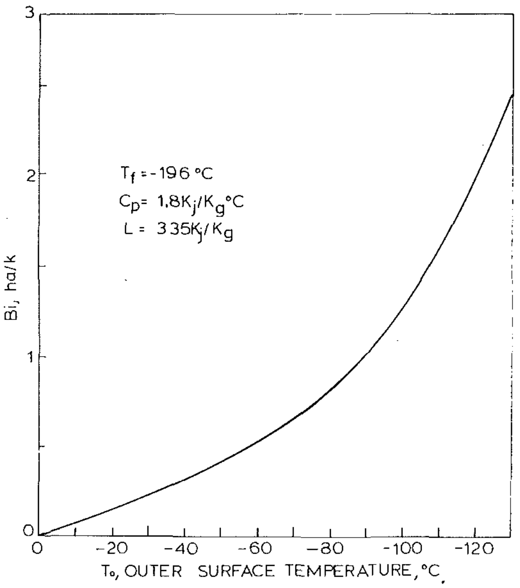

Fig. 5 The specific Biot number, as a function of the outer surface temperature

From equations (31) and (32) and Fig. 3 a simple criterion can be found for the range of cooling rates in an organ, if

$$B^* \le 0.6$$

the range of cooling rates in the organ is

$$H \ge \frac{\partial T}{\partial t}(x, t) \ge 0.8H$$

$$0 \le x \le 2\ell_{\min}; \quad 0 \le \tau \le \frac{T_{ph} - T_{\min}}{H}$$

In Fig. 4, the position of the change of phase front (given by equation (28)) is presented as a function of the outer surface cooling rate for different outer surface temperatures. The cooling rates on the change of phase front for those temperatures are presented as well. It is obvious from Fig. 4 that, if a narrow range of cooling rates is required for experimental or preservation purposes in an organ of a considerable volume it is possible to achieve this requirement for cooling rates on the order of magnitude of 10^0 °C/min, but it is not possible to achieve it for cooling rates on the order of magnitude of 10^2 °C/min or higher. For outer surface cooling rates of the order of magnitude of 10^1 °C/min, the criteria resulting from Fig. 3 and equations (31) and (32) have to be employed in order to determine the likelihood of having a narrow range of cooling rates in the frozen organ. The variation of the specific Biot number, defined by equation (36) for different outer surface temperatures has been calculated from equation (35) and is presented in Fig. 5. The use of Fig. 5 will be demonstrated by an example. It can be observed from Fig 4 that if a tissue is frozen so that a cooling rate of 100°C/min is imposed on its outer surface, the change of phase front will be at a distance of 4 mm from the outer surface when the outer surface temperature has reached −100°C. Fig. 5 shows that for this outer surface temperature the required Biot number is 1.1. A value for the heat transfer coefficient can be found from the data mentioned above by using equation (36).

$$h = \frac{\mathrm{Bi}\, k}{a}$$

or

$$h = \frac{(1.2)(2.3)}{4.10^{-3}} = 632\ \mathrm{Nm/m^2\,K}$$

This value of h is high for a gas flow and it is obvious that if such a problem is encountered the coolant should be liquid nitrogen.

Experiment

An experiment has been conducted with the intention of correlating the outer surface temperature with the change of phase front position following a freezing protocol similar to that discussed in the analytical part of this paper. Water has been used in the experiment as a first order simulation of biological tissue. The experimental apparatus consists of a laboratory test tube on a cooling stage (Fig. 6) cooled by a flow of low temperature gaseous nitrogen whose temperature is controlled by a preprogrammed controller. The controller and the coolant fluid system are employed in a cryomicroscope and were described in detail by Ushiyama in [6]. A 9 mm ID transparent plexiglass laboratory test tube with a wall thickness of 1 mm has been glued with epoxy on 0.25 mm stainless steel sheet which covers a 9 mm hole in the cooling chamber made of phenolic laminate. Water was introduced in the tube and the change of phase front was observed as it advanced from the bottom of the tube. The diameter of the tube was chosen so

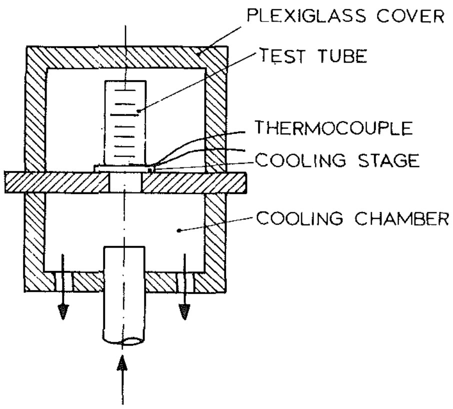

Fig. 6 Schematic drawing of the cooling stage

that the heat losses across the outer surface of the tube were negligible relative to the heat flux extracted from the bottom for the range of cooling rates of interest. The design is a good representation of the one-dimensional case.

The temperature of the stainless steel sheet at the surface in contact with the water was measured by means of a 0.05 mm copper constantan thermocouple connected to the controller and a chart recorder. The tube had a scale covering half its circumference printed on the inside (in order to avoid parallax) and divided into increments of 2.5 mm. The whole apparatus was positioned so that there was a distance of approximately 5 cm between the tube and the chart recorder and a distance of 15 cm between the tube and a GBC-ITC, T.V. camera which was focussed on a plane midway between the tube and the chart recorder. A certain cooling rate was set on the controller and the freezing process including the data on the chart were recorded magnified on a video tape thus making it possible to continuously correlate the position of the freezing front and the temperature of the outer surface which dropped with a constant cooling rate.

The experimental results for a number of cooling rates have been compared with the analytical results obtained from equations (26) and (28) and are presented in Fig. 7. A very good correlation was found for temperatures of the outer surface as low as −45°C. It has been further observed that for a cooling rate of approximately 10°C/min and the existing experimental set-up, the lowest temperature reached was approximately −45°C.

Conclusions

A perturbation method has been employed to analyze the problem of freezing a biological tissue when a predetermined constant cooling rate is imposed on its outer surface. Based on this analysis, the following conclusions can be drawn:

1 When an organ or tissue is frozen in such a way that the outer surface temperature decreases at a constant rate, H, to a certain minimum temperature, $T_{\min}$, the range of cooling rates in the frozen medium up to the instant that the minimum temperature is reached is narrow and varies only between H and $0.8\,H$.

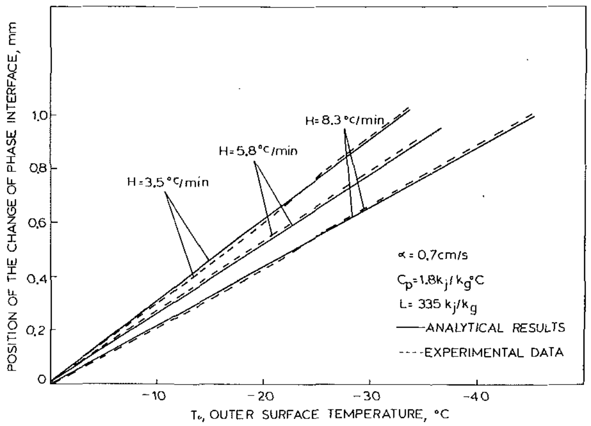

Fig. 7 Position of the freezing front as a function of outer surface temperature, analytical and experimental results

2 The range of cooling rates in an organ of a complex shape frozen by this method can be evaluated by a dimensionless number which includes the thermophysical and geometrical data of that tissue or organ.

3 If a narrow range of cooling rates is required in a frozen organ or tissue (for experimental or preservation purposes), it is most likely that this requirement can be achieved with cooling rates of the order of magnitude of 10^0 °C/min, but most likely could not be achieved for cooling rates on the order of magnitude of 10^2 °C/min or higher. For the intermediate range of cooling rates the dimensionless number mentioned above should be employed to determine whether in a specific tissue it is possible to achieve the narrow range of cooling rates.

4 The analytical results compare well with experimental measurements. The results presented in this paper could facilitate the determination of the range of cooling rates in an organ of irregular shape frozen according to the freezing program analyzed in this paper. This information could be helpful in the analysis of an experimental procedure whose purpose would be to find a correlation between cooling rates and post freezing organ viability.

References

1 Meryman, H. T., 1966: "Review of Biological Freezing" *Cryobiology*, Academic Press, London.

2 Mazur, P., 1966: "Physical and Chemical Basis of Injury in Single Celled Micro-Organisms Subjected to Freezing and Thawing," *Cryobiology*, Academic Press, London.

3 Ockendon, T. R. and Hodgkins, R. W. eds., 1975: "Moving Boundary Problems in Heat Flow and Diffusion," Clarendon Press, Oxford.

4 Landau, H. G., 1950: "Heat Conduction in a Melting Solid," *Quarterly of Applied Mathematics*, Vol. 8, pp. 81–94.

5 Huang, G. L. and Shim, Y. P., 1976: "Perturbation Solutions of Moving Boundary Problems," *Int. J. Heat Mass Transfer*, Vol. 19, pp. 690–696.

6 Ushiyama, M., 1973: "Volumetric Changes in Saccharomyces Cervisiaé During Freezing at Constant Cooling Velocities," SB/SM Thesis, Department of Mechanical Engineering, M.I.T., Cambridge, MA.

M. N. Özişik
J. C. Uzzell, Jr.

Department of Mechanical and Aerospace Engineering
North Carolina State University,
Raleigh, N.C. 27650

Exact Solution for Freezing in Cylindrical Symmetry with Extended Freezing Temperature Range

The problem of solidification by a line heat sink in an infinite medium with cylindrical symmetry for a substance having an extended freezing temperature range between the solidus and liquidus temperatures is solved exactly for two different cases characterizing the distribution of the solid fraction within the two-phase zone. In one of the models, the solid fraction is assumed to vary linearly with the temperature and in the other solidification within the two-phase zone is assumed to have a linear relationship with the distance. The analysis is applicable for both eutectic and solid solution alloys.

Introduction

The exact solutions of phase change problems are limited to a few idealized situations because the interface between the phases is moving as the latent heat is absorbed or liberated; as a result the location of the solid liquid interface is not known *a priori* and must follow as part of the solution. The problems so posed are nonlinear and the solutions involve considerable difficulties; however, a limited body of literature exists. Most of the exact solutions are discussed in [1]; some of the recent work includes the solution for a semi-infinite body with extended freezing temperature range [2] and the solution for freezing of humid porous half-space [3]. Most of the solutions are for a half-space in the rectangular coordinate system. It appears that the exact solution in the cylindrical coordinate system is limited to the problem of freezing (or melting) by a line heat sink (or source) in cylindrical symmetry solved by Paterson [4] and reported in [1]. Furthermore, all the existing solutions except the one reported in [2] are for a phase change process appropriate for pure substances in which the phase change takes place at a discrete melting (or solidification) temperature; as a result, the solid and liquid regions are separated by a sharp interface at the melting point temperature of the material. In the case of a binary system the latent effect occurs in an extended zone between the solidus and liquidus temperatures, as a result a two-phase region (called a mushy region) may exist between the purely solid and purely liquid phases. This two-phase region is bounded by two isothermal interfaces, one at the solidus temperature and the other at the liquidus temperature. In the present investigation a phase change problem of this type is solved in cylindrical symmetry for solidification caused by a line heat sink located at $r = 0$.

Analysis

A line heat sink of strength Q,W/m, is located at $r = 0$ in a large body of liquid which is initially at a uniform temperature T_i higher than the liquidus temperature T_2 of the material. The heat sink is activated at time $t = 0$ and absorbs heat continuously for times $t > 0$. As a result the solidification starts at the origin and propagates in the positive r-direction. For a binary system considered here the solidification takes place over a two-phase zone consisting of solid and liquid mixture contained between the purely solid and purely liquid phases. The present study is concerned with the determination of one-dimensional transient temperature distribution in each of the phases and the locations of the solidus and liquidus fronts as a function of time. All thermophysical properties of each phase are assumed to remain constant, but may differ for different phases. The convective velocity resulting from volumetric effects is considered negligible. As the solid is continuously formed within the two-phase region, the heat released during solidification is treated as a volumetric heat generation term, in the manner of [5, 6], expressed as

$$g(r, t) = \rho L \frac{df_s}{dt}. \tag{1}$$

Here, ρ is the density, L is the latent heat per unit mass and f_s is the solid fraction within the two-phase zone. Thus, the rate of change of solid fraction with respect to the time in the two-phase zone provides a heat generation effect. The relative amount of solid phase present in an alloy at any temperature is readily determined from the phase diagram by the application of the lever rule [7] or a solid-fraction temperature relationship can be written [6]. In the present analysis, we considered two different models for the determination of f_s in the two-phase zone.

Model I. In this model, a linear relationship is assumed between the solid fraction and the temperature, such that in the two-phase zone f_s is represented by

$$f_s = f_{su}\left(1 - \frac{T_t - T_1}{T_2 - T_1}\right) \tag{2}$$

where $T_t \equiv T_t(r, t)$ is the temperature within the two-phase zone, T_1 and T_2 are the solidus and liquidus temperatures respectively. Clearly, the solid fraction f_s has a value of zero at the liquidus front and f_{su} at

---

Contributed by the Heat Transfer Division for publication in the JOURNAL OF HEAT TRANSFER. Manuscript received at the Joint Transfer Division February 13, 1978.

the solidus front. For an alloy system showing an eutectic the value of f_{su} depends upon the alloy composition. If the alloy composition lies between the horizontal extremities of the eutectic composition, f_{su} is the solid fraction at the eutectic temperature. For an alloy outside the eutectic range f_{su} is unity.

Model II. In this model, the process of solidification within the two-phase zone is assumed to have a linear relationship with the distance, expressed in the form

$$f_s = f_{su}(1 - R), \quad \text{where} \quad R = \frac{r - S_1(t)}{S_2(t) - S_1(t)}. \tag{3}$$

Here, r is the radial distance from the origin, $S_1(t)$ and $S_2(t)$ are the locations of the solidus and liquidus fronts, respectively.

Solution for Model I

The differential equations of heat condition for the solid, two-phase and liquid regions are given respectively as

$$\frac{1}{r}\frac{\partial}{\partial r}\left(r\frac{\partial T_s}{\partial r}\right) = \frac{1}{\alpha_s}\frac{\partial T_s(r,t)}{\partial t} \quad 0 < r < S_1(t),\ t > 0 \tag{4}$$

$$\frac{1}{r}\frac{\partial}{\partial r}\left(r\frac{\partial T_t}{\partial r}\right) + \frac{\rho L}{k_t}\frac{df_s}{dt} = \frac{1}{\alpha_t}\frac{\partial T_t(r,t)}{\partial t} \quad S_1(t) < r < S_2(t),\ t > 0 \tag{5}$$

$$\frac{1}{r}\frac{\partial}{\partial r}\left(r\frac{\partial T_\ell}{\partial r}\right) = \frac{1}{\alpha_\ell}\frac{\partial T_\ell(r,t)}{\partial t} \quad r > S_2(t),\ t > 0. \tag{6}$$

The heat generation term appearing in equation (5) results from the heat released in the two-phase zone according to equation (1).

The heat sink at the origin should satisfy the following energy balance equation

$$\lim_{r\to 0}\left(2\pi r k_s \frac{\partial T_s}{\partial r}\right) = Q. \tag{7}$$

The boundary conditions at the solidus front are

$$T_s(r,t) = T_t(r,t) = T_1 \quad \text{at} \quad r = S_1(t),\ t > 0 \tag{8a}$$

$$k_s\frac{\partial T_s}{\partial r} - k_t\frac{\partial T_t}{\partial r} = \rho L(1 - f_{su})\frac{ds_1(t)}{dt} \quad \text{at} \quad r = S_1(t),\ t > 0 \tag{8b}$$

where the right-hand side of equation (8*b*) accounts for the liberation of latent heat resulting from the liquid fraction $(1 - f_{su})$ in the two-phase region just at the solidus front. The boundary conditions at the liquidus front are

$$T_t(r,t) = T_\ell(r,t) = T_2 \quad \text{at} \quad r = S_2(t),\ t > 0 \tag{9a}$$

$$k_t\frac{\partial T_t}{\partial r} = k_\ell\frac{T_\ell}{\partial r} \quad \text{at} \quad r = S_2(t),\ t > 0. \tag{9b}$$

The boundary condition at $r \to \infty$ is taken as

$$T_\ell(r,t) = T_i \quad \text{as} \quad r \to \infty\ t > 0 \tag{10}$$

and the initial condition for the liquid phase as

$$T_\ell(r,t) = T_i \quad \text{for} \quad t = 0, r > 0. \tag{11}$$

In this model, the solid fraction f_s in the two-phase zone is given by equation (2). Then

$$\frac{df_s}{dt} = -\frac{f_{su}}{T_2 - T_1}\frac{\partial T_t(r,t)}{\partial t}. \tag{12}$$

Introducing equation (12) into (5), the differential equation for the two-phase zone takes the form

$$\frac{1}{r}\frac{\partial}{\partial r}\left(r\frac{\partial T_t}{\partial r}\right) = \frac{1}{\alpha_t{}^*}\frac{\partial T(r,t)}{\partial t} \tag{13a}$$

where

$$\frac{1}{\alpha_t{}^*} \equiv \frac{\rho L f_{su}}{k_t(T_2 - T_1)} + \frac{1}{\alpha_t}. \tag{13b}$$

Thus, the assumption f_s is a linear function of temperature as defined by equation (2) removed the nonhomogeneous generation term from the differential equation for the two-phase zone. Now the analysis of the problem is reduced to the solution of the three homogeneous equations (4), (6), and (13), subject to the boundary and initial conditions given by equations (7) through (11). The solutions of these three homogeneous equations are chosen in the forms

$$T_s(r,t) = C_1 Ei(-r^2/4\alpha_s t) + C_2 \quad 0 < r < S_1(t) \tag{14}$$

$$T_t(r,t) = C_3 Ei(-r^2/4\alpha_t{}^*t) + C_4 \quad S_1(t) < r < S_2(t) \tag{15}$$

$$T_\ell(r,t) = C_5 Ei(-r^2/4\alpha_\ell t) + C_6 \quad r > S_2(t) \tag{16}$$

where $Ei(-z)$ is the exponential integral function [8] and C_i's, i = 1 to 6, are the integration constants. The notation $E_1(x)$ has also been used for $-Ei(-x)$ in other references. Clearly, these equations satisfy the differential equations (4), (6), and (13). The integration constants are determined by utilizing the six boundary conditions given by equations (7), (8*a*), (9*a*), and (10); the coefficients determined in this manner also satisfy the initial condition (11) for the liquid phase. The resulting solutions are given as

$$T_s(r,t) = T_1 + \frac{Q}{4\pi k_s}\left[Ei(-r^2/4\alpha_s t) - Ei(-\lambda^2)\right] \quad 0 < r < S_1(t) \tag{17a}$$

$$T_t(r,t) = \frac{T_2 - T_1}{Ei(-\eta^2) - Ei(-\lambda^2\alpha_s/\alpha_t{}^*)}Ei(-r^2/4\alpha_t{}^*t) + \frac{T_1 Ei(-\eta^2) - T_2 Ei(-\lambda^2\alpha_s/\alpha_t{}^*)}{Ei(-\eta^2) - Ei(-\lambda^2\alpha_s/\alpha_t{}^*)} \quad S_1(t) < r < S_2(t) \tag{17b}$$

$$T_\ell(r,t) = T_i - \frac{T_i - T_2}{Ei(-\eta^2\alpha_t{}^*/\alpha_\ell)}Ei(-r^2/4\alpha_\ell t) \quad r > S_2(t) \tag{17c}$$

where, in the process of obtaining these solutions, we introduced two unknown constants λ and η defined as

$$\lambda = S_1(t)/2(\alpha_s t)^{1/2} \quad \text{or} \quad S_1(t) = 2\lambda(\alpha_s t)^{1/2} \tag{18a}$$

$$\eta = S_2(t)/2(\alpha_t t^*)^{1/2} \quad \text{or} \quad S_2(t) = 2\eta(\alpha_t{}^*t)^{1/2}. \tag{18b}$$

and λ and η are both positive quantities.

Finally, when equations (17) and (18) are introduced into the interface energy balance equations (8*b*) and (9*b*) the following two transcendental equations are obtained for the determination of the parameters λ and η:

$$\frac{Q}{4\pi}e^{-\lambda^2} - \frac{k_t(T_2 - T_1)}{Ei(-\eta^2) - Ei(-\lambda^2\alpha_s/\alpha_t{}^*)}e^{-\lambda^2\alpha_s/\alpha_t{}^*} = \lambda^2\alpha_s(1 - f_{su})\rho L, \tag{19a}$$

$$k_t\frac{T_2 - T_1}{Ei(-\eta^2) - Ei(-\lambda^2\alpha_s/\alpha_t{}^*)}e^{-\eta^2} = k_\ell\frac{T_2 - T_i}{Ei(-\eta^2\alpha_t{}^*/\alpha_\ell)}e^{-\eta^2\alpha_t{}^*/\alpha_\ell}. \tag{19b}$$

Nomenclature

B_n = defined by equation (25*b*)
f_s = solid fraction in the two-phase region
f_{su} = solid fraction in the two-phase region at the solidus front
$g(r,t)$ = internal heat generation defined by equation (1), W/m^3
k = thermal conductivity, W/m°C
L = latent heat, Ws/kg
Q = strength of the line heat sink, W/m
r = radial space coordinate
$S_1(t), S_2(t)$ = the locations of the solidus and liquidus fronts respectively, m
t = time, s
T = temperature, °C
T_1, T_2, T_i = solidus, liquidus, and initial temperatures respectively
α_{t^*} = defined by equation (13b)
α = thermal diffusivity, m^2/s (i.e., $\alpha_s = k_s/\rho C_s$)
λ, η = parameters defined by equations (18) or (20)
ρ = density, kg/m^3

Subscripts

ℓ, s, t = refer to the liquid, solid and two-phase regions respectively

Once λ and η are determined from the solution of equations (19), the temperatures in the solid, two-phase and liquid region are obtained from equations (17) and the locations $S_1(t)$ and $S_2(t)$ of the solidus and liquidus fronts from equations (18). The foregoing solutions are exact because the differential equations, the boundary and initial conditions are all satisifed by the solutions (17).

Solution for Model II

In this case the governing differential equations and the boundary conditions are exactly the same as those given above by equations (4–6) and (7–11) respectively. The only difference is that the solid fraction f_s within the two-phase zone is a function of position. Thus, the generation term cannot be combined with the time derivative term as has been done for the previous model; as a result the differential equation (5) for the two-phase zone remains nonhomogeneous. To determine a particular solution for this nonhomogeneous equation, an explicit form is needed for the heat generation term. A functional form for df_s/dt can be established by assuming $S_1(t)$ and $S_2(t)$ vary with the time as

$$S_1(t) = 2\lambda(\alpha_s t)^{1/2}, \quad S_2(t) = 2\eta(\alpha_t t)^{1/2}, \tag{20}$$

where the constants λ and η are yet to be determined. When equations (3) and (20) are introduced into equation (5), the differential equation for the two-phase zone takes the form

$$\frac{1}{r}\frac{\partial}{\partial r}\left(r\frac{\partial T_r}{\partial r}\right) + H\frac{r}{t^{3/2}} = \frac{1}{\alpha_t}\frac{\partial T_t(r,t)}{\partial t} \tag{21a}$$

where the constant H is defined as

$$H = \frac{\rho L f_{su}}{4k_t(\eta\alpha_t^{1/2} - \lambda\alpha_s^{1/2})}. \tag{21b}$$

The analysis of the problem now involves the solution of equations (4), (6) and (21) subject to the boundary conditions (7) through (11). The solutions of these three differential equations are chosen in the forms

$$T_s(r,t) = A_1 Ei(-r^2/4\alpha_s t) + A_2 \quad 0 < r < S_1(t) \tag{22}$$

$$T_t(r,t) = A_3 Ei(-r^2/4\alpha_t t) + A_4 + T_{tp}(r,t) \quad S_1(t) < r < S_2(t) \tag{23}$$

$$T_\ell(r,t) = A_5 Ei(-r^2/4\alpha_\ell t) + A_6 \quad r > S_2(t) \tag{24}$$

where $T_{tp}(r,t)$ is a particular solution of equation (21) and A_i's, $i = 1$ to 6, are the constants of integration.

A particular solution of equation (21) is determined by the method of series expansion, and the resulting particular solution is obtained as

$$T_{tp}(r,t) = \sum_{n=0}^{\infty} B_n\left(\frac{r}{t^{1/2}}\right)^{2n+3} \tag{25a}$$

where

$$B_n = \frac{(-1)^{n+1}\rho L f_{su}[(n+1)!]}{2k_t(\eta\alpha_t^{1/2} - \lambda\alpha_s^{1/2})\alpha_t^{n}(2n+3)[(n+3)!]}. \tag{25b}$$

The integration constants A_i's are determined by the application of the six boundary conditions given by equations (7, 8a, 9a) and (10). The solutions obtained in this manner satisfy the initial condition (11) for the liquid phase and are given as

$$T_s(r,t) = T_1 + \frac{Q}{4\pi k_s}[Ei(-r^2/4\alpha_s t) - Ei(-\lambda^2)] \quad \text{in} \quad 0 < r < S_1(t) \tag{26a}$$

$$\begin{aligned} T_t(r,t) = {} & \frac{T_2 - T_1 + \sum_{n=0}^{\infty} B_n[(2\lambda\alpha_s^{1/2})^{2n+3} - (2\eta\alpha_t^{1/2})^{2n+3}]}{Ei(-\eta^2) - Ei(-\lambda^2\alpha_s/\alpha_t)} Ei\left(-\frac{r^2}{4\alpha_t t}\right) + \\ & + \frac{T_1 Ei(-\eta^2) - T_2 Ei(-\lambda^2\alpha_s/\alpha_t) - \sum_{n=0}^{\infty} B_n[(2\lambda\alpha_s^{1/2})^{2n+3} Ei(-\eta^2) - (2\eta\alpha_t^{1/2})^{2n+3} Ei(-\lambda^2\alpha_s/\alpha_t)]}{Ei(-\eta^2) - Ei(-\lambda^2\alpha_s/\alpha_t)} + \\ & + \sum_{n=0}^{\infty} B_n\left(\frac{r}{t^{1/2}}\right)^{2n+3} \quad \text{in} \quad S_1(t) < r < S_2(t) \end{aligned} \tag{26b}$$

$$T_\ell(r,t) = T_i - \frac{T_i - T_2}{Ei(-\eta^2\alpha_t/\alpha_\ell)} Ei(-r^2/4\alpha_\ell t) \quad \text{in} \quad r > S_2(t). \tag{26c}$$

When equations (26) and (20) are introduced into the interface energy balance equations (8b) and (9b), the following two transcendental equations are obtained for the determination of the parameters λ and η:

$$\begin{aligned} & \frac{Q}{4\pi}e^{-\lambda^2} - k_t\frac{(T_2 - T_1) + \sum_{n=0}^{\infty} B_n[(2\lambda\alpha_s^{1/2})^{2n+3} - (2\eta\alpha_t^{1/2})^{2n+3}]}{Ei(-\eta^2) - Ei(-\lambda^2\alpha_s/\alpha_t)} \times \\ & \times e^{-\lambda^2\alpha_s/\alpha_t} - \frac{k_t}{2}\sum_{n=0}^{\infty} B_n(2n+3)(2\lambda\alpha_s^{1/2})^{2n+3} \\ & = \lambda^2\alpha_s(1 - f_{su})\rho L, \end{aligned} \tag{27a}$$

$$\begin{aligned} & k_t\frac{(T_2 - T_1) + \sum_{n=0}^{\infty} B_n[(2\lambda\alpha_s^{1/2})^{2n+3} - (2\eta\alpha_t^{1/2})^{2n+3}]}{Ei(-\eta^2) - Ei(-\lambda^2\alpha_s/\alpha_t)} \times \\ & \times e^{-\eta^2} + \frac{k_t}{2}\sum_{n=0}^{\infty} B_n(2n+3)(2\eta\alpha_t^{1/2})^{2n+3} \\ & = k_\ell\frac{T_2 - T_i}{Ei(-\eta^2\alpha_t/\alpha_\ell)}e^{-\eta^2 t/\alpha_\ell}. \end{aligned} \tag{27b}$$

Numerical Example and Discussion

To illustrate the application of the present analysis, we now consider the solidification of an aluminum-copper alloy containing five percent copper. The physical properties of the solid and liquid phases are taken as [5].

$k_s = 197.3$ W/m°C
$k_\ell = 181.7$ W/m°C
$C_s = 1046.7$ Ws/kg°C,
$C_\ell = 1256$ Ws/kg°C
$\rho = 2723.2$ kg/m^3
$L = 395{,}403$ Ws/kg
$T_1 = 547.8$°C
$T_2 = 642.2$°C
$f_{su} = 0.8952$

and k_t and C_t for the two-phase zone are approximated as

$$k_t = \frac{k_s + k_\ell}{2} = 185.5 \text{ W/m°C}$$

$$C_t = \frac{C_s + C_\ell}{2} = 1151.35 \text{ Ws/kg°C}$$

It is assumed that the liquid phase is initially at a uniform temperature $T_i = 648.9$°C.

The Model I is applied for the analysis of this problem and the calculations are performed for heat sink of strengths taken as:

$Q = 20{,}000$; 30,000; 40,000; 50,000 and 70,000 W/m.

The values of the parameters λ and η associated with this model are determined from the solution of the coupled equations (19*a*, *b*). A modified Newton's method described in [9] is used for the calculations. Since a small number is generally determined from the algebraic sum of many large numbers, it was found necessary to retain a large number of significant digits in these calculations.

Table 1 lists the values of λ and η for Model-I for the set of input parameters given above and for several different values of the heat sink strength Q.

Fig. 1 shows the location of the solidus (S_1) and liquidus (S_2) fronts as a function of time for a heat sink of strength Q = 50,000 W/m. Fig. 2 shows the temperature distribution as a function of the radial position for the solid, two-phase and liquid regions at the time t = 1 hr after the start of solidification for a heat sink of strength Q = 50,000 W/m.

The two solid fraction models defined by equations (2) and (3), provide two possible exact solutions for the solidification problem considered in this study. The first model which is equivalent to that originally suggested in [10] and applied with the electric analogy method for the solidification of castings in slab geometry has found good agreement with experiments. The second model has been used in [5] to solve a phase change problem approximately by Goodman's integral technique in the rectangular coordinate system. By performing the analysis for the cases $f_s/f_{su} = 1 - \overline{X}^n$, where $n = 1, 2, 3$ and $\overline{X}$ is the equivalent of R in the rectangular coordinates, it has been shown that the solid fraction distribution is not the dominant factor as far as temperature distribution and the rate of solidification are concerned.

Acknowledgment

The authors would like to thank Professor J. A. Bailey for his helpful discussions. This work was supported in part through the National Science Foundation Grant ENG 77-12949.

Table 1 The variation of λ and η with Q for Model I for the system parameters considered in the example

Q(W/m)	λ	η
20,000	0.00102	0.8367
30,000	0.00712	0.9777
40,000	0.01879	1.0724
50,000	0.03377	1.1433
70,000	0.06694	1.2476

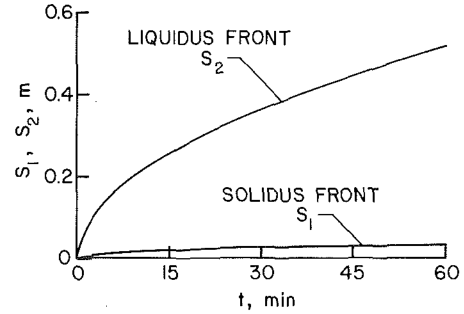

Fig. 1 Growth of solidus (S_1) and liquidus (S_2) fronts with time for Q = 50,000 W/m

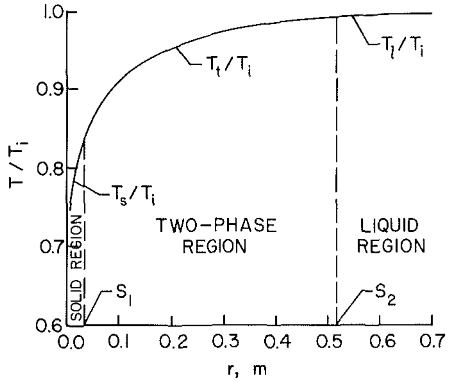

Fig. 2 Temperature distribution for Q = 50,000 W/m at time t = 1 hr for T_i = 648.9°C

References

1 H. S. Carslaw and J. C. Jaeger, *Conduction of Heat in Solids*, 2d ed., Oxford at the Clarendon Press, London, 1959.

2 S. H. Cho and J. E. Sunderland, "Heat Conduction Problems with Melting and Freezing," ASME JOURNAL OF HEAT TRANSFER, Vol. 91, 1969, pp. 421-426.

3 M. D. Mikhailov, "Exact Solution for Freezing of Humid Porous Half-Space," *Int. J. Heat Mass Transfer*, 19, 1976, pp. 651-655.

4 S. Paterson, "Propagation of a Boundary of Fusion," *Proc. Glasgow Math. Assoc.*, *1*, pp. 42-47.

5 R. H. Tien and G. E. Geiger, "A Heat-Transfer Analysis of the Solidification of a Binary Eutectic System," ASME JOURNAL OF HEAT TRANSFER, Vol. 89, 1967, pp. 230-234.

6 R. H. Tien and G. E. Geiger, "The Unidimensional Solidification of a Binary Eutectic System with a Time Dependent Surface Temperature," ASME JOURNAL OF HEAT TRANSFER, Vol. 90, 1968, pp. 27-31.

7 L. H. Van Vlack, *Elements of Materials Science*, 2d ed., Addison-Wesley Publishing Co., Reading, Mass., 1967, pp. 234-269.

8 N. N. Lebeder. *Special Functions and Their Applications*, Prentice-Hall, Inc., Englewood Cliffs, N. J., 1965.

9 K. M. Brown, "A Quadratically Convergent Newton-like Method Based Upon Gaussian Elimination," *SIAM Journal on Numerical Analysis*, 6, 1969, pp. 560-569.

10 V. Paschkis, Studies on Solidification of Castings, *Trans. Am. Foundryman's Assoc.*, 53, 1945, pp. 90-101.

Ralph L. Webb
Department of Mechanical Engineering,
The Pennsylvania State University,
University Park, PA 16802

A Generalized Procedure for the Design and Optimization of Fluted Gregorig Condensing Surfaces

This paper summarizes the general theory of the Gregorig fluted condensing surface, and includes advances since Gregorig's original publication. These include Bromley, et al.'s mathematical description for the geometrical shape of the convex surface, and definition of the "optimum" fluted surface geometry established by Zener and Lavi. However, their optimization is applicable to only one of a family of possible convex surface shapes. This paper extends the work of Zener and Lavi to define the optimum geometry as a function of the included angle of the convex surface. This broader optimization analysis will support calculation of economically optimum fluted surface designs. Calculated results are presented for ammonia condensing on vertical fluted tubes and compared with existing experimental data. The expected performance of real condensers is discussed, relative to the idealized conditions assumed in the analysis. Finally, the paper outlines a step-by-step procedure for the design of the fluted surface and construction of the convex surface profile.

Introduction

In 1954, Gregorig [1]proposed a method of using surface tension forces to enhance laminar film condensation on a vertical surface. Fig. 1 illustrates a horizontal cross section thru the wall of a vertical fluted tube.

Although Gregorig's concept is well known, the details of the theory and design procedure are not readily available. The Gregorig paper, published in German, gives an equation to calculate the film thickness on the convex surface using a graphical procedure. And the procedure required for design of the concave drainage channel was not specified. Richter's 1957 M.S. Thesis [2] defines specific procedures to design the Gregorig surface. However, this was not published. Later, Bromley, et al. [3] defined the geometrical shape of the Gregorig surface and provided certain fundamental geometrical relationships for this curve shape, which are useful in design. Finally, Zener and Lavi [4] proposed a method for calculating the geometry of an optimized fluted surface, accounting for both the convex and concave surfaces. However, the equations they present are applicable to only one convex surface shape. For practical reasons one may wish to define the optimum design for other possible convex surfaces. Thus, there have been several advances since Gregorig's original paper. There has been no comprehensive summary of those several advances. And, since each author uses a different nomenclature, it is difficult to quickly grasp the state-of-the-art.

The purpose of this paper is threefold: 1) Using a consistent nomenclature, summarize the general theory of fluted surface design as defined by Gregorig, and extended by others, 2) to outline a clear design procedure, 3) to extend the optimization analysis of Zener and Lavi to include a broader range of optimized surface shapes.

The Convex Surface

Gregorig's equation results from a force balance between the pressure gradient due to surface tension forces and the viscous forces on an element of the condensate film. The surface tension induced pressure gradient is $dP/ds = \sigma\, d(1/r)/ds$. Gregorig proposed that the radius be varied over S to maintain a constant driving force, dP/ds. This will establish a constant film thickness, δ, over the convex arc length, S.

Since $h_s = k/\delta$, the Gregorig surface yields a constant condensation coefficient over the entire convex surface arc length, S. The geometrical shape of the convex surface must satisfy the relation $(1/r^2)dr/ds$ = constant. The resulting equation developed by Gregorig for the convex surface is

$$\frac{1}{r_0}-\frac{1}{r}=\frac{3\mu k \Delta T s^2}{2\rho\lambda\sigma g_c \delta^4}=\frac{3}{2B}\frac{s^2}{\delta^4} \tag{1}$$

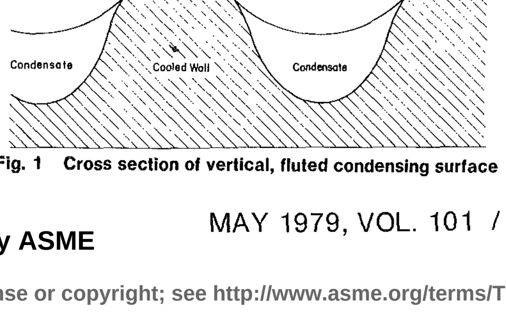

Fig. 1 Cross section of vertical, fluted condensing surface

Contributed by the Heat Transfer Division for publication in the JOURNAL OF HEAT TRANSFER. Manuscript received by the Heat Transfer Division April 21, 1978.

In equation (1), r_0 is the convex surface radius at the crest and r is the radius at any point s on the surface. This equation defines how the radius must be varied to attain a specified and constant film thickness over the surface profile. At the termination of the convex surface, $1/r = 0$, which satisfies the requirement $d(1/r)/ds$ = constant. Later analysis by Zener and Lavi confirmed that Gregorig's surface shape is indeed the optimum.

Setting $1/r = 0$ and $s = S$ in equation (1), the resulting film thickness is

$$\delta = \left(\frac{3}{2B} r_0 S^2\right)^{1/4} \qquad (2)$$

Gregorig provides little detailed description on the use of equation (1) to construct the convex surface shape. No specific information is given on the design of the concave drainage surface.

Bromley presents more detail on the geometrical shape of the convex surface. Generalized equations for the arc length are possible if s is replaced by its geometrical equivalent $\int r d\theta$. As shown in the Appendix, the general equations for construction of the convex surface are given by equations (3) and (4). S is the arc length to the end of the convex profile at which $\theta = \theta_m$.

$$\frac{\theta}{\theta_m} = \frac{s}{r_0\theta_m} - \frac{4}{27}\left(\frac{s}{r_0\theta_m}\right)^3 \qquad (3)$$

$$\frac{r_0}{r} = 1 - \frac{4}{9}\left(\frac{s}{r_0\theta_m}\right)^2 \qquad (4)$$

The film thickness can be expressed in several forms as shown in the Appendix. Then, the condensation coefficient is given by $h_s = k/\delta$, where

$$\frac{1}{\delta} = \left(\frac{B\theta_m}{S^3}\right)^{1/4} = \left(\frac{2B}{3r_0S^2}\right)^{1/4} = \left(\frac{8}{27}\frac{B}{r_0^3\theta_m^2}\right)^{1/4} \qquad (5)$$

For a given crest radius r_0, there are a family of surface shapes which satisfy the Gregorig criterion dP/ds = constant. Fig. 2 illustrates several of these Gregorig profiles. Each surface has the same r_0, but ends at a different θ_m. The arc length of each surface is given by equation ($A3$). The third form of equation (5) shows that $\delta \alpha \theta_m^{1/2}$. So, smaller condensation coefficients will prevail for larger values of θ_m (longer arc length S). In the discussion on optimized surface design, we will show that large values of θ_m actually yield higher performance, when the condensation coefficient is based on the projected area of the convex and concave surfaces.

Design Procedure for the Convex Surface

The design procedure for the convex surface is:

1 Arbitrarily specify θ_m and calculate the term B which is defined by fluid properties.

2 Establish condensation coefficient:
  a. Alternate 1: Specify crest radius r_0 and calculate δ by equation (2) (or the second form of equation (5)). Then $h_s = k/\delta$.
  b. Alternate 2: Arbitrarily specify the desired h_s and calculate $\delta = k/h_s$. Then calculate r_0 by the third form of equation (5).

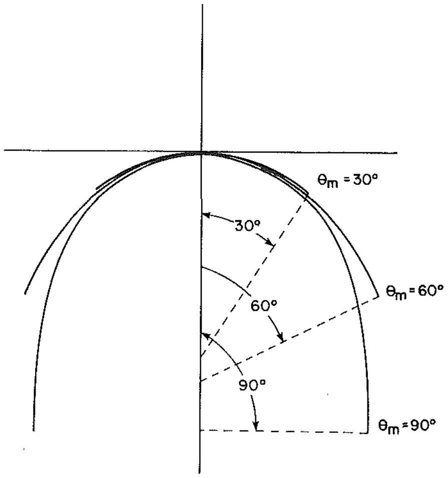

Fig. 2 Convex surface profiles

3 The geometrical shape of the convex surface $s(r, \theta)$ is computed using equation (3). Construction of the curve is discussed in a following section.

The Drainage Groove

The remaining part of the fluted surface problem is to design the concave drainage groove. The normal procedure is to use a semicircular channel of constant radius. The channel radius may be selected so that the gravity drained channel operates at full capacity at the bottom of the tube. The condensing area per drainage groove is $A_d = 2SL$. The volumetric flow rate of condensate to be drained is

$$\dot{V} = \frac{2SL{\cdot}U\Delta T_m}{\rho\lambda} = \frac{2SL{\cdot}h_s\Delta T}{\rho\lambda} \qquad (6)$$

Two analyses have been performed for the capacity of the semicircular concave channel. The models assumed by Richter, and by Zener and Lavi are shown in Figs. 3(b) and 3(a), respectively.

Both analyses assume, at maximum capacity, the drainage channel is filled to the inflection point. Richter assumes no curvature of the liquid film is present. Zener and Lavi assume that a curved interface exists, due to the liquid-surface contact angle.

Assuming laminar flow, Richter established the capacity for the channel of Fig. 3(a) by a force balance. The cross-sectional area of this channel is $A_d = \pi d^2/8$. His analysis gives for the channel average velocity at full capacity

$$u_m = \frac{d^2 g}{16\nu} \qquad (7)$$

From continuity, $\dot{V} = u_m A_d$, giving

$$\dot{V} = \frac{\pi d^4 q}{128\nu} \qquad (8)$$

Zener and Lavi's analysis gives a 50 percent smaller channel capacity

Nomenclature

A_d = flow cross section of drainage channel
b = projection of fluted surface ($p + d$)
$B = \rho\lambda\sigma g_c/\mu k\Delta T$ (equation (1))
d = width of drainage groove
$F_1 = k(B\theta_m)^{1/4}$ (equation (13))
$F_2 = (256\nu/\pi g)(2L\Delta T/\rho\lambda)$(equation (15))
g = gravitational constant
g_c = dimensional constant 32.17 $\mathrm{lb_m ft/lb_f s^2}$
h = heat transfer coefficient, h_b, projected area, h_i, tube internal surface, h_s, convex surface arc length S, h_0, smooth surface
k = thermal conductivity of condensing liquid
$K = 3/2B\delta^4$ (equation (A-2))
L = length of condensing surface
p = projection of convex surface
r = radius of convex surface, r, at any point on arc, r_0, at crest
s = arc length measured along convex surface
S = value of s at $\theta = \theta_m$
ΔT = temperature difference between vapor and condensing surface, ΔT_m coolant to vapor ΔT
u_m = average velocity in drainage channel
U = overall heat transfer coefficient
$\dot{V}$ = volumetric flow rate in drainage channel
$\beta = p/2S$
δ = condensate film thickness
θ = angular coordinate, measured from crest of convex surface
θ_m = value of θ at end of convex surface, where $1/r = 0$
λ = latent heat
μ = dynamic viscosity of condensate
ν = kinematic viscosity of condensate
ρ = density of condensate
σ = surface tension of condensate

$$\dot{V} = \frac{\pi d^4 g}{256\nu} \tag{9}$$

The capacity predicted by Zener and Lavi seems more reasonable, since a contact angle less than 90 deg may be expected.

Using equation (9), the required condensate channel diameter is obtained by equating equations (6) and (9).

$$d = \left(\frac{256\nu}{\pi g} \cdot \frac{2SL \cdot U\Delta T_m}{\rho\lambda}\right)^{1/4} = \left(\frac{256\nu}{\pi g} \cdot \frac{2SL \cdot h_s\Delta T}{\rho\lambda}\right)^{1/4} \tag{10}$$

where

$$\frac{1}{2SU} = \frac{1}{h_i A_i} + \frac{1}{2Sh_s} \tag{11}$$

assuming the temperature drop across the tube wall is zero.

Optimum Gregorig Surfaces

Three variables define the geometry of the Gregorig convex surface, θ_m, r_0 and S. The previously discussed design procedure requires initial specification of two of the three geometric variables. Then the width d of the concave drainage channel is sized to handle the condensate load. Among the four geometric variables θ_m, r_0, S, d, two are dependent variables. For any θ_m, there is a family of possible surfaces, each having a different S or r_0. It is logical to ask if one of these surfaces, for a specified θ_m, yields an optimum design. Using the nomenclature of Fig. 4, we define the "optimum design" as follows: the optimum design will yield the maximum condensation coefficient (h_b) based on the projected area of the fluted surface, or the nominal tube diameter. The nominal tube diameter is defined as the diameter measured through the inflection point between the convex and concave surface. By this criterion, we wish to maximize

$$h_b = \frac{2S}{p + d} h_s \tag{12}$$

where h_b is the condensation coefficient based on the projected area $b = p + d$.

Zener and Lavi compute the optimum arc length S for a surface geometry having $p = S$, which occurs when $\theta_m = \pi/2$. For this case, they show that the optimum geometry has $d = 4S$. We will show later that the maximum h_b will occur when $\theta_m = \pi/2$. However, there are practical and economic reasons why one may not wish to design for $\theta_m = \pi/2$. For example, this may require excessive tube wall thickness. So the economic optimum may exist for some $\theta_m \leq \pi/2$.

The optimum may be found by writing equation (12) as a function of S. By setting the derivative of this function equal to zero, we then define the value of S that makes h_b a maximum.

To write equation (12) as a function of S, we use the first form of equation (5) with $h_s = k/\delta$. We may write $h_s = F_1/S^{3/4}$ where

$$F_1 \equiv k(B\theta_m)^{1/4} \tag{13}$$

The projected area of the convex surface, p, is expressed as $p \equiv 2\beta S$. Making these substitutions in equation (12) we obtain

$$\frac{2F_1}{h_b} = 2\beta S^{3/4} + dS^{-1/4} \tag{14}$$

Next, it is necessary to express the diameter of the drainage channel, d, in terms of S. Substituting $F_1/S^{3/4}$ for h_s in equation (10)

$$d = \left[\frac{256\nu}{\pi g} \cdot \frac{2SL\Delta T}{\rho\lambda} \cdot \frac{F_1}{S^{3/4}}\right]^{1/4}$$

Letting

$$F_2 = \frac{256\nu}{\pi g} \cdot \frac{2L\Delta T}{\rho\lambda} \tag{15}$$

$$d = (F_1F_2)^{1/4} S^{1/16} \tag{16}$$

Substitution of equation (16) in (14) gives

$$\frac{2F_1}{h_b} = 2\beta S^{3/4} + (F_1F_2)^{1/4} S^{-3/16} \tag{17}$$

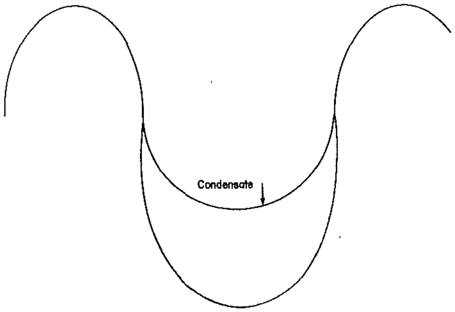

Fig. 3(*a*) Zener and Lavi [4]

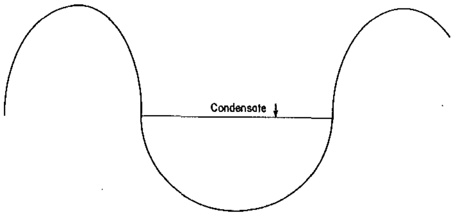

Fig. 3(*b*) Richter [2]

Fig. 3 Drainage channel models

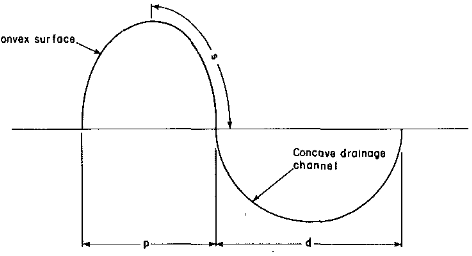

Fig. 4 Nomenclature for calculation of optimum design

Setting the derivative of this function equal to zero, we find

$$S_{\mathrm{opt}} = \left[\frac{(F_1F_2)^{1/4}}{8\beta}\right]^{16/15} \tag{18}$$

Combining equation (16) and (18), we obtain

$$d = 8\beta S_{\mathrm{opt}} \tag{19}$$

Substitution of equations (18) and (19) in equation (14) gives the value of h_b associated with S_{opt}

$$h_b = 1.055\, F_1\, (\beta F_1 F_2)^{-.2} \tag{20}$$

Substitution of equation (19) in (14) gives a simpler equation for S_{opt}, than equation (18)

$$S_{\mathrm{opt}} = \left[\frac{1}{5\beta}\frac{F_1}{h_b}\right]^{4/3} \tag{21}$$

We have constructed convex surface profiles for $\theta_m = \pi/6$, $\pi/3$, and $\pi/2$ (Fig. 2) and graphically determined the relation $\beta = p/2S$. Fig. 5 shows a graph of β versus θ_m. This figure may be used to obtain values of β for any θ_m.

The optimization procedure is equivalent to that used by Zener and Lavi. Our method uses a conventional nomenclature and mathematical procedure in interests of clarity, whereas Zener and Lavi use a less conventional nomenclature and more elegant mathematics. Zener and Lavi's optimization is restricted to the case for $\beta = 1$, or $p = 2S$. For this case, equation (17) shows that $d = 4S$, in agreement with Zener and Lavi.

Equation (20) shows that h_b is a maximum if $\theta_m = \pi/2$. Any value of $\theta_m < \pi/2$ yields a smaller value for h_b. We suspect that practical and economic consideration may dictate the use of $\theta_m < \pi/2$.

The procedure for calculating the optimum design is:

1 arbitrarily establish θ_m and L. Read β from Fig. 5;
2 compute parameters B, F_1 and F_2 for the convex surface;
3 calculate h_b by equation (20);

4 calculate S_{opt} and d by equations (21) and (19), respectively;
5 $r_0 = 2S_{\text{opt}}/3\theta_m$ by equation (A-3).

Interpretation of Analytical Results

The design procedure does not allow the designer to arbitrarily fix h_b. The calculated value of h_b is the maximum value for the specified L and θ_m. If the calculated value of h_b is larger than desired, it may be reduced by increasing the vertical tube length ($h_b \propto L^{-.2}$) or use of a smaller θ_m since $h_b \propto \theta_m{}^{.2}$. The smaller θ_m may allow reduced tube wall thickness. Since $r_0 \propto \theta_m{}^{-14/15}$, reduced θ_m would permit larger values for the crest radius, r_0.

For the optimum design, with any value of θ_m, note that $p/(p + d) = .2$. Thus, 80 percent of the projected area consists of the concave drainage channel. If the analysis is based on Richter's assumption of a flat liquid interface in the drainage channel, the result would be the same. However, the calculated S_{opt} and d would be 17 percent smaller and h_b 15 percent larger.

Figs. 6 and 7 show the predicted results for ammonia condensing at 50°F with $\Delta T = 4°\text{F}$. The curves are prepared for tube lengths of 4, 10, 20, and 40 ft. (1.2 to 12 m). The condensation coefficient is based on the projected area of the flutes. To base the condensation coefficient on the total fluted surface area, the values for $\theta_m = \pi/6$, $\pi/3$ and $\pi/2$ should be divided by 1.47, 1.52, and 1.66, respectively. Fig. 6 shows that a 40 percent higher h_b is obtained with $\theta_m = \pi/2$ than for $\theta_m = \pi/6$. However, a thicker tube wall would be required if the inner surface is smooth. The crest radius, r_0, varies from .009 to .026 in. (.22 to .66 mm) for $L = 4$ ft (1.2 m) and .005 to .015 in. (.13-.38 mm) for $L = 40$ ft (12 m). Recall that the drainage channel is apportioned 80 percent of the projected surface area. This requires a pitch spacing ($p + d$) between .09 and .14 in. (2.3 to 3.5 mm). The dimensions of the convex and concave channels may be obtained from Fig. 7 using the relation $p = .2(p + d)$ and $d = .8(p + d)$. The augmentation based on the projected surface area, h_p/h_{Nu}, is of interest. Here, h_{Nu} refers to the condensation coefficient on a smooth vertical tube as given by Nusselt's theory for laminar film condensation. The calculated values range from 3.4 ($L = 4$ ft) to 3.8 ($L = 40$ ft) for $\theta_m = \pi/2$. If the augmentation is based on the total surface area, the above predicted values are reduced to 2.2 and 2.4.

We have compared our predicted results with experimental data on fluted tubes. D. G. Thomas [5] reports data for steam taken by him, as well as other data by Gregorig and Lustenader. They show augmentation ratios (based on total surface area) in the range of 4 to 8 for tube lengths between one and two ft. Combs and Murphy [6] tested two 4 ft long fluted tubes with ammonia. For the same heat flux used in our predictions, they found augmentation values (based on total surface area) of 4 to 6. Uehara, et al. report augmentation ratios of 1.5 to 2 based on total surface area.

It appears that the predicted performance of the "optimized" surface designs is less than some of the reported experimental values. We suggest two reasons for this unexpected result. First, we have neglected condensation on the concave surface. Second, the drainage channel width is much larger than those used on the experimental surfaces. Our optimized drainage channels are 80 percent of the total projected area. The experimental surfaces use drainage channel widths on the order of 50 percent of the projected area. Thus, it appears that the condensation on the concave surfaces is too large to be neglected. The analysis selects the drainage channel size to be filled to capacity at the bottom of the tube, so we hesitate to recommend a reduced channel size. However, if vapor shear or other phenomena exist which tend to reduce the condensate thickness on the drainage channel, a reduced size is warranted.

Application to Heat Exchanger Design

The theoretical analysis assumes idealistic conditions which may not occur in real condensers. It is worthwhile to examine the major assumptions in view of expected real effects. Gregorig assumed laminar condensation on a constant temperature surface. The surface tension forces establish a thin film, and the flow length over the convex surface is so short that a very low Reynolds number (Re < 10) is obtained.

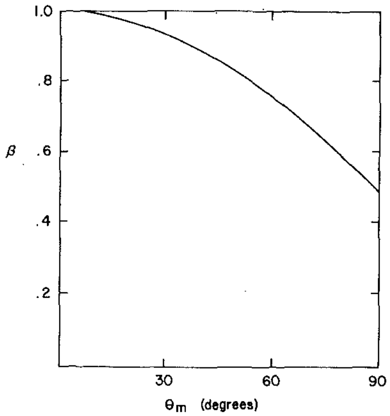

Fig. 5 Graph of β versus θ_m

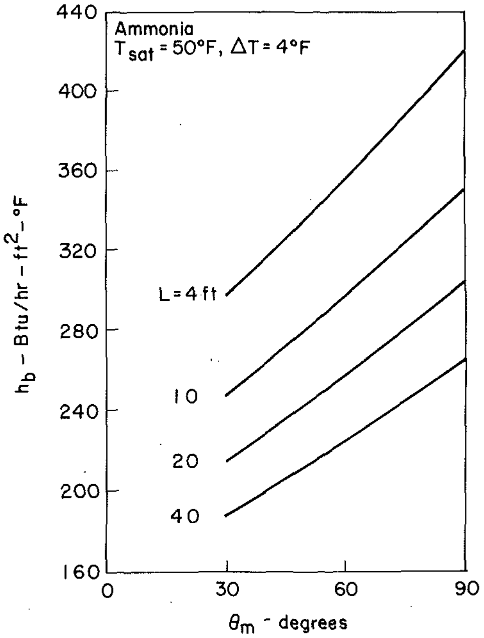

Fig. 6 h_b versus θ_m for condensation of ammonia on optimum fluted surface geometry. $T_{\text{sat}} = 50°\text{F}$, $\Delta T = 4°\text{F}$

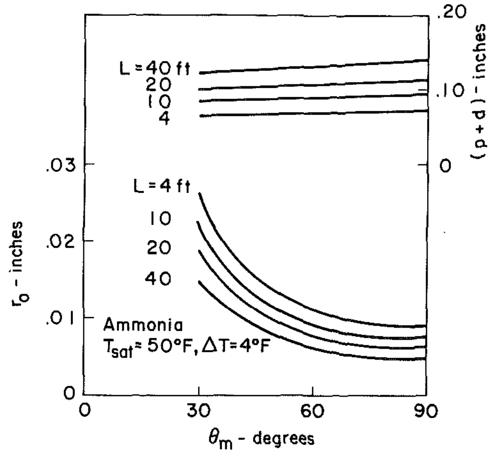

Fig. 7 ($p + d$) and r_0 versus θ_m for condensation of ammonia on optimum fluted surface geometry. $T_{\text{sat}} = 50°\text{F}$, $\Delta T = 4°\text{F}$

The theory assumes no condensation on the concave portion of the profile. We have previously stated that this assumption is too conservative. The film thickness in the drainage channel is zero at the top of the tube and attains its maximum value at the bottom of the tube.

If the heat transfer to the concave channel is included in the analysis, we would find that the condensation coefficient decreases from the top to the bottom of the tube. The drainage channel behavior is further dependent on the shape of the liquid interface. We have noted how the results will differ for the Richter versus Zener and Lavi drainage channel assumptions. The presence of vapor shear will reduce the required drainage channel size and yield increased heat transfer coefficient in the concave channel.

The inclusion of real wall effects suggests that the assumption of a constant wall temperature is probably unattainable. Since the heat flux is larger on the convex surface than on the concave surface, the metal and film temperatures will be smaller on the concave portion of the surface. Thus, the film temperature will cool as it moves from the crest of the convex surface toward the concave surface. This reducing film temperature will establish an increased surface tension gradient for removal of condensate from the convex surface. Perhaps the major question is what temperature should be assumed for the design. We suggest calculation of the interfacial temperature at the crest of the convex surface, assuming one-dimensional conduction across the wall. The heat conduction in the wall is further influenced by the geometry of the inner surface and the thermal conductivity of the tube wall. If the inner surface is smooth, the temperature drop across the wall is increased causing a higher film temperature at the convex crest.

Construction of the Gregorig Profile

The convex surface profile is constructed graphically or by digital computer using equations (3) and (4).

Table 1 lists the values of r/r_0 and θ/θ_m computed from equations (3) and (4) for 15 equal ΔS increments. Using these tabled values, Gregorig profiles for any θ_m may be constructed. The procedure to calculate a profile for any specified θ_m is:

1 Calculate a table of values of $\theta = (\theta/\theta_m)\,\theta_m$ and $\Delta S/r_0 = (\Delta S/r_0\theta_m)\,\theta_m$ using θ/θ_m and $\Delta S/r_0\theta_m$ from Table 1. Then the values of r/r_0, $\Delta S/r_0$ and θ are known for each of the 15 increments.

2 The geometrical profile may be constructed in 15 consecutive increments using the known values of r/r_0, θ and $\Delta S/r_0$ at each increment.

References

1 Gregorig R., "Hautkondensation an feingewellten Oberflächen bei Beruksichtigung der Oberflächenspannungen," *Zeitchrift für angewandte Mathematik und Physik*, Vol. V, 1954, pp. 36–49.

2 Richter, R., Rensselaer Polytechnic Institute, M.S. Thesis, 1958, Department of Mechanical Engineering.

3 Bromley, L. A., Hymphreys, R. F., Murray, W., "Condensation on and Evaporation from Radially Grooved Rotating Disks," ASME JOURNAL OF HEAT TRANSFER, Feb. 1966, pp. 80–88.

4 Zener C., and Lavi, A., "Drainage Systems for Condensation," ASME *Journal of Engineering for Power*, Vol. 96, 1974, pp. 209–215.

5 Thomas, D. G., "Enhancement of Film Condensation Rate on Vertical Tubes by Longitudinal Fins," *AIChE Journal*, July 1968, pp. 644–649.

6 Combs S. K., and Murphy, R. W., "Experimental studies of OTEC Heat Transfer Condensation of Ammonia on Vertical Fluted Tubes," *Proc. 5th Ocean Thermal Energy Conversion Conf.*, Miami Beach, Fla., Feb. 20–22, 1978. DOE Report CONF-780236, Vol. 3, Sec. 6, pp. 111–122.

7 Uehara, H., Masutani K., and Miyoshi, M., "Heat Transfer Coefficients of Condensation on Vertical Fluted Tubes," Ibid., Sec. 6, pp. 146–160.

Table 1 Tabled Geometric Values for the Gregorig Surface
r/r_0 and θ/θ_m versus $\Delta S/r_0\theta_m$

$\Delta S/r_0\theta_m$	r/r_0	θ/θ_m
.1	1.0045	.09985
.1	1.0181	.19981
.1	1.0417	.29600
.1	1.0766	.39052
.1	1.1250	.48148
.1	1.1905	.56800
.1	1.2784	.64919
.1	1.3975	.72415
.1	1.5625	.79200
.1	1.8000	.85185
.1	2.1635	.90281
.1	2.7778	.94400
.1	4.0178	.97452
.1	7.7586	.99348
.1	∞	1.0000

$\sum \Delta S/r_0\theta_m = S/r_0\theta_m = 1.5$

APPENDIX

Mathematical Description of the Convex Surface

Bromley, et al. [3] have shown that a generalized form of equation (1) may be developed by replacing the arc length S by $\int r d\theta$. Thus,

$$\int^r d\theta = \int^s \frac{1}{r}\,ds \tag{A1}$$

where $1/r$ is given by equation (1). The result of the integration is

$$\theta = \frac{s}{r_0} - K\frac{s^3}{3} \tag{A2}$$

where

$$K = \frac{3\mu k \Delta I}{2\sigma\rho\lambda g_c \delta^4} = \frac{3}{2B}\cdot\frac{1}{\delta^4}$$

Letting $\theta = \theta_m$ when $1/r = 0$, equations (1) and (A-2) give the following forms for θ_m.

$$\theta_m = \frac{2K}{3}S^3 = \frac{2}{3}K^{-1/2}\,r_0{}^{-3/2} = \frac{2S}{3r_0} \tag{A3}$$

A generalized equation for the convex surface is given by equation (A4) and (A5). Equations (A3) and (A4) are obtained by solving the second form of equation (A3) for K and substituting in equation (1) and equation (A2), respectively.

$$\frac{\theta}{\theta_m} = \frac{s}{r_0\theta_m} - \frac{4}{27}\left(\frac{s}{r_0\theta_m}\right)^3 \tag{A4}$$

$$\frac{r_0}{r} = 1 - \frac{4}{9}\left(\frac{s}{r_0\theta_m}\right)^2 \tag{A5}$$

Equation (A5) is a simpler form than given by Bromley, et al.

K. C. Poon
R. C. H. Tsou[2]
Y. P. Chang

Department of Mechanical Engineering
State University of New York at Buffalo
Buffalo, NY 14260

Solution of Anisotropic Problems of First Class by Coordinate-Transformation[1]

In an earlier paper, it was suggested to divide heat conduction problems in anisotropic media into three classes for the systematic presentation of their analytical solutions. It is shown in this paper that a large number of the first-class problems governed by differential equations of hyperbolic, parabolic and elliptic types with boundary conditions of the first, second, third and fourth kinds can be transformed into those for isotropic media. Solutions of two illustrative problems are shown while those of more complicated problems will be reported in subsequent papers.

1 Introduction

Since Stokes (1851), the study on anisotropic boundary value problems has been of great interest in applied sciences, ranging from crystal physics, geomechanics, elasticity and electro-magnetics to heat and mass transfer [1, 2, 3]. In spite of their importance, analytical studies have been limited to special or simple cases [4–10], due to the following mathematical difficulties: (1) an anisotropic medium which is homogeneous in one coordinate system becomes heterogeneous in other coordinate systems; (2) the partial differential equation can be separated only conditionally and therefore it is not possible to find in most cases the general solutions with respect to each of the spatial variables; (3) as a consequence of (2) it is very difficult to find a solution satisfying all the boundary conditions for bounded regions.

According to the degree of mathematical difficulty, it was suggested to divide anisotropic problems into three classes [9]. To clarify this classification, let u be the sought function in rectangular coordinates (x_i, $i = 1, 2, 3$) and the boundary conditions on $u(x_i, t)$ may be written in the general form:

$$C_0u_t + C_1 \sum_{i=1}^{3} a_{ji}u_{x_i} + C_2u = f \text{ on } S_j, \text{ for } t > 0 \qquad (1.1)$$

Where C's are constants and all but one may be zero simultaneously, a_{ji} the anisotropic coefficients of the medium; t is the time; S_j the surface segment describable by a single value of x_j; the subscripts t and x_i of u denote the differentiation of u with respect to t and x_i, respectively; and f is an absolutely integrable function over S_j and time. The boundary condition (1.1) reduces to the first kind (Dirichlet) for $C_0 = C_1 = 0$, the second kind (Neumann) for $C_0 = C_2 = 0$ and the third kind (mixed, or radiative) for $C_0 = 0$. For brevity, we shall refer to condition (1.1) as the fourth kind, whose physical meaning depends on the sought function u. In the case of heat conduction, for instance, u denotes the temperature and therefore (1.1) represents heating or cooling of surface S_j by a perfect conductor [11]. If the region is bounded by not more than two surfaces normal to one coordinate with boundary conditions of any one of the four kinds, then the problem is categorized as the first class. The second class is for regions completely or partially bounded with boundary conditions of any kind only on the surface or surfaces normal to one coordinate but of either the first or second kind on other surfaces. The third class is for open or bounded regions which do not fall into the first and second classes. The definition of the first class, however, is somewhat over-extended. For instance, for an infinite slab with anisotropy in cylindrical coordinates, the problem does not belong to the first class. A more accurate definition should be made by taking into account the separability conditions of the partial differential equations, as will be discussed when we report the solution of problems of the second class in the near future.

In this article, we shall consider only problems of the first class with anisotropy homogeneous in rectangular and circular cylinder coordinate systems. This class of problems encompasses regions of a free space, an infinite slab, a half space in rectangular coordinates, a free space bounded internally by an infinite, circular-cylindrical surface, and infinite solid and hollow cylinders. It will be shown that many of these problems can be transformed from anisotropic to isotropic. We shall describe the differential equation in a form as general as possible so as to show that the method is applicable to a wide range of anisotropic problems. As to the solution of specific problems in the present paper, we consider only the heat conduction in a translationally moving cylinder and in a rotating cylinder.

2 Anisotropy in Rectangular Coordinates

Consider the differential equation in the general form:

---

[1] This study was supported in part by the National Science Foundation, ENG 76-83367.

[2] R. C. H. Tsou made the initial study on three-dimensional anisotropy in cylindrical coordinates in 1973, now is with General Electric, San Jose, CA 95125.

Contributed by the Heat Transfer division for publication in the JOURNAL OF HEAT TRANSFER. Manuscript received by the Heat Transfer Division July 19, 1978.

$$a_1u_{tt} + a_2u_t + b_i(t)u_{x_i} - a_{ij}u_{x_ix_j} + a_3u = A(x_i, t), t > 0 \quad (2.1)$$

where the summation convention has been used; a's are known constants of real values; $b_i(t)$ are continuous functions of time, t, a_{ij} the anisotropic coefficients forming a symmetric second-order tensor with $a_{ii} > 0$ and $a_{ii}a_{jj} > a_{ij}^2$ for $i \neq j$, and $A(x_i, t)$, where $i = 1, 2, 3$, is an absolutely integrable function over the domain under investigation. The equation for $a_1 \neq 0$ is of hyperbolic type and is often encountered in elastodynamics and electro-magnetics [3, 5]. It also represents one of several formulations for the heat conduction in a medium with the finite speed of heat propagation [12–14].

The initial conditions on $u(x_i, t)$ can be written as follows:

$$u = F_1(x_i),\ u_t = F_2(x_i) \text{ for } t = 0 \quad (2.2)$$

The boundary conditions on $u(x_i, t)$ depend on the region in question. If x_j extends from negative infinity to positive infinity, we impose that

$$u = \text{finite as } |x_j| \to \infty \quad (2.3)$$

To show that all terms involving cross-derivatives, i.e., $a_{ij}u_{x_ix_j}$ for $i \neq j$, can be removed so that the resultant equation will be reduced to the form for an isotropic medium, it is sufficient to consider the region bounded by two parallel infinite planes ($0 < x_1 < L$, $|x_2|, |x_3| < \infty$)

$$\begin{aligned} &C_0u_t - C_1a_{1i}u_{x_i} + C_2u = f_1(x_2, x_3, t),\ x_1 = 0 \\ &\qquad\qquad\qquad\qquad\qquad\qquad t > 0 \quad (2.4) \\ &C_0'u_t + C_1'a_{1i}u_{x_i} + C_2'u = f_2(x_2, x_3, t),\ x_1 = L \end{aligned}$$

where primed C's are known constants and all but one of them can be zero simultaneously so that boundary conditions of the other three kinds are included.

We now introduce the new spatial variables:[3]

$$\xi_1 = x_1;\ \xi_2 = \frac{1}{\beta_{12}}(x_2 - \nu_{12}x_1);$$

$$\xi_3 = \frac{1}{\sigma}\left(x_3 - \epsilon x_1 - \frac{\gamma}{\beta_{12}^2}x_2\right) \quad (2.5)$$

where

$$\nu_{ij} = a_{ij}/a_{11};\ \beta_{12}^2 = \nu_{22} - \nu_{12}^2;\ \gamma = \nu_{23} - \nu_{12}\nu_{13};$$

$$\epsilon = \nu_{13} - \nu_{12}\frac{\gamma}{\beta_{12}^2};\ \sigma^2 = \beta_{13}^2 - \frac{\gamma^2}{\beta_{12}^2};\ \beta_{13}^2 = \nu_{33} - \nu_{13}^2 \quad (2.6)$$

By the well-known chain-rule, it can be easily shown that the set of equations (2.1–2.4) are transformed into the following set:

$$a_1u_{tt} + a_2u_t + b_i'(t)u_{\xi_i} - a_{11}u_{\xi_i\xi_i} + a_3u = A(\xi_i, t), t > 0 \quad (2.7)$$

$$u = F_1(\xi_i);\ u_t = F_2(\xi_i);\ i = 1, 2, 3, \text{ for } t > 0 \quad (2.8)$$

$$\begin{aligned} &C_0u_t - C_1a_{11}u_{\xi_1} + C_2u = f_1(\xi_2, \xi_3, t),\ \xi_1 = 0 \qquad t > 0 \quad (2.9) \\ &C_0'u_t + C_1'a_{11}u_{\xi_1} + C_2'u = f_2(\xi_2, \xi_3, t),\ \xi_1 = L \\ &\qquad u = \text{finite for } |\xi_2|, |\xi_3| \to \infty \end{aligned}$$

The Jacobian of the transformation can be readily found as $(\beta_{12}\sigma)$. Note that these equations are identical in form with those for an isotropic medium in the transformed space.

If $a_1 = 0$, then (2.7) reduces to parabolic type. It may represent the heat conduction with heat generation in an isotropic medium which moves at the velocity whose components are:

$$V_i(t) = b_i'(t)/(\rho C) \quad (2.10)$$

where ρ and C are the density and specific heat of the medium. For this case, however, we are referring to a set of moving coordinate system with functions A and f's described in terms of the moving coordinates, and a convective term is to be added to the lefthand side of (2.4) which will doom the transformation of the anisotropic problem into the isotropic one. Thus, for a moving medium, we exclude boundary conditions of the fourth kind, unless $V_1 = 0$.

If $a_1 = a_2 = 0$, $b_i(t)$ = constant, and A is independent of time, then (2.7) reduces to elliptic type which may represent the steady-state heat conduction provided that $C_0 = C_0' = 0$ and f_1 and f_2 are time-invariant and expressible in terms of the moving coordinates.

3 Anisotropy in Circular Cylinder Coordinates

Consider the differential equation in circular cylinder coordinates (r, θ, z):

$$\begin{aligned} &a_1u_{tt} + a_2u_t + a_3u + b_2(t)\,u_\theta + b_3(t)u_z \\ &\qquad - a_{11}\left(u_{rr} + \frac{1}{r}u_r + \frac{2\nu_{12}}{r}u_{r\theta} + \frac{\nu_{22}}{r^2}u_{\theta\theta} + 2\nu_{13}u_{rz}\right. \\ &\qquad\qquad \left. + \frac{2\nu_{23}}{r}u_{\theta z} + \frac{\nu_{13}}{r}u_z + \nu_{33}u_{zz}\right) = A(r, \theta, z, t) \quad (3.1) \end{aligned}$$

where the double subscripts in the anisotropic property-coefficients 1, 2, and 3 denote r, θ, and z, respectively; and subscripts t, r, θ and z of u designate the differentiation with respect to these variables. The initial conditions may be described in the same manner as (2.2):

$$u = F_1(r, \theta, z),\ u_t = F_2(r, \theta, z), \text{ for } t = 0 \quad (3.2)$$

The boundary conditions on u will depend on the region to be concerned. To show the transformation of anisotropic problems, it suffices to consider only an infinite hollow cylinder ($r_1 < r < r_2$, $0 \leq \theta \leq 2\pi$, $|z| < \infty$), with boundary conditions of the fourth kind:

$$\begin{aligned} &C_0u_t - C_1a_{11}\left(u_r + \frac{\nu_{12}}{r}u_\theta + \nu_{13}u_z\right) + C_2u = f_1(\theta, z, t),\ r = r_1 \\ &C_0'u_t + C_1'a_{11}\left(u_r + \frac{\nu_{12}}{r}u_\theta + \nu_{13}u_z\right) + C_2'u = f_2(\theta, z, t),\ r = r_2 \end{aligned} \quad (3.3)$$

In addition to these, we impose that

$$\begin{aligned} &u(r, \theta, z, t) = u(r, \theta + 2n\pi, z, t),\ n = \pm1, \pm2, \pm3\ldots \\ &u = \text{finite for } |z| < \infty \end{aligned} \quad (3.4)$$

By introducing the new spatial variables:[4]

$$\eta = r;\ \xi = \frac{1}{\beta_{13}}(z - \nu_{13}r);\ \phi = \frac{1}{\beta_{12}}(\theta - \nu_{12}lnr) \quad (3.5)$$

the set of equations (3.1–3.4) can be transformed into the following set:

$$\begin{aligned} &a_1u_{tt} + a_2u_t + a_3u + \frac{b_2(t)}{\beta_{12}}u_\phi + \frac{b_3(t)}{\beta_{13}}u_{\xi\xi} \\ &\qquad - a_{22}\left(u_{\eta\eta} + \frac{1}{\eta}u_\eta + \frac{1}{\eta^2}u_{\phi\phi} + \frac{2\gamma}{\beta_{13}\eta}u_{\phi\xi} + u_{\xi\xi}\right) = A(\eta, \theta, \xi, t) \end{aligned} \quad (3.6)$$

Nomenclature

A = source function
a, b, c = coefficients
F = initial conditions
f = boundary data
k_{ij} = thermal conductivity coefficients
u = dependent variable, temperature
$\nu_{ij} = k_{ij}/k_{11}$
$\gamma, \epsilon, \beta_{ij}, \sigma$ = anisotropic parameters
ξ, η, ζ, ϕ = transform coordinates
$b_1' = b_1$

$$b_2' = \frac{1}{\beta_{12}}(b_2 - \nu_{12}b_1)$$

$$b_3' = \frac{1}{\sigma}\left(b_3 - \frac{b_2\gamma}{\beta_{12}^2} - \epsilon b_1\right)$$

---

[3] These new variables can be seen from equation (3.9) [9] or obtained by the linear transformation but the process is very lengthy.

[4] This transformation can be seen from (10) or obtained by the investigation of separability of variables as well as by intergral transforms [15, 16].

$$C_0u_t - C_1a_{11}u_\eta + C_2u = f_1(\phi, \xi, t),\ \eta = r_1$$
$$C_0'u_t + C_1'a_{11}u_\eta + C_2'u = f_2(\phi, \xi, t),\ \eta = r_2 \tag{3.7}$$

and we impose that

$$u(\eta, \phi, \xi, t) = u\left(\eta, \phi + \frac{2n\pi}{\beta_{12}}, \xi, t\right), n = \pm 1, \pm 2, \pm 3 \ldots \tag{3.8}$$
$$u = \text{finite for } |\xi| \to \infty$$

The Jacobian of the transformation is $(\beta_{12}\beta_{13})$.

Note that one cross-derivative term, $2\gamma u_{\phi\xi}/(\beta_{13}\eta)$ remains in (3.6). It can be easily shown that this term can be removed by taking an integral transform with the kernel $e^{in\phi}/\sqrt{2\pi}$ and that the auxiliary equation can be further transformed, by a change of the dependent and independent variables, into Kummer's equation. Therefore, we may tentatively conclude that the anisotropic problem (3.1–3.4) in general cannot be reduced into the corresponding isotropic one with the present transformation. However, it can be seen from (3.6) that the transformation is successful for the following three cases:

1 three-dimensional anisotropy with $\gamma = \nu_{23} - \nu_{12}\nu_{13} = 0$
2 two-dimensional anisotropy in r and θ
3 two-dimensional anisotropy in r and z.

4 Example 1—Moving Ring Heat-Source

Solutions of the first-class problems of heat conduction in stationary media, with anisotropy in rectangular coordinates have been reported in [9] and those for two-dimensional problems with anisotropy in polar coordinates in [10, 15]. Solutions of specific three-dimensional problems in circular cylinder coordinates are more involved and require more than the space available here [16]. Therefore, in the present work, we consider only the solution of two simpler problems for a moving medium.

A ring heat-source which generates heat at the constant rate of q' per unit length and moves over the surface of an infinite solid cylinder of radius r_0 in the axial direction (z) at constant velocity V. The cylinder is initially at zero temperature and there is convective heat loss at the surface $r = r_0$ to the surroundings of temperature zero. The material is symmetric with respect to any plane passing through the cylinder axis. Specializing (3.6–3.7) to this case, we obtain the governing equations of the temperature as follows:

$$\frac{1}{\alpha_1}\left(u_t + \frac{V}{\beta_{13}}u_\xi\right) - \left(u_{\eta\eta} + \frac{1}{\eta}u_\eta + u_{\xi\xi}\right) = \frac{1}{k_{11}}q'\delta(r - r_0)\delta(z - 0) \tag{4.1}$$

$$u = 0, 0 \le \eta < r_0, |\xi| < \infty, t = 0 \tag{4.2}$$

$$u_\eta + hu = 0,\ \eta = r_0$$
$$u = \text{finite},\ \eta = 0 \qquad t > 0 \tag{4.3}$$

where we have replaced a_{11} by k_{11}, the thermal conductivity coefficient in r-direction; C_1' by unity; C_2'/a_{11} by h, i.e., the convective heat transfer coefficient divided by k_{11}; α_1 is the thermal diffusivity in r-direction; and η and ξ have been defined in (3.5). The solution of the problem (4.1–4.3) in steady state has been reported in [17] and that for unsteady states in [18]. Making use of the Green's function given in [18] and noting that the Jacobian of transformation is β_{13}, we find the Green's function associated with the present anisotropic problem as:

$$\mathrm{G}(r, z, t|r', z', t') = \frac{1}{2\pi r_0^2\beta_{13}\sqrt{\pi\alpha_1(t - t')}}$$
$$\times \exp\left\{-\frac{[(z - z') - \nu_{13}(r - r') - V(t - t')]^2}{4\alpha_1\beta_{13}^2(t - t')}\right\}$$
$$\cdot \sum_{n=1}^{\infty} \frac{J_0(\lambda_nr)J_0(\lambda_nr')}{\left[1 + \left(\frac{h}{\lambda_n}\right)^2\right]J_0^2(\lambda_nr_0)}e^{-\alpha_1\lambda_n^2(t-t')} \tag{4.4}$$

where λ_n are the roots of the transcendental equation:

$$hJ_0(\lambda r_0) - \lambda J_1(\lambda r_0) = 0 \tag{4.5}$$

and J_0 and J_1 are the Bessel functions of the first kind, orders zero and one.

By the well known Green's formula, the temperature field is given by,

$$u(r, z, t) = \frac{2\pi r_0\alpha_1q'}{k_{11}}\int_0^t \mathrm{G}(r, z, t|r_0, 0, t')dt'$$
$$= \frac{q'}{2r_0\beta_{13}k_{11}}\left(\frac{\alpha_1}{\pi}\right)^{1/2} \cdot \sum_{n=1}^{\infty} \frac{J_0(\lambda_nr)}{\left[1 + \left(\frac{h}{\lambda_n}\right)^2\right]J_0(\lambda_nr_0)}$$
$$\times \int_0^t \exp\left\{-\alpha_1\lambda_n^2\tau - \frac{[z - \nu_{13}(r - r_0) - V\tau]^2}{4\alpha_1\beta_{13}^2\tau}\right\}\frac{d\tau}{\sqrt{\tau}} \tag{4.6}$$

Setting the upper limit of the integral in (4.6) to infinity gives the steady-state solution:

$$u(r, z) = \frac{q'}{k_{11}r_0}\sum_{n=1}^{\infty} \frac{J_0(\lambda_nr)}{\left[1 + \left(\frac{h}{\lambda_n}\right)^2\right]\left[\left(\frac{V}{2\alpha_1}\right)^2 + (\lambda_n\beta_{13})^2\right]^{1/2}J_0(\lambda_nr_0)}$$
$$\cdot \exp\left[-\frac{1}{\beta_{13}^2}\left\{\left[\left(\frac{V}{2\alpha_1}\right)^2 + \lambda_n^2\beta_{13}^2\right]^{1/2}|z - \nu_{13}(r - r_0)|\right.\right.$$
$$\left.\left. - \frac{V}{2\alpha_1}[z - \nu_{13}(r - r_0)]\right\}\right] \tag{4.7}$$

We nondimensionalize (4.6) and (4.7) and change the variable of integration for the unsteady-state solution to obtain

$$u(\bar{r}, \bar{z}, \mathrm{Fo})\frac{k_{11}}{q'} = \frac{2}{\beta_{13}}\left(\frac{\mathrm{Fo}}{\pi}\right)^{1/2}\sum_{n=1}^{\infty} \frac{J_0(\lambda_n\bar{r})}{\left[1 + \left(\frac{\mathrm{Bi}}{\lambda_n}\right)^2\right]J_0(\lambda_n)}$$
$$\cdot \int_0^1 \exp\left[-\mathrm{Fo}\,\lambda_n^2\mu^2 - \frac{[2\mathrm{PeFo}\mu^2 - \bar{z} + \nu_{13}(\bar{r} - 1)]^2}{4\beta_{12}^2\mathrm{Fo}\mu^2}\right\}d\mu \tag{4.8}$$

$$u(\bar{r}, \bar{z})\frac{k_{11}}{q'} = \sum_{n=1}^{\infty} \frac{J_0(\lambda_n\bar{r})}{\left[1 + \left(\frac{\mathrm{Bi}}{\lambda_n}\right)^2\right]J_0(\lambda_n)[\mathrm{Pe}^2 + (\lambda_n\beta_{13})^2]^{1/2}}$$
$$\cdot \exp\left[-\frac{1}{\beta_{13}^2}\{(\mathrm{Pe}^2 + \lambda_n^2\beta_{13}^2)^{1/2}|\bar{z} - \nu_{13}(\bar{r} - 1)|\right.$$
$$\left. - \mathrm{Pe}[\bar{z} - \nu_{13}(\bar{r} - 1)]\}\right] \tag{4.9}$$

where

$$\bar{r} = \frac{r}{r_0}; \bar{z} = \frac{z}{r_0}; \mathrm{Pe} = \frac{Vr_0}{2\alpha_1}, \text{ the Peclet number;}$$
$$\mathrm{Bi} = hr_0, \text{ the Biot number; } \mathrm{Fo} = \frac{\alpha_1t}{r_0^2}, \text{ the Fourier number}$$
$$(\mathrm{Bi})J_0(\lambda) - \lambda J_1(\lambda) = 0 \tag{4.10}$$

Note that the integration limits in (4.8) are definite and that the integral is unity at the source point, ($\bar{r} = 0, \bar{z} = 0, \mu = 0$). Consequently, its numerical calculation can be handled with more facility than the original equation (4.6). This technique of changing from an indefinite to a definite integral applies not only to the present problem, but also to other heat conduction problems where the indefinite integral may even be improper.

5 Steady-State Heat Conduction in a Rotating Solid Cylinder

Consider a solid cylinder of radius r_0 which rotates about its axis at the constant angular velocity Ω and loses heat by convection at its surface. If all the prescribed data are independent of time t and position z, and the material is symmetric in the z-direction, then the problem to be solved can be stated in terms of the transformed coordinates as follows:

$$\frac{\omega}{\alpha_1}u_\phi - \left(u_{\eta\eta} + \frac{1}{\eta}u_\eta + \frac{1}{\eta^2}u_{\phi\phi}\right) = \frac{1}{k_{11}}q(\eta, \phi), 0 \le \eta < r_0 \tag{5.1}$$
$$u_\eta + hu = f(\phi),\ \eta = r_0 \tag{5.2}$$

$$u(\eta, \phi) = u\left(\eta, \phi + \frac{2\pi n}{\beta_{12}}\right), n = \pm 1, \pm 2, \pm 3, \ldots \tag{5.3}$$

$$u = \text{finite}, \eta = 0$$

where functions $q(\eta, \xi)$ and $f(\phi)$ are assumed to be bounded and at least piecewise continuous; and $\omega = \Omega/\beta_{12}$. If $\mathrm{G}(r, \theta|r', \theta')$ is the Green's function associated with the problem, then the solution for $u(r, \theta)$ is

$$u(r, \theta) = \frac{1}{k_{11}} \int_0^r \int_0^{2\pi} q(r', \theta')\mathrm{G}(r, \theta|r', \theta')r'dr'd\theta' - r_0 \int_0^{2\pi} f(\theta') \frac{\partial}{\partial n'} \mathrm{G}(r, \theta|r_0, \theta')d\theta' \tag{5.4}$$

where n' is the conormal so that

$$\frac{\partial}{\partial n'} = \frac{\partial}{\partial r'} + \frac{\nu_{12}}{r_0} \frac{\partial}{\partial \theta'} \tag{5.5}$$

The Green's function G satisfies the homogeneous equations (5.1) and (5.2) and the conditions (5.3) except at the source point. We seek the solution for $\mathrm{G}(\eta, \phi|\eta', \phi')$ in the form:

$$\mathrm{G} = \sum_{n=-\infty}^{\infty} R(\eta|\eta', n)e^{in\beta_{12}(\phi - \phi')} \tag{5.6}$$

where $R(\eta|\eta', n)$ satisfies

$$R_{\eta\eta} + \frac{1}{\eta} R_\eta - \left(\frac{n^2\beta_{12}{}^2}{\eta^2} + i\omega_n{}^2\right) R = -\frac{1}{\alpha_1\eta} \delta(\eta - \eta') \tag{5.7}$$

$$R_\eta + hR = 0, \eta = r_0$$

$$R = \text{finite}, \eta = 0 \tag{5.8}$$

with $\omega_n{}^2 = \omega n\beta_{12}/\alpha_1$. The solution of (5.7) satisfying (5.8) for $\eta < \eta'$, is

$$R(\eta|\eta', \mathrm{n}) = -\frac{u_1(\eta)u_2(\eta')}{\eta' W(u_1, u_2)} \tag{5.9}$$

and for $\eta > \eta'$, we just interchange η and η', where $W(u_1, u_2)$ is the Wronskian of u_1 and u_2 and

$$u_1(\eta) = I_\upsilon(i^{1/2}\omega_n\eta) \tag{5.10}$$

$$u_2(\eta) = [hK_\nu(i^{1/2}\,\omega_n r_0) + i^{1/2}\omega_n K_\nu{}'(i^{1/2}\omega_n r_0)]I_\nu(i^{1/2}\omega_n\eta) - [hI_\nu(i^{1/2}\omega_n r_0) + i^{1/2}\omega_n I_\nu{}'(i^{1/2}\omega_n r_0)]K_\nu(i^{1/2}\omega_n\eta) \tag{5.11}$$

where $\nu = n\beta_{12}$; I_ν and K_ν are the modified Bessel functions of the first and second kinds, respectively; the prime in I_υ and K_υ denotes the differentiation with respect to the argument.

Substituting $R(\eta|\eta', n)$ into (5.6), arranging real and imaginary part and transforming back to the original coordinates, we obtain for $r < r'$:

$$\mathrm{G}(r, \theta|r', \theta') = \frac{\epsilon}{\alpha_1\beta_{12}} \sum_{n=0}^{\infty} \left[\frac{M_1(\omega_n r)[N_2(r, \theta|r', \theta', \omega_n) - N_1(r, \theta|r', \theta', \omega_n)]}{h^2M_1{}^2(\omega_n r_0) + \omega_n{}^2M_2{}^2(\omega_n r_0) + 2h\omega_n M_2(\omega_n r_0)M_1(\omega_n r_0)} \cdot \frac{1}{\cos[\psi_2(\omega_n r_0) - \psi_1(\omega_n r_0)]}\right] \tag{5.12}$$

where $\epsilon = 1$ if $n = 0$ and 2 otherwise.

$$\begin{aligned} N_1(r, \theta|r', \theta', \omega_n) = {} & [\omega_n{}^2M_2(\omega_n r_0)\{M_1(\omega_n r')M_4(\omega_n r_0) \\ & \cdot \cos[\psi_1(\omega_n r) + \psi_1(\omega_n r') - \psi_2(\omega_n r_0) + \psi_4(\omega_n r_0)] \\ & - M_2(\omega_n r_0)M_3(\omega_n r') \cos[\psi_1(\omega_n r) + \psi_3(\omega_n r')]\} \\ & + h^2M_1(\omega_n r_0)\{M_1(\omega_n r')M_3(\omega_n r_0) \cos[\psi_1(\omega_n r) \\ & + \psi_1(\omega_n r') - \psi_1(\omega_n r_0) + \psi_3(\omega_n r_0)] \\ & - M_1(\omega_n r_0)M_3(\omega_n r') \cos[\psi_1(\omega_n r) + \psi_3(\omega_n r')]\} \\ & + h\omega_n M_2(\omega_n r_0)\{M_1(\omega_n r')M_3(\omega_n r_0)' \\ & \cdot \cos[\psi_1(\omega_n r) + \psi_1(\omega_n r') - \psi_2(\omega_n r_0) + \psi_3(\omega_n r_0)] \\ & - M_1(\omega_n r_0)M_3(\omega_n r') \\ & \cdot \cos[\psi_1(\omega_n r) - \psi_2(\omega_n r_0) + \psi_1(\omega_n r_0) + \psi_3(\omega_n r')]\} \\ & + h\omega_n M_1(\omega_n r_0)\{M_1(\omega_n r')M_4(\omega r_0) \\ & \cdot \cos[\psi_1(\omega_n r) + \psi_1(\omega_n r') - \psi_1(\omega_n r_0) + \psi_3(\omega_n r_0) \\ & - M_2(\omega_n r_0)M_3(\omega_n r') \\ & \cdot \cos[\psi_1(\omega_n r) + \psi_2(\omega_n r_0) - \psi_1(\omega_n r_0) + \psi_3(\omega_n r')]\}] \\ & \cdot \cos n\left[(\theta - \theta') - \nu_{12} \ln \frac{r}{r'}\right] \end{aligned} \tag{5.13}$$

$$M_1(\omega_n s) = [\mathrm{ber}_\nu{}^2(\omega_n s) + \mathrm{bei}_\nu{}^2(\omega_n s)]^{1/2}$$

$$M_2(\omega_n s) = [\mathrm{ber}_\nu{}'^2(\omega_n s) + \mathrm{bei}_\nu{}'^2(\omega_n s)]^{1/2}$$

$$M_3(\omega_n s) = [\mathrm{ker}_\nu{}^2(\omega_n s) + \mathrm{kei}_\nu{}^2(\omega_n s)]^{1/2}$$

$$M_4(\omega_n s) = [\mathrm{ker}_\nu{}'^2(\omega_n s) + \mathrm{kei}_\nu{}'^2(\omega_n s)]^{1/2} \tag{5.14}$$

$$\psi_1(\omega_n s) = \tan^{-1} \frac{\mathrm{bei}_\nu(\omega_n s)}{\mathrm{ber}_\nu(\omega_n s)};\ \psi_2(\omega_n s) = \tan^{-1} \frac{\mathrm{bei}_\nu{}'(\omega_n s)}{\mathrm{ber}_\nu{}'(\omega_n s)}$$

$$\psi_3(\omega_n s) = \tan^{-1} \frac{\mathrm{kei}_\nu(\omega_n s)}{\mathrm{ker}_\nu(\omega_n s)};\ \psi_4(\omega_n s) = \tan^{-1} \frac{\mathrm{kei}_\nu{}'(\omega_n s)}{\mathrm{ker}_\nu{}'(\omega_n s)}$$

and $N_2(r, \theta|r', \theta', \omega_n)$ is given by the same expression (5.13) except by replacing all cosine functions with sine functions. For $r > r'$, we just interchange r and r' except in $\cos n[(\theta - \theta') - \nu_{12}\ln r/r']$ and $\sin n[(\theta - \theta') - \nu_{12}\ln r/r']$.

With the Green's function known, the temperature distribution can be calculated from (5.4) for any bounded and at least piecewise continuous, prescribed-functions f and q. It can be easily shown by setting $\nu_{12} = 0$, $\beta_{12} = 1$, $f = 0$ and $q = q_0\delta(r - r_0)\delta(\theta - 0)$ that the problem reduces to one for a generatrix source rotating over a cylinder of isotropic medium at constant angular velocity Ω which has been reported in [18, 19].

6 Some Calculated Results

The ring source problem has great importance in metal cutting, in heat treatment processes (moving of a rod from one chamber to another) and in the emergency cooling of nuclear reactors. Therefore, some calculated results for this problem are shown in this section. Figs. 1 and 2 show the temperature histories at the cylinder surface for different values of Biot and Peclet numbers for a given anisotropic medium. Temperature distributions in the cylinder for steady state are plotted in Figs. 3 and 4. To investigate the anisotropic effects, temperature fields for isotropic and orthotropic media are also shown in these figures. For the anisotropic medium with $\nu_{13} = 0.5$, $\beta_{13} = 0.95$, the following interesting results can be readily seen either from (4.8) and (4.9) or Figs. 1–4.

1 Since $\beta_{13} \simeq 1$, the temperature at the surface of the cylinder is almost the same for isotropic and anisotropic cases.

2 The larger the value of ν_{13}, the more the temperature curves in the interior of the cylinder shifted to the negative direction of z in spite of the fact that the direction of motion changed. Since β_{13} is smaller than unity, the anistropy gives higher maximum temperature for given values of r.

3 For a given value of r, temperature curves for isotropic and anisotropic media intersect at a certain point, say $\bar{z}_0$. For $\bar{z} > \bar{z}_0$, the temperature is lower in the anisotropic medium but higher for $\bar{z} < \bar{z}_0$. As $|\bar{z}| \gg \bar{z}_0$, the temperature curves for all anisotropies have similar behavior differing only by scale and approach to zero as $|\bar{z}|$ goes to infinity. Therefore β_{13} can be looked upon as a scale factor for anisotropic and orthotropic cases, respectively, the larger the β_{13}, the flatter are the temperature curves.

7 Discussions and Concluding Remarks

As stated in an earlier paper [11], β_{ij} must be positive and ν_{ij} for $i \neq j$ can be either positive or negative depending on the selection of coordinates with respect to the medium's anisotropic structure. From the definition of γ in (2.6) for both coordinate systems, it is seen that it can be positive or negative and is a measure of the coupling effect of the three-dimensional anisotropy to the temperature field. Similar interpretation can be given to ϵ as defined in (2.6). However, the anisotropic parameter σ is to be real and positive, i.e., $\beta_{13} > \gamma/\beta_{12}$. If $\sigma < 0$, then the anisotropic problem can no longer be transformed into

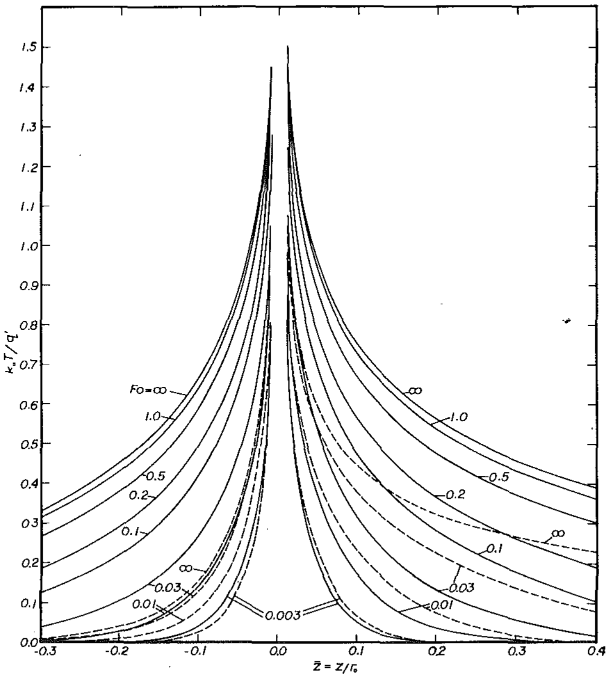

Fig. 1 Surface Temperature History for Bi = 1.0, $\nu_{33} = 1.2$, $\nu_{13} = 0.5$, — Pe = 0.50, - - - Pe = 5.00

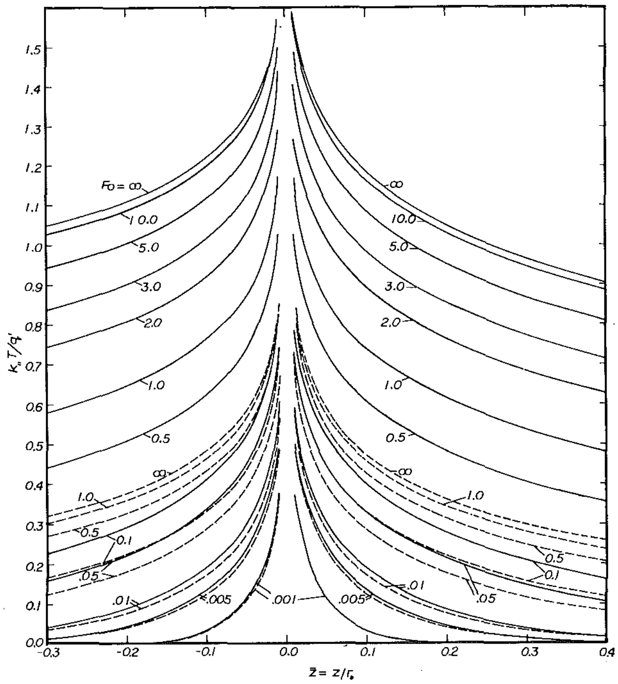

Fig. 2 Surface Temperature History for Pe = −0.50, $\nu_{33} = 4.0$, $\nu_{13} = 0.5$, — Bi = 0.10, - - - Bi = 1.00

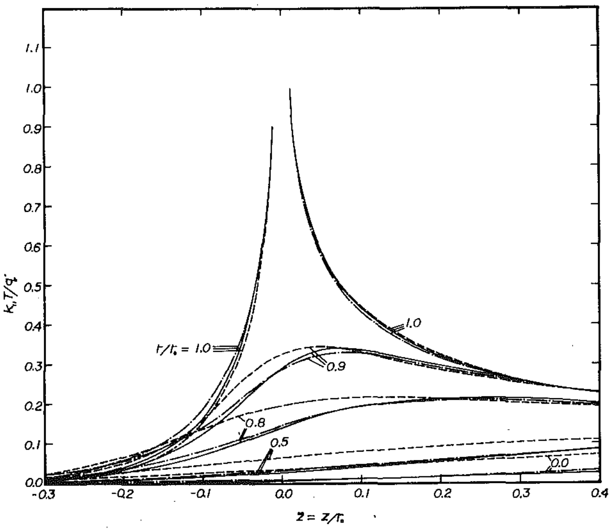

Fig. 3 Temperature Distribution in Steady State for Bi = 1.0, Pe = −5.0, — isotropic ($\nu_{33} = 1.0$), - - - anisotropic ($\nu_{33} = 1.2$, $\nu_{13} = 0.5$), – • – • – orthotropic ($\nu_{33} = 1.2$)

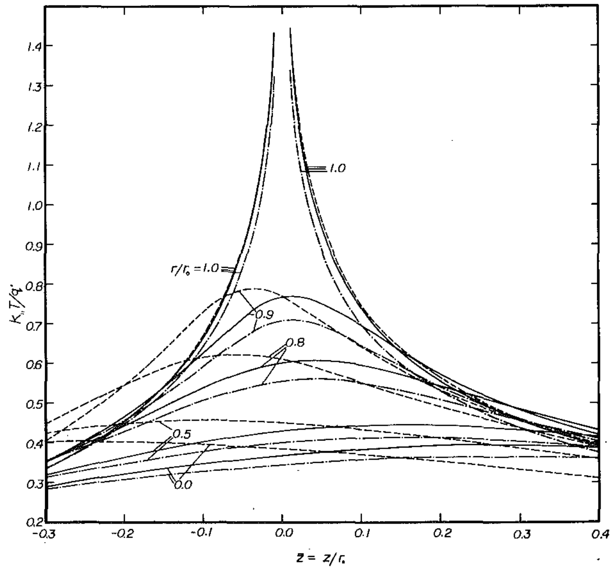

Fig. 4 Temperature Distribution in Steady State for Bi = 1.0, Pe = 0.5, — isotropic ($\nu_{33} = 1$), - - - anisotropic ($\nu_{33} = 1.2$, $\nu_{13} = 0.5$), — • — • — orthotropic ($\nu_{33} = 1.2$)

the correspondingly isotropic. This, however, does not necessarily reflect that the anisotropic problem has no solution, as was remarked in [9]. In view of the the parallelisms of ν_{13} and β_{13} in Section 6 (or ν_{12} and β_{12} in Section 5) and ν_{12}, ϵ, γ and σ for three-dimensional anisotropy in rectangular coordinates and ν_{12}, ν_{13}, γ and β's in cylindrical coordinates, we may refer to anisotropic property parameters ν_{12}, ν_{13}, γ and ϵ as the shifting factors and β's as scale factors of temperature curves.

Solutions of specific problems, particularly those with boundary conditions of the fourth kind, those of three-dimensional anisotropy in cylindrical coordinates, those with finite speed of heat propagation and those of the second class will be reported in the near future.

References

1 Wooster, W. A., *A Textbook on Crystal Physics*, University Press, Cambridge, 1938.

2 Nye, J. Y., *Physical Properties of Crystals*, Clarendon Press, Oxford, 1960.

3 Born, M., and Wolf, E., *Principles of Optics*, Ch. 14, Pergamon Press, 1975.

4 Kuprudeze, V. D., *Potential Methods in the Theory of Elasticity*, Ch. 9, Israel Programs for Scientific Translation, 1965.

5 Hearmon, R. F. S., *An Introduction to Applied Anisotropic Elasticity*, University Press, Oxford, 1961.

6 Clement, D. L., "Thermal Stress in an Anisotropic Elastic Half-Space," *SIAM J. Appl. Math.*, Vol. 24, No. 1, 1973, pp. 332–337.

7 Tauchert, T. R. and Akoz, A. Y., "Stationary Temperature and Stress Fields in Anisotropic Elastic Slab," ASME *Journal Applied Mechanic*, Sept. 1975, pp. 647–650.

8 Berman, R., et al., "Anisotropic Heat Conduction in HCP He," *Journal of Physics*, Vol. 6, 1973, pp. 2119–2131.

9 Chang, Y. P., "Analytical Solution for Heat Conduction in Anisotropic Media in Infinite Semi-Infinite and Two-Plane-Bounded Regions," *International Journal of Heat Mass Transfer*, Vol. 20, 1977.

10 Chang, Y. P. and Tsou, C. H., "Heat Conduction in an Anisotropic Medium, Homogeneous in Cylindrical Coordinates, Unsteady States," ASME JOURNAL OF HEAT TRANSFER., Feb. 1977, pp. 41–47.

11 Carslaw, H. S. and Jaeger, J. C., *Conduction of Heat in Solids*, Clarendon Press, Oxford, 1959.

12 Morse, P. M. and Feshback, H., *Methods of Theoretical Physics*, McGraw-Hill, New York, 1953, pp. 865–869.

13 Truesdell, C. and Noll, W., *Handbuch der Physik*, Flugge S. Ed., Springer-Verlag, Berlin, 1965.

14 Curtin, M. E. and Pipkin, A. C., "A General Theory of Heat Conduction with Finite Wave Speeds," *Ach. Rat. Mech. Anal.*, Vol. 31, 1968, p. 113.

15 Chang, Y. P. and Tsou, C. H., "Heat Conduction in an Anisotropic Medium Homogeneous in Cylindrical Coordinates, Steady States," ASME JOURNAL OF HEAT TRANSFER, Vol. 99, pp. 132–134, 1977.

16 Poon, K. C., "Analytical Solution for Heat Conduction in Cylindrically Anisotropic Media at Rest and in Motion with Infinite and Finite Speed of Heat Propagation," PhD Dissertation, Mechanical Engng., SUNY at Buffalo, (in preparation).

17 Watts, R. G., "Temperature Distributions in Solid and Hollow Cylinders due to a Moving Circumferential Ring Heat Source," ASME JOURNAL OF HEAT TRANSFER, Vol. 91, pp. 465–470, 1969.

18 Kang, C. S. and Chang, Y. P., "A System of Concentrated and Distributed Heat Sources over a Translationally and Rotationally Moving Cylinder," *International Journal of Heat Mass Trans.*, Vol. 18, pp. 109–121, 1975.

19 Des Ruisseaux, N. R. and Zerkle, R. C., "Temperature in Semi-Infinite and Cylindrical Bodies Subjected to Moving Heat Sources and Surface Cooling," ASME JOURNAL OF HEAT TRANSFER, Vol. 92, 1970, pp. 456–464.

D. A. Wesley
Mem. ASME

Thermal Test and Analysis Division,
Sandia Laboratories,
Albuquerque, N.M. 87115

Thin Disk On A Convectively Cooled Plate—Application To Heat Flux Measurement Errors[1]

An analysis is made of the steady-state thermal processes associated with a thin disk affixed to a convectively cooled solid plate. The disk represents a thermopile heat flux gauge. In the first part of the paper, the heat conduction problem of the plate is solved for the simplified condition where the heat flow through the disk is axially one-dimensional. It was found that the local divergence of the heat flux field within the plate owing to the presence of the disk may result in a gauge reading that underestimates the heat transfer rate. Also, a sizeable local plate temperature augmentation can occur. Furthermore, the analysis yields dimensional estimates of the region where the temperature and heat flux fields within the plate are significantly altered by the presence of the disk. An adjunct to the foregoing analysis develops a one-dimensional conduction factor which is useful in determining when the heat flow through the disk can be considered to be axially one-dimensional.

Introduction

This paper is concerned with the steady-state heat transfer processes associated with a thin circular disk affixed to a convectively cooled plate. The plate face opposite the disk has a constant heat flux thermal boundary condition. This physical situation is illustrated in Fig. 1. No thickness or thermal conductivity constraints are imposed on the plate. The disk, however, has radius, thickness, and thermal conductivity restrictions. These restrictions are consistent with the thermal boundary conditions associated with axial one-dimensional heat flow through the disk.

Consideration of this problem is motivated by the measurement of heat fluxes from convectively cooled surfaces by thermopile heat flux gauges. A thermopile heat flux gauge consists basically of an insulating wafer fitted with a number of thermoelectric junctions [1]. Various sizes and geometric shapes of these gauges are commercially available, but attention will be focused here on a thin circular disk. The additional thermal resistance of a disk affixed to a plate causes a local temperature increase and a divergence of the heat flux in the plate. The result is that the magnitude of the mean heat flux at the interface between the gauge and plate is less than the constant heat flux at the opposite face of the plate. This effect causes the gauge reading to be lower and therefore not indicative of the heat flux that is convected from the surface of the undisturbed plate.

Differences between the thermal operating conditions and those existing during calibration will typically cause a change in the proportionality between the emf output and the heat flow through the gauge. Factors that cause this change are:

1 temperature dependence of the thermal conductivity of the gauge,

2 temperature dependence of the Seebeck coefficient associated with the thermopile (see [2]), and

3 significant departure from an axial one-dimensional heat flow through the wafer.

The error in the heat flux gauge reading that occurs due to the temperature dependence of items (1) and (2) may be estimated with a mean gauge temperature relationship. Some commercially available gauges have a thermocouple embedded in the wafer which provides data to perform this type of correction. The error recorded in item (3)

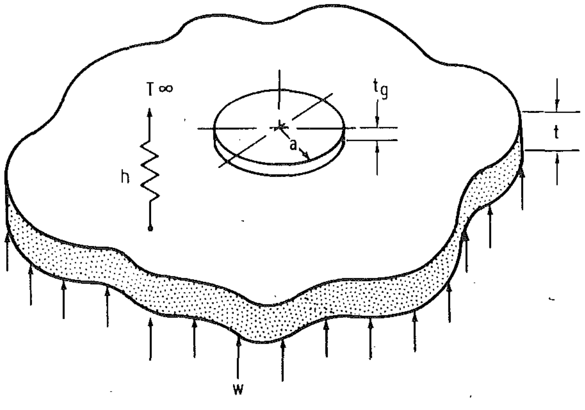

Fig. 1 Pictorial representation of the physical situation

---

[1] This work was supported by the Department of Energy.

Contributed by The Heat Transfer Division for publication in The JOURNAL OF HEAT TRANSFER. Manuscript received by The Heat Transfer Division June 5, 1978.

is more difficult to estimate since the heat flux field within the gauge is governed by the thermal conductivity and the boundary conditions. A section of this paper will be devoted to developing a method for determining when the mean heat flow through the gauge may be considered to be axially one-dimensional.

The heat conduction problem for the configuration shown in Fig. 1 may be formulated in various degrees of complexity. At the extreme level of complexity is a coupled heat conduction problem that requires the specification of the convective heat transfer coefficient over the entire surface of the disk and plate. The complete mathematical description of the thermal and hydrodynamic boundary layers at the disk and plate surface is complex. Specification of the convective heat transfer coefficient would, therefore, be difficult. A simplification to the problem may be made by neglecting the heat loss from the edge of the thin disk. An additional simplification may be made by assuming that the convective heat transfer coefficient at the disk face is constant and equal to the constant convective coefficient at the plate surface. This assumption would not be valid when the disk is located in a region where the thermal boundary layer is growing rapidly or when the disk would trip the boundary layer from laminar to turbulent. These simplified boundary conditions are consistent with a one-dimensional axial heat flux field within the disk provided that the radial temperature gradient at the interface between the disk and plate is small.

The assumption of one-dimensional heat flow through the disk allows the thermal resistance of the disk and the convective heat transfer resistance to be lumped together. The result is an effective convective heat transfer coefficient h_e,

$$h_e = \left(\frac{1}{h} + \frac{t_g}{k_g}\right)^{-1} \tag{1}$$

which applies to a disk sized area on the plate surface. This problem is schematically represented in Fig. 2. Here t_g and k_g are the disk thickness and thermal conductivity, respectively. Note that the value of h_e can never exceed the value of h.

Two different cases of the heat conduction problem, depicted in Fig. 2, will be investigated here. These two cases are formed by permitting the radius b, which defines the location of an insulated boundary, to be finite or taken in the limit as b approaches infinity. The limiting case, which is perhaps the most common, corresponds physically to a disk affixed to a radially large plate.

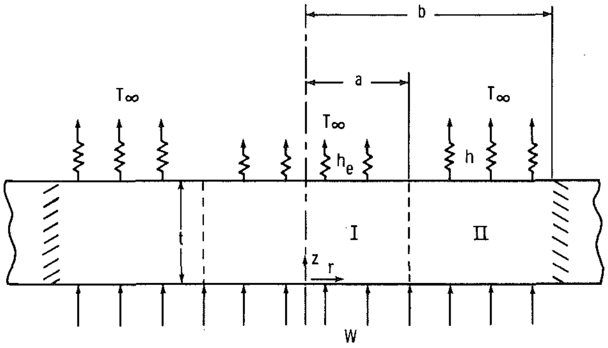

Fig. 2 Schematic representation of the simplified physical situation

Although the literature contains problem solutions where the convective heat transfer coefficient varies over a flat surface (examples are reported in [3–5]) there do not appear to be any published results for the problem of the present investigation.

Analysis

Heat Conduction through the Plate. The method which was used to determine the temperature field within the plate is based on the observation that the classical separation of variables approach will yield solution representations for each of two regions of the plate. Although the literature contains a number of problems [6–10], described mathematically by Laplace's equation, that have utilized this solution method, the author is aware of only two heat conduction studies [11, 12] that have utilized this technique. This solution method is believed to offer computational advantages over numerical finite-difference approaches.

A cross-sectional view of the two mathematical regions of the plate is shown in Fig. 2. The two regions are denoted by numerals I and II respectively. Region I is a cylinder of length t and radius a, and region II is an annulus of length t with inside radius a and outside radius b. The temperature representation of each region can be expressed in terms of an infinite series. The coefficients of these two series solutions can be evaluated by equating the temperatures ($T_{\rm I}$ and $T_{\rm II}$) and the heat fluxes ($-k\partial T_{\rm I}/\partial r$ and $-k\partial T_{\rm II}/\partial r$) at the interface between the two regions ($r = a, 0 \le z \le t$).

The number of independent parameters characteristic of this problem are minimized by introducing the dimensionless quantities

$$\bar{z} = \frac{z}{t}, \bar{r} = \frac{r}{a}, \bar{b} = \frac{b}{a} \tag{2a}$$

$$\mathrm{Bi} = \frac{ht}{k}, \mathrm{Bi}_e = \frac{h_e t}{k} \tag{2b}$$

$$\overline{T}_{\rm I} = \frac{T_{\rm I} - T_\infty}{T_w - T_\infty}, \overline{T}_{\rm II} = \frac{T_{\rm II} - T_\infty}{T_w - T_\infty} \tag{2c}$$

where T_w is the spatially uniform convective surface temperature in the absence of the disk. In the limiting case where $\bar{b}$ approaches infinity, T_w serves to specify the convective surface temperature at large $\bar{r}$. This temperature can be represented in terms of other thermal parameters as

$$T_w = \frac{w}{h} + T_\infty \tag{3}$$

The governing partial differential equations for regions I and II cannot be readily solved by the separation of variables method due to the nonhomogeneous spatially constant heat flux boundary at the

Nomenclature

A_n = dimensionless series coefficient
a = disk radius
Bi = Biot number, ht/k
Bi_e = effective Biot number, $h_e t/k$
B_m = dimensionless series coefficient
b = plate radius
$\bar{b}$ = dimensionless plate radius, b/a
$\bar{b}_\infty$ = dimensionless plate radius, equation (34)
C_f = conduction factor
h = convective heat transfer coefficient
h_e = effective convective heat transfer coefficient, equation (1)
k = plate thermal conductivity
k_g = disk thermal conductivity
r = radial coordinate
$\bar{r}$ = dimensionless radial coordinate
$T_{\rm I}$ = region I temperature representation
$T_{\rm II}$ = region II temperature representation
$T_{\rm disk}$ = disk temperature representation
T_w = plate surface temperature, equation (3)
T_∞ = temperature of external fluid environment
$\overline{T}_{\rm I}$ = dimensionless region I temperature
$\overline{T}_{\rm II}$ = dimensionless region II temperature
$\overline{T}$ = dimensionless disk temperature
t = plate thickness
t_g = disk thickness
w = uniform heat flux at the plate surface
z = axial coordinate
$\bar{z}$ = dimensionless axial coordinate, z/t
δ_m = eigenvalue, equation (12)
θ_1 = dimensionless region I temperature
θ_2 = dimensionless region II temperature
λ_n = eigenvalue, equation (11)

Subscripts

k = integer value, $(0 < k \le \infty)$
m = integer value, equation (12)
n = integer value, equation (11)

Superscripts

N = order of the A_n determinant
∞ = infinite order A_n determinant

plate surface. This obstacle can be removed through the use of the principle of superposition [13]. The superposition principle permits the temperature representation in each region to be expressed as the sum of the axial linear and spatially nonuniform temperature contributions

$$\overline{T}_{\rm I} = \theta_1 + {\rm Bi}(1 - \bar{z}) + \frac{\rm Bi}{{\rm Bi}_e} \tag{4a}$$

$$\overline{T}_{\rm II} = \theta_2 + {\rm Bi}(1 - \bar{z}) + 1 \tag{4b}$$

Here θ_1 and θ_2 represent the dimensionless nonuniform contributions of regions I and II, respectively. The governing equations together with the resulting homogeneous boundary conditions expressed in terms of the variable θ appear as follows:

Region I

$$\frac{\partial^2\theta_1}{\partial\bar{r}^2} + \frac{1}{\bar{r}}\frac{\partial\theta_1}{\partial\bar{r}} + \left(\frac{a}{t}\right)^2\frac{\partial^2\theta_1}{\partial\bar{z}^2} = 0 \tag{5a}$$

$$\theta_1(0, \bar{z}) \text{ is bounded} \tag{5b}$$

$$\frac{\partial\theta_1}{\partial\bar{z}}(\bar{r}, 0) = 0 \tag{5c}$$

$$\frac{\partial\theta_1}{\partial\bar{z}}(\bar{r}, 1) = -{\rm Bi}_e\theta_1(\bar{r}, 1) \tag{5d}$$

Region II

$$\frac{\partial^2\theta_2}{\partial\bar{r}^2} + \frac{1}{\bar{r}}\frac{\partial\theta_2}{\partial\bar{r}} + \left(\frac{a}{t}\right)^2\frac{\partial^2\theta_2}{\partial\bar{z}^2} = 0 \tag{6a}$$

$$\frac{\partial\theta_2}{\partial\bar{r}}(\bar{b}, \bar{z}) = 0 \tag{6b}$$

$$\frac{\partial\theta_2}{\partial\bar{z}}(\bar{r}, 0) = 0 \tag{6c}$$

$$\frac{\partial\theta_2}{\partial\bar{z}}(\bar{r}, 1) = -{\rm Bi}\theta_2(\bar{r}, 1) \tag{6d}$$

The boundary condition (6b) applies when the dimensionless radius $\bar{b}$ is finite. In the limit as $\bar{b}$ approaches infinity, equation (6b) is replaced with

$$\lim_{\bar{b}\to\infty} \theta_2(\bar{b}, \bar{z}) \text{ is bounded} \tag{7}$$

The two remaining relations that couple regions I and II can be formulated by noting that the temperature and the heat flux must be continuous at the interface between the two regions.

$$\theta_1(1, \bar{z}) + \frac{\rm Bi}{{\rm Bi}_e} = \theta_2(1, \bar{z}) + 1 \tag{8a}$$

$$\frac{\partial\theta_1}{\partial\bar{r}}(1, \bar{z}) = \frac{\partial\theta_2}{\partial\bar{r}}(1, \bar{z}) \tag{8b}$$

The solution of equations (5a) and (6a) by the separation of variables method yields the nonuniform temperature contributions for regions I and II.

$$\theta_1(\bar{r}, \bar{z}) = \sum_{n=1}^{\infty} A_n I_0(\lambda_n\bar{r}) \cos\left(\frac{t\lambda_n\bar{z}}{a}\right) \tag{9}$$

$$\theta_2(\bar{r}, \bar{z}) = \sum_{m=1}^{\infty} B_m \left\{I_0(\delta_m\bar{r}) + \frac{I_1(\delta_m\bar{b})}{K_1(\delta_m\bar{b})} K_0(\delta_m\bar{r})\right\} \cos\left(\frac{t\delta_m\bar{z}}{a}\right) \tag{10a}$$

Equation (9) remains unchanged when the radius b is taken in the limit as $\bar{b}$ approaches infinity. The solution representation of region II, however, changes to

$$\lim_{\bar{b}\to\infty} \theta_2(\bar{r}, \bar{z}) = \sum_{m=1}^{\infty} B_m K_0(\delta_m\bar{r}) \cos\left(\frac{t\delta_m\bar{z}}{a}\right) \tag{10b}$$

The symbols I_x and K_x denote modified Bessel functions of the first and second kinds respectively. The symbols λ_n and δ_m represent eigenvalues which are defined by the following equations:

$$\frac{t\lambda_n}{a} \tan\left(\frac{t\lambda_n}{a}\right) = {\rm Bi}_e \tag{11}$$

$$n = 1, 2, 3, \ldots$$

$$\frac{t\delta_m}{a} \tan\left(\frac{t\delta_m}{a}\right) = {\rm Bi} \tag{12}$$

$$m = 1, 2, 3, \ldots$$

The eigenvalues for the present investigation were determined by solving equations (11) and (12) with a numerical iteration scheme.

The A_n and B_m coefficients that appear in equations (9) and (10) have yet to be determined. The first step in this evaluation procedure is the substitution of the θ_1 and θ_2 parameters into equation (8a). By applying orthogonality to this equality, an expression for the A_n coefficients in terms of the B_m coefficients will be obtained.

$$A_n = D_n + \sum_{m=1}^{\infty} B_m E_{mn} \tag{13}$$

Here, D_n and E_{mn} are defined as

$$D_n = \frac{\left\{1 - \dfrac{\rm Bi}{{\rm Bi}_e}\right\} \dfrac{a}{\lambda_n t} \sin\left(\dfrac{\lambda_n t}{a}\right)}{I_0(\lambda_n)\left\{\dfrac{1}{2} + \dfrac{a}{4t\lambda_n}\sin\left(\dfrac{2t\lambda_n}{a}\right)\right\}} \tag{14}$$

$$E_{mn} = \frac{\dfrac{a}{2t}\left\{I_0(\delta_m) + I_1\dfrac{(\delta_m\bar{b})K_0(\delta_m)}{K_1(\delta_m\bar{b})}\right\}\left\{\dfrac{\sin\left[\dfrac{t}{a}(\lambda_n - \delta_m)\right]}{(\lambda_n - \delta_m)} + \dfrac{\sin\left[\dfrac{t}{a}(\lambda_n + \delta_m)\right]}{(\lambda_n + \delta_m)}\right\}}{I_0(\lambda_n)\left\{\dfrac{1}{2} + \dfrac{a}{4t\lambda_n}\sin\left(\dfrac{2t\lambda_n}{a}\right)\right\}} \tag{15a}$$

When $\bar{b}$ is taken in the limit as $\bar{b}$ approaches infinity the E_{mn} expression becomes

$$\lim_{\bar{b}\to\infty} E_{mn} = \frac{\dfrac{a}{2t}K_0(\delta_m)\left\{\dfrac{\sin\left[\dfrac{t}{a}(\lambda_n - \delta_m\right]}{(\lambda_n - \delta_m)} + \dfrac{\sin\left[\dfrac{t}{a}(\lambda_n + \delta_m)\right]}{(\lambda_n + \delta_m)}\right\}}{I_0(\lambda_n)\left\{\dfrac{1}{2} + \dfrac{a}{4t\lambda_n}\sin\left(\dfrac{2t\lambda_n}{a}\right)\right\}} \tag{15b}$$

Similarly, by substituting θ_1 and θ_2 into equation (8b) and applying orthogonality results in an expression for the B_m coefficients in terms of the A_n coefficients.

$$B_m = \sum_{k=1}^{\infty} A_k F_{km} \tag{16}$$

When the dimensionless radius $\bar{b}$ is finite, F_{km} is defined by

$$F_{km} = \frac{\lambda_k I_1(\lambda_k)\dfrac{a}{2t}\left\{\dfrac{\sin\left[\dfrac{t}{a}(\lambda_k - \delta_m)\right]}{(\lambda_k - \delta_m)} + \dfrac{\sin\left[\dfrac{t}{a}(\lambda_k + \delta_m)\right]}{(\lambda_k + \delta_m)}\right\}}{\delta_m\left\{I_1(\delta_m) - \dfrac{I_1(\delta_m\bar{b})K_1(\delta_m)}{K_1(\delta_m\bar{b})}\right\}\left\{\dfrac{1}{2} + \dfrac{a}{4t\delta_m}\sin\left(\dfrac{2t\delta_m}{a}\right)\right\}} \tag{17a}$$

In the limit as $\bar{b}$ approaches infinity the F_{km} expression changes to

$$\lim_{\bar{b}\to\infty} F_{km} = \frac{-\lambda_k I_1(\lambda_k)\dfrac{a}{2t}\left\{\dfrac{\sin\left[\dfrac{t}{a}(\lambda_k - \delta_m)\right]}{(\lambda_k - \delta_m)} + \dfrac{\sin\left[\dfrac{t}{a}(\lambda_k + \delta_m)\right]}{(\lambda_k + \delta_m)}\right\}}{\delta_m K_1(\delta_m)\left\{\dfrac{1}{2} + \dfrac{a}{4t\delta_m}\sin\left(\dfrac{2t\delta_m}{a}\right)\right\}} \tag{17b}$$

The substitution of equation (16) into equation (13) produces a relation between all of the A_n coefficients.

$$A_n = D_n + \sum_{k=1}^{\infty} A_k G_{kn} \tag{18}$$

Here G_{kn} is defined as

$$G_{kn} = \sum_{m=1}^{\infty} F_{km} E_{mn} \tag{19}$$

To obtain the value of each A_n coefficient by the use of equation (18) would require the solution of an infinite determinant. It can be shown that as successively larger $N \times N$ determinants are solved the value of each A_n approaches a definite limit. The value of this limit is what would be obtained if an infinite number of terms were taken. Extrapolation formulas have been utilized as a means of obtaining the same limit to a given number of significant figures. A two constant extrapolation formula that is reported in [6] is

$$A_n^{(N)} = A_n^{(\infty)} + \frac{C_1}{N} + \frac{C_2}{N^2} \tag{20}$$

The $A_n^{(\infty)}$, C_1, and C_2 unknowns in equation (20) can be evaluated by the solution of three simultaneous equations. Each equation requires a distinct $A_n^{(N)}$ value. These values can be obtained from the solution of three different A_n determinants. Each determinant must differ in order from the preceding by $N - 2$. Hence, only values obtained from successive odd or even determinants are suitable for use in solving equation (20).

The solution representation of the temperature field within region I provides a means of estimating several errors that may be present in a thermopile heat flux gauge reading. These errors originate from two separate sources: (1) the local divergence of the heat flux field within the plate and (2) the temperature dependence of the thermal conductivity and the Seebeck coefficient.

The local divergence of the heat flux field within the plate results in a difference between the heat flux at the interface between the gauge and plate and the spatially constant heat flux at the opposite face of the plate. Therefore, a fractional part of the energy that enters that area of the plate directly opposite the gauge will flow around the gauge. This net heat loss from region I gives rise to a misleadingly low gauge reading (i.e., a gauge error). The percentage difference between the heat entering region I and the heat lost through the interface between the gauge and plate is

$$\text{percent error} = \left\{1 + \frac{2}{\text{Bi}}\int_0^1 \frac{\partial \bar{T}_I}{\partial \bar{z}}(\bar{r}, 1)\bar{r}d\bar{r}\right\} \times 100 \tag{21}$$

The temperature dependence of the thermal conductivity and the Seebeck coefficient of a specific gauge may change the proportionality between the heat flow through the gauge and the emf output. The mean temperature of the gauge is the basis for correcting the error in the output. If the gauge is thin and the temperature gradient within the gauge is not large, then the radial mean temperature of the interface between the gauge and the plate provides a good approximation of the mean gauge temperature. The radial mean interface temperature ($\bar{T}_{\text{mean}}$) can be determined from

$$\bar{T}_{\text{mean}} = 2\int_0^1 \bar{T}_I(\bar{r}, 1)\bar{r}d\bar{r} \tag{22}$$

This approximation may be somewhat in error if the axial temperature gradient within the gauge is large and the governing thermal and electrical gauge properties change appreciably with temperature. If the axial temperature drop across the gauge is taken into account then equation (22) can be improved. The resulting dimensionless equation for the mean gauge temperature is

$$\text{Mean Temp.} = \bar{T}_{\text{mean}}\left(\frac{\dfrac{\text{Bi}}{2} + \dfrac{k_g t}{k t_g}}{\text{Bi} + \dfrac{k_g t}{k t_g}}\right) \tag{23}$$

Equation (23) provides an excellent estimate of the mean gauge temperature for all but the most severe operating conditions.

One-Dimensional Conduction Factor. As earlier remarked, a significant departure from axial one-dimensional heat flow through a thermopile heat flux gauge can lead to an error in the gauge reading. A locally distorted heat flux field at the edge of the gauge is inevitable. [1] suggests that edge effects produce a negligible error in the gauge reading if the gauge is constructed with the thermopile junctions located at least five times the gauge thickness from the edge of the gauge. There is no indication that the recommended thermopile region was derived with consideration given to a spatially distorted temperature at the interface between the gauge and heat transferring surface. Equation (9) implies that a radially nonuniform temperature is typical at the interface between a gauge and plate. It is obvious that the heat flux field within the gauge is governed by the entire conductive/convective thermal system. A specific gauge design, therefore, may not insure against an error due to a distorted heat flux within the gauge which results from an unfavorable thermal system.

A one-dimensional conduction factor, which provides an indication of when the mean heat flow through a thin disk can be considered to be axially one-dimensional, will be developed in the following analysis. The factor was formulated with consideration given to the entire thermal system illustrated in Fig. 1. Recall that the previous plate heat conduction analysis utilized a simplified thermal boundary condition which was based on the assumption of an axial linear temperature gradient within a disk affixed to a plate. In view of this, it appears that the conduction factor would serve a twofold purpose: first, predicting when the previous plate heat conduction results are no longer valid and, second, indicating when an error may be present in a thermopile type heat flux gauge reading due to a significant departure from an axial one-dimensional heat flow through the gauge.

A disk of radius a and thickness t_g is attached to the plate shown in Fig. 2. The axis of the disk coincides with the z coordinate. A dimensionless temperature is required in addition to those dimensionless parameters defined by equations (2a), (2b), and (2c). This is the dimensionless temperature distribution of the disk and is defined as

$$\overline{T} = \frac{T_{\text{disk}} - T_\infty}{T_w - T_\infty} \tag{24}$$

It is convenient to express the dimensionless heat conduction equation of the disk in the integral form.

$$\left(\frac{t}{a}\right)^2 \int_0^1 \int_1^{1+t_g/t} \bar{r} \left(\frac{\partial^2 \overline{T}}{\partial \bar{r}^2} + \frac{1}{\bar{r}} \frac{\partial \overline{T}}{\partial \bar{r}}\right) d\bar{z} d\bar{r} = - \int_0^1 \bar{r} \frac{\partial \overline{T}}{\partial \bar{z}} \left(\bar{r}, 1 + \frac{t_g}{t}\right) d\bar{r} + \int_0^1 \bar{r} \frac{\partial \overline{T}}{\partial \bar{z}} (\bar{r}, 1) d\bar{r} \tag{25}$$

This equation allows for heat loss at the edge of the gauge.

The mean value theorem of integral calculus states that a $\bar{\xi}$ exists within the thin gauge ($t_g \ll a$) such that $1 \le \bar{\xi} \le 1 + t_g/t$ where

$$\int_1^{1+t_g/t} \bar{r} \left(\frac{\partial^2 \overline{T}}{\partial \bar{r}^2} + \frac{1}{\bar{r}} \frac{\partial \overline{T}}{\partial \bar{r}}\right) d\bar{z} = \frac{t_g}{t} \bar{r} \left\{\frac{\partial^2 \overline{T}}{\partial \bar{r}^2} (\bar{r}, \bar{\xi}) + \frac{1}{\bar{r}} \frac{\partial \overline{T}}{\partial \bar{r}} (\bar{r}, \bar{\xi})\right\} \tag{26}$$

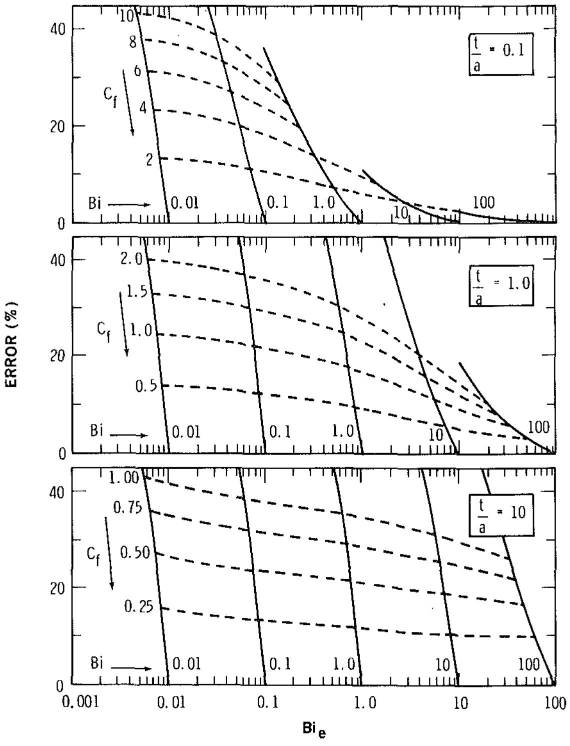

Fig. 3 Conduction factor and plate conduction errors for the case where $\bar{b}$ approaches infinity

For physically realistic convective boundary conditions at the edge of the gauge and significant differences between Bi_e and Bi, $\bar{\xi}$ may be approximated as being equal to unity, i.e., $\bar{\xi} \simeq 1$. The boundary conditions where this approximation would prove invalid occur when the disk and plate interface temperature approaches a constant (Bi_e approaches Bi) or when the convective heat transfer coefficient at the edge of the disk becomes large when compared with that at the disk face. As Bi_e approaches Bi the problem defined in the previous analysis begins to disappear as would any interest in a one-dimensional conduction factor. [14] indicates that a large reduction in heat transfer occurs at the edge of the gauge as opposed to the opposite being true.

Both partial derivatives on the right hand side of equation (25) may be represented in terms of other thermal parameters. Noting that the local convective heat flux at the disk surface is given by $h(T_{\text{disk}} - T_\infty)$, it follows that

$$-\frac{\partial \overline{T}}{\partial \bar{z}} \left(r, 1 + \frac{t_g}{t}\right) = \frac{k}{k_g} \mathrm{Bi}\, \overline{T} \left(\bar{r}, 1 + \frac{t_g}{t}\right) \tag{27}$$

The local heat flux at the interface between the disk and plate must be conserved, that is

$$\frac{\partial \overline{T}}{\partial \bar{z}} (\bar{r}, 1) = \frac{k}{k_g} \frac{\partial \overline{T}_I}{\partial \bar{z}} (\bar{r}, 1) \tag{28}$$

Let a conduction factor C_f be defined as

$$C_f = \frac{t}{a} \left| \frac{\int_0^1 \bar{r} \left\{\frac{\partial^2 \overline{T}_I}{\partial \bar{r}^2} (\bar{r}, 1) + \frac{1}{\bar{r}} \frac{\partial \overline{T}_I}{\partial \bar{r}} (\bar{r}, 1)\right\} d\bar{r}}{\int_0^1 \bar{r} \frac{\partial \overline{T}_I}{\partial \bar{z}} (\bar{r}, 1) d\bar{r}} \right| \tag{29}$$

Equation (9) in the previous analysis section enables one to easily evaluate the integrals in the C_f expression.

When equation (25) is expressed in terms of the preceding quantities developed in equations (26–29), a relation between the magnitudes of the radial, axial, and convective heat transport contributions is obtained

$$\frac{t_g k_g}{ak} C_f = 1 + \left| \frac{\mathrm{Bi} \int_0^1 \bar{r} \overline{T} \left(\bar{r}, 1 + \frac{t_g}{t}\right) d\bar{r}}{\int_0^1 \bar{r} \frac{\partial \overline{T}_I}{\partial \bar{z}} (\bar{r}, 1) d\bar{r}} \right| \tag{30}$$

Thus, when the product of the conduction factor, the disk to plate thermal conductivity ratio, and the disk thickness to radius ratio is much less than unity, i.e.,

$$\frac{t_g k_g}{ak} C_f \ll 1 \tag{31}$$

the mean heat flow through the disk can be considered to be axially one-dimensional.

Results and Discussion

The following results were generated with a CDC 6600 digital computer. Convergence of the mathematical series that were utilized in producing the data was obtained when the addition of a single term caused the final result to differ by not more than 0.0001. Depending upon the thermal input parameters, convergence was achieved with from 7 to 56 terms.

Plate Conduction Error and Conduction Factor. Attention will be initially focused on the plate heat conduction error results which are presented in Fig. 3. The error results, identified by the unbroken curves in the figure, were generated from equation (21) for the limiting case where $\bar{b}$ approaches infinity. Fig. 3 also contains the one-dimensional conduction factor results which are identified by the dashed (broken) curves.

The figure is subdivided into three semi-logarithmic graphs, each of which contains the results for a specific plate thickness to disk radius ratio (t/a). In each graph, the percentage error as a function of the effective Biot number (Bi_e) is plotted for five Biot numbers (Bi) between 0.01 and 100. Inspection of the error curves reveals a pattern with Bi_e whereby the error decreases monotonically toward zero as Bi_e approaches Bi. Furthermore, the $Bi = 0.01$ and 0.1 curves of the three semilogarithmic graphs are nearly linear showing a very slight convex shape. The $Bi = 100$ curves are slightly concave.

The error curves in Fig. 3 generally indicate that a slight departure in Bi_e from Bi can result in a significant error. Exceptions occur at large Bi and small t/a values. It is obvious that the thermopile type heat flux gauge user will reduce plate heat conduction errors by selecting specific gauges that minimize the difference between Bi_e and Bi. Equations (1) and (2*b*) clearly shows that the reduction of the difference between Bi_e and Bi ultimately requires a reduction in the t_g/k_g ratio.

The conduction factor (C_f), in addition to the plate conduction error, is a function of the Bi_e, Bi, and t/a parameters. It is natural, therefore, to plot the conduction factor results on the plate conduction error graphs. The conduction factor results, which were generated from equation (29), are represented by dashed curves in Fig. 3.

Two characteristics of the conduction factor are of importance to the thermopile heat flux gauge user. First, a gauge attached to a thicker plate is less likely to incur errors caused by a departure from an axial one-dimensional conduction field within the gauge than the same gauge attached to a thin plate. Second, a gauge operating with a significant difference between Bi_e and Bi is more prone toward a one-dimensional conduction departure error. It must be emphasized that equation (31) represents the criteria to be met for reducing errors of this type. Furthermore, it is obvious that gauges which are subject to thermal conditions that result in sizeable plate conduction errors also run a greater risk of errors caused by a distorted heat flux field within the gauge.

Approximate Mean Gauge Temperature. Equation (22) affords the thermopile type heat flux gauge user a means of correcting errors of a different class. This type of error, which was addressed earlier, results from the temperature dependence of the thermal and electrical properties of the gauge. The approximate mean gauge temperature provides a basis for estimating an error of this kind.

Fig. 4 was prepared for the case where $\bar{b}$ approaches infinity (i.e., a radially infinite plate). The figure is subdivided into three graphs for Biot numbers of 0.01, 1.0 and 100. Each graph contains the plots of the dimensionless approximate mean disk temperature ($\bar{T}_{\text{mean}}$) as a function of the Bi_e/Bi ratio.

The results shown in Fig. 4 are useful in estimating the local plate temperature increase as well as providing a means of correcting errors caused by the temperature dependence of the gauge properties. For significant differences between Bi_e and Bi, quite large temperature increases can occur. With present commercially available gauges, some Bi_e/Bi values in the figure may not represent practicable operating conditions.

Region of Influence. It may be necessary to estimate that region of the plate where the temperature and heat flux fields are not significantly altered by the presence of the disk. This may be of interest, for example, in determining when the previous results (Figs. 3 and 4) for the radially infinite plate are valid. It must be born in mind that there is no actual sharp division between that region of the plate where the thermal fields are altered and that region where the fields are not altered. Hence, a rather arbitrary means of defining this boundary must be adopted. The method which was chosen here consists of obtaining a dimensionless radius $\bar{b}_\infty$ where

$$\text{Error}_{(\bar{b}_\infty)} = 0.99\ \text{Error}_{(\infty)} \tag{32}$$

Fig. 5 clearly shows the region of the plate where the thermal fields within the plate are changed due to the presence of the gauge. From the figure, $\bar{b}_\infty$ may be as small as 1.1 to as large as 10.0. The thermal disturbance is more localized for small t/a and large Bi values. These results provide a definitive estimate of the region of the plate that is thermally altered by the presence of a specific thermopile heat flux gauge.

Concluding Remarks

It has been shown that small differences between Bi_e and Bi can result in meaningfully large errors caused by the divergence of the heat flux field within the plate. Significant augmentations of the approx-

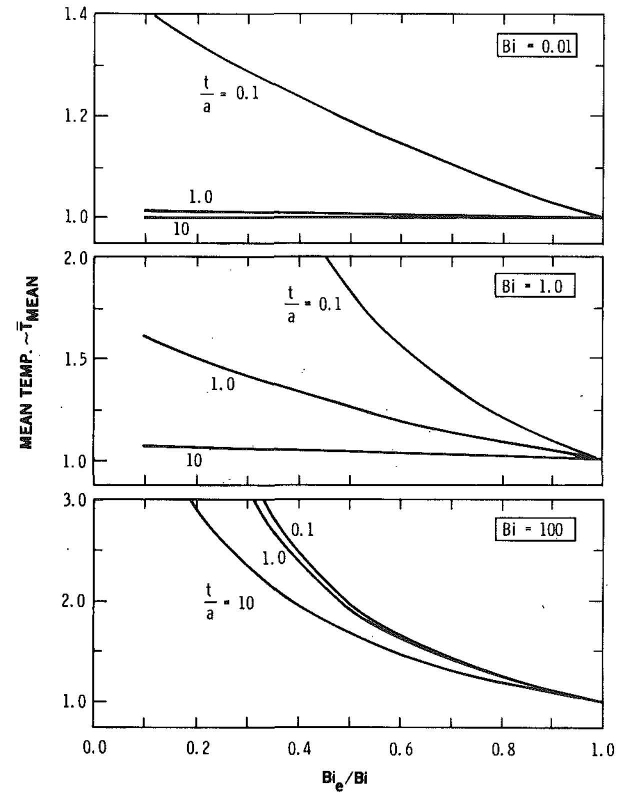

Fig. 4 Approximate mean gauge temperature for the case where $\bar{b}$ approaches infinity

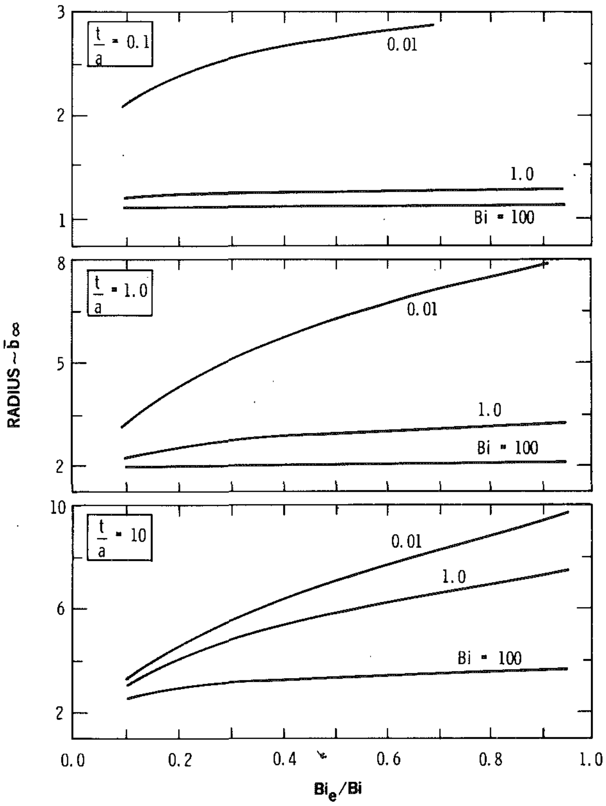

Fig. 5 Region of the plate where the temperature and heat flux fields are altered

imate mean gauge temperature can also result from small differences between Bi_e and Bi. Furthermore, thermal operating conditions that are conducive to plate conduction errors also increase the probability of errors resulting from a significant departure from an axial one-dimensional heat flux field within the gauge. The mean heat flux field within the gauge can be regarded as axially one-dimensional if $C_f t_g k_g / ak \ll 1$. Reduction of the type of errors that are addressed in this paper ultimately require the selection of a specific gauge that minimizes the t_g/k_g ratio.

The use of the results shown in Figs. 3–5 requires values of Bi_e, Bi, and t/a. Convective heat transfer coefficients are often calculated from temperature sensor and heat flux gauge measurements. Therefore, the actual value of Bi, and consequently Bi_e, is not known. The error results shown in Fig. 3, for example, may be utilized with a measured Bi value by employing an iteration technique.

An iteration method that has proved successful consists of calculating approximate Bi and Bi_e values from the measured heat flux and temperature data. With these values, Fig. 3 will yield a plate conduction error. The error in turn may be used to correct the measured heat flux value. The corrected heat flux value is used in calculating new approximate Bi and Bi_e values. This procedure is repeated until Bi converges to a number of significant figures. This iteration method, when applied to specific heat flux gauge applications, has converged to 0.01 percent of the actual value with four iterations.

References

1 Hager, N. E., Jr., "Thin Foil Heat Meter," *Rev. Sci. Instr.*, Vol. 36, 1965, p. 1564.

2 *Manual On The Use of Thermocouples In Temperature Measurement*, American Society for Testing and Materials Tech. Pub. 470, 1970, p. 2.

3 Holy, Z. J., "Temperature and Thermoelastic Stress Fields in an Infinite Half-Space due to Axisymmetric Surface Heat Transfer, Part I. Iterative-perturbation Solution of Integral-Equation Formulation," *Nucl. Eng. Design* Vol. 5, 1967, p. 255.

4 Holy, Z. J., "Temperature, and Thermoelastic Stress Fields in an Infinite Half-Space due to Axisymmetric Surface Heat Transfer, Part II. Solution by Laguerre Polynomial Approximations," *Nucl. Eng. Design*, Vol. 5, p. 364.

5 Holy, Z. J., "A Synthesis Technique for Variable Surface Heat Transfer," *Nucl. Eng. Design*, Vol. 8, 1968, p. 289.

6 Smythe, W. R., "Flow Over Thick Plate with Circular Hole," *J. Appl. Phy.*, Vol. 23, 1952, p. 447.

7 Kirkham, D., "Potential and Capacity of Concentric Coaxial Capped Cylinders," *J. Appl. Phy.*, Vol. 28, 1957, p. 724.

8 Kirkham, D., "Exact Theory of Flow Into a Partially Penetrating Well," *J. Geophy. Res.*, Vol. 64, 1959, p. 1317.

9 Enfros, A. L., "Potential Distribution Near a Cylindrical Probe," *Soviet Phy., Tech. Phy.*, Vol. 5, 1961, p. 954.

10 Kelman, R. B., "Axisymmetric Potentials in Composite Geometries: Finite Cylinder and Half Space," *Cont. Diff. Egs.*, Vol 2, 1963, p. 421.

11 Kelman, R. B., "The Steady Temperature Interior to a Finite or Semi-Infinite Cylinder with a Discontinuous Radiation Condition," *J. Math. Mech.*, Vol. 14, 1965, p. 881.

12 Schmitz, R. A., "Heat Flux Through a Strip-Heated Flat Plate," ASME JOURNAL OF HEAT TRANSFER, Vol. 92, 1970, p. 201.

13 Myers, G. E., *Analytical Methods in Conduction Heat Transfer*, McGraw-Hill, New York, 1971, p. 151.

14 Chilcott, R. E., "A Review of Separated and Reattaching Flows with Heat Transfer," *Int. J. Heat Mass Trans.*, Vol. 10, 1967, p. 783.

P. M. Sforza
Professor of Mechanical and Aerospace Engineering.
Mem. ASME

W. Stasi
Research Associate.

Aerodynamics Laboratories,
Polytechnic Institute of New York,
Farmingdale, N. Y.

Heated Three-Dimensional Turbulent Jets

An experimental investigation of heated three-dimensional turbulent free jets is presented. Emphasis is placed on the basic character of such flows and their relation to their unheated counterparts and to heated axisymmetric jets. Temperature and velocity distributions indicate that these flow fields may be characterized by three distinct regions in terms of the axis decays: a potential core region where axis values are close to the exit values, a characteristic decay region wherein the axis decays are dependent upon orifice geometry, and an axisymmetric decay region where the axis decay is axisymmetric in nature and thus independent of orifice geometry. These regions are not exactly the same for temperature as for velocity, the former being shifted somewhat upstream of the latter. Half-width data indicate that heated three-dimensional jets change shape as they proceed downstream, ultimately becoming axisymmetric in nature, regardless of initial orifice shape. Profile characteristics and similarity are discussed as well as cross-plane contours of pertinent flow variables. Some of the effects of initial conditions and exit flow quality on the subsequent development of three-dimensional jets are shown and the sensitivity of such flows to these factors is described.

Introduction

Three-dimensional jet flow fields display several interesting features not apparent in their two-dimensional and axisymmetric counterparts. Since these simpler flow geometries are limiting cases of the three-dimensional flow, it is necessary that a better understanding of the general case be developed in order to more fully appreciate the consequences of the theories of shear flow turbulence that are based primarily on experience with the extreme cases. Such understanding will surely promote improved predictive capabilities for free turbulent shear flows. In addition, engineering practice requires, for the interim, experimentally inspired empiricisms capable of providing reasonably accurate information on three-dimensional shear flows.

The first author and his students have studied, in some detail, the behavior of constant property three-dimensional turbulent shear flows [1, 2] as well as heat and mass transfer in axisymmetric turbulent jets [3] and heat transfer in three-dimensional turbulent jets [4]. Recently emerging interest in such flows among other researchers is evidenced by the experimental work on heated slot jets by Sfeir [5] and the encouraging attempts at numerical analysis of constant property three-dimensional turbulent jets by McGuirk and Rodi [6].

The objective of this paper is to illustrate the character of heated three-dimensional turbulent free jets and to relate them, where possible, to their unheated three-dimensional counterparts as well as to heated axisymmetric free jets. We will consider jets issuing at exit velocities in the range of 60 to 90 m/s from orifices of various geometry at temperatures considerably (25°C to 125°C) higher than that of the motionless surroundings. Structural aspects of these flows which will be addressed include velocity and temperature fields and cross-plane contours of flow properties.

Experimental Apparatus

The experiments reported here were performed in the jet facility of the Aerodynamics Laboratories of the Polytechnic Institute of New York. Several different, but similar, stations in the facility were used in the course of these studies, which were performed over a period of years. They each consist, basically, of a fiberfax insulated cylindrical settling chamber with provision for instrumentation at various internal locations for monitoring of chamber pressure and temperature and internal screens upstream of the jet exit. The air supplied to the chamber is first allowed to settle in a large reservoir, after which it is passed through a silica gel matrix for moisture removal. A nichrome wire electric resistance heater, coiled about a portion of the chamber supply pipe, is monitored by an automatic control unit in order to keep the temperature of the supply air constant at the desired level.

The present investigation included isothermal (heater off) conditions as well as operation at elevated chamber temperatures (100°C to 200°C). The downstream end of the chamber accepts various endplates into which orifices of various geometry are machined. The endplates (both metal and bakelite endplates have been used) are thick enough to allow the upstream (inlet) side of the orifice to be contoured with a radius on the order of the (shortest) characteristic dimension of the orifice. Thus the orifices may be considered to be short converging nozzles. It will become apparent, it is hoped, from the subsequent discussion of results that initial conditions such as orifice details, exit profile uniformity, etc., are quite important in determining the nature of the near field of the jet flow. This becomes particularly evident in the case of three-dimensional free jets because of the distinctive character of such flows in the near field.

Contributed by the Heat Transfer Division and presented at The Winter Annual Meeting, Atlanta, Georgia, November 27–December 2, 1977 of THE AMERICAN SOCIETY OF MECHANICAL ENGINEERS. Manuscript received by the Heat Transfer Division February 6, 1978. Paper No. 77-WA/HT-27.

Typical features of the jet facilities used in this investigation are shown in Fig. 1. Most of the data (the detailed studies) presented here were obtained in a vertically oriented jet, as is shown in the illustration. Effects of horizontally issuing heated jets are most pronounced for orifice geometries with e approximately equal to unity, and are described in [7]. The large contraction in area from settling chamber to orifice (70:1) maintains low speed in the settling chamber (less than 1 m/s) and ensures low streamwise turbulent intensity at the exit. The orifice itself is machined out of the endplate and includes a radius on the order of half the endplate thickness. It has been our experience that exit radii less than this can lead to what is apparently a separation condition within the orifice with subsequent spurious downstream behavior.

The major problem in heated jet studies is connected with heat loss, by various means, from the settling chamber to its surroundings. This can lead to altered conditions in the test room, unwanted convection currents, and nonuniform exit temperature profiles. In order to minimize these effects the chamber was heavily insulated and materials of low heat conductivity were used where possible to thermally isolate the chamber. Within the chamber, six relatively coarse mesh (2mm × 2mm) screens were installed to promote temperature uniformity. Typical exit profiles of velocity and temperature for the rectangular slot of slenderness ratio $e = 0.1$ are shown in Fig. 2.

Several different types of instrumentation were used: pitot and thermocouple probes, and a specially designed isokinetic sampling probe described in some detail by Sforza and Mons [3]. Many of the temperature field measurements reported herein were obtained by means of various thermocouple probes while the more detailed measurements of the velocity and temperature field presented here for the particular case of the jet from an orifice of slenderness ratio $e = 0.1$ were performed with the isokinetic sampling probe. This latter has the capability of measuring mean values of mass, momentum, and enthalpy flux, from which the more conventional variables such as mass-averaged mean velocity (see Favre [8], Laufer [9]) and mean temperature may be deduced. Measurements of turbulence quantities were not made in this study. The objective here is to illustrate the basic character of the three-dimensional flow field in the case of combined heat and momentum transfer.

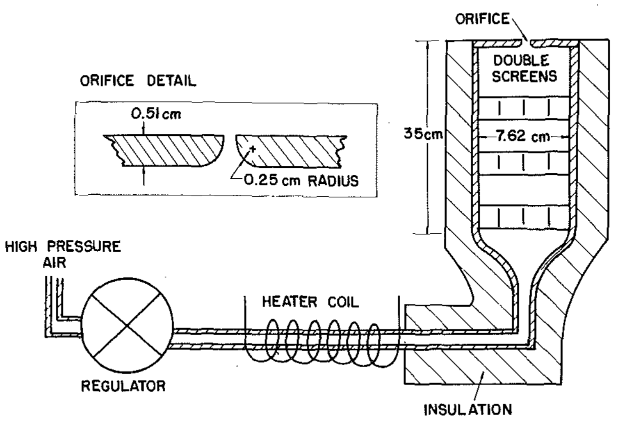

Fig. 1 Schematic diagram of typical heated jet facility

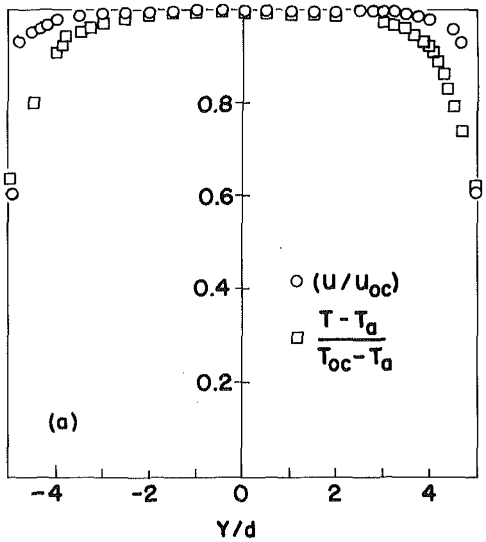

Fig. 2(*a*) The plane $z = 0$

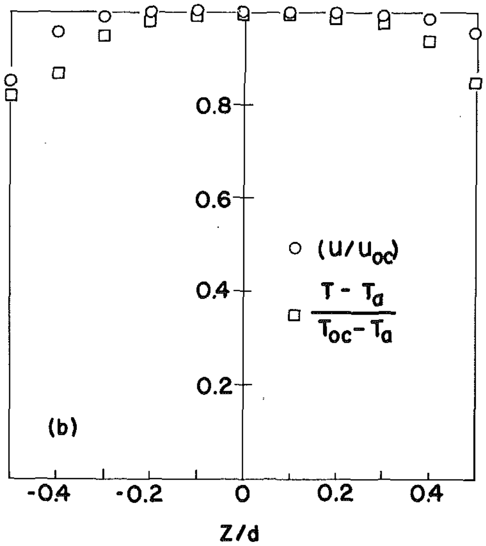

Fig. 2(*b*) The plane $y = 0$

Fig. 2 Initial profiles of velocity and temperature for a rectangular slot jet of $e = 0.1$

Nomenclature

c_p = specific heat at constant pressure
d = characteristic orifice height
d' = diameter of a circular orifice of area equal to that of a given orifice
d_t = effective thermal diameter
e = orifice slenderness ratio, d/l
e_r = reference value of e, equal to 0.1 here
l = characteristic orifice length
m = exponent in decay law for axis temperature excess
n = exponent in decay law for axis velocity decay
T = mean stagnation temperature
U = mean velocity component in the streamwise direction
$\tilde{U}$ = mass-averaged velocity, $\overline{\rho U}/\bar{\rho}$
x = streamwise coordinate
y = transverse coordinate
z = transverse coordinate
ρ = density

Subscripts

a = conditions in the ambient atmosphere
AD = axisymmetric decay region
o = axial conditions
oc = axial condition at orifice exit
PC = potential core region
½ = conditions at the half-width location

Superscripts

$(\bar{\ })$ = $(\ )/d$ for length variables and temporal mean for flow quantities
$(\tilde{\ })$ = $(\ )/(de_r/e)$

Probe positioning in the plane of the orifice was achieved by a manually activated two-degree of freedom traversing mechanism capable of being incremented in intervals of 0.127mm. This unit is positioned in the streamwise direction by a motor and lead screw unit capable of increments of 0.254mm.

The Flow Field

It has been shown by Sforza, et al. [1] that the constant density three-dimensional turbulent jet may be characterized by three distinct regions in the axis velocity decay. This has been substantiated for heated jets as well by Sfeir [5] who considered slender rectangular jets of slenderness ratio $e = 0.1, 0.05, 0.033$. The temperature field is similarly described by the distinctive features of the axis temperature excess decay. In general, the flow field appears as depicted in Fig. 3, and the various regions may be described as follows:

(a) Potential Core (*PC*) Region: Here the flow is characterized by constant values of axis velocity and temperature excess, equal to, or very close to the exit values.

(b) Characteristic Decay (*CD*) Region: In this second region the maximum velocity and temperature excess decay as a constant power of X, the axial coordinate. The exponent in this power law decay is dependent on orifice geometry; thus the decay in this region is termed "characteristic" of the particular orifice geometry considered.

(c) Axisymmetric Decay (*AD*) Region: This final decay region illustrates the tendency of all jets to approach axisymmetry far from the exit, independent of orifice geometry. Here, both the axis velocity and temperature excess are proportional to x^{-1}.

The major difference between the axis decay of velocity and temperature excess is that the *CD* and *AD* regions begin somewhat sooner for the latter. This is apparently indicative or the more rapid mixing of heat compared to mixing of momentum.

Axis Decays

The axial variation of the temperature excess, $(T_0 - T_a)/(T_{oc} - T_a)$, as determined by thermocouple probes, is shown in Fig. 4 for various types of orifice geometries. It is to be noted that as the orifice approaches an axisymmetric configuration the extent of the *CD* region decreases until it is no longer discernible. Detailed tests have not yet been performed to determine more accurately the value of slenderness ratio at which this occurs, but the results of [2], for constant property three-dimensional jets, indicates that this value is $e \cong 4$. The streamwise distance is nondimensionalized with respect to d', the diameter of a circular jet of cross-sectional area equal to that of the orifice in question. Note that all the data falls in a relatively narrow band far downstream, indicating the developing independence of orifice geometry as distance from the orifice grows, and the fact that the total heat content of the jet is well-scaled by $(T_{oc} - T_a)$ and d'. The use of d' is tantamount to using the more accurate thermal diameter, a characteristic dimension based on the actual integral of the heat flux at the exit, i.e.,

$$d_t = \left[\int_{-\infty}^{+\infty} \int_{-\infty}^{+\infty} \rho U c_p (T - T_a)\, dydz \right]^{1/2} \Bigg/ \left[\frac{\pi}{4} \rho U c_p (T - T_a) \right]_{oc}^{1/2}$$

However, accurate measurement of the exit profiles is often quite difficult in practice and the use of d' is suggested for engineering purposes, providing reasonably uniform exit profiles are expected. Our experience indicates that for such cases d' is usually accurate to within ten percent of the proper value, d_t, mentioned above.

Some more detailed results for the particular case of the slot jet of slenderness ratio $e = 0.1$ are shown in Fig. 5. The mass flux probe was used in obtaining this data for mass-averaged velocity, $\tilde{U} = \overline{\rho U}/\bar{\rho}$ (see Favre [8] and Laufer [9]), and temperature. The velocity data for both the isothermal and heated cases are seen to be virtually identical, save for the typical upstream shift of the data for the heated case, which is most likely due to the slightly lower total momentum of the heated jet for a given chamber pressure. The temperature excess data compares the heated $e = 0.1$ jet with an axisymmetric jet and illustrates

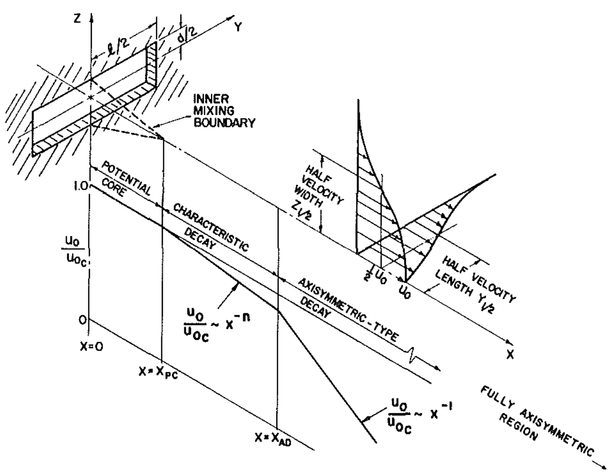

Fig. 3 Schematic diagram of a three-dimensional free jet flow field showing the various flow regions typically encountered

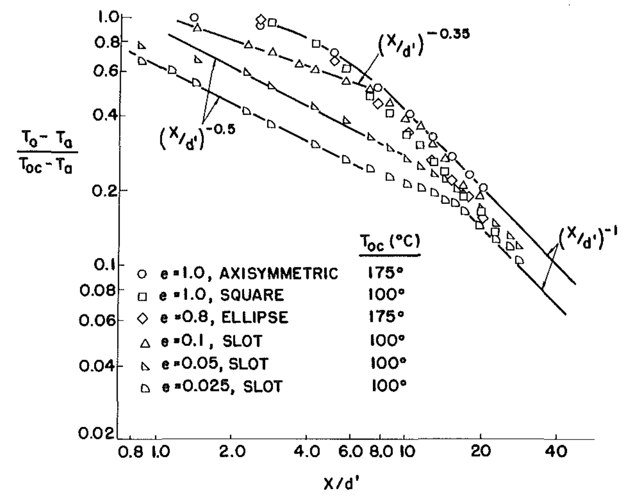

Fig. 4 Variation of normalized centerline temperature excess as a function of nondimensional streamwise distance

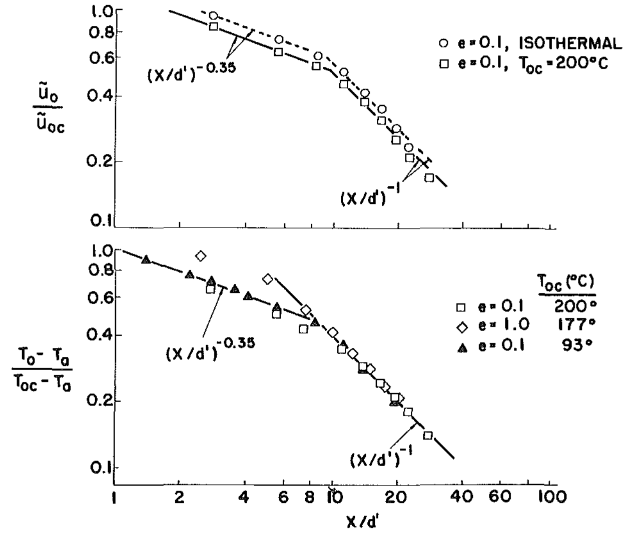

Fig. 5 Centerline variation of flow properties: (a) mass-averaged velocity for heated and isothermal slot jets with $e = 0.1$ (b) temperature excess for $e = 0.1$ slot jet and $e = 1.0$ axisymmetric jet

the difference in axis decay in the near field and the equivalence in the far field. The shaded symbols are results from a thermocouple probe in the flow of a different $e = 0.1$ jet in a different test bay in our facility and are shown in order to supplement the presently available data obtained from the isokinetic sampling probe.

A summary of the data on the exponent in the power law fits to the axis decay of velocity and temperature excess is shown in Fig. 6. Included is past and present data from our laboratories as well as some isothermal results from the work of Becher [10], which was performed in the context of heating and ventilation, and the recent work of Sfeir on heated three-dimensional jets [5]. It is found here that the exponent in the decay law for temperature excess is $m \cong 0.5$ for the *CD* region of slender jets, $e \leq 0.05$, which is in agreement with the results of [5]. On the other hand, for $e = 0.1$, we find that the exponent $m \simeq 0.35$, which is equal to the value for the exponent of the velocity decay law for this case. The results of [9], for the same orifice geometry, indicate a value of 0.5, as for the more slender slots. The reasons for this discrepancy are not clear, although several factors may be considered. The results of [5] for this case show some unusual behavior in the region of interest (see Fig. 1(*a*) of [5]). Furthermore, Fig. 5 of [6] shows results taken from [2] (cold jet) and also from [5] in which little difference is seen between the two experimental results. Probably more important than these indications is the fact that Sfeir [5] makes use of two extreme configurations for his orifices, in the sense that one type is a sharp-edged orifice, i.e., a thin plate with a rectangular slot in it, and the other is a long channel of constant cross-section. These stand in contrast to the short, smooth, converging nozzle-type orifices used in the present study. Indeed it appears that the few discrepancies between the results of this report and those of Sfeir [5] are most likely due to the alteration of the character of the exit flow field. It is likely that this important factor of nozzle configuration and its influence on exit flow quality; i.e., the uniformity of the exit profiles, the existence of a vena contracta effect, presence of turbulence, etc., can now be isolated by employing the sensitivity of three-dimensional jets to it. It seems that an exciting avenue of research on shear flow development may be opened by virtue of some of the small but noticeable effects producible in three-dimensional jets by alterations of the exit flow. Some other effects of this type, aside from the changes in axis decay features, are addressed throughout this study.

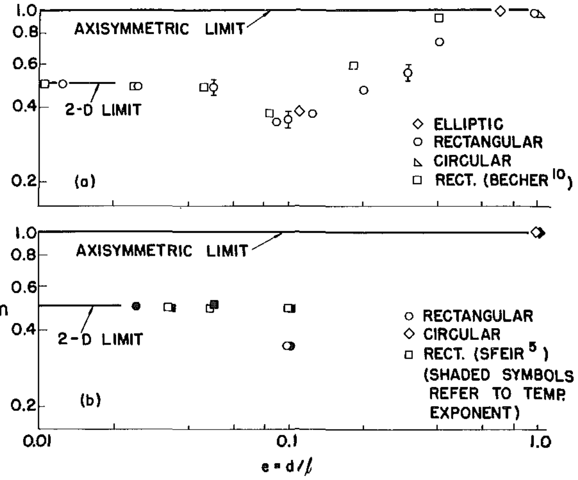

Fig. 6 Variation of exponent in the power laws for axis decay of velocity and temperature excess in the *CD* region as a function of orifice slenderness ratio: (a) isothermal jets (b) heated jets

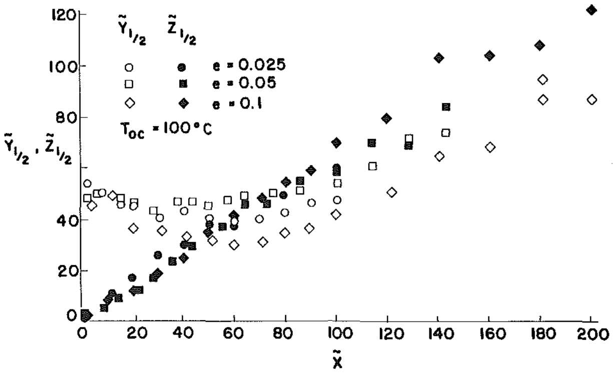

Fig. 7 Composite plot of thermal half-widths of three-dimensional slot jets of various slenderness ratio illustrating correlative effect of coordinate stretching

Half-Width Growth

The behavior of the thermal half-widths in the two principal coordinate directions for different geometries is shown in Fig. 7. It is seen that there exists a reasonable degree of correlation between the various jets when an appropriately stretched coordinate system is used. As suggested in [2], the X, Y, and Z coordinates are normalized with respect to $d(e_r/e)$, where e_r is a reference slenderness ratio chosen here to be 0.1.

Note that the typical characteristic of the velocity field of the constant property three-dimensional free jet, the "cross-over" of the half-widths, is also present in the case of the thermal half-widths. Thus we see that for three-dimensional heated jets, the major axis half-width decreases initially while the minor axis half-width grows; at some intermediate station they cross over, grow similarly, but at different rates and finally tend to approach each other far downstream where the jet tends to axisymmetry. This cross-over point is found to coincide approximately with the streamwise location of the start of axisymmetric type temperature decay, i.e., X_{AD}.

A detailed description of the thermal and velocity half-widths for the $e = 0.1$ heated jet is given by Figs. 8 and 9, respectively. In the former figure, the previously mentioned cross-over phenomena is clearly evident and the approach to axisymmetry is well-illustrated. The $Y_{1/2}$ and $Z_{1/2}$ data neatly bound the axisymmetric heated jet half-width data and tend to approach it far downstream. Experiments on the ellipse of fineness ratio $e = 0.8$ (7) have even shown a second cross-over point in the far field indicating an "oscillation" of the flow field about the axisymmetric counterpart flow field. The half-widths for the velocity field of the $e = 0.1$ jet are shown in Fig. 9. The same qualitative behavior as for the thermal half-widths is found, although the cross-over point occurs sooner for the latter, as is typical in three-dimensional heated jets. Typically, the thermal half-widths are greater than the velocity half-widths. Also shown on the figure are data for an isothermal $e = 0.1$ jet; comparison indicates that the $Z_{1/2}$ growth for the heated jet is augmented, while the $Y_{1/2}$ growth is somewhat suppressed.

Similar results are found in [5], although it again becomes apparent that the nozzle characteristics do cause some alterations in half-width behavior. The sharp-edged nozzle results reported there are very close in behavior to those shown here. However, the long channel-like nozzle tends to suppress the "necking-down" of $Y_{1/2}$. In studies on three-dimensional wall jets, Sforza and Herbst [11] show a similar effect, which was attributed to the altered mass entrainment characteristics imposed on the flow by the presence of a solid boundary tangent to the mainstream direction. It may be possible that the different initial flow profiles caused by the shear flow in the long channel nozzle case of Sfeir [5] may induce reduced entrainment capabilities for such configurations. Indeed, it has been suggested by Trentacoste and Sforza [2] that the near field entrainment is strongly influenced by three-dimensional vortex structures, the generation of which is dependent upon exit conditions such as shear stress distribution and turbulence characteristics.

Profile Characteristics

Profiles of flow variables in the two principal planes have been obtained and are found to display characteristics similar to those described for constant property three-dimensional jets in [1] and [2]. That is, in the *AD* region the normalized temperature profiles are found to be equivalent when plotted against either $Y/Y_{1/2}$ or $Z/Z_{1/2}$,

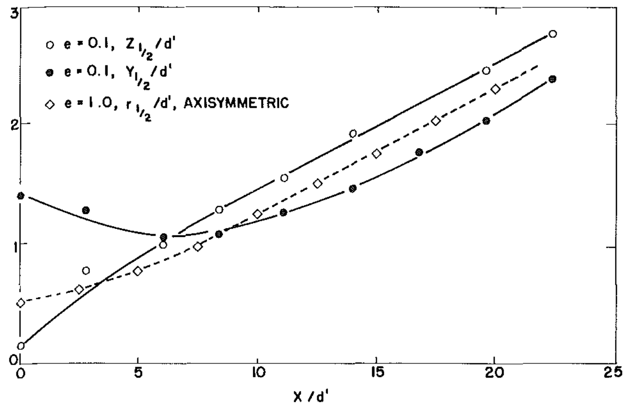

Fig. 8 Thermal half-widths in the planes Y = 0 and Z = 0 for the $e = 0.1$ slot jet with $T_{oc} = 200°C$. Also shown is the half-radius for an axisymmetric jet with $T_{oc} = 175°C$

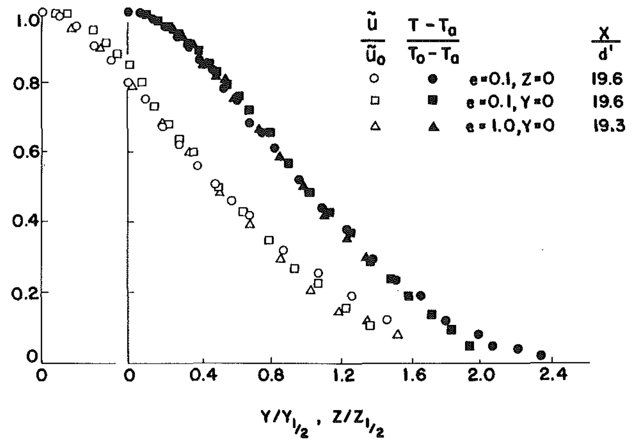

Fig. 10 Normalized profiles of mass-averaged velocity and temperature excess for the heated ($T_{oc} = 200°C$) slot jet of $e = 0.1$ in the *AD* region. Also shown is the case of a heated ($T_{oc} = 175°C$) axisymmetric jet

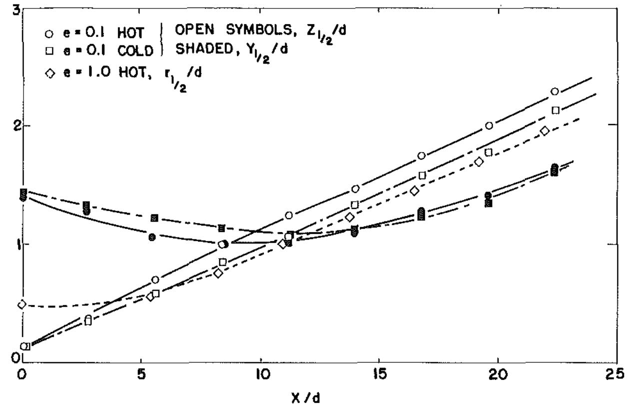

Fig. 9 Mass averaged velocity half-widths in the planes $Y = 0$ and $Z = 0$ for the $e = 0.1$ slot jet under heated ($T_{oc} = 200°C$) and isothermal conditions. Also shown is the case of an axisymmetric heated jet with $T_{oc} = 175°C$

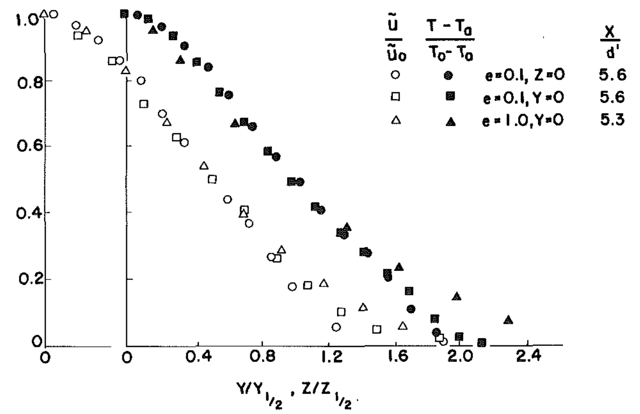

Fig. 11 Normalized profiles of mass-averaged velocity and temperature excess for the heated ($T_{oc} = 200°C$) slot jet of $e = 0.1$ in the *CD* region. Also shown is the case of a heated ($T_{oc} = 175°C$) axisymmetric jet in a similar region

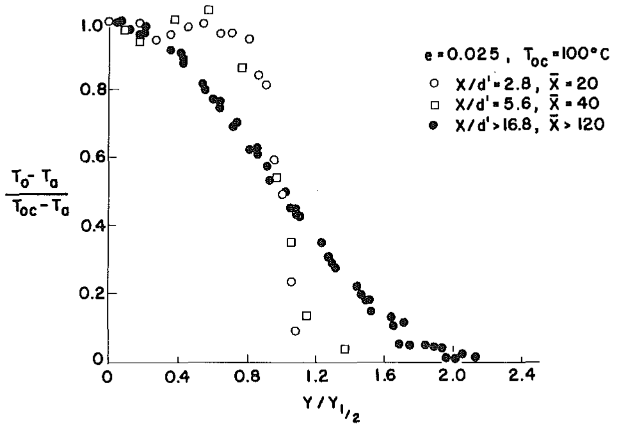

Fig. 12 Normalized profiles of temperature excess at various stream-wise stations for a heated ($T_{oc} = 100°C$) jet of $e = 0.025$ showing the approach to similarity and the presence of temperature irregularities in the *CD* region

for all jets tested, and the typical axisymmetric result therefore can serve to describe all three-dimensional jets in the *AD* region, as shown for the $e = 0.1$ jet in Fig. 10. On the other hand, in the *CD* region, where orifice geometry effects are important it is found that the degree of similarity achieved is not as pronounced (Fig. 11). The same effects are observed for the velocity field of the $e = 0.10$ jet as shown in Figs. 10 and 11. Temperature "irregularities" typical of the *CD* region of slender three-dimensional jets, in planes Z = constant, such as those described in [1] and [2] for the velocity field of constant property three-dimensional jets have also been noted (Fig. 12). We have always maintained that these effects were due, in large part, to large scale vortex structures surrounding the jet in the near field, and were therefore essentially inviscid interactions with the turbulent flow field. The effects of such structures were described in [2], while Viets and Sforza [12] carried out theoretical and experimental studies on the motion of such bilaterally symmetric vortex rings. Holdeman and Foss [13] have proposed a vortex stretching model based on some of these ideas, and more recent work has been performed by Rockwell [14].

Sfeir [5] also shows temperature and velocity irregularities with the characteristic "saddle-back" shape described in [2]. His results are for the $e = 0.10$ jet, for which case our results show very minor features of this type. However, he also illustrates the change in the magnitude of the irregularities for the two different nozzle geometries, the sharp-edged nozzles having more pronounced overshoots than the long channel-like nozzle. It may be that the sharp-edged nozzle issues forth with a vena contracta of some type due to the sharp edges and this produces a jet configuration, just beyond the exit, which has a much more slender cross-section than the orifice. Such a condition would be tantamount to using a narrower slot, i.e., a smaller effective e value. This would be consistent with the observed results of more pronounced overshoots for the sharp-edged nozzle case.

Cross-Plane Contours

The heated rectangular slot jet of slenderness ratio $e = 0.1$ was studied in detail with the mass flux probe at one station in the *CD*

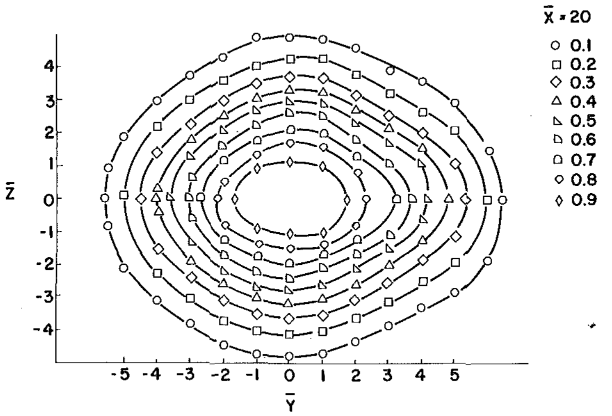

Fig. 13 Normalized contours of constant mass flux $(\overline{\rho U}/\overline{\rho U_0})$ for the heated (T_{oc} = 200°C) slot jet of e = 0.1 in the plane x/d = 20, i.e., in the *CD* region

region ($\bar{x}$ = 20) and one station in the *AD* region ($\bar{x}$ = 60). Data for mass, momentum, and enthalpy flux sufficient for generating contour plots of these variables in the planes $\bar{x}$ = 20 and 60 were obtained. For the purposes of the present report such contours are presented only for mass flux; the other properties displayed similar behavior.

Lines of constant mass flux, faired through the available data points, at the station $\bar{x} \approx 20$ are shown in Fig. 13. Note that the contours are somewhat like rounded lozenges with their major axes aligned with the major axis of the e = 0.1 orifices, i.e., $\bar{z}$ = 0. Further downstream, $\bar{x}$ = 60, in the *AD* region, the mass flux contours are found to be roughly elliptical, as shown in Fig. 14. Here, however, the major axes of the ellipses are aligned with the minor axis of the orifice, i.e., $\bar{y}$ = 0. These plots provide another illustration of the cross-over phenomenon described in the discussion on half-width growth.

It is evident that the three-dimensionality of the flow is quite strong, and it may bear repeating that the momentum flux and enthalpy flux follow the same trends. Indeed, the ellipticity of the contours in the *AD* region has also been shown for the velocity field of isothermal jets by Trentacoste and Sforza [2].

Conclusions

Experiments on heated three-dimensional turbulent free jets indicate that these flows may be characterized by three distinct regions in terms of the axis property decays: a potential core region where axis values are close to the exit values, a characteristic decay region wherein the axis decays are dependent upon orifice geometry, and an axisymmetric decay region where the axis decay is axisymmetric in nature and thus independent of orifice geometry. These regions are not exactly the same for temperature as for velocity, the former being shifted somewhat upstream of the latter.

Half-width data indicate that heated three-dimensional jets change (cross-sectional) shape as they proceed downstream. The major axis half-width decreases initially while the minor axis half-width grows; at some intermediate station they cross over, grow similarly, but at different rates and finally tend to approach each other far downstream where the jet tends to axisymmetry.

Cross-plane contours illustrate the altering shape of three-dimensional jets as described above. Measurements shown here, and those of other investigations, e.g., Flora and Goldschmidt [15], indicate that the nature of the orifice exit flow conditions play a large role in the development of the near field jet characteristics. It is suggested that three-dimensional jets would serve as excellent test cases for investigating the effects of initial conditions in turbulent mixing, because their downstream development seems particularly sensitive to them.

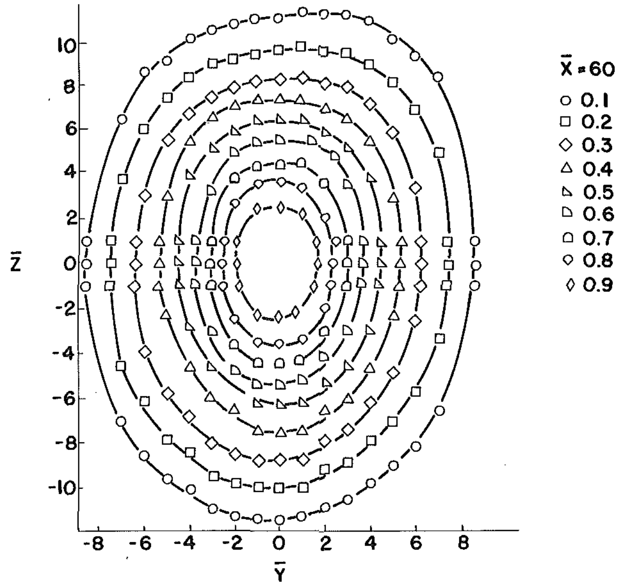

Fig. 14 Normalized contours of constant mass flux $(\overline{\rho U}/\overline{\rho U_0})$ for the heated (T_{oc} = 200°C) slot jet of e = 0.1 in the plane x/d = 60, i.e., the *AD* region

Acknowledgment

This research was supported in part by the Air Force Office of Scientific Research under Contract No. AF 49(638)-1623, Project No. 9781-01; and by the Advanced Research Projects Agency of the Department of Defense, monitored by the U. S. Army Research Office-Durham under Contract No. DAHC04-69-C-0077, ARPA Order No. 1442.

References

1 Sforza, P. M., Trentacoste, N. P., and Steiger, M. H.: "Studies on Three-Dimensional Viscous Jets," *AIAA Jl.*, Vol. No. 4, 5, May, 1966, pp. 800–806.

2 Trentacoste, N. P. and Sforza, P. M., "Further Experimental Results for Three-dimensional Free Jets," *AIAA Jl.*, Vol. No. 5, May, 1967, pp. 885–891.

3 Sforza, P. M. and Mons, R. F., "Mass, Momentum, and Energy Transport in Turbulent Free Jets," *Int. J. Heat Mass Transfer*, Vol. 21, 1978, pp. 371–384.

4 Sforza, P. M., "Three-Dimensional Free Jets and Wall Jets—Applications to Heating and Ventilation," *Proc. of the 1977 International Centre for Heat and Mass Transfer in Buildings*, Dubrovnik, Yugoslavia, Sept. 1977, Hemisphere Publishing Co., Washington, D. C., 1978.

5 Sfeir, A. A., "The Velocity and Temperature Fields of Rectangular Jets," *International Jl. of Heat and Mass Trans.*, Vol. 19, 1976, pp. 1289–97.

6 McGuirk, J. J. and Rodi, W., "The Calculation of Three-Dimensional Turbulent Free Jets," International Symposium on Turbulent Shear Flows, Pennsylvania State University, April 18–20, 1977.

7 Trentacoste, N. P. and Sforza, P. M., "Studies in Homogeneous and Nonhomogeneous Free Turbulent Jets", AIAA Paper No. 70-130, AIAA 8th Aerospace Sciences Meeting, New York, Jan. 1970.

8 Favre, A.: "Statistical Equations of Turbulent Gases," *Problems of Hydromechanics and Continuum Mechanics, SIAM*, Philadelphia, PA, 1969, pp. 231–266.

9 Laufer, J., "Turbulent Shear Flows of Variable Density," *AIAA Jl.*, Vol. No. 7, 4, April, 1969, pp. 606–712.

10. Becher, P., "Calculation of Jets and Inlets in Ventilation," *I. Kommission Hos. Jul. Gjellerups Forlag*, Copenhagen, 1949.

11 Sforza, P. M. and Herbst, G., "A Study of Three-Dimensional Incompressible Turbulent Wall Jets," *AIAA Journal*, Vol. 8, No. 2, Feb. 1970, pp. 276–383.

12 Viets, H. and Sforza, P. M., "Dynamics of Bilaterally Symmetric Vortex Rings", *Physics of Fluids*, Vol. 15, No. 2, 1972, pp. 230–240.

13 Holdeman, J. D. and Foss, J. F., "The Initiation, Development and Decay of the Secondary Flow in a Bounded Jet," ASME *Journal of Fluids Engineering*, Vol. 97 Sept. 1975, pp. 342–352.

14 Rockwell, D. O., "Vortex Stretching Due to Shear Layer Instability," ASME *Jl. of Fluids Engineering*, Vol. 99, March 1977, pp. 240–244.

15 Flora, J. J. and Goldschmidt, V. W., "Virtual Origins of a Free Plane Turbulent Jet", *AIAA Jl.*, Vol. 7, No. 12, December, 1969, pp. 2344–2346.

D. E. Kooker
Research Physical Scientist.

C. W. Nelson
Research Physical Scientist.

U. S. Army Ballistic Research Laboratory
Aberdeen Proving Ground, MD 21005

Numerical Solution of Solid Propellant Transient Combustion

Three thermal theories of solid propellant combustion, [1, 2, 3], all based on the quasi-steady flame assumption, were subjected to a rapidly rising external pressure field simulating a gun combustion chamber. Transient burning rates were computed by four different numerical solution methods; the best results were obtained with an invariant imbedding scheme. The numerical predictions show that (1) burning rate "runaway" is a numerical difficulty and is not a solution to the models, (2) the final state of an intrinsically unstable model at constant pressure is composed of repeating finite-amplitude spikes, and (3) the dynamic burning rate from a linearly-stable model can be many times greater than $r = ap^n$.

Introduction

Current theories of gun interior ballistics rely on, and are sensitive to, the steady-state burning rate "law," $r = ap^n$, to model combustion of solid propellant grains. This power law often provides a good correlation of constant-pressure burning rates obtained in strand burner experiments. However, when the combustion chamber pressurization rate can exceed 100 MPa/ms, the use of instantaneous pressures in the same relationship implies a burning-rate adjustment which may not occur. The possibility of dynamic burning rate excursions warrants further investigation.

The rate of solid propellant decomposition depends heavily on heat released in the flame region and at the gas/solid interface. The instantaneous energy flux to the surface of the reactive solid is controlled to a large extent by competition in the gas phase between convection, heat conduction, species diffusion, and chemical reactions. A comprehensive time-dependent model incorporating this level of detail has yet to be accomplished. On the other hand, very few experimental measurements are available to set values of constants, delineate controlling chemical reaction steps, and validate predictions. Measurements of temperature profiles are impeded by the steep gradients near the regressing surface and by uncertain resolution of the surface location with time. Instantaneous regression rates have not been measured during rapid pressure changes because of formidable difficulties.

An alternative is to examine the thermal-wave combustion theories originally developed for the study of combustion instability and/or extinguishment in solid propellant rocket motors. It is our purpose here to investigate the behavior of three such models, Krier, et al., [1], Levine and Culick [2], and Kooker and Zinn [3], in a rapidly increasing pressure field. All three models are based on the quasi-steady flame assumption, i.e., the gas-phase flame region should respond and adjust to pressure changes at least an order of magnitude faster than the solid-phase thermal wave. Hence, regression rate is controlled by the response of the thermal wave in the unburned solid.

The quasi-steady flame assumption precludes a description of propellant ignition. The initial condition, instead, is the thermal wave associated with a steady-state burning rate at the initial value of pressure. This condition relates to the gun problem in the following way: In large artillery, a time delay (up to 200 ms) occurs between the first operation of the primer and the onset of rapid pressurization. Depending on chamber size, the pressure can remain below 1000 psia while ignition and flamespreading are completed. It is reasonable to assume that, before the onset of the rapid pressure transient, a given propellant grain has ignited and attained its steady-state burning rate corresponding to the low value of pressure. Note also that, in the examples that follow, the time-dependent pressure field and the resulting propellant burning rate are uncoupled; a prescribed time-dependent pressure is simply imposed at the edge of the flame zone. This was done to create a more controlled numerical experiment though it is physically unrealistic. Preliminary calculations of closed-chamber combustion where propellant burning rate dictates the pressure transient can be found in [4].

Analysis

Derivation of Combustion Models. The derivation of each of the three models is based on a common set of simplifying assumptions. It is assumed that (1) the solid propellant combustion process can be described in a single spatial dimension, (2) the unburned propellant is homogeneous, incompressible, and inert, (3) the solid is converted into gas by a global pyrolysis reaction which occurs at an infinitesimally thin interface, and (4) the gas-phase flame is quasi-steady and remains anchored to the interface. As a direct result of these assumptions, all three models, when written for the coordinate system shown in Fig. 1, reduce to the following initial/boundary value problem describing the thermal-wave in the unburned solid propellant:

$$\Theta_\tau + R\Theta_\eta - \Theta_{\eta\eta} = 0 \qquad (-\infty < \eta \leqslant 0) \tag{1}$$

initial condition $\Theta(\eta, 0) =$ (1a)

$$\text{boundary conditions}\begin{cases}\Theta(-\infty, \tau) = 0 & (1b)\\ \Theta_\eta(0, \tau) = & (1c)\end{cases}$$

$$\text{with } R = R(\Theta_s) \tag{1d}$$

Contributed by the Heat Transfer Division of THE AMERICAN SOCIETY OF MECHANICAL ENGINEERS and presented at the AIChE Heat Transfer Conference, Salt Lake City, Utah, August 15–17, 1977. Revised manuscript received by the Heat Transfer Division February 6, 1978. Paper No. 77-HT-17.

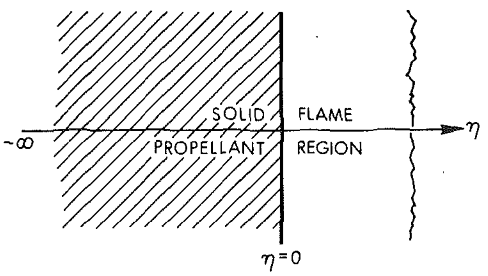

Fig. 1 Combustion model configuration

where the particular form of G and R depends on the model in question. The initial condition is taken to be the thermal-wave corresponding to an assumed steady-state burning rate. Equation (1*b*) of the boundary conditions enforces the cold-solid temperature at infinity, while equation (1*c*) is the result of an energy balance at the interface and includes the contribution of the gas-phase flame. The point of departure of the three models is the flame analysis and the postulated global pyrolysis reaction (equation (1*d*)). Details of the derivations can be found in [4].

The gradient boundary condition in the Krier, et al., model is given by

$$\Theta_\eta(0,\tau) = RH + [P^{2n}\,(P^{n/m} - H)]/R \tag{2}$$

where

$$R = \Theta_s{}^m \tag{3}$$

The power law dependence of R on surface temperature is used as an approximation to an Arrhenius reaction rate. The appearance of the pressure exponent n in equation (2) is the result of assuming that the steady-state burning rate of the propellant is $\bar{r} = a\bar{p}^n$. Thus, if the pressure is held constant, the time-dependent model will predict a value of burning rate identical to this steady state law when all transient portions of the solution have died away. Of course, for a given value of pressure in an arbitrary time-dependent situation, the heat feedback from the gas-phase flame will not necessarily equal its steady-state value at that pressure.

For the Levine/Culick model, the gradient boundary condition is

$$\Theta_\eta(0,\tau) = R\left[H + (\Theta_s - 1)\left(1 - \frac{c_p}{c_s}\right)\right] + P^{2n}\left\{(1 - H) + \frac{c_p}{c_s}\frac{E}{A}\left[\frac{1}{1 + \frac{n_s - n}{E}\ln P} - 1\right]\right\}\Bigg/ R \tag{4}$$

where

$$R = P^{n_s} \exp\left[\frac{A(\Theta_s - 1)}{1 + \frac{A}{E}(\Theta_s - 1)}\right] \tag{5}$$

Although somewhat disguised, equation (5) is an unsteady Arrhenius expression. *For all computations shown in the present paper*, $n_s \equiv 0$. Similar to [1], the Levine/Culick model will also predict a value of burning rate identical to $a\bar{p}^n$ when the pressure is held constant and the transient portion of the solution has vanished.

In the Kooker/Zinn model, the flame region is assumed to be controlled by the simple one-step global reaction,

$$\text{Oxidizer} + \text{Fuel} \rightarrow \text{Products}$$

which leads to the gradient boundary condition,

$$\Theta_\eta(0,\tau) = R\left[H + (\Theta_s - 1)\left(1 - \frac{c_p}{c_s}\right)\right] + Z\frac{P^{\hat{\beta}}}{R} \tag{6}$$

with R given by equation (5) when $n_s = 0$. The unknown constant, Z, is determined by the interface energy balance at the initial condition, i.e.,

$$Z = 1 - H \tag{7}$$

Although this model does not incorporate a power law burning rate expression, the differences at steady state are small [4].

Numerical Solution Methods. Predictions of the time-dependent burning rate for each combustion model require the solution to equation (1) using the appropriate interface boundary condition (equation (2) for Krier, et al.; equation (4) for Levine and Culick; equation (6) for Kooker and Zinn). An exact analytical solution is not possible since the primary equation and the boundary conditions are coupled and nonlinear. Because of the potential difficulty introduced by the nonlinearity, the present study examined four different numerical solution techniques, each of which has been used in previous investigations to solve combustion problems of this type. The objective is to see if the desired solution is independent of the method used to obtain it.

Each numerical technique is expressed in the following notation. The superscripts n and $n + 1$ refer to the current time level (where the solution is known) and the new time level, respectively. The subscripts $j - 1$, j, $j + 1$ refer to an arbitrary interior mesh point, j, and its two adjacent neighbors. For reasons to be discussed, the mesh point distribution is nonuniform and hence $\Delta\eta_j \equiv \eta_j - \eta_{j-1}$ and $\Delta\eta_{j+1} \equiv \eta_{j+1} - \eta_j$ are not necessarily equal. For convenience, define

Nomenclature

a = constant in burning rate law, $r = ap^n$
$A = E(1 - T_\infty/T_{so})$, $[n - d]$
c_s, c_p = specific heat of solid and gas, respectively
E; $E_s = E_s/\mathcal{R}_o T_{so}$, $[n - d]$; activation energy of surface reaction
G = defined in equation (1c), $[n - d]$
$H = \bar{Q}_s/c_s\,(T_{so} - T_\infty)$, $[n - d]$
k_s, k_g = thermal conductivity of solid and gas, respectively
m = exponent in equation (3)
$\dot{m}$ = mass flow rate = $\rho_s r$
n = pressure exponent in burning rate law, $r = ap^n$
n_s = pressure exponent in equation (5)
p; P = pressure; p/p_o $[n - d]$
Q_s, Q_f = heat release per unit mass for surface reaction and flame reaction, respectively
r; R = surface regression rate; r/r_o, $[n - d]$
R_s = R computed from a steady state expression, usually $R_s = P^n$, $[n - d]$
t = time
T; T_{so}; T_∞ = temperature; initial surface temperature; cold-solid temperature
x = distance coordinate, normal to propellant surface
$Z = \dfrac{c_p}{c_s}\left(\dfrac{T_{so}}{T_{so} - T_\infty}\right)\Lambda_o{}^2$, $[n - d]$
$\alpha = k_s/\rho_s c_s$, thermal diffusivity
$\hat{\beta}$ = reaction order (see equation (6))
β = defined in equation (18)
$\eta = x(r_o/\alpha)$, $[n - d]$
Θ; $\Theta_s = \dfrac{T - T_\infty}{T_{so} - T_\infty}$, $[n - d]$; nondimensional surface temperature
$D\Theta_j$ = defined in equation (8)
$DD\Theta_j$ = defined in equation (9)
$\Lambda_o{}^2 = k_g Q_f \omega_o/(\dot{m}_o{}^2 c_p{}^2 T_{so})$, $[n - d]$
ρ_s, ρ_g = density of solid and gas, respectively
$\tau = t(r_o{}^2/\alpha)$, $[n - d]$
ω = mass production rate

Superscript

$^{-}$= at steady state

Subscript

o = initial conditions
j = grid point
η = partial derivative with respect to η

$$D\Theta_j \equiv \frac{\Delta\eta_j{}^2\Theta_{j+1} + (\Delta\eta_{j+1}{}^2 - \Delta\eta_j{}^2)\,\Theta_j - \Delta\eta_{j+1}{}^2\,\Theta_{j-1}}{\Delta\eta_j\Delta\eta_{j+1}\,(\Delta\eta_j + \Delta\eta_{j+1})} \qquad (8)$$

$$\simeq \Theta_\eta \text{ at point } j,$$

$$DD\Theta_j \equiv 2\frac{\Delta\eta_{j+1}(\Theta_{j-1} - \Theta_j) + \Delta\eta_j(\Theta_{j+1} - \Theta_j)}{\Delta\eta_j\Delta\eta_{j+1}\,(\Delta\eta_j + \Delta\eta_{j+1})} \qquad (9)$$

$$\simeq \Theta_{\eta\eta} \text{ at point } j$$

Then the four numerical techniques when applied to equation (1) can be written as,

(A) Explicit [$O(\Delta\tau, \Delta\eta_{\max}{}^2)$, stable for $\Delta\tau < ½\,\Delta\eta_{\min}{}^2$]

$$\frac{\Theta_j{}^{n+1} - \Theta_j{}^n}{\Delta\tau} + R^n(D\Theta_j{}^n) - DD\Theta_j{}^n = 0 \qquad (10)$$

(B) Full Implicit [$O(\Delta\tau, \Delta\eta_{\max}{}^2)$, stable for any $\Delta\tau$]

$$\frac{\Theta_j{}^{n+1} - \Theta_j{}^n}{\Delta\tau} + R^{n+1}\,(D\Theta_j{}^{n+1}) - DD\Theta_j{}^{n+1} = 0 \qquad (11)$$

(C) Crank-Nicolson Implicit [$O(\Delta\tau^2, \Delta\eta^2{}_{\max})$, stable for any $\Delta\tau$]

$$\frac{\Theta_j{}^{n+1} - \Theta_j{}^n}{\Delta\tau} + \frac{1}{2}\{R^{n+1}\,(D\Theta_j{}^{n+1}) - DD\Theta_j{}^{n+1} + R^n(D\Theta_j{}^n) - DD\Theta_j{}^n\} = 0 \qquad (12)$$

(D) Invariant Imbedding Implicit [$O(\Delta\tau, \Delta\eta^2{}_{\max})$, stable for any $\Delta\tau$] See derivation in [4].

The coupling between the unknowns at $j - 1$, j, and $j + 1$ in Methods (B) and (C) leads to a tridiagonal matrix which is inverted with the standard Thomas Algorithm.

All the methods generate a finite difference equation (FDE) which is only an approximation to the true partial differential equation (PDE). The relationship between the two is based on Taylor series expansions and, using Method (B) as an example, can be written as,

$$\text{FDE} = \text{PDE} - \frac{\Delta\tau}{2}\Theta_{\tau\tau} + [R\Delta\eta_j\Delta\eta_{j+1} + 2(\Delta\eta_j - \Delta\eta_{j+1})](\Theta_{\eta\eta\eta}/6)$$
$$+ [R\Delta\eta_j\Delta\eta_{j+1}\,(\Delta\eta_{j+1} - \Delta\eta_j) - 2(\Delta\eta_j{}^2 - \Delta\eta_j\Delta\eta_{j+1} + \Delta\eta_{j+1}{}^2)]\,(\Theta_{\eta\eta\eta\eta}/24) \qquad (13)$$

For equally-spaced mesh points, this reduces to the more familiar form,

$$\text{FDE} = \text{PDE} - \frac{\Delta\tau}{2}\Theta_{\tau\tau} + (2R\Theta_{\eta\eta\eta} - \Theta_{\eta\eta\eta\eta})\,(\Delta\eta^2/12) \qquad (14)$$

Based on equation (14), the formal order of accuracy is $O(\Delta\tau)$ and $O(\Delta\eta^2)$. However, unless the derivative terms are uniformly small, the formal argument can be misleading. Since the present combustion problem involves a thermal profile which may have very steep gradients near the interface, the spatial mesh must be closely spaced in this region (i.e., $\Delta\eta \ll 1$); otherwise the truncation error will swamp the desired solution. Although no single mesh system will be optimal for all problems, Method (D) was used to determine a 231 grid point system [21 points, $-0.01 \leqslant \eta \leqslant 0$; 30 points, $-0.10 \leqslant \eta < -0.01$; 50 points, $-2.00 \leqslant \eta < -0.10$; 130 points, $-15.00 \leqslant \eta < -2.00$] such that the numerical solution for an extreme combustion problem was independent of further rearrangement and additional points.

The problem of nonlinearity must also be treated with care. Each numerical method effectively linearizes equation (1) in some manner. Furthermore the interface boundary condition, which must be applied at the new time level $n + 1$, is a nonlinear function of the surface temperature at $n + 1$. This requires an iteration procedure where the integration of equation (1) and the application of the boundary condition are updated cyclically. Convergence is assumed when the difference between the R used in equation (1) and the R which follows from the boundary condition is less than a specified tolerance (in this study, 10^{-8} using double precision computation). A crucial point concerning the size of the time step $\Delta\tau$ enters here. Although Methods (B–D) are theoretically stable for an unrestricted time step, the iteration procedure is *not*. For those combustion problems where the surface temperature is changing rapidly with time, the time step must be appropriately restricted to keep the numerical solution from diverging. No mathematical proof is offered to support this conclusion. However, in the present investigation, the time step was continuously monitored and appropriately reduced if the number of cycles required for convergence of the iteration exceeded five.

Model Equation. The limiting accuracy of the numerical solution computed by Methods (A–D) can be estimated with an example denoted as the model equation. An exact analytical solution is available ([5], p. 389) since both the equation and the boundary conditions are linear. Using the present notation, this system can be written as

$$\Theta_\tau + R\Theta_\eta - \Theta_{\eta\eta} = 0 \;[\tau \geq \tau_o, -\infty < \eta \leq 0] \qquad (15)$$

$$\text{initial condition} \qquad \Theta(\eta, \tau_o) = \Theta_o\,(\eta) \qquad (15a)$$

$$\text{boundary conditions} \begin{cases} \Theta(-\infty, \tau) = 0 & (15b) \\ \Theta_\eta(0,\tau) = H\left[\Theta(0, \tau) + \dfrac{T_\infty}{T_{so} - T_\infty}\right] & (15c) \end{cases}$$

where R and H are constants.

For an example problem with an unrealistically high surface heating rate, the predicted numerical solution, based on the same grid mesh system used in the combustion problems, and the exact solution are indistinguishable on the scale of a usual plot. The maximum error occurs at the surface $\eta = 0$, and was within 1 percent for Method (D). Furthermore, using Method (D), the magnitude of the error at a given time level decreased as the size of the step $\Delta\tau$ decreased. Method (A) may be equally accurate for this linear problem but the diffusion stability restriction on the time step is so small that the method is not competitive economically. For this reason, it was eliminated. For Methods (B) and (C), the maximum surface temperature error was within 2 percent, but the expected convergence as the time step was decreased did not always materialize. This can be traced to errors in the tridiagonal matrix inversion used by both Methods (B) and (C). Using a uniform mesh system as an example, the diagonal element of the matrix is given by

$$1 + \frac{2\Delta\tau}{\Delta\eta^2} \qquad (16)$$

while the off-diagonal elements are

$$\frac{R\Delta\tau}{2\Delta\eta} \pm \frac{\Delta\tau}{\Delta\eta^2} \qquad (17)$$

For time steps at or below the diffusion stability limit and with $R \ll 2/\Delta\eta$, diagonal dominance is assured. However, when using large time steps *and* nonlinear spacing (variable $\Delta\eta$), the absolute value of the diagonal term can change by orders of magnitude from one corner of the matrix to the other. This can create the same type of errors in the matrix inversion process as does loss of diagonal dominance. These errors can easily overpower the temporal truncation error in the finite difference equation, leading to the result that a decrease in $\Delta\tau$ does not produce the expected increase in accuracy. For this example, however, the loss in accuracy is minimal.

On the basis of the linear model equation, it is concluded that Methods (B–D) yield nearly equal results with acceptable accuracy. The results from the linear model equation are not intended to be conclusive proof of accuracy for the combustion models to follow, but rather an estimate of the expected lower error bound. It should be stressed that the influence of the nonlinearity in the three combustion models has *not* been assessed in this exercise.

Results

Burning Rate Response to a Sudden Compression. The purpose of this investigation is to compute the burning rate response to a rapidly increasing pressure field which simulates the gun combustion chamber environment. A similar problem is posed in [1] for the behavior of a rocket engine during a sudden compression. Several numerical computations in [1] are based on the pressure profile described by

$$P(\tau) = 1.0 + \Delta P\,[1.0 - \exp(-\beta\tau)] \tag{18}$$

With $\Delta P = 2.5$ and $\beta = 1.0$, this expression approximates an experimental test run reported in [1]. Equation (18) is not a good representation of a typical gun pressure time-history. However, it is relevant to the gun problem if viewed as a large amplitude pressure wave suddenly passing over a propellant grain which is burning at steady state. Such a situation could conceivably develop during a malfunction. For this reason, any results which follow from equation (18) are of interest to the present analysis. A set of computations showing the sensitivity of the Krier, et al. model to changes in the value of surface heat release, H, is reproduced here in Fig. 2 (see Fig. 9 in [1]). The unbounded burning rate predicted for $H = 0.80$ is one of several calculations used as evidence of burning rate runaway, also called "intrinsic instability of burning rate." A similar runaway condition was reported in [2] as the result of a sinusoidal pressure oscillation.

Because of the adverse influence that burning rate runaway would have in a gun system, the decision was made to examine each model in detail to determine the cause of the unbounded result and when it might occur. A first step was to use Method (D) to recompute the Krier, et al. results for $H = 0.80$ shown in Fig. 2. The recomputed results are shown in Fig. 3; no runaway condition is indicated and the burning rate returns to the same value as $H = 0.75$ at a nondimensional time of approximately 1.2. Further computations of this case, however, showed that Method (D) will also predict a divergent solution if the time step restriction imposed by the iteration procedure is removed or a sufficient number of mesh points near the propellant interface are eliminated.

There is considerable interest in the relationship between a possible runaway condition and the intrinsic instability limit of the mathematical model. A linearized analysis based on small perturbation theory yields this limit as the neutral stability curve separating regions of stable and unstable response. Since a small disturbance in the linearly unstable regime eventually provokes an unbounded response, the theory implies that a solid propellant combustion model operating in this regime will not admit[1] a uniform steady-state burning rate even at constant pressure.

Hence, some additional computations were performed to determine the response to a uniform pressure field when the combustion model is at or beyond the intrinsic instability limit. Using the Krier, et al. model and the propellant parameters of Fig. 3, this limit is achieved at a value of $H = 0.8333$ (see [1]). The burning rate response (Method D) to an imposed pressure of $P(\tau) \equiv 1$, when $H = 0.8333$, is shown in Fig. 4. This damped oscillatory response is stimulated only by the numerical discretization of the initial thermal wave; the pressure at the edge of the flame zone was identically unity. The period of the natural oscillation is approximately 1.45. Repeating this computation with $H = 0.88$, which forces the model well into the unstable regime, produces the pattern of large amplitude "spikes" shown in Fig. 5. The maximum amplitude of the repeating spike is approximately 77, with a period of 1.36. Further computations have shown that this maximum amplitude increases with increasing H, but the solution remains bounded and does not run away to infinity.

A related question concerns the possibility that a large amplitude disturbance may evoke a runaway response from a linearly stable model. Such a problem was studied in [6], where a series of sinusoidal pressure oscillations with increasing amplitude were imposed on the Kooker and Zinn model (early version). The results of Fig. 14 in [6] demonstrate that a sufficient amplitude disturbance will produce large-amplitude repeating spikes from a linearly stable model, but the burning rate response remains bounded.

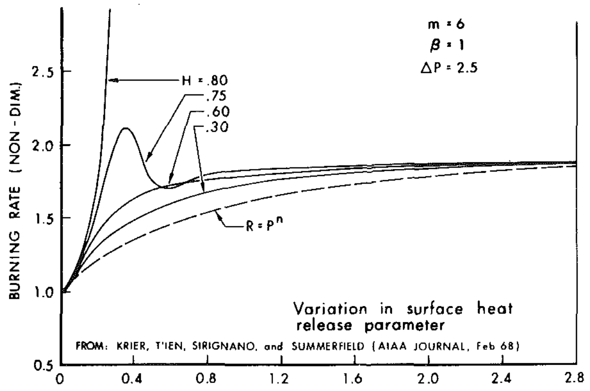

FROM: KRIER, T'IEN, SIRIGNANO, and SUMMERFIELD (AIAA JOURNAL, Feb 68)

Fig. 2 Burning rate response of Krier, et al.'s model (Original Results)

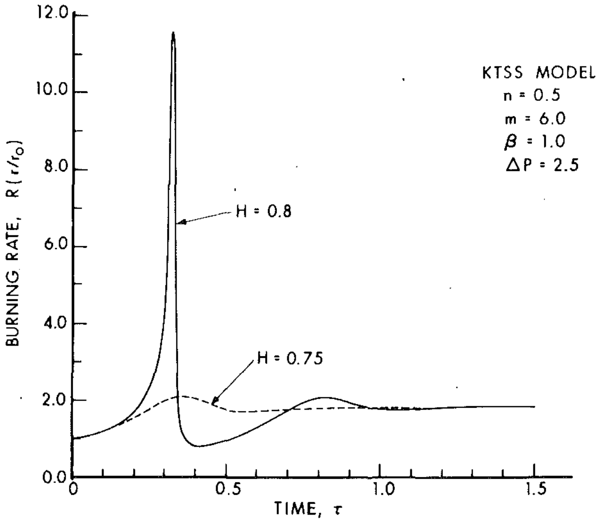

Fig. 3 Burning rate response of Krier, et al.'s model (Recomputed Results)

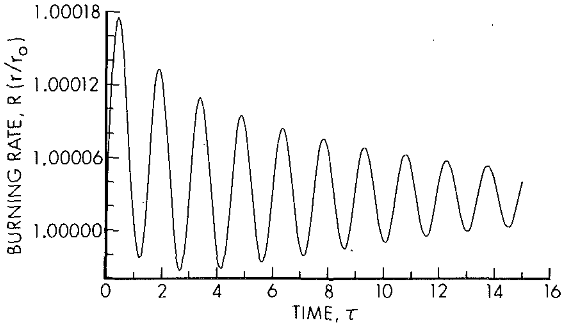

Fig. 4 Response of Krier, et al.'s model to $P(\tau) \equiv 1$ at intrinsic instability limit ($H = 0.8333$, $n = 0.5$, $m = 6.0$)

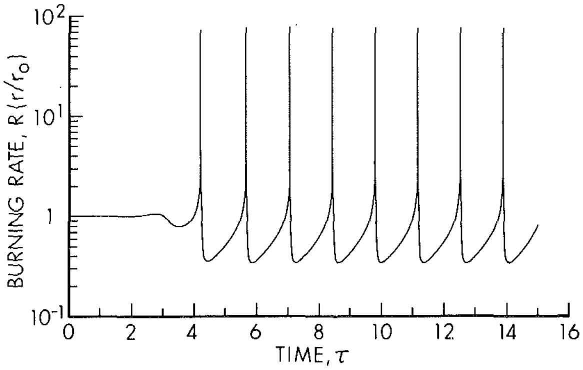

Fig. 5 Response of Krier, et al.'s model to $P(\tau) \equiv 1$ when intrinsically unstable ($H = 0.88$, $n = 0.5$, $m = 6.0$)

---

[1] The authors are indebted to the referee for insight on this point.

A strong resemblance to the repeating spike burning rate phenomenon has been reported in the Russian literature for a related problem. Reference [7] considers gasless combustion of a solid propellant (or explosive) which burns by means of a single, in-depth, irreversible, condensed-phase reaction. The equations solved are identical to those used by Bradley ([8] with $a = 1$) in his study of radiant ignition of a reactive solid. Since the model does not consider regression of a gas/solid interface, the burning rate quoted in [7] is the velocity of the reaction front maximum as it moves into the unreacted solid. For certain combinations of heat release and activation energy, the velocity of the reaction front pulsates in a manner similar to the above results.

To the authors' knowledge, large amplitude spikes in propellant burning rate have never been observed experimentally. However, this may not be so surprising when one considers the small time scale involved and the fact that static pressure in the combustion chamber is the usual quantity monitored. If a spike or large amplitude excursion did occur, its presence could be obscured by gas-phase damping and remain undetected by a wall pressure gage. Hence, the possibility exists that this type of behavior is a triggering mechanism for combustion instabilities.

Also of interest is a comparison of all three combustion models under *identical linearly-stable input conditions when driven by the* same exponential pressure profile (equation (18)). Fig. 6 shows the results (Method D) of such a comparison when $H = 0.8, n = 0.67$, and the remaining parameters are those of Table 1. Qualitatively, the burning rate response of each model is the same. The large value of peak burning rate predicted by the Krier, et al. model can be traced to the assumption that $c_p = c_s$, which removes the damping term, $R(\Theta_s - 1)(1 - c_p/c_s)$, from the gradient boundary condition. Since it could easily be replaced in the model, this is considered a minor point in the present investigation. Note that all three models exhibit a consistent trend which cannot be characterized by a function of $d \ln P/d\tau$. To dramatize this point, consider the following expression for transient burning rate derived recently by Krier [9] from a perturbation analysis of the Krier, et al. model. Using the present notation,

$$R(\tau) = R_s \left[1 + \Psi(P) \frac{n}{R_s{}^2} \frac{d \ln P}{d\tau} \right] \tag{19}$$

where

$$\Psi(P) = \frac{\left(1 - \frac{1}{m} P^{n/m}\right)}{\left[P^{n/m}\left(2 + \frac{1}{m}\right) - 2H\right]}, \quad P = P(\tau).$$

The prediction following from equation (19) is plotted in Fig. 6 for comparison with the full nonlinear solution of the Krier, et al. Model. In this example, no correlation exists between the two results in the time interval 0 → 1.0.

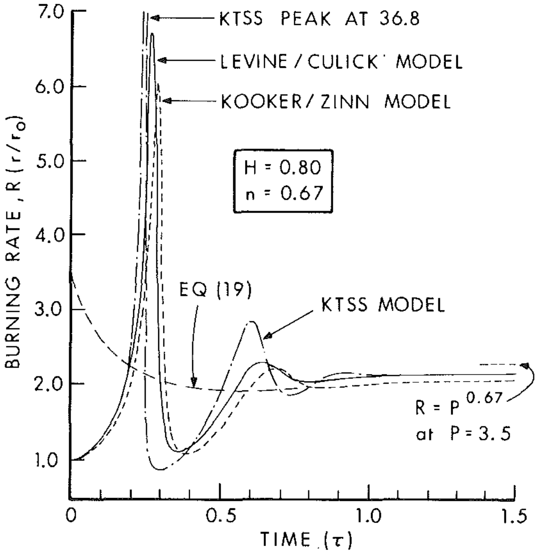

Fig. 6 Comparison of model predictions for burning rate response to exponential pressure profile ($\Delta P = 2.5, \beta = 1.0$)

Table 1 Assumed propellant parameters

$\rho_s = 1.54$ gm/cm^3
$c_s = 1.55$ J/gm-K (0.37 cal/gm-K)
$k_s = 0.0031$ J/cm-s K (7.3×10^{-4} cal/cm-s K)
$\Rightarrow \alpha = 1.28 \times 10^{-3}$ cm^2/s
$T_\infty = 298$ K
$E_s = 0.0628$ MJ/mole (15 kcal/mole) (m = 6.2, Krier, et al.)
$c_p = 1.72$ J/gm-K (0.41 cal/gm-K)
$k_g = 0.00156$ J/cm-s K (3.72×10^{-4} cal/cm-s K)
$r_o = 0.75$ cm/s
$p_o = 6.9$ MPa (1000 psia
$T_{so} = 623$ K
} steady-state initial conditions

Burning Rate Response in a Simulated Gun Combustion Chamber. A typical gun propellant is assumed to be represented by the parameters given in Table 1. Also required is a value for the surface heat release, H, associated with the global pyrolysis reaction. This is possibly the most difficult parameter to estimate since a single reaction which converts solid to gas does not exist in the actual combustion process. The present investigation will rely on experimental studies such as [10] in which estimates are made of the amount of heat released in the surface zone of a double-base propellant, with and without catalysts, under steady state conditions. These results indicate that a value of approximately 418 J/gm (100 cal/gm) would be compatible with the assumed initial conditions of Table 1. This implies a range of values for H between 0.8 and 0.9. Other investigators have inferred values of H from 0.5 to 0.85 for double-base propellants.

The pressure variation to be imposed at the edge of the flame zone in the combustion models is obtained from an experimental firing of the 105 mm Tank Gun. For the purpose of the numerical solution, a time origin ($\tau = 0$) is established at the point where the gun pressure is equal to 6.9 MPa (1000 psi). From this origin, approximately 1.3 nondimensional time units (~3ms) are required to reach the peak pressure of 393 MPa (57,000 psi). In this study, the pressure reaches only about 30 MPa at the end of the time of interest.

An example of the burning rate response to the above-mentioned gun pressure-time history is shown in Figs. 7 and 8 for the Levine and Culick Model using Method (D). All the cases are linearly stable. The results are plotted as R/R_s, where R_s is the steady state value of burning rate based on the instantaneous value of pressure and the pressure exponent, $n = 0.67$. Note that, at first, R/R_s falls below one, indicating that the thermal wave which controls burning rate does not respond instantaneously to the increasing pressure. The figures clearly show the sensitivity as H increases. For a value of $H = 0.83$, the numerical solution indicates a maximum dynamic overshoot of approximately 10. To see if this behavior follows from unrealistic variations of the temperature distribution in the solid propellant, thermal profiles for three points in time (as denoted by the symbols in Fig. 8) are plotted in Fig. 9. The curve for $\tau = 0$ is the initial thermal wave at steady state which decays to $1/e$ of the surface value in a distance of α/r_o (or $\eta = 1$). The rise to the maximum burning rate is driven primarily by the surface heat release term, RH. At the maximum surface temperature of 820 K, the boundary condition is finally overpowered by heat conduction into the unburned solid. The burning rate then declines due to the combined effects of (1) rapid heat conduction into the solid resulting from the steep temperature gradient near the surface, and (2) the heat sink created by low temperature propellant suddenly uncovered by the large regression rate. However, the rate of heat release in the flame zone continues to increase with the increasing pressure. Thus, a new dynamic cycle begins.

An important observation can be made from the results shown in Figs. 3–8. The interval of time equal to $\alpha/r_o{}^2$ ($\Delta\tau = 1$, nondimensionally) is commonly referred to as the characteristic response time of the thermal wave, i.e., the time required for a significant change in

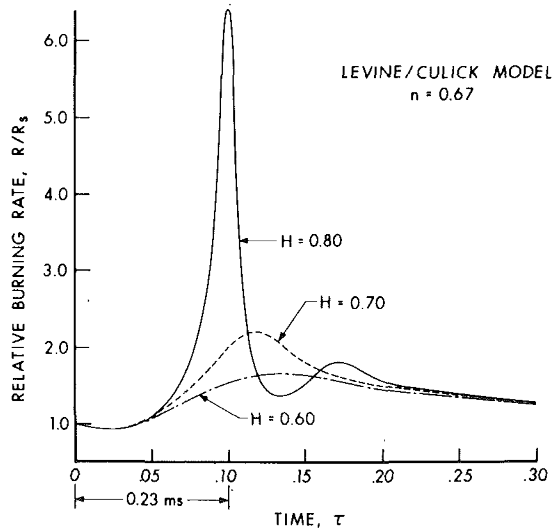

Fig. 7 Relative burning rate response to gun pressure-time history

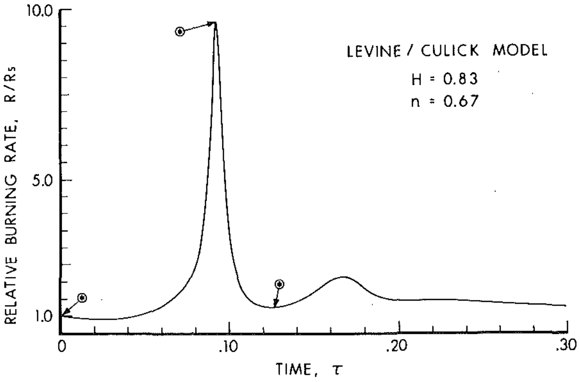

Fig. 8 Relative burning rate response to gun pressure-time history

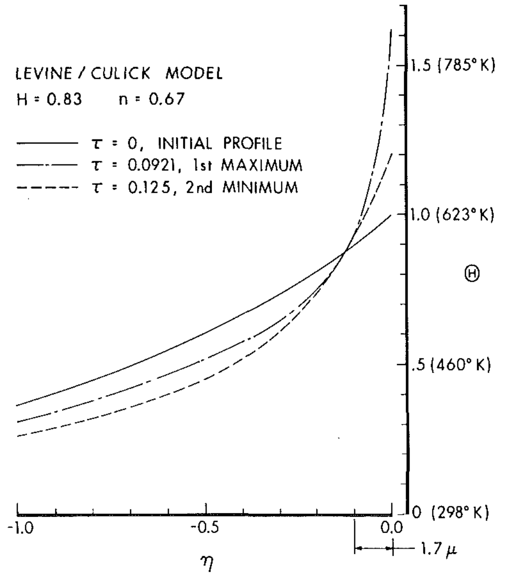

Fig. 9 Temperature profiles in unburned solid propellant for time points indicated in Fig. 8

burning rate as the result of a change in the environment. The current results show, however, that significant changes in burning rate can occur within a small fraction of this time. This is also true as the combustion model approaches the intrinsic instability limit, in which case the characteristic response time would be the period of the natural oscillation.

The three numerical methods of integration (Methods (B, C, D)) show a close agreement for the case in Fig. 7 except near the peak burning rate. In the vicinity of the peak, Method (D) predicts a larger value than Methods (B) and (C) which are coincident. After considerable study, it was determined that the difference is attributable to errors in the matrix inversion process used by both Methods (B) and (C). For these implicit solutions where the time step is much larger than the explicit diffusion stability limit, a loss of diagonal dominance can occur when the regression rate R is large (essentially, a cell Reynolds number problem). In a special exercise, the time step $\Delta\tau$ and the grid spacing $\Delta\eta_j$ near the propellant interface were manipulated to maintain diagonal dominance as the regression rate became large; the numerical result for peak burning rate then matched the Method (D) result to within a fraction of a percent. This verifies the hypothesis but the required manipulation is uneconomical. For reasons beyond the scope of this study, Method (D) (invariant imbedding) is not subject to the diagonal dominance limitation and is considered the superior method, in both accuracy and economy.

Conclusions

Burning rate runaway is a numerical difficulty and is not a solution to the thermal-wave combustion models. The nonlinear models admit large-amplitude spikes in burning rate, but the numerical solution remains finite.

When the combustion model is beyond the intrinsic instability limit as determined by a linear stability analysis, the final unstable state is composed of repeating, finite-amplitude spikes.

For the example cases discussed here, significant changes in burning rate can occur within a time interval much smaller than either $\sigma/r_0{}^2$ or the period of the natural oscillation at the intrinsic instability limit.

Given the major assumption of a quasi-steady flame region, all three combustion models predict nearly the same burning rate response, regardless of the differences in the analysis of the gas-phase flame zone. The dominant influence is the response of the thermal wave in the unburned solid.

When the combustion models are driven by a gun pressure-time history, the combustion response at low pressure (early time) can be much greater than the "steady-state" prediction, $r = ap^n$, while the response at high pressure returns asymptotically to $r = ap^n$.

References

1 Krier, H., Tien, J. S., Sirignano, W. A., and Summerfield, M., "Nonsteady Burning Phenomena of Solid Propellants: Theory and Experiments," *AIAA Journal*, Vol. 6, No. 22, Feb. 1968 pp. 278–285.

2 Levine, J. N., and Culick, F. E. C., "Nonlinear Analysis of Solid Rocket Combustion Instability," AFRPL-TR-74-45, Oct. 1974.

3 Kooker, D. E., and Zinn, B. T., "Numerical Investigation of Nonlinear Axial Instabilities in Solid Rocket Motors," US Army Ballistic Research Laboratory, BR1-CR-141, March 1974, AD No. 776954.

4 Kooker, D. E., and Nelson, C. W., "Numerical Solution of Three Solid Propellant Combustion Models During a Gun Pressure Transient," US Army Ballistic Research Laboratory, BRL-R-1953, Jan. 1977, AD No. AO35250.

5 Carslaw, H. S., and Jaeger, J. C., *Conduction of Heat in Solids*, Oxford Press, 2nd Edition, 1959.

6 Kooker, D. E., and Zinn, B. T., "Triggering Axial Instabilities in Solid Rockets: Numerical Predictions," AIAA/SAE 9th Propulsion Conference, AIAA Paper 73-1298, 1973.

7 Shkadinskii, K. G., Khaikin, B. I., and Merzhanov, A. G., "Propagation of a Pulsating Exothermic Reaction Front in the Condensed Phase," *Fizika Goreniya i Vzryva*, Vol. 7, No. 1, 1971, pp. 19–28.

8 Bradley, H. H., Jr., "Theory of Ignition of a Reactive Solid by Constant Energy Flux," *Comb. Sci. and Tech.*, Vol. 2, 1970, pp. 11–20.

9 Krier, H., "Solid Propellant Burning Rate During a Pressure Transient," *Comb. Sci. and Tech.*, Vol. 5, 1972, pp. 69–73.

10 Kubota, N. et al., "An Experimental Study of the Site and Mode of Action of Platonizers in Double Base Propellants," *AIAA Journal*, Vol. 12, No. 12, 1974, pp. 1709–1714.

A. M. Kanury
Department of Aerospace and Mechanical Engineering, University of Notre Dame, Notre Dame, Ind. 46556

D. J. Holve
Department of Mechanical Engineering, Stanford University, Stanford, Calif. 94305

Response of Building Components to Heating in a Fire

This paper deals with the response of building components such as walls, doors, etc. exposed to the severe thermal atmospheres created by accidental fires in structures. The standard fire test ASTM E-119 of the American Society for Testing and Materials, which is used to measure this response, is considered for a theoretical analysis. Only the thermal aspects of the problem are examined. Through dimensional, order-of-magnitude, and phenomenological analyses of the governing equations of an idealized model, a variety of conclusions are drawn. These conclusions are consistent with various successful current fire protection design practices. Deviations of the idealized theoretical model from the practical operating conditions of the actual test are carefully noted for consideration in the future refinements of the analysis.

Introduction

The current state of the art of flammability and fire testing is largely empirical. In order to make reliable and economical fire safety predictions and designs, there is need for theoretical analysis of the various fire phenomena based on both the existing and future fire tests.

The overall objective of the work reported in this paper is to develop a better understanding of the ASTM E-119 Standard Fire Test [1] through theoretical analysis to identify its merits and shortcomings, to discover effective ways of interpreting its measurements to the level of safety in a fire, and thus to contribute towards fire safety prediction and design in structures. The analysis would also reveal how various physical, chemical and structural variables influence the fire endurance of a construction member.

The ASTM E-119 Standard Test measures fire resistive properties of walls, partitions, columns, beams and girders, floors, roofs and ceilings, and frames and facings. The Underwriters' Laboratory [2] and the National Fire Protection Association [3] equivalent tests are designated, respectively, UL-263 and NFPA-251. The test procedure, scrupulously detailed in the ASTM Standards, requires incorporation of the test specimen assembly in its full size as a partition in a large furnace that resembles a compartment in a structure. One side of the partition is exposed to a gas fire whose temperature (averaged over nine thermocouples) follows a prescribed history. The test procedure defines the performance of the member or assembly as "the period of resistance to standard exposure elapsing before the first critical point in behavior is observed" [1]. The critical point is marked (1) by the passage of flames or of gases, through the member or assembly, hot enough to ignite cotton waste, or (2) by the transmission of heat through the member or assembly to raise the temperature of the unexposured surface to 250°F (139°C) above the initial temperature. Load-bearing walls and partitions are required to sustain the applied load during the test. An option is available to subject the member or assembly to withstand a hose-stream impact.

Model Formulation

In the following theoretical model, only the thermal and thermochemical aspects of the fire endurance of a wall are considered. To this effect, several idealizations are made.

1 Passage of flames or of gases through the wall assembly is greatly facilitated during a test by leaks through seams, joints, cracks, etc. Whereas seams and joints usually arise in the process of fabrication of the assembly, cracks would normally develop in an uncontrollable way during the test. Furthermore, walls in a real structure will show cracks at random due to settlement and vibration. Add to this the fact that plumbing, electrical and ducting installations require much drilling and cutting. One can thus expect cracks and holes to evolve in a random, stochastic manner. The present model ignores this stochastic element.

2 The temperature of the unexposed surface is measured by a number of thermocouples each of which is placed under a standard asbestos pad. A careful examination of the thermal properties of the asbestos stipulated by the ASTM standard relative to the properties of a typical species of wood employed in construction practice leads one to conclude that the asbestos pads do little more than serve as shields for thermal radiation and as controlled convection surfaces. Furthermore, estimates of heat loss rate at the back-face under actual test conditions show that this loss is safely negligible. The present theory thus uses the temperature measured under the asbestos pads to be synonymous with the temperature of the back-face.

3 The ASTM standard stipulates that the test assembly be subjected to a superimposed load on bearing-walls during the test. Whereas degeneration of load-bearing ability due to exposure to fire is an important aspect in determining the endurance of a wall, the present model ignores this structural mechanics aspect of the problem. Also ignored are the details of bonding between laminates and their failure. Thus the study reported here is stressed to be but the first step in a comprehensive investigation which integrates the structural mechanics with fire dynamics.

4 In the present study, the walls are assumed to be solid slabs in which heat transfer occurs by one-dimensional conduction.

After the specimen slab is installed in the furnace and the furnace temperature is allowed to rise according to a programmed standard

---

Contributed by the Heat Transfer Division for publication in The JOURNAL OF HEAT TRANSFER. Manuscript received by the Heat Transfer Division August 16, 1978.

$T_f(t)$ curve, heat is convected and radiated transiently to the specimen surface from the furnace gases and walls. A fraction of the heat flux received by the specimen surface is transferred into the interior of the solid by transient conduction while the rest is reradiated to the furnace environment.

As a result of the heat flow into the solid, the temperature at the surface and at all stations in the interior rises gradually with time. The steepest thermal gradients are confined to a relatively thin thermal layer [4] near the exposed surface so that at depths beyond this layer, the solid is at its initial temperature without responding to the thermal perturbation imposed at the surface. As the surface temperature increases with time, so also does the thickness of the thermal layer. The problem in this first stage of the fire is determination of these dependencies and of the transient temperature profile.

As heating continues, the surface temperature exceeds a certain level beyond which pyrolysis of the solid occurs at a measurable rate. A pyrolysis layer penetrating into the solid is subsequently formed. In this second stage, the problem is to determine the variation of the transient temperature profile, and hence, the surface temperature with time, and the propagation of the thermal and pyrolysis waves into the solid. Further heating causes the thermal wave to reach the unexposed backface of the slab. Beyond this stage, the problem becomes one of determining the propagation rate of the pyrolysis layer and temporal variation of the temperature across the solid. Two important variables calculated in this stage are: (1) the time at which the backface temperature reaches 250°F (139°C) above the initial temperature, and (2) the time at which the pyrolysis layer reaches the backface. The shorter of these two times is taken here to determine the fire resistance of the specimen.

The preceding description is adequate even for walls that are composite in structure, i.e., having two or more slabs of different materials in intimate contact. The interface boundary conditions are, of course, additionally needed.

Variables of Concern. The above description of the idealized physical model reveals that the standard fire endurance of a construction component depends on certain characteristics governed by the following three groups of variables: (1) *Exposure*—The time history of the furnace gas temperature, the furnace wall temperature (and the associated thermal equilibrium), the effective emissivity of the gas phase and the walls, the flow and ventilation in the furnace, scaling of the exposed surface, absorptivity of the surface, etc. (2) *Specimen Material(s)*—Thermal conductivity, density, and specific heat of the material, internal contact resistances in composite solids, initial temperature, dimensions and other geometry/structure-related data, moisture content, pyrolysis kinetics (vapor pressure data for noncharring materials), effective latent heat of pyrolytic vaporization, conductivity, specific heat, density, latent heats and temperature of transformation of any heat-absorbing additives in the construction materials, physical and chemical properties of the glues used, if any, specific heat and molecular weight of the pyrolysates, kinetics and energetics of secondary char-catalyzed transformations experienced by the pyrolysate flow, etc. (3) *Boundaries*—Convective and radiative loss characteristics of the backface; the temperature of air adjacent to the backface, thermal, physical, and chemical properties of protective coatings, if any, etc.

Mathematical Model. We deal with charring materials comprising the construction wall. The geometry chosen is that of a slab. Thermal properties are considered variant with density in a prescribed manner. The char formed in pyrolysis is assumed to be structurally strong enough to avoid crumbling and erosion. The ventilation in the furnace is assumed to be low enough to preclude ablative consumption of the surface char. In the presence of the pyrolysate flow, the surface char is assumed to be nonglowing in the time zone of interest. Secondary, char-catalyzed, chemical transformations in the pyrolysate flow are neglected so as to render the problem tractable.

In formulating the model, the time-variant radiant/convective heating of the surface by the time-variant furnace gas and wall temperature is the most important consideration. While some ingenuity is needed to solve the problem with the transient boundary conditions, experience [5] indicates that the macroscopic charring rate is relatively insensitive to the specific time-wise distribution of the exposure so long as it is not in the form of intermittently spaced narrow spikes. The energy conservation in the slab is then described by the following equation.

$$\frac{\partial}{t}(\rho_a h_a + \rho_c h_c) = \frac{\partial}{\partial x} K \frac{\partial T}{\partial x} + \frac{\partial}{\partial x}(\dot{m}_g'' h_g) + Q_p \frac{\partial \rho}{\partial t} \tag{1}$$

where t is time, x is depth beneath the exposed surface, ρ is density, h is enthalpy, K is the porous solid conductivity, T is temperature, $\dot{m}_g''$ is the pyrolysis gas mass flux, and Q_P is the energy required to produce a unit mass of the pyrolysates. Suppose wood of density ρ_w when pyrolyzed produces per unit volume $(\rho_w - \rho_c)$ kg of pyrolysates and ρ_c kg of residual char. At any instant of partial decomposition when the wood density is $\rho(t)$, the pyrolysates yet to be released amount to $(\rho(t) - \rho_c)$ kg/m^3 of wood. Then, the degree of completeness of pyrolysis is given by

$$\lambda \equiv 1 - \left[\frac{\rho(t) - \rho_c}{\rho_w - \rho_c}\right] \tag{2}$$

When $\lambda = 0$, the pyrolysis has not occurred. When λ is unity, the pyrolysis is complete. If wood is viewed to consist of reactive material of density ρ_a, which transforms in pyrolysis into gases and char, it is obvious that, initially, all the wood is reactive, so that $\rho_a = \rho_w$ and that, finally, no part of the char is reactive, so that $\rho_a = 0$. Thus, the degree of pyrolysis may be defined in an alternative way, viz:

$$\lambda \equiv 1 - \frac{\rho_a}{\rho_w} \tag{3}$$

The above two definitions of λ lead to a relationship between the hypothetical active component density and the instantaneous density of partially pyrolyzed wood:

Nomenclature

$a, b,$ = indices
a_p = pyrolysis preexponential factor
B' = mass transfer driving force
Bi* = Biot number
C_P = specific heat, J/kgK
Da, Da′, D̃a, D̃a′ = Damköhler numbers
E = pyrolysis activation energy, J/mole
g = gravitational constant, m/s^2
h = enthalpy, J/kg
h^* = heat transfer coefficient, W/m^{2}K
K = thermal conductivity, W/mK
ℓ = wall thickness, m
L_p = heat of gasification, J/kg
$\dot{m}''$ = mass flux, kg/m^{2}s
n = index
Pe = Peclet number
Pr = Prandtl number

$\dot{q}''$ = heat flux, W/m^2
Q_p = enthalpy of pyrolysis, J/kg
R = universal gas constant, J/mole K
t = time, s
T = temperature, K
u = velocity, m/s
x = depth, m
α = thermal diffusivity, m^2/s
ϵ = emissivity
λ = degree of completeness of pyrolysis
μ = nondimensional mass flux
ν = kinematic viscosity, m^2/s
ρ = density, kg/m^3
σ = Stefan-Boltzmann constant, W/m^{2}K^4
ξ = nondimensional depth
θ = nondimensional temperature
τ = nondimensional time

Subscripts

1 = front layer of solid
2 = substrate solid
av = average
∞ = ambient
a = active
b = backface
c = char
f = flame
g = gas
i = initial, and interfacial
n = net
r = resistance
R = residue
s = exposed surface
w = wood
p = pyrolysis

$$\frac{\rho(t)-\rho_c}{\rho_w-\rho_c}=\frac{\rho_a}{\rho_w} \tag{4}$$

This relation is entirely consistent with the existing conceptions [6, 7] of the macroprocess of wood pyrolysis. The total instantaneous density of partially decomposed wood $\rho(t)=\rho_a(t)+\rho_R(t)$. Initially, $\rho=\rho_a=\rho_w$, and the residual density $\rho_R=0$. As the active component disappears, gases and char appear. The rates are related by

$$-\frac{d\rho}{\rho_w-\rho_c}=-\frac{d\rho_a}{\rho_w}=\frac{d\rho_R}{\rho_c} \tag{5}$$

The reaction rate in equation (1) is assumed to be given by a first-order Arrhenius rate equation:

$$\frac{d\rho}{dt}=-a_p\rho_a\exp[-E/RT(t)] \tag{6}$$

which, by equation (4), becomes

$$\frac{d\rho}{dt}=-a_p\left[\frac{\rho-\rho_c}{\rho_w-\rho_c}\cdot\rho_w\right]\exp[-E/RT(t)] \tag{7}$$

The enthalpies in equation (1) are defined by taking the initial temperature T_∞ as reference.

$$h_a\equiv\int_{T_\infty}^{T}C_{Pa}dT;\quad h_c\equiv\int_{T_\infty}^{T}C_{Pc}dT;\quad h_g\equiv\int_{T_\infty}^{T}C_{Pg}dT$$

The significance of equation (1) is simple. The left-hand term is the rate of increase of the total sensible enthalpy of an element in the solid. The right-hand terms are the excess conductive flux into the control element, the rate of convective heat transfer resulting from the outflow of the pyrolyzates, and the local energy sink caused by pyrolysis, respectively. K is the effective thermal conductivity of the porous solid matrix whose pores are filled with the pyrolyzates. The internal convection term is always negative, since the outflow of gases convects heat always opposing the inward conduction. A thorough thermal contact between the porous matrix and the flowing pyrolyzates is assumed.

The mass flux varies with depth depending on the rate of the local gas generation. Thus, continuity of mass is expressed by

$$\frac{\partial\dot{m}''}{\partial x}=\frac{\partial\rho}{\partial t} \tag{9}$$

or, on integration,

$$\dot{m}''(x,t)=\int_{\ell}^{x}\frac{\partial\rho(x,t)}{\partial t}dx$$

Accumulation of gases to build up local pressure internally is ignored.

The heat of gasification is an illusive property. Kung [7] developed the reasons underlying this illusion by relating the heat of gasification with the heat of pyrolysis. By performing product differentiation of the terms in equation (1), substituting equations (5), (8), and (9) and rearranging, the following alternative for equation (1) is obtained.

$$\rho C_P\frac{\partial T}{\partial t}=\frac{\partial}{\partial x}K\frac{\partial T}{\partial x}+\dot{m}''C_{Pg}\frac{\partial T}{\partial x}+L_P\frac{\partial\rho}{\partial t} \tag{10}$$

where

$$\rho C_P\equiv\rho_aC_{Pa}+\rho_RC_{PR}$$

$$L_P\equiv Q_P+h_g+\frac{h_c\rho_c}{\rho_w-\rho_c}-\frac{h_a\rho_w}{\rho_w-\rho_c} \tag{11}$$

The temperature dependence of the heat of gasification L_P is evident from this last result.

Equations (7), (9), and (10) are three equations for the three unknowns of the problem $\rho(x,t)$, $\dot{m}_g''(x,t)$ and $T(x,t)$. Appropriate boundary and initial conditions are needed to solve this set. For time less than zero, $T(x,0)=T_\infty$, $\rho(x,0)=\rho_w$ and $\dot{m}_g''(x,0)=0$. At the exposed surface $x=0$, the net heat flux $\dot{q}_n''$ is given by the sum of incident radiative and convective fluxes from the furnace, which attempts to simulate the exposure fire, less the reradiative flux from the surface to the furnace. The radiation terms may be linearized for a first approximation so that the net radiant flux is written as $h_r(T_f-T_s)$, with the radiative heat transfer coefficient h_r equal to $\sigma\epsilon T^3$ where σ is Stefan-Boltzmann constant, ϵ is emissivity lying between the surface and furnace flame emissivities and T is a similarly representative temperature. Thus the surface boundary condition may be stated in a simple form

$$\dot{q}_n''=K\frac{\partial T}{\partial x}\bigg|_{x=0}=h^*(T_f-T_s) \tag{12}$$

where $h^*=h_r+h_c$, h_c being the convective heat transfer coefficient. In [9], the convective heat transfer rate for the standard ASTM furnace is estimated to be about 4 kW/m^2. The surface temperature T_s varies with time as dictated by the balance (equation (12)) between the solid phase conduction and gas phase radiation/convection.

The furnace temperature T_f is, as mentioned, a prescribed function of time. The ASTM standard presents a programmed $T_f(t)$. By performing an energy balance on the compartment, Kawagoe and Sekine [8] theoretically obtained the time-variation of the flame temperature which closely approximates the empirical furnace temperature-time history of the ASTM standard. A variety of mathematical representations of the $T_f(t)$ are available in the literature [9–11] each with its merits and shortcomings. The simplest of these representations is given by the ISO formula [11],

$$T_f-T_\infty=345\log_{10}(1+8t) \tag{13}$$

in which the temperature T is in centigrade and time t is in seconds. This exposure temperature history has the character of a never-dying fire to which fuel is fed by an external control. The temperature rises rapidly first and then slowly. That the fuel in a real situation is finite and depletable is completely unacknowledged by the ASTM/ISO temperature-time history. In order to correct this deficiency, from the knowledge of compartment fires which start small, grow, reach a maximum, burn more or less steadily for a finite duration, and then decay due to fuel depletion, one can presume that the room temperature varies with time according to

$$(T_f-T_\infty)/T_{f\max}=(t/t_{\max})\exp([1-(t/t_{\max})^2]/2) \tag{14}$$

where $T_{f\max}$ is the maximum temperature attained in the compartment and $t_{\max}$ is the time at which this maximum is first attained. These two adjustable parameters depend upon such variables as the room geometry, ventilation, fuel content and distribution.

The backface of the exposed slab loses heat by natural convection as its temperature progressively rises. In [9], some estimations are presented to show that if the backface temperature rise above the ambient temperature (T_b-T_∞) is not substantially large, the backface loss may be safely ignored. Thus, the second boundary condition is

$$\dot{q}_b''=-K\frac{\partial T}{\partial x}\bigg|_{x=\ell}\approx 0 \tag{15}$$

Furthermore, if composite walls are involved, continuity of temperature at each of the interfaces has to be stipulated by the following two equations:

$$K_1\frac{\partial T}{\partial x}\bigg|_1=K_2\frac{\partial T}{\partial x}\bigg|_2 \tag{16a}$$

$$T_1=T_2 \tag{16b}$$

Considerations may also be extended to examine the influence of an air space in the wall such as that produced by the presence of studs.

Kung [7] has solved equations (7), (9), (10) numerically for a prescribed constant exposure heat flux at $x=0$. Bamford, et al. [12] solved them for the constant T_f condition.

Dimensional and Order-of-Magnitude Analyses

Consider the equations developed in the preceding section. If one ignores the internal convection and pyrolysis endothermicity in equation (10),

$$\rho C_P \frac{\partial T}{\partial t} = \frac{\partial}{\partial x} K \frac{\partial T}{\partial x} \tag{17a}$$

By defining nondimensional time $\tau \equiv Kt/\rho C_P \ell^2$, depth $\xi \equiv x/\ell$, and temperature $\theta \equiv (T - T_\infty)/(T_f - T_\infty)$ (assuming that T_f is constant), the above equation reduces to

$$\frac{\partial \theta}{\partial \tau} = \frac{\partial^2 \theta}{\partial \xi^2} \tag{17b}$$

The boundary conditions equation (12) and (15) reduce to the following (with $\mathrm{Bi}^* \equiv h^* \ell/K$).

$$\left.\frac{\partial \theta}{\partial \xi}\right|_s = -\mathrm{Bi}^*[1 - \theta(0, \tau)]; \quad \left.\frac{\partial \theta}{\partial \xi}\right|_b = 0 \tag{18}$$

The solution of the problem is thus expected to be of the form

$$\theta = \theta(\xi, \tau; \quad \mathrm{Bi}^*) \tag{19}$$

To attain a given temperature rise at a given depth under a given boundary condition Biot number, the time required is given by τ = constant. This simple argument leads to the conclusion that the fire resistance of a slab is given by

$$\frac{Kt_r}{\rho C_P \ell^2} = \text{constant} \tag{20}$$

That is, thicker solids with high volumetric heat capacity and low thermal conductivity offer longer endurance times.

In a thermally thin wall, the solution will take the form $\theta \equiv \theta(\xi, \tau')$ where $\tau' \equiv \tau \cdot \mathrm{Bi}^*$. The fire resistance is then given by τ' = constant. That is,

$$\frac{h^* t_r}{\rho C_P \ell} = \text{constant} \tag{21}$$

The conductivity disappears from the solution because the internal thermal gradients vanish. Note that while in the former case, $t_r \propto \ell^2$, in the latter case, $t_r \propto \ell$. Complete solutions are expected to indicate $t_r \propto \ell^n$, where $1 < n < 2$.

In order to test the implications of equations (20) and (21), the available data [4, 12, 14, 15] on charring time of wood slabs of different species and thicknesses are plotted in Fig. 1. No account is taken in this plot for the variation of thermal properties between different wood species. Nor is the heat transfer coefficient ascribed with the specific values pertaining to individual experiments. Thus, all that this figure shows is the dependence of t_r on ℓ. According to equations (20) and (21), $t_r \propto \ell^2$ in the conduction-controlled regime and $t_r \propto \ell$ in the exposure-controlled regime. The straight lines in the figure indicate these two proportionalities. It appears that within the range of the presented data, the internal conduction is irrelevant and the resistance time is governed by the exposure conditions.

Comparatively more complete dimensional analyses may be made by making some simplifying assumptions regarding the pyrolysis kinetics. Suppose that all pyrolysis occurs abruptly at a distinct temperature, T_p. This supposition removes the need to consider the complicated chemical rate equation given by equation (7) and conceptually gives rise to a surface within the slab where all the wood is suddenly transformed to char with an energy absorption. This surface, $x = \ell_1$, which is at T_P, moves inward at some velocity which gives the charring rate. Ahead of the moving pyrolysis front is the virgin wood and behind it is char through which the pyrolyzates flow with $\dot{m}_g''(t)$ independent of depth (due to equation (9)). Assume that the char remains intact. Denoting the char domain by 1 and virgin zone by 2, the energy equation and boundary conditions become the following:

$$K_1 \frac{\partial^2 T}{\partial x^2} - \dot{m}_g'' C_{Pg} \frac{\partial T}{\partial x} = \rho_1 C_{P1} \frac{\partial T}{\partial t} \quad \text{(char)} \tag{22}$$

$$K_2 \frac{\partial^2 T}{\partial x^2} = \rho_2 C_{P2} \frac{\partial T}{\partial t} \quad \text{(wood)} \tag{23}$$

At the exposed surface, (subscript s),

$$-K_1 \left.\frac{\partial T}{\partial x}\right|_s = h_s^*(T_f - T_s) \tag{24}$$

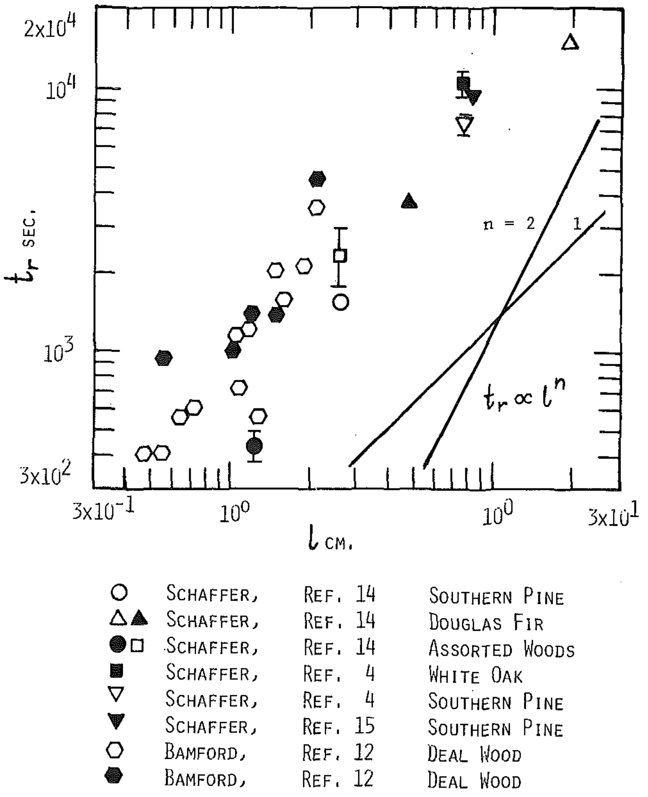

Fig. 1 Charring times of wood slabs of different thicknesses

At the interface i located at $x = \ell_1$

$$K_1 \left.\frac{\partial T}{\partial x}\right|_{i-} - K_2 \left.\frac{\partial T}{\partial x}\right|_{i+} = (\rho_2 - \rho_1) L_p \frac{d\ell_1}{dt} = L_p \dot{m}_g'' \tag{25}$$

$$T = T_p \tag{26}$$

At the backface, (subscript b),

$$-K_2 \left.\frac{\partial T}{\partial x}\right|_b = h_b(T_b - T_\infty) \tag{27}$$

Initially,

$$0 \le x \le \ell, \quad T = T_\infty, \quad \ell_1 = 0 \tag{28}$$

We further assume that

$$\dot{m}_g'' = at^b \tag{29}$$

Then, by defining

$$\xi \equiv x/\ell, \quad \tau \equiv K_2 t/\rho_2 C_{P2} \ell^2, \quad \theta \equiv (T - T_\infty)/(T_f - T_\infty) \tag{30}$$

we obtain the following dimensionless equations:

$$\frac{\partial^2 \theta}{\partial \xi^2} - \mathrm{Pe}\tau^{\mathrm{b}} \frac{\partial \theta}{\partial \xi} = \frac{\alpha_2}{\alpha_1} \frac{\partial \theta}{\partial \tau} \tag{22a}$$

$$\frac{\partial^2 \theta}{\partial \xi^2} = \frac{\partial \theta}{\partial \tau} \tag{23a}$$

$$\left.\frac{\partial \theta}{\partial \xi}\right|_{\mathrm{s}} = \mathrm{Bi}^*{}_{\mathrm{s}}(1 - \theta_{\mathrm{s}}) \tag{24a}$$

$$\left.\frac{\partial \theta}{\partial \xi}\right|_{i-} - \frac{K_2}{K_1} \left.\frac{\partial \theta}{\partial \xi}\right|_{i+} = \mathrm{Da}' \tau^b \tag{25a}$$

$$\theta_i = \theta_P \tag{26a}$$

$$\left.\frac{\partial \theta}{\partial \xi}\right|_b = \mathrm{Bi}_b \theta_P \tag{27a}$$

$$\mu = \tau^b \tag{29a}$$

Initially,

$$0 \le \xi \le 1, \quad \theta = 0, \quad \mu = 0 \qquad (28a)$$

The problem thus involves the following nondimensional variables:

Independent:

$$\xi \equiv (x/\ell); \qquad \tau \equiv (\alpha_2 t/\ell^2);$$

$$\alpha_2/\alpha_1; \qquad K_2/K_1;$$

$$\mathrm{Bi}_s{}^* \equiv (h_s{}^*\ell/K_1); \qquad \mathrm{Bi}_b \equiv (h_b\ell/K_2);$$

$$\theta_p \equiv (T_p - T_\infty)/(T_f - T_\infty);$$

$$Pe \equiv (aC_{Pg}\ell/K_1)(\ell^2/\alpha_2)^b;$$

$$\mathrm{Da}' \equiv \left[\frac{I_p}{T_f - T_\infty}\cdot\frac{a\ell}{K_1}\cdot\left(\frac{\ell^2}{\alpha_2}\right)^b\right] \equiv \left[\frac{L_p}{C_{Pg}(T_f - T_\infty)}\right]\cdot \mathrm{Pe} \equiv \mathrm{Da}\cdot\mathrm{Pe}$$

Dependent:

$$\theta \equiv (T - T_\infty)/(T_f - T_\infty); \quad \theta_s \equiv (T_s - T_\infty)/(T_f - T_\infty);$$

$$\theta_b \equiv (T_b - T_\infty)/(T_f - T_\infty); \quad \mu \equiv (\dot{m}_g{}''/a)(\alpha_2/\ell^2)^b$$

The solution for the fire endurance time of the slab will assume the form

$$f(\tau_r, \mathrm{Pe}, \alpha_2/\alpha_1, K_2/K_1, \mathrm{Bi}_s{}^*, \mathrm{Bi}_b\theta_b, \theta_p, \mathrm{Da}) = 0 \qquad (31)$$

This eight-parameter problem is immensely complex, in spite of the assumptions made regarding the pyrolysis kinetics and mass flux dependency on time. The manner in which the 17 different variables combine to fewer (i.e., eight) variables, however, is of crucial interest. Further simplifications are necessary to reduce the parameters even more. For instance, if the backface heat losses are ignorable, the backface Biot number vanishes. If the char and virgin solid properties are not significantly different, the ratios of thermal diffusivities and of conductivities become equal to unity. Thus,

$$f(\tau_r, \mathrm{Pe}, \mathrm{Bi}_s{}^*, \theta_p, \mathrm{Da}) = 0 \qquad (32)$$

In the case just described, T_f is fixed to convect heat to the specimen; the exposed surface temperature, T_s, increases with time, and hence, the net flux received, $h_s{}^*(T_f - T_s)$, decreases with time. Suppose the heat flux, $\dot{q}_s{}''$, is a prescribed constant so that $(T_f - T_s)$ is kept fixed by increasing T_f with time as required by the surface temperature. Then the normalizing temperature is $\dot{q}_s{}''\ell/K_2$ so that $\tilde{\theta} \equiv (T - T_\infty)\cdot K_2/\dot{q}_s{}''\ell$. Despite this change, equations (22*a*), (23*a*), and (26*a*–29*a*) remain unaltered. Equations (24*a*) and (25*a*) alter to

$$\left.\frac{\partial\theta}{\partial\xi}\right|_s = -\frac{K_2}{K_1} \qquad (24b)$$

$$\left.\frac{\partial\theta}{\partial\xi}\right|_{i-} - \left.\frac{\partial\theta}{\partial\xi}\right|_{i+} = \tilde{\mathrm{D}}\mathrm{a}'\cdot\tau^b \qquad (25b)$$

where

$$\tilde{\mathrm{D}}\mathrm{a} \equiv L_pK_2/\dot{q}_s{}''C_{Pg}\ell, \quad \tilde{\mathrm{D}}\mathrm{a}' \equiv \tilde{\mathrm{D}}\mathrm{a}\cdot\mathrm{Pe}$$

The net effect of this boundary condition is to reduce the need for the exposed surface Biot number and to use in its place the ratio of thermal conductivities. Thus, the eight-parameter problem corresponding to equation (31) takes the form

$$f(\tau_r, \mathrm{Pe}, \alpha_2/\alpha_1, K_2/K_1, \tilde{\mathrm{D}}\mathrm{a}, \theta_p, \mathrm{Bi}_b\tilde{\theta}_b) = 0 \qquad (33)$$

We consider the first term containing the endurance time as the dependent variable and the other six as independent variables. The second, third, and fourth terms are related to transport properties and may be combined in an as yet unknown manner. Energy conservation and physical intuition suggest that the remaining energy sink terms can, in principle, be combined by summation.

$$\frac{1}{\dot{q}_s{}''}\left[\frac{K_2L_p}{C_{Pg}\ell} + \frac{K_2(T_p - T_\infty)}{\ell} + h_b(T_b - T_\infty)\right] \equiv \frac{1}{B'} \qquad (34)$$

The bracketed quantity is an estimate of energy demand for pyrolysis, for preheating of the solid to pyrolysis temperature, and for backface heat losses; $\dot{q}_s{}''$ is the supply to meet this demand. The ratio of supply-to-demand fluxes may be denoted by B', which is a mass transfer driving force [13], a high value of which indicates a shorter endurance time. Even though the total problem is nonlinear because of the inherent transience, the admittedly crude argument presented above with linear summation provides an intuitively consistent, practical, and useful index B' to characterize the fire resistance of walls.

Phenomenological Analyses

With mere algebraic arguments the gross effects of various variables on the fire endurance time can be deduced by conducting simple overall energy and mass balances on the slab exposed to heating.

For instance, suppose a heat flux $\dot{q}_s{}''$ is incident on the specimen surface. To completely char the slab of thickness ℓ, this incident energy in time t_r has to be equal to the sum of four different quantities: the sensible heat required to raise the original solid to pyrolysis temperature; the latent heat required to pyrolyze the solid; the sensible heat consumed to raise char from the pyrolysis temperature to the final higher temperature, and the heat loss through the backface. Considering a unit cross section throughout,

$$\dot{q}_s{}''t_r \approx \rho_2C_{P2}(T_p - T_\infty)\ell + (\rho_2 - \rho_1)\ell L_P + \rho_1C_{P1}(T_c - T_p)\ell + h_b(T_b - T_\infty)t_r$$

$$\begin{matrix}\text{Heat}\\\text{Input}\end{matrix} \approx \text{virgin solid} + \text{pyrolysis} + \text{char heating} + \text{backface heatloss}$$

The backface temperature, T_b, in the loss term is taken to be somewhere between T_∞ and T_c. Resolving for the resistance time t_r,

$$t_r \approx \frac{\ell[\rho_2C_{P2}(T_p - T_\infty) + (\rho_2 - \rho_1)L_p + \rho_1C_{P1}(T_c - T_p)]}{[\dot{q}_s{}'' - h_b(T_b - T_\infty)]} \qquad (35)$$

The data of Fig. 1 again confirm this linear dependency of t_r on ℓ. Mass balance constrains the outflow of pyrolyzates in time t_r to correspond to the total mass loss suffered by the sample. That is, $(\rho_2 - \rho_1)\ell \approx \dot{m}_g{}''t_r$, so that

$$\dot{m}_g{}'' \approx (\rho_2 - \rho_1)\ell/t_r \qquad (36)$$

Note the similar features shared by equations (34) and (35) and, hence, how dimensional analysis and phenomenological analysis go hand in hand in developing a better understanding of the problem. It is obvious from equation (35) that the fire endurance time may be enhanced by increasing the value of the numerator and decreasing the value of the denominator—either by decreasing the exposure flux or by increasing the backface heat losses. Liquid-filled metal wall components essentially provide an increased backface heat loss, whereas external "protection" with insulating coatings essentially provides a decrease in the exposure flux itself. Equation (35) could be more rigorously obtained by conducting an order-of-magnitude analysis on equations (1), (7), (9), and (12).

Equations (1), (7), and (9), for instance, indicate that the resistance time t_r is of the order

$$t_r \sim \frac{\ell[\rho C_P\Delta T + \Delta\rho C_{Pg}\Delta T + L_p\Delta\rho]}{K\Delta T/\ell} \qquad (37)$$

where ΔT is the characteristic internal temperature differential, $\Delta\rho$ is the characteristic internal density differential and C_{Pg} is the pyrolyzate specific heat. Note immediately from equation (37) that the resistance time is longer for materials of higher density, ρ, higher specific heat, C_P, higher virgin-to-char density differential, $\Delta\rho$, higher pyrolysis temperature, higher endothermicity, lower conductivity, and larger thickness. It is intriguing to note that a higher convective capacity of the pyrolyzate flow increases the resistance time not only directly by the energy dissipation mechanism evident in equations (1) and (37), but also indirectly by "blocking" the surface flux caused by transpiration. This can be seen by eliminating K from equation (37) through an order-of-magnitude analysis on equation (12). The result is

$$t_r \approx \frac{\ell[\rho C_P \Delta T + \Delta\rho C_{Pg} \Delta T + L_P \Delta\rho + \Delta\rho C_{Pg} \Delta T_{fs}]}{h^* \Delta T_{fs}} \quad (38)$$

where ΔT_{fs} is the characteristic temperature difference between the furnace and the specimen surface. Whereas the first C_{Pg} term of equation (38) appears directly from equation (37), the second C_{Pg} term appears as a result of the boundary condition, equation (12). It is important to further note that the resistance time t_r is given by equation (37) in the conductive control regime and by equation (38) in the exposure heat flux control regime. In the former case, $t_r \propto \ell^2$ whereas in the latter, $t_r \propto \ell$. Fig. 1 indicates that the latter of these two alternative control mechanisms best describes the available data.

Note that addition of stabilizers and retardants to the solid increases the numerator of equation (38) (through an increase in ΔT, $\Delta\rho$, C_{Pg}, and L_p). The effect of retardants on the denominator (i.e., on ΔT_{fs} and h^*) is minor. Flame inhibitors, on the other hand, increase resistance time, t_r, by dominantly decreasing the denominator of equation (38) through a drastic decrease in ΔT_{fs}, and by affecting the numerator only weakly.

Also note that reductions in the characteristic scale, furnace and specimen emissivities, and the view factor cause an increase in t_r, but t_r may also be increased by reducing the temperature characteristic differential ΔT_{fs}. This is an obvious inference, for if in the limiting case there were no fire in the room, ΔT_{fs} is zero so that the resistance time t_r is infinite.

The preceding deductions result from a rather crude magnitude analysis to give the trends but not precise numerical answers. Despite the crudeness in analysis, however, the above treatment captures much of what has been reported in the literature.

Concluding Remarks

It is clear from these discussions that valuable information could be developed by an application of the sciences of heat transfer and combustion to such pragmatic problems as fire resistance of building components. The ASTM E-119 test is described here physically, this description is expressed in mathematics, and the mathematical model is qualitatively examined. The qualitative deductions of this paper are in excellent accord with the intuitive rationale employed in the existing design practice.

Acknowledgments

The work reported here is partially supported by the National Bureau of Standards under contract (No. 4-36105) with Stanford Research Institute. The authors wish to thank Mr. D. Gross of NBS who monitored this project. Appreciation is also expressed to Mr. S. B. Martin of SRI who managed the mavericks.

References

1 1977 Annual Book of *ASTM Standards,* Part 18, American Society for Testing and Materials, 1916 Race Street, Philadelphia, Pa., 1977, pp. 739–759.

2 "UL 263 Fire Test," Underwriters Laboratory, Inc., June 1964.

3 "Fire Codes" NFPA 251, Vol. 4, No. 251-1 National Fire Protection Association, 1965.

4 Schaffer, E. L., "Charring Rate of Selected Woods," Forest Products Lab., Research Paper 69, U. S. Forest Service, Madison, Wisconsin, 1967.

5 Kanury, A. M., "Rate of Charring Combustion in a Fire," 14th Symposium (International) on Combustion, The Combustion Institute, Pittsburgh, Pa., 1973, pp. 1131–1142.

6 Kanury A. M., and Blackshear, Jr., P. L., "Some Considerations Pertaining to the Problem of Wood-Burning," *Combustion Science and Technology,* Vol. 1, 1970, pp. 339–356.

7 Kung, H. C., "A Mathematical Model of Wood Pyrolysis," *Combustion and Flame,* Vol. 18, 1972, pp. 185–195.

8 Kawagoe, K., and Sekine, T., "Estimation of Fire Temperature-Time Curve in Rooms," Building Research Institute Occasional Report No. 11, 1963.

9 Kanury A. M., and Holve, D. J., "A Theoretical Analysis of the ASTM E-119 Standard Fire Test of Building Construction and Materials," Final Rept. NBS Contract No. 4-36105, Stanford Research Institute, Menlo Park, California, 94025, 1975.

10 Lie, T. T., *Fire and Buildings,* Applied Science Publishers, 1972.

11 Williams-Leir, G., "Analytic Equivalents of Standard Fire Temperature Curves," *Fire Technology,* Vol. 9, 1973, pp. 132–136.

12 Bamford, C. H., Crank, J., and Malan, D. H., "The Combustion of Wood," *Proc. Camb. Phil. Soc.* Vol. 46, 1946 pp. 166–182.

13 Spalding, D. B., *Some Fundamentals of Combustion,* Butterworths, London, 1955.

14 Schaffer, E. L., "Review of Information Related to the Charring Rate of Wood," Research Note No. FPL-0145 of the Forest Products Laboratory, U.S. Department of Agriculture, Madison, Wisconsin, Nov. 1966.

15 Schaffer, E. L., "An Approach to Mathemetical Prediction of Temperature Rise Within a Semi-Infinite Wood Slab Subjected to High-Temperature Conditions," *Pyrodynamics,* Vol. 2, 1965, pp. 117–132.

S. W. Van Sciver
R. W. Boom
Applied Superconductivity Laboratories
University of Wisconsin
Madison, Wisc. 53706

Heat Transfer from Aluminum to He II—Application to Superconductive Magnetic Energy Storage

Heat transfer problems associated with large scale Superconductive Magnetic Energy Storage (SMES) are unique due to the proposed size of a unit. The Wisconsin design consists of a cryogenically stable magnet cooled with He II at 1.8 K. The special properties of He II ($T < 2.17$ K) provide an excellent heat transfer medium for magnet stability. Design values are determined from an experimental study of heat transfer from aluminum to He II. Under near saturated conditions we observe a maximum surface heat flux of 1.7 W/cm^2 at 1.91 K and a recovery at 0.7 W/cm^2. The advantages of operating the magnet under subcooled conditions are exemplified by improved heat transfer. The maximum at 1.89 K and 1.3 atm pressure is 2.3 W/cm^2 with recovery enhanced to 1.9 W/cm^2. A conservative maximum heat flux of 0.5 W/cm^2 with an associated temperature difference of 0.5 K has been chosen for design. Elements of the experimental study as well as the design will be discussed.

Introduction

Large scale superconductive magnetic energy storage is being considered as an alternate storage scheme for the electric utilities. Serious feasibility studies under way at the University of Wisconsin and at Los Alamos Scientific Laboratory, have shown that a superconducting magnetic system can provide a highly efficient method of electrical storage provided the size of the unit exceeds about 1000 MWh [1].

The configuration of a unit is shown in Fig. 1. Economic analysis dictates that the magnet, which is a thin shelled segmented solenoid, be buried in subterranean bedrock. The rock structure provides a large fraction of the magnet support for the rather low cost of excavation. Load bearing struts made of fiber reinforced composites provide thermal isolation of the cryogenic environment. System optimization has suggested that the magnet consist of a composite aluminum stabilized NbTi conductor cooled by 1.8 K He II, also known as superfluid helium.

The choice of He II, instead of normal pool boiling helium at 4.2 K, results from a comparison between the cost of NbTi and refrigeration for the unit. Since the current density of NbTi at 1.8 K and 5 T is roughly twice that at 4.2 K and 5 T, the savings in material costs more than compensate for the added refrigeration required for lower temperature operation.

Figure 2 displays a cross section schematic of the conductor design. There are four major components to the design: cruciform, stabilizer, superconductor and shell [2]. A structural cruciform, made of high strength aluminum, is needed to carry the hoop-stress due to magnetic loading. Eight high purity aluminum wedges are designed to carry the current under fault conditions where the superconductor loses its current carrying capacity. The superconductor, which is a braid of NbTi in a copper matrix, is located between the high purity aluminum and the high strength aluminum shell. The thin high strength aluminum shell forms the conductor exterior. Complete containment is necessary since magnetic loading fully yields the high purity aluminum. The current capability of an 8 cm diameter conductor is about 286 KA at 2.5 T.

A significant portion of the energy storage magnet design considerations has to do with the thermal design of the aluminum stabilized composite conductor. Under fault conditions, the current migrates to the high purity aluminum generating heat due to resistive losses. For a given resistivity of the high purity aluminum, the wedge is sized

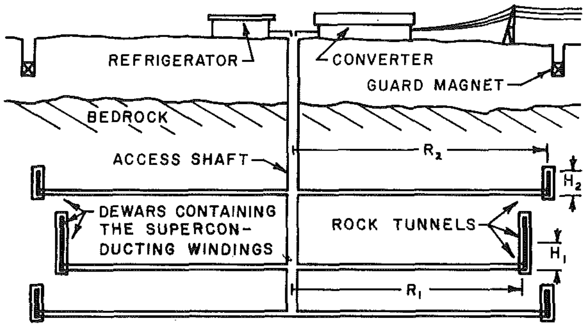

Fig. 1 Conceptual design of a 1000 MWh superconductive energy storage magnet. Typical dimensions: R_1 = 68 m, R_2 = 75 m, H_1 = H_2 = 7.5 m

---

Contributed by the Heat Transfer Division for publication in the JOURNAL OF HEAT TRANSFER. Manuscript received by the Heat Transfer Division August 11, 1978.

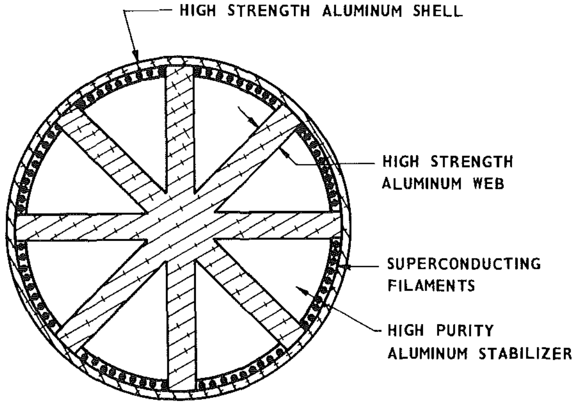

Fig. 2 **Cross-sectional schematic of aluminum stabilized conductor**

by establishing the limitations in heat transfer to the helium. These limits can be determined from basic heat transfer research.

In the following paper we report results from an experiment designed to measure heat transfer from aluminum to He II. The range of temperatures investigated is from 1.5 K to 2.1 K with pressures from saturated vapor pressure, about 0.02 atm, to the critical pressure, 2.3 atm. The data shows clear advantages for subcooling and operation at as low a temperature as possible taking into account refrigeration power requirements.

Experiment

A schematic of the experimental apparatus is shown in Fig. 3. The heat transfer samples studied to date are machined from high purity aluminum. The area of contact between the aluminum and helium is 1.48 cm^2. Results from measurements on sample No. 1, 99.99 percent purity and residual resistance ratio ($R_{4.2K}/R_{300K}$) of 500, were reported previously [3]. Sample No. 2, machined from 99.999 percent aluminum with a resistance ratio of approximately 1500, has been used in most of the work which is reported here. The samples are attached to the end of a thin walled, 0.02 cm, stainless steel tube, 21 cm long and 1.37 cm ID.

The heat transfer measurement consists of applying heat at the lower end of the sample and measuring the temperature difference across the Al-He II boundary, ΔT. The value of ΔT is determined by extrapolation of the temperatures measured in the aluminum and helium to the interface. Heat is applied by joule heating a 335 Ω strain gage epoxied to the lower end of the sample. Axial heat flow is guaranteed by surrounding the assembly by a vacuum container. Temperatures are measured with matched ⅛ watt Ohmite carbon resistors, nominal resistance 75 Ω. Uncertainty in the surface temperature difference is ±3 mK.

A pressure container surrounding the vacuum can is filled through a needle valve connected to the helium bath. Pressure is applied through a capillary tube joined to an external gas handling system. Regulation of the pressure in the subcooled work is achieved manually to a precision of ±0.04 atm. Further details of the experimental apparatus have been reported elsewhere [3–5].

Results and Discussion

We summarize the heat transfer characteristics of the experimental setup in Fig. 4. Two heat transfer and boiling curves are shown. The data at saturated vapor pressure and 1.91 K is for sample No. 1. All subcooled data, including the plotted results at 1.89 K and 1.27 atm, are associated with sample No. 2. The general features of these data are similar. On increasing the applied heat flux, the temperature of the sample increases continuously to a maximum occurring around 2 W/cm^2 but dependent upon applied pressure and temperature. This region of the heat transfer curve is dominated by the Kapitza resistance.

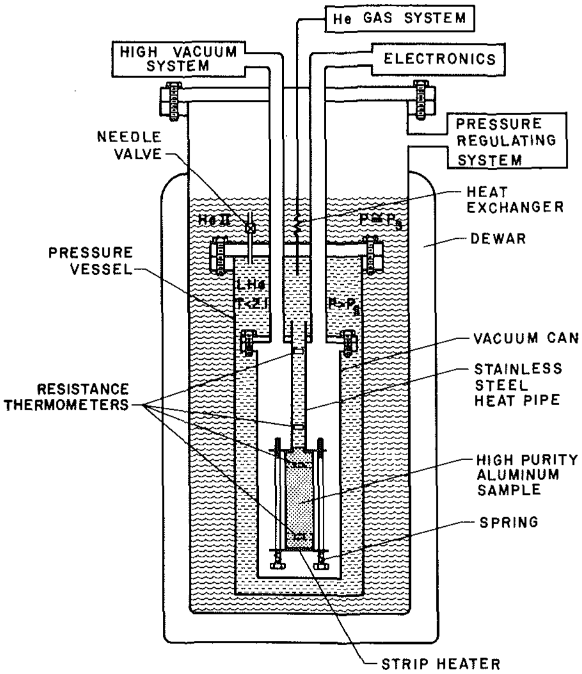

Fig. 3 **Schematic of heat transfer experimental apparatus**

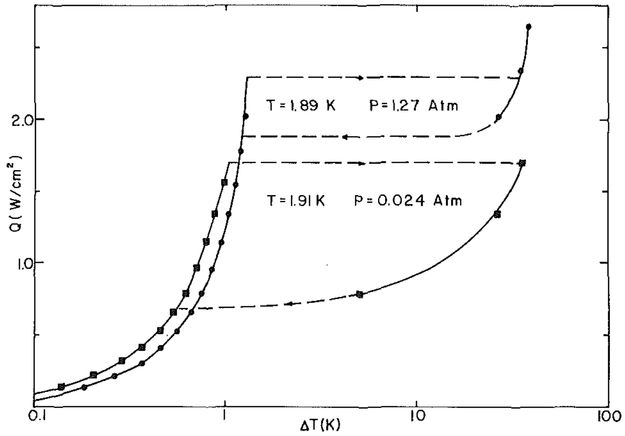

Fig. 4 **Heat transfer and boiling curves near 1.9 K and for two pressures**

Above the peak heat flux surface boiling occurs and the temperature of the sample increases by an order of magnitude. For the saturated case, the boiling is accompanied by low frequency oscillations, of the order of several Hertz. The noise frequency is much higher for the pressurized system and appears to increase with applied pressure. Also accompanying the boiling in the pressurized system are rather macroscopic regions of He I. This effect is first observed as a temperature excursion above the λ-transition of the resistor nearest the helium-aluminum interface. Similar effects have been seen by Caspi, et al. [6], although their experiment is of different geometry to the present work.

Nomenclature

A = Gorter-Mellink mutual friction constant
C = coefficient of the generalized Kapitza conductance
h = generalized Kapitza conductance
L = length of tube
m = a constant
P = pressure
Q = heat flux
Q^* = peak heat flux
R = electrical resistance
S = entropy
T = absolute temperature
T_b = bath temperature
T_0 = transition temperature
T_s = surface temperature
ρ_n = normal fluid density
ρ_s = superfluid density

On reducing the applied heat flux below the peak it is found that the sample does not immediately recover to the Kapitza regime. Instead, the heat transfer curves have a considerable hysteresis. The amount of hysteresis appears to be strongly dependent on the applied pressure. This subject will be discussed in more detail in what follows. The features of these heat transfer results which will be emphasized in the discussion are the critical heat fluxes and the Kapitza conductance.

Critical Heat Fluxes. The peak heat flux in the heat transfer to He II is determined by the size of the temperature difference which can be sustained by the bulk *He* II [7, 8]. The temperature gradient develops as a result of the mutual friction between two components of the fluid, superfluid and normal fluid. For the special case when the channel dimensions are relatively large (dia > 1 mm), the temperature gradient has a well established form,

$$\nabla T = \frac{A\rho_n}{S}\left(\frac{Q}{\rho_s ST}\right)^m \tag{1}$$

where m is a constant with value approximately 3 and A is the Gorter-Mellink mutual function constant. The quantity x has been shown to be a significant function of temperature [9].

The above expression can at least in principle be used to explain the peak heat fluxes in a heat transfer experiment. The helium near the surface of the heater is subcooled below saturated vapor pressure by either the hydrostatic head or the applied pressure. Thus, the peak heat flux is defined by the amount of heat needed to raise the helium at the surface to the transition temperature, T_0. For axial heat flow, integration of equation (1) results in an expression for the peak heat flux,

$$Q^* = \left[\frac{1}{L}\int_{T_b}^{T_0} \frac{S}{A\rho_n}(\rho_s ST)^m \, dT\right]^{1/m} \tag{2}$$

where T_b is the saturation temperature of the bath and L is the length of the tube.

We can increase the peak heat flux to a maximum by subcooling to pressures above the λ-point, $P > 0.05$ atm, thus allowing the integral in equation (2) to be taken to its maximum temperature of 2.17 K. This effect distinguishes the two heat transfer curves in Fig. 4. The peak heat flux in the near saturation case is due to the hydrostatic head which provides a small subcooling. At 1.91 K, the peak is about 1.7 W/cm^2 for a hydrostatic head of 36 cm, which allows a maximum temperature difference in the helium of about 0.06 K. In the subcooled work, the temperature difference can be much larger, about 0.28 K at 1.89 K and 1.27 atm, which qualitatively explains the increase in the peak to 2.3 W/cm^2.

Figure 5 is a plot of the peak heat flux as a function of bath pressure. At constant bath temperature, an increase of the applied pressure above saturation raises the peak heat flux to a maximum occurring near the λ-point. Further increasing the pressure tends to reduce the peak as seen in the high pressure data ($P \gtrsim 1$ atm). A similar pressure dependence in the peak heat flux has been seen by Linnet and Frederking [8]. This effect is understandable in terms of the reduced effective thermal conductivity of the He II, which results from pressurization [5, 10].

Integrating equation (2) for different pressures predicts a monotonically decreasing peak heat flux. This analysis for 1.89 K is shown by the solid curve in Fig. 5. The agreement is very close indicating that the pressure dependence, like the temperature dependence, of the peak heat flux in He II can be understood in terms of the fluid conductivity. Therefore, from the standpoint of the peak heat flux, there exists a broad maximum in the heat transfer capability occurring in the range 0.1 to 1 atm.

The recovery heat flux appears to be affected more strongly by pressure. The value near saturation and 1.91 K is about 0.7 W/cm^2. Subcooling increases the recovery monotonically with pressure. Near the critical pressure ($P \sim 2.3$ atm) the two critical heat fluxes converge at a value of about 2 W/cm^2. This effect appears to result from the enhanced film boiling heat transfer that occurs with subcooling. Recovery may be controlled by a minimum temperature difference in the film boiling required [5].

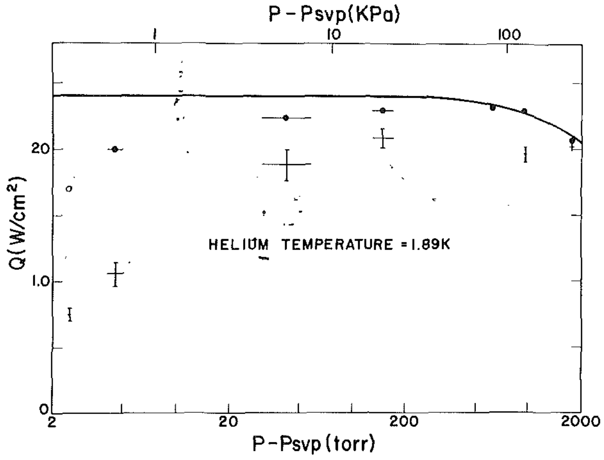

Fig. 5 Peak and recovery heat fluxes versus applied pressures at 1.89 K. Open data point is at 1.91 K

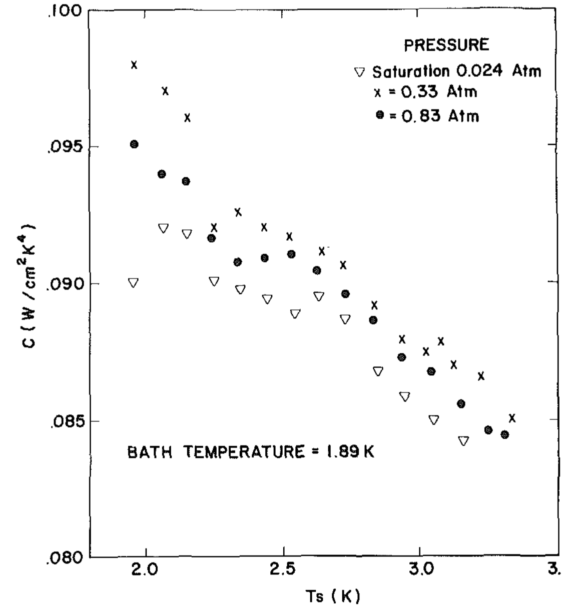

Fig. 6 Coefficient of generalized Kapitza conductance versus surface temperature and pressure

Kapitza Conductance. The region of the heat transfer curve which is less than the critical heat flux can be considered the Kapitza regime. Unlike nucleate boiling heat transfer, no bubbles form in bulk He II. Rather there is an exchange of energy across the boundary via thermal wave (phonon) scattering [11]. The thermal resistance is related to the mismatch between the two bulk media as well as surface conditions. Using an analytic expansion of the radiative energy transfer, we can develop an empirical relationship for the heat transfer in this region. We define the Kapitza conductance for finite ΔT as $h = Q/\Delta T$, where Q is the surface heat flux. The form of the generalized Kapitza conductance can be written [12],

$$h = CT^3 f(\Delta T/T)\,\Delta T \tag{3}$$

where $f = 1 + \frac{3}{2}\Delta T/T + (\Delta T/T)^2 + \frac{1}{4}(\Delta T/T)^3$ and C is an empirical factor which can vary by a factor of five depending on material [13, 14]. The strength of the above analysis is in its ability to predict the temperature dependence of h. However, the theoretical magnitude is far from correct and we must rely on experimental determined values for the coefficient, C. We have reported the value of C for sample No. 1 to be 0.108 ± 0.005 W/cm^{2}K^4 [3]. Plotted in Fig. 6 are the experimental values for sample No. 2 at 1.89 K and three pressures versus surface temperature T_s. The empirical form of equation (3) is similar to that of sample No. 1, allowing an adequate estimate to be deduced from the data. Over the full range of surface temperatures,

C has a value of 0.090 ± 0.005 $\mathrm{W/cm^2K^4}$. These values of Kapitza conductance are somewhat higher than previously reported measurements on aluminum by Mittag [15] and Denner [16].

One of the goals of the subcooled work was to determine whether the Kapitza conductance has a pressure dependence in the high heat flux regime. It can be seen in Fig. 6 that no significant pressure effect exists within the uncertainty of these results. This observation is consistent with earlier work on copper [17] for small temperature differences but conflicts with Madsen and McFadden [18] who showed a substantial change in Kapitza conductance with pressure at large temperature differences. The small variations in these results (about 2 percent in C) appear to be the consequence of cycling the sample to room temperature, thereby allowing a certain amount of surface contamination to occur.

Application to Magnet Design

There are two primary areas where heat transfer data is of critical importance to design of large scale superconductive magnetic energy storage. These subjects deal with the stability of the conductor and design of heat exchangers for a pressurized system.

The correct approach to the problem of cryogenic stability of magnets has yet to be established. A common method, although perhaps not the best, is to equate the heat generated in steady state with all the current being carried by the stabilizer, to the peak or recovery heat flux [19]. Under these circumstances, we can employ the data from this experiment to establish limits for heat fluxes and associated temperature drops for an aluminum stabilized magnet in He II. For example, if we design the conductor for a surface heat flux of 0.5 $\mathrm{W/cm^2}$ at 1.8 K, which is quite conservative, the associated surface temperature difference would be about 0.5 K. Operation of the system in the subcooled regime may prove to be a valuable modification of the design. Under these circumstances, we may consider raising the design heat flux substantially.

There are a number of distinct advantages to operation of a magnet system in subcooled rather than saturated He II. These points are summarized below:

(1) Improved peak heat flux,
(2) Improved recovery heat flux,
(3) No penalty in Kapitza conductance.

In addition, since the dielectric strength of helium gas is approximately proportional to density, subcooled operation also inhibits voltage breakdown [20]. Judging from the positive features that a subcooled system would bring, a design which takes advantage of these effects is encouraged.

In Fig. 7 we display a cross-sectional schematic of a conductor-dewar assembly for superconductive magnetic energy storage. The major components of the system are indicated. The conductor turns which make up the magnet, are contained in the high pressure liquid side, $P \sim 1$ atm. Heat loads are transmitted through the heat exchanger to the low pressure helium bath, which is connected directly to the refrigeration system. The load bearing struts, shown only schematically here, must be connected to the low pressure side to avoid taking the steady state heat loads through the heat exchanger. Design of the heat exchanger must provide an adequate path for heat loads resulting from conductor fault conditions, while allowing for only small temperature differences between the high and low pressure baths. Radiation and conduction heat loads are intercepted at optimized intermediate stations [21].

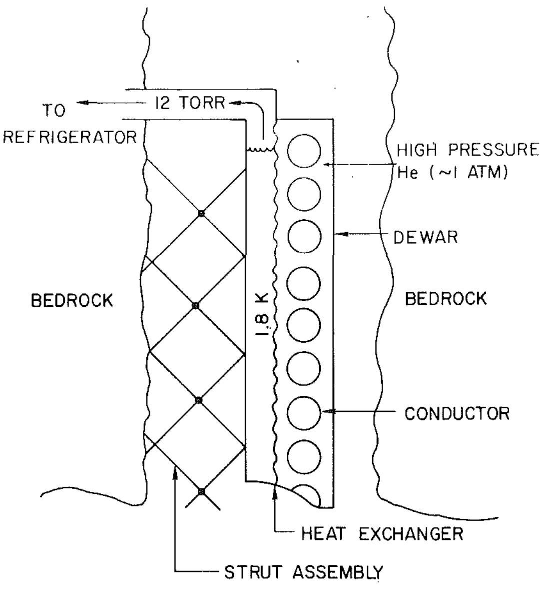

Fig. 7 Schematic design of conductor-dewar assembly which allows for operation in subcooled He II

In addition to the design of the heat exchanger, a pressurized cooling system requires an increased helium inventory. We have estimated, based on steady state heat flow in the bulk liquid, that twice as much helium could be required in this design. However, the comparison may be too severe since it does not include the necessary margins of safety.

Conclusions

The results of the above experiment to measure heat transfer from aluminum to He II indicate that subcooling creates definite advantages for magnet stabilization. The improvement in heat transfer is most noticeable in the recovery heat flux, which is almost three times higher in the subcooled work as compared to that near saturation.

Incorporation of these findings into the design of large scale superconducting energy storage magnets poses several problems. In addition to the design of the heat exchanger for such a system, a difficulty not previously addressed is that the subcooled system will probably require a larger helium inventory.

Acknowledgment

This work is supported by the U.S. Department of Energy under grant no. EY-76-C-02-2844.

References

1 *Wisconsin Superconductive Energy Storage Project,* Vol. II, University of Wisconsin, Madison, Wisc., Jan. 1976.

2 Ladkany, S. G., "High Current Al-TiNb Composite Conductors for Large Energy Storage Magnets," *Advances in Cryogenic Engineering,* Vol. 24, 1978, pp. 374–382.

3 Van Sciver, S. W., "Kapitza Conductance of Aluminum and Heat Transport from a Flat Surface Through a Large Diameter Tube to Saturated He II," *Advances in Cryogenic Engineering,* Vol. 23, 1978, pp. 340–348.

4 Van Sciver, S. W., "Cryostabilization of Large Superconducting Magnets Using Pool Boiled Helium II," *7th Symposium on Engineering Problems in Fusion Research,* Knoxville, Tenn., IEEE Publication No. 77CH1267-4-NPS, pp. 690–694.

5 Van Sciver, S. W., "Kapitza Conductance of Aluminum and Heat Transport Through Subcooled He II," *Cryogenics,* Vol. 18, No. 9, 1978, pp. 521–527.

6 Caspi, S., Lee, J. Y., and Frederking, T. H. K., "Oscillatory and Hysteretic Phenomena during Lambda Transition (He II-He I) Above the Thermodynamic Critical Pressure in the Presence of Heat Flow," *Advances in Cryogenic Engineering,* Vol. 23, 1978, pp. 349–357.

7 Arp, V., "Heat Transport Through Helium II," *Cryogenics,* Vol. 10, No. 4, 1970, pp. 96–105.

8 Linnet, C. and Frederking, T. H. K., "Thermal Conditions at the Gorter-Mellink Counterflow Limit Between 0.01 and 3 Bar," *Journal Low Temperature Physics,* Vol. 21, No. 3/4, 1975, pp. 447–462.

9 Vinen, W. F., "Mutual Friction in a Heat Current in Liquid Helium II, I. Experiments on Steady Heat Currents," *Proceedings Royal Society of London,* Vol. A240, No. 1220, 1957, pp. 114–127.

10 Allen, J. F. and Ganz, E., "The Influence of Pressure on the Thermal Conductivity of Liquid He II," *Proceedings Royal Society of London,* Vol. A171, No. A945, 1939, pp. 242–250.

11 Khalatnikov, I. M., *Introduction to the Theory of Superfluidity,* W. A. Benjamin, New York, 1965, Chap. 23.

12 Clement, B. W. and Frederking, T. H. K., "Thermal Boundary Resistance and Related Peak Flux During Supercritical Heat Transport From a Horizontal Surface Through a Short Tube to a Saturated Bath of Liquid He II," *Proceedings International Institute of Refrigeration Commission I,* International Institute of Refrigeration, 1966, pp. 49–59.

13 Irey, R. K., "Heat Transport in Liquid Helium II," *Heat Transfer at Low Temperatures,* Plenum, New York, 1975, pp. 325–355.

14 Synder, N. S., "Thermal Conductance at the Interface of a Solid and Helium II (Kapitza Conductance)," N.B.S. Technical Note No. 385, Dec. 1968, Institute of Basic Standards, National Bureau of Standards, Boulder, Col.

15 Mittag, K., "Kapitza Conductance and Thermal Conductivity of Copper Niobium and Aluminum in the Range from 1.3 K to 2.1 K," *Cryogenics*, Vol. 13, No. 2, 1973, pp. 94–99.

16 Denner, H. D., "Kapitza Resistance of Lead, Copper, Aluminum and Nickel Between 0.3 K and 1.4 K," *Proceedings of 6th Intern. Cryogenic Engineering Conference*, IPC Science and Technology Press, Guildford, England, 1976, pp. 348–352.

17 Challis, L. J., Dransfeld, K. and Wilks, J., "Heat Transfer Between Solids and Liquid Helium II," *Proceedings Royal Society of London*, Vol. A260, No. 1300, 1961, pp. 31–46.

18 Madsen, R. A. and McFadden, P. W., "Heat Transfer to an Unsaturated Bath of Liquid Helium II," *Advances in Cryogenic Engineering*, Vol. 13, 1968, pp. 617–623.

19 Kantrowitz, A. R., and Stekly, Z. J. J., "A New Principle for the Construction of Stabilized Superconducting Coils," *Applied Physics Letters*, Vol. 6, No. 3, Feb. 1965, pp. 56–57.

20 Hwang, K. F., "Dielectric Strength of Helium Vapor and Liquid at Temperatures Between 1.4 and 4.2 K," *Advances in Cryogenic Engineering*, Vol. 23, 1978, pp. 110–117.

21 Hilal, M. A. and McIntosh, G. E., "Cryogenic Design for Large Superconducting Energy Storage Magnets," *Advances in Cryogenic Engineering*, Vol. 21, 1976, pp. 69–77.

Errata

Erratum: G. B. Wallis, H. J. Richter: "An Isentropic Streamtube Model for Flashing Two-Phase Vapor-Liquid Flow", published in the November 1978 issue of the *Journal of Heat Transfer*, pp. 595–600.

The ordinate in Fig. 12 should read 10^3/kg/m^{2}s instead of 10^4 kg/m^{2}s.

journal of heat transfer

technical notes

This section contains shorter technical papers. These shorter papers will be subjected to the same review process as that for full papers.

Radiative and Convective Transfer for Real Gas Flow through a Tube with Specified Wall Heat Flux

C. W. Clausen[1] and T. F. Smith[2]

Nomenclature

A_w = inside surface area of tube wall zone, m^2

b = width of volume and surface zones, m

B = ratio of zone width to inside tube radius, $2b/D$

BNO = Boltzmann number, $\rho u c_p/\sigma T^3{}_{g,e}$

$\overrightarrow{GG}$ = directed flux area, volume zones, m^2

$\overrightarrow{GS}(\overrightarrow{SG})$ = directed flux area, volume and surface zones, m^2

K = total absorption coefficient, 1/m

N = number of volume and wall surface zones

Q = dimensionless wall heat flux, $q/\sigma T^4{}_{g,e}$

$\overrightarrow{SS}$ = directed flux area, surface zones, m^2

St = Stanton number

θ = dimensionless temperature, $T/T_{g,e}$

Introduction

The purpose of this study is to examine the interaction of radiative transfer with convective transfer for slug flow of an absorbing-emitting gas in a black wall circular tube with specified wall heat flux. Axial gas and wall temperature distributions are sought utilizing the zone method of solution where gas radiative properties are described by the weighted sum of gray gases model. The tube system treated here is similar to that studied by Nakra and Smith [1] with the exception that the prescribed duct wall temperature has been replaced with the wall heat flux boundary condition and axial variation of the Stanton number has been included. Details of the analysis and solution procedures may be found in [1] and [2].

Analysis

Performing a zonal analysis similar to that previously reported [1], steady-state energy balances for volume and wall zones, respectively, are expressed as

$$\left[\sum_{j=1}^{N}(\overrightarrow{G_jG_i}\theta^4{}_{g,j}+\overrightarrow{S_jG_i}\theta^4{}_{w,j})+\overrightarrow{S_eG_i}+\overrightarrow{S_0G_i}\theta^4{}_{s,0}\right]\Big/A_w - K_iD\theta^4{}_{g,i}+\frac{\mathrm{BNO}}{2B}(\theta_{g,i-1}-\theta_{g,i}) + \mathrm{BNO}\,\mathrm{St}_i(\theta_{w,i}-\theta_{g,i})=0 \quad (1)$$

$$\left[\sum_{j=1}^{N}(\overrightarrow{\mathrm{G_jS_i}}\theta^4{}_{g,j}+\overrightarrow{S_jS_i}\theta^4{}_{w,j})+\overrightarrow{S_eS_i}+\overrightarrow{S_0S_i}\theta^4{}_{s,0}\right]\Big/A_w - \theta^4{}_{w,i}+\mathrm{BNO}\,\mathrm{St}_i(\theta_{g,i}-\theta_{w,i})+Q_i=0 \quad (2)$$

where temperatures are referenced to the inlet gas temperature and $\theta_{g,i-1} = 1$ when $i = 1$ corresponding to the inlet gas temperature. The wall heat flux is based on the inside tube diameter D. For the results presented here, the inlet and outlet surfaces are porous and are assigned the inlet and outlet gas temperatures, respectively. Results from a more comprehensive analysis [2] which includes wall conduction in equation (2) illustrate that wall conduction has a negligible influence on gas temperatures and, furthermore, affects wall temperatures only for wall elements near the tube ends.

Axial variation of convective coefficient is considered in this analysis to account for entrance effects. The following correlation as recommended by Siegel and Keshock [3] for turbulent flow is employed

$$\frac{\mathrm{St}}{\mathrm{St}_\infty} = 1 + \frac{1}{2(x/D)^{5/6}} \quad (3)$$

where the subscript ∞ denotes the value of St for fully developed flow as evaluated from the Nusselt number correlations.

Gas radiative properties are evaluated from the weighted sum of gray gas model. Weighting factors and pressure absorption coefficients [1] for an equimolal mixture of carbon dioxide and water vapor at a combined partial pressure of 0.2206 atm and a total pressure of 1 atm are employed here. Directed flux areas are expressed in terms of the weighting factors and direct exchange areas. Direct exchange areas for a zone width to radius ratio of 0.25 [4] are utilized in this investigation. Thus, the tube length is divided into ten zones for tube length to diameter ratio $L/D = 1.25$.

Results and Discussion

Representative results for axial gas and wall temperature distributions are displayed in Fig. 1 for several values of BNO and uniform wall heat fluxes. All results apply for $\mathrm{St}_\infty = 0.01$, $D = 0.6$ m and $L/D = 1.25$. The upper portion of this figure corresponds to heating gas results where the inlet gas temperature is 556 K and positive wall heat fluxes are imposed. The lower portion shows cooling gas cases for an inlet gas temperature of 1944 K and heat extraction from the wall. Values of Q are limited by the requirement that temperatures must fall within the range of 556 to 1944 K as specified by the correlations for gas properties.

The heating gas results illustrate that gas and wall temperatures increase with axial distance. However, wall temperatures may decrease near the duct exit due to radiative loss to the cooler outlet surface. This latter finding is particularly evident for the higher values of BNO where a relatively small increase in gas temperature occurs. As BNO decreases, gas and wall temperatures increase and are nearly identical for the stagnant gas case where only radiative transfer exists. Similar but opposite trends are observed for the cooling gas results.

For the constant St cases, wall temperature distributions become

---

[1] Lawrence Livermore Laboratories, Livermore, CA

[2] Assoc. Professor, Division of Energy Engineering, The University of Iowa, Iowa City, Iowa 52242, Mem. ASME.

Contributed by the Heat Transfer Division for publication in the JOURNAL OF HEAT TRANSFER. Manuscript received by the Heat Transfer Division December 22, 1977.

symmetric as BNO increases. This behavior is attributed to the gas experiencing a smaller temperature change for the higher values of BNO. Thus, the outlet surface is at nearly the same temperature as the inlet surface and the radiant exchange terms are almost symmetric. Results are also presented in Fig. 1 for an axial variation of St. For comparison purposes, St $\approx$ 6 St_∞ at x/L = 0.05 corresponding to the midpoint of the first zone and 1.4 St_∞ at the tube exit for L/D = 1.25. The variable St produces lower wall temperatures but has a negligible influence on gas temperatures. Entrance effects are more predominant for wall zones near the duct inlet and are especially important for the higher magnitudes of BNO. The influence of St_∞ is examined later.

The general dependency of gas and wall temperatures on BNO and wall heat flux is similar over the entire tube length. Thus, gas and wall temperatures corresponding to the last zone are displayed in Fig. 2 as a function of BNO for several values of Q corresponding to the more common cooling gas case. All results are for a constant St. Horizontal curves labeled BNO = 0 depict gas and wall temperatures for a stagnant gas. The minimum value for BNO for larger heat fluxes is evident by the termination of several curves for gas temperatures where corresponding wall temperatures fall outside the range for gas radiative properties. Gas and wall temperatures coincide for $Q = -0.01$ and separate as necessitated by decreasing Q.

The influence of St_∞ is illustrated in Fig. 3 where results for cooling cases are presented for both axially varying and uniform St with St_∞ = 0, 0.005 and 0.01. Gas temperatures are shown only for St_∞ = 0.01 since they are insensitive to St_∞. Wall temperatures particularly near the entrance exhibit a strong dependence on St.

Fig. 4 presents effects of varying the tube length on gas and wall temperature distributions. Results are shown for values of L/D ranging from 1.25 to 5. Longer ducts necessitate smaller heat flux magnitudes or larger values of BNO to maintain wall temperatures within the required limits. Entrance effects are displayed only for L/D = 5 where St $\approx$ 1.1 St_∞ at the duct outlet. The outlet surface temperature has a strong influence on the temperature distributions particularly those for the wall and is even felt by the wall zones near the duct inlet. This latter finding is attributed to the transparent component of the gas. For L/D = 5 wall and gas temperature differ-

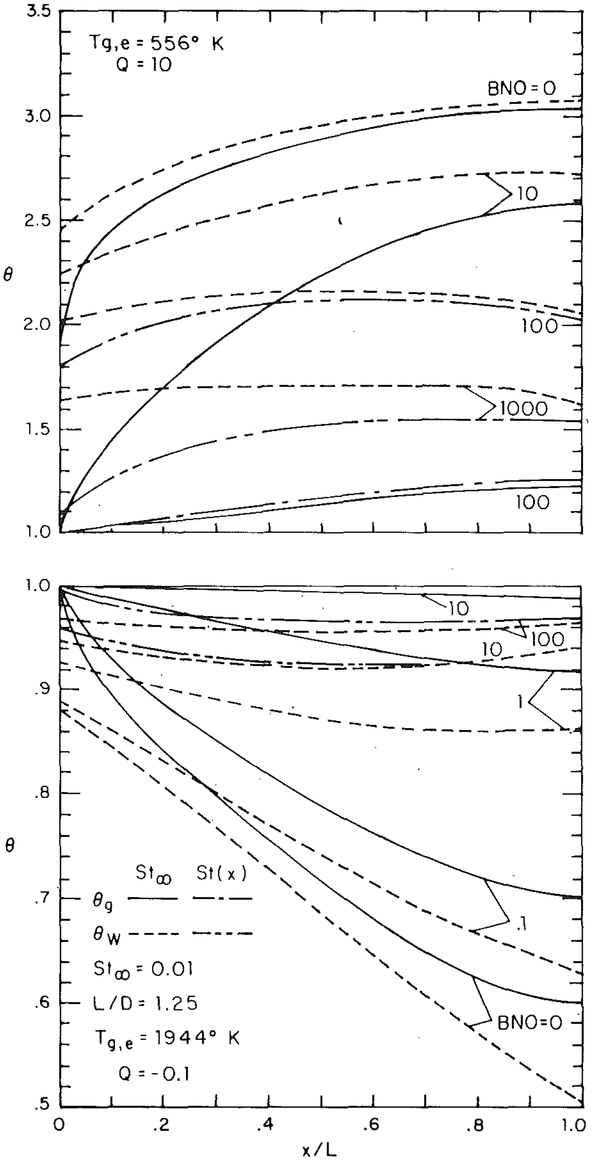

Fig. 1 Axial gas and wall temperature distributions

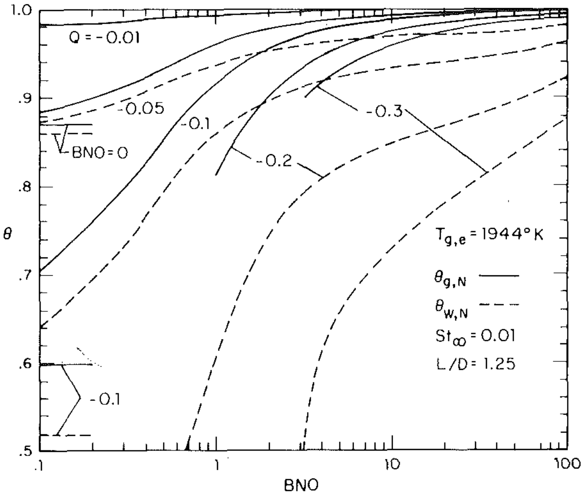

Fig. 2 Outlet gas and wall temperatures

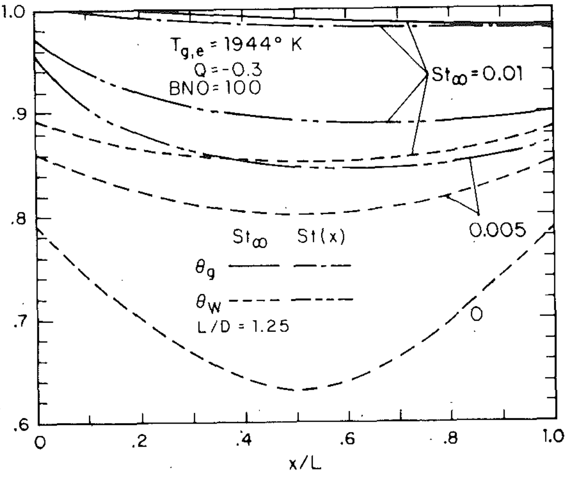

Fig. 3 Influence of the Stanton number

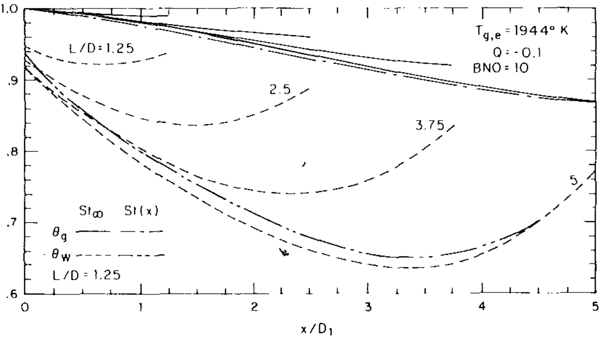

Fig. 4 Effect of length to diameter ratio

ences display a general increase with axial location. Results for longer ducts, however, are necessary in order to define the fully developed conditions.

References

1 Nakra, N. K. and Smith, T. F., "Combined Radiation-Convection for a Real Gas," ASME JOURNAL OF HEAT TRANSFER, Vol. 99, 1977, pp. 60–65.

2 Clausen, C. W., "Radiative and Convective Transfer for Real Gas Flow Through a Tube with Specified Wall Heat Flux," M.S. Thesis, Mechanical Engineering Program, The University of Iowa, 1977.

3 Siegel, R. and Keshock, E. G., "Wall Temperature in a Tube with Forced Convection, Internal Radiation Exchange and Axial Wall Heat Conduction," NASA TN D-2116, 1964.

4 Nakra, N. K., Smith, T. F. and Hering, R. G., "Direct Exchange Areas for Cylindrical Enclosures," Division of Energy Engineering, The University of Iowa TR-E-001-76, 1976.

Surface Radiative Exchange in Rod Bundles

C. L. Tien[1], R. A. Sanchez[2], D. A. Mandell[2], and C. T. McDaniel[2]

Introduction

Radiative exchange within a bundle of rods or tubes constitutes an important concern in many heat transfer systems such as reactor fuel bundles, boiler tube banks, etc. Accurate calculation of this radiative exchange is most formidable, particularly considering the geometric complexity and the interaction of surface radiation and convection with the interstitial absorbing and scattering medium. Even for the simple case of radiative exchange in a bundle of diffusely radiating rods immersed in a radiatively nonparticipative medium (e.g., vacuum, air), the calculation could become quite complicated and cumbersome. Previous applications [1] often treat the radiative heat transfer in a simplified manner, using uniform radiosity for each tube. The total heat transfer is then accurately predicted through development of empirical "convective" heat transfer coefficients from experimental data on prototypical geometries. However, a more mechanistic split between the radiative and convective heat transfer components is desirable to improve prediction generality and basic understanding of the phenomena involved.

General formulation of surface radiative exchange is commonly cast in the form of an integral equation [2]. Since few exact analytical solutions are available and exact numerical solutions are often impractical in terms of cost and effort, approximate methods have been widely employed for engineering applications. In particular, the lumped-system approximation which assumes uniform-radiosity surface elements has received considerable attention. The accuracy of the obtained results for radiative interchange can always be improved by subdividing further the lumped element. Such subdivisions result in an increasingly large number of algebraic equations, which combined with calculation of the associated configuration factors F_{ij} may again render the numerical solution impractical. Without further subdivision, the lumped-system approximation can also be improved by carrying out higher-order corrections. Indeed, it has been shown that the ordinary lumped-system approximation represents the first-order approximation in an iterative solution of the governing integral equation [3–5]. A second-order approximation, however, requires the tedious calculation of the second-order configuration factor, F_{ijk}, which is the fraction of energy leaving surface i that reaches surface k by way of surface j. Another similar correction method [6, 7] is based on the use of $F_{ij}\,F_{jk}$ to approximate F_{ijk}. It is the purpose of the present note to introduce and assess a convenient, approximate method for evaluating the radiative interchange in rod bundles.

The Anistropic Factor

Recently, Andersen [8] suggested a semi-empirical method, which appears especially convenient in calculating surface radiation exchange in rod bundles. In formulation, this method is nearly identical to the case with surfaces having both diffuse and specular components [2], although their conceptual bases are quite different. For the calculation of radiation in rod bundles, the radiosity of each rod is often assumed uniform, thus constituting one radiation node per rod in the radiation resistance network. Some rods, however, may have very non-uniform radiosity distributions depending on the neighboring rods and bounding surfaces. For instance, the side of the corner rods in a fuel-rod bundle facing the cold channel wall has a very different radiosity from that of the back side facing inner rods. Without subdividing each rod into several uniform-radiosity nodes, Andersen assumed that for each rod, say rod i, a fraction $(1 - \mu_i)$ of the irradiation H_{ji} is reflected isotropically and the rest μ_i is reflected directly back to its source, rod j. The anisotropic factor μ_i was suggested by Andersen as ½ for rods and $\pi/4$ for bounding surfaces on the basis of a simple semi-empirical argument.

It is interesting to note that the anisotropic factor μ can be related to the second-order configuration factor in accordance with the second-order approximation. From their respective definitions, there follows:

$$F_{jij} = F_{ji}\,[(1 - \mu_i)\,F_{ij} + \mu_i] \tag{1}$$

or

$$\mu_i = \frac{F_{jij} - F_{ij}F_{ji}}{F_{ji}\,(1 - F_{ij})} \tag{2}$$

When N surfaces surround surface i, then the result becomes:

$$\mu_i = \frac{\sum_{j=1}^{N} F_{jij} - \sum_{j=1}^{N} F_{ij}F_{ji}}{\sum_{j=1}^{N} F_{ji} - \sum_{j=1}^{N} F_{ij}F_{ji}} \tag{3}$$

The value of μ_i so obtained, however, is still approximate since it is based on the second-order approximation.

Numerical Examination

In order to shed some light on various approximate calculation schemes without being excessively tangled in geometric complexity, a simple system consisting of three rods surrounded by a rectangular boundary is considered. The system schematic is shown in Fig. 1. Due to the insulated horizontal boundaries, the present system also represents the case of three columns of rods kept at 1000, 1600, and 1000°F, respectively, and bounded by two infinite surfaces at 500°F. Even for this simple case, considerable numerical work must be carried out for a careful numerical examination. In addition to the ordinary multi-nodal computation, second-order configuration factors are calculated from the Monte-Carlo method [9]. A larger number of cases have been calculated, but only some representative results will be presented below to illustrate the major findings.

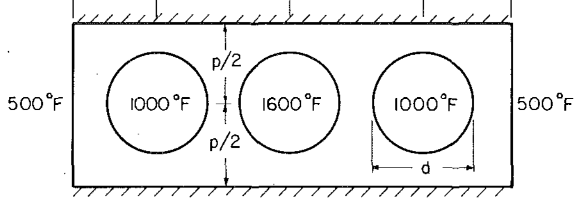

Fig. 1 Schematic of the system

---

[1] Department of Mechanical Engineering, University of California, Berkeley, CA. Fellow, ASME

[2] Nuclear Energy Engineering Division, General Electric Company, San Jose, CA.

Contributed by the Heat Transfer Division for publication in the JOURNAL OF HEAT TRANSFER. Manuscript received by the Heat Transfer Division September 21, 1978.

ences display a general increase with axial location. Results for longer ducts, however, are necessary in order to define the fully developed conditions.

References

1 Nakra, N. K. and Smith, T. F., "Combined Radiation-Convection for a Real Gas," ASME Journal of Heat Transfer, Vol. 99, 1977, pp. 60–65.
2 Clausen, C. W., "Radiative and Convective Transfer for Real Gas Flow Through a Tube with Specified Wall Heat Flux," M.S. Thesis, Mechanical Engineering Program, The University of Iowa, 1977.
3 Siegel, R. and Keshock, E. G., "Wall Temperature in a Tube with Forced Convection, Internal Radiation Exchange and Axial Wall Heat Conduction," NASA TN D-2116, 1964.
4 Nakra, N. K., Smith, T. F. and Hering, R. G., "Direct Exchange Areas for Cylindrical Enclosures," Division of Energy Engineering, The University of Iowa TR-E-001-76, 1976.

Surface Radiative Exchange in Rod Bundles

C. L. Tien[1], R. A. Sanchez[2], D. A. Mandell[2], and C. T. McDaniel[2]

Introduction

Radiative exchange within a bundle of rods or tubes constitutes an important concern in many heat transfer systems such as reactor fuel bundles, boiler tube banks, etc. Accurate calculation of this radiative exchange is most formidable, particularly considering the geometric complexity and the interaction of surface radiation and convection with the interstitial absorbing and scattering medium. Even for the simple case of radiative exchange in a bundle of diffusely radiating rods immersed in a radiatively nonparticipative medium (e.g., vacuum, air), the calculation could become quite complicated and cumbersome. Previous applications [1] often treat the radiative heat transfer in a simplified manner, using uniform radiosity for each tube. The total heat transfer is then accurately predicted through development of empirical "convective" heat transfer coefficients from experimental data on prototypical geometries. However, a more mechanistic split between the radiative and convective heat transfer components is desirable to improve prediction generality and basic understanding of the phenomena involved.

General formulation of surface radiative exchange is commonly cast in the form of an integral equation [2]. Since few exact analytical solutions are available and exact numerical solutions are often impractical in terms of cost and effort, approximate methods have been widely employed for engineering applications. In particular, the lumped-system approximation which assumes uniform-radiosity surface elements has received considerable attention. The accuracy of the obtained results for radiative interchange can always be improved by subdividing further the lumped element. Such subdivisions result in an increasingly large number of algebraic equations, which combined with calculation of the associated configuration factors F_{ij} may again render the numerical solution impractical. Without further subdivision, the lumped-system approximation can also be improved by carrying out higher-order corrections. Indeed, it has been shown that the ordinary lumped-system approximation represents the first-order approximation in an iterative solution of the governing integral equation [3–5]. A second-order approximation, however, requires the tedious calculation of the second-order configuration factor, F_{ijk}, which is the fraction of energy leaving surface i that reaches surface k by way of surface j. Another similar correction method [6, 7] is based on the use of $F_{ij}\,F_{jk}$ to approximate F_{ijk}. It is the purpose of the present note to introduce and assess a convenient, approximate method for evaluating the radiative interchange in rod bundles.

The Anistropic Factor

Recently, Andersen [8] suggested a semi-empirical method, which appears especially convenient in calculating surface radiation exchange in rod bundles. In formulation, this method is nearly identical to the case with surfaces having both diffuse and specular components [2], although their conceptual bases are quite different. For the calculation of radiation in rod bundles, the radiosity of each rod is often assumed uniform, thus constituting one radiation node per rod in the radiation resistance network. Some rods, however, may have very non-uniform radiosity distributions depending on the neighboring rods and bounding surfaces. For instance, the side of the corner rods in a fuel-rod bundle facing the cold channel wall has a very different radiosity from that of the back side facing inner rods. Without subdividing each rod into several uniform-radiosity nodes, Andersen assumed that for each rod, say rod i, a fraction $(1 - \mu_i)$ of the irradiation H_{ji} is reflected isotropically and the rest μ_i is reflected directly back to its source, rod j. The anisotropic factor μ_i was suggested by Andersen as ½ for rods and $\pi/4$ for bounding surfaces on the basis of a simple semi-empirical argument.

It is interesting to note that the anisotropic factor μ can be related to the second-order configuration factor in accordance with the second-order approximation. From their respective definitions, there follows:

$$F_{jij} = F_{ji}\,[(1 - \mu_i)\,F_{ij} + \mu_i] \tag{1}$$

or

$$\mu_i = \frac{F_{jij} - F_{ij}F_{ji}}{F_{ji}\,(1 - F_{ij})} \tag{2}$$

When N surfaces surround surface i, then the result becomes:

$$\mu_i = \frac{\sum_{j=1}^{N} F_{jij} - \sum_{j=1}^{N} F_{ij}F_{ji}}{\sum_{j=1}^{N} F_{ji} - \sum_{j=1}^{N} F_{ij}F_{ji}} \tag{3}$$

The value of μ_i so obtained, however, is still approximate since it is based on the second-order approximation.

Numerical Examination

In order to shed some light on various approximate calculation schemes without being excessively tangled in geometric complexity, a simple system consisting of three rods surrounded by a rectangular boundary is considered. The system schematic is shown in Fig. 1. Due to the insulated horizontal boundaries, the present system also represents the case of three columns of rods kept at 1000, 1600, and 1000°F, respectively, and bounded by two infinite surfaces at 500°F. Even for this simple case, considerable numerical work must be carried out for a careful numerical examination. In addition to the ordinary multi-nodal computation, second-order configuration factors are calculated from the Monte-Carlo method [9]. A larger number of cases have been calculated, but only some representative results will be presented below to illustrate the major findings.

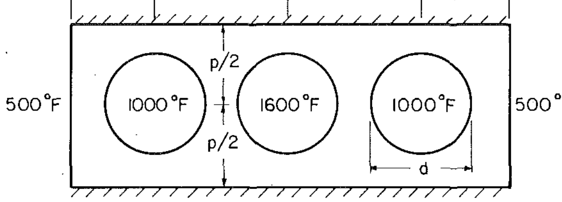

Fig. 1 Schematic of the system

---

[1] Department of Mechanical Engineering, University of California, Berkeley, CA. Fellow, ASME

[2] Nuclear Energy Engineering Division, General Electric Company, San Jose, CA.

Contributed by the Heat Transfer Division for publication in the Journal of Heat Transfer. Manuscript received by the Heat Transfer Division September 21, 1978.

Table 1 Values of Q (Btu/hr) and μ for $d/p = 0.77$ and different ρ's

ρ	0.1	0.3	0.5	0.7	0.9
Q_1	10616	8669	6458	4022	1386
Q_2	10304	8091	5949	3751	1344
Q_8	10227	7854	5706	3603	1319
Q_{24}	10197	7796	5649	3567	1312
$Q^{I}(=Q_1)$	10616	8669	6458	4022	1386
Q^{II}	10623	8670	6447	3989	1360
Q_μ	10003	7473	5318	3339	1260
μ_r	0.5	0.5	0.5	0.5	0.5
μ_c	0.120	0.183	0.179	0.166	0.143

Table 1 shows the radiative heat transfer rate Q, leaving all three rods for $d/p = 0.77$ and various surface reflectivities, ρ. The number of subdivided surfaces for each cylinder is shown by the number subscript on Q. The values of Q are decreasing as the number of surfaces per cylinder increases from one to twenty-four and are asymptotically approaching a limit which can be regarded as the exact solution to the problem. The anisotropic solution Q_μ refers to the total heat transfer as calculated by using the anisotropic factor concept with averaged values of μ_c and μ_r calculated from equation (3), where subscripts c and r refer to surrounding cooled walls and rods, respectively. Untabulated data show that for d/p increasing from 0.1 to 0.99, μ_r increases from 0.3 to 0.7 approximately, while μ_c increases from 0.04 to 0.4 as compared to Andersen's suggested values of 0.5 for μ_r and $\pi/4$ for μ_c. The Q_μ solution underpredicts the radiative heat transfer with a maximum difference between Q_{24} and Q_μ of 6.4 percent for $\rho = 0.7$, Q_1 is 12.8 percent above Q_{24}. In all cases, Q_μ provides considerable improvement over Q_1 in accuracy.

Also shown in Table 1 are radiative heat transfer results from the lumped approximation (one uniform-radiosity surface per rods), Q^{I}, and the second-order approximation, Q^{II}. They give virtually identical results. This is true for all values of d/p. Thus the second-order solutions renders little improvement over the standard lumped analysis when rod bundles are being considered.

The last two rows of Table 1 present the results of a parametric study of the most appropriate values of μ_r and μ_c for use in the anisotropic formulation. From both Andersen's suggestion and the calculation method based on the second-order approximation, it is logical to fix the value of μ_r as 0.5 but to determine μ_c from the best fit to Q_{24}. The fact that the resulting range of μ_c is relatively narrow (0.12–0.18) greatly enhances the effectiveness of this approximate calculation method. Based on the present study, a good value for μ_c would be 0.15 instead of $\pi/4$ as suggested by Andersen. An additional parametric study based on a five-by-five bundle in a square enclosure further substantiates the present finding that the anisotropic formulation can be used effectively; also, as the number of rods increases, the effect of boundary radiation becomes less, and the solution is less sensitive to the value of μ_c.

Conclusion

The anisotropic formulation is a convenient way of accurately accounting for non-uniform radiosity of the rod and channel surfaces in the calculation of the radiative interchange. Based on this study, anisotropic reflection factors (μ) of 0.5 for the rods and 0.15 for the surrounding channel walls are recommended.

Acknowledgment

The authors wish to express their deep appreciations to Drs. G. E. Dix, B. S. Shiralkar and J. G. M. Andersen for their helpful discussions and comments.

References

1 Dix, G. E. and Andersen, J. G. M., "Spray Cooling Heat Transfer for a BWR Fuel Bundle," Symposium on the Thermal and Hydraulic Aspects of Nuclear Reactor Safety, Vol. 1, ASME, 1977, pp. 217–248.

2 Sparrow, E. M. and Cess, R. D., *Radiation Heat Transfer*, McGraw-Hill, New York, 1978, Chapters 3 and 5.

3 Love, T. J., *Radiative Heat Transfer*, Charles E. Merrill, Inc., Columbus, OH, 1968, Appendix V.

4 Love, T. J. and Turner, W. D., "High-Order Approximations for Lumped System Analysis of Evacuated Enclosures," *AIAA Progress in Astronautics and Aeronautics: Thermal Design Principles of Spacecraft and Entry Bodies*, Vol. 21, edited by J. T. Bevans, Academic Press, New York, 1969, pp. 3–19.

5 Turner, W. D., and Camacho-Almonte, J., "Second-Order Approximation for Radiative Heat Transfer between Simple Two-Dimensional Surfaces," *AIAA Journal*, Vol. 14, 1976, pp. 5–6.

6 Bevans, J. T. and Edwards, D. K., "Radiation Exchange in an Enclosure with Directional Wall Properties," ASME JOURNAL OF HEAT TRANSFER, Vol. 87, 1965, pp. 388–396.

7 Bobco, R. P., "A Script-F Matrix Formulation for Enclosures with Arbitrary Surface Emission and Reflection Characteristics," ASME JOURNAL OF HEAT TRANSFER, Vol. 93, 1971, pp. 33–40.

8 Andersen, J. G. M., "CORECOOL, A Model for the Temperature Distribution and Two Phase Flow in a Fuel Element under LOCA Conditions," NEDO-21325, General Electric Company, San Jose, California, 1976.

9 Siegel, R. and Howell, J. R., *Thermal Radiation Heat Transfer*, McGraw-Hill Book Company, New York, 1972, Chapter 11.

Evaluation of Intergrating Sphere Surfaces for Infrared Pyrradiometers

R. Birkebak[1] and Md. Alamgir[2]

Nomenclature

A_d, A_i = area of detector receiving surface, inlet port area, mm^2
A_s, A_w = total surface area of sphere and active sphere area for reflection, mm^2
E = radiant flux entering the sphere, W
e = emission power, W/m^2
k = proportionality constant for the detector, $W/\mu v$
Q_c, O_k = convective and conductive energy transfer rated from the detector, W
Q_d, O_i, Q_w = radiant energy transfer rate to the detector by self interchange, from the source, and from the sphere wall, respectively, W
T = temperature, K
V, V_c, V_d = detector output, μv
θ = angle of incidence
ρ = surface directional reflectance
$\bar{\rho}_w$ = average wall reflectance, $[\rho_w(A_w/A_s) + \rho_d(A_d/A_s)]$

Subscripts

a = ambient
c = shutter closed, convention
d = detector
i = source, inlet port
k = conduction
0 = reference state, detector
w = sphere wall

Introduction

The integrating sphere radiometer has been used to monitor solar radiation [1] and its use was initially limited to the solar spectrum because of the lack of a suitable diffuse reflecting surface in the infrared. However, during the mid-1960's and later, several surfaces were found which could be used in the infrared. Birkebak and Eckert [2] used a sulfur coated integrating sphere while McCullough, et al. [3] used NaCl as a wall coating. Wood and Smith [4] observed that gold coated grit surfaces were good infrared diffuse reflectors. Birkebak [5, 6] had already recognized this and had patented an integrating sphere pyrradiometer (ISP) which used aluminized roughened metal or plastic surfaces.

We have employed three surfaces which are diffusely reflecting [7]

---

[1] Research Professor, University of Kentucky, Lexington, KY. Mem. ASME

[2] Research Assistant, University of Kentucky, Lexington, KY.

Contributed by the Heat Transfer Division for publication in the JOURNAL OF HEAT TRANSFER. Manuscript received by the Heat Transfer Division April 20, 1978

Table 1 Values of Q (Btu/hr) and μ for $d/p = 0.77$ and different ρ's

ρ	0.1	0.3	0.5	0.7	0.9
Q_1	10616	8669	6458	4022	1386
Q_2	10304	8091	5949	3751	1344
Q_8	10227	7854	5706	3603	1319
Q_{24}	10197	7796	5649	3567	1312
$Q^{I}(=Q_1)$	10616	8669	6458	4022	1386
Q^{II}	10623	8670	6447	3989	1360
Q_μ	10003	7473	5318	3339	1260
μ_r	0.5	0.5	0.5	0.5	0.5
μ_c	0.120	0.183	0.179	0.166	0.143

Table 1 shows the radiative heat transfer rate Q, leaving all three rods for $d/p = 0.77$ and various surface reflectivities, ρ. The number of subdivided surfaces for each cylinder is shown by the number subscript on Q. The values of Q are decreasing as the number of surfaces per cylinder increases from one to twenty-four and are asymptotically approaching a limit which can be regarded as the exact solution to the problem. The anisotropic solution Q_μ refers to the total heat transfer as calculated by using the anisotropic factor concept with averaged values of μ_c and μ_r calculated from equation (3), where subscripts c and r refer to surrounding cooled walls and rods, respectively. Untabulated data show that for d/p increasing from 0.1 to 0.99, μ_r increases from 0.3 to 0.7 approximately, while μ_c increases from 0.04 to 0.4 as compared to Andersen's suggested values of 0.5 for μ_r and $\pi/4$ for μ_c. The Q_μ solution underpredicts the radiative heat transfer with a maximum difference between Q_{24} and Q_μ of 6.4 percent for $\rho = 0.7$, Q_1 is 12.8 percent above Q_{24}. In all cases, Q_μ provides considerable improvement over Q_1 in accuracy.

Also shown in Table 1 are radiative heat transfer results from the lumped approximation (one uniform-radiosity surface per rods), Q^{I}, and the second-order approximation, Q^{II}. They give virtually identical results. This is true for all values of d/p. Thus the second-order solutions renders little improvement over the standard lumped analysis when rod bundles are being considered.

The last two rows of Table 1 present the results of a parametric study of the most appropriate values of μ_r and μ_c for use in the anisotropic formulation. From both Andersen's suggestion and the calculation method based on the second-order approximation, it is logical to fix the value of μ_r as 0.5 but to determine μ_c from the best fit to Q_{24}. The fact that the resulting range of μ_c is relatively narrow (0.12–0.18) greatly enhances the effectiveness of this approximate calculation method. Based on the present study, a good value for μ_c would be 0.15 instead of $\pi/4$ as suggested by Andersen. An additional parametric study based on a five-by-five bundle in a square enclosure further substantiates the present finding that the anisotropic formulation can be used effectively; also, as the number of rods increases, the effect of boundary radiation becomes less, and the solution is less sensitive to the value of μ_c.

Conclusion

The anisotropic formulation is a convenient way of accurately accounting for non-uniform radiosity of the rod and channel surfaces in the calculation of the radiative interchange. Based on this study, anisotropic reflection factors (μ) of 0.5 for the rods and 0.15 for the surrounding channel walls are recommended.

Acknowledgment

The authors wish to express their deep appreciations to Drs. G. E. Dix, B. S. Shiralkar and J. G. M. Andersen for their helpful discussions and comments.

References

1 Dix, G. E. and Andersen, J. G. M., "Spray Cooling Heat Transfer for a BWR Fuel Bundle," Symposium on the Thermal and Hydraulic Aspects of Nuclear Reactor Safety, Vol. 1, ASME, 1977, pp. 217–248.

2 Sparrow, E. M. and Cess, R. D., *Radiation Heat Transfer*, McGraw-Hill, New York, 1978, Chapters 3 and 5.

3 Love, T. J., *Radiative Heat Transfer*, Charles E. Merrill, Inc., Columbus, OH, 1968, Appendix V.

4 Love, T. J. and Turner, W. D., "High-Order Approximations for Lumped System Analysis of Evacuated Enclosures," *AIAA Progress in Astronautics and Aeronautics: Thermal Design Principles of Spacecraft and Entry Bodies*, Vol. 21, edited by J. T. Bevans, Academic Press, New York, 1969, pp. 3–19.

5 Turner, W. D., and Camacho-Almonte, J., "Second-Order Approximation for Radiative Heat Transfer between Simple Two-Dimensional Surfaces," *AIAA Journal*, Vol. 14, 1976, pp. 5–6.

6 Bevans, J. T. and Edwards, D. K., "Radiation Exchange in an Enclosure with Directional Wall Properties," ASME JOURNAL OF HEAT TRANSFER, Vol. 87, 1965, pp. 388–396.

7 Bobco, R. P., "A Script-F Matrix Formulation for Enclosures with Arbitrary Surface Emission and Reflection Characteristics," ASME JOURNAL OF HEAT TRANSFER, Vol. 93, 1971, pp. 33–40.

8 Andersen, J. G. M., "CORECOOL, A Model for the Temperature Distribution and Two Phase Flow in a Fuel Element under LOCA Conditions," NEDO-21325, General Electric Company, San Jose, California, 1976.

9 Siegel, R. and Howell, J. R., *Thermal Radiation Heat Transfer*, McGraw-Hill Book Company, New York, 1972, Chapter 11.

Evaluation of Intergrating Sphere Surfaces for Infrared Pyrradiometers

R. Birkebak[1] and Md. Alamgir[2]

Nomenclature

A_d, A_i = area of detector receiving surface, inlet port area, mm^2
A_s, A_w = total surface area of sphere and active sphere area for reflection, mm^2
E = radiant flux entering the sphere, W
e = emission power, W/m^2
k = proportionality constant for the detector, $W/\mu v$
Q_c, O_k = convective and conductive energy transfer rated from the detector, W
Q_d, O_i, Q_w = radiant energy transfer rate to the detector by self interchange, from the source, and from the sphere wall, respectively, W
T = temperature, K
V, V_c, V_d = detector output, μv
θ = angle of incidence
ρ = surface directional reflectance
$\bar{\rho}_w$ = average wall reflectance, $[\rho_w(A_w/A_s) + \rho_d(A_d/A_s)]$

Subscripts

a = ambient
c = shutter closed, convention
d = detector
i = source, inlet port
k = conduction
0 = reference state, detector
w = sphere wall

Introduction

The integrating sphere radiometer has been used to monitor solar radiation [1] and its use was initially limited to the solar spectrum because of the lack of a suitable diffuse reflecting surface in the infrared. However, during the mid-1960's and later, several surfaces were found which could be used in the infrared. Birkebak and Eckert [2] used a sulfur coated integrating sphere while McCullough, et al. [3] used NaCl as a wall coating. Wood and Smith [4] observed that gold coated grit surfaces were good infrared diffuse reflectors. Birkebak [5, 6] had already recognized this and had patented an integrating sphere pyrradiometer (ISP) which used aluminized roughened metal or plastic surfaces.

We have employed three surfaces which are diffusely reflecting [7]

---

[1] Research Professor, University of Kentucky, Lexington, KY. Mem. ASME

[2] Research Assistant, University of Kentucky, Lexington, KY.

Contributed by the Heat Transfer Division for publication in the JOURNAL OF HEAT TRANSFER. Manuscript received by the Heat Transfer Division April 20, 1978

in the infrared and present a critical evaluation of the ISP performance using these surfaces. The instrument described in this paper can be used either as a pyrradiometer or pyrgeometer. The results presented are for long wave length black body hemispherical radiation.

Description of Surfaces

We have used the concepts of Birkebak [5, 6] and Wood and Smith [4] for generating diffusely reflecting surfaces. Such a surface consists of multilayers of adhesive, silicon carbide particles, SC, filler, *F*, and reflecting materials. The acrylic filler material is used to fill and round out the spaces between the scattering particles. The top reflecting materials used were either vapor deposited aluminum or a bronze enamel acrylic spray paint.

The surfaces were applied directly to the interior of 0.1 m dia sphere whose interior had been sand blasted. The details of the surface preparation and description are given by Alamgir [7]. The basic surface descriptions from substrate to coating are:

Surface 1,	180 grit (SC)-*F*-40 μm glass beads-*F*-Al.,
Surface 2,	180 grit (SC)-*F*-320 grit (SC)-*F*-Al,
Surface 3,	180 grit (SC)-bronze enamel.

Experimental Apparatus

The experimental apparatus used consisted of 1) three integrating spheres, 2) a thin film thermopile, 3) a goniometric system and focused black body source, 4) a 2π sterradian black body source and 5) associated amplifiers and recorders.

The integrating spheres were constructed of aluminum. Their inside diameter was 101.6 mm, the inlet port 49.5 mm in diameter, and the detector port 12.5 mm in diameter. These spheres were milled into aluminum cylinders 150 mm in diameter and into which coolant flow passages had been machined [7]. The spheres were coated with the surfaces described previously. The thermopile used was a thin film type developed at AEDC [8] and had a receiving area of 123.3 mm^2.

A schematic diagram of the goniometric system used for wall diffuseness measurements is shown in Fig. 1. The sphere was held in a fixed position and the source-optics rotated about an axis passing through and parallel to the entrance port and in the plane A-B. The system was adjustable for 9 deg steps from 0 to 90 degs. A shutter was provided so that the small black body source could be blocked off from the sphere. The whole system was housed in an insulated box one meter on a side and painted black on its interior surfaces.

A 2π sterradian black body source was used to simulate a thermal environment. It consisted of a 0.2 m dia hemisphere which could be electrically heated or cooled by a circulating coolant. The ISP was placed on the diametral plane of this source.

Measurement of Surface Diffuseness and Reflectance

The diffuseness of an integrating sphere wall coating was measured by irradiating the sphere entrance port with collimated black body radiation at different angles of incidence.

It can easily be shown that the output of a detector on the sphere wall is

$$V_d(\theta) = k\rho_w E_i(\theta)\,(A_d/A_s)(1/(1-\bar{\rho}_w)) \tag{1}$$

$$= f(e_i, A_i, (A_d/A_s), \rho_w, \bar{\rho}_w)\cos\theta \tag{1-a}$$

where $E_i(\theta) = e_i A_i \cos\theta$ is the irradiance from the black body source, and A_i is the inlet port area, A_s is the sphere area, A_d is the detector area, and ρ_w and $\bar{\rho}_w$ are reflectances.

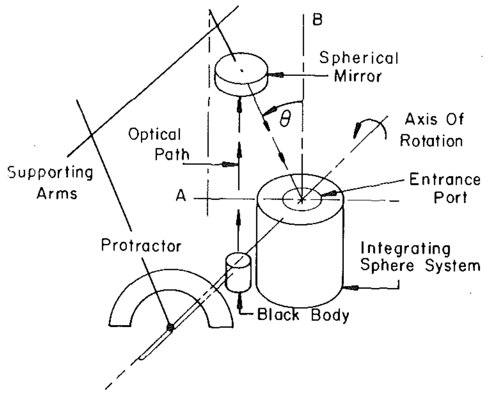

Fig. 1 Schematic diagram of goniometer apparatus

If the sphere coating is diffusely reflecting, the output $V_d(\theta)$ should then be the $\cos\theta$. Any deviations from $\cos\theta$ is a measure of the coating's nondiffuseness.

Pyrradiometer Analysis

The analysis is based upon the assumption that the irradiance is from a 2π diffuse source and the detector is able to view the entrance port A_i.

An energy balance written on the detector gives

$$Q_i + Q_w + Q_d = e_d A_d + Q_c + Q_k \tag{2}$$

where Q_i is the incoming radiation from the source;

$$Q_i = e_i A_i \left(\frac{A_d}{A_s}\right)\left(\frac{1}{1-\bar{\rho}_w}\right), \tag{3}$$

Q_w is the emitted radiation from the wall,

$$Q_w = e_w A_w \left(\frac{A_d}{A_s}\right)\left(\frac{1}{1-\bar{\rho}_w}\right), \tag{4}$$

Q_d is the radiant interchange of the detector with itself,

$$Q_d = e_d A_d \rho_w \left(\frac{A_w}{A_s}\right)\left(\frac{A_d}{A_s}\right)\left(\frac{1}{1-\bar{\rho}_w}\right) \tag{5}$$

The first term on the right of equation (2) is the emitted flux from the detector, Q_c represents any convective heat transfer and Q_k is the conductive heat transfer from the detector. We will assume that the output of the detector is proportional to Q_k

$$Q_k = kV \tag{6}$$

where k (W/μv) is the detector constant and V is its output in microvolts. Let V_0 represent the condition when $T_d = T_w = T_i \neq T_a$. then

$$k\Delta V = Q_{\text{net}}\,(\text{Radiation}) - \Delta Q_c = Q_{\text{net}} \tag{7}$$

If the detector constant k is known, then the 2π environmental radiation E_i can be calculated by solving equations (2–6) for E_i.

Results and Conclusions

Wall diffuseness and Reflectance. The diffuseness of the three types of integrating sphere wall coatings was checked for black body source temperatures of 366, 422, 477 and 533 K. At each angular position two readings of the detector output were taken, one with the shutter open, V, and the other with the shutter closed, V_c. The second reading corresponded to the detector output due to background radiation. The detector response at $\theta = 18$ deg was used to normalize the data. For angles less than 18 deg a portion of the specular component is lost through the entrance port. It is assumed that at this angle of incidence, the cosine relationship is exactly satisfied. The data were evaluated using

$$((V - V_c)/(V(18\text{ deg}) - V(18\text{ deg})_c)\cos 18\text{ deg} \tag{8}$$

The data were also corrected for the finite thickness (0.5 mm) of the lip on the entrance port which for larger angle of illumination reduced the port area.

Fig. 2 shows the percent deviation of the normalized detector output from the cosine distribution for the three coatings studied. The data are the average values for the four source temperatures used. The scatter in the data is attributed to slight variations in surface finish at various positions. All three surfaces appear to be diffuse reflectors up to 72 deg with a variation of +1.5 to −3 percent from a cosine distribution. At 81 deg the surfaces are within −6.5 percent of the cosine distribution. The results indicate that all three surfaces are satisfac-

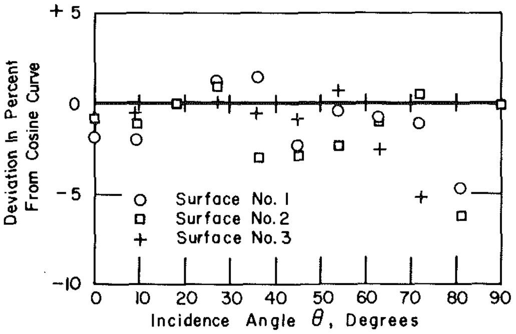

Fig. 2 Surface coating reflection distribution deviation from a diffuse surface

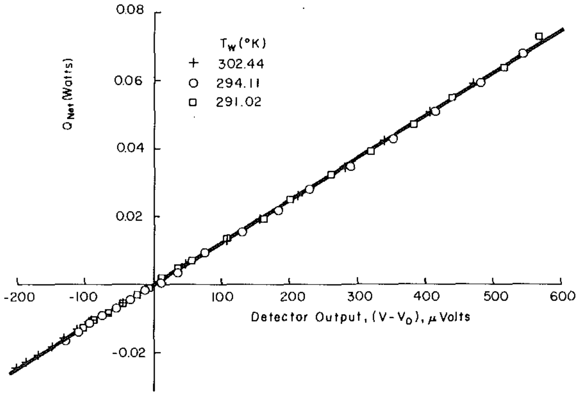

Fig. 3 Pyrradiometer calibration curve for the 2π black body source

tory diffusers of infrared radiation when used in an integrating sphere.

The reflectances of the coatings were determined for source temperatures from 366 to 533 K. Details of the test procedure are given in [7].

The average wall reflectance $\bar{\rho}_w$ of surface coating no. 1, was 0.818, for surface no. 2, 0.911 and for surface no. 3, 0.896. The lower value for coating no. 1 was caused by non-uniform surface coating of the aluminum film and was verified by inspecting the surface with an optical comparator.

A value of 0.94 was reported by Sherrel [9] for a gold coated grit surface. A higher wall reflectance value is desirable, however, the 4 percent difference between our results and Sherrel's becomes less important when ease of surface preparation and cost is considered.

The ISP with costing no. 2 was calibrated using the 2π sterradian black body source. The source temperature, T_i, was varied from 278 to 353 K while the ISP wall temperature, T_w, was varied from 291 to 303 K. In addition, the reference temperature, T_d, of the thermopile and air temperature, T_a, were measured. The thermopile output was amplified and then recorded with a DVM.

The experimental data were used in equation (7) along with the area measurements. A least square curve fitting method was employed to determine the constant k. The resulting equation is $Q_{\text{net}} = 1.2498 \times 10^{-4}\,\Delta V - 1.59 \times 10^{-4}$ where the value of k has the units (W/μV). The results of Q_{net} are shown in Fig. 3 and the data for E_i are represented by the correlation equation with a mean deviation of ± 2 percent. The offset Q_{net} for ΔV of zero is the result of our inability to completely account for the detector heat losses.

We have developed an ISP which responds to directional radiation in a cosine manner and in which the detector is shielded from most environmental effects. The system is simple to construct and to use.

Acknowledgments

The authors gratefully acknowledge the financial support from the Mechanical Engineering Department of the University of Kentucky.

References

1 McCullough, B. A., et al., "An Intensity and Uniformity Monitor for Solar Simulators," *J. of Space Craft and Rockets,* Vol. 4, 1967, pp. 1114–1116.

2 Birkebak R. C., and Eckert, E. R. G., "Effect of Roughness of Metal Surfaces on Angular Distribution of Monochromatic Reflected Radiation," ASME JOURNAL OF HEAT TRANSFER, 87, 1965, pp. 85–94.

3 McCullough, B. A., et al., "A Vacuum Integrating Sphere for In-Situ Reflectance Measurements at 77k from 0.5 to 10 Microns," *Progress in Astronautics and Aeronautics,* ed. by G. Heller, Vol. 20, 1967, pp. 137–150.

4 Wood B. E., and Smith, A. M., "An Investigation of Infrared Diffuser Surfaces," Arnold Engineering Development Center Report No. AEDC-TR-22, 1974.

5 Birkebak, R. C., "Infrared Detector Utilizing an Integrating Sphere Radiometer," Patent No. 3, 222, 522; U.S. Patent Office, 1965

6 Birkebak, R. C., "Apparatus and Method of Measuring the Emissivity of an Object," Patent No. 3,401, 263; U.S. Patent Office, 1968.

7 Alamgir, Md., "An Experimental Study of the Integrating Sphere for Diffuse Infrared Radiation Measurements," M.S. Thesis, Department of Mechanical Engineering, University of Kentucky, 1977.

8 Frazine, D. F., "The Design and Construction of Thin Film Radiation Thermopiles," Arnold Engineering Development Center Report No. AEDC-TR-66-38, 1966.

9 Sherrel, F. G., "Determination of Hemispherical Emittance by Measurements of Infrared Bihemispherical Reflectance," Arnold Engineering Development Center Report No. AEDC-TR-69-213, 1969.

Surface Wetted Area during Transition Boiling in Forced Convective Flow

H. S. Ragheb[1] **and S. C. Cheng**[1]

Introduction

During a loss-of-coolant accident (LOCA) in a water cooled nuclear reactor, some portions of the core are under the transition boiling heat transfer mode. The transition boiling mode is most efficient at its lower temperature boundary which corresponds to the critical heat flux (CHF). Immediately after CHF, the heated surface can no longer support the continuous liquid contact, and heat transfer deteriorates due to the increase of area covered by dry patches.

The heated surface during transition boiling is partially wet and partially covered by vapor. Hence a convenient way to deal with transition boiling is to assume that it is a combination of both unstable nucleate boiling and unstable film boiling alternately existing at any given location at the heated surface. The variation of heat transfer rate with temperature is primarily a result of the change in the fraction of time that each boiling mode exists at a given location as stated by Berenson [1].

Following Berenson's description of the transition boiling mode, Kalinin, et al. [2] weighted the two heat transfer components (nucleate and film boiling) by f_k, the fraction of surface that is wet. The total heat flux q_t is then expressed as

$$q_t = q_{NB} f_k + q_{FB}\,(1 - f_k) \qquad (1)$$

and

$$f_k = \frac{q_t - q_{FB}}{q_{NB} - q_{FB}} \qquad (2)$$

where q_{NB} and q_{FB} represent nucleate boiling and film boiling, respectively, assuming that both expressions can be extrapolated into the transition boiling régime. Knowing q_{NB} and q_{FB} from correlations, and using experimental data of q_t, one can obtain the expression of f_k in terms of T_w, wall temperature, T_{max}, wall temperature at maximum heat flux, and $T_{\min}$, wall temperature at minimum heat flux.

---

[1] Department of Mechanical Engineering University of Ottawa, Ottawa, Canada

Contributed by the Heat Transfer Division for publication in the JOURNAL OF HEAT TRANSFER. Manuscript received by the Heat Transfer Division September 29, 1978.

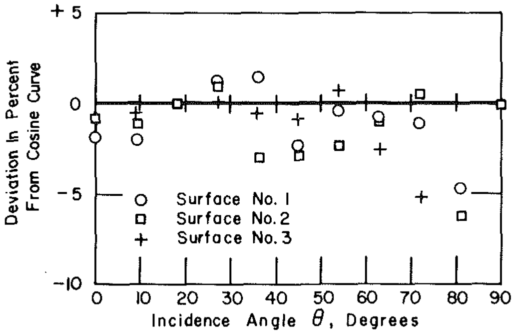

Fig. 2 Surface coating reflection distribution deviation from a diffuse surface

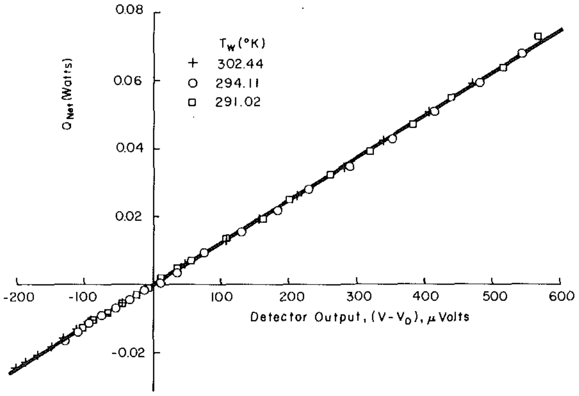

Fig. 3 Pyrradiometer calibration curve for the 2π black body source

tory diffusers of infrared radiation when used in an integrating sphere.

The reflectances of the coatings were determined for source temperatures from 366 to 533 K. Details of the test procedure are given in [7].

The average wall reflectance $\bar{\rho}_w$ of surface coating no. 1, was 0.818, for surface no. 2, 0.911 and for surface no. 3, 0.896. The lower value for coating no. 1 was caused by non-uniform surface coating of the aluminum film and was verified by inspecting the surface with an optical comparator.

A value of 0.94 was reported by Sherrel [9] for a gold coated grit surface. A higher wall reflectance value is desirable, however, the 4 percent difference between our results and Sherrel's becomes less important when ease of surface preparation and cost is considered.

The ISP with costing no. 2 was calibrated using the 2π sterradian black body source. The source temperature, T_i, was varied from 278 to 353 K while the ISP wall temperature, T_w, was varied from 291 to 303 K. In addition, the reference temperature, T_d, of the thermopile and air temperature, T_a, were measured. The thermopile output was amplified and then recorded with a DVM.

The experimental data were used in equation (7) along with the area measurements. A least square curve fitting method was employed to determine the constant k. The resulting equation is $Q_{\text{net}} = 1.2498 \times 10^{-4}\, \Delta V - 1.59 \times 10^{-4}$ where the value of k has the units (W/μV). The results of Q_{net} are shown in Fig. 3 and the data for E_i are represented by the correlation equation with a mean deviation of ± 2 percent. The offset Q_{net} for ΔV of zero is the result of our inability to completely account for the detector heat losses.

We have developed an ISP which responds to directional radiation in a cosine manner and in which the detector is shielded from most environmental effects. The system is simple to construct and to use.

Acknowledgments

The authors gratefully acknowledge the financial support from the Mechanical Engineering Department of the University of Kentucky.

References

1 McCullough, B. A., et al., "An Intensity and Uniformity Monitor for Solar Simulators," *J. of Space Craft and Rockets,* Vol. 4, 1967, pp. 1114–1116.

2 Birkebak R. C., and Eckert, E. R. G., "Effect of Roughness of Metal Surfaces on Angular Distribution of Monochromatic Reflected Radiation," ASME JOURNAL OF HEAT TRANSFER, 87, 1965, pp. 85–94.

3 McCullough, B. A., et al., "A Vacuum Integrating Sphere for In-Situ Reflectance Measurements at 77k from 0.5 to 10 Microns," *Progress in Astronautics and Aeronautics,* ed. by G. Heller, Vol. 20, 1967, pp. 137–150.

4 Wood B. E., and Smith, A. M., "An Investigation of Infrared Diffuser Surfaces," Arnold Engineering Development Center Report No. AEDC-TR-22, 1974.

5 Birkebak, R. C., "Infrared Detector Utilizing an Integrating Sphere Radiometer," Patent No. 3, 222, 522; U.S. Patent Office, 1965

6 Birkebak, R. C., "Apparatus and Method of Measuring the Emissivity of an Object," Patent No. 3,401, 263; U.S. Patent Office, 1968.

7 Alamgir, Md., "An Experimental Study of the Integrating Sphere for Diffuse Infrared Radiation Measurements," M.S. Thesis, Department of Mechanical Engineering, University of Kentucky, 1977.

8 Frazine, D. F., "The Design and Construction of Thin Film Radiation Thermopiles," Arnold Engineering Development Center Report No. AEDC-TR-66-38, 1966.

9 Sherrel, F. G., "Determination of Hemispherical Emittance by Measurements of Infrared Bihemispherical Reflectance," Arnold Engineering Development Center Report No. AEDC-TR-69-213, 1969.

Surface Wetted Area during Transition Boiling in Forced Convective Flow

H. S. Ragheb[1] **and S. C. Cheng**[1]

Introduction

During a loss-of-coolant accident (LOCA) in a water cooled nuclear reactor, some portions of the core are under the transition boiling heat transfer mode. The transition boiling mode is most efficient at its lower temperature boundary which corresponds to the critical heat flux (CHF). Immediately after CHF, the heated surface can no longer support the continuous liquid contact, and heat transfer deteriorates due to the increase of area covered by dry patches.

The heated surface during transition boiling is partially wet and partially covered by vapor. Hence a convenient way to deal with transition boiling is to assume that it is a combination of both unstable nucleate boiling and unstable film boiling alternately existing at any given location at the heated surface. The variation of heat transfer rate with temperature is primarily a result of the change in the fraction of time that each boiling mode exists at a given location as stated by Berenson [1].

Following Berenson's description of the transition boiling mode, Kalinin, et al. [2] weighted the two heat transfer components (nucleate and film boiling) by f_k, the fraction of surface that is wet. The total heat flux q_t is then expressed as

$$q_t = q_{NB} f_k + q_{FB}(1 - f_k) \tag{1}$$

and

$$f_k = \frac{q_t - q_{FB}}{q_{NB} - q_{FB}} \tag{2}$$

where q_{NB} and q_{FB} represent nucleate boiling and film boiling, respectively, assuming that both expressions can be extrapolated into the transition boiling régime. Knowing q_{NB} and q_{FB} from correlations, and using experimental data of q_t, one can obtain the expression of f_k in terms of T_w, wall temperature, T_{max}, wall temperature at maximum heat flux, and $T_{\min}$, wall temperature at minimum heat flux.

---

[1] Department of Mechanical Engineering University of Ottawa, Ottawa, Canada

Contributed by the Heat Transfer Division for publication in the JOURNAL OF HEAT TRANSFER. Manuscript received by the Heat Transfer Division September 29, 1978.

Kalinin, et al. obtained two functions for f_k, one being exponential decay with increasing T_w.

Tong and Young [3] suggested that the total heat flux q_t is a sum of two components, i.e.,

$$q_t = q_{TB} + q_{FB} \tag{3}$$

where q_{TB} is the transition boiling component which decays with increasing T_w (see Fig. 4). They obtained an empirical, exponential decay expression for q_{TB} in terms of T_w and x, quality. Hsu and Graham [4] related this expression to the fraction of wetted area. Recently, Tong [5] suggested that the wetted area fraction can be related to q_{TB} by

$$f_T = q_{TB}/q_{NB} \tag{4}$$

where q_{NB} can be approximated by $q_{\rm CHF}$ in the transition boiling regime.

The purpose of this study is (1) to examine the measurements of the wetted area during a quenching process using an electric probe, and (2) to compare these measurements with the predictions of Kalinin and Tong. The study involving the electric probe in detecting the phase change on a heated surface has been reported in [6, 7].

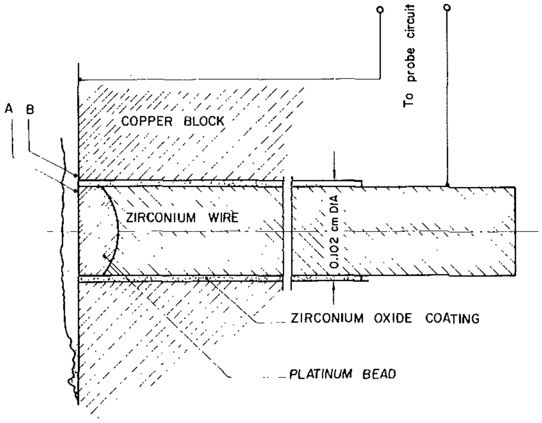

Fig. 1 Probe configuration

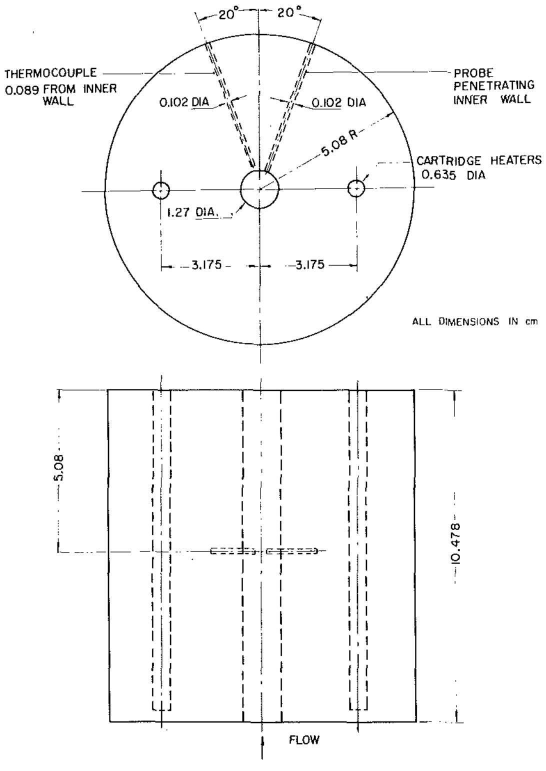

Fig. 2 Test section

Experimental Apparatus

Fig. 1 shows schematically the configuration of the probe. The probe made of zirconium wire coated by a platinum tip is suited for high temperature operation. It can detect the presence of liquid droplets contact on the heated surface by measuring voltage drop between the platinum tip (as one electrode) and the heating surface (as another electrode). The test section with the probe and the adjacent thermocouple is shown in Fig. 2. Tests were conducted for water at atmospheric pressure under flow boiling conditions with G, mass flux, varying from 34–102 kg/m^{2}s and $\Delta T_{\rm sub}$, inlet subcooling, varying from 0–28 °C. Further details of the experimental apparatus and procedures may be found in [6, 7].

Results and Discussion

Fig. 3 shows an example of the probe signal and the adjacent thermocouple signal for a typical rewetting run. The region BC characterizes the transition boiling mode where the wetted area increases with time. The boiling curve constructed as shown in Fig. 4 was based on the temperature-time trace of the thermocouple (Fig. 3) using the technique developed in [8].

For a typical point in transition boiling, the quantities of q_t, q_{NB}, and q_{FB} defined in the Kalinin's approach are illustrated in Fig. 4. q_{NB} has been extrapolated to $T_{\rm min}$ and q_{FB} to $T_{\rm max}$. The extrapolation of q_{FB} in this case being a horizontal line is due to the fact that film boiling is almost independent of wall superheat under the present flow conditions [9–11], q_{TB} defined by Tong and Young is also indicated in the figure.

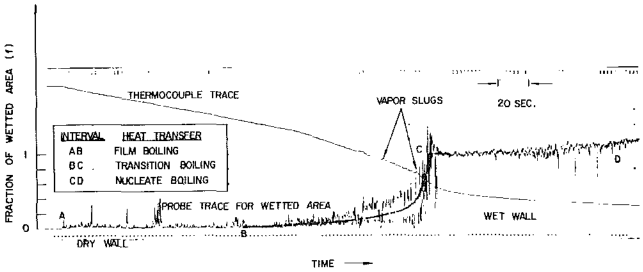

Fig. 3 Signals recorded from the probe and the thermocouple in flow boiling

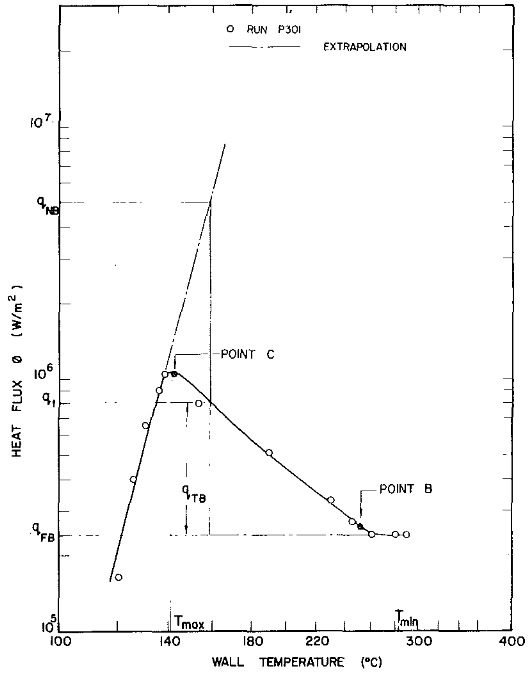

Fig. 4 Boiling curve of water for $G = 68$ kg/m^{2}s $8\Delta T_{\rm sub} = 27.8$ °C

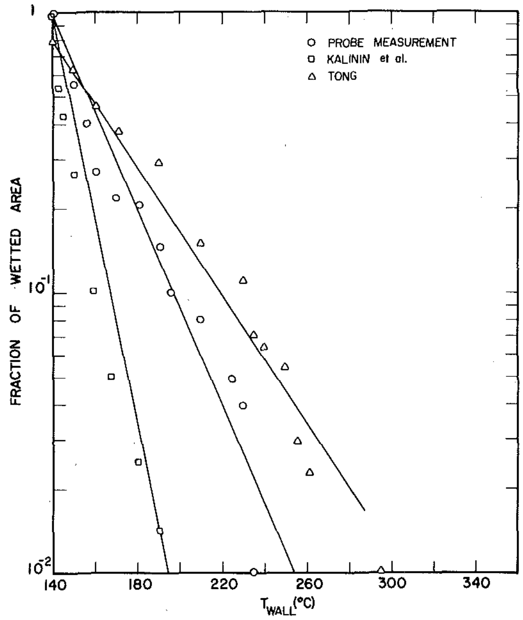

Fig. 5 Comparison of measured and predicted fraction of wetted area

The predicted fraction of wetted area using equations (2) and (4) based on the boiling curve of Fig. 4 is shown in Fig. 5. The measured fraction of wetted area by the probe is also presented in Fig. 5 for comparison. This is obtained from Fig. 3 by assuming $f = 1$ at CHF and $f = 0$ at the minimum heat flux (to be explained later), the points (as a function of time) in between are read directly from the graph. Since the time coordinate is related to T_w in the data reduction process, thus f versus T_w can be obtained as shown. In general, both measured and predicted results display a same exponential trend (which becomes a straight line in a semi-log plot). The predicted wetted area using Tong's expression is in closer agreement with the probe measurement, except at CHF. As seen from Figs. 3 and 4, (1) the onset of intermittent wetting at point B is very close to the minimum heat flux, hence it can be assumed $f = 0$ at the minimum heat flux, and (2) the onset of continuous liquid contact at point C coincides with the CHF point, and furthermore, point C approaches the mean value of voltage drop from the nucleate boiling side (continuous liquid contact) as indicated in Fig. 3, thus $f = 1$ can be assumed at CHF.

The agreement between the probe measurement and Tong's expression suggests a new method of predicting transition boiling. If q_{CHF} and q_{FB} are given, with the measured fraction of wetted area by the probe, transition boiling can be calculated from equations (3) and (4).

Conclusions

1 The fraction of wetted area predicted using Kalinin's approach in transition boiling under flow conditions compares favorably with the probe measurement.

2 Transition boiling under flow conditions can be predicted if (1) q_{CHF} and q_{FB} are given, and (2) the measured fraction of wetted area from the probe is available.

3 This study provides some insight of transition boiling phenomenon through the measurement of the fraction of wetted area. It is hoped that this will lead to improved modelling of the transition boiling process.

Acknowledgments

Financial support from the U.S. Nuclear Regulatory Comission is acknowledged.

References

1 Berenson, P. J. "Experiments in Pool-Boiling Heat Transfer," *Int. J. of Heat and Mass Transfer,* Vol. 5, 1962, pp. 985–999.

2 Kalinin, E. K., Berlin, I. I., Kostyuk, V. V., and Nosova, E. M. "Heat Transfer in Transition Boiling of Cryogenic Liquids," *Proceedings, Cryogenics Engineering Conference,* Queen's University, Kingston, Ontario, Canada, 1975, pp. 273–277.

3 Tong, L. S., and Young, J. D. "A Phenomenological Transition and Film Boiling Heat Transfer Correlation," *Proc. of the 5th Int. Heat Transfer Conference,* Vol. IV, Tokyo, Japan, 1974, pp. 120–124.

4 Hsu, Y. Y. and Graham, R. W., *Transport Processes in Boiling and Two-Phase Systems,* McGraw-Hill, 1976, pp. 254–256.

5 Tong, L. S. "Heat Transfer in Reactor Safety," *Proceedings, 6th Int. Heat Transfer Conference,* Vol. 6, Toronto, Canada, 1978, p. 296.

6 Ragheb, H. S., Cheng, S. C., and Groeneveld, D. C. "Measurement of Transition Boiling Boundaries in Forced Convective Flow," *Int. J. of Heat and Mass Transfer* (in press).

7 Ragheb, H. S., "Development of Electric Probes to Detect Phase Change at a Heated Surface," M.A.Sc. Thesis, Univ. of Ottawa, 1977.

8 Cheng, S. C., Heng, K. T., and Ng, W., "A Technique to Construct a Boiling Curve from Quenching Data Considering Heat Loss," *Int. J. of Multiphase Flow,* Vol. 3, 1977, pp. 495–499.

9 Cheng, S. C., Ng, W., Heng, K. T. and Groeneveld, D. C., "Measurements of Transition Boiling Data Under Forced Convective Conditions," ASME JOURNAL OF HEAT TRANSFER, Vol. 100, 1978, pp. 382–384.

10 Fung, K. K., "Forced Convective Transition Boiling," M.A.Sc. Thesis, Dept. of Mechanical Engineering, University of Toronto, 1976.

11 Newbold, F. J., Ralph, J. C., and Ward, J. A., "Post-Dryout Heat Transfer Under Low Flow and Low Quality Conditions," AERE-R8390, 1976.

Correlation of Burnout Data for Disk Heaters Cooled by Liquid Jets[1]

J. H. Lienhard[2] and M. Z. Hasan[3]

Elsewhere in this issue Katto and Shimizu [1] present excellent new observations of the peak or "burnout" heat flux, $q_{\max}$, for liquid jets impinging on horizontal disk heaters. Recently Lienhard and Eichhorn [2] offered the following correlation for the burnout heat flux, $q_{\max}$, in this situation:

$$\frac{\phi\beta}{f(r)} = \left(\frac{\beta^3}{We_f}\right)^A, \tag{1}$$

where

$$\phi \equiv \frac{q_{\max}}{\rho_g h_{fg} u_f};\; We_f \equiv \frac{\rho_f u_f^2 D}{\sigma};\; r \equiv \frac{\rho_f}{\rho_g};\; \beta \equiv \frac{D}{d}, \tag{2}$$

and where ρ_f and ρ_g are the saturated liquid and vapor densities, h_{fg} is the latent heat of the liquid, σ is the surface tension, u_f and d are the jet velocity and diameter, and D is the heater diameter. The function, $f(r)$, cannot be obtained theoretically so the value of $f(r) \sim r^{0.725}$ was borrowed from an earlier correlation of their own data [3, 4] by Monde and Katto [3]. The exponent, A, requires further explanation:

Equation (1) was based upon a stability criterion that says: burnout will occur when the rate at which kinetic energy of the evaporated liquid is added to the escaping mixture exceeds the rate at which the newly created surface of droplets consumes mechanical energy. To complete this balance it was argued on the basis of the droplet formation literature that

$$\text{droplet diameter} \sim d/\beta\,[We_f\phi^2\beta]^a f_1(r), \tag{3}$$

where $f(r)$ was an unknown function and a was an unknown exponent. It is important to note that a might depend on either r or We_f without violating the rationale in [2]. The function A was

$$A \equiv \frac{1-3a}{3-6a} = A(r \text{ or } We_f). \tag{4}$$

---

[1] We are pleased to acknowledge the NSF for supporting this work under Grant ENG 77-25029

[2] Professor, Boiling and Phase Change Laboratory, Mechanical Engineering Department, University of Kentucky, Lexington, KY 40506. Fellow, ASME.

[3] Research Assistant, Boiling and Phase Change Laboratory, Mechanical Engineering Department, University of Kentucky, Lexington, KY 40506.

Contributed by the Heat Transfer Division for publication in the JOURNAL OF HEAT TRANSFER. Manuscript received by the Heat Transfer Division January 11, 1979.

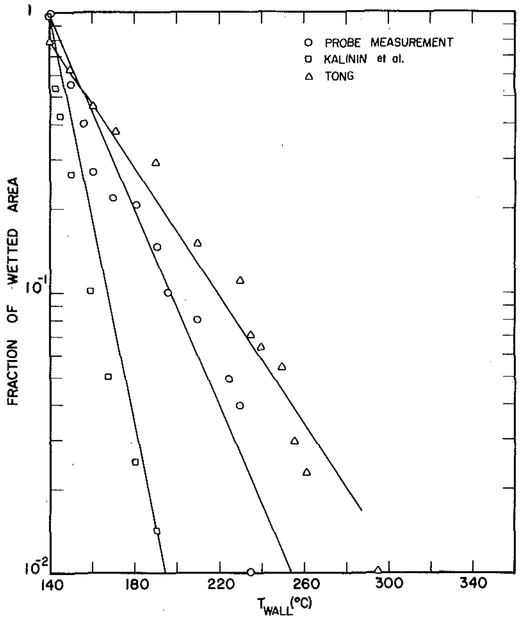

Fig. 5 Comparison of measured and predicted fraction of wetted area

The predicted fraction of wetted area using equations (2) and (4) based on the boiling curve of Fig. 4 is shown in Fig. 5. The measured fraction of wetted area by the probe is also presented in Fig. 5 for comparison. This is obtained from Fig. 3 by assuming $f = 1$ at CHF and $f = 0$ at the minimum heat flux (to be explained later), the points (as a function of time) in between are read directly from the graph. Since the time coordinate is related to T_w in the data reduction process, thus f versus T_w can be obtained as shown. In general, both measured and predicted results display a same exponential trend (which becomes a straight line in a semi-log plot). The predicted wetted area using Tong's expression is in closer agreement with the probe measurement, except at CHF. As seen from Figs. 3 and 4, (1) the onset of intermittent wetting at point B is very close to the minimum heat flux, hence it can be assumed $f = 0$ at the minimum heat flux, and (2) the onset of continuous liquid contact at point C coincides with the CHF point, and furthermore, point C approaches the mean value of voltage drop from the nucleate boiling side (continuous liquid contact) as indicated in Fig. 3, thus $f = 1$ can be assumed at CHF.

The agreement between the probe measurement and Tong's expression suggests a new method of predicting transition boiling. If q_{CHF} and q_{FB} are given, with the measured fraction of wetted area by the probe, transition boiling can be calculated from equations (3) and (4).

Conclusions

1 The fraction of wetted area predicted using Kalinin's approach in transition boiling under flow conditions compares favorably with the probe measurement.

2 Transition boiling under flow conditions can be predicted if (1) q_{CHF} and q_{FB} are given, and (2) the measured fraction of wetted area from the probe is available.

3 This study provides some insight of transition boiling phenomenon through the measurement of the fraction of wetted area. It is hoped that this will lead to improved modelling of the transition boiling process.

Acknowledgments

Financial support from the U.S. Nuclear Regulatory Comission is acknowledged.

References

1 Berenson, P. J. "Experiments in Pool-Boiling Heat Transfer," *Int. J. of Heat and Mass Transfer,* Vol. 5, 1962, pp. 985–999.

2 Kalinin, E. K., Berlin, I. I., Kostyuk, V. V., and Nosova, E. M. "Heat Transfer in Transition Boiling of Cryogenic Liquids," *Proceedings, Cryogenics Engineering Conference,* Queen's University, Kingston, Ontario, Canada, 1975, pp. 273–277.

3 Tong, L. S., and Young, J. D. "A Phenomenological Transition and Film Boiling Heat Transfer Correlation," *Proc. of the 5th Int. Heat Transfer Conference,* Vol. IV, Tokyo, Japan, 1974, pp. 120–124.

4 Hsu, Y. Y. and Graham, R. W., *Transport Processes in Boiling and Two-Phase Systems,* McGraw-Hill, 1976, pp. 254–256.

5 Tong, L. S. "Heat Transfer in Reactor Safety," *Proceedings, 6th Int. Heat Transfer Conference,* Vol. 6, Toronto, Canada, 1978, p. 296.

6 Ragheb, H. S., Cheng, S. C., and Groeneveld, D. C. "Measurement of Transition Boiling Boundaries in Forced Convective Flow," *Int. J. of Heat and Mass Transfer* (in press).

7 Ragheb, H. S., "Development of Electric Probes to Detect Phase Change at a Heated Surface," M.A.Sc. Thesis, Univ. of Ottawa, 1977.

8 Cheng, S. C., Heng, K. T., and Ng, W., "A Technique to Construct a Boiling Curve from Quenching Data Considering Heat Loss," *Int. J. of Multiphase Flow,* Vol. 3, 1977, pp. 495–499.

9 Cheng, S. C., Ng, W., Heng, K. T. and Groeneveld, D. C., "Measurements of Transition Boiling Data Under Forced Convective Conditions," ASME JOURNAL OF HEAT TRANSFER, Vol. 100, 1978, pp. 382–384.

10 Fung, K. K., "Forced Convective Transition Boiling," M.A.Sc. Thesis, Dept. of Mechanical Engineering, University of Toronto, 1976.

11 Newbold, F. J., Ralph, J. C., and Ward, J. A., "Post-Dryout Heat Transfer Under Low Flow and Low Quality Conditions," AERE-R8390, 1976.

Correlation of Burnout Data for Disk Heaters Cooled by Liquid Jets[1]

J. H. Lienhard[2] and M. Z. Hasan[3]

Elsewhere in this issue Katto and Shimizu [1] present excellent new observations of the peak or "burnout" heat flux, $q_{\max}$, for liquid jets impinging on horizontal disk heaters. Recently Lienhard and Eichhorn [2] offered the following correlation for the burnout heat flux, $q_{\max}$, in this situation:

$$\frac{\phi\beta}{f(r)} = \left(\frac{\beta^3}{We_f}\right)^A, \tag{1}$$

where

$$\phi \equiv \frac{q_{\max}}{\rho_g h_{fg} u_f};\; We_f \equiv \frac{\rho_f u_f^2 D}{\sigma};\; r \equiv \frac{\rho_f}{\rho_g};\; \beta \equiv \frac{D}{d}, \tag{2}$$

and where ρ_f and ρ_g are the saturated liquid and vapor densities, h_{fg} is the latent heat of the liquid, σ is the surface tension, u_f and d are the jet velocity and diameter, and D is the heater diameter. The function, $f(r)$, cannot be obtained theoretically so the value of $f(r) \sim r^{0.725}$ was borrowed from an earlier correlation of their own data [3, 4] by Monde and Katto [3]. The exponent, A, requires further explanation:

Equation (1) was based upon a stability criterion that says: burnout will occur when the rate at which kinetic energy of the evaporated liquid is added to the escaping mixture exceeds the rate at which the newly created surface of droplets consumes mechanical energy. To complete this balance it was argued on the basis of the droplet formation literature that

$$\text{droplet diameter} \sim d/\beta\,[We_f\phi^2\beta]^a f_1(r), \tag{3}$$

where $f(r)$ was an unknown function and a was an unknown exponent. It is important to note that a might depend on either r or We_f without violating the rationale in [2]. The function A was

$$A \equiv \frac{1-3a}{3-6a} = A(r \text{ or } We_f). \tag{4}$$

---

[1] We are pleased to acknowledge the NSF for supporting this work under Grant ENG 77-25029

[2] Professor, Boiling and Phase Change Laboratory, Mechanical Engineering Department, University of Kentucky, Lexington, KY 40506. Fellow, ASME.

[3] Research Assistant, Boiling and Phase Change Laboratory, Mechanical Engineering Department, University of Kentucky, Lexington, KY 40506.

Contributed by the Heat Transfer Division for publication in the JOURNAL OF HEAT TRANSFER. Manuscript received by the Heat Transfer Division January 11, 1979.

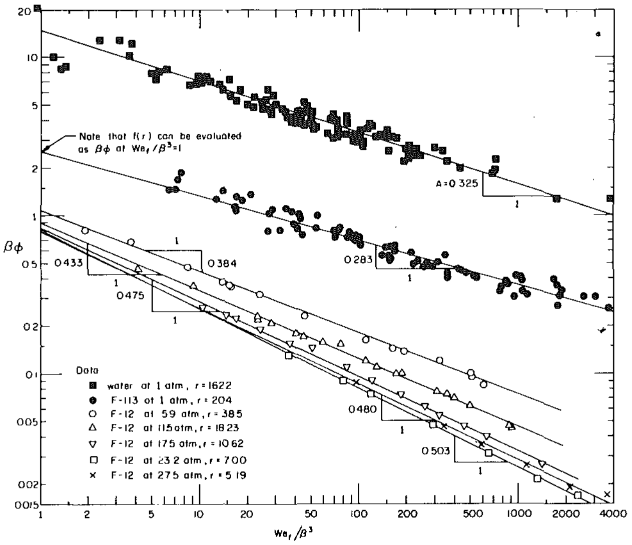

Fig. 1 Determination of $f(r)$ and $A(r)$

In [2] A was found to depend weakly on We_f if $f(r)$ was taken to be $\sim r^{0.725}$. Now that Katto and Shimizu have provided an excellent set of data over a vastly extended range of r, let us leave f and A as undetermined functions for the moment.[4] Then we plot $\phi\beta$ against We_f/β^3 in Fig. 1, for the collected data of [1, 3, 4].

The data in Fig. 1 define a unique straight line for each value of r. The slope of each line is equal to A, and its intercept at $\beta^3/We_f = 1$ is equal to $f(r)$. These functions are plotted in Fig. 2[5] on the basis of faired lines through the data[6] in Fig. 1. Notice that they define perfectly smooth curves. $A(r)$ is a complicated function bounded between approximately $1/4$ and $1/2$, and it can be approximated within ±3 percent over the range $1622 \geqslant r \geqslant 5$, by the expression:

$$A(r) \simeq 0.4346 + 0.1027 \ln r - 0.0474 (\ln r)^2 + 0.00426 (\ln r)^3 \quad (5)$$

Actually it is more convenient to pick a value of A from Fig. 2 for use in computations than it is to use equation (5). The function $f(r)$ can also be read from Fig. 2, although it is given exactly by the straight line:

$$f(r) = 0.744 + 0.0084\, r \quad (6)$$

The present correlation—equation (1) with values of $A(r)$ and $f(r)$ from Fig. 2 is virtually the same as that given in [2] except in that the present functions $A(r)$ and $f(r)$ are valid over a large range of r. In [2] the function $A(r)$ was not spelled out since data were only available for two values of r, and the power law function of Katto, et al. was used for $f(r)$. His power law function matched equation (6) very closely at the two values of r that were previously available.

With known values of the functions, $f(r)$ and $A(r)$, we plot the final correlation for the 250 data points given in [1, 3, 4] on $\Phi\beta/f(r)$ versus $(\beta^3/We_f)^{A(r)}$ coordinates in Fig. 3. The correlation is very good—it brings more than 95 percent of the data together within ±20 percent. It also is interesting to note that the high data scatter is concentrated on the right-hand side of Fig. 3. This is the region of low velocity in which Froude number influences might be making themselves felt in the upward and downward facing nozzles used in the experiments.

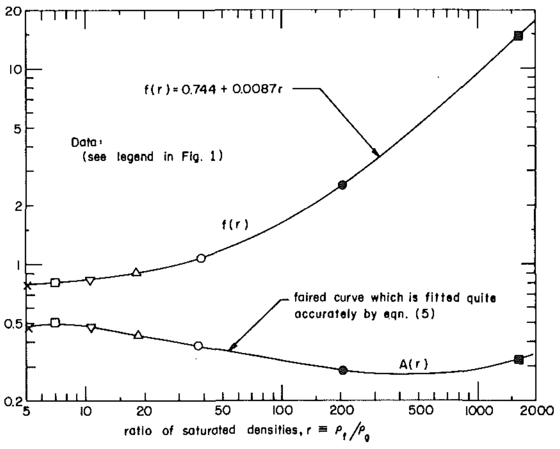

Fig. 2 The functions $f(r)$ and $A(r)$

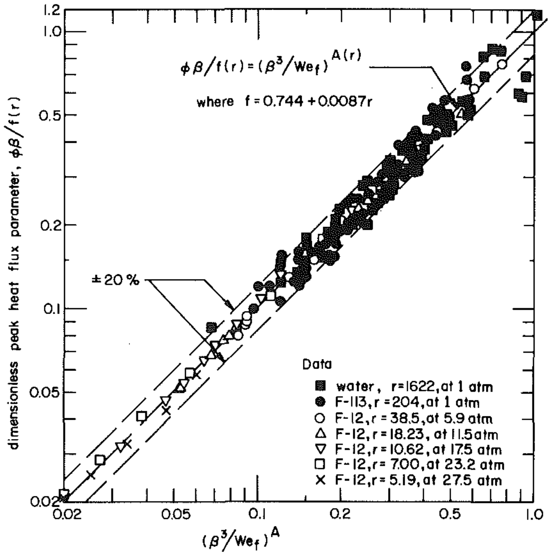

Fig. 3 Correlation of burnout heat flux data

The scatter on the left half of the correlation and for all data with $r < 50$ is only ±7 percent.

It also is interesting to see that Katto and Shimizu's I and V regions—while they do not lend any discontinuity to our correlation—can be identified. $q_{\max}$ will be u_f-independent when $A = 1/2$. With reference to Fig. 2, we see that this occurs when r is small, as they indicate. Notice too that the 27.9 bar (or 27.4 atm) data correlate perfectly in the present scheme because the correct value of $f(r)$ has been used. Of course, the reader should recognize that Katto and Shimizu are carrying through a general strategy of correlation which Katto and his coworkers have adapted to other systems as well. While we believe that equation (1) gives an improved correlation in this system, we do not intend that it should replace their general strategy.

References

1 Katto, Y., and Shimizu, M., "Upper Limit of CHF in the Forced Convection Boiling on a Heated Disc with a Small Impinging Jet," ASME JOURNAL OF HEAT TRANSFER, Vol. 101, May 1979. pp. 265–269.

2 Lienhard, J. H., and Eichhorn, R., "On Predicting Boiling Burnout for Heaters Cooled by Liquid Jets," *Int. J. Heat Mass Transfer*, (in press).

3 Monde, M., and Katto, Y., "Burnout in High Heat-Flux Boiling System with an Impinging Jet," *Int. J. Heat and Mass Transfer*, Vol. 21, 1978, pp. 295–305.

4 Katto, Y., and Monde, M., "Study of Mechanisms of Burnout with an Impinging Jet," *Proceedings of the 5th Int. Heat Transfer Conf., Tokyo*, Vol. IV, B6.2, Japan, 1974.

---

[4] We are most grateful to Professor Katto for his permission to use these data.

[5] The use of logarithmic coordinates in Fig. 2 has no physical significance and it is used only to accommodate a wide range of numbers on our graph.

[6] These faired lines deviate almost imperceptibly from the calculated regression lines through the data.